

DISSERTATION

NEW APPROACHES TO FLUOROMODIFICATIONS OF ELECTRON ACCEPTOR
MOLECULES FOR ORGANIC PHOTOVOLTAICS

Submitted by

Colin P. Brook

Department of Chemistry

In partial fulfillment of the requirements

For the Degree of Doctor of Philosophy

Colorado State University

Fort Collins, Colorado

Fall 2021

Doctoral Committee:

Advisor: Steven H. Strauss

Amy L. Prieto

Alan J. Kennan

Martin P. Gelfand

Copyright by Colin P. Brook 2021

All Rights Reserved

ABSTRACT

NEW APPROACHES TO FLUOROMODIFICATIONS OF ELECTRON ACCEPTOR MOLECULES FOR ORGANIC PHOTOVOLTAICS

The overall goal of this work is to advance fundamental science and applications of organic electron acceptors based on fluorinated fullerenes and polycyclic aromatic hydrocarbons. The synthetic part of the dissertation focused on the development of new synthetic approaches towards the fluoromodification of large conjugated organic molecules and on the improvements of existing methods for the preparation of high-performing fullerene-based *n*-type semiconductors.

Chapter 1 describes development and application of a new configuration of the gradient-temperature gas-solid reactor for the efficient and high-yielding trifluoromethylation of fullerenes. Significant improvements were achieved in the yields and selectivity of bis-trifluoromethylated C₆₀ and C₇₀ fullerenes: 2-fold and 10-fold yield increase compared to prior state of the art, respectively. An approach to maintain a constant reactive gas pressure in the reactor has been introduced by creating a liquid-gas reservoir of CF₃I by submerging the reservoir in one of several low-temperature slush baths available that resulted in improvements in both yields and selectivity for trifluoromethylfullerenes, while also solving a problem of previously unproductive use of the gaseous reagent.

Chapter 2 presents the author's work in partnership with the National Renewable Energy Lab (NREL) aimed at investigation of the prominent stabilizing effect of perfluoroalkylated fullerenes on the rate of photobleaching of common high-performance donor-polymers used in OPV devices, compared to the pure polymer films and blends with prototypical non-fluorinated fullerene,

PC₆₀BM. It is demonstrated that rationalizing complex photobleaching behaviour ultimately required consideration of the electron affinity of the fullerene as well as the relative miscibility of the polymer–fullerene blend. The ability of the bis-trifluoromethylfullerene and Fauxhawk fullerene to stabilize certain donor materials against photodegradation, to blend well with fluorinated (and even certain non-fluorinated) polymers, and to quench excited states efficiently was thoroughly studied and correlated with structure-property relationships amongst several polymer donor and fullerene acceptor combinations.

Chapter 3 describes a new approach to the direct fluoromodification of polycyclic aromatic hydrocarbons based on replacing commonly used perfluoroalkyl groups (C_nF_{2n+1}, or R_F) with perfluorobenzyl groups (C₆F₅CF₂, or Bn_F). For the first time, solution-phase direct perfluorobenylation of an electron-rich perylene (PERY) and electron-poor perylene diimide (PDI), has been achieved. Five new *bay*- and *peri*-substituted compounds of perylene, PERY-(Bn_F)_n, where *n* = 1, 2 and 3; and three new *bay*-substituted compounds of perylene diimide, PDI-(Bn_F)_n, where *n* = 1, 2; were synthesized and fully characterized, revealing that electron withdrawing Bn_F group is comparable to R_F in increasing acceptor strength of new compounds.

Chapter 4 deals with a new type of annulative pi-extension (APEX) reaction discovered in this work that occurs via reductive dehydrofluorination/aromatization reactions involving perfluorobenzylated PDI compounds, that afforded fluorinated benzoperylene and coronene-based derivatives with prodigious electron acceptor properties. Another type of annulation leading to the transition-metal free formation of new compounds with all-carbon seven-membered rings across the *bay* regions of PDIs, consequently forming as rare examples of a newly-recognized fundamental type of conformational isomers, named akamptisomers, is also reported here for the first time. Studies of the likely reaction pathways in both types of reactions and effects of varying

reaction parameters on the preferred product formation are presented. Single crystal crystallographic studies of many of the new compounds prepared in this work provide rich and unique data for in-depth analysis of the solid-state packing motifs and influences of the type and position of fluorinated functional groups on the intermolecular interactions, and ultimately, charge transport in these new organic n-type semiconductor materials.

TABLE OF CONTENTS

ABSTRACT.....	ii
LIST OF TABLES.....	viii
LIST OF FIGURES.....	ix
LIST OF SCHEMES.....	xv
CHAPTER 1. IMPROVED SYNTHESSES OF <i>BIS</i> -TRIFLUOROMETHYLATED C ₆₀ /C ₇₀ FULLERENES AND C ₆₀ (CF ₃) _N (N = 4–6) AS ROBUST ELECTRON ACCEPTORS FOR ORGANIC OPTOELECTRONICS.....	1
1.1. Introduction.....	1
1.1.1. General comments on free radical addition to fullerenes.....	3
1.1.2. Gradient temperature gas-solid reactor background and modification strategy thereof.....	5
1.2. Results and Discussion.....	9
1.2.1. Gradient temperature gas-solid reactor improvements from prior state of the art.....	9
1.2.2. Optimization of GTGS-IV reactor variables to favor 60-2-1.....	10
1.2.3. Improved yield of 60-2-1 with precise temperature control using.....	14
1.2.4. Improved yield of 70-2-1 with precise temperature control (GTGS-VI).....	15
1.2.5. Constant (low) pressure trifluoromethylation using GTGS-V and slush baths.....	16
1.2.5.1. Effects of hot-plate temperature on TMF product distribution at 28 Torr CF ₃ I.....	18
1.2.5.2. Improved yield of 60-4-2 using a constant 28 Torr of CF ₃ I.....	19
1.2.5.3. Effects of constant (low) pressures of CF ₃ I on TMF product distribution.....	20
1.2.5.4. Results using other perfluoroalkyl iodides at constant (low) pressures with C ₆₀	20
1.2.5.5. Preparation of low TMC ₇₀ Fs using a constant (low) pressure of CF ₃ I.....	21
1.3. Conclusions.....	23
1.4. Experimental section.....	24
1.4.1. Reagents and solvents.....	24
1.4.2. Instrumentation.....	24
1.4.3. GTGS reactor general procedures.....	25
1.4.3.1. GTGS-IV and VI.....	25
1.4.3.2. GTGS-V with LGR.....	25
1.4.3.3. Slush baths used for LGR and their resulting CF ₃ I vapor pressures.....	26
1.4.3.4. Workup and sample preparation for analysis.....	26
1.5. Supplemental Information.....	26
1.5.1. GTGS reactor external hot-plate temperature and internal temperature comparison.....	26
1.6. Tables and Figures.....	28
CHAPTER 1 REFERENCES.....	41
CHAPTER 2. APPLICATION OF PERFLUOROALKYLATED FULLERENES IN ORGANIC PHOTOVOLTAICS.....	43
2.1. Introduction.....	44
2.2. Results and Discussion.....	49
2.2.1. Photobleaching of neat films and blends with PC ₆₀ BM and 60-2-1.....	49
2.2.2. Time-resolved photoluminescence quenching of PC ₆₀ BM and 60-2-1 blends.....	52
2.2.3. Scanning tunneling spectroscopy/microscopy of select PC ₆₀ BM and 60-2-1 blends.....	54
2.2.4. Photoconductance of select of PC ₆₀ BM and 60-2-1 blends.....	57

2.2.5. OPV Device Work with 60-2-1	59
2.2.5.1. Spin Coated OPV Cells.....	59
2.2.5.2. Vapor Deposited OPV Cells.....	59
2.2.6. Photobleaching of blends with Faux-Hawk Fullerene.....	61
2.3. Conclusions.....	63
2.4. Experimental Section.....	64
2.4.1. Materials	64
2.4.2. Photobleaching.....	64
2.4.2.1. Sample preparation and ageing.....	64
2.4.2.2. PCE11 films.....	65
2.4.2.3. TPD-BDT films	66
2.4.2.4. TPD-BDT(OEH) and TPD-CPDT films.....	66
2.4.2.5. BT-BDT films.....	66
2.4.2.6. FBT-BDT films.....	66
Tables and Figures	67
CHAPTER 2 REFERENCES	83
CHAPTER 3. PERFLUOROBENZYLATION OF ELECTRON-RICH PERYLENE AND ELECTRON-DEFICIENT PERYLENE DIIMIDES —SYNTHESIS, ISOLATION, AND CHARACTERIZATION OF PRODUCTS	88
3.1. Introduction.....	88
3.2. Direct C-H Perfluorobenylation of Perylene: Synthesis and Isolation	90
3.3. Direct C-H Perfluorobenylation of Perylene Diimides: Synthesis and Isolation.....	93
3.4. Structural Characterization of Perfluorobenzylated Perylenes.....	98
3.4.1. X-ray crystallography.	98
3.4.2. NMR spectroscopy.....	101
3.5. Structural Characterization of Perfluorobenzylated Diimide products.....	102
3.5.1. X-ray crystallography.	102
3.5.2. NMR spectroscopy.....	102
3.6. Conclusions.....	104
3.7. EXPERIMENTAL SECTION.....	105
3.7.1. Materials and Methods.....	105
3.7.2. Synthesis of PERY-(Bn _F) _n	107
3.7.2.1. NMR chemical shifts, coupling constants, yields of isolated PERY-(Bn _F) _n	108
3.7.3. Synthesis of N,N'-bis(pentafluorophenyl)perylene diimide (PDI).....	109
3.7.4. Synthesis of PDI(-(Bn _F) _n).....	110
3.8. Tables and Figures	112
CHAPTER 3 REFERENCES	166
CHAPTER 4. NEW APPROACHES TO FLUOROANNULATION OF PAHS	168
4.1. Introduction.....	168
4.2. Investigation into PDI-perfluorobenylation side-reactions in DMSO	170
4.3. Effects of reaction variables on product distribution and PDI conversion	176
4.3.1. Reaction optimization in DMSO: effects of reduced copper, Bn _F I sequential addition	176
4.3.2. Testing alternative solvents: reaction results and PDI-1-Bn _F stability	180
4.4. Cascade synthesis of bis(perfluorophenyl) <i>benzo</i> [<i>g,h,i</i>]perylene diimide: isolation, characterization, and effects of reducing agent.....	186

4.4.1. Discovery and isolation of bis(perfluorophenyl)benzo[g,h,i]perylene diimide.....	186
4.5. Na ₂ S ₂ O ₃ promoted cascade perfluorobenylation and annulation of PDIs to give a chiral bay-bay annulated seven membered ring derivative.....	190
4.5.1. Synthesis and isolation.....	191
4.5.2. Isolation of PDI-C7H2 (and BPDI) derivatives.....	192
4.5.2.1. Primary HPLC separation: isolation of PDI-C7H2 and BPDI (and PDI).....	192
4.5.2.2. Secondary and tertiary HPLC separation: isolation of PDI- <i>cis</i> (C7H2) ₂ (F1F2), PDI- <i>trans</i> (C7H2) ₂ (F1F3) and PDI-C7FH (F1F4) (Figure 4.32).....	193
4.5.2.3. Quaternary HPLC separation: isolation of PDI-1-Bn _F , BPDI-C7H2, PDI-C7H2-5-Bn _F	195
4.6. Structural Characterization of PDI derivatives from this work.	196
4.6.1. X-ray Crystallography	196
4.7. Mechanistic insight and DFT calculation for bis(perfluorophenyl)benzo[g,h,i]perylene diimide formation.....	203
4.8. Electrochemical properties and absorption spectra of fluoromodified PAHs	204
4.8.1. Redox properties of PERY(Bn _F) _n in solution, comparison to PERY(CF ₃) _n	204
4.8.2. Redox properties of PDI(Ph _F) ₂ and its derivatives in the gas and solution phase. ...	205
4.8.3. Absorption spectra of PDI and its derivatives	207
4.9. Conclusions.....	208
4.10. Experimental section.....	209
4.10.1. Materials and Methods.....	209
4.10.2. General procedure for PDI perfluorobenylation and stability experiments	211
4.10.3. General reaction procedure for BPDI derivatives (3a,b)	212
4.10.4. General reaction procedure for PDI-C7H2 derivatives (4a,b,d).....	213
4.11. Tables and Figures	215
CHAPTER 4 REFERENCES	306
LIST OF ACRONYMS AND ABBREVIATIONS	309

LIST OF TABLES

Table 1: Experimental data for the trifluoromethylation of C ₆₀ using GTGS-IV.....	28
Table 2: Conditions and results for the trifluoromethylation of C ₆₀ and C ₇₀ using GTGS-VI.....	29
Table 3: Conditions and results for the trifluoromethylation of C ₆₀ and C ₇₀ with constant low pressures of CF ₃ I gas	30
Table 2.1: Lifetime of neat and blended films aged in air.....	67
Table 2.2: Quenching efficiencies (%) with standard deviations.....	68
Table 2.3: Device characteristics of photovoltaic solar cells of PCE11	68
Table 2.4: DFT calculated HOMO/LUMO values donor molecule.....	69
Table 2.5: Summary of photovoltaic figures of merit for BHJ devices with DCV5T-F ₂ (3,3)-Me ₄ (2,2,4,4).....	69
Table 2.6: Summary of photovoltaic figures of merit for PHJ devices with DCV5T-F ₂ (3,3)-Me ₄ (2,2,4,4) as donor.....	69
Table 3.1. Reaction conditions for direct perfluorobenzylation.....	112
Table 3.2. Crystal data and final refinement parameters for the PERY-1-1 and PERY-2-1 X-ray diffraction structures.....	113
Table 3. Crystal data and final refinement parameters for PDI-1-B _{NF} and PDI-1,2-(B _{NF}) ₂ X-ray diffraction ^a	114
Table 4.1. Stability experiments for PDI perfluorobenzylation reaction's substrates and products.....	215
Table 4.2. Reaction conditions tested for perfluorobenzylation of PDI(Ph _F) in DMSO	215
Table 4.3 Reaction conditions tested for perfluorobenzylation of PDI(Ph _F).....	215
Table 4.4. Reaction conditions tested for perfluorobenzylation of PDI(Ph _F) in PhCN resulting in BPDI(Ph _F).....	216
Table 4.5. Reaction conditions to generate PDI-C ₇ H ₂ derivatives.....	216
Table 4.6. Half-peak reduction potentials of PERY derivatives.....	217
Table 4.7. Electrochemical properties of PDI derivatives	217
Table 4.8. The seven compounds characterized by single-crystal X-ray diffraction described in this chapter ^a	218
Table 4.9. Crystal data and final refinement parameters for five X-ray diffraction structures deposited with the Cambridge structural database ^a	219

LIST OF FIGURES

Figure 1.1: Schlegel diagrams of TMFs studied in this work.....	31
Figure 1.2: Alternate configurations of the gradient-temperature gas–solid (GTGS) reactor.....	33
Figure 1.3: HPLC chromatogram of crude product mixture from rxn. 5.	34
Figure 1.4: HPLC chromatogram of crude product mixture from rxn. <i>i</i>	34
Figure 1.5: HPLC chromatogram of crude product mixture from rxn. <i>ii</i>	34
Figure 1.6: ¹⁹ F-NMR taken in CDCl ₃ of crude product mixture of reaction G	35
Figure 1.7: Schematic diagram of GTGS reactor equipped with LGR.....	36
Figure 1.8: HPLC chromatograms of crude product mixtures from rxns. A to E using GTGS-V equipped with a LGR.....	37
Figure 1.9: HPLC chromatogram of crude product mixtures for rxns. C and F using GTGS-V equipped with a LGR.....	38
Figure 1.10: HPLC chromatogram of crude product mixtures from rxns. B and G–I using GTGS-V equipped with a LGR.....	39
Figure 1.11: HPLC chromatogram of crude product mixtures from rxn. J using GTGS-V equipped with a LGR.....	40
Figure 1.12: HPLC chromatogram of crude product mixtures from rxns. K and L using GTGS reactor configuration V equipped with a LGR	40
Figure 2.1: Chemical structure of polymers and fullerenes used in this study	70
Figure 2.2: Representative examples of neat and 1:1 by weight blends of PCE11 films photobleaching over time.....	71
Figure 2.3: Fraction of light absorbed over time measured at λ_{\max} for films of neat polymer and fullerene blends.....	72
Figure 2.4: Comparison of T_{80} and T_{60} values for neat and blended films	73
Figure 2.5: Comparison of T_{80} and T_{60} values for neat and blended films	74
Figure 2.6: PL decays for neat and fullerene blends.....	75
Figure 2.7: Differential tunnel conductance (dI/dV) versus voltage characteristics of (a) BT-BDT and (b) PCE11.....	76
Figure 2.8: dI/dV images corresponding to ~10 nm thick active layer films prepared on Au (111) and imaged under inert atmosphere	77
Figure 2.9: The product of charge carrier yield (ϕ) and sum of local hole and electron mobilities ($\Sigma\mu$).....	78
Figure 2.10: Fraction of light absorbed over time measured at λ_{\max} for films of neat polymer and fullerene blends—including FHF	79
Figure 2.11: reproduction of Figure 2.10 showing the stable rate of photodegradation after the initial rapid absorbance drop.....	80
Figure 2.12: J - V plots (left) and EQE spectra (right).....	81
Figure 2.13: Device architecture for BHJ devices with 60-2-1 (acceptor) and DCV5T-F ₂ (3,3)-Me ₄ (2,2,4,4) (donor).	82
Figure 2.14: Structure of DCV5T-F ₂ (3,3)-Me ₄ (2,2,4,4).	82
Figure 3.1. Top: General reaction scheme for direct perfluorobenzoylation of perylene.....	115
Figure 3.2. NMR spectra of crude reaction 1a	116
Figure 3.3. ¹⁹ F-NMR spectrum of crude reaction mixture 1a	117

Figure 3.4. ^{19}F -NMR spectrum of crude reaction mixture 1b	118
Figure 3.5. HPLC chromatograms of pure PERY and crude 1a and 1b reaction mixtures.....	119
Figure 3.6. General reaction scheme for direct perfluorobenylation of perylene showing differences in reaction conditions between 1b and 1c	120
Figure 3.7. Positive-ion ESI mass spectrum of crude reaction mixture from reaction 1c	121
Figure 3.8. HPLC chromatograms of crude product mixtures 1b and 1c	122
Figure 3.9. Structure and numbering of all possible isomers of derivatized perylenes containing 1–2 BnF groups	123
Figure 3.10. Structure and numbering of all possible isomers containing 3–4 BnF groups.....	124
Figure 3.11. Top: General reaction scheme for direct perfluorobenylation of PDI and nomenclature for unique positions. Bottom: Drawings of molecular structures of isolated PDI- $(\text{BnF})_n$ compounds	125
Figure 3.12. ^{19}F -NMR spectrum of crude reaction mixture 2a	126
Figure 3.13. ^{19}F -NMR spectrum of crude reaction mixture 2b	127
Figure 3.14. Example of primary separation by flash chromatography.	128
Figure 3.15. HPLC chromatogram of secondary separation post flash chromatography	128
Figure 3.16. The molecular X-ray structures of 3-PERY($\text{CF}_2\text{C}_6\text{F}_5$) (PERY-1-1) and 3,10-PERY($\text{CF}_2\text{C}_6\text{F}_5$) ₂ (PERY-2-1).....	129
Figure 3.17. Parallel perspective drawings of the π - π overlap of perylene $\text{C}(\text{sp}^2)$ aromatic cores in the structures of PERY-1-1 (a) and PERY-2-1.....	129
Figure 3.18. The structure of PERY-1-1.....	130
Figure 3.19. Side perspective of crystal structure packing of PERY, PERY-1-1, and PERY-2-1	131
Figure 3.20. Top view of PERY-2-1 through single column of perylene cores	131
Figure 3.21. The structure of PERY-2-1.....	132
Figure 3.22. The structure of PERY-2-1.....	133
Figure 3.23. Intermolecular interactions between PERY-2-1 molecules of adjacent columns ..	133
Figure 3.24. Single crystal X-ray structure and packing of PERY-1-1	134
Figure 3.25. Single crystal X-ray structure and packing of PERY-2-1	135
Figure 3.26. Simplified view of PERY-2-1 solid state packing between adjacent rows of perylene columns.....	136
Figure 3.27. ^{19}F -NMR spectra of mono- and bis-substituted products.	137
Figure 3.28. ^1H -NMR spectrum of PERY-1-1 in CDCl_3	138
Figure 3.29. ^{19}F -NMR spectrum of PERY-1-1 in CDCl_3	139
Figure 3.30. ^1H -NMR spectrum of PERY-1-2 in CDCl_3	140
Figure 3.31. ^1H -NMR spectrum of PERY-1-2 aromatic region in CDCl_3	140
Figure 3.32. ^{19}F -NMR spectrum of PERY-1-2 in CDCl_3	141
Figure 3.33. Positive-ion ESI mass spectrum of PERY-2-1.....	142
Figure 3.34. ^1H -NMR spectrum of PERY-2-1 in CDCl_3	142
Figure 3.35. ^{19}F -NMR spectrum of PERY-2-1 in CDCl_3	143
Figure 3.36. Positive-ion ESI mass spectrum of PERY-3-1.....	144
Figure 3.37. ^1H -NMR spectrum of PERY-3-1 in CDCl_3	144
Figure 3.38. ^{19}F -NMR spectrum of PERY-3-1 in CDCl_3	145
Figure 3.39. Positive-ion ESI mass spectrum of PERY-3-2 fraction.	146
Figure 3.40. ^1H -NMR spectrum of PERY-3-2 in CDCl_3	146
Figure 3.41. ^{19}F -NMR spectrum of PERY-3-2 in CDCl_3	147

Figure 3.42. ¹⁹ F-NMR spectra of benzylic region for fraction i	148
Figure 3.43. ¹⁹ F-NMR spectra of benzylic region for fraction ii	149
Figure 3.44. ¹⁹ F-NMR spectra of benzylic region for reaction 1c , fraction iii	150
Figure 3.45. ¹⁹ F-NMR spectrum of largest fraction (vi) from reaction 1c	151
Figure 3.46. Drawings of the X-ray structures of PDI-1-Bn _F (left) and PDI-1,7-(Bn _F) ₂ (right).	152
Figure 3.47. ¹⁹ F NMR aromatic region of purified PDI-1-(Bn _F) ₁	153
Figure 3.48. ¹⁹ F-NMR spectrum of PDI-1-Bn _F in CDCl ₃	154
Figure 3.49: Closeup view of signals in ¹⁹ F-NMR spectrum of PDI-1-Bn _F	155
Figure 3.50: ¹ H-NMR spectrum of PDI-1-Bn _F in CDCl ₃	156
Figure 3.51: ¹ H-NMR spectrum of PDI-1-Bn _F in CDCl ₃ showing from 2.5 to 9.5 ppm.	157
Figure 3.52: ¹⁹ F-NMR spectrum of PDI-1,6-(Bn _F) ₂ in CDCl ₃	158
Figure 3.53: Closeup view of signals in ¹⁹ F-NMR spectrum of PDI-1,6-(Bn _F) ₂	159
Figure 3.54: ¹ H-NMR spectrum of PDI-1,6-(Bn _F) ₂ in CDCl ₃	160
Figure 3.55: ¹ H-NMR spectrum of PDI-1,6-(Bn _F) ₂ in CDCl ₃ showing from 2.5 to 9.5 ppm.	161
Figure 3.56: ¹⁹ F-NMR spectrum of PDI-1,7-(Bn _F) ₂ in CDCl ₃	162
Figure 3.57: Closeup view of signals in ¹⁹ F-NMR spectrum of PDI-1,7-(Bn _F) ₂	163
Figure 3.58: ¹ H-NMR spectrum of PDI-1,7-(Bn _F) ₂ in CDCl ₃	164
Figure 3.59: ¹ H-NMR spectrum of PDI-1,7-(Bn _F) ₂ in CDCl ₃ showing from 2.5 to 9.5 ppm.	165
Figure 4.1. Top: Balanced chemical equation for direct perfluorobenylation of PDI. Bottom: Proposed mechanism for the perfluorobenylation of PDI (and PERY)	220
Figure 4.2. Concentration of perfluorobenzyl iodide (Bn _F I) over time when heated in DMSO and in the presence of copper.	221
Figure 4.3. ¹⁹ F-NMR spectrum of perfluorobenzyl iodide (Bn _F I) over time when heated in DMSO and in the presence of copper.	222
Figure 4.4. Negative-ion ESI mass spectrum of PDI after heating for 8 hours at 145 C in DMSO with copper.	223
Figure 4.5. Mass spectrum of crude product mixture of reaction 2a	223
Figure 4.6. Negative-ion ESI mass spectrum of PDI-1-Bn _F	224
Figure 4.7. Change in ¹ H NMR spectra of PDI-1-Bn _F after decomposition.	224
Figure 4.8. Negative-ion ESI mass spectrum of PDI-1-Bn _F after decomposition with copper ..	225
Figure 4.9. Negative-ion ESI mass spectrum of PDI-1-Bn _F after thermal decomposition (without copper)	226
Figure 4.10. HPLC chromatogram of crude perfluorobenylation reactions of PDI-1-Bn _F after thermal decomposition.	226
Figure 4.11. Comparison between UV-vis absorption profiles of unreacted PDI, PDI-1-Bn _F and the major decomposition product.	227
Figure 4.12. HPLC chromatograms of crude product mixtures of 145 °C reactions from Table 4.2.	228
Figure 4.13: ¹⁹ F NMR spectrum of fraction-a in Figure 4.12 (ca. 3–4 min) from reaction 2d ..	229
Figure 4.14. ¹ H-NMR of crude perfluorobenylation reactions of PDI in NMP after heating for 2 hours at 145 °C with copper (rxn. 2c with NMP instead of DMSO).	229
Figure 4.15. ¹⁹ F-NMR of crude perfluorobenylation reactions of PDI in NMP after heating for 2 hours at 145 °C with copper (rxn. 2c with NMP instead of DMSO).	230
Figure 4.16. Mass spectrum of crude perfluorobenylation reactions of PDI in NMP after heating for 2 hours at 145 °C with copper (rxn. 2c with NMP instead of DMSO).	230
Figure 4.17: HPLC chromatogram of crude perfluorobenylation reactions of PDI in PhCl. ...	231

Figure 4.18: Negative-ion ESI mass spectrum of crude reaction mixture of perfluorobenylation reaction of PDI in PhCl.....	231
Figure 4.19. HPLC chromatogram of crude perfluorobenylation reactions of PDI in ODCB.	232
Figure 4.20. Negative-ion ESI mass spectrum of crude reaction mixture of perfluorobenylation reaction of PDI in ODCB.....	232
Figure 4.21. ¹⁹ F-NMR spectra of aliquots taken over time of perfluorobenylation reaction of PDI in PhCN with 4 equiv. of Bn _F I and 8 equiv. of copper.....	233
Figure 4.22. Negative-ion ESI mass spectrum of crude perfluorobenylation reaction of PDI in PhCN with 4 equiv. of Bn _F I and 8 equiv. of copper.....	234
Figure 4.23. HPLC chromatogram of crude perfluorobenylation reaction of PDI in PhCN with 4 equiv. of Bn _F I and 8 equiv. of copper.....	234
Figure 4.24: Top: General reaction scheme for direct perfluorobenylation and annulation of PDI with nomenclature for unique positions. Bottom: Drawings of molecular structures of isolated perylene diimides, PDI(Bn _F) _n , and benzoperylene diimides, BPDI(Bn _F) _n	235
Figure 4.25. HPLC chromatograms of crude perfluorobenylation reactions of PDI in PhCN.	236
Figure 4.26 Stacked ¹⁹ F-NMR spectra of crude reactions 3c (top), 3d (middle), and 3e.....	237
Figure 4.27. Stacked negative-ion ESI mass spectra of crude reactions 3c (top) and 3d (bottom).....	237
Figure 4.28. HPLC separations of reaction 3b , showing chromatogram for 470 nm wavelength detection.....	238
Figure 4.29 General reaction scheme for direct perfluorobenylation and annulation of PDI with nomenclature for unique positions.....	239
Figure 4.30. HPLC chromatograms of crude product mixture of reaction 4a	240
Figure 4.31. Example of primary separation of reaction 4b.	241
Figure 4.32 Example of secondary and tertiary separation of reaction 4b.	242
Figure 4.33. Stacked ¹⁹ F-NMR spectra of major fractions shown in Figure 4.32.	243
Figure 4.34. Closeup view of aromatic region of Figure 4.33.....	243
Figure 4.35. Example of quaternary separation of reaction 4b, F1F5, to give pure PDI-1-Bn _F	244
Figure 4.36. Example of quaternary separation of reaction 4b, F1F6.	244
Figure 4.37. The literature structure of (C ₃ F ₇ CH ₂) ₂ PDI.	245
Figure 4.38. The literature structure of (Ph _F) ₂ PDI-1,7-F ₂	246
Figure 4.39. Ball-and-stick plots for the seven structures listed in Table 4.8.....	247
Figure 4.40. Thermal ellipsoid plots for the first five structures listed in Table 4.8.....	248
Figure 4.41. Views of the structures of (Ph _F) ₂ PDI-1-Bn _F and (Ph _F) ₂ PDI-1,7-(Bn _F) ₂ showing the distortions of the PDI aromatic cores from planarity.....	249
Figure 4.42. Views of the structures of (Ph _F) ₂ PDI-1-Bn _F and (Ph _F) ₂ PDI-1,7-(Bn _F) ₂ showing the packing of molecules in the unit cells.....	250
Figure 4.43. A portion of the unit cell in the donor/acceptor co-crystal structure of PYRN/(Ph _F) ₂ PDI-1,12- <i>cyclo</i> -CH ₂ C ₆ F ₄	251
Figure 4.44. Parallel projection drawing of the PYRN donor (grey C atoms) and one of its neighboring (Ph _F) ₂ PDI-1,12- <i>cyclo</i> -CH ₂ C ₆ F ₄ acceptors in the donor/acceptor co-crystal structure.....	252
Figure 4.45. The PDI enantiomers in the donor/acceptor co-crystal X-ray structure of PYRN/(Ph _F) ₂ PDI-1,12- <i>cyclo</i> -CH ₂ C ₆ F ₄	253
Figure 4.46. The X-ray structure of 5-ethyl-5,6-dihydro-11 <i>H</i> -dibenzo[<i>b,e</i>]azepine-6-thione, oriented to highlight the boat configuration of the seven-membered ring.....	254

Figure 4.47. Four drawings of the structure of $(\text{Ph}_F)_2\text{PDI-1,12-cyclo-CH}_2\text{C}_6\text{F}_4$ oriented to highlight the boat configuration of the seven-membered rings.....	255
Figure 4.48. A portion of the unit cell in the donor/acceptor co-crystal structure of $\text{PERY}/(\text{Ph}_F)_2\text{PDI-8-Bn}_F\text{-1,12-cyclo-CH}_2\text{C}_6\text{F}_4$	256
Figure 4.49. Parallel projection drawings of the PERY donors (grey C atoms) on either side of the $(\text{Ph}_F)_2\text{PDI-8-Bn}_F\text{-1,12-cyclo-CH}_2\text{C}_6\text{F}_4$ acceptor in the co-crystal structure of $\text{PERY}/(\text{Ph}_F)_2\text{PDI-8-Bn}_F\text{-1,12-cyclo-CH}_2\text{C}_6\text{F}_4$	257
Figure 4.50. The nonplanar conformations of the seven-membered rings in the cis isomer $(\text{Ph}_F)_2\text{PDI-1,12:6,7-(cyclo-CH}_2\text{C}_6\text{F}_4)_2$	258
Figure 4.51. Drawings of $(\text{Ph}_F)_2\text{PDI-1,12:6,7-(cyclo-CH}_2\text{C}_6\text{F}_4)_2$ (<i>cis</i> ; top) and $(\text{Ph}_F)_2\text{PDI-1,12:7,6-(cyclo-CH}_2\text{C}_6\text{F}_4)_2$ (<i>trans</i> ; bottom).	259
Figure 4.52. Drawings of $(\text{Ph}_F)_2\text{PDI-1,12:6,7-(cyclo-CH}_2\text{C}_6\text{F}_4)_2$ (<i>cis</i> ; top) and $(\text{Ph}_F)_2\text{PDI-1,12:7,6-(cyclo-CH}_2\text{C}_6\text{F}_4)_2$ (<i>trans</i> ; bottom) rotated 90°	260
Figure 4.53. (Top) The DFT-optimized structures of the <i>up,down</i> and <i>up,up</i> seven-membered ring conformers of the <i>cis</i> isomer $(\text{Ph}_F)_2\text{PDI-1,12:6,7-(cyclo-CH}_2\text{C}_6\text{F}_4)_2$	261
Figure 4.54. Fragments of the DFT <i>cis-up,up</i> isomer of $(\text{Ph}_F)_2\text{PDI-1,12:6,7-(cyclo-CH}_2\text{C}_6\text{F}_4)_2$	262
Figure 4.55. The X-ray structure of $(\text{Ph}_F)_2\text{PDI-1,12-benzo(Ph}_F)_2$	263
Figure 4.56. The packing of molecules in the X-ray structure of $(\text{Ph}_F)_2\text{PDI-1,12-benzo(Ph}_F)_2$	264
Figure 4.57 Possible pathways to formation of BPDI (and <i>bis</i> BPDI) and its derivatives.	265
Figure 4.58. The DFT-optimized structure of the putative intermediate $(\text{Ph}_F)_2\text{PDI-1,12-(Bn}_F)_2$	265
Figure 4.59. Left) change in $E_{p/2}^{0/-}$ as a function of number of Bn_F groups substituted onto perylene.	266
Figure 4.60. Cyclic voltammogram of PERY-1-1, PERY-2-1, PERY-3-1 and PERY-3-2 taken in 0.1 M $\text{N}(n\text{Bu})_4\text{ClO}_4$ in dimethoxyethane,	267
Figure 4.61. Cyclic voltammograms of PDI, PDI-1- Bn_F , and PDI-1,7- $(\text{Bn}_F)_2$, taken in 0.1 M TBAPF_6 in DCM	268
Figure 4.62. Cyclic voltammograms of PDI and BPDI taken in 0.1 M TBAPF_6 in DCM.....	269
Figure 4.63. Cyclic voltammograms of PDI, PDI-C7H2, PDI- <i>cis</i> (C7H2)2 and PDI- <i>trans</i> (C7H2)2 taken in 0.1 M TBAPF_6 in DCM	270
Figure 4.64. UV-vis absorbance spectra of PDI, BPDI, and their respective perfluorobenzylated derivatives.	271
Figure 4.65. UV-vis absorbance spectra of PDI and PDI-C7H2 derivatives.....	272
Figure 4.66. $^1\text{H-NMR}$ spectrum of BPDI in CDCl_3	273
Figure 4.67. $^{19}\text{F-NMR}$ spectrum of BPDI in CDCl_3	274
Figure 4.68. Expanded aromatic region of BPDI	275
Figure 4.69. Closeup view of BPDI's $^{19}\text{F-NMR}$	276
Figure 4.70. $^1\text{H-NMR}$ spectrum of <i>bis</i> BPDI in CDCl_3	277
Figure 4.71. $^{19}\text{F-NMR}$ spectrum of <i>bis</i> BPDI in CDCl_3	278
Figure 4.72. Expanded aromatic region of <i>bis</i> BPDI's $^{19}\text{F-NMR}$ spectrum.....	279
Figure 4.73. Closeup view of <i>bis</i> BPDI's $^{19}\text{F-NMR}$	280
Figure 4.74. Comparison between $^{19}\text{F-NMR}$ spectra of PDI, BPDI, and <i>bis</i> BPDI.....	281
Figure 4.75. $^1\text{H-NMR}$ spectrum of BPDI-6- Bn_F in CDCl_3	282
Figure 4.76. $^{19}\text{F-NMR}$ spectrum of BPDI-6- Bn_F in CDCl_3	283
Figure 4.77. Closeup view of BPDI-6- Bn_F 's $^{19}\text{F-NMR}$	284
Figure 4.78. $^1\text{H-NMR}$ spectrum of PDI-C7H2 in CDCl_3 from 2.4 to 9.6 ppm.	285

Figure 4.79. ^{19}F -NMR spectrum of PDI-C7H2 in CDCl_3	286
Figure 4.80. Expanded aromatic region of PDI-C7H2's ^{19}F -NMR spectrum	287
Figure 4.81. Closeup view of PDI-C7H2's ^{19}F -NMR	288
Figure 4.82. ^1H -NMR spectrum of PDI-C7HF in CDCl_3 from 2.4 to 9.6 ppm.	289
Figure 4.83. ^{19}F -NMR spectrum of PDI-C7HF in CDCl_3	290
Figure 4.84. Expanded aromatic region of PDI-C7HF's ^{19}F -NMR spectrum	291
Figure 4.85. Closeup view of PDI-C7HF's ^{19}F -NMR	292
Figure 4.86. ^1H -NMR spectrum of PDI- <i>cis</i> (C7H2) ₂	293
Figure 4.87. ^{19}F -NMR spectrum of PDI- <i>cis</i> (C7H2) ₂ in CDCl_3	294
Figure 4.88 Expanded aromatic region of PDI- <i>cis</i> (C7H2) ₂ 's ^{19}F -NMR spectrum.....	295
Figure 4.89. Closeup view of PDI- <i>cis</i> (C7H2) ₂ 's ^{19}F -NMR.....	296
Figure 4.90. ^1H -NMR spectrum of PDI- <i>trans</i> (C7H2) ₂ in CDCl_3 from 2.4 to 9.6 ppm.....	297
Figure 4.91. ^{19}F -NMR spectrum of PDI- <i>trans</i> (C7H2) ₂ in CDCl_3	298
Figure 4.92. Expanded aromatic region of PDI- <i>trans</i> (C7H2) ₂ 's ^{19}F -NMR spectrum.....	299
Figure 4.93. Closeup view of PDI- <i>trans</i> (C7H2) ₂ 's ^{19}F -NMR.....	300
Figure 4.94. ^1H -NMR spectrum of PDI-C7H2-BnF in CDCl_3 from 2.4 to 9.6 ppm.	301
Figure 4.95. ^{19}F -NMR spectrum of PDI-C7H2-BnF in CDCl_3	302
Figure 4.96. Expanded aromatic region of PDI-C7H2-BnF's ^{19}F -NMR spectrum.....	303
Figure 4.97. First of two closeup views of PDI-C7H2-BnF's ^{19}F -NMR signals	304
Figure 4.98. Second of two closeup views of PDI-C7H2-BnF's ^{19}F -NMR signals.....	305

LIST OF SCHEMES

Scheme 1: Possible elementary steps during fullerene trifluoromethylation in GTGS reactor.... 32

CHAPTER 1.
Improved Syntheses of *Bis*-trifluoromethylated C₆₀/C₇₀ Fullerenes and C₆₀(CF₃)_n (n = 4–6) as Robust Electron Acceptors for Organic Optoelectronics

1.1. Introduction

Of the many n-type semiconductor materials available for organic electronics, C₆₀ and C₇₀ fullerenes and their derivatives continue to be of interest, particularly in organic photovoltaics (OPVs), as the electron-acceptor materials.¹ Recently there has been an increased interest in using fluorinated materials for their improved stability and often overall better device performance compared to their non-fluorinated counterparts both in OPVs and organic field effect transistors (OFETs).² However, for the most part studies of organic electronic devices using fluorinated materials contain either fluorinated electron-donor materials and/or fluorinated non-fullerene electron-acceptor compounds.² Studies of fluorine-containing fullerenes on the other hand, such as perfluoroalkyl fullerenes (PAFs), in organic devices have been rarely reported, despite their favorable properties: they are more thermally stable than the commonly used non-fluorinated fullerenes and exhibit a wide range of high electron affinities.³⁻⁵

One of the challenges of accessibility of PAF materials for applied research is low selectivity in the perfluoroalkylation of C₆₀ (and even more so C₇₀). Most reported syntheses generate a multitude of different isomers with varying degrees of perfluoroalkyl additions and/or have very low conversion of fullerene starting material.⁶ This inevitably results in low yields of the desired compound(s) and often requires several stages of HPLC separation to remove unwanted side products. Consequently, this has hindered more extensive investigation into the use of PAFs as potentially better performing electron acceptors for OPVs and other electronic devices.

One notable class of PAFs that has gotten attention as an organic *n*-type material are trifluoromethylated C₆₀-fullerenes (TMC₆₀Fs, C₆₀(CF₃)_n). The simplest among them is the bis-adduct C₆₀(CF₃)₂ (1,7-bis(trifluoromethyl)-C₆₀-fullerene), colloquially referred to as **60-2-1**.⁶⁻⁷ In particular, C₆₀(CF₃)₂ (**60-2-1**, see Figure 1.1 for adopted isomer notations and Schlegel diagrams) and other low *n* number (4–6) TMC₆₀Fs have been shown to improve the photostability of certain active layers in OPV thin films compared to PC₆₀BM, especially, if they were paired with fluorinated donors.⁸⁻¹⁰ Moreover, C₆₀(CF₃)₂ (**60-2-1**) gave some of the highest microwave conductivity when paired with a high performance fluorinated polymer, even higher than when the same polymer was paired with well-studied fullerene acceptor phenyl-C₆₁-butyric acid methyl ester (PCBM), suggesting it could be ideal for high-performance all-fluorinated OPVs.¹⁰

Further exploration of such TMC₆₀F acceptors depends on their availability in practical amounts required to test device conditions for fabrication. Moreover, many OPV devices have shown significant improvement in performance when using the C₇₀ material instead of C₆₀ of the respective fullerene derivative due to better light absorption properties;¹¹ but the reported yields for C₇₀(CF₃)₂₋₆ compounds are very low in direct synthesis (1-2%), and in one report, their preparation involved thermally induced transalkylation using higher TMC₇₀Fs and pristine C₇₀ in sealed ampoules.¹² Therefore, to materialize the benefits of TMF acceptors in organic electronics, efficient syntheses with improved yields and selectivity for the desired TMC₆₀Fs and TMC₇₀Fs are required.

In this chapter, a new configuration of the in-house built gradient-temperature gas-solid (GTGS) reactor developed by the author is described that led to significant improvements in the syntheses of 60-2-1 and other low *n*-number TMC₆₀Fs compared to the current state-of-the-art.⁵ Furthermore, detailed and systematic study of effects of reaction parameters on product

distribution in the modified reactor have resulted in the first efficient method of preparation of 70-2-1.

The modified GTGS reactor is equipped with a slush-bath cooled liquid-gas reservoir (LGR) which maintains constant low pressures of CF₃I and can significantly improve the product distribution to favor other low *n*-number products for both C₆₀ and C₇₀ TMFs.

1.1.1. General comments on free radical addition to fullerenes

Prior studies of free radical additions to fullerenes have demonstrated facile syntheses of polyadducts, but it is thermodynamically difficult if not impossible to selectively generate the simplest derivatives, the bis-adducts, as the major products in such reactions. In the case of free radical halogenation, the bis-fluoro and bis-chloro adducts were isolated as minor products in small amounts;¹³⁻¹⁴ while, to the best of the knowledge of the author, there are currently no examples of the bis-bromofullerenes being isolated. Not surprisingly, this is also the case with the free radical trifluoromethylation, where theoretical and experimental studies have shown that the difference in stability between the bis (2-) and 4-adducts, or a 4- and 6-adducts (and so on) is such that the number of additions progressively increases the stability of the adduct, favoring more additions until some thermodynamic plateau is reached or the fullerene is saturated.¹⁵

Notably, the free radical trifluoromethylation of C₆₀ and C₇₀ can form certain higher adducts selectively with very good yields for a single isomer. For example, C₆₀(CF₃)₁₂ was prepared by heating C₆₀ with excess CF₃I in a sealed ampoule at 440 °C for 2 days, with 84% isolated yield based on starting C₆₀.¹⁶ Another example is selective preparation of a single-isomer C₇₀(CF₃)₁₀ (89 mol% in the product by NMR) in the reaction between C₇₀ and CF₃I at 530 °C for 90 minutes in the flow tube reactor.¹⁷⁻¹⁸ In general, these thermodynamic products are favored by increasing reaction time, increasing reaction temperature, and with an increasing ratio of CF₃I to C₆₀; which

also improves the conversion of C₆₀.¹⁵ However, applying conditions that favor generation of lower adducts, the kinetic products in this case, have been shown to result in low yields of the desired compound due to incomplete conversion of C₆₀ and mixed product distribution: for example, the highest yielding synthesis for 60-2-1 currently in the literature is only stated to be 21–25% based on HPLC chromatogram peak area,⁵⁻⁶ where the majority of the product mixture composed of unreacted C₆₀. These effects are even more pronounced in the trifluoromethylation of C₇₀, where the bis-adduct was only obtainable directly with <2% yield.⁵

Interestingly, this has the effect of not only limiting the maximum theoretical yield of lower adducts under idealized thermodynamic conditions, but further limits the yield of specific isomers of those adducts that are precursors to the most thermally stable TMFs. This is the case even if the specific isomer in question is the most thermodynamically favored of the possible same-numbered CF₃ adducts.

For example, of the most thermodynamically favored tetrakis-adducts, 60-4-2 is known to be the most stable by a non-negligible degree (–8.1 kJ/mol difference) compared to the next most stable isomer, 60-4-1 (see Figure 1.1 for isomer structure).¹⁵ However, 60-4-2 has only been isolated as a minor product; and is often only observed as the oxidized form (60-4-2-O) due to its high reactivity towards oxidation in light while dissolved in an organic solvent.¹⁹ This discrepancy between the actual yield of 60-4-2 relative to 60-4-1 can be reasoned both thermodynamically and kinetically; in that 60-4-2 undoubtedly forms faster than 60-4-1 for aforementioned reasons, which in theory should make it the more abundant compound in the product mixture; but 60-4-2 is intrinsically more reactive towards further radical addition due to its reactive fulvene moiety, which leads to the isomer pattern of 60-6-2 shown in Figure 1.1. Moreover, statistically it is more likely that 60-4-2 will react favorably with a CF₃ radical compared to 60-4-1; there are multiple

positions on 60-4-2 where a CF_3 group can add directly without isomerization to generate either 60-6-1 or 60-6-2, the two most stable hexakis-adducts.¹⁵ On the other hand, 60-4-1 cannot directly form 60-6-2 without isomerization, and only forms 60-6-1 (one out of the two 60-6 isomers). This results in a greater abundance of 60-4-1 than 60-4-2 in the product mixtures (if either are present in measurable amounts). Improving relative yields of “elusive fulvene fullerene” 60-4-2 is desirable for further selective derivatization of the reactive fulvene moiety it contains and exploring its properties as a strong acceptor material.

1.1.2. Gradient temperature gas-solid reactor background and modification strategy thereof

Prior work to directly synthesize TMFs with trifluoromethyl iodide (CF_3I) at low pressures has been achieved using a gradient temperature gas-solid (GTGS) reactor previously developed in the Strauss–Boltalina lab (see GTGS-I in upper left of Figure 1.2 for detailed diagram of the basic design, the gas-handling system is absent for clarity).^{5, 20} The GTGS reactor consists of a quartz thimble with a flat bottom where the solid fullerene sample sits; the thimble is then connected via a compression joint to a 1 liter headspace (to act as a pressure ballast) which is connected through a closeable Teflon valve to a gas-manifold. The gas manifold is equipped with a CF_3I gas tank, external vacuum, and a pressure transducer (0-1000 Torr range) to monitor the pressure of CF_3I (see Figure 1.7 for simplified schematic diagram). The 1-liter ballast has an additional compression joint allowing for a water-chilled cold finger to be inserted into the quartz thimble, such as GTGS-III in Figure 1.2. The quartz thimble is placed onto a special plate furnace, so that the bottom of the quartz thimble is in contact with its heating element which acts as the “hot plate”. The hot plate has a thermocouple positioned between the heating element and the bottom of the quartz thimble in order to monitor its temperature (T_{hp}) directly.

By using the GTGS reactor for the trifluoromethylation of C₆₀ instead of commonly used sealed glass ampoules, it is possible to sequester some of the low adducts as they are being generated by depositing them on the surface of the cold finger or reactor walls (the kinetic products in these reactions) so that they do not continue to react further. At the same time, the reaction is allowed to continue so the conversion of C₆₀ is not as limited, improving the overall yield of the desired TMF over the theoretical yield possible by thermodynamic control alone.¹⁵ The general concept of the GTGS reactor design and operation is based on the experimental fact that the vapor pressure of trifluoromethyl fullerenes increases with the number of CF₃ groups attached to the cage, while the sublimation temperatures decrease, correspondingly. This trend has specifically been documented with select lower TMFs in thermal vapor deposition experiments in ultra-high vacuum. It was observed that the temperature required to achieve the same rate of deposition (0.2 Å/s) for C₆₀, 60-2-1 and 60-4-1 progressively and significantly decreased; from 450 °C to 360 °C and finally 280 °C, respectively.²¹ The closed GTGS reactor system has two temperature zones: the “hot zone” and the “cold zone”. As can be seen in Figure 2, the “hot zone” represents a small region of the reactor atop the hot plate with heat insulation covering it made out of either refractory brick (50 mm insulation) or fused silica wool (e.g. 10 mm for the general GTGS configuration “I”, abbreviated as **GTGS-I**). In this hot zone region, the solid fullerenes can react with gaseous CF₃I forming TMFs, which sublime and spend some time in the gas phase—still within the hot zone where they may or may not continue to react with CF₃ radicals—until they reach “cold zone” with lower temperature, then deposit and cease to react. Outside the “hot zone”, the temperatures are not sufficiently high for the thermally induced homolytic CF₃-I bond-cleavage and thus, for reactions of CF₃ radicals with fullerenes. A thermally-induced heterogeneous reaction that occurs

in the “hot zone” of GTGS reactor between solid fullerene and gaseous CF_3I reagent is a complex process to control and it is likely to involve several elementary steps, as depicted in Scheme 1.⁵

The GTGS reactor allows for the kinetic products formed to be isolated out of the hot zone before they would otherwise react further to give more thermodynamically favored compounds. Importantly, at the elevated temperatures used for the GTGS reactor, C_{60} has a non-negligible vapor pressure;²² and thus partial sublimation of C_{60} takes place, implying that there is likely a limit to maximizing the TMF yield via increasing the reaction temperature without sacrificing conversion of C_{60} due to sublimation.

Prior research that involved GTGS configurations I–III (**GTGS-I–III**) showed that the product distribution of TMFs formed depends on the concentration of CF_3 radicals and the residence time of the fullerene species in the hot zone (the total time spent in the hot zone either as a solid or in the gas phase).⁵ Several experimental factors that increase the concentration of CF_3 radicals and/or residence times of the fullerene species both favor the formation of $\text{C}_{60}/\text{C}_{70}(\text{CF}_3)_{n>6}$, (referred to henceforth as “higher TMFs”) and improve fullerene starting material conversion. Those experimental factors relevant for this work include (i) CF_3I pressure ($P(\text{CF}_3\text{I})$), (ii) temperature of the hot zone, and (iii) size of the hot zone.

The interest of this work is to improve the conversion of C_{60} while maintaining a product distribution which favors the formation of $\text{C}_{60}/\text{C}_{70}(\text{CF}_3)_{n\leq 6}$ (referred to as “lower TMFs”), and ideally to sufficiently favor a specific single isomer to generate it in high yields (thereby removing the necessity of multiple stages of purification to separate it from other TMFs) for device testing. Before designing new experiments to fulfill this goal, it is useful to describe what has been established in prior work that would help to improve these outcomes, i.e., conversion and selectivity.

Note that these general remarks are based on reactions performed on the small scale (ca. 5–10 mg of C₆₀ starting material) using GTGS-I unless otherwise stated.

- i. As the initial CF₃I pressure ($P(\text{CF}_3\text{I})$) is decreased, lower TMFs are favored while less C₆₀ is converted.
- ii. The highest yields of 60-2-1 were achieved using low pressures ($P(\text{CF}_3\text{I}) = 5\text{--}45$ Torr).
- iii. Increasing the size of the hot zone from 10 to 50 mm, GTGS-I to II in Figure 1.2, resulted in greater conversion of C₆₀ but the product distribution favored higher TMFs.
- iv. Using a 10 mm hot zone with an added cold finger, GTGS-III, resulted in a lower conversion of C₆₀ than in GTGS-I while the product distribution shifted towards lower TMFs compared to the product distribution in GTGS-I.
- v. Using both a 50 mm hot zone and a cold finger (GTGS-IV) was not investigated in prior work.
- vi. Three different temperatures for the hot plate (T_{hp}) were tested: 550, 600 and 670 °C; as T_{hp} increased, there was an increase in the amount of C₆₀ conversion. The exception was for the lowest pressure, 5 Torr, at which 670 °C-product had more unreacted C₆₀ than the product obtained at 600 °C; likely it is due to C₆₀ subliming faster than it can react at higher T_{hp} and reduced pressures.
- vii. The product distribution of TMFs changed as T_{hp} increased, but how was also dependent on $P(\text{CF}_3\text{I})$; in general, for reactions carried out at $P(\text{CF}_3\text{I}) \leq 45$ Torr, the product distribution shifted towards lower TMFs at higher T_{hp} ; while at $P(\text{CF}_3\text{I}) = 135$ Torr, the composition shifted towards lower TMFs at lower T_{hp} .

1.2. Results and Discussion

1.2.1. Gradient temperature gas-solid (GTGS) reactor improvements from prior state of the art

Knowing from prior work that the most favorable conditions for generating 60-2-1 are with $P(\text{CF}_3\text{I}) = 5\text{--}45$ Torr and T_{hp} (hot plate temperature) of 600 or 670 °C gives a useful starting point to optimize for yield and selectivity of 60-2-1. Moreover, it was using $P(\text{CF}_3\text{I}) = 10$ Torr at $T_{\text{hp}} = 670$ °C which previously achieved a very high selectivity and the highest yield for 60-2-1 with respect to the C_{60} (21% yield by HPLC), albeit at the expense of low conversion, since most of the crude material was unreacted C_{60} . Therefore, the author initially investigated these low pressures to generate 60-2-1 in greater yields, while also maintaining a favorable product distribution for generating 60-2-1 as selectively as possible.

A problem using these lower pressures is that the rate of reaction can be slow to prepare products in a reasonable amount of time, especially if more than 5–10 mg of fullerene is being used. One can partly circumvent this problem by increasing the size of the hot zone from the 10 mm to a 50 mm insulation. However, as has also been previously observed, the larger hot zone increases conversion of C_{60} , but also favors higher TMFs; presumably by increasing the residence time of the TMFs (or C_{60}) in the gas phase, i.e., giving them ample time to react further with the gaseous CF_3 radicals.⁵ Therefore, in this work, the author used a new GTGS reactor configuration—a combination of a large 50-mm hot zone and cold finger placed just 10 mm above the fullerene bed (GTGS-IV). By employing the cold finger as well as the larger hot zone with GTGS-IV, it is possible to increase the conversion of C_{60} while also favoring lower TMFs. This can be reasoned as improving the conversion of C_{60} much like what was previously observed when increasing the size of the hot zone in going from GTGS-I to II,⁵ while also shortening the residence

time sublimed TMFs spend in the hot zone and thereby suppressing their further trifluoromethylation by allowing them to deposit closer/sooner than above the 50 mm insulation.

Notably, in this work it was observed that when both the cold finger and the 50 mm insulation are used together in GTGS-IV, there is no sublimate on the side walls of the reactor above the hot zone; which is always observed when the small (10 mm) hot zone is used, with or without the cold finger (GTGS-I and III). Instead, for GTGS-IV all sublimed fullerenes deposited solely onto the base of the cold finger suggesting that the close distance of the cold finger to the non-sublimed fullerenes provides a shorter path length for sublimation and subsequently it should reduce the number of gas-phase reactions of TMFs, even with a large hot zone. Consequently, these factors lead to improving the product distribution towards lower TMFs.

In addition to slower reaction rates, when using low pressures ($P(\text{CF}_3\text{I})=5\text{--}45$ Torr) with the GTGS reactor, another concern is that the rate of sublimation of unreacted C_{60} increases, too. This is even more noticeable at higher hotplate temperatures: for example, using $P(\text{CF}_3\text{I})=10$ Torr and $T_{\text{hp}}=670$ °C resulted in high selectivity for 60-2-1, but more than half of the crude material was unreacted C_{60} that had sublimed and thus could no longer react outside of the hot zone.⁵ For this reason, to improve the yield of 60-2-1 (and other low TMFs for that matter), it is clearly beneficial to use 600 °C instead of 670 °C for this goal.

1.2.2. Optimization of GTGS-IV reactor variables to favor 60-2-1

The general conditions used with GTGS-IV to favor the formation of 60-2-1 were as follows: C_{60} starting material (ca. 50–100 mg) was finely ground using a mortar and pestle, $P(\text{CF}_3\text{I}) = 10\text{--}15$ Torr, $T_{\text{hp}} = 600$ °C \pm 10 °C, and reaction times were ranging from 10 to 18 h (see Table 1).

It is relevant that as the CF_3I gas is consumed during the course of these reactions, there is a noticeable pressure drop in CF_3I . This not only changes the rate of sublimation for all TMFs and

C₆₀, for better or worse, but also lowers the concentration of CF₃I available as the reaction proceeds, slowing the rate of conversion of C₆₀ as time goes on. In practice, this can be overcome by frequently stopping the reaction, evacuating the gas in the GTGS reactor, and replenishing the CF₃I back to its starting pressure to continue the reaction anew. But this is cumbersome, inevitably increases CF₃I waste, and does not necessarily improve the yield of the desired compound. For example, when starting with $P(\text{CF}_3\text{I}) = 15$ Torr and replenishing the gas pressure midway through reactions 1 and 2 (Table 1) it resulted in relatively good isolated yields for 60-2-1 (20% and 22% isolated based on starting mass of C₆₀, respectively). These two reactions were carried out using the same conditions to demonstrate sufficient reproducibility between identical reactions, so that results could be compared when conditions were altered. Notably, and somewhat counter-intuitively, in reaction 3 the CF₃I gas was not replenished and was simply depleted over time, and this resulted in a significantly higher isolated yield of 28% for 60-2-1 compared to the yields in reactions 1 and 2.

It might be intuitive at first to assume that a decrease in $P(\text{CF}_3\text{I})$ over time—essentially a decrease in the concentration of CF₃I—should in fact lower the isolated yield of 60-2-1 compared to when CF₃I is refilled: as this should slow the rate of trifluoromethylation. In that, if CF₃I is not refilled halfway during the reaction, then the trifluoromethylation rate of C₆₀ will be comparatively slow for the last half of the reaction resulting in a lower conversion of C₆₀ and less 60-2-1 being generated overall. However, this neglects the fact that unless the 60-2-1 has sublimed out of the hot zone, it will continue to react with CF₃ radicals to generate higher adducts and thereby lowering the relative abundance of 60-2-1. Moreover, later in the reaction process, as the amount of 60-2-1 increases relative to the amount of C₆₀ in the hot zone, eventually the rate of reaction for the trifluoromethylation of 60-2-1 to generate higher adducts will eventually be greater than the rate

of formation *for* 60-2-1 from the diminishing amount of unreacted C₆₀. Therefore, the yield of 60-2-1 is expected to be maximized when the rate of conversion of C₆₀ into 60-2-1 is increased *and* subsequent conversion of 60-2-1 into higher TMFs is hindered.

With this in mind, if $P(\text{CF}_3\text{I})$ is held constant over the course of the reaction, the sublimation rate of TMFs and C₆₀ will also be constant. Likewise, the rate of reactions with respect to the concentration of CF₃I will also be constant for all fullerenes in the hot zone. Conversely, if the pressure of CF₃I is not being maintained constant and instead is decreasing during the reaction, then the reaction rate of 60-2-1 with CF₃ radicals will progressively slow down, while the rate of sublimation will increase for all fullerenes. This allows 60-2-1 to sublime faster as the reaction proceeds, while slowing subsequent trifluoromethylation: hindering the formation of higher adducts while allowing the remaining C₆₀ to continue to react. Hence, allowing $P(\text{CF}_3\text{I})$ to decrease as the reaction proceeds will benefit the *selectivity* towards 60-2-1 and should thereby improve the isolated yield. This can explain why replenishing the CF₃I midway during reactions *1 and 2* with 15 Torr is actually not beneficial to increasing the yield of 60-2-1 as compared to reaction 3.

Investigating the scalability of these reactions with GTGS-IV, when the same conditions as reaction 3 were used but at twice the scale of C₆₀ starting material (from 50 to 100 mg, reaction 4) there was a decrease in the isolated percent yield, from 28% to only 16%. However, this was possible to overcome by simply increasing the reaction time from 10 to 16 hours (rxns. 4 and 5 in Table 1, respectively); resulting in an isolated yield of 28%, the same as reaction 3 using 50 mg of C₆₀.

Working on the hypothesis that lower pressures favor 60-2-1 and that the previous most favorable conditions to generate 60-2-1 were utilizing a $P(\text{CF}_3\text{I})$ of 10 Torr, it was investigated if with GTGS-IV using 10 Torr would also be beneficial. When lowering the initial CF₃I pressure to

10 Torr (rxns. 6 and 7) compared to 15 Torr (rxns. 1-4), the total reaction time had to be extended to 18 hours instead of 10 to allow the majority of the fullerene material to sublime. As expected, using lower pressure resulted in a lower C₆₀ conversion but also gave a lower yield of 60-2-1. Moreover, increasing the time of the reaction inevitably requires the reactor to be left unattended and possible temperature fluctuations unmonitored. The heating element used in GTGS-I, II or III studied in prior work or GTGS-IV studied in this work, is controlled manually with a Variac variable-transformer and can undergo potential temperature swings of up to ± 10 °C within less than a 30-minute timespan, and even greater if not monitored. Typically, the temperature of the hot plate does “stabilize” (does not change more than 1.0 °C within an hour) but starts to drop at a later time if the reactions are longer than a few hours. Here, it was observed that when leaving the reaction going overnight (16 or 18 hours total) after the hot plate temperature was stable for at least 2 hours the day before, the hot plate temperature was always lower than the temperature it was left at, by as much as 27 °C in the case of reaction 7. To overcome these inconsistent conditions, the hotplate heating element was equipped with a programmable control box and is discussed in the following section.

It should be noted that with the goal of efficiently generating 60-2-1 in sufficient quantities for device application, the author of this dissertation deemed it ideal to compare the isolated yield of highly pure 60-2-1 only after separation by HPLC so that the correlations between reaction conditions and product yield are accurately monitored (see Table 1). On the other hand, previous studies typically reported the percent yield of 60-2-1 calculated based on integration of HPLC peak area, which inevitably deviates from the isolated yield by mass of purified product, due to either a discrepancy caused by natural losses in the purification process or known discrepancies in the

extinction coefficient and lambda max (λ_{\max}) between C₆₀, 60-2-1 and other TMFs in the chromatogram.

For example, the chromatogram of product of reaction 5 (Figure 1.3) shows that under the HPLC conditions used, there is baseline separation between C₆₀ and 60-2-1 allowing to calculate a 42 % yield of 60-2-1 based on peak area integration; while this amounts to an isolated yield of 28% for 60-2-1 (two thirds of the 42 % yield expected based on HPLC peak area). In that light, with the highest yielding reaction for 60-2-1 previously reported as 21% based on HPLC peak area, and no data for isolated yield given, it can be assumed that if it were *isolated* to 95+% purity, then it would be noticeably lower than 21%, although the exact degree to which the yield would be lowered, cannot be determined *a priori* from the HPLC chromatogram alone, for the reasons previously discussed. Nonetheless, comparison of the % yield of 60-2-1 by HPLC reported previously⁵ with the results obtained by the author unequivocally indicates at least two-fold improvement.

1.2.3. Improved yield of 60-2-1 with precise temperature control using

In order to maintain more consistent temperatures during the reaction as well as allow for more precise comparisons between reaction temperature and the final product distribution, the hotplate heating element was equipped with a programmable control box, which itself was attached to the thermocouple nestled between the hot plate and the base of the reactor, allowing for direct feedback whether 10 or 50 mm insulation is used (GTGS-V and VI in Figure 1.2, respectively). This allowed the control box to adjust the applied voltage automatically and subtly over time to maintain the desired T_{hp} from 590 to 620 °C $\pm < 2$ °C.

With GTGS-VI in hand, and with the general optimized conditions to favor 60-2-1 determined using GTGS-IV (particularly, rxns. 3 and 5), it is now possible to maintain reliably precise (narrow) temperature ranges within optimized conditions and to improve reproducibility between

reactions; subsequently allowing for more detailed comparisons of the product distributions obtained in reactions with different T_{hp} . Moreover, by using GTGS-VI instead of IV, it is possible to examine effects of the temperature more accurately than in the prior studies. For example, it allowed for comparisons between the product distributions in the series of reactions with 5 °C increments in T_{hp} , revealing that $T_{\text{hp}} = 605$ °C gives a greater yield and is more selective for 60-2-1 than when $T_{\text{hp}} = 600$ °C was used under otherwise similar conditions (see more discussion in following section).

For these reasons, to favor the formation of 60-2-1 using GTGS-VI the conditions were chosen similar to reactions 3 and 5 above, that is $P(\text{CF}_3\text{I}) = 15$ Torr and a 10 hour reaction time; but an elevated (and more precise) hot plate temperature of $T_{\text{hp}} = 605$ °C \pm 2 °C was used, resulting in reaction (i) in Table 2 (see Figure 1.4 for chromatogram). The most significant difference in the composition of products is the large increase in 60-4-2 content when GTGS-VI is used compared to GTGS-IV, while the relative distribution of other TMFs is very similar between the two experiments, as is the conversion of C_{60} . This might be why a slight decrease in the relative HPLC peak area for 60-2-1 for reaction (i) (Figure 1.4) for observed compared to reaction 5 in (Figure 1.3). Interestingly, when analyzing the crude material of reaction (i) by ^{19}F -NMR (see Figure 1.6), only measurable signals for 60-2-1, 60-4-2 and 60-4-1 are observed, with integrations ratios of 5.4/2.5/1.0, respectively, representing a selectivity of 61% for 60-2-1 by ^{19}F -NMR.

1.2.4. Improved yield of 70-2-1 with precise temperature control (GTGS-VI)

When these same conditions were applied for C_{70} substrate instead of C_{60} , a significant improvement was observed in the yield of 70-2-1 (19%), conversion of C_{70} (61%), and even more so the selectivity (31% of total TMF peak area), compared to the literature data, which reported <2% yield for generating 70-2-1.^{5, 12, 23} While this is not as selective (or high yielding)

as with C₆₀, it is important to note that C₇₀ has a much lower vapor pressure compared to C₆₀, and, therefore, C₇₀ derivatives are expected to sublime at a higher temperature than analogous C₆₀ derivatives. Moreover, the rate of the trifluoromethylation of C₇₀ is comparable to that of C₆₀ at the same reaction temperature. Hence, the rate of sublimation of lower TMC₇₀Fs is typically not fast enough for them to sublime out of the hot zone before they are converted into higher TMC₇₀Fs. This naturally makes the GTGS reactor less suited for kinetic control of C₇₀ trifluoromethylations compared to C₆₀. In fact, most of the crude product mixture in reaction (ii) was not sublimed; and the non-sublimed product-residue contained the majority of the 70-2-1 compound present compared to the sublimate deposited onto the cold finger. This suggests that the rate of reaction for 70-2-1 with CF₃ radicals to generate higher TMFs is significantly faster than the rate of sublimation for 70-2-1 thereby limiting the ability to control the product distribution with the GTGS, compared to the C₆₀ case. Furthermore, a lower symmetry D_{5h}-C₇₀ molecule may form more regioisomers for a given n(CF₃) compared to high-symmetry I_h-C₆₀, which makes the TMC₇₀Fs product mixtures even more complex.

1.2.5. Constant (low) pressure trifluoromethylation using GTGS-V and slush baths

While it was shown that a decreasing pressure over time in the GTGS reactor can be favorable for the synthesis of 60-2-1 and 70-2-1, this is not necessarily the case for other lower TMFs; their generation requires preventing both C₆₀ and 60-2-1 from subliming so they react further. As discussed above, there is a more substantial difference between the sublimation temperature of higher TMFs and C₆₀ compared to 60-2-1 and C₆₀. This suggests that tetrakis-adducts and higher addition products will more efficiently separate out of the hot zone compared to 60-2-1 at temperatures and pressures where C₆₀ has negligible vapor pressure. Moreover, the decrease in the rate of reaction as P(CF₃I) decreases, which was beneficial for the selective synthesis of 60-2-1,

will needlessly extend the reaction time for the synthesis of other lower TMFs. For such reasons, it would be preferred to have a system which is capable of maintaining relatively constant pressure applied throughout the reaction. Prior attempts at this idea have utilized a gas flow tube reactor, and the GTGS reactor has been configured with a flow tube in place of the cold finger (not shown here),⁵ but these methods do not (easily) allow for control over the exact pressure and do not allow for low pressures. Moreover, this significantly increases CF₃I waste, especially if the reaction is slow to proceed.

An approach proposed in this work to overcome these problems is to control the vapor pressure of CF₃I using cold slush baths to cool a region of the GTGS reactor where CF₃I can condense; in so doing limiting the maximum pressure of CF₃I throughout the GTGS reactor to that of the vapor pressure of CF₃I at the temperature of the slush bath used, regardless of how high the temperature is elsewhere in the GTGS reactor. In practice, this can be accomplished by simply attaching an additional glass tube with a closeable valve to the GTGS gas line (referred to as the GTGS-line), and submerging part of it into a cold slush bath (must be colder than boiling point of CF₃I). A general schematic diagram of the GTGS-line is shown in Figure 1.7. With this modification and a slush bath of the appropriate temperature, it is possible to add CF₃I gas to the GTGS-line whereby it will condense in the glass tube once it has reached the CF₃I equilibrium vapor pressure at the temperature of the respective slush bath. This glass tube, when open to the GTGS reactor (through the GTGS-line), acts as a liquid-gas reservoir (LGR) and will maintain a constant vapor pressure of CF₃I throughout the GTGS reactor, regardless of the temperature in other regions. When there is excess of CF₃I(*l*) in the LGR while a trifluoromethylation reaction is happening in the GTGS reactor, the CF₃I(*g*) will be consumed in the hot zone of the reactor and be replaced by the excess CF₃I(*l*) vaporizing from the LGR, giving a continuous feed and maintaining a constant pressure of

$\text{CF}_3\text{I}_{(g)}$ throughout the GTGS reactor. Subsequently it ensures a constant rate of reaction and sublimation for the TMFs and C_{60} in the hot zone.

The melting point of CF_3I is listed as $-110\text{ }^\circ\text{C}$ (often simply as $<-78\text{ }^\circ\text{C}$) with a boiling point of $-22.5\text{ }^\circ\text{C}$.²⁴ Consequently, slush baths that are colder than $-22.5\text{ }^\circ\text{C}$ are potentially useable in this system as they will not over-pressure the GTGS reactor. Fortunately, it was found that a dry-ice/isopropyl alcohol mixture ($\text{CO}_2(\text{s})/\text{IPA}$) resulted in a CF_3I pressure of approximately 28 Torr—within the desired range for low TMFs and 60-2-1. Conveniently, $\text{CO}_2(\text{s})/\text{IPA}$ baths are comparatively easy and inexpensive to setup compared to slush baths cooled with liquid nitrogen and, if done properly, can maintain their own temperature for over 10 hours without additional $\text{CO}_2(\text{s})$ being added. For these reasons, $\text{CO}_2(\text{s})/\text{IPA}$ slush baths were used as a point of principle for this method. Note that the temperature of the $\text{CO}_2(\text{s})/\text{IPA}$ baths were consistently measured at $-80\text{ }^\circ\text{C}$ rather than the expected value of $-78\text{ }^\circ\text{C}$, presumably due to higher altitude decreasing the sublimation temperature of dry-ice (Fort Collins CO is at an elevation of 1525 m from sea level).

1.2.5.1. Effects of hot-plate temperature on TMF product distribution at 28 Torr of CF_3I

Five control experiments using the LGR half-submerged in a $\text{CO}_2(\text{s})/\text{IPA}$ slush bath were performed with the same amount of starting material (ca. 55 mg C_{60}) and reaction time (8 h) at hot plate temperatures ranging from 595 to 615 $^\circ\text{C}$, in 5 $^\circ\text{C}$ increments. GTGS-V was used to have a smaller hot zone above the base of the cold finger so as to limit the number of recombination reactions between CF_3 radicals before they can come into contact with the fullerenes; wastefully accelerating the depletion of the $\text{CF}_3\text{I}_{(l)}$ in the LGR. The results of this series of reactions, including yield and relative abundance of the major TMFs products, are given in Table 3; HPLC chromatograms of representative aliquots of the crude product mixtures are shown in Figure 1.8.

By comparing the chromatograms in Figure 1.8 and the data in Table 3, the following general trends can be deduced from reactions A–E.

- 1) At the lowest temperature studied, 595 °C (A), a significant presence of higher TMFs in the product was noted. It can be hypothesized that the rate of sublimation for lower TMFs is very slow at 595 °C, so they continue to react in the hot zone shifting the product distribution towards higher TMFs. As temperatures were increased from 595 to 605 °C (A to C), the selectivity for 60-2-1 increases significantly from 29 to 42 %.
- 2) Upon further temperature increase from 605 to 615 °C (C to E), relative abundance of the tetrakis- and hexakis-adducts, such as 60-4-1, 60-6-1, and most notably 60-4-2, increases, whereas the relative amount of 60-2-1 falls. Interestingly, relative abundance of 60-4-2 continuously increases (in both yield and selectivity) as the temperature is increased from A to E. This unexpectedly high yield suggest that higher temperatures favor 60-4-2 over 60-4-1.
- 3) For the selective synthesis of 60-2-1, 605 °C (rxn. C) is the most favorable temperature in both yield and selectivity, albeit at the expense of lower conversion of C₆₀ compared to reactions D and E. At the same time, higher temperature can be used to favor the tetrakis- and hexakis-adducts, in particular, 60-4-2.

1.2.5.2. Improved yield of 60-4-2 using a constant 28 Torr of CF₃I

Based on these observations, it was hypothesized that it could be possible to increase the yield of 60-2-1 in reaction C further by allowing it to react longer under the same conditions. However, when this was tested by letting the reaction go for 10 hours instead of 8, only a moderate increase in C₆₀ conversion was observed (81% compared to 79%). Instead, it can be seen from the chromatogram shown in Figure 1.9 that there is a significant increase in the amount of 60-4-2, with a 21% yield by HPLC area rather than 16%, consequentially decreasing relative yield of 60-

2-1. Presumably, this extra time allowed for any non-sublimed 60-2-1 to continue reacting with CF_3I to form 60-4-2 (and other TMFs) at a faster rate than the remaining C_{60} was reacting to generate more 60-2-1. Additionally, unlike the 8-hour reactions (A–E), all material had sublimed in the 10-hour reaction (F). Therefore, without removing the 60-2-1 more efficiently before it can react, this appears to be near the limit for maximizing both the conversion of C_{60} and the yield of 60-2-1 with this method. Interestingly, this provides what is believed to be the highest yielding reaction to date for 60-4-2.

1.2.5.3. Effects of constant (low) pressures of CF_3I on TMF product distribution

For obtaining lower pressures than in reactions A–E, slush baths closer to the temperature of CF_3I 's melting point are needed. Some liquid nitrogen ($\text{N}_{2(l)}$) slush baths were investigated in this work as a point of principle (rxns. G–I in Table 3) to demonstrate that it is possible to obtain constant low vapor pressures of CF_3I over the range desirable for lower TMFs (see Figure 1.10 for chromatograms of the products obtained under such conditions). Indeed, by using these colder slush baths it is possible to achieve selectivity over 50% for 60-2-1, and even as high as 65.6% when the pressure was kept constant at 9 torr (rxn. I). However, the yield is decreased due to the greater abundance of unreacted C_{60} . Moreover, while use of the ($\text{N}_{2(l)}$) slush baths have been shown to indeed successfully maintain very low pressure, and indeed improve the selectivity for 60-2-1, ($\text{N}_{2(l)}$) slush baths are non-trivial to maintain and can cause drops in the pressure while mixing in more $\text{N}_{2(l)}$ throughout the reaction. This makes them less practical to use than a CO_2/IPA slush bath with the LGR.

1.2.5.4. Results using other perfluoroalkyl iodides at constant (low) pressures with C_{60}

It is noteworthy that the author also sought to investigate this synthetic approach with other gaseous perfluoroalkyl iodides. Particularly of interest was pentafluoroethyl iodide ($\text{C}_2\text{F}_5\text{I}$) to

generate $C_{60}(C_2F_5)_2$, which has previously only been made in low yields of <2%,⁵ as well as *n*- C_3F_7I . Unfortunately, it was observed that C_2F_5I and *n*- C_3F_7I required several hours to reach their respective equilibrium vapor pressures at -80 °C ($CO_2(s)$ /IPA slush bath temperature). It did not matter if the gas was being condensed while over-pressured, or if the condensed gas was being vaporized when opened to a closed system under static vacuum: the rate for the gas to reach its vapor pressure was several hours in either case. It is believed this partly explains why when using the same conditions as reaction C above, but with C_2F_5I gas instead of CF_3I , it resulted in <1% conversion of C_{60} : presumably, the gas is “replaced” at this slow rate after some of it is consumed in the reaction. For this reason, these higher perfluoroalkyl iodides do not seem appropriate for this reaction system, while other reactive gasses still may be utilized in such systems.

1.2.5.5. Preparation of low TMC₇₀Fs using a constant (low) pressure of CF_3I .

Previous reports on trifluoromethylation of C_{70} showed that yields of lower C_{70} -TMFs are notoriously low, and can even require multi-step synthesis.^{5-6, 12} In particular, when using the GTGS low-pressure methods similar to C_{60} , the highest yield achieved was <2% for 70-2-1; and most of C_{70} remained unreacted.⁵ It was only when increasing the pressure above 135 Torr that any reasonable conversion was achieved producing higher TM C_{70} Fs, while lower TMC₇₀Fs were present only in negligible amounts. Notably, the C_{70} substrate was almost completely consumed to generate isomers of $C_{70}(CF_3)_8$ and $C_{70}(CF_3)_{10}$ in high yields.

In this work, using the LGR-GTGS with a $CO_2(s)$ /IPA slush bath, the reaction of C_{70} (50 mg) with CF_3I for 8 hours at 610 °C afforded an 11% yield of 70-2-1 (based on HPLC chromatogram peak area, rxn. J shown in Figure 1.11), among other lower TMC₇₀Fs and a high conversion of C_{70} starting material (91% converted C_{70} based on HPLC).

Analyzing the crude product mixture that was deposited onto the cold finger after subliming out of the hot zone (referred to here as the “product-sublimate” or simply “sublimate”) separately from the product mixture that remains at the base of the GTGS thimble (the “product-residue” or simply “residue”) shows a significant difference between the product distribution of the two samples. More interestingly, when using either a lower or higher temperature compared to reaction J, the distribution of TMC₇₀Fs and C₇₀ does not change substantially for the product-sublimate (compare chromatograms shown in Figure 1.12 for rxns. K and L); while there is a significant difference in their distribution when analyzing the product-residue (chromatograms represented in Figure 1.12 with dotted lines).

Notably, the product-residue obtained at 600 °C (rxn. K) had considerably less unreacted C₇₀ compared to 620 °C (rxn. L); while the distribution of the TMFs present in the residue at 600 °C favored lower TMFs compared to 620 °C. The residue of reaction K (600 °C) had more 70-2-1 and 70-4-2 compared to the sublimate of reaction K, whereas at elevated temperatures with reaction L (620 °C), the distribution of TMFs is very similar between the residue and the substrate; although the residue of reaction L contains significantly more unreacted C₇₀ compared to the substrate.

Therefore, changing the temperature does not appear to have a significant impact on the product distribution of the sublimed material. Taking this into account and the fact that C₇₀ has a higher sublimation temperature compared to C₆₀,²² it could indicate that the reaction rate for the progressive trifluoromethylation of C₇₀ is much faster than the sublimation rate of lower TMC₇₀Fs, at least at the temperatures and pressures used here.

This is indicated by the observation that higher temperatures result in greater abundance of C₇₀ in the residue while also favoring higher TMFs; suggesting that at 620 °C the C₇₀ material is not

readily subliming before it reacts, but once a reaction occurs to make a bis-adduct, it is faster for (several) additional CF_3 groups to be added before the TMC_{70}F is able to sublime. Moreover, at lower reaction temperatures (rxn. K) the same TMC_{70}F product distribution is observed in the sublimate as with the higher temperatures' sublimate (rxn L), but the product distribution is different in the residue at the lower temperature and favors lower TMFs: suggesting that the sublimation rate of lower TMC_{70}Fs is not different enough from C_{70} relative to their reaction rates into higher adducts to allow for their sublimation and deposition onto the cold zone before they react. This suggest that, despite these promising initial results that showed improved relative yields of 70-2-1 compared to the literature overall, use of the GTGS reactor for development of selective trifluoromethylation methods for C_{70} is not as advantageous as for C_{60} .

1.3. Conclusions.

The results presented in this Chapter demonstrate that systematic optimization of the reaction conditions, including a new reactor configuration, for trifluoromethylation of fullerenes in the gradient-temperature-gas-solid reactor yielded significant improvements in the yields and selectivity of 60-2-1 and 70-2-1 compared to previously reported works. In the latter case, a nearly 10x fold increase in the yield was achieved compared to the literature data. This optimization opened a convenient route to prepare these TMFs with high purity and using a less laborious purification protocol and to make them available for testing in optoelectronic devices (see Ch.2). Furthermore, for the first time, it was possible to synthesize 60-4-2, a valuable TMF with the fulvene-like addition pattern, with relatively high yield. This compound has been shown to be a valuable synthon for further highly selective functionalization, due to the presence of a uniquely short and highly reactive double bond in the structure.²⁵ Another substantial modification of the GTGS method involved the use of a liquid-gas reservoir (LGR) for CF_3I cooled by submerging it

in the low-temperature slush bath thereby maintaining constant gas pressure in the reactor. This led to further improvements in yields and selectivity for a number of lower TMFs, and also solved the problem of previously unproductive use of the gaseous reagent. Such approach is transferrable to reactions of other organic substrates and possibly other reactive gases, when maintaining constant low pressures is critical for effective and selective functionalization.

1.4. Experimental section

1.4.1. Reagents and solvents

The following reagents and solvents were used as received unless otherwise indicated: C₆₀ (MTR Ltd, >99.5%); C₇₀ (MTR Ltd, >98.0%); Trifluoromethyl iodide (SynQuest Labs, abbr. CF₃I, 99%); chloroform-*d* (abbr. CDCl₃; Cambridge Isotope Laboratories, 99.8%), hexafluorobenzene (abbr. C₆F₆; Sigma-Aldrich, >99.5% NMR grade); toluene (Honeywell, HPLC grade); heptane (Sigma-Aldrich, HPLC grade).

1.4.2. Instrumentation

High Performance Liquid Chromatography (HPLC) for separation and analysis was conducted using a Shimadzu liquid chromatography instrument (CBM-20A control module, SPD-20A UV-Vis detector, LC-6AD pump, manual injector valve). The HPLC columns utilized were the COSMOSIL Buckyprep and Bucky-M, both semi-preparative scale (10 mm I.D. x 250 mm, Nacalai Tesque, Inc.), at a flow rate of 5 and 7 mL min⁻¹, respectively. Fluorine-19 NMR spectra were collected on a Varian (Agilent) 400NMR spectrometer equipped with Automated Tuning in a CDCl₃ solution. ¹⁹F NMR spectra were acquired at 376.1 MHz, using 1 second relaxation time and 45 ° pulse angle. ¹⁹F chemical shifts are reported in ppm using hexafluorobenzene as the internal standard (C₆F₆: $\delta = -164.9$). UV-vis absorption spectra were recorded on a Perkin Elmer Lambda 19 spectrometer.

1.4.3. GTGS reactor general procedures

For all reactions discussed here, the quartz thimble depicted in Figure 1.7 was dry loaded with C₆₀ (or C₇₀) (ca. 50–100 mg); ensuring all material was evenly spread across the base of the thimble and none was stuck on the sidewalls before continuing. This thimble was then attached to the rest of the GTGS reactor by an O-ring gasket connecting to the 1-liter reactor headspace that can be isolated from the GTGS gas manifold; either with or without an attached LGR if one was used. The entire GTGS-manifold was then closed to external atmosphere and placed under dynamic vacuum overnight to remove trace residual solvents adsorbed onto the solid fullerene material. The GTGS reactor was prepared in either configuration IV, V (with LGR), or VI as shown in Figure 1.2, and continued as follows.

1.4.3.1. GTGS-IV and VI

The GTGS manifold was closed to the vacuum line and CF₃I is slowly added (10 or 15 Torr). The quartz thimble and 1-liter headspace above it is then closed off from the rest of the manifold so that there is ca. 1-liter of CF₃I gas at the respective pressure used (measured at room temperature). Once closed, the pre-heated hotplate with 50 mm insulation is raised into contact with the base of the reactor and adjusted to give the desired hot plate temperature (T_{hp}). After the given reaction time, the hot plate is removed (lowered) and the reactor allowed to cool before opening to vacuum, removing any unreacted gaseous CF₃I.

1.4.3.2. GTGS-V with LGR

Once equipped with a liquid gas reservoir (LGR) (see Figure 1.7) and after evacuating overnight, the GTGS manifold is then closed to vacuum and excess CF₃I is added (at least 200 Torr). At this point, the LGR is half-submerged into a slush bath, causing CF₃I to condense and the pressure to equilibrate to the vapor pressure at the temperature of the slush bath over the course

of 5–10 minutes. The pre-heated hotplate, attached with a 10 mm insulator block, was then raised into contact with the base of the reactor and set to the desired hot plate temperature (T_{hp}). After the given reaction time, the hot plate is removed (lowered) and the reactor allowed to cool before opening to vacuum; removing any unreacted gaseous CF_3I . Note that at this point, the LGR can be closed off before evacuating the manifold in order to recycle any unreacted condensed CF_3I .

1.4.3.3. Slush baths used for LGR and their resulting CF_3I vapor pressures

$P(CF_3I) = 28$ Torr is the vapor pressure obtained at a temperature of -80 °C, using a dry-ice/isopropyl alcohol (CO_2/IPA) slush bath. $P(CF_3I) = 22$ Torr is the vapor pressure at -83 °C, using a liquid nitrogen/ethyl acetate ($N_{2(l)}/EtOAc$) slush bath. $P(CF_3I) = 12$ Torr is the vapor pressure at -90 °C, using a $N_{2(l)}/heptane$ slush bath. $P(CF_3I) = 9$ Torr is the vapor pressure at -95 °C, using a $N_{2(l)}/toluene$ slush bath.

1.4.3.4. Workup and sample preparation for analysis

After a reaction is finished, the GTGS reactor and manifold are left under dynamic vacuum overnight to remove all iodine biproduct that deposits onto the cold finger as large crystals. Once there are no more visible iodine crystals or vapor in the GTGS reactor, the sublimate on the cold finger is dissolved and with excess toluene (100 mL), combined with the sublimation residue (unless otherwise stated), and sonicated for 30 minutes. (This is to ensure all unreacted C_{60} is dissolved prior to HPLC analysis.) An aliquot from the dilute crude solution is then analyzed by HPLC. Note that all glassware used to hold the dissolved product mixture was wrapped and covered in aluminum foil to prevent photooxidation of the products from sunlight.

1.5. Supplemental Information

1.5.1. GTGS reactor external hot-plate temperature and internal temperature comparison

All measurements given for the reaction temperature are for the external temperature of the hot plate—measured in between the hotplate and the base of the reactor. In contrast, the internal reaction temperature (that which the fullerene material is experiencing) is expected to be different and there is a measurable temperature drop between the two. While one cannot measure it directly during the reaction, control experiments were done heating the GTGS reactor while it is open to allow a thermocouple to be placed on the inside so as to measure the “external” hot-plate temperature and the “internal” reaction temperature. When this was done at an external temperature of 600 °C, the internal temperature was measured as 525 °C. While when external temperature of 620 °C was used it gave an internal temperature of 535 °C. These values are likely to differ slightly or fluctuate during the actual reaction, which in contrast is under reduced pressure with continuously subliming and reacting material.

1.6. Tables and Figures

Table 1: Experimental data for the trifluoromethylation of C₆₀ using GTGS-IV.

Rxn.	Starting C ₆₀ (mg)	T _{hp} (°C)	Time (h)	P(CF ₃ I) (Torr)	Refilled CF ₃ I?	Isolated 60-2-1 (mg) ^a	Percent yield of 60-2-1 (%) ^c	Conversion of C ₆₀ by HPLC ^b (%)
1	53.8	600 ± 10	10	15	Yes	12.8	20	81
2	51.9	600 ± 10	10	15	Yes	13.7	22	83
3	55.1	600 ± 10	10	15	No	18.4	28	85
4	102.9	600 ± 10	10	15	No	20.2	16	71
5	107.8	600 ± 20	16	15	No	36.6	28	82
6	54.8	600 ± 27 ^d	18	10	No	12.1	19	81
7	52.5	600 ± 14 ^e	18	10	No	14.3	23	86

^a Isolated yield is for 60-2-1 after HPLC separation with a minimum 95% purity (verified by HPLC) and with no detectible signals of other TMFs by 19F-NMR.

^b Conversion is based on HPLC peak area and calculated by subtracting the percent of remaining C₆₀ from 100%; where the percent of C₆₀ is calculated by dividing the HPLC peak area of C₆₀ by the total peak area and multiplying this by 100%.

^c Percent yield is calculated by dividing the isolated yield of 60-2-1 by the theoretical yield based on the amount of C₆₀ starting material used.

^d Hot plate was found at 573 °C when left overnight at an original temperature of 600 °C.

^e Hot plate was found at 586 °C when left overnight at an original temperature of 600 °C.

Table 2: Conditions and results for the trifluoromethylation of C₆₀ and C₇₀ using GTGS-VI

Rxn.	Substrate (mg)	$T_{\text{hp.}}$ (°C)	$P(\text{CF}_3\text{I})$ (Torr)	Time (h)	C ₆₀ (C ₇₀) conversion (%)	Yield ^a and abundance ^b (%)		
						60(70)-2-1	60-4-2	60-4-1
<i>i</i>	C ₆₀ , 55	605 ± 2	15	15	80	39.0 48.4 (60.6)^c	18.6 23.1	8.3 10.3
<i>ii</i>	C ₇₀ , 50	610 ± 2	15	15	61	19.1 31.5	-	-

^a Yield based on area of the specified TMF peak in the chromatogram divided by the total peak area including unreacted C₆₀ (or C₇₀).

^b Percent abundance is always depicted as bold and calculated by dividing the specified TMF peak in the chromatogram by the total peak area of all products (i.e., 2–11 minutes) unless otherwise stated.

^c percent abundance determined based on integration values in ¹⁹F-NMR of the crude product mixture, shown in Figure 1.6.

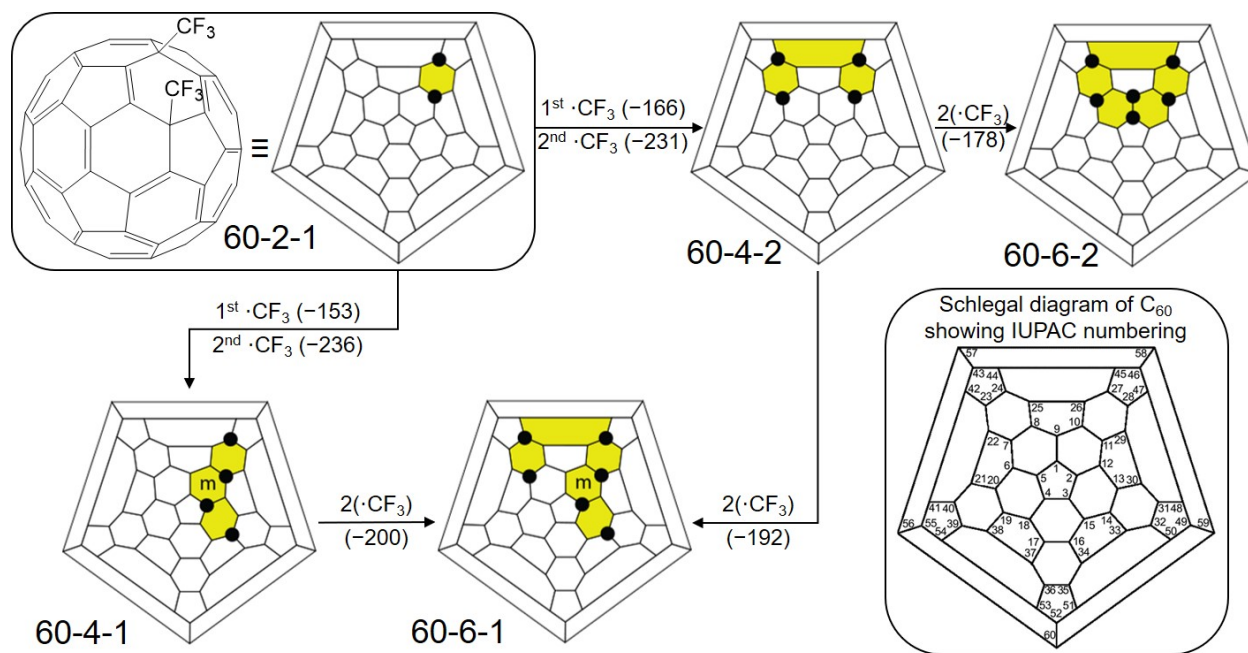
Table 3: Conditions and results for the trifluoromethylation of C₆₀ and C₇₀ with constant low pressures of CF₃I gas using the GTGS reactor equipped with a slush-bath-cooled LGR.

Rxn.	<i>T</i> _{hp} (°C)	<i>P</i> (CF ₃ I) (Torr)	Time (h)	Conversion of C ₆₀ (%)	Yield ^a and abundance^b (%)			
					60-2-1	60-4-2	60-4-1	60-6-1
A	595	28	8	73	20.0 27.7	10.2 14.0	8.0 11.1	8.4 11.6
B	600	28	8	83	22.3 27.0	12.0 14.5	11.2 13.5	9.8 11.8
C	605	28	8	79	31.5 40.0	15.8 20.0	10.9 13.8	6.7 8.5
D	610	28	8	90	30.4 33.9	19.2 21.3	11.4 12.7	9.7 10.7
E	615	28	8	84	22.4 26.7	19.6 23.3	11.1 13.2	9.8 11.7
F	605	28	10	81	17.1 21.1	21.1 26.0	9.3 11.4	11.2 13.8
G	600	22	8	83	31.0 37.4	18.4 22.2	9.9 11.9	7.8 9.5
H	600	12	6	59	30.6 52.0	3.3 5.5	10.4 17.6	3.6 6.1
I	600	9	8	45	29.4 65.6	1.9 4.3	5.3 11.8	2.5 5.7

Each reaction was performed with ca. 55 mg of C₆₀ starting material. See experimental section for information on the slush baths used.

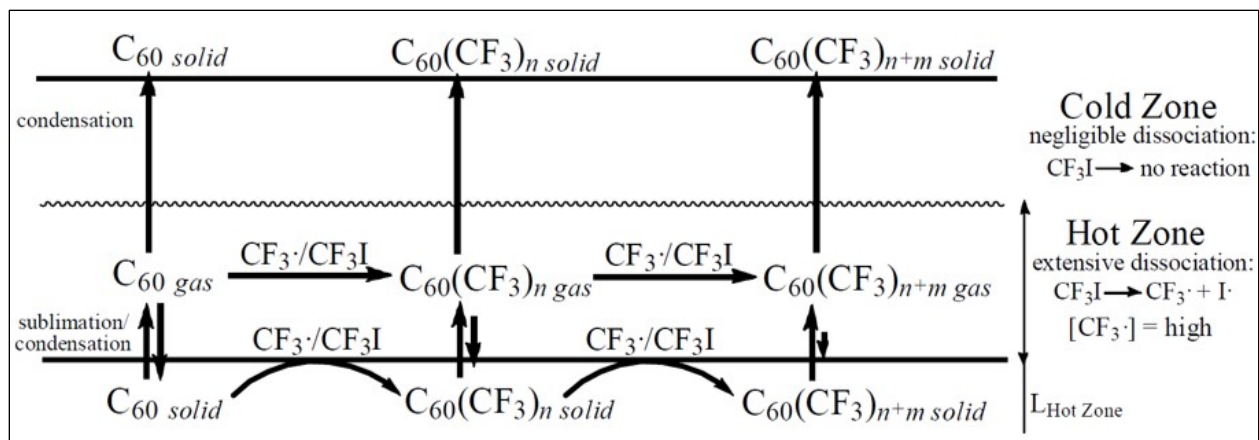
^a Yield based on area of the specified TMF peak in the chromatogram divided by the total peak area, including C₆₀.

^b Percent abundance is always depicted as bold and calculated by dividing the specified TMF peak in the chromatogram by the total peak area of all products (i.e., 2–11 minutes) unless otherwise stated.



Isomer abbreviation ^a	CF ₃ addition locants with fixed 1,7-positions ^b	Isomer abbreviation ^a	CF ₃ IUPAC-approved addition locants ^c
60-2-1	1, 7	60-2-1	1,7
60-4-1	1, 7, 23, 40	60-4-1	1,6,11,18
60-4-2	1, 7, 11, 27	60-4-2	1,7,11,24
60-6-1	1, 7, 11, 23, 27, 40	60-6-1	1,6,11,18,24,27
60-6-2	1, 7, 11, 24, 25, 27	60-6-2	1,6,9,12,15,18

Figure 1.1: Schlegel diagrams of TMFs studied in this work with notations adopted from references 7 and 17, showing major pathways for the consecutive addition of ·CF₃. The corresponding enthalpies of addition for the most stable 1st and 2nd (or pair) of CF₃ group(s) to give the corresponding isomer are listed in parentheses (kJ·mol⁻¹, DFT) and taken from reference 15. Black circles denote CF₃ groups, yellow ribbons connect two (or more) para- or meta-CF₃ groups on the same hexagon. Upper left inset shows 3D structure and Schlegel diagram for 60-2-1. Mid right inset shows generic C₆₀ Schlegel diagram showing IUPAC numbering taken from reference 6. a) isomer abbreviations where first number represents the type of fullerene (C₆₀ in this case), second number is the number of CF₃ groups on the fullerene cage and the last number is the “isomer number”.⁶ b) non-standard locants with fixed 1,7-positions to show the addition pattern as CF₃ groups are added. c) IUPAC-approved locants positions based on the lowest locant number possible for the structure.



Scheme 1: Possible elementary steps during fullerene trifluoromethylation in GTGS reactor, reprinted from reference 5 with permission. The elementary processes that occur during fullerene trifluoromethylation are: (i) thermolysis of CF_3I producing CF_3 radicals; (ii) sublimation of C_{60} from the hot zone; (iii) trifluoromethylation of the surface layer of the solid C_{60} (and further trifluoromethylation of so-formed solid TMFs) in the hot zone; (iv) sublimation of TMFs from the hot zone; (v) trifluoromethylation of the subliming C_{60} and TMFs in the gas phase; and (vi) condensation of C_{60} and TMFs from the gas phase into the cold zone. Trifluoromethylation of fullerenes is treated as an irreversible process; it is also assumed that the sublimation of fullerenes and TMFs out of the cold zone does not take place.

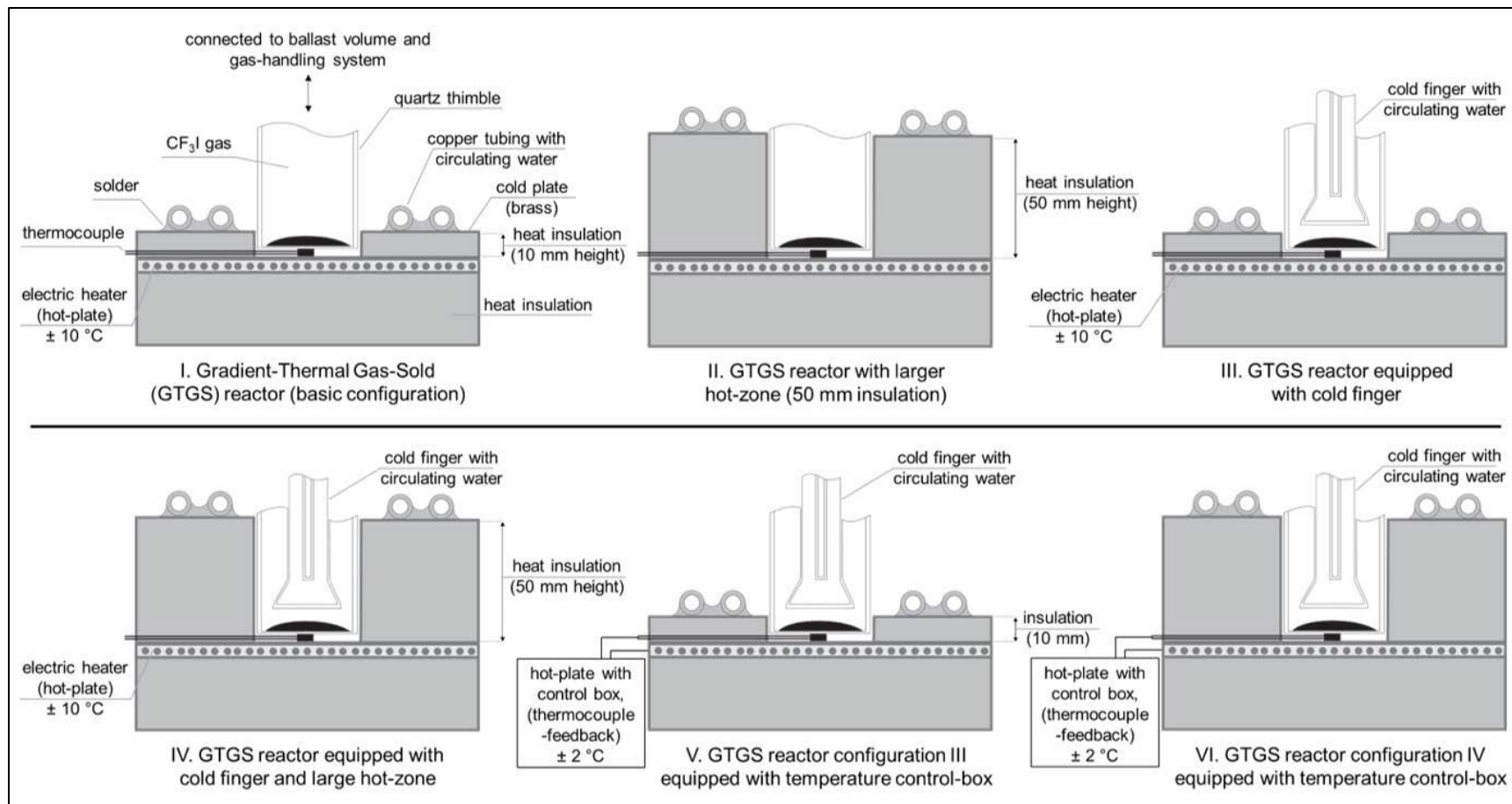


Figure 1.2: Alternate configurations of the gradient-temperature gas–solid (GTGS) reactor used in prior work (I–III on the top) and new configurations used in this work (IV–VI on the bottom); abbreviated as GTGS-X, where X=I–VI and signifies one of the six configurations shown above. The heating element in configurations I-IV is controlled manually using a Variac to compensate for fluctuations in the hot plate temperature (T_{hp}) over time, measured by the thermocouple sandwiched between the quartz thimble hot plate. This allowed the temperature to be maintained within 10 °C of the desired T_{hp} . The hot-plate control box used in GTGS-V and -VI allows for T_{hp} to be held constant within a 2 °C range of the set point temperature. I) GTGS reactor basic configuration, 10 mm hot zone; II) GTGS reactor with 50 mm hot zone; III) GTGS reactor with 10 mm hot zone and equipped with cold finger; IV) GTGS reactor with 50 mm hot zone and equipped with cold finger; V) GTGS-III modified with a digital temperature control box for the hot-plate, equipped with a thermocouple placed between the quartz thimble and hot-plate to supply a direct feedback loop. VI) GTGS-IV modified with a digital temperature control box for the hot-plate, equipped with a thermocouple placed between the quartz thimble and hot-plate to supply a direct feedback loop.

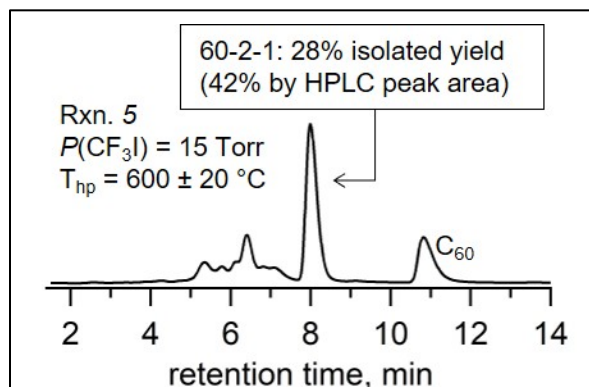


Figure 1.3: HPLC chromatogram of crude product mixture from rxn. 5. A mixture of 1:1 toluene:heptane was used as the eluent at a flow rate of 7 mL min^{-1} on a Bucky-M column; detector set to 300 nm.

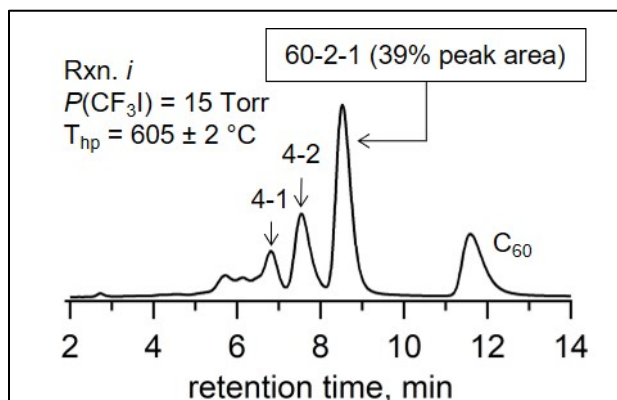


Figure 1.4: HPLC chromatogram of crude product mixture from rxn. *i*. A mixture of 1:1 toluene:heptane was used as the eluent at a flow rate of 7 mL min^{-1} on a Bucky-M column; detector set to 300 nm.

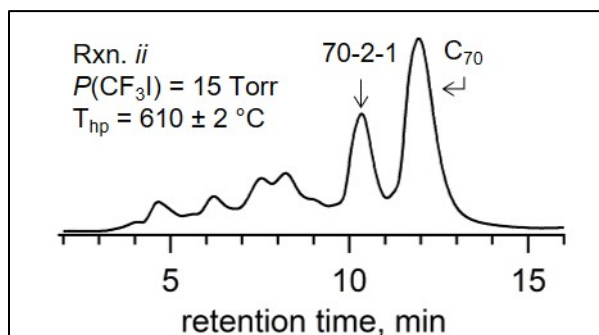


Figure 1.5: HPLC chromatogram of crude product mixture from rxn. *ii*. Toluene was used as the eluent at a flow rate of 5 mL min^{-1} on a Buckyprep column; detector set to 300 nm.

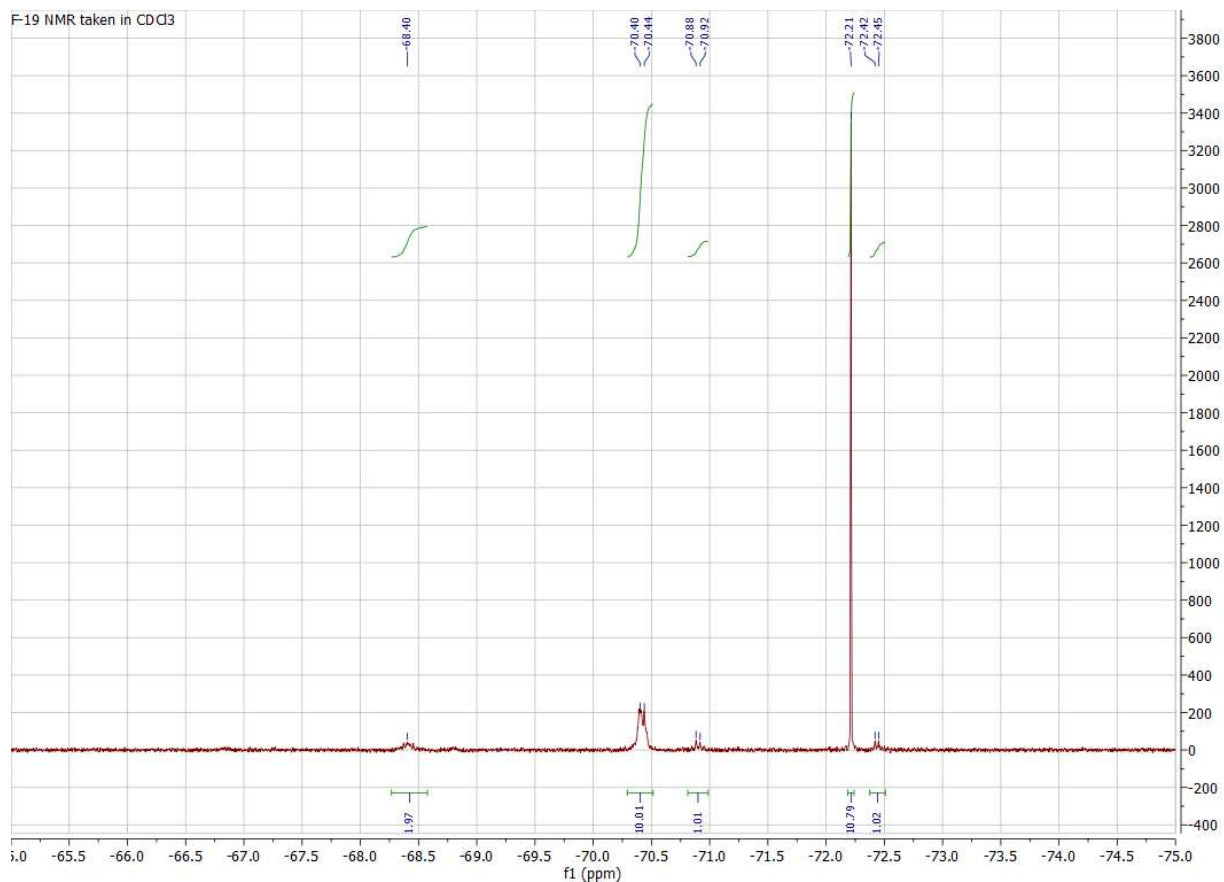


Figure 1.6: ¹⁹F-NMR taken in CDCl₃ of crude product mixture of reaction G, the highest yielding reaction for 60-2-1. Note that the only measurable signals above the baseline are for 60-2-1 (-72.2 ppm), 60-4-1 (-68.4, -70.9, and -72.44 ppm) and 60-4-2 (-70.42 ppm) at a ratio of about 5.4/1.0/2.5, respectively. Thereby the selectivity of 60-2-1 based on NMR for this method is 60.6%.

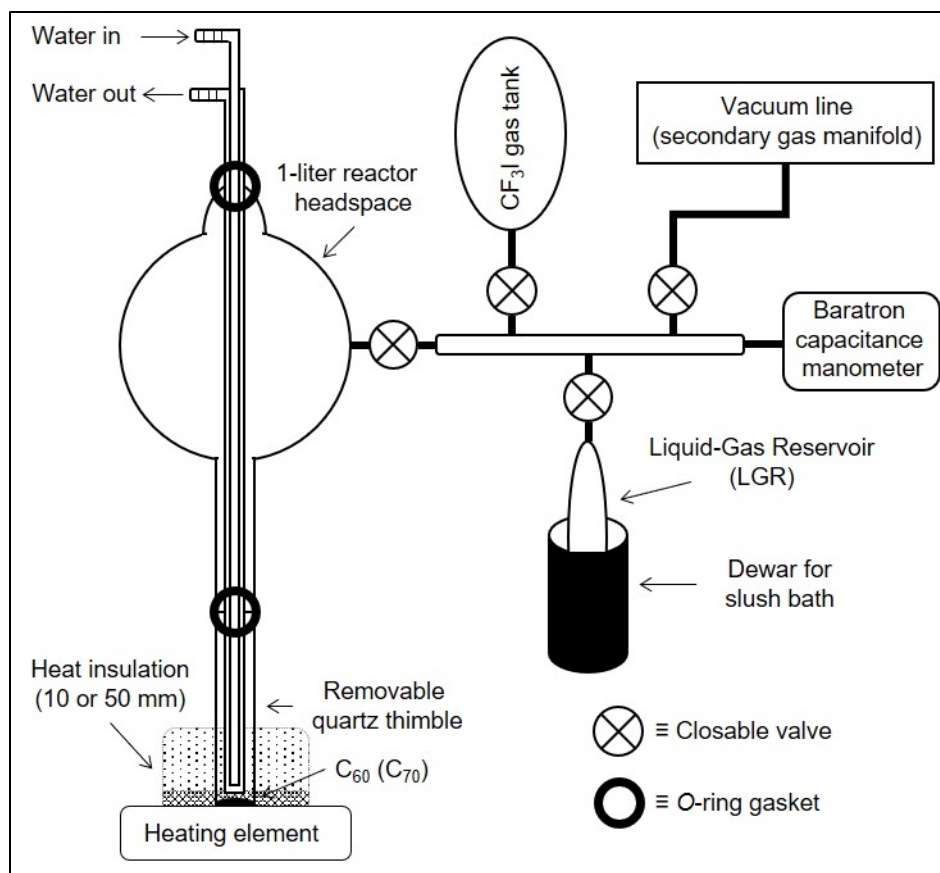


Figure 1.7: Schematic diagram of GTGS reactor equipped with LGR.

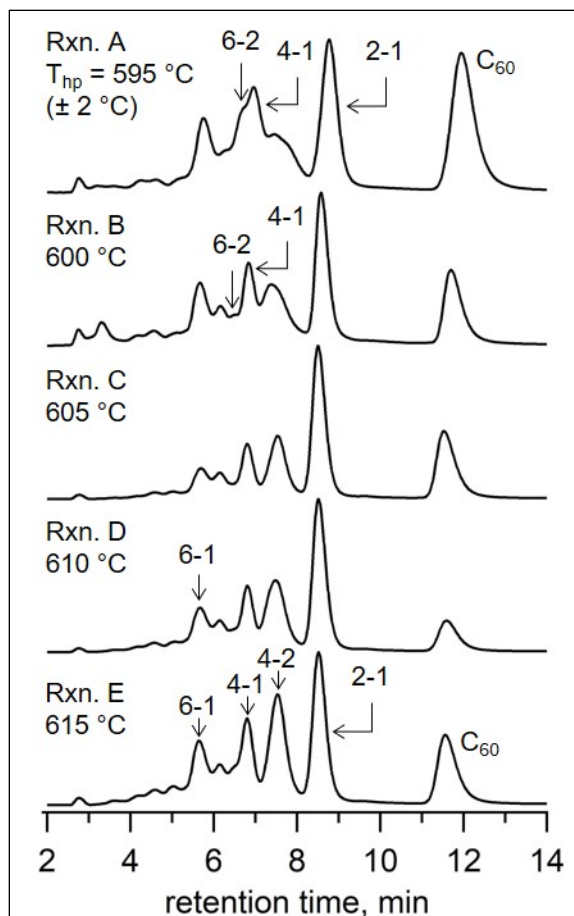


Figure 1.8: HPLC chromatograms of crude product mixtures from rxns. A to E using GTGS-V equipped with a LGR cooled in an CO₂/IPA slush bath; see Table 3 for reaction conditions. Each temperature shown is the measured T_{hp} value ± 2 °C for the respective reaction. A mixture of 1:1 toluene:heptane was used as the eluent at a flow rate of 7 mL min⁻¹ on a Bucky-M column; detector set to 300 nm.

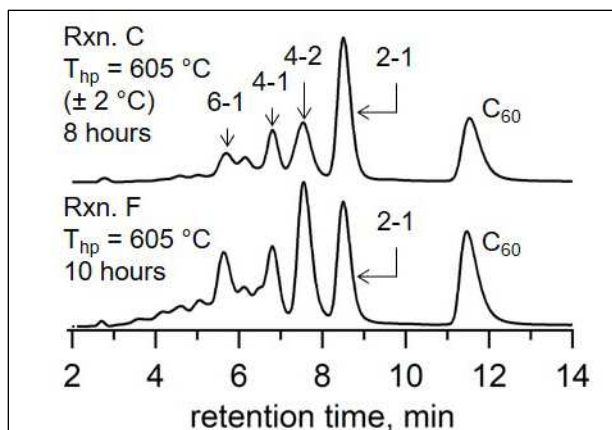


Figure 1.9: HPLC chromatogram of crude product mixtures for rxns. C and F using GTGS-V equipped with a LGR cooled in an CO_2/IPA slush bath; conditions for rxn. C and F are identical except for reaction time (8 and 10 hours, respectively), see Table 3 for reaction conditions. Each T_{hp} value shown is $\pm 2\text{ }^{\circ}\text{C}$ for the respective reaction. A mixture of 1:1 toluene:heptane was used as the eluent at a flow rate of 7 mL min^{-1} on a Bucky-M column; detector set to 300 nm.

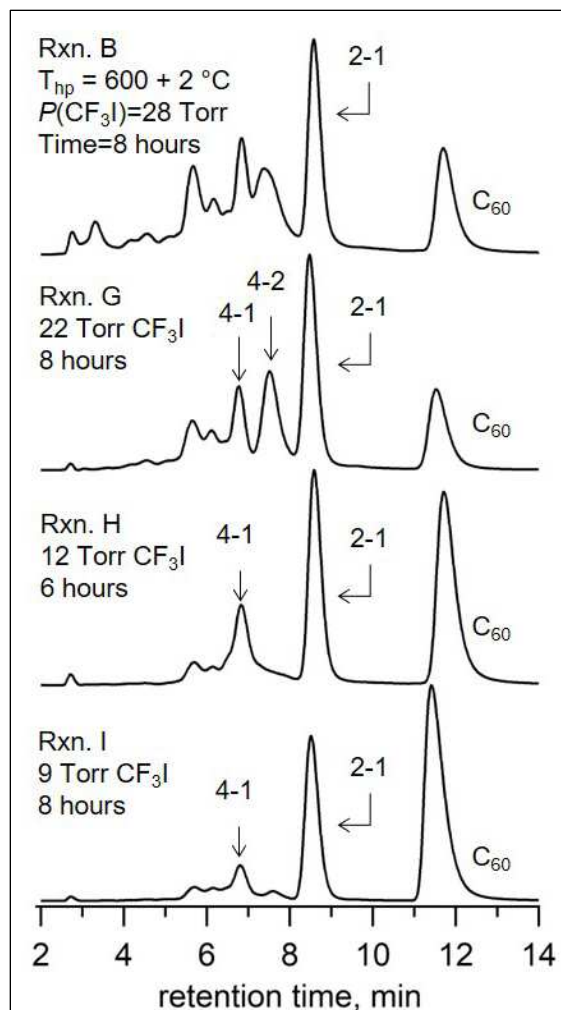


Figure 1.10: HPLC chromatogram of crude product mixtures from rxns. B and G–I using GTGS-V equipped with a LGR cooled in varying slush baths to give different CF₃I vapor pressures; for all reactions shown, $T_{hp} = 600 \pm 2 \text{ }^\circ\text{C}$ (see Table 3 for reaction conditions). $P(\text{CF}_3\text{I})$ is the measured vapor pressure of CF₃I with excess CF₃I condensed in the LGR utilizing various slush baths (see experimental section). A mixture of 1:1 toluene:heptane was used as the eluent at a flow rate of 7 mL min⁻¹ on a Bucky-M column; detector set to 300 nm.

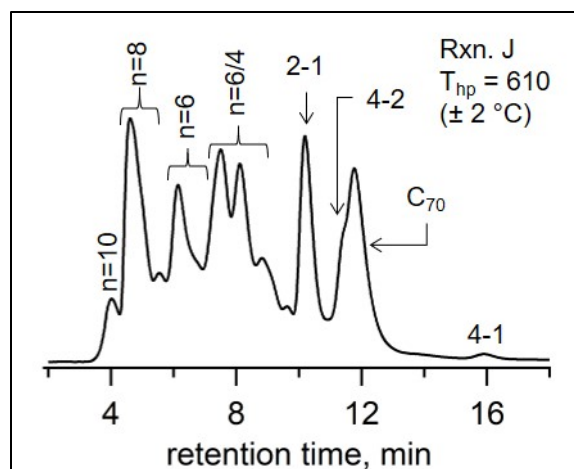


Figure 1.11: HPLC chromatogram of crude product mixtures from rxn. J using GTGS-V equipped with a LGR cooled in an CO₂/IPA slush bath (constant 28 Torr of CF₃I). HPLC chromatogram of products from C₇₀ reaction with CF₃I in GTGS reactor set to 610 C for 8 hours. Toluene was used as the eluent at a flow rate of 5 mL min⁻¹ on a Buckyrep column; detector set to 300 nm.

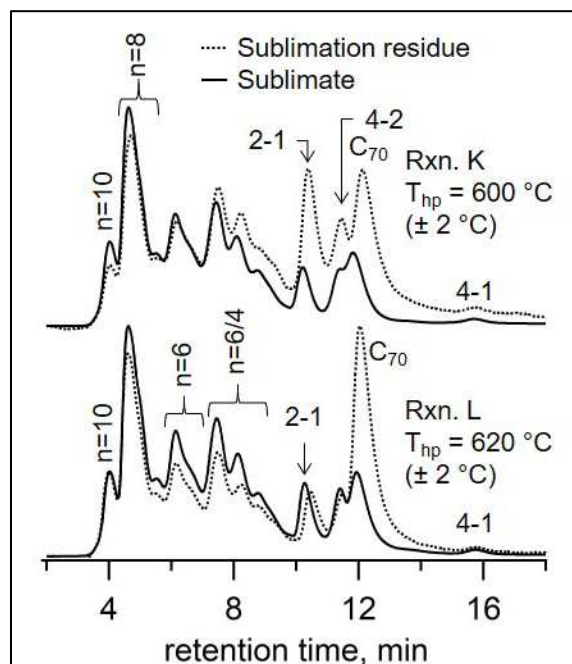


Figure 1.12: HPLC chromatogram of crude product mixtures from rxns. K and L using GTGS reactor configuration V equipped with a LGR cooled in an CO₂/IPA slush bath (constant 28 Torr of CF₃I), showing the difference in the sublimation residue compared to the sublimate of each reaction. HPLC chromatogram of products from C₇₀ reaction with CF₃I in GTGS reactor set to 600 and 620 °C, respectively, for 8 hours each. Toluene was used as the eluent at a flow rate of 5 mL min⁻¹ on a Buckyrep column; detector set to 300 nm.

CHAPTER 1 REFERENCES

1. Ganesamoorthy, R.; Sathiyam, G.; Sakthivel, P., Review: Fullerene based acceptors for efficient bulk heterojunction organic solar cell applications. *Sol. Energy Mater. Sol. Cells* **2017**, *161*, 102-148.
2. Fan, Q.; Méndez-Romero, U. A.; Guo, X.; Wang, E.; Zhang, M.; Li, Y., Fluorinated Photovoltaic Materials for High-Performance Organic Solar Cells. *Chemistry – An Asian Journal* **2019**, *14* (18), 3085-3095.
3. Larson, B. W.; Whitaker, J. B.; Popov, A. A.; Kopidakis, N.; Rumbles, G.; Boltalina, O. V.; Strauss, S. H., Thermal [6,6] → [6,6] Isomerization and Decomposition of PCBM (Phenyl-C61-butyric Acid Methyl Ester). *Chem. Mater.* **2014**, *26* (7), 2361-2367.
4. San, L. K.; Bukovsky, E. V.; Larson, B. W.; Whitaker, J. B.; Deng, S. H. M.; Kopidakis, N.; Rumbles, G.; Popov, A. A.; Chen, Y.-S.; Wang, X.-B.; Boltalina, O. V.; Strauss, S. H., A faux hawk fullerene with PCBM-like properties. *Chemical Science* **2015**, *6* (3), 1801-1815.
5. Kuvychko, I. V.; Whitaker, J. B.; Larson, B. W.; Raguindin, R. S.; Suhr, K. J.; Strauss, S. H.; Boltalina, O. V., Pressure effect on heterogeneous trifluoromethylation of fullerenes and its application. *J. Fluorine Chem.* **2011**, *132* (10), 679-685.
6. Boltalina, O. V.; Popov, A. A.; Kuvychko, I. V.; Shustova, N. B.; Strauss, S. H., Perfluoroalkylfullerenes. *Chem. Rev.* **2015**, *115* (2), 1051-1105.
7. Popov, A. A.; Kareev, I. E.; Shustova, N. B.; Stukalin, E. B.; Lebedkin, S. F.; Seppelt, K.; Strauss, S. H.; Boltalina, O. V.; Dunsch, L., Electrochemical, Spectroscopic, and DFT Study of C₆₀(CF₃)_n Frontier Orbitals (n = 2–18): The Link between Double Bonds in Pentagons and Reduction Potentials. *J. Am. Chem. Soc.* **2007**, *129* (37), 11551-11568.
8. Garner, L. E.; Nellissery Viswanathan, V.; Arias, D. H.; Brook, C. P.; Christensen, S. T.; Ferguson, A. J.; Kopidakis, N.; Larson, B. W.; Owczarczyk, Z. R.; Pfeilsticker, J. R.; Ramamurthy, P. C.; Strauss, S. H.; Boltalina, O. V.; Braunecker, W. A., Photobleaching dynamics in small molecule vs. polymer organic photovoltaic blends with 1,7-bis-trifluoromethylfullerene. *Journal of Materials Chemistry A* **2018**, *6* (11), 4623-4628.
9. Nellissery Viswanathan, V.; Ferguson, A. J.; Pfeilsticker, J. R.; Larson, B. W.; Garner, L. E.; Brook, C. P.; Strauss, S. H.; Boltalina, O. V.; Ramamurthy, P. C.; Braunecker, W. A., Strategic fluorination of polymers and fullerenes improves photostability of organic photovoltaic blends. *Org. Electron.* **2018**, *62*, 685-694.
10. Brook, C. P.; Paul, G.; Viswanathan, V. N.; Satyanarayana, S.; Panidhara, K. M.; Larson, B. W.; Ferguson, A. J.; Pal, A. J.; Ramamurthy, P. C.; Strauss, S. H.; Boltalina, O. V.; Braunecker, W. A., Molecular insights into photostability of fluorinated organic photovoltaic blends: role of fullerene electron affinity and donor–acceptor miscibility. *Sustainable Energy & Fuels* **2020**, *4* (11), 5721-5731.
11. Zhang, F.; Zhuo, Z.; Zhang, J.; Wang, X.; Xu, X.; Wang, Z.; Xin, Y.; Wang, J.; Wang, J.; Tang, W.; Xu, Z.; Wang, Y., Influence of PC60BM or PC70BM as electron acceptor on the performance of polymer solar cells. *Sol. Energy Mater. Sol. Cells* **2012**, *97*, 71-77.
12. Semivrazhskaya, O. O.; Rybalchenko, A. V.; Kosaya, M. P.; Lukonina, N. S.; Mazaleva, O. N.; Ioffe, I. N.; Troyanov, S. I.; Tamm, N. B.; Goryunkov, A. A., Lower trifluoromethyl[70]fullerene derivatives: novel structural data and a survey of electronic properties. *Electrochim. Acta* **2017**, *255*, 472-481.
13. Boltalina, O. V.; Lukonin, A. Y.; Street, J. M.; Taylor, R., C60F2 exists! *Chem. Commun.* **2000**, (17), 1601-1602.
14. Kuvychko, I. V.; Streletskii, A. V.; Shustova, N. B.; Seppelt, K.; Drewello, T.; Popov, A. A.; Strauss, S. H.; Boltalina, O. V., Soluble chlorofullerenes C(60)Cl(2,4,6,8,10). Synthesis, purification, compositional analysis, stability, and experimental/theoretical structure elucidation, including the X-ray structure of C(1)-C(60)Cl(10). *J. Am. Chem. Soc.* **2010**, *132* (18), 6443-6462.
15. Ignat'eva, D. V.; Goryunkov, A. A.; Ioffe, I. N.; Sidorov, L. N., Trifluoromethylation of Fullerenes: Kinetic and Thermodynamic Control. *The Journal of Physical Chemistry A* **2013**, *117* (48), 13009-13017.

16. Troyanov, S. I.; Dimitrov, A.; Kemnitz, E., Selective Synthesis of a Trifluoromethylated Fullerene and the Crystal Structure of C₆₀(CF₃)₁₂. *Angew. Chem. Int. Ed.* **2006**, *45* (12), 1971-1974.
17. Shustova, N. B.; Strauss, S. H.; Boltalina, O. V., High-Yield Synthesis of a Single Asymmetric Isomer of C₇₀(CF₃)₁₀ by High-Temperature Radical Trifluoromethylation. In *Efficient Preparations of Fluorine Compounds*, Roesky, H. W., Ed. Wiley & Sons: Hoboken, New Jersey, 2013; pp 447-449.
18. Kirsch, P., *Efficient Preparations of Fluorine Compounds. Edited by Herbert W. Roesky.* 2013; Vol. 52, p 5914-5914.
19. Whitaker, J. B.; Kuvychko, I. V.; Shustova, N. B.; Chen, Y.-S.; Strauss, S. H.; Boltalina, O. V., An elusive fulvene 1,7,11,24-C₆₀(CF₃)₄ and its unusual reactivity. *Chem. Commun.* **2014**, *50* (10), 1205-1208.
20. Kuvychko, I. V. Chloro-, aryl-, and perfluoroalkylfullerenes. doctoral dissertation, Colorado State University 2009.
21. Reeves, B. J.; Brook, C. P.; Gerdes, O.; Deng, S. H. M.; Yuan, Q.; Wang, X.-B.; Strauss, S. H.; Boltalina, O. V.; Walzer, K., Fluorous Fullerene Acceptors in Vacuum-Deposited Photovoltaic Cells. *Solar RRL* **2019**, *3* (7), 1900070.
22. Pan, C.; Chandrasekharaiah, M. S.; Agan, D.; Hauge, R. H.; Margrave, J. L., Determination of sublimation pressures of a fullerene (C₆₀/C₇₀) solid solution. *The Journal of Physical Chemistry* **1992**, *96* (16), 6752-6755.
23. Dorozhkin, E. I.; Ignat'eva, D. V.; Tamm, N. B.; Goryunkov, A. A.; Khavrel, P. A.; Ioffe, I. N.; Popov, A. A.; Kuvychko, I. V.; Streletskiy, A. V.; Markov, V. Y.; Spandl, J.; Strauss, S. H.; Boltalina, O. V., Synthesis, Characterization, and Theoretical Study of Stable Isomers of C₇₀(CF₃)_n (n = 2, 4, 6, 8, 10). *Chemistry – A European Journal* **2006**, *12* (14), 3876-3889.
24. Iodotrifluoromethane SDS No. 1100J01 [Online]. <http://synquestlabs.com/msds/1100/1100-J-01.pdf> (accessed 3/24).
25. Whitaker, J. B. Preparation, regioselective chemistry, and electronic properties of perfluoroalkylfullerenes. doctoral dissertations, Colorado State University 2000-2019 - CSU Theses and Dissertations, 2013.

CHAPTER 2.

Application of Perfluoroalkylated Fullerenes in Organic Photovoltaics

In this chapter, the photostability study of select organic photovoltaic (OPV) active layers containing high-performance polymer donors blended with either perfluoroalkyl fullerenes or PC₆₀BM as the fullerene acceptor is described. The obtained results are then correlated to both the electron affinity and/or miscibility between the fullerene acceptor and polymer donor of each blend. Sixteen total combinations of active layer blends were studied using PC₆₀BM, 60-2-1 (C₆₀(CF₃)₂), or Faux-Hawk Fullerene (FHF), along with six films of neat high-performance donor polymers (two fluorinated and four non-fluorinated donors). The structures and abbreviated names of each polymer and fullerene are shown in Figure 2.1. Miscibility of blends containing 60-2-1 (C₆₀(CF₃)₂) or PCBM was probed using a combination of time-resolved photoluminescence (TRPL) measurements and scanning tunneling microscopy (STM) imaging. The results of these photobleaching studies and measurements of donor-acceptor miscibility, considered alongside additional photoconductance measurements and preliminary device work, provide new molecular-level optimization insights for improving the long-term stability of OPV active layers.

All films were prepared and photobleached by the author of this dissertation at the National Renewable Energy Lab (NREL) under the supervision of Dr. Wade Braunecker, with the exception of films containing the polymer TPD-CPDT which were prepared and photobleached by graduate student Vinila Viswanathan at NREL. Donor molecules were either purchased or were prepared by Dr. Wade Braunecker at NREL. Both perfluoroalkylated fullerenes, 60-2-1 and FHF, were prepared by the author of this dissertation at CSU (discussed on Chapter 1). Time-resolved microwave conductivity (TRMC) measurements were performed by Dr. Bryon Larson and Dr. Andrew Ferguson at NREL. TRPL and STS/STM measurements were performed by graduate

student Guatam Paul in the laboratory of Prof. Amlan Pal at the School of Physical Sciences, Indian Association for the Cultivation of Science. Spin coated devices were prepared by graduate students Sandeep Satyanarayana and Kumar M. Panidhara in the laboratory of Prof. Praveen Ramamurthy at the Department of Materials Engineering, Indian Institute of Science. Vapor deposited devices were prepared by Strauss Boltalina lab group member Brain Reeves at Heliatek, GmbH in Dresden, DE under the supervision of Dr. Karsten Walzer.

2.1. Introduction

The potential for organic photovoltaics (OPVs) to offer an inexpensive source of renewable energy in the form of lightweight and flexible modules²⁶⁻²⁷ has been driving extensive research efforts in the field.²⁸⁻³⁰ With reports of single junction³¹⁻³² and tandem cells³³ now exceeding 17% power conversion efficiencies (PCEs), along with recent advances in large area printing of OPV modules,^{26, 34} the technology is becoming increasingly commercially viable. However, while encapsulation of the active layer can extend the operational lifetimes of certain OPV systems from days to years,³⁵⁻³⁶ the intrinsic instability of the active layer remains a pertinent obstacle to the wide-spread real-world application of OPV technology.^{34-35, 37} While there are multiple known pathways that contribute to degradation,³⁷⁻⁴⁰ thermal instability of the active layer morphology and irreversible photobleaching of the active layer components are typically the most detrimental.

The most favorable active layer architecture in high performance devices is the bulk heterojunction (BHJ), which exists as a metastable state consisting of interpenetrating domains of an electron donating material (typically a small molecule or conjugated polymer) and an electron accepting material (typically a fullerene derivative, although efficient non-fullerene acceptors are becoming more common³⁰). The BHJ architecture maximizes both the amount of donor–acceptor contacts for charge generation and separation, and produces morphologies that facilitate charge

transport to the electrodes.⁴¹ However, because it is a metastable state, the BHJ is intrinsically susceptible to degradation under operating conditions through phase separation over time. While less common, some blends containing very crystalline polymers have even been observed to phase separate at room temperature when kept in the dark.⁴² In principle, improving the general miscibility between the donor and acceptor should help prevent phase separation, thereby improving the thermal stability of the active layer morphology by corollary.⁴³ In fact, several recent studies have demonstrated correlations between good polymer–fullerene miscibility and critical device metrics, such as improved charge collection efficiency⁴⁴ and fill factor.⁴⁵ Furthermore, by understanding temperature-dependent miscibility, the stability and mixing behaviours of certain components of polymer solar cells have been optimized at processing and operating temperatures.⁴⁶

Perhaps, even more detrimental than phase separation to device performance is exposure of the active layer to light in the presence of oxygen. This can cause the donor polymer to undergo complete irreversible photobleaching within several minutes to a few days if the active layer is not encapsulated.⁴⁷ While encapsulation with various materials is quite effective at slowing (though not eliminating) oxygen and moisture permeation to the active layer,³⁶ the anti-fouling properties, adhesion, and the ability of PV polymeric encapsulants to preclude moisture and oxygen can also degrade over time.⁴⁸ Thus, any improvements to the intrinsic photo-oxidative stability of the OPV active layer would help extend the useful lifetime of a working device.

Currently, the primary mechanism involved in photobleaching of the donor polymer in the presence of oxygen is believed to proceed via a radical pathway.⁴⁹ It has been proposed that both the polymer and fullerene can donate photogenerated electrons to diatomic oxygen to form a superoxide radical anion, and that the radical anion is in turn responsible for degrading the

polymer. Moreover, it has been shown that there is a strong inverse correlation between the electron affinity (EA) of the fullerene acceptor and the rate of photobleaching of the donor polymer in BHJ blends.⁴⁷ In a series of five fullerenes with EAs ranging from 3.77 eV to 4.07 eV, PC₆₀BM had the highest EA and demonstrated the greatest stabilizing effect, regardless of the donor polymer tested. The results implied that the higher the EA of the fullerene, that is the deeper its lowest unoccupied molecular orbital (LUMO), the more stable the polymer donor in the blend became towards photo-oxidation. Noteworthy, among OPV researchers, the term “electron affinity” is not used as strictly defined by the IUPAC (the electron affinity is the negative of the energy change when adding an electron to the neutral species in the gas phase, EA_(g)); instead, the EA value (or alternatively -E_{LUMO}) is calculated from the equation: EA(X) = -E_{LUMO}(X) = E⁺⁰(Fe(Cp)₂) + E_{1/2}^{0/-}, where E⁺⁰(Fe(Cp)₂) is formal potential of Fc⁺/Fc redox couple,⁵⁰ which, depending on the literature source can have values from 4.4 to 5.38 eV. This leads to large discrepancies in the cited EA values for the same acceptor materials. For example, in ref. 47 E⁺⁰(Fe(Cp)₂) = 4.8 eV was used, while in this study, E⁺⁰(Fe(Cp)₂) = 5.1 eV was used as recommended by ref 50 for estimation of EA of acceptors (see Figure 1.1). Thus, EA(PCBM) has two significantly different values, 4.07 eV (ref. 22) and 3.96 eV (this work), respectively, slight variations in the E_{1/2}^{0/-} may either contribute to larger differences or partially cancel them out.⁵⁰ Thus, a more accurate way to compare acceptor strength is to use the EA_(g) when possible, or E_{1/2}^{0/-}, if CV measurements are done under similar conditions.

Trifluoromethylfullerenes (TMFs) are typically more intrinsically photo-oxidatively and thermally stable than PC₆₀BM, which can degrade over time into PC₆₀BM-oxide,⁵¹⁻⁵² or partially decompose and isomerize upon heating into more stable compounds.³ The LUMO energies tend to be much deeper than PC₆₀BM due to strong electron withdrawing nature of fluorine atoms.

Furthermore, LUMO energies of TMFs are tunable through the number of $-CF_3$ additions to a fullerene and their relative locations on the cage (addition patterns), suggesting they are promising materials for improving the stability of the donor polymer in OPV blends. The simplest TMF, 60-2-1 ($C_{60}(CF_3)_2$), has a LUMO energy ca. 220 meV deeper than PC₆₀BM.⁵³ Indeed, the recent collaborative work of the author and NREL showed that 60-2-1 could stabilize the initial rate of photobleaching in small molecule and polymer blends by a factor of 15 relative to PC₇₀BM.⁵⁴ However, phase-separation of 60-2-1 from the small molecule donor material was observed that resulted in dramatic acceleration of the photobleaching rate in less than 24 h of white light exposure. Those results suggest that if there is a substantial difference in miscibility between different fullerenes and a given donor material, the EA of the fullerene alone should not be considered as the only factor determining its stabilizing effect.⁵⁵ Additionally, while many TMFs are known to be highly crystalline materials,⁵⁶ recent work has demonstrated that polymer–fullerene miscibility has more influential effects than the crystallinity of single components on certain optimization parameters in polymer–fullerene solar cells.⁵⁷ Indeed, the miscibility of several high performance donor–acceptor combinations has been correlated with improved device performance.^{44, 58-59} The results suggest that understanding and improving the miscibility of TMFs with common high performance donor materials or their derivatives could be an effective strategy for improving the intrinsic stability of the active layer, as well as the overall efficiency of devices.

Incidentally, fluorinated donor polymers have received notable interest as components of high performance OPV active layers.^{30, 60-64} Fluorine substitution into the polymer backbone has been shown to impart a number of beneficial effects on the material as an OPV donor: strategic fluorination can (i) increase polymer crystallinity,⁶⁵ which in turn can improve both charge mobility⁶⁶ and photostability;⁶⁷ (ii) tune the optoelectronic properties of the donor material;⁶⁸ and

(iii) strongly influence dipole moments in the material that in turn affect charge separation and recombination.⁶⁹ Specific fluorine interactions can also have a strong influence on the solid-state morphology of active layer blends,^{29, 64, 70-72} and they have recently been employed by Braunecker et al. at NREL to influence long-range structural order in other organic conjugated systems such as covalent organic frameworks.⁷³

In this work, several high performance OPV polymers and their structural analogues were studied, shown in Figure 2.1. Copolymers based on thienopyrrolodione (TPD) have been widely studied with a variety of electron rich comonomers, most notably derivatives of benzodithiophene (BDT),⁷⁴ but also comonomers such as cyclopentadithiophene (CPDT).⁷⁵ Depending on the side chains, TPD-BDT copolymers have been optimized above 8.5% PCE with conventional device structures⁷⁶ and TPD-CPDT above 6%.⁷⁵ TPD-BDT polymers are known to be some of the most photo-oxidatively stable copolymers that simultaneously display high OPV efficiencies, while also being widely commercially available. The polymer commercially known as PCE11 (shown in Figure 2.1, see Experimental Section for full name) and its analogues have displayed optimized efficiencies near 11%,⁷⁷ and one can reason that the fluorinated aromatic units in the backbone may serve to improve miscibility with the fluorinated fullerene through well-known phenyl-perfluorophenyl stacking interactions.⁷³ Polymer donors that were structurally related to PCE11 were also synthesized by combining either the fluorinated or non-fluorinated benzothiadiazole (BT) unit with the BDT comonomer. A wide-variety of these BT-BDT materials have been synthesized in the literature, with many of the materials exceeding 5-6% efficiency.⁷⁸

2.1.1. Herein, case studies investigating several combinations of fluorinated and non-fluorinated high-performance donor polymers with PC₆₀BM, 60-2-1, and Faux-Hawk Fullerene (FHF) are presented. The miscibility between components in the blends composed of one of the select

polymers and one of the acceptors, PC₆₀BM or 60-2-1, were probed using time-resolved photoluminescence (TRPL) and scanning tunneling microscopy (STM). The obtained results and the fullerene's respective EA values were correlated with the overall photo-oxidative stability of the active layer and then, with the intrinsic photoconductance of the active layer material. Unoptimized spin-coated and vapor deposited OPV devices were fabricated using 60-2-1 as the acceptor as a proof of concept, and the set of OPV figures of merit were determined. Finally, studies of photobleaching of blends of select polymers with Faux-Hawk Fullerene (FHF) were carried out to get insights into effects of lower EA of this acceptor, and a different chemical nature of its fluorinated functional group than those of 60-2-1 (fluorophenyl vs. CF₃).

2.2. Results and Discussion

2.2.1. Photobleaching of neat films and blends with PC₆₀BM and 60-2-1

For each polymer and fullerene used in this study, non-encapsulated films of neat polymer and blends of 1:1 by mass of polymer–fullerene were aged in air under a quad array of tungsten halogen lamps with intensity ~ 0.7 suns (70 mW/cm²). The surface temperature of the substrates under the lamp was recorded as 60 °C. The spin coating procedures were optimized for each blend (as described in the Experimental Section) such that each film had an initial absorbance of ca. 0.3 absorbance units at the red-edge λ_{max} (see Figure 2.2 for a representative example); absorbance spectra were measured periodically over the course of several days to weeks. Absorbance data at the red-edge λ_{max} for each film was used to evaluate the time required to bleach each film to 80% and then 60% of its initial absorbance (T_{80} and T_{60} , respectively). The results were repeated in triplicate, with average degradation lifetimes recorded in Table 2.1. The overall decrease in the absorbance spectrum, and for some polymers the blue shift in λ_{max} , is consistent with the loss of conjugation in the polymer backbone that occurs during photodegradation of the material.⁴⁹

Before discussing important nuances in the photobleaching data, the following general observations should be made about the results listed in Table 2.1. First, in all twelve blends, the addition of a fullerene to the polymer resulted in improved stability over the neat polymer system. Second, the apparent rates of degradation can change dramatically between the T_{80} and T_{60} , either stabilizing or accelerating depending on a given sample (*vide infra*). Indeed, recent literature results have shown that phase separation of the polymer and fullerene can happen with time; this phenomenon has been independently observed both with blends of 60-2-1⁵⁴ and in systems with PCE11.⁴² Finally, in some cases the fluorinated fullerene acts as a more efficient stabilizer of the polymer towards photodegradation, and in other cases PC₆₀BM is more efficient.

The data on photobleaching behavior of the three TPD-based polymers (-BDT(OEH), -BDT, and -CPDT, entries 1-3 in Table 2.1) are shown in the top of Figure 2.2. The graphs show comparison of the decrease in fraction of light absorbed (FA) over time for the studied systems. The behavior varied significantly from one system to another for both the neat samples and the blends. For example, with regards to the neat polymer films, the TPD-CPDT bleached approximately one order of magnitude faster than both TPD-BDT-based polymers. Though it cannot be said conclusively why the CPDT unit is intrinsically less stable, the α -hydrogens on the side chains of conjugated OPV monomers are known to be particularly susceptible to degradation by free radical abstraction,⁴⁷ and such α -hydrogens are not present in either BDT monomer unit like they are in CPDT. Regarding the blends, there was a marked difference in the stabilizing effects of the two fullerenes amongst these TPD-polymers. For example, the TPD-CPDT blend with 60-2-1 was five times more stable than a blend with PC₆₀BM (determined from T_{80}), as might be anticipated from the lower lying LUMO of the fluorinated fullerene based on all the aforementioned observed trends. However, the TPD-BDT blend with 60-2-1 was only marginally

more stable towards photodegradation than a blend with PC₆₀BM, with a T_{80} of 46 h vs. 41 h with PC₆₀BM; for the TPD-BDT(OEH) blends, the trend was actually inverted, with PC₆₀BM being a more effective stabilizer than 60-2-1. Based on this observation, it was hypothesized that the TPD-BDT(OEH) may not be as miscible with 60-2-1 as it is with PC₆₀BM, which is discussed in more detail in subsequent sections.

When comparing the photobleaching behavior of BT-based materials over time, shown in the bottom of Figure 2.2, the most important observation, perhaps, was that for both fluorinated donors (FBT-BDT and PCE11), 60-2-1 was a more efficient stabilizer of the polymer towards photodegradation than PC₆₀BM by a factor of two to three, whereas all the other polymers investigated (with the exception of TPD-CPDT) saw either no or only a small improvement in the photostability with 60-2-1 relative to PC₆₀BM. Furthermore, the relative rate of photobleaching of PCE11 in the PC₆₀BM blend appeared to increase over time relative to the 60-2-1 blend when T_{60} and T_{80} values are compared in Table 1 (or look at Figure 2.2 which shows how the photobleaching dynamics for PCE11 films change past the T_{60} value). Indeed, PCE11 is known to phase separate with time from PC₆₀BM, even when kept in the dark as a result of thermally driven phase separation.⁴² These results suggest the PCE11–60-2-1 system may remain more intimately blended relative to PCE11–PC₆₀BM. For the non-fluorinated BT-BDT polymer, the opposite trend was true; the PC₆₀BM blend was *slightly* more stable than that with the 60-2-1, although both had significant stabilizing effects.

Overall, the photobleaching behavior in these blends is complex and cannot be simply rationalized based solely on the relative electron affinity of the two fullerenes. In reality, it is difficult to disentangle the effects of photo and thermal stability of the blends. It was observed in prior research that small amounts of photo-induced degradation of OPV donors can lead to phase

instability that, in turn, accelerates additional photodegradation.⁵⁴ However, one can hypothesize that varying degrees of intimate mixing of the components in these blends were, at least partially, responsible for the trends and behavior observed. Thus, photoluminescence quenching measurements, presented in the next section, were used to tease out foundational molecular insights into these phenomena and subsequently investigate the morphology of several representative blends using scanning tunneling microscopy imaging.

2.2.2. Time-resolved photoluminescence (TRPL) quenching of PC₆₀BM and 60-2-1 blends

Photoluminescence (PL) quenching has previously been used to study polymer–fullerene intercalation,⁷⁹ relative fullerene distributions in mixtures of amorphous and semicrystalline polymers,⁸⁰ and, most recently, by the author and his NREL collaborators to probe the phase separation of a small molecule donor and 60-2-1 with time during a photobleaching experiment.⁵⁴ While it is acknowledged that PL quenching is only an indirect measurement of miscibility, stronger PL quenching is generally associated with smaller domain sizes and more intimate mixing,⁸¹ which one can contend would help explain the photobleaching data. In light of this, time-resolved PL measurements were performed to probe the miscibility of each donor and acceptor by comparing the relative degree of PL quenching between PC₆₀BM and 60-2-1 for each polymer used in this study. The measurements for a given polymer series were normalized by the number of excitation pulses and then by the fraction of absorbed light at the excitation wavelength (details for each polymer and further discussion are given in the Experimental Section). PL decays were obtained by integrating the total PL counts over the full PL spectrum and plotting *vs.* time (Figure 2.6). The quenching efficiencies were then calculated from the neat and blend PL decays integrated between 0 and 2 ns and are summarized in Table 2.2.

Let us focus first on the quenching efficiencies of the TPD-based polymers shown in Figure 2.6, which were all greater than 98% efficient for both PC₆₀BM and 60-2-1. Interestingly, for the TPD-based polymers, the increased stabilization toward photobleaching is correlated with the greater PL quenching efficiency. For example, in the case of TPD-BDT(OEH), the polymer was more stabilized toward photodegradation by PC₆₀BM than by 60-2-1, and the PL quenching by PC₆₀BM was more efficient for this polymer than by 60-2-1 (99.7 vs. 99.2%, respectively). In contrast, the other two TPD polymers were more stabilized by 60-2-1 than by PC₆₀BM, and PL quenching by 60-2-1 was more efficient in both cases.

Now when analyzing PL data for the three BT-based polymers, a similar trend is observed. The upper right portion of Figure 2.6 shows that the PL of PCE11 was moderately more efficiently quenched by 60-2-1 compared to PC₆₀BM, noting that 60-2-1 had the greater stabilizing effect on this polymer. Moreover, PC₆₀BM was more stabilizing for BT-BDT and was a far more efficient quencher of that polymer's PL. Finally, the data for FBT-BDT might be considered an outlier, as 60-2-1 had the greater stabilizing effect on FBT-BDT, while the quenching efficiencies with 60-2-1 were slightly lower (98.2% vs. 98.5% with PC₆₀BM). However, when comparing the relative quenching data for FBT-BDT and BT-BDT, it is observed that the substitution of fluorine into the polymer backbone dramatically improved quenching efficiency with 60-2-1, from 92.4 to 98.2%; consistent with the photobleaching results that 60-2-1 had a greater relative stabilizing effect on FBT-BDT than BT-BDT compared to PC₆₀BM.

The results for these twelve systems strongly suggest that a full rationalization of the photobleaching data requires consideration of both the electron affinity of the fullerene and the relative miscibility of the polymer–fullerene blend. These results are coupled with a more direct probe of morphology, microscopy studies, in the next section.

2.2.3. Scanning tunneling spectroscopy/microscopy of select PC₆₀BM and 60-2-1 blends

Scanning tunneling spectroscopy (STS) coupled with scanning tunneling microscopy (STM) is a powerful technique for probing nanoscale morphology in semiconductor materials.⁸²⁻⁸⁵ Indeed, the STS/STM technique has been employed to determine the band edges of nanostructures,⁸⁴ to map the band structure in a pn-junction with nanometer resolution,⁸⁶ to investigate cross-sectional interfaces in model BHJ OPV systems,⁸⁷ and was recently used by Braunecker et al. at NREL to probe the influence of additives on polymer and fullerene domain size in an OPV active layer.⁴¹ With this technique, transient conductance (dI/dV) images can be used to differentiate semiconductor components based upon their electronic levels and localized density of states (DOS), *i.e.*, polymer and fullerene HOMO and LUMO levels. The materials in a BHJ can therefore be mapped throughout a given sample. The bias-dependent localized DOS distributions obtained with tunnel conductance (dI/dV) images for blends of PCE11 and BT-BDT with the two fullerene derivatives were examined. Since these measurements are non-trivial, it was necessary to down select from twelve polymer–fullerene systems to four (blends with PCE11 and BT-BDT). These particular systems were chosen because (1) they represented the two most stable polymers investigated in this work, and because (2) one polymer (BT-BDT) was more stabilized by PC₆₀BM and the other (PCE11) was more stabilized by 60-2-1.

As the contact and high internal resistances of thick (~100 nm) active layers typically employed in OPV devices are known to skew STS/STM results, morphologies of ~10 nm thick active layers were investigated and cast at higher spin speeds from stock solutions of the same concentration as those used for the preparation of blends for photobleaching. The neat films of the polymers were first analyzed by STS at various positions throughout the films in order to ascertain the local DOS and to locate the HOMO and LUMO levels. To obtain a single measurement, the tip was held at a

fixed position and sample bias was swept from 2.5 V to -2.5 V while the differential tunnel conductance (dI/dV) spectrum was measured simultaneously using a lock-in amplifier. This allowed for the measurement of the dI/dV versus voltage plot that would correlate to the nanoscale electronic levels. As the sample is biased in both the negative and positive voltage range, the first peaks nearest to 0 V in both bias directions in the dI/dV spectrum correspond to occupied and unoccupied states, respectively. For neat materials, dI/dV curves afford accurate information regarding the relative positions of HOMO and LUMO energy levels with respect to the Fermi level. For example, Figure 2.7 shows histograms of the distributions of local DOS of BT-BDT HOMO and LUMO levels. Each histogram (represented with bars) was compiled from dI/dV spectra from at least 100 different measurements/positions. The STS characteristics of the pure materials then allowed for distinguishing between donor and acceptor components in the blends based on their energy levels. To analyze the dI/dV images of BHJ's in the meaningful manner, one needs to know the energy levels of at least one component (donor or acceptor) of the BHJ. Figure 2.7c represents the energy levels (HOMO and LUMO) of the donor polymers (PCE11 and BT-BDT) of the four selected polymer–fullerene systems obtained from Figure 2.7a and Figure 2.7b.

Figure 2.8 illustrates STM dI/dV images corresponding to blends prepared with PCE11 (left) and BT-BDT (right). The data were recorded at a constant sample bias of -0.95 V to view BT-BDT and -0.70 V for PCE11 in the BHJs, selected to specifically probe the HOMO level of the polymers. At these biases, conductance will by and large occur through the donor polymer, thus allowing for the visualization of the polymer donor domains as brighter (magenta) regions. The green regions in these images represent domains with very low DOS, and, hence, can be considered fullerene-rich, while the intermediate DOS in the blue regions are likely to represent domains mixed with polymer and fullerene. As the aim is to correlate this morphology data with the

measured PL data from the quenching experiments, described in the previous section, the focus and discussion hereafter will be on the qualitative size and clustering behavior of the polymer (magenta) domains in Figure 2.8, starting first by comparing the differences between two different fullerenes for a given polymer.

The image corresponding to the PCE11:PC₆₀BM film in the lower left corner of Figure 2.8 suggests that both the polymer and fullerene-rich domains are more clustered in comparison to the PCE11:60-2-1 film in the upper left corner, where domains are smaller and appear more evenly dispersed. Quantitative analysis of the images reveals that the magenta (polymer rich) regions represent 1.9% of the area of the PCE11:PC₆₀BM images, whereas the polymer-rich regions represent just 1.2% of the area in the PCE11:60-2-1 images. While those differences are small, the results are consistent with the PL quenching data that indicates 60-2-1 is the more efficient quencher for this polymer. A comparison of the polymer-rich domains in the two BT-BDT images shows the opposite trend; the larger magenta (polymer) domains represent 2.7% of the area in the BT-BDT:60-2-1 film, compared to just 0.4% in BT-BDT:PC₆₀BM. This data is also consistent with the PL quenching efficiencies, as PC₆₀BM was found to be a far more efficient PL quencher than 60-2-1 in films with BT-BDT (98.4% with vs. 92.4%, respectively).

Now let us compare the difference between the two polymers for a given fullerene. PC₆₀BM quenches the PL of BT-BDT (98.4%) more efficiently than that of PCE11 (95.6%), and, as would be anticipated from that data, polymer-rich domains of BT-BDT are smaller (compare magenta spots in the lower two images of Figure 2.8). Similarly, 60-2-1 quenches the PL of PCE11 (97.0%) more efficiently than that of BT-BDT (92.4%), and domains of PCE11 are clearly smaller (compare magenta spots in the upper two images Figure 2.8). The STM images are thus fully consistent with the PL quenching data and the photobleaching trends, where 60-2-1 is more

efficient at stabilizing PCE11 toward photodegradation, and PC₆₀BM is more efficient at stabilizing BT-BDT. These data support the hypothesis that a full rationalization of the photobleaching data requires consideration of the electron affinity of the fullerene as well as the relative miscibility of the polymer–fullerene components in the blend.

2.2.4. Photoconductance of select of PC₆₀BM and 60-2-1 blends

Time-resolved microwave conductivity (TRMC) is a useful technique for probing and studying photoinduced charge generation in OPV blends.⁸⁸⁻⁹¹ The TRMC setup used here, along with the general methodology and principles for TRMC, have been thoroughly discussed elsewhere.⁹²⁻⁹⁴ Furthermore, TRMC has recently been used to screen new photovoltaic materials for their potential performance in OPV devices.^{68, 94-96} Here, six different samples on quartz substrates, including the neat polymers of PCE11 and BT-BDT along with their blends of PC₆₀BM and 60-2-1, were prepared in order to probe the intrinsic photoconductance properties of these materials. The optical density of each film was relatively low (between 0.1 and 0.2 absorbance units), with the films being slightly thinner than those used for the photodegradation experiments. The principal figure-of-merit (the ‘yield-mobility product’, $\phi\Sigma\mu$), derived from the microwave data is proportional to the product of the sum of the local mobilities ($\Sigma\mu$) of free carriers and the overall yield of free charge carrier generation (ϕ) per absorbed photon.⁹² While $\phi\Sigma\mu$ is a complex parameter, the relative miscibility of donor polymers and fullerene acceptors will necessarily influence the generation of free charge carriers, and in this work, it was investigated how the TRMC figure of merit might thus be influenced in these different blends.

The TRMC figure of merit was recorded over four orders of excitation intensity, shown in Figure 2.9, which allows the analysis of the transition from a regime where higher order processes influence the measured signal towards intensity-independent recombination processes as the

excitation intensity is decreased. The $\phi\Sigma\mu$ values at lowest absorbed photon flux of blend films show between one and two orders of magnitude increase relative to the neat polymer, indicating a high yield of free charges per photon absorbed when the acceptor is present. As noted in a previous section, PL quenching in the BT-BDT-PC₆₀BM blend was significantly more efficient than in the blend with 60-2-1 (98.4 vs. 92.1%, respectively). Those PL results appear to correlate with the more pronounced TRMC signal in BT-BDT-PC₆₀BM blends at all excitation intensities, which would be consistent with more efficient exciton dissociation in that blend. For the case of fluorinated PCE11 blended with either PC₆₀BM or 60-2-1, the latter appears to reach the intensity-independent $\phi\Sigma\mu$ regime at almost two orders of magnitude higher in excitation intensity than the former. While the exact origin of this phenomenon is unclear, it may be due to enhanced mixing of the 60-2-1 within PCE11 that, in turn, favors more exciton to carrier conversion as opposed to higher order exciton quenching processes that can limit ϕ .⁹⁷ The fact that the peak $\phi\Sigma\mu$ product is higher at the lowest intensity for the PC₆₀BM blend may be due to a higher electron mobility contribution to the signal compared to 60-2-1.⁹⁸

For both blends of PCE11, the peak $\phi\Sigma\mu$ is amongst the highest values that have been recorded for OPV films in the literature.⁶⁸ The BT-BDT polymer blends, on the other hand, are between one and two orders of magnitude lower than the signals for PCE11. The general magnitude of the TRMC figure of merit for both PCE11 and BT-BDT polymers are thus consistent with literature device efficiencies attained for PCE11/PC₆₀BM near 11%⁷⁷ and for derivatives of BT-BDT/PC₆₀BM closer to 3-4%.⁷⁸ The fact that the blend of PCE11 with 60-2-1 exhibits a generally comparable response to that with PC₆₀BM in terms of overall magnitude is quite notable. That promising result suggests there is nothing intrinsically limiting in the 60-2-1 blend that would prevent efficient devices from being constructed with this fullerene as the acceptor.

That being said, TRMC does not probe differences in open circuit voltages (V_{oc}), which will necessarily be lower for a given polymer in devices with 60-2-1 vs. PC₆₀BM as the LUMO of the former is ca. 220 mV deeper. While extensive device optimization with 60-2-1 was outside the scope of this work, preliminary device data was obtained and is presented in the following section.

2.2.5. OPV Device Work with 60-2-1

2.2.5.1. Spin Coated OPV Cells

BHJ devices were initially fabricated using PCE11–PC₆₀BM blends to understand the necessities and difficulties of processing PCE11. These processing conditions resulted in an active layer thickness of 300 nm. The JV characteristics and EQE for the best device are shown in the top of Figure 2.12. Device efficiencies near 9% were achieved (Table 2.3), approaching the record literature efficiencies reported near 11% PCE for this polymer.⁷⁷

The optimal processing conditions for PCE11–PC₆₀BM were then used for devices with 60-2-1 as acceptor. Initial devices with 60-2-1 and PCE11 gave a low 0.26% PCE, highlighting the need to develop a unique set of processing conditions for this blend. It was attempted to use thinner active layers by spinning a polymer concentration of 5 mg/mL at a rate of 2200 rpm. The resulting absorber thickness was 50–60 nm and hence resulted in low photocurrents. However, device efficiencies improved to 1.6% (Table 2.3). Attempts to spin coat PCE11 and 60-2-1 blends to even thinner active layers by further increasing spin speeds and/or reducing the concentration of polymer and fullerene stock solutions generally resulted in poor film quality that did not further improve device efficiency. The results ultimately suggest that the thickness dependent morphology of 60-2-1 blends will be an important parameter for spin-coating to optimize in future work when new polymers with deeper energy levels are designed and tailored for application with 60-2-1.

2.2.5.2. Vapor Deposited OPV Cells.

BHJ devices with 60-2-1 or C₆₀ as the acceptor and the molecular donor DCV5T-F₂(3,3)-Me₄(2,2,4,4) (structure shown in Figure 2.14) in the active layer were prepared and their device figures of merit are shown in Table 2.5 (cells B1-B6). When comparing cells B5 and B6 in Table 2.5, there was no a decrease in fill factor (FF). Interestingly, both devices have significantly higher V_{oc} than predicted by the difference in HOMO and LUMO of the donor and acceptor, respectively (see Table 2.4 for DFT calculated HOMO/LUMO values of donor molecule). This allowed for good PCEs of 3.5 and 3.8 % in cells B5 and B6. The performance characteristics of these devices can be regarded as particularly promising when considering that the reported data here are largely for un-optimized devices, i.e., fluorinated acceptor simply replaced C₆₀ in the cells that were optimized for the latter. Therefore, losses in the voltage and resulting PCE can be mitigated by judicious choice of donor material with lower HOMO levels (B1 and B2). The only optimization condition tested was the temperature of the substrate during deposition of the BHJ layer, where it was found that deposition at 50 °C leads to better FF, V_{oc}, and J_{sc} than deposition at 70 °C.

Planar Hetero Junction (PHJ) devices with 60-2-1 or C₆₀ as the acceptor and DCV5T-F₂(3,3)-Me₄(2,2,4,4) as the molecular donor in the active layer were also prepared and their device figures of merit are shown in Table 2.6 (cells P1–P4). In the PHJ architecture, the layers of the donor and acceptor are not mixed as in BHJ, so the D/A interface is smaller, it is therefore not surprising the OPV figures of merit are lower. In addition, the donor material has been designed originally to match energetically with C₆₀ (as evidenced by high V_{oc} value in Table 2.6) and not with lower LUMO 60-2-1. Overall, the highest PCE achieved in these tests for 60-2-1 -based OPV cells was ca. 4%, i.e., 80% lower than that of C₆₀-based cells.

It should be noted that while these 60-2-1 devices underperformed their PC₆₀BM and C₆₀ counterparts in spin-coated and vapor deposited devices, respectively, the polymer and small

molecule donors have not yet been optimized as high-performance donors for use with low-LUMO 60-2-1 acceptor.

Nevertheless, the TRMC results above suggest that 60-2-1 possesses sufficient intrinsic photoconductance properties to produce high efficiency devices, assuming it is blended with polymers or small molecules with appropriately deep energy levels to produce high open circuit voltages. To the best of the author's knowledge, 60-2-1 is one of very few fullerene derivatives that can be successfully used for vapor-deposited photovoltaic cell fabrication, which allows for a more precise control of the morphology of active layers compared to the solution-based spin-coating methods.

2.2.6. Photobleaching of blends with Faux-Hawk Fullerene

In addition to measuring the stabilizing effect of the TMF 60-2-1 compared to PC₆₀BM, four select polymers of the six tested above were also blended with faux-hawk fullerene (FHF), (see molecular structure in Figure 1.1) and photobleached over time. The EA_(g) of FHF (2.81 eV)⁴ is almost right between PC₆₀BM (2.63 eV)⁹⁹ and 60-2-1 (2.92 eV)¹⁰⁰ and, one can hypothesize that it should, therefore, have a stabilizing effect on the donor polymer somewhere between the effect of the other two fullerenes, all other parameters in the blend being equal. While limitations of instrument availability and project time constraints did not allow for more complete investigation, including the device performance or miscibility of these FHF blends by STM-STS, as was done for 60-2-1 (see sections 2.2.3 and 2.2.4 above) it is, nevertheless, possible to infer valuable information from the photobleaching data described in this section and test the above hypothesis of the EA effect on stability. It is noteworthy that for the polymer blends with FHF tested in this work, it was observed that, in general, films were visibly less uniform in appearance than blends prepared with PC₆₀BM or 60-2-1 with the same polymers. Subsequently, most FHF blends initially

had a more rapid rate of photobleaching compared to either of the two other fullerenes tested: note a rapid drop in absorbance within the first few hours, shown in Figure 2.10.. This was then followed by a much more gradual and almost linear rate of photobleaching for the next few days or weeks. It is hypothesized here that this is due to the FHF films not being well blended, forming more regions of isolated polymer that photobleached at a rate similar to that of neat polymer films.

After this initial drop in absorbance, which is observed, to some extent, for all blends analyzed in this study, the degradation rates for FHF blends depicted in Figure 2.10 notably slowed: suggesting that the remaining polymer in the blend is intimately mixed with the respective fullerene, stabilizing the polymer from photobleaching. This “degradation rate” is measured as the slope of the best fit line for absorbance measurements of a given blend taken over time, depicted in Figure 2.11.

When comparing photobleaching of the FHF blends with the two fluorinated polymers, FBT-BDT and PCE11, and similar blends with PCBM and 60-2-1 (see top of Figure 2.11) there appears to be a clear correlation between the increasing EA of each fullerene and the stabilizing effect it has on the polymer. Indeed, in the case of both fluorinated polymers, PC₆₀BM is the least stabilizing, and 60-2-1 is the most stabilizing, while FHF is in-between the two. It is exactly what would be expected based on the fullerene’s EA alone.

Interestingly, this trend does not hold true when comparing the two non-fluorinated polymers BT-BDT and TPD-BDT(OEH), shown at the bottom of Figure 2.11. In these blends, FHF is actually the least stabilizing acceptor for either polymer tested, while PC₆₀BM was either the most stabilizing or essentially the same as 60-2-1 (as is the case for BT-BDT). This further suggests that the non-fluorinated polymers are not as miscible with FHF compared to PC₆₀BM and subsequently are not as stabilized by FHF. At the same time, fluorinated polymers are more miscible both with

FHF and 60-2-1 (compared to their non-fluorinated polymer analogs) and are more stabilized when blended with them compared to PC₆₀BM. Thus, the empirical observation that stronger acceptors are better for photostability of the blends can only apply when good miscibility of donor and acceptor is achieved.

2.3. Conclusions

While a significant research focus in the field of OPV over the last decade has revolved around improving device efficiencies, this work aims to advance the state of OPV science by providing molecular insight and more foundational understanding around the photostability of OPV donor–acceptor blends. It was demonstrated that rationalizing complex photobleaching behaviour ultimately required consideration of the electron affinity of the fullerene *as well as* the relative miscibility of the polymer–fullerene blend. The ability of 60-2-1 (and FHF) to stabilize certain donor materials towards photodegradation, to blend well with fluorinated (and even certain non-fluorinated) polymers, and to quench excited states efficiently was thoroughly demonstrated and correlated with structure-property relationships amongst several polymer donor and fullerene acceptor combinations. The methodology and guiding principles in this work set the stage for a new paradigm in OPV materials development, including the design of more intrinsically oxidatively stable donor materials whose LUMO levels are otherwise too deep to work in conjunction with PC₆₀BM or other traditional acceptors in an OPV device, but whose energetics would make 60-2-1, other fluorinated fullerenes,⁵⁶ or fluorinated small molecule acceptors¹⁰¹ more optimal substitutes.

2.4. Experimental Section

2.4.1. Materials

60-2-1 (also referred to as $C_{60}(CF_3)_2$) was synthesized according to literature procedure⁵ and purified to >99% purity as determined by HPLC, ^{19}F NMR, and APCI-MS. PC₆₀BM was purchased from Nano-C, Inc., was >99% pure, and was used without further purification. Poly[(5,6-difluoro-2,1,3-benzothiadiazol-4,7-diyl)-alt-(3,3''-di(2-octyldodecyl)-2,2';5',2'';5'',2'''-quaterthiophen-5,5'''-diyl)], also known as PCE11 ($M_n = 74$ KDa, $M_w/M_n = 1.76$) was purchased from California Organic Semiconductors, Inc., as were the stannylated BDT monomer and brominated FBT units. The brominated BT unit was purchased from TCI. BT-BDT and FBT-BDT copolymers in Figure 1 were synthesized from these commercially available monomers according to literature procedures.⁷⁸ TPD-BDT ($M_n = 14$ KDa, $M_w/M_n = 2.74$) and TPD-BDT(EH) ($M_n = 12$ KDa, $M_w/M_n = 2.88$) were purchased from Ossila. TPD-CPDT was synthesized according to a literature procedure.⁷⁵ All other reagents employed in this study were obtained from commercial sources at the highest available purity and used without further purification.

2.4.2. Photobleaching

2.4.2.1. Sample preparation and ageing.

Details of the photobleaching apparatus are provided elsewhere.¹⁰² All films were cast in air onto 1×2 cm² quartz substrate, previously cleaned by brushing with detergent followed by sequential ultrasonication in acetone and isopropanol. Unless otherwise stated, films were cast from 70 μ L solutions of 1:1 chlorobenzene/*o*-dichlorobenzene, at a spin rate of 600 RPM for 30 s followed by 2000 RPM for another 60 s. The films were then kept in the dark overnight to dry. Solutions containing 12 mg/mL were used to cast films of neat-polymer; this was also used to mix

with equal amounts of fullerene solution of the same concentration (12 mg/mL in this case) for casting their respective film-blends. Each solution was heated and stirred for at least 1 h prior to casting to ensure all components were dissolved and well blended. Films containing the same polymer were prepared on the same day and photobleached together—after drying overnight in the dark—on a rotating spinner to account for differences in the lamp output; allowing each film to be exposed to the same conditions and intensity of light throughout the aging process. This allowed for a maximum of twelve films to be photobleached at the same time. Radiative heating from the lamps kept the samples at a temperature of 65 °C. Films were prepared to give an initial max absorbance of 0.2–0.3 for each film tested in this study. Alteration to the general procedure just described are listed below for the given polymer blend, the goal being to maintain a similar initial absorbance value between all films tested. Unless otherwise stated, three films of each neat polymer and blend were prepared and the absorbance measurements were taken at three distinct positions (of each of the three films), giving nine data points for each film type at each time interval the absorbance was measured at. Films were photobleached until there was no substantial change in the absorbance value or after 30 days of photobleaching, whichever process was sooner.

2.4.2.2. PCE11 films

A solution of PCE11 (6 mg/mL) was heated at 110 °C for 1 h with stirring prior to use. 100 μ L of this was cast onto a hot substrate (also heated to 110 °C) at a spin rate of 1200 RPM for 60 s. To avoid the polymer from crashing out solution during the process of casting, the quartz substrate was heated using a hot plate set to 110 °C for 1 minute prior to transferring to onto the vacuum-chuck. The pipette tip used was warmed by wrapping in aluminum foil and placing on a hot plate (set to 110 °C) for 1 minute before use. The vacuum-chuck was heated by placing a hot aluminum metal block on it, which was previously heated on the same hot plate, onto the top of the chuck for

10 s and removed immediately prior to casting. *PCBM blends*; solutions were cast at a spin rate of 1000 RPM for 30 s followed by 2000 RPM for 60 s. *60-2-1 blends*; solutions were cast at a spin rate of 700 RPM for 30 s followed by 2000 RPM for 60 s.

2.4.2.3. TPD-BDT films

A 50 μ L solution of 6 mg/mL of polymer was cast at a spin rate of 500 RPM for 30 s, then increased to 2000 RPM 60 s. *60-2-1 blends*; solutions were cast at a spin rate of 500 RPM for 10 s followed by 2000 RPM for 60 s.

2.4.2.4. TPD-BDT(OEH) and TPD-CPDT films

A solution of 7.5 mg/mL of polymer was heated at 110 °C for 1 h with stirring to fully dissolve, and cast while hot. Note the quartz substrate itself was not heated for these films.

2.4.2.5. BT-BDT films

Solutions of neat polymer were mixed while heated at 80 °C for 2 h to thoroughly dissolve, before cooling back to RT. Solutions (once cooled) were cast at a spin rate of 800 RPM for 60 s.

2.4.2.6. FBT-BDT films

A solution of FBT-BDT (6 mg/mL) was heated at 90 °C for 1 h with stirring prior use. 100 μ L of this was cast onto a RT substrate at a spin rate of 700 RPM for 10 s followed by 2000 RPM for 60 s. Note that both PCE11 and FBT-BDT films change color when heated in solution, from a greenish blue to a red magenta color, but revert when cooled down.

Tables and Figures

Table 2.1: Lifetime of neat and blended films aged in air.

Polymer	Blend	T_{80} (h)	Relative ^(a) T_{80}	T_{60}	Relative ^(a) T_{60}
TPD- BDT(OEH)	Neat	19	-	58	-
	PC ₆₀ BM	86	4.5	288	5.0
	60-2-1	60	3.2	192	3.3
TPD-BDT	Neat	16	-	65	-
	PC ₆₀ BM	41	2.6	106	1.6
	60-2-1	46	2.9	137	2.1
TPD-CPDT	Neat	1.6	-	6.6	-
	PC ₆₀ BM	2.2	1.4	7.7	1.2
	60-2-1	11	6.9	28	4.2
PCE11	Neat	53	-	91	-
	PC ₆₀ BM	72	1.4	173	1.9
	60-2-1	91	1.7	360	4.0
FBT-BDT	Neat	9.6	-	21	-
	PC ₆₀ BM	20	2.1	58	2.8
	60-2-1	58	6.0	161	7.7
BT-BDT	NEAT	17	-	67	-
	PC ₆₀ BM	163	9.6	648	9.7
	60-2-1	108	6.4	624	9.3

^a Relative value of T_{80} and T_{60} for a given blend were calculated by normalizing them to the T_{80} and T_{60} values for their respective neat polymer film. See Figure 2.4 Figure 2.5 for graphical representation of T_{80} and T_{60} values.

Table 2.2: Quenching efficiencies (%) with standard deviations.

Polymer	PC ₆₀ BM	60-2-1
TPD-BDT(OEH)	99.7 ± 0.1	99.2 ± 0.3
TPD-BDT	98.4 ± 0.4	99.6 ± 0.4
TPD-CPDT	97.9 ± 0.6	99.2 ± 0.1
BT-BDT	98.4 ± 0.2	92.4 ± 0.7
FBT-BDT	98.5 ± 0.5	98.2 ± 0.5
PCE11	95.6 ± 0.6	97.0 ± 0.4

Table 2.3: Device characteristics of photovoltaic solar cells of PCE11

Fullerene	V _{oc} (V)	J _{sc} (mA/cm ²)	FF (%)	η (%)	R _s (Ωcm ²)	R _{sh} (Ωcm ²)
PC ₆₀ BM	0.78	17.3	66	8.9	6.1	567
60-2-1	0.49	6.40	50	1.6	16	302

Table 2.4: DFT calculated HOMO/LUMO values donor molecule.

Donor	HOMO (eV)	LUMO (eV)
DCV5T-F ₂ (3,3)-Me ₄ (2,2,4,4)	-5.139	-3.986

Table 2.5: Summary of photovoltaic figures of merit for BHJ devices with DCV5T-F₂(3,3)-Me₄(2,2,4,4).

Cell	Fullerene on ITO (10 nm)	BHJ layer thickness (nm)	Substrate temp. (°C)	J _{sc} (mA/cm ²)	FF (%)	V _{oc} (V)	PCE (%)
B1	C ₆₀	20	70	6.9	68.2	0.97	4.6
B2	C ₆₀	30	70	8	65.2	0.98	5.1
B3	60-2-1	20	70	6	53.2	0.73	2.3
B4	60-2-1	30	70	6	51.2	0.55	1.7
B5	60-2-1	20	50	6.6	62.5	0.85	3.5
B6	60-2-1	30	50	7	62.7	0.86	3.8

In each case, the fullerene on ITO was also the fullerene used in a BHJ layer with DCV5T-F₂(3,3)-Me₄(2,2,4,4). Devices made in accordance with Figure 2.13.

Table 2.6: Summary of photovoltaic figures of merit for PHJ devices with DCV5T-F₂(3,3)-Me₄(2,2,4,4) as donor.

Cell	Acceptor	Donor	J _{sc} (mA/cm ²)	FF (%)	V _{oc} (V)	PCE (%)
P1	C ₆₀	6	5.5	53.5	1.06	3.1
P2	C ₆₀	10	5.2	49	1.05	2.7
P3	60-2-1	6	4.5	58.5	0.97	2.6
P4	60-2-1	10	4.8	51.2	0.97	2.4

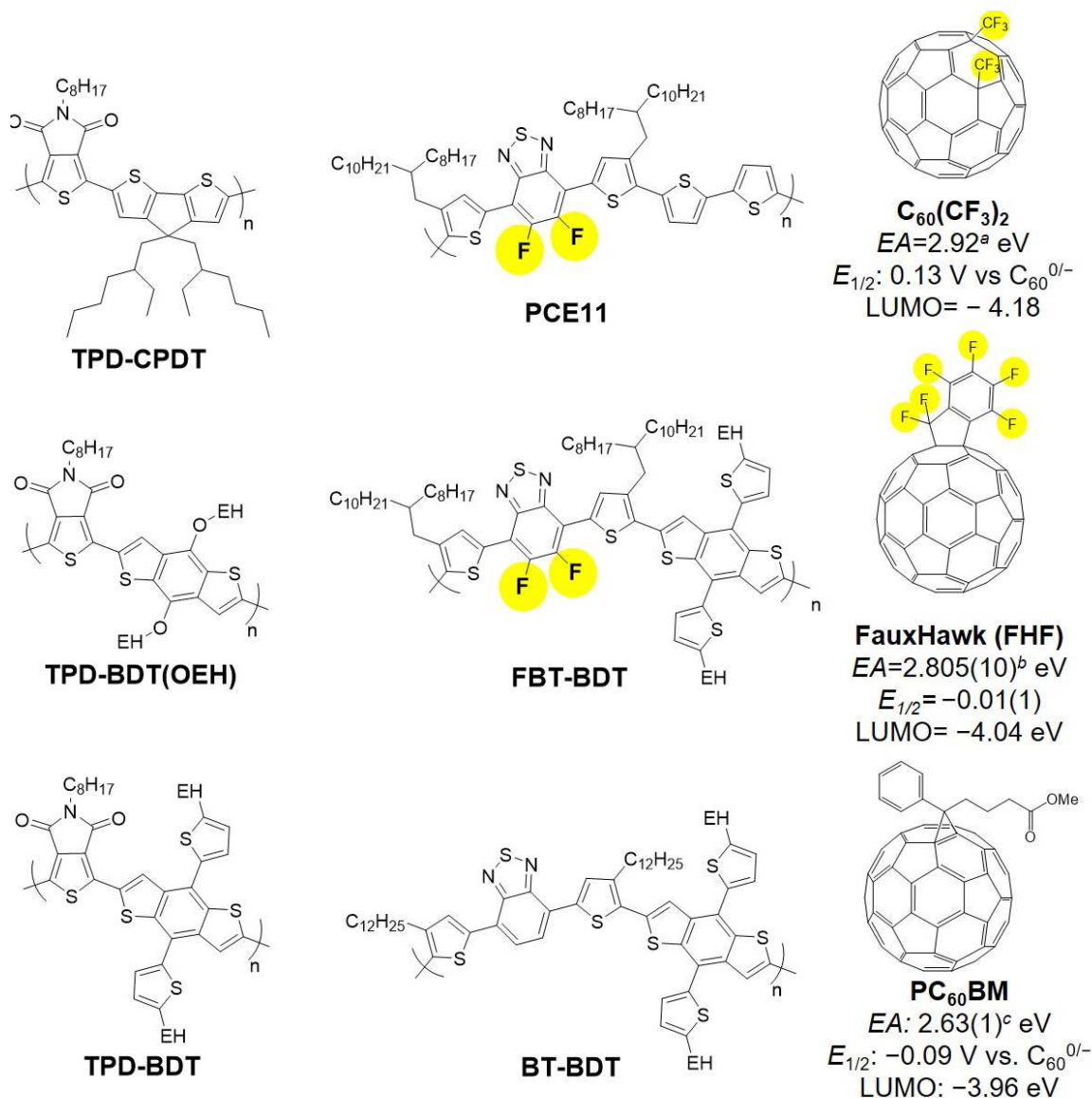


Figure 2.1: Chemical structure of polymers and fullerenes used in this study. Fluorine atoms are labeled in yellow for clarity. a) EA values taken from reference ¹⁰⁰; b) EA values taken from reference ⁴; c) EA values taken from reference ⁹⁹. For each fullerene, gas phase EA values were measured by low-temperature PES. *E*_{1/2}^{0/-} values are from CV performed in o-DCB. LUMO energies were calculated with CV data using: LUMO = -((*E*_{1/2}^{0/-} vs. Fe(Cp)₂⁺⁰) + 5.1); with C₆₀^{0/-} = - 1.05 (V) vs. Fe(Cp)₂⁺⁰. LUMO energies were calculated from CV data: LUMO = -((*E*_{1/2}^{0/-} vs. Fe(Cp)₂⁺⁰) + 5.1) eV, where C₆₀^{0/-} = 1.05 (eV) vs. Fe(Cp)₂⁺⁰. *E*_{1/2}^{0/-} values are taken from the literature of CVs performed in o-DCB⁵³ with Fe(Cp)₂⁺⁰ as an internal reference. EH denotes branched ethyl-hexyl side chains.

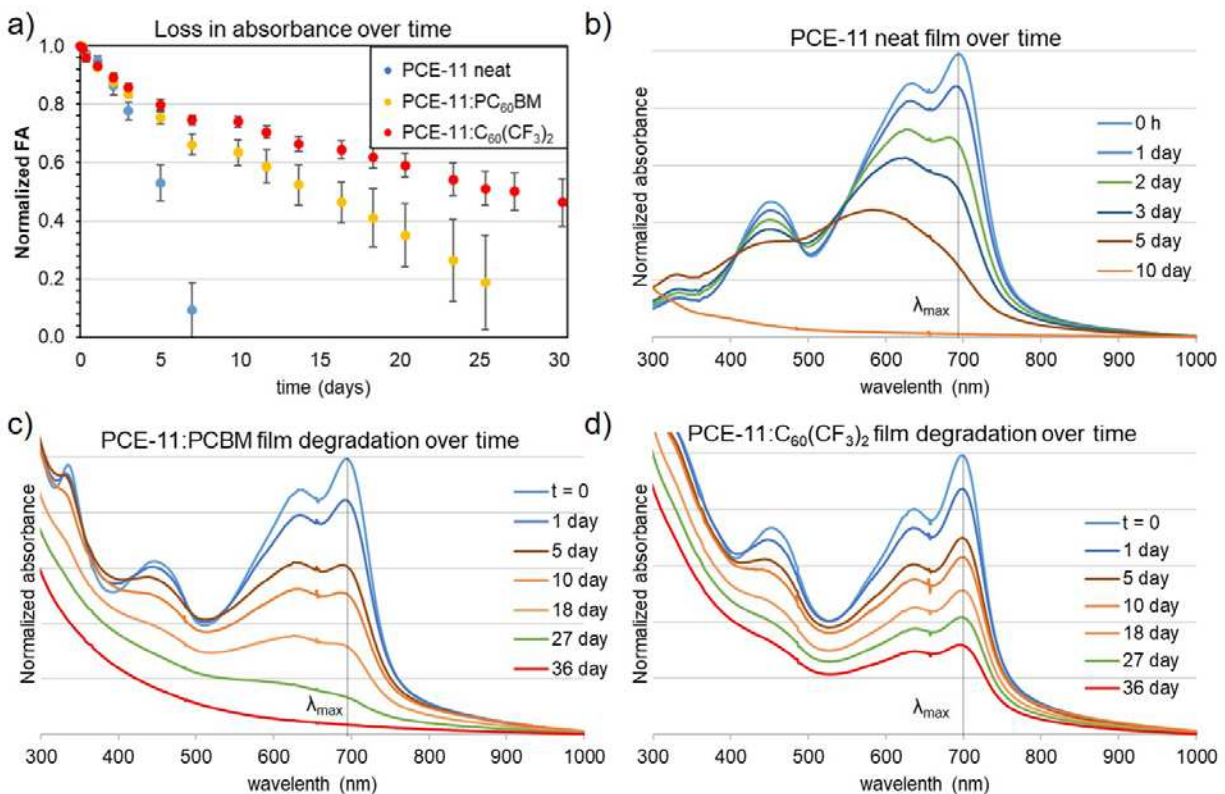


Figure 2.2: Representative examples of neat and 1:1 by weight blends of PCE11 films photobleaching over time. a) Fraction of absorbed light over time measured at λ_{\max} for PCE11 films (extension of graph shown in Figure 2.3). b–d) Representative examples of normalized absorption spectra taken over time for films of... b) neat PCE11; c) blend with PC₆₀BM; d) blend with C₆₀(CF₃)₂ (60-2-1).

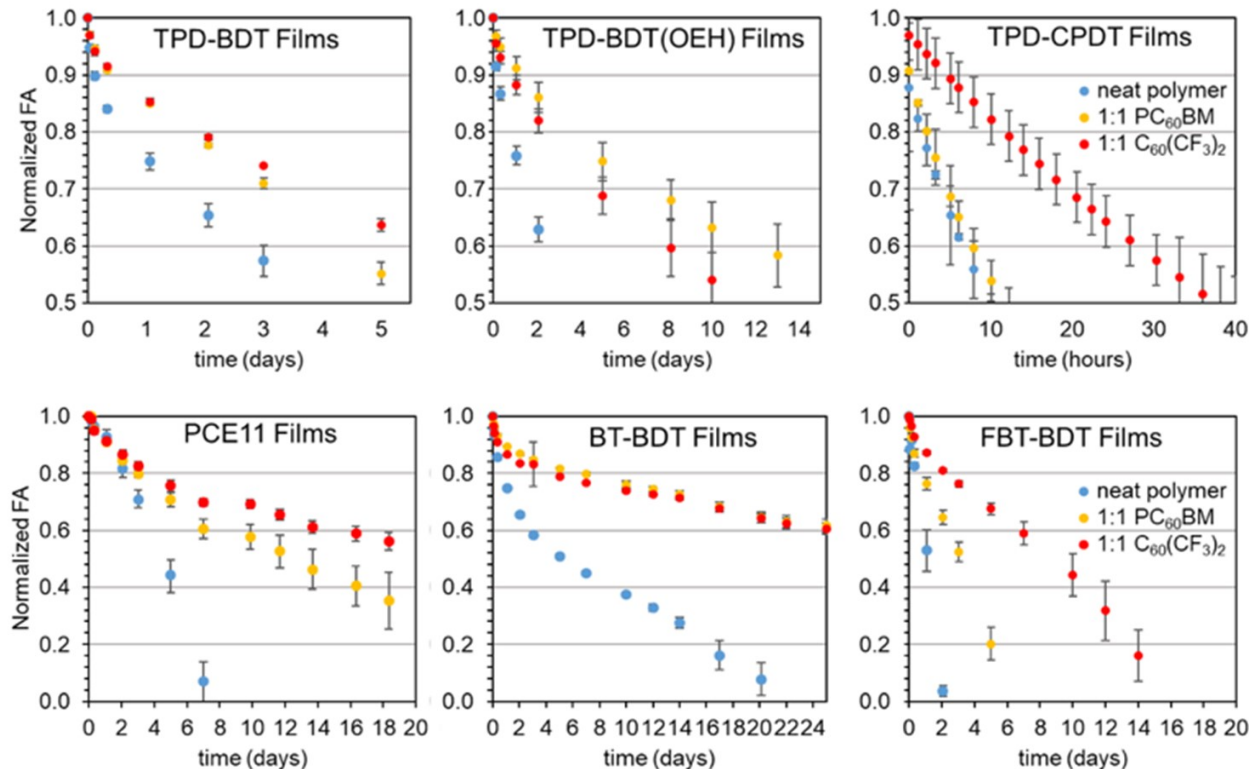


Figure 2.3: Fraction of light absorbed over time measured at λ_{\max} for films of neat polymer and fullerene blends containing TPD-BDT, TPD-BDT(OEH) and TPD-CPDT (top left to top right), and PCE11, BT-BDT, and FBT-BDT (bottom left to right). Inset in the right most graph shows color key for each film type. All neat films are represented in blue. 1:1 (by mass) blends of polymer with PC₆₀BM and C₆₀(CF₃)₂ (60-2-1) are orange and red, respectively. Note, the x-axes are not at the same scale; each figure shows degradation up to the T_{60} values for the most stable fullerene blend for that given polymer. Error bars represent the maximum and minimum absorbance values recorded for films of the same blend type, where three films of each blend were prepared and consistently measured at three distinct positions (for a total of 9 measurements for each absorbance value shown above).

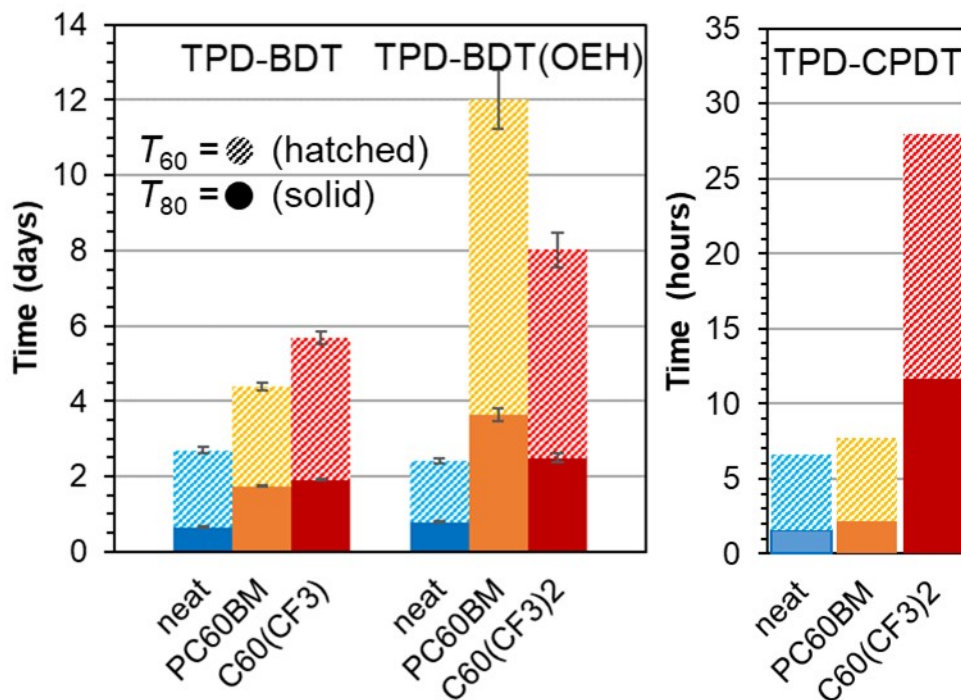


Figure 2.4: Comparison of T_{80} and T_{60} values for neat and blended films from Figure 2.3—using the same color key. Solid bars represent the average time it takes for a given film to irreversible photobleach to 80% of the initial absorbance value (T_{80}), hatched bars represent the additional time to reach 60% of the initial absorbance value (T_{60}). (left) films of TPD-BDT and TPD-BDT(OEH) T_{80} and T_{60} values in units of days. (right): films of TPD-CPDT T_{80} and T_{60} values in units of hours.

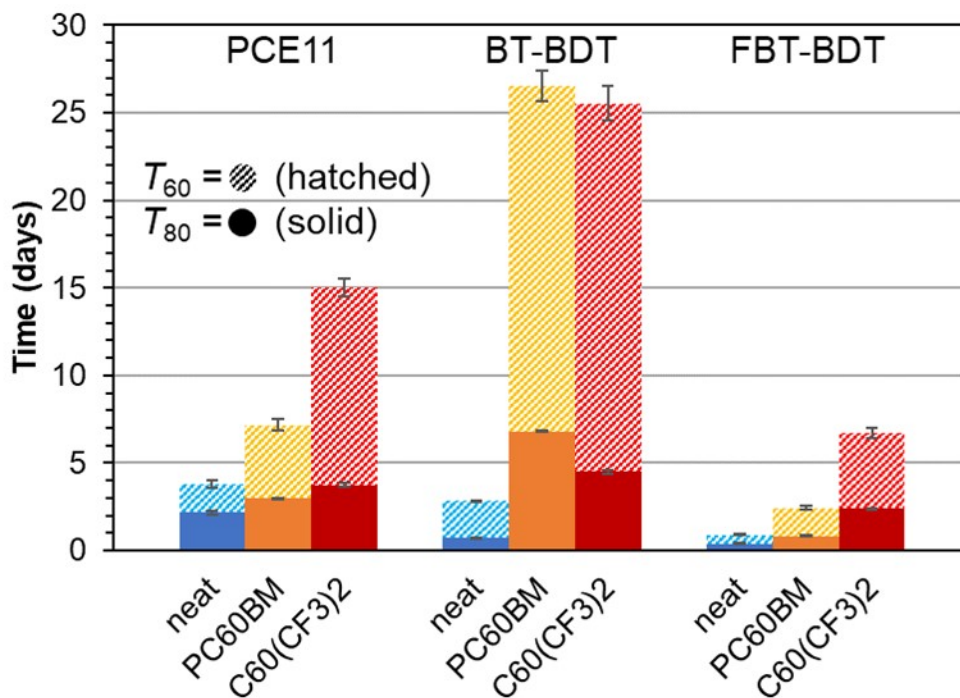


Figure 2.5: Comparison of T_{80} and T_{60} values for neat and blended films from Figure 2.3—using the same color key. Solid bars represent the average time it takes for a given film to irreversibly photobleached to 80% of the initial absorbance value (T_{80}), hatched bars represent the additional time to reach 60% of the initial absorbance value (T_{60}).

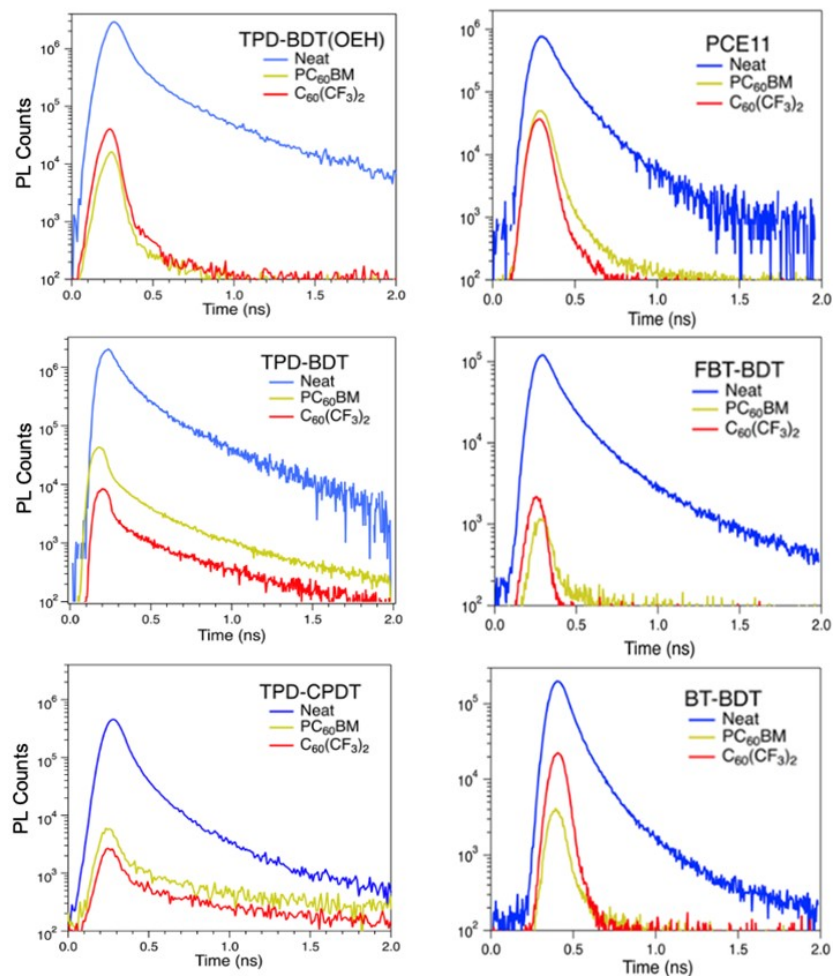


Figure 2.6: PL decays for neat and fullerene blends of TPD-BDT(OEH), TPD-BDT, and TPD-CPDT (top, center, and bottom left, respectively), as well as PCE-11, FBT-BDT, and BT-BDT (top, center, and bottom right, respectively). All neat films are represented in blue. Polymer blends (1:1 by mass) with PC₆₀BM and C₆₀(CF₃)₂ are coloured orange and red, respectively. TPD-CPDT data was reproduced in part with permission.¹⁰³

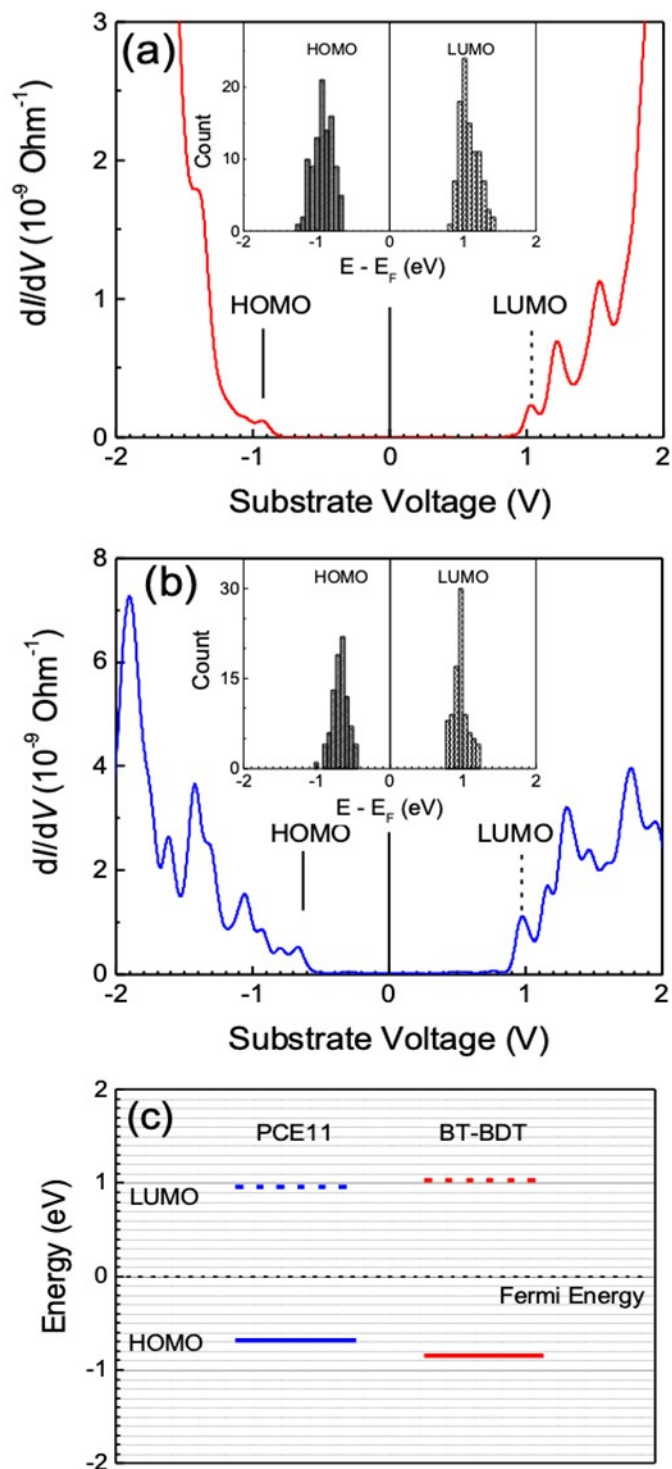


Figure 2.7: Differential tunnel conductance (dI/dV) versus voltage characteristics of (a) BT-BDT and (b) PCE11 with marked HOMO and LUMO positions and corresponding histograms (inset) of HOMO and LUMO positions obtained from many dI/dV spectra. (c) Energy level diagram of PCE11 and BT-BDT.

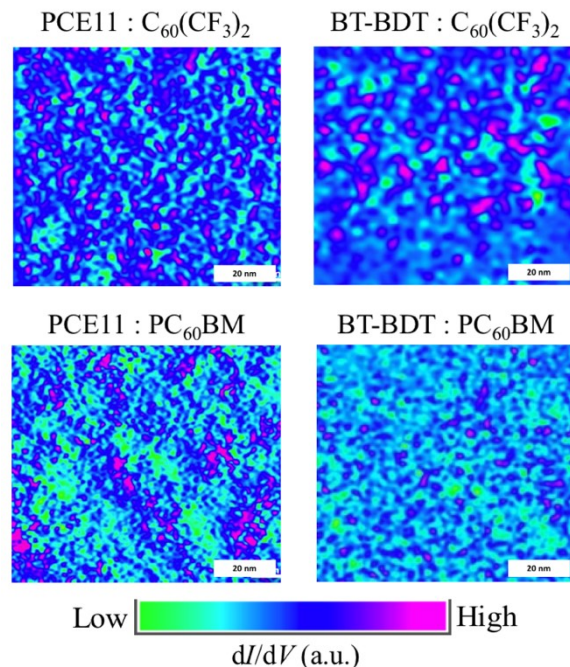


Figure 2.8: dI/dV images corresponding to ~ 10 nm thick active layer films prepared on Au (111) and imaged under inert atmosphere. Left panel: PCE11. Right panel: BT-BDT. Upper panel: blends with $C_{60}(CF_3)_2$. Lower panel: blends with $PC_{60}BM$. Images were recorded at -0.95 V for BT-BDT and -0.70 V for PCE11, probing the HOMO of the polymers. Hence, magenta regions correspond to polymer donor-rich domains, green to fullerene-rich domains, and blue regions can be considered to represent mixed-domains. White scale bar represents 20 nm.

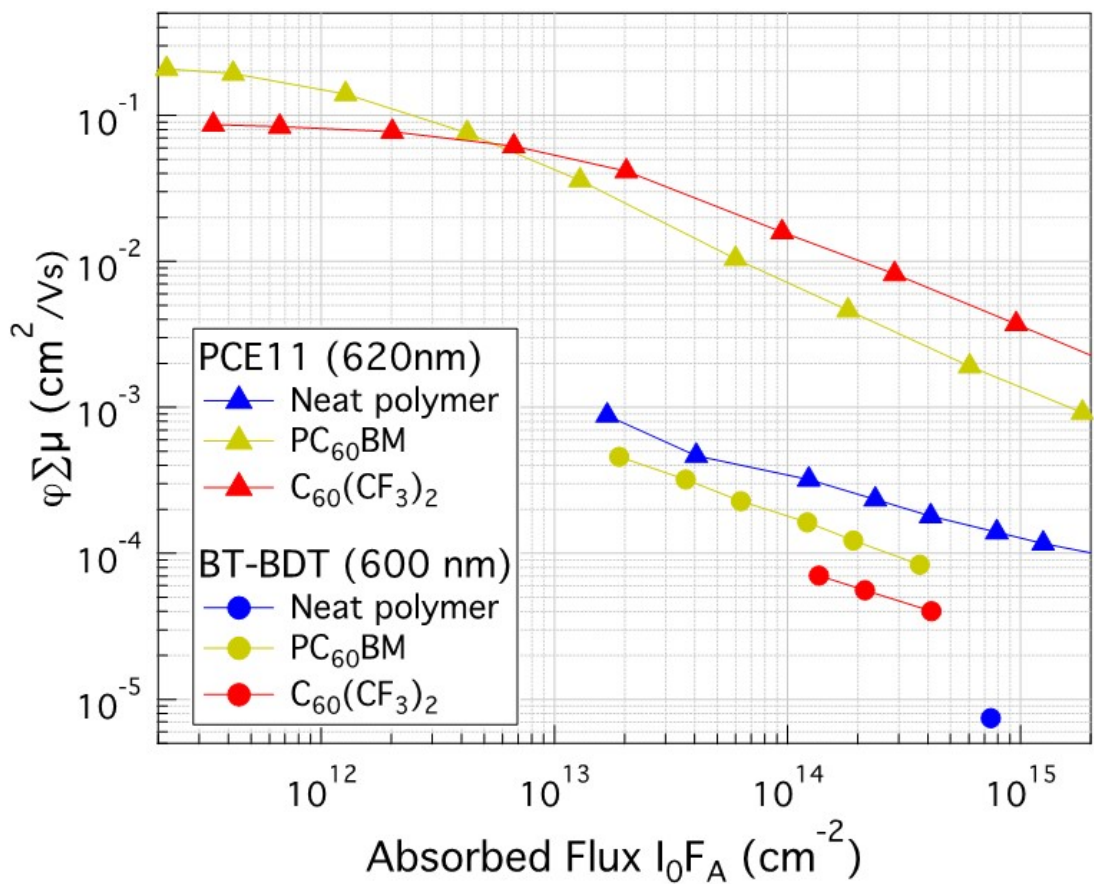


Figure 2.9: The product of charge carrier yield (ϕ) and sum of local hole and electron mobilities ($\Sigma\mu$) is illustrated over a range of intensities spanning several orders of magnitude at a laser excitation wavelength of 620 nm for PCE11 samples (triangles) and 600 nm for BT-BDT samples (circles).

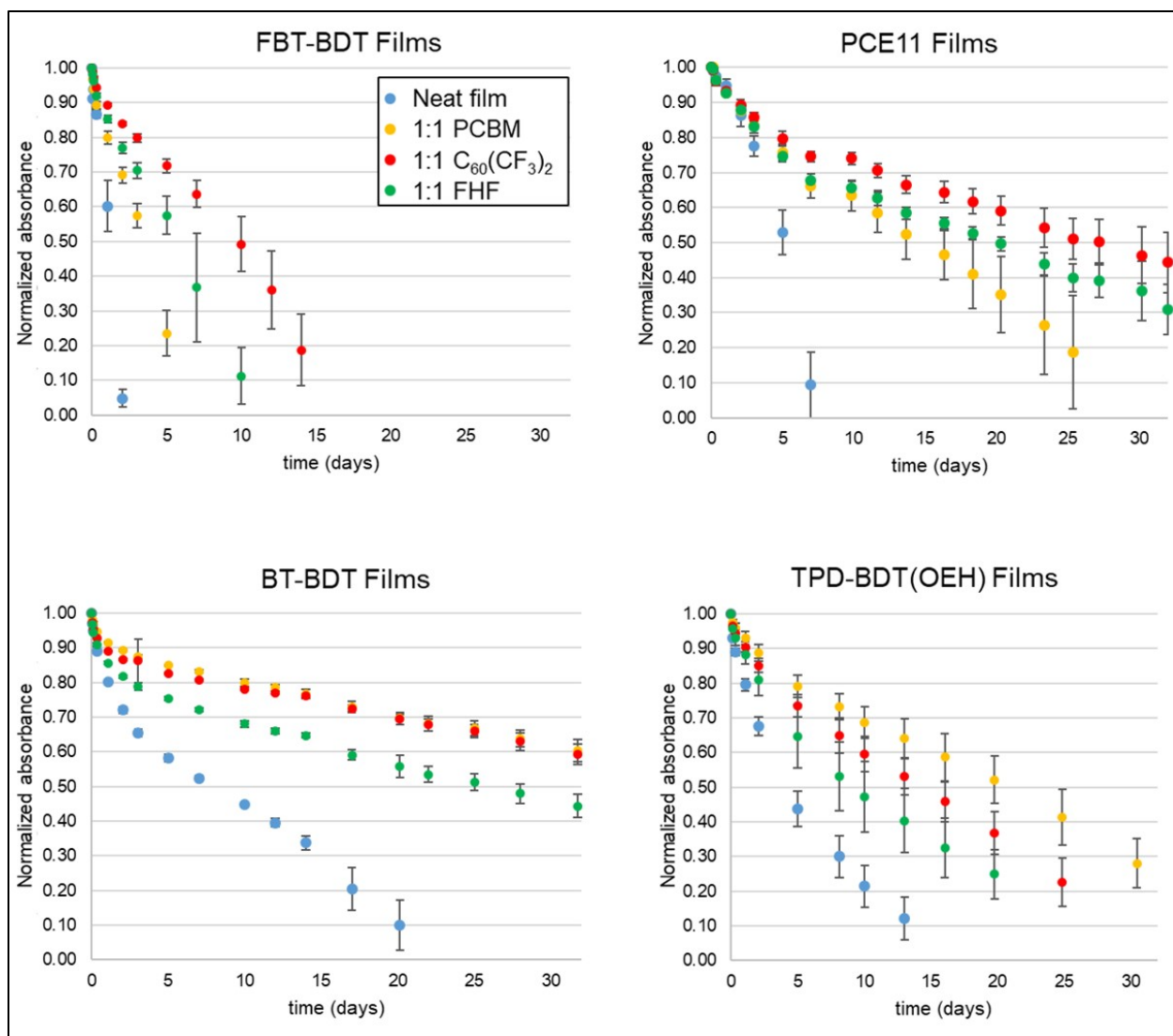


Figure 2.10: Fraction of light absorbed over time measured at λ_{\max} for films of neat polymer and fullerene blends—including FHF—containing fluorinated FBT-BDT or PCE11 (top) and non-fluorinated BT-BDT and TPD-BDT(OEH) (bottom). Inset in the left most graph shows color key for each film type. All neat films are represented in blue; 1:1 (by mass) blends of polymer with PC₆₀BM, C₆₀(CF₃)₂, and FHF are orange, red, and green respectively. Each x-axis is set to the same scale (30-days) regardless of rate of film degradation for the respective polymer and blends. Error bars represent the maximum and minimum absorbance values recorded for films of the same blend type, where three films of each blend were prepared and consistently measured at three distinct positions (for a total of 9 measurements for each absorbance value shown above).

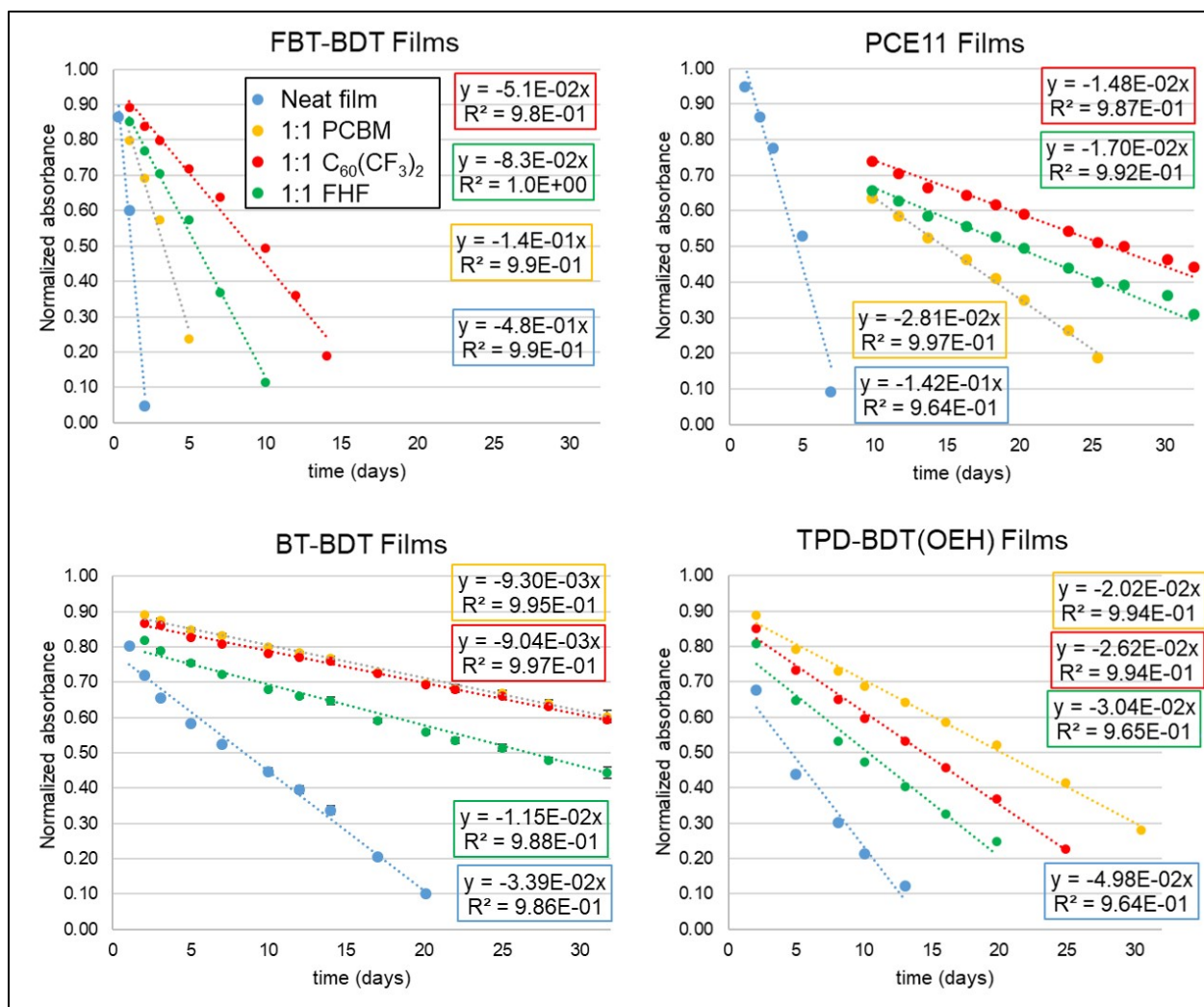


Figure 2.11: reproduction of Figure 2.10 showing the stable rate of photodegradation after the initial rapid absorbance drop. Best-fit lines shown were calculated from the slope of the line after the initial absorbance drop (all data points shown are after the initial rapid absorbance drop for clarity, see Figure 2.10 for prior data points not included in calculating the best fit line). Inset equation in each graph for the best fit lines and their R² values for the respective polymer blend; inset in the top-left graph shows color key for each film type; all neat films are represented in blue. 1:1 (by mass) blends of polymer with PC₆₀BM, C₆₀(CF₃)₂, and FHF are orange, red, and green respectively.

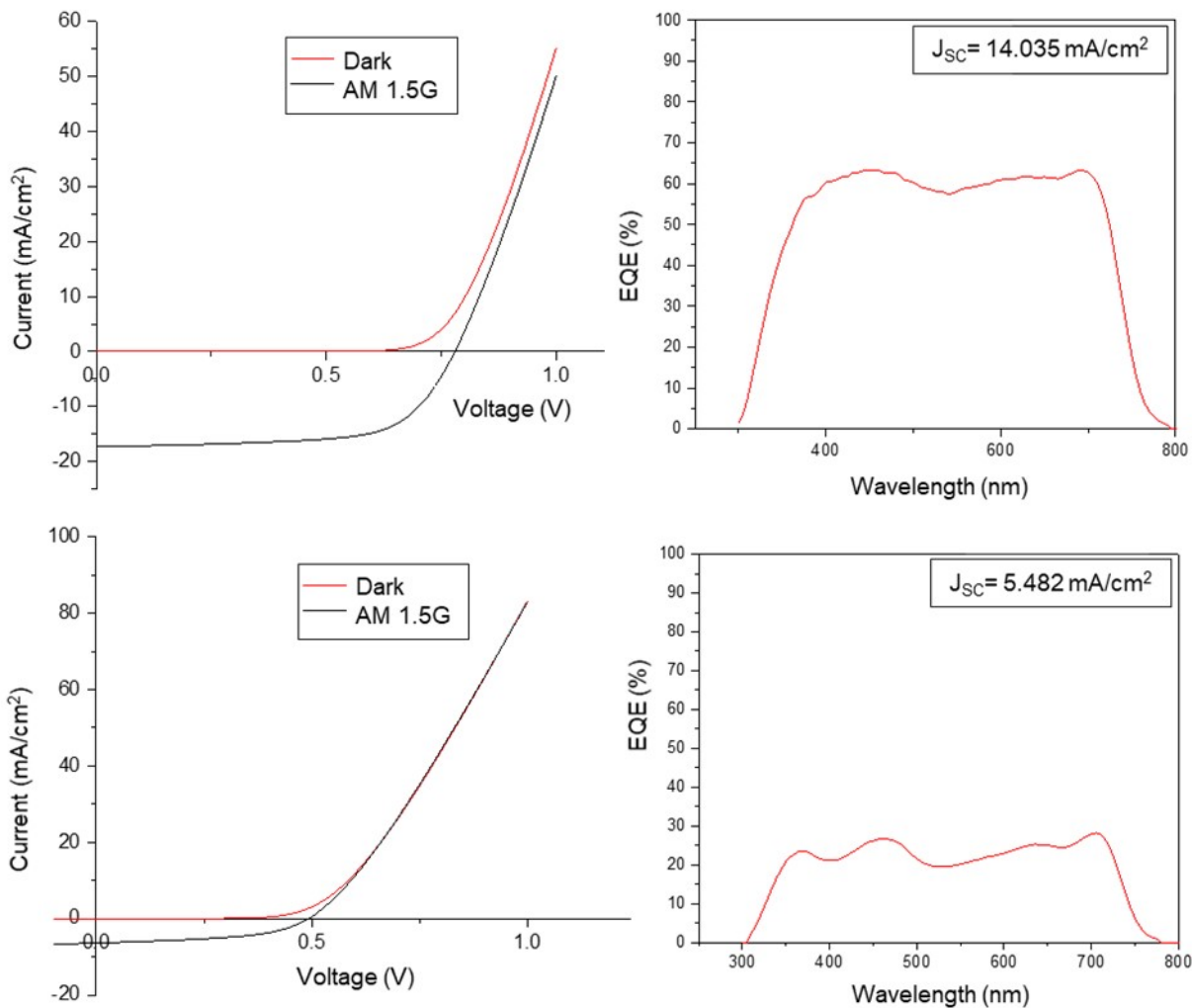


Figure 2.12: J - V plots (left) and EQE spectra (right) for the highest performing PCE11:PC₆₀BM device (8.9% PCE, top) and PCE11:60-2-1 device (1.6% PCE, bottom).

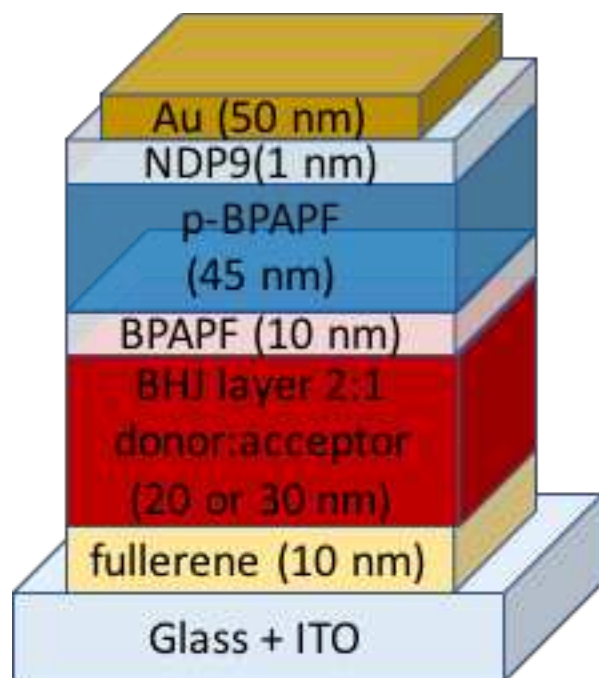


Figure 2.13: Device architecture for BHJ devices with 60-2-1 (acceptor) and DCV5T-F₂(3,3)-Me₄(2,2,4,4) (donor).

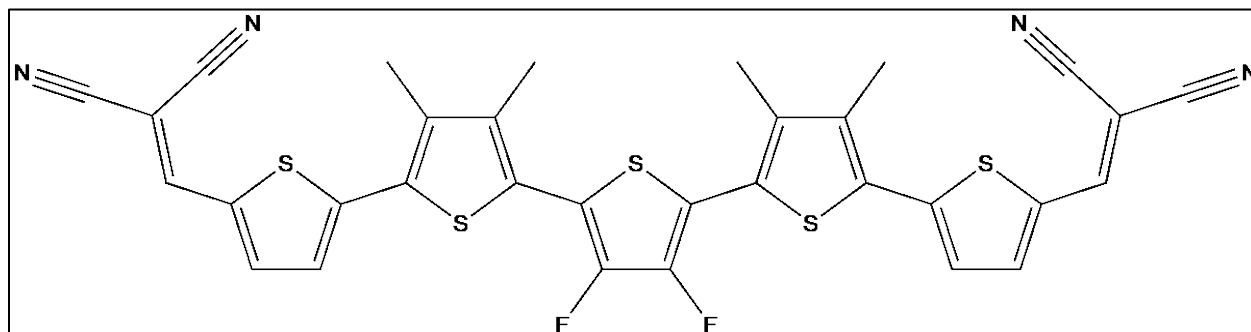


Figure 2.14: Structure of DCV5T-F₂(3,3)-Me₄(2,2,4,4).

CHAPTER 2 REFERENCES

3. Larson, B. W.; Whitaker, J. B.; Popov, A. A.; Kopidakis, N.; Rumbles, G.; Boltalina, O. V.; Strauss, S. H., Thermal [6,6] → [6,6] Isomerization and Decomposition of PCBM (Phenyl-C61-butylbutyric Acid Methyl Ester). *Chem. Mater.* **2014**, *26* (7), 2361-2367.
4. San, L. K.; Bukovsky, E. V.; Larson, B. W.; Whitaker, J. B.; Deng, S. H. M.; Kopidakis, N.; Rumbles, G.; Popov, A. A.; Chen, Y.-S.; Wang, X.-B.; Boltalina, O. V.; Strauss, S. H., A faux hawk fullerene with PCBM-like properties. *Chemical Science* **2015**, *6* (3), 1801-1815.
5. Kuvychko, I. V.; Whitaker, J. B.; Larson, B. W.; Raguindin, R. S.; Suhr, K. J.; Strauss, S. H.; Boltalina, O. V., Pressure effect on heterogeneous trifluoromethylation of fullerenes and its application. *J. Fluorine Chem.* **2011**, *132* (10), 679-685.
26. Andersen, T. R.; Dam, H. F.; Hosel, M.; Helgesen, M.; Carle, J. E.; Larsen-Olsen, T. T.; Gevorgyan, S. A.; Andreasen, J. W.; Adams, J.; Li, N.; Machui, F.; Spyropoulos, G. D.; Ameri, T.; Lemaitre, N.; Legros, M.; Scheel, A.; Gaiser, D.; Kreul, K.; Berny, S.; Lozman, O. R.; Nordman, S.; Valimaki, M.; Vilkmann, M.; Søndergaard, R. R.; Jørgensen, M.; Brabec, C. J.; Krebs, F. C., Scalable, ambient atmosphere roll-to-roll manufacture of encapsulated large area, flexible organic tandem solar cell modules. *Energy Environ. Sci.* **2014**, *7* (9), 2925-2933.
27. Krebs, F. C.; Espinosa, N.; Hösel, M.; Søndergaard, R. R.; Jørgensen, M., 25th Anniversary Article: Rise to Power – OPV-Based Solar Parks. *Adv. Mater.* **2014**, *26* (1), 29-39.
28. Wadsworth, A.; Ashraf, R. S.; Abdelsamie, M.; Pont, S.; Little, M.; Moser, M.; Hamid, Z.; Neophytou, M.; Zhang, W.; Amassian, A.; Durrant, J. R.; Baran, D.; McCulloch, I., Highly Efficient and Reproducible Nonfullerene Solar Cells from Hydrocarbon Solvents. *ACS Energy Lett.* **2017**, *2* (7), 1494-1500.
29. Deng, D.; Zhang, Y.; Zhang, J.; Wang, Z.; Zhu, L.; Fang, J.; Xia, B.; Wang, Z.; Lu, K.; Ma, W.; Wei, Z., Fluorination-enabled optimal morphology leads to over 11% efficiency for inverted small-molecule organic solar cells. *Nat. Commun.* **2016**, *7*, 13740.
30. Zhao, W.; Li, S.; Yao, H.; Zhang, S.; Zhang, Y.; Yang, B.; Hou, J., Molecular Optimization Enables over 13% Efficiency in Organic Solar Cells. *J. Am. Chem. Soc.* **2017**, *139* (21), 7148-7151.
31. Lin, Y.; Adilbekova, B.; Firdaus, Y.; Yengel, E.; Faber, H.; Sajjad, M.; Zheng, X.; Yarali, E.; Seitkhan, A.; Bakr, O. M.; El-Labban, A.; Schwingenschloegl, U.; Tung, V.; McCulloch, I.; Laquai, F.; Anthopoulos, T. D., 17% Efficient Organic Solar Cells Based on Liquid Exfoliated WS₂ as a Replacement for PEDOT:PSS. *Adv. Mater.* **2019**, *31* (46), 1902965.
32. Cui, Y.; Yao, H.; Hong, L.; Zhang, T.; Tang, Y.; Lin, B.; Xian, K.; Gao, B.; An, C.; Bi, P.; Ma, W.; Hou, J., 17% efficiency organic photovoltaic cell with superior processability. *Natl. Sci. Rev.* **2020**, *7*, 1239-1246.
33. Meng, L.; Zhang, Y.; Wan, X.; Li, C.; Zhang, X.; Wang, Y.; Ke, X.; Xiao, Z.; Ding, L.; Xia, R.; Yip, H.-L.; Cao, Y.; Chen, Y., Organic and solution-processed tandem solar cells with 17.3% efficiency. *Science* **2018**, *361* (6407), 1094-1098.
34. Kang, H.; Kim, G.; Kim, J.; Kwon, S.; Kim, H.; Lee, K., Bulk-Heterojunction Organic Solar Cells: Five Core Technologies for Their Commercialization. *Adv. Mater.* **2016**, *28* (36), 7821-7861.
35. Mateker, W. R.; Sachs-Quintana, I. T.; Burkhard, G. F.; Cheacharoen, R.; McGehee, M. D., Minimal Long-Term Intrinsic Degradation Observed in a Polymer Solar Cell Illuminated in an Oxygen-Free Environment. *Chem. Mater.* **2015**, *27* (2), 404-407.
36. Adams, J.; Spyropoulos, G. D.; Salvador, M.; Li, N.; Strohm, S.; Lucera, L.; Langner, S.; Machui, F.; Zhang, H.; Ameri, T.; Voigt, M. M.; Krebs, F. C.; Brabec, C. J., Air-processed organic tandem solar cells on glass: toward competitive operating lifetimes. *Energy Environ. Sci.* **2015**, *8* (1), 169-176.
37. Mateker, W. R.; McGehee, M. D., Progress in Understanding Degradation Mechanisms and Improving Stability in Organic Photovoltaics. *Adv. Mater.* **2017**, *29* (10), 1603940-n/a.
38. Jørgensen, M.; Norrman, K.; Gevorgyan, S. A.; Tromholt, T.; Andreasen, B.; Krebs, F. C., Stability of Polymer Solar Cells. *Adv. Mater.* **2012**, *24* (5), 580-612.

39. Grossiord, N.; Kroon, J. M.; Andriessen, R.; Blom, P. W. M., Degradation mechanisms in organic photovoltaic devices. *Org. Electron.* **2012**, *13* (3), 432-456.
40. Mateker, W. R.; Douglas, J. D.; Cabanetos, C.; Sachs-Quintana, I. T.; Bartelt, J. A.; Hoke, E. T.; El Labban, A.; Beaujuge, P. M.; Frechet, J. M. J.; McGehee, M. D., Improving the long-term stability of PBDTTPD polymer solar cells through material purification aimed at removing organic impurities. *Energy Environ. Sci.* **2013**, *6* (8), 2529-2537.
41. Garner, L. E.; Bera, A.; Larson, B. W.; Ostrowski, D. P.; Pal, A. J.; Braunecker, W. A., Promoting Morphology with a Favorable Density of States Using Diiodooctane to Improve Organic Photovoltaic Device Efficiency and Charge Carrier Lifetimes. *ACS Energy Lett.* **2017**, *2* (7), 1556-1563.
42. Li, N.; Perea, J. D.; Kassar, T.; Richter, M.; Heumueller, T.; Matt, G. J.; Hou, Y.; Güldal, N. S.; Chen, H.; Chen, S.; Langner, S.; Berlinghof, M.; Unruh, T.; Brabec, C. J., Abnormal strong burn-in degradation of highly efficient polymer solar cells caused by spinodal donor-acceptor demixing. *Nat. Commun.* **2017**, *8*, 14541.
43. Muller, C.; Bergqvist, J.; Vandewal, K.; Tvingstedt, K.; Anselmo, A. S.; Magnusson, R.; Alonso, M. I.; Moons, E.; Arwin, H.; Campoy-Quiles, M.; Inganäs, O., Phase behaviour of liquid-crystalline polymer/fullerene organic photovoltaic blends: thermal stability and miscibility. *J. Mater. Chem.* **2011**, *21* (29), 10676-10684.
44. Treat, N. D.; Varotto, A.; Takacs, C. J.; Batara, N.; Al-Hashimi, M.; Heeney, M. J.; Heeger, A. J.; Wudl, F.; Hawker, C. J.; Chabynyc, M. L., Polymer-Fullerene Miscibility: A Metric for Screening New Materials for High-Performance Organic Solar Cells. *J. Am. Chem. Soc.* **2012**, *134* (38), 15869-15879.
45. Ye, L.; Hu, H.; Ghasemi, M.; Wang, T.; Collins, B. A.; Kim, J.-H.; Jiang, K.; Carpenter, J. H.; Li, H.; Li, Z.; McAfee, T.; Zhao, J.; Chen, X.; Lai, J. L. Y.; Ma, T.; Bredas, J.-L.; Yan, H.; Ade, H., Quantitative relations between interaction parameter, miscibility and function in organic solar cells. *Nature Mater.* **2018**, *17* (3), 253-260.
46. Ye, L.; Collins, B. A.; Jiao, X.; Zhao, J.; Yan, H.; Ade, H., Miscibility–Function Relations in Organic Solar Cells: Significance of Optimal Miscibility in Relation to Percolation. *Adv. Energy Mater.* **2018**, *8* (28), 1703058.
47. Hoke, E. T.; Sachs-Quintana, I. T.; Lloyd, M. T.; Kauvar, I.; Mateker, W. R.; Nardes, A. M.; Peters, C. H.; Kopidakis, N.; McGehee, M. D., The role of electron affinity in determining whether fullerenes catalyze or inhibit photooxidation of polymers for solar cells. *Adv. Energy Mater.* **2012**, *2* (11), 1351-1357.
48. Carvalho de Oliveira, M. C.; Cardoso, A. S. A. D.; Viana, M. M.; Lins, V. d. F. C., The causes and effects of degradation of encapsulant ethylene vinyl acetate copolymer (EVA) in crystalline silicon photovoltaic modules: A review. *Renewable Sustainable Energy Rev.* **2018**, *81*, 2299-2317.
49. Hintz, H.; Egelhaaf, H. J.; Peisert, H.; Chassé, T., Photo-oxidation and ozonization of poly(3-hexylthiophene) thin films as studied by UV/VIS and photoelectron spectroscopy. *Polym. Degrad. Stab.* **2010**, *95* (5), 818-825.
50. Cardona, C. M.; Li, W.; Kaifer, A. E.; Stockdale, D.; Bazan, G. C., Electrochemical Considerations for Determining Absolute Frontier Orbital Energy Levels of Conjugated Polymers for Solar Cell Applications. *Adv. Mater.* **2011**, *23* (20), 2367-2371.
51. Tournebize, A.; Bussièrre, P.-O.; Rivaton, A.; Gardette, J.-L.; Medlej, H.; Hiorns, R. C.; Dagnon-Lartigau, C.; Krebs, F. C.; Norrman, K., New Insights into the Mechanisms of Photodegradation/Stabilization of P3HT:PCBM Active Layers Using Poly(3-hexyl-d13-Thiophene). *Chem. Mater.* **2013**, *25* (22), 4522-4528.
52. San, L. K.; Bukovsky, E. V.; Larson, B. W.; Whitaker, J. B.; Deng, S. H. M.; Kopidakis, N.; Rumbles, G.; Popov, A. A.; Chen, Y.-S.; Wang, X.-B.; Boltalina, O. V.; Strauss, S. H., A faux hawk fullerene with PCBM-like properties. *Chem. Sci.* **2015**, *6* (3), 1801-1815.
53. Popov, A. A.; Kareev, I. E.; Shustova, N. B.; Stukalin, E. B.; Lebedkin, S. F.; Seppelt, K.; Strauss, S. H.; Boltalina, O. V.; Dunsch, L., Electrochemical, Spectroscopic, and DFT Study of C₆₀(CF₃)_n Frontier Orbitals (n = 2-18): The Link between Double Bonds in Pentagons and Reduction Potentials. *J. Am. Chem. Soc.* **2007**, *129* (37), 11551-11568.

54. Garner, L. E.; Nellisery Viswanathan, V.; Arias, D. H.; Brook, C. P.; Christensen, S. T.; Ferguson, A. J.; Kopidakis, N.; Larson, B. W.; Owczarczyk, Z. R.; Pfeilsticker, J. R.; Ramamurthy, P. C.; Strauss, S. H.; Boltalina, O. V.; Braunecker, W. A., Photobleaching dynamics in small molecule vs. polymer organic photovoltaic blends with 1,7-bis-trifluoromethylfullerene. *J. Mater. Chem. A* **2018**, *6* (11), 4623-4628.
55. Nellisery Viswanathan, V.; Ferguson, A. J.; Pfeilsticker, J. R.; Larson, B. W.; Garner, L. E.; Brook, C. P.; Strauss, S. H.; Boltalina, O. V.; Ramamurthy, P. C.; Braunecker, W. A., Strategic fluorination of polymers and fullerenes improves photostability of organic photovoltaic blends. *Org. Electron.* **2018**, *62*, 685-694.
56. Boltalina, O. V.; Popov, A. A.; Kuvychko, I. V.; Shustova, N. B.; Strauss, S. H., Perfluoroalkylfullerenes. *Chem. Rev.* **2015**, *115* (2), 1051-1105.
57. Zhang, C.; Langner, S.; Mumyatov, A. V.; Anokhin, D. V.; Min, J.; Perea, J. D.; Gerasimov, K. L.; Osvet, A.; Ivanov, D. A.; Troshin, P.; Li, N.; Brabec, C. J., Understanding the correlation and balance between the miscibility and optoelectronic properties of polymer–fullerene solar cells. *J. Mater. Chem. A* **2017**, *5* (33), 17570-17579.
58. Huang, W.; Gann, E.; Chandrasekaran, N.; Prasad, S. K. K.; Chang, S.-Y.; Thomsen, L.; Kabra, D.; Hodgkiss, J. M.; Cheng, Y.-B.; Yang, Y.; McNeill, C. R., Influence of Fullerene Acceptor on the Performance, Microstructure, and Photophysics of Low Bandgap Polymer Solar Cells. *Adv. Energy Mater.* **2017**, *7* (11), 1602197-n/a.
59. Han, G.; Guo, Y.; Duan, R.; Shen, X.; Yi, Y., Importance of side-chain anchoring atoms on electron donor/fullerene interfaces for high-performance organic solar cells. *J. Mater. Chem. A* **2017**, *5* (19), 9316-9321.
60. Zhang, Q.; Yan, L.; Jiao, X.; Peng, Z.; Liu, S.; Rech, J. J.; Klump, E.; Ade, H.; So, F.; You, W., Fluorinated Thiophene Units Improve Photovoltaic Device Performance of Donor–Acceptor Copolymers. *Chem. Mater.* **2017**, *29* (14), 5990-6002.
61. Bauer, N.; Zhang, Q.; Zhu, J.; Peng, Z.; Yan, L.; Zhu, C.; Ade, H.; Zhan, X.; You, W., Donor polymer fluorination doubles the efficiency in non-fullerene organic photovoltaics. *J. Mater. Chem. A* **2017**, *5* (43), 22536-22541.
62. Viswanathan, V. N.; Rao, A. D.; Pandey, U. K.; Kesavan, A. V.; Ramamurthy, P. C., Molecular-level architectural design using benzothiadiazole-based polymers for photovoltaic applications. *Beilstein J. Org. Chem.* **2017**, *13*, 863-873.
63. Chochos, C. L.; Leclerc, N.; Gasparini, N.; Zimmermann, N.; Tatsi, E.; Katsouras, A.; Moschovas, D.; Serpetzoglou, E.; Konidakis, I.; Fall, S.; Leveque, P.; Heiser, T.; Spanos, M.; Gregoriou, V. G.; Stratakis, E.; Ameri, T.; Brabec, C. J.; Avgeropoulos, A., The Role of Chemical Structure in Indacenodithienothiophene-alt-Benzothiadiazole Copolymers for High Performance Organic Solar Cells With Improved Photo-Stability Through Minimization of Burn-in Loss. *J. Mater. Chem. A* **2017**.
64. Yuan, J.; Ford, M. J.; Zhang, Y.; Dong, H.; Li, Z.; Li, Y.; Nguyen, T.-Q.; Bazan, G. C.; Ma, W., Toward Thermal Stable and High Photovoltaic Efficiency Ternary Conjugated Copolymers: Influence of Backbone Fluorination and Regioselectivity. *Chem. Mater.* **2017**, *29* (4), 1758-1768.
65. Stuart, A. C.; Tumbleston, J. R.; Zhou, H.; Li, W.; Liu, S.; Ade, H.; You, W., Fluorine substituents reduce charge recombination and drive structure and morphology development in polymer solar cells. *J. Am. Chem. Soc.* **2013**, *135* (5), 1806-15.
66. Reichenbacher, K.; Suss, H. I.; Hulliger, J., Fluorine in crystal engineering--"the little atom that could". *Chem. Soc. Rev.* **2005**, *34* (1), 22-30.
67. Heumueller, T.; Mateker, W. R.; Sachs-Quintana, I. T.; Vandewal, K.; Bartelt, J. A.; Burke, T. M.; Ameri, T.; Brabec, C. J.; McGehee, M. D., Reducing burn-in voltage loss in polymer solar cells by increasing the polymer crystallinity. *Energy Environ. Sci.* **2014**, *7* (9), 2974-2980.
68. Oosterhout, S. D.; Kopidakis, N.; Owczarczyk, Z. R.; Braunecker, W. A.; Larsen, R. E.; Ratcliff, E. L.; Olson, D. C., Integrating theory, synthesis, spectroscopy and device efficiency to design and characterize donor materials for organic photovoltaics: a case study including 12 donors. *J. Mater. Chem. A* **2015**, *3* (18), 9777-9788.

69. Lu, L.; Yu, L., Understanding low bandgap polymer PTB7 and optimizing polymer solar cells based on it. *Adv. Mater.* **2014**, *26* (26), 4413-30.
70. Berger, R.; Resnati, G.; Metrangolo, P.; Weber, E.; Hulliger, J., Organic fluorine compounds: a great opportunity for enhanced materials properties. *Chem. Soc. Rev.* **2011**, *40* (7), 3496-3508.
71. Sun, H.; Tottempudi, U. K.; Mottishaw, J. D.; Basa, P. N.; Putta, A.; Sykes, A. G., Strengthening π - π Interactions While Suppressing Csp²-H \cdots π (T-Shaped) Interactions via Perfluoroalkylation: A Crystallographic and Computational Study That Supports the Beneficial Formation of 1-D π - π Stacked Aromatic Materials. *Cryst. Growth Des.* **2012**, *12* (11), 5655-5662.
72. Omorodion, H.; Twamley, B.; Platts, J. A.; Baker, R. J., Further Evidence on the Importance of Fluorous-Fluorous Interactions in Supramolecular Chemistry: A Combined Structural and Computational Study. *Cryst. Growth Des.* **2015**, *15* (6), 2835-2841.
73. Braunecker, W. A.; Hurst, K. E.; Ray, K. G.; Owczarczyk, Z. R.; Martinez, M. B.; Leick, N.; Kuehlen, A.; Sellinger, A.; Johnson, J. C., Phenyl/perfluorophenyl stacking interactions enhance structural order in 2D covalent organic frameworks. *Cryst. Growth Des.* **2018**, *18* (7), 4160-4166.
74. Yao, H.; Ye, L.; Zhang, H.; Li, S.; Zhang, S.; Hou, J., Molecular Design of Benzodithiophene-Based Organic Photovoltaic Materials. *Chem. Rev.* **2016**, *116* (12), 7397-7457.
75. Li, Z.; Tsang, S.-W.; Du, X.; Scoles, L.; Robertson, G.; Zhang, Y.; Toll, F.; Tao, Y.; Lu, J.; Ding, J., Alternating Copolymers of Cyclopenta[2,1-b;3,4-b']dithiophene and Thieno[3,4-c]pyrrole-4,6-dione for High-Performance Polymer Solar Cells. *Adv. Funct. Mater.* **2011**, *21* (17), 3331-3336.
76. Cabanetos, C.; El Labban, A.; Bartelt, J. A.; Douglas, J. D.; Mateker, W. R.; Frechet, J. M. J.; McGehee, M. D.; Beaujuge, P. M., Linear Side Chains in Benzo[1,2-b:4,5-b']dithiophene-Thieno[3,4-c]pyrrole-4,6-dione Polymers Direct Self-Assembly and Solar Cell Performance. *J. Am. Chem. Soc.* **2013**, *135* (12), 4656-4659.
77. Liu, Y.; Zhao, J.; Li, Z.; Mu, C.; Ma, W.; Hu, H.; Jiang, K.; Lin, H.; Ade, H.; Yan, H., Aggregation and morphology control enables multiple cases of high-efficiency polymer solar cells. *Nature Commun.* **2014**, *5*, 5293.
78. Gao, C.; Wang, L.; Li, X.; Wang, H., Rational design on D-A conjugated P(BDT-DTBT) polymers for polymer solar cells. *Polym. Chem.* **2014**, *5* (18), 5200-5210.
79. Rance, W. L.; Ferguson, A. J.; McCarthy-Ward, T.; Heeney, M.; Ginley, D. S.; Olson, D. C.; Rumbles, G.; Kopidakis, N., Photoinduced Carrier Generation and Decay Dynamics in Intercalated and Non-intercalated Polymer:Fullerene Bulk Heterojunctions. *ACS Nano* **2011**, *5* (7), 5635-5646.
80. Sajjad, M. T.; Ward, A. J.; Kästner, C.; Ruseckas, A.; Hoppe, H.; Samuel, I. D. W., Controlling Exciton Diffusion and Fullerene Distribution in Photovoltaic Blends by Side Chain Modification. *J. Phys. Chem. Lett.* **2015**, *6* (15), 3054-3060.
81. Yi, X.; Peng, Z.; Xu, B.; Seyitliyev, D.; Ho, C. H. Y.; Danilov, E. O.; Kim, T.; Reynolds, J. R.; Amassian, A.; Gundogdu, K.; Ade, H.; So, F., Critical Role of Polymer Aggregation and Miscibility in Nonfullerene-Based Organic Photovoltaics. *Adv. Energy Mater.* **2020**, *10* (8), 1902430.
82. Banin, U.; Cao, Y.; Katz, D.; Millo, O., Identification of atomic-like electronic states in indium arsenide nanocrystal quantum dots. *Nature* **1999**, *400* (6744), 542-544.
83. Wang, L.; Chen, Q.; Pan, G. B.; Wan, L. J.; Zhang, S.; Zhan, X.; Northrop, B. H.; Stang, P. J., Nanopatterning of donor/acceptor hybrid supramolecular architectures on highly oriented pyrolytic graphite: a scanning tunneling microscopy study. *J. Am. Chem. Soc.* **2008**, *130* (40), 13433-13441.
84. Mocatta, D.; Cohen, G.; Schattner, J.; Millo, O.; Rabani, E.; Banin, U., Heavily doped semiconductor nanocrystal quantum dots. *Science* **2011**, *332* (6025), 77-81.
85. Chien, T. Y.; Kourkoutis, L. F.; Chakhalian, J.; Gray, B.; Kareev, M.; Guisinger, N. P.; Muller, D. A.; Freeland, J. W., Visualizing short-range charge transfer at the interfaces between ferromagnetic and superconducting oxides. *Nat. Commun.* **2013**, *4*, 2336.
86. Bera, A.; Dey, S.; Pal, A. J., Band mapping across a pn-junction in a nanorod by scanning tunneling microscopy. *Nano letters* **2014**, *14* (4), 2000-2005.

87. Shih, M. C.; Huang, B. C.; Lin, C. C.; Li, S. S.; Chen, H. A.; Chiu, Y. P.; Chen, C. W., Atomic-scale interfacial band mapping across vertically phased-separated polymer/fullerene hybrid solar cells. *Nano letters* **2013**, *13* (6), 2387-2392.
88. Braunecker, W. A.; Owczarczyk, Z. R.; Garcia, A.; Kopidakis, N.; Larsen, R. E.; Hammond, S. R.; Ginley, D. S.; Olson, D. C., Benzodithiophene and Imide-Based Copolymers for Photovoltaic Applications. *Chem. Mater.* **2012**, *24* (7), 1346-1356.
89. Braunecker, W. A.; Oosterhout, S. D.; Owczarczyk, Z. R.; Larsen, R. E.; Larson, B. W.; Ginley, D. S.; Boltalina, O. V.; Strauss, S. H.; Kopidakis, N.; Olson, D. C., Ethynylene-Linked Donor-Acceptor Alternating Copolymers. *Macromolecules* **2013**, *46* (9), 3367-3375.
90. Braunecker, W. A.; Oosterhout, S. D.; Owczarczyk, Z. R.; Kopidakis, N.; Ratcliff, E. L.; Ginley, D. S.; Olson, D. C., Semi-random vs Well-Defined Alternating Donor-Acceptor Copolymers. *ACS Macro Lett.* **2014**, *3* (7), 622-627.
91. Oosterhout, S. D.; Braunecker, W. A.; Owczarczyk, Z. R.; Ayzner, A. L.; Toney, M. F.; Olson, D. C.; Kopidakis, N., Molecular engineering to improve carrier lifetimes for organic photovoltaic devices with thick active layers. *Org. Electron.* **2017**, *47*, 57-65.
92. Ferguson, A. J.; Kopidakis, N.; Shaheen, S. E.; Rumbles, G., Dark carriers, trapping, and activation control of carrier recombination in neat P3HT and P3HT:PCBM blends. *J. Phys. Chem. C* **2011**, *115* (46), 23134-23148.
93. Dayal, S.; Kopidakis, N.; Rumbles, G., Photoinduced electron transfer in composites of conjugated polymers and dendrimers with branched colloidal nanoparticles. *Faraday Discuss.* **2012**, in press.
94. Savenije, T. J.; Ferguson, A. J.; Kopidakis, N.; Rumbles, G., Revealing the Dynamics of Charge Carriers in Polymer:Fullerene Blends Using Photoinduced Time-Resolved Microwave Conductivity. *J. Phys. Chem. C* **2013**, *117* (46), 24085-24103.
95. Owczarczyk, Z. R.; Braunecker, W. A.; Oosterhout, S. D.; Kopidakis, N.; Larsen, R. E.; Ginley, D. S.; Olson, D. C., Cyclopenta[c]thiophene-4,6-dione-Based Copolymers as Organic Photovoltaic Donor Materials. *Adv. Energy Mater.* **2014**, *4* (11), 1301821.
96. Saeki, A.; Yoshikawa, S.; Tsuji, M.; Koizumi, Y.; Ide, M.; Vijayakumar, C.; Seki, S., A Versatile Approach to Organic Photovoltaics Evaluation Using White Light Pulse and Microwave Conductivity. *J. Am. Chem. Soc.* **2012**, *134* (46), 19035-19042.
97. Ferguson, A. J.; Kopidakis, N.; Shaheen, S. E.; Rumbles, G., Quenching of excitons by holes in poly(3-hexylthiophene) films. *J. Phys. Chem. C* **2008**, *112*, 9865-9871.
98. Larson, B. W.; Reid, O. G.; Coffey, D. C.; Avdoshenko, S. M.; Popov, A. A.; Boltalina, O. V.; Strauss, S. H.; Kopidakis, N.; Rumbles, G., Inter-Fullerene Electronic Coupling Controls the Efficiency of Photoinduced Charge Generation in Organic Bulk Heterojunctions. *Adv. Energy Mater.* **2016**, *6* (24), n/a.
99. Larson, B. W.; Whitaker, J. B.; Wang, X.-B.; Popov, A. A.; Rumbles, G.; Kopidakis, N.; Strauss, S. H.; Boltalina, O. V., Electron Affinity of Phenyl-C61-Butyric Acid Methyl Ester (PCBM). *The Journal of Physical Chemistry C* **2013**, *117* (29), 14958-14964.
100. Kuvychko, I. V.; Whitaker, J. B.; Larson, B. W.; Folsom, T. C.; Shustova, N. B.; Avdoshenko, S. M.; Chen, Y.-S.; Wen, H.; Wang, X.-B.; Dunsch, L.; Popov, A. A.; Boltalina, O. V.; Strauss, S. H., Substituent effects in a series of 1,7-C60(RF)2 compounds (RF = CF3, C2F5, n-C3F7, i-C3F7, n-C4F9, s-C4F9, n-C8F17): electron affinities, reduction potentials and E(LUMO) values are not always correlated. *Chemical Science* **2012**, *3* (5), 1399-1407.
101. Aldrich, T. J.; Matta, M.; Zhu, W.; Swick, S. M.; Stern, C. L.; Schatz, G. C.; Facchetti, A.; Melkonyan, F. S.; Marks, T. J., Fluorination Effects on Indacenodithienothiophene Acceptor Packing and Electronic Structure, End-Group Redistribution, and Solar Cell Photovoltaic Response. *J Am Chem Soc* **2019**, *141* (7), 3274-3287.
102. Tremolet de Villers, B. J.; O'Hara, K. A.; Ostrowski, D. P.; Biddle, P. H.; Shaheen, S. E.; Chabinyk, M. L.; Olson, D. C.; Kopidakis, N., Removal of Residual Diiodooctane Improves Photostability of High-Performance Organic Solar Cell Polymers. *Chem. Mater.* **2016**, *28* (3), 876-884.
103. Tang, M. L.; Bao, Z., Halogenated Materials as Organic Semiconductors. *Chem. Mater.* **2011**, *23* (3), 446-455.

CHAPTER 3.

Perfluorobenylation of Electron-Rich Perylene and Electron-Deficient Perylene Diimides —Synthesis, Isolation, and Characterization of Products

3.1. Introduction

The direct C-H fluorination (i.e., replacement of hydrogen with fluorine atoms) of organic electronic materials can impose significant improvements on the chemical and physical properties of conjugated small molecules and polymers alike used as either donor or acceptor materials¹⁰⁴⁻¹⁰⁸ (as also discussed in chapter 2). Furthermore, introduction of fluorinated functional groups, such as perfluoroalkyl (R_F) and perfluoroaryl (A_{RF}) moieties in polycyclic aromatic hydrocarbons (PAH) has received interest in the field of organic electronics for their ability to beneficially (and more significantly than direct fluorination) modulate the chemical and physical properties of PAHs for use as ambipolar and *n*-type materials.¹⁰⁹ For example, perfluoroalkylation has a much greater electron-withdrawing effect than simple fluorination on aromatic compounds, while the bulkier groups allow for more control over the solid-state packing.¹⁰⁹ This allows for tuning the optical and electronic properties as well as the controlling the crystal packing and morphology in blends. Moreover, the strong electron withdrawing ability of R_F increases the electron affinity and subsequently improves stability towards notorious oxidation of *n*-type materials.

Perylene (PERY) and its chemical derivatives are widely used as active materials in organic electronics as well as fluorescent dyes and pigments.¹¹⁰⁻¹¹¹ Exploration of new synthetic approaches towards derivatization of perylenes has recently intensified due to their excellent performance in organic photovoltaics (OPVs) and organic field effect transistors (OFETs).¹¹²⁻¹¹³ For example, the introduction of R_F groups was shown to strengthen π - π interactions,¹¹⁴ increase charge carrier mobility, and improve air stability.¹¹⁵ In one computational study of the charge

transport properties of (poly)trifluoromethylated polycyclic aromatic hydrocarbons (PAHs), PERY(CF₃)₄ was predicted to be an ambipolar material with comparably high hole and electron mobilities. Improved solid-state electrical conductivity was attributed to the more efficient columnar π - π stacking in the solid phase compared to the herringbone-sandwich packing motif of underivatized PERY.¹¹⁶⁻¹¹⁷ However, experimental device studies of such derivatives have been hampered by their low availability. The reported synthetic method for PERY(CF₃)_n ($n > 1$) derivatives requires harsh reaction conditions (i.e., high temperatures (300–360 °C) and pressure (in sealed glass ampoules), and it suffers from poor yields of desired compounds due to low selectivity.¹¹⁸

Alternatively, an electron-deficient derivative of perylene, perylene diimide (PDI), is one of the most investigated compounds among PAHs in the last decade; notably due to their versatile absorption, fluorescence, *n*-type semiconducting abilities, and photostability.¹¹⁹ Moreover, PDIs with varying imide groups can be prepared directly from PTCDA (and a primary-amine of choice) which is less than a twentieth of the price of underivatized PERY as of this writing; thus significantly decreasing the cost per molecule. The derivatization of PDIs can take place on either the *ortho* or *bay* regions, undergo annulation across the bay, and/or undergo dimerization (and trimerization/tetramerization).¹¹⁹⁻¹²⁰ These modifications generally require either an activation step before substitution, such as bromination, or a noble-metal catalysts—or both.

It was recently demonstrated by former Strauss-Boltalina group member Tyler Clikeman that it is possible to directly trifluoromethylate PTCDA without prior activation by controlled heating in the gas/solid phase using the GTGS reactor: generating substituted products containing 2–4 CF₃ groups on PTCDA which were subsequently converted into their respective PDIs.¹²¹ After trifluoromethylation, the PDI materials were air-stable, soluble in organic solvents, and thermally

robust allowing for vapor deposition as well as solution processing. However, the reported synthetic method for PDI-(CF₃)_n (n > 1) derivatives requires high temperatures (500 °C) and result in a mixture of products (and isomers thereof). Consequently, the major product, PDI-1,7-(CF₃)₂, is only obtained in a yield of 21%; without much control available to improving the selectivity more towards a single isomer (or number of CF₃ groups).

In this work, an alternative approach to fluoromodification of perylene and PDI is studied that is based on replacing commonly used perfluoroalkyl groups (C_nF_{2n+1}, or R_F) with perfluorobenzyl groups (C₆F₅CF₂, or Bn_F).^{109, 122} The Strauss-Boltalina group recently determined that Bn_F can be directly substituted onto a curved polycyclic aromatic hydrocarbon corannulene under more moderate conditions than required for CF₃ substitutions, and that Bn_F has a similar electron withdrawing effect as CF₃.¹²³ One can also expect a different (and likely more favorable for charge transport than in the case of bulky and electrically insulating R_F groups) type of solid-state intermolecular electronic coupling due to the presence of flexible C₆F₅ moieties that are known to exhibit strong inter- or intramolecular π - π interactions with electron-rich phenyl groups (if present) in the solid phase.¹²⁴⁻¹²⁵ To the knowledge of the author, except for the prior group Strauss-Boltalina work on perfluorobenylation of corannulene, mentioned above, no studies were reported on the perfluorobenylation of PAHs.

3.2. Direct C-H Perfluorobenylation of Perylene: Synthesis and Isolation

Figure 3.1 shows the general reaction scheme for the direct perfluorobenylation of PERY that was used in this work to prepare several members of a new family of PERY(Bn_F)_n compounds shown in the lower part of Figure 3.1. To find suitable conditions for preparation of PERY(Bn_F)_n derivatives, PERY was initially heated with two equiv. of Bn_FI in DMSO with copper-mediator at 120 °C for 24 hours (rxn. **1a** in Table 3.1); analogous to the conditions used by Li et al. for the

radical perfluoroalkylation of PAHs with perfluoroalkyl iodides.¹²² This reaction gave a mixture of products consisting predominately of two isomers of mono-substituted derivatives in the *peri*- (PERY-1-1) and *bay*- (PERY-1-2) positions (see Figure 3.1 for molecular structures and notations) in 1.6:1 ratio, according to the NMR spectra of the crude product mixture (see Figure 3.2 for more detail). The ¹H-NMR spectrum shown at the top of Figure 3.2 shows only a moderate 60% conversion of PERY was achieved in reaction **1a**; in comparison, when Li et al. carried out their reaction of PERY and two equiv. of perfluorooctyl iodide (C₈F₁₇I) at 120 °C, high regioselectivity towards *peri*- monosubstituted product with yield of 65% (after removing unreacted PERY) was reported.¹²⁶ This indicated a difference in reactivity between C₈F₁₇I and BnFI towards PERY and the necessity to further optimize perfluorobenylation conditions.

Increasing the reaction temperature to 145 °C, doubling the amount of the BnFI reagent, and increasing total reaction time to 48 h (reaction **1b**, in Table 3.1) resulted in significantly improved conversion and higher substitution degree compared to reaction **1a**. Notably, the ¹⁹F-NMR spectra of the crude products in Figure 3.3 and Figure 3.4 show several new products being generated in **1b** (Figure 3.4) that are not observed in the spectrum of **1a** (Figure 3.3). Moreover, the middle of Figure 3.5 shows the chromatogram of reaction **1a**, consisting of a large amount of unreacted PERY and only two other major peaks (the products PERY-1-1 and PERY-1-2); in comparison, the bottom of Figure 3.5 shows the chromatogram of reaction **1b**, where there is only trace amounts of unreacted PERY and greater degree of substitutions on PERY. Then, the reaction was scaled up to isolate minor products (5-fold increase, reaction **1c**), keeping all reaction parameters the same as in the reaction **1b**, except for addition of rigorous stirring of the reaction mixture with a magnetic stir bar (see Figure 3.6 for comparison of conditions and resulting chromatograms). This yielded unexpectedly significant changes to the product distribution: when agitation during

the reaction was limited to just that of refluxing solvent in the reaction tube as in reaction **1a**, predominant formation of *mono*-substituted perylenes was observed; in reaction **1c**, on the other hand, predominant products were tris- substituted perylenes (see details below) even though the stoichiometric reagent ratio was the same as in reaction **1a**. Furthermore, electrospray ionization mass spectrometry (ESI-MS) analysis of the crude product from reaction **1c** revealed that substitution of up to 5 Bn_F groups per PERY was achieved, albeit the major products were bis- and tris-substituted compounds (Figure 3.7). Improved conversion in reaction **1c** compared to reaction **1b** is an expected outcome of improved reagent mixing whereas such strong influence on the degree of substitution and hence product distribution was not anticipated.

Five new compounds were isolable from these two reaction products in sufficient quantities and purity to characterize further (see Figure 3.1 for structures). Reaction **1b** yielded high-purity samples of PERY-1-1, PERY-1-2, and PERY-2-1 after one stage of HPLC separation as shown in Figure 3.8, top. Minor fractions labeled as i and ii were identified as mixtures containing PERY-2 isomers, each having two of the four possible isomers with both *bay* and *peri* substitutions (see Figure 3.9, Figure 3.42, and Figure 3.43 for analysis). Note that fraction ii also contained unreacted PERY (nearly 50% by ¹H-NMR). Components of smaller fraction iii were not unambiguously identified in reaction **1a**.

Analysis of the elution of PERY(Bn_F)_n indicates that retention times (t_R) appear to increase as more Bn_F groups are added to the *peri* position (t_R(PERY-1-1) < t_R(PERY-2-1), while the derivatives with Bn_F on the *bay* position have lower retention times (t_R(PERY-1-2) < t_R(PERY-1-1)). It is hypothesized by the author that separation of components of PERY(Bn_F)_n mixtures with the use of Cosmosil Buckyprep column is largely based on the π–π interactions with the electron-rich pyrene stationary phase. When functional groups are substituted onto the *bay* positions (as in

PERY-1-2) it causes twisting of the perylene core and subsequently hinders possible π - π interaction with the stationary phase.¹²⁷ Another opposite factor at play here is increasing electron deficiency of the PERY core in PERY(BnF)_n as the substitution degree increases causing stronger donor-acceptor π - π interactions with electron-rich pyrene of the stationary phase. One can then infer that having substitutions on both the *bay* and *peri* positions (as in PERY-2 isomers identified in fractions i and ii) may result in partial cancelling out the above effects and result in the retention times close to underivatized PERY.

Reaction **1c** afforded isolation of two isomers of PERY-3 from the largest fraction (iv), by either simple solvent extraction (PERY-3-1) or an additional HPLC separation in methanol (PERY-3-2) as shown in the inset of Figure 3.8. Small amounts of a non-symmetric tetrakis-substituted isomer with two groups on the *peri* positions and two on the *bay* positions ((PERY-4-1, see Figure 3.44) were isolated from fraction iii, its exact substitution pattern is currently unknown.

3.3. Direct C-H Perfluorobenylation of Perylene Diimides: Synthesis and Isolation

The perylene diimide used in this work, *N,N'*-bis(pentafluorophenyl)perylene diimide (henceforth referred to simply as PDI), is already partially fluorinated and was prepared according to literature with modifications (see experimental section for details).¹²⁸⁻¹²⁹

It is noteworthy that in contrast to the plethora of possible isomers for 1-4 substitutions of PERY due to the four *bay* and four *peri* positions available (see Figure 3.9 and Figure 3.10), the number of possible isomers of PDIs is limited. With the four *peri* positions protected by the imide groups, there is a significant decrease in the possible number of substitutions and isomers thereof: from 2 isomers to 1 for the mono-product(s), and from 8 isomers to 2 for the bis-products (see Figure 3.9 for possible bis-perylene isomers). Noteworthy, formation of the higher PDI

substitution products (e.g. tris- and tetrakis) might be hindered under certain reaction conditions from lack of sterically available positions. This is under the assumption that the *ortho*-positions of PDIs (and PERY) are not reactive enough to be substituted before saturation of all possible *bay* (and *peri*) positions is achieved, if even then. Furthermore, it is assumed that Bn_F groups cannot be adjacent to each other on PDI (or PERY): for example, *peri* and *ortho* as well as *ortho* and *bay* positions on the same ring are too sterically hindered to fit, as are two adjacent *bay* positions (across the same *bay*-region) and two *peri* positions across a fissure from each other. This conjecture is in agreement with prior studies of trifluoromethyl PDIs by the Strauss-Boltalina group: even under the harsh thermal conditions, products with adjacent CF₃ groups were not formed;¹²¹ note that CF₂C₆F₅ (Bn_F) is bulkier than CF₃. Hence, the derivatization of PDIs ought to be more selective—generate fewer products but each in greater relative abundance—compared to the perfluorobenylation of PERY.

Figure 3.11 shows the general reaction scheme for the direct perfluorobenylation of PDI that was used in this work to prepare three new PDI-(Bn_F)_n compounds (*n* = 1–2), shown in the lower part of Figure 3.11. To find suitable conditions for the preparation of PDI-(Bn_F)_n compounds, PDI was initially heated with 2 equiv. of Bn_FI in DMSO with copper-mediator at 120 °C for 24 hours (rxn. **2a**, in Table 3.1). This reaction resulted in a mixture of products; the major product was a mono-substituted derivative, PDI-1-Bn_F, while there were two isolable minor bis-substituted products, PDI-1,6-(Bn_F)₂ and PDI-1,7-(Bn_F)₂, found in a ratio of 9.3:1.0:1.5 respectively according to the ¹⁹F-NMR spectrum of the crude product. In comparison, the PDI starting material was at a relative abundance of 14.8 based on the integration value in the ¹⁹F-NMR spectrum, achieving only a moderate 44% conversion of PDI into Bn_F-substituted derivatives. This result was similar to what was observed for the perfluorobenylation of PERY described in the previous section: the

perfluorobenylation of PDI at 120 °C resulted in relatively low conversion of starting material compared to the perfluoroalkylation by Li et al.

Indeed, after chromatographic separation reaction **2a** resulted in a 5.0% isolated yield of highly pure PDI-1-Bn_F, and less than 1% for either isolated bis-adduct, PDI-1,6-(Bn_F)₂ and PDI-1,7-(Bn_F)₂, (isolation discussed more below). In contrast, the perfluoroalkylation of another PDI derivative by Li et al. using either perfluorobutyl- (C₄F₉I) or perfluorooctyl-iodide (C₈F₁₇I) resulted in good isolated yields of 57% and 60% for the monosubstituted products PDI-1-C₄F₉ and PDI-1-C₈F₁₇, respectively; while the bis-perfluoroalkyl isomers (1,6 and 1,7) generated were collected together to give collective yields of 18% for PDI-(C₄F₉)₂ and 14% for PDI-(C₈F₁₇)₂. From this, one can infer that under the conditions used here, there is a difference in the reactivity between perfluoroalkyl- and perfluorobenzyl-radicals for the direct substitution onto PDI, and thereby the necessity to optimize the perfluorobenylation conditions.

Interestingly, following the same method as with PERY above—i.e., increasing the reaction temperature to 145 °C (from 120 °C), doubling the amount of Bn_FI reagent, and increasing the total reaction time to 48 hours (rxn. **2b** in Table 3.1)—resulted in greater conversion according to the ¹⁹F-NMR spectra of the crude product mixtures (compare Figure 3.12 for **2a** with Figure 3.13 for **2b**). However, when comparing between the spectra of crude products from reactions **2a** and **2b**, one can see the PDI-(Bn_F)_n product distribution does not change drastically, while the signals from the PDI starting material decrease in relative intensity in reaction **2b** compared to reaction **2a**. Indeed, the ratio PDI-1-(Bn_F)₂, PDI-1,6-(Bn_F)₂, and PDI-1,7-(Bn_F)₂ products for reaction **2b** is 7.5:1.0:1.2, respectively, close to the ratio found in **2a**. But this is relative to 5.0 for the amount of PDI starting material, which would indicate a conversion of at least 66% for reaction **2b** (compared to 44% for rxn. **2a**). More surprisingly, there is a disproportionate amount of fluorine signals in

the aromatic region (generally defined as ca. -135--170 here) per benzylic F(CF₂) fluorine signal (generally defined here as ca. -70--94 ppm).

To explain briefly, each Bn_F group has one triplet for the two benzylic fluorines F(CF₂), and three signals for the five aromatic fluorines (*ortho*-Bn_F, 2F; *meta*-Bn_F, 2F; *para*-Bn_F, 1F). In the case of Bn_FI, this results in a 2:5 ratio of benzylic to aromatic fluorines. Each PDI in this work (including the starting material) also has two sets of pentafluorophenyl groups which show up as three aromatic signals for the 10 aromatic fluorines (*ortho*-Ph_F, 4F; *meta*-Ph_F, 4F; *para*-Ph_F, 2F). Consequently, substituting a single Bn_F group onto PDI results in a benzylic to aromatic fluorine ratio of 2:15 (or 1:7.5); having two groups (PDI-(Bn_F)₂) will result in a ratio of 4:20 (or 1:5); PDI-(Bn_F)₃ will be 6:25 (or 1:4.17); and finally, PDI-(Bn_F)₄ will be 8:30 (or 1:3.75).

Therefore, if the aromatic fluorines of PDI starting material are taken into account in the ¹⁹F-NMR spectrum (as in, at least one signal from the PDI starting material is isolated and can be used to subtract out the relative intensity of the PDI Ph_F groups from the aromatic region) and there is not unreacted Bn_FI left over, then one can expect a ratio of the benzylic region to aromatic region to be no higher than that of mono-substituted derivatives at 2:15 (1:7.5). On the other end of the spectrum, one would not expect a ratio lower than that of PDI-(Bn_F)₄ at 8:30, if it could be prepared in the first place. Curiously, in reaction **2a** (120 C) this ratio is much higher than the maximum 2:15: after taking into account unreacted PDI—by setting the integration value for the starting material's *ortho*-Ph_F (2F) to 2, then subtracting out 10 from the resulting value for the total aromatic region—the ratio of benzylic to aromatic fluorines is 2.17 to 27.87, or 2.00:25.7 (1:12.8) indicating that there is (are) some side product(s) generated which have aromatic signals without benzylic fluorines being present on them; however, they could not be isolated or easily

characterized further. Moreover, these unidentified products are even in greater abundance going from reaction **2a** to **2b**.

It is interesting to note that in the reactions with PERY (see prior section) there was no apparent deviation from the expected 2:5 benzylic to aromatic ratio for PERY-Bn_F products in reaction **1a** (see Figure 3.3 for ¹⁹F-NMR spectrum of rxn. **1a**); while the crude ¹⁹F-NMR spectra of rxn. **1b** does have a difference from expected (2.0:6.8, see Figure 3.4), but this is a small difference in comparison to reaction **2a** or **2b** with PDI.

In total, three new PDI-(Bn_F)_n compounds were isolable by performing two stages of separation (see Figure 3.11 for structures). Initial separation by silica column chromatography—illustrated in the left of Figure 3.14 as a developed TLC plate—was used to isolate unreacted PDI as the third (bottom) fraction and pure *mono*-substituted product, PDI-1-Bn_F, in the second (middle) fraction; all other products coeluted together and were collected as the first (top) fraction for secondary separation. The right of Figure 3.14 shows the ¹⁹F NMR spectra of each of the three isolated fractions. Individual *bis*-isomers, PDI-1,6-(Bn_F)₂ and PDI-1,7-(Bn_F)₂, could be isolated using HPLC via a Cosmosil Buckyprep column using MeCN as the eluent (Figure 3.15).

It's noteworthy that when flash chromatography is not performed prior to HPLC separation with the Buckyprep column, then the unreacted PDI and PDI-1-Bn_F product stick to (and clog) the HPLC column while using MeCN as the eluent. This then required a stronger eluent to remove them from the column, such as toluene; which, in turn, does not allow for the separation between *bis*-isomers.

The high affinity for the pyrene stationary phase of underivatized PDI is consistent with the chromatographic results for the perfluorobenzylated PERY described above. Namely, if the perylene core remains flat after electron withdrawing groups are introduced, as is the case for *peri*

substituted PERY(Bn_F) products (and the imide groups on PDIs), then the perylene core will be more electron deficient and subsequently have a greater retention time due to the more favorable π - π interactions with the rigidly flat and electron-rich pyrene stationary phase. Conversely, substitutions of Bn_F groups on the *bay* distort the perylene core's two naphthalene subunits from planarity, impeding π - π overlap with the pyrene stationary phase and leading to a decrease in the retention time compared to unsubstituted PERY or PDI. Interestingly, the relative differences in stationary phase affinity (judged by their retention times) caused by the presence of one or two substituents on the *bay* position of PDI molecules are significantly larger compared to the difference for analogous mono- and bis-substituted on the *bay* positions in PERY molecules. This is undoubtedly due to fact that underivatized PDI is already highly electron deficient, (with EA of 3.01 eV) so the relative change in electron affinity per substituted Bn_F group is much smaller than for PERY molecules, which have lower EA and smaller π system. As a result, it makes the effect of decreased π - π overlap due to twisting the perylene core more substantial on *bay*-substituted PDI derivatives, thereby significantly lowering the relative retention time; while with *bay*-substituted PERY the increase in electron affinity partially offsets these affects, and the retention time stays very close to unsubstituted PERY.

3.4. Structural Characterization of Perfluorobenzylated Perylenes

3.4.1. X-ray crystallography.

Crystals of 3-PERY(CF₂C₆F₅) and 3,10-PERY(CF₂C₆F₅)₂ (PERY-1-1 and PERY-2-1 respectively) suitable for single-crystal X-ray diffraction were grown by evaporation of dichloromethane–methanol solutions. Data collection and refinement parameters are listed in Table 3.2. Thermal ellipsoid plots of the individual molecules are shown in Figure 3.16. The perylene cores of both molecules are essentially planar. For PERY-1-1, the average deviation of

the core C(sp²) atoms from their least-squares plane is ± 0.034 Å (the individual values range from -0.053 to 0.048 Å). For PERY-2-1, the average deviation is ± 0.050 Å (the individual values range from -0.092 to 0.077 Å).

Parallel pairs of PERY-1-1 molecules have extensive π - π overlap, as shown in Figure 3.17. The least-squares planes of the perylene cores are rigorously parallel. The nine C(sp²) atoms of one molecule that overlap the π system of its neighbor have perpendicular out-of-plane displacements that range from 3.346 to 3.417 Å and average 3.381 Å. These pairs are arranged in herringbone layers in crystallographic *bc* planes and are stacked in the crystallographic *a* direction, as shown in Figure 3.18. The structure of one of the two known polymorphs of unsubstituted PERY also exhibits herringbone sandwich layers in crystallographic *bc* planes that are stacked in the *a* direction with perpendicular out-of-plane displacements that range from 3.371 to 3.437 Å and average 3.412 Å as shown in Figure 3.19. Interestingly, in the structure of PERY-2-1 the molecules in form continuous stacks with two similar types of π - π overlap, as also shown in Figure 3.17 (and Figure 3.20).

The perpendicular distances of the C(sp²) atoms in one perylene core from the π systems of its two types of neighbors average 3.488 and 3.501 Å, not nearly as close as in PERY-1-1 (the perylene cores are rigorously parallel). These stacks form layers of perylene cores in crystallographic *bc* planes, with the layers separated by layers of the perfluorobenzyl substituents, as shown in Figure 3.21. The perylene cores in neighboring stacks are tilted 35.6° , as shown in Figure 3.22, where there are multiple C-H \cdots F interactions as close as 2.4 Å (see Figure 3.23). Within the fluorous layers formed by the perfluorobenzyl substituents, there are multiple intermolecular F \cdots F contacts (not shown) that range from 2.7 – 2.9 Å. Alternate views to compare

the crystal packing of PERY-1-1 and PERY-2-1, including space filling models, are shown in Figure 3.24 and Figure 3.25, respectively.

Such a significant change in the solid-state packing from fluoromodification has been observed before. For example, Okamoto et al. prepared 5,11-diphenyltetracene (PPT) and 5-perfluorophenyl-11-phenyltetracene (FPPT) and compared their solid-state interactions in single crystals and hole-mobility in OFETs.¹³⁰ They observed that PPT had no measurable π - π interactions between tetracene cores of neighboring molecules. In contrast, FPPT formed rows of planar tetracene cores with close π - π stacking ranging from 3.30 to 3.35 Å, with the side Ph and Ph_F groups forming columns with the neighboring PhF and Ph, respectively, with the close H...F distances of 2.4 Å between neighbors, which is believed to be a major pathway for electron transport. Not surprisingly, FPPT showed high hole-mobilities of $4.2 \times 10^{-2} \text{ cm}^2/\text{V}\cdot\text{s}$ in OFETs, more than two orders of magnitude greater than PPT under the same conditions.

It is worth mentioning that an increase (or decrease) in the π - π distance does not imply improved (hampered) mobility. For example, the orthorhombic polymorph of single-crystal rubrene, which has one of the highest mobility values in OFETs of $40 \text{ cm}^2/\text{V}\cdot\text{s}^2$, has relatively long π - π distances of 3.74 Å.¹³¹ At the same time, its parent PAH tetracene, which has closer π - π distances of 2.56 Å,¹³² has a mobility an order of magnitude lower in single-crystal OFETs.¹³³ The decreased mobility has been partly attributed to the negligible π - π overlap between adjacent slip-stacked molecules, compared to significant overlap with orthorhombic rubrene despite the greater distance between tetracene cores.¹³⁴ We note here that PERY-2-1 has a significant overlap between perylene cores within the same column and has π - π distances less than those of single crystal rubrene. Thus, it can be considered for future testing as an organic semiconductor in OFETs.

3.4.2. NMR spectroscopy.

Obtaining crystallographic data for two of the five isolated compounds aided NMR-based structural elucidations for those remaining compounds, which single crystals were not of sufficient quality for X-ray diffraction. Since PERY-1-1 has a single Bn_F group on the *peri* position, as found from the crystallographic data, this allowed for the determination of the fingerprint chemical shift region for the benzylic $\text{F}(\text{CF}_2)$ signals in the ^{19}F NMR spectrum for *peri* substitution at $-\delta$ 86 as shown in Figure 3.27. The other isolated mono-substituted PERY, PERY-1-2, might either have the substitution on the *bay* or *ortho* position. The observed ^{19}F chemical shift for $\text{F}(\text{CF}_2)$ of $-\delta$ 73 cannot be definitively assigned to either of them without additional information, however, the absence of the two singlets in the experimental ^1H NMR spectrum rules out the *ortho* isomer, leading to conclusion that PERY-1-2 is a *bay*-substituted derivative. In the ^{19}F NMR spectra of both compounds shown in Figure 3.27, the chemical shifts of the three aromatic multiplets of $\text{F}(\text{C}_6\text{F}_5)$ are practically indistinguishable, whereas chemical shifts of benzylic $\text{F}(\text{CF}_2)$ are sensitive to the position on the PERY core. Similarly, CF_3 -substituted PERY derivatives, studied by the Strauss-Boltalina group previously, showed distinct substitution-site dependent chemical shift regions in ^{19}F NMR spectra.^{118, 127}

Both PERY-3-1 and PERY-3-2 show resonances for two $-\text{CF}_2-$ groups in their ^{19}F -NMR spectra in the *peri* region (ca. -86 ppm), and one $-\text{CF}_2-$ in the *bay* region (ca. -72 ppm). There is no through-space coupling between the $-\text{F}(\text{CF}_2)-$ in either compound, which indicates there are no adjacent $-\text{CF}_2-$ groups (e.g. *ortho* with either an adjacent *peri* or *bay*, or two adjacent *peri* positions). The two proposed PERY-3 isomers shown in Figure 3.1 are the only structures that fulfil this condition and give a singlet in their respective ^1H -NMR spectra (see Figure 3.37 and Figure 3.40). Any other substitution pattern with two Bn_F groups in the *peri* position and one on

the *bay* would result in only doublets (and one triplet). However, it is not possible to distinguish between these isomers from these results alone.

Notably, no spectroscopic evidence was found that *ortho*-substitution took place in reactions **1a** or **1b**, suggesting it to be the least reactive site on PERY under applied reaction conditions. Examples of direct substitutions on the *ortho* positions with CF₃ groups exist, however, they require high temperatures (300–360 °C) and are only observed in polysubstituted PERY(CF₃)_n, where $n > 4$, i.e., where it was the least sterically hindered position available.¹¹⁸

3.5. Structural Characterization of Perfluorobenzylated Diimide products

3.5.1. X-ray crystallography.

Crystals of PDI-1-Bn_F and PDI-1,7-(Bn_F)₂ suitable for single-crystal X-ray diffraction were grown by evaporation of dichloromethane–methanol solutions. Data collection and refinement parameters are listed in Table 3. Side and top view drawings of X-ray structures of the individual molecules are shown in Figure 3.46. The presence of the Bn_F substituents results in significant distortions of the PDI core from planarity, also shown in Figure 3.46. The distortions from planarity can be quantified by determining the twist angle made by the least-squares planes of the two naphthalene moieties (NAPHs) of the PDI core. For PDI-1-Bn_F, the two NAPHs are individually planar, with average out-of-plane displacements of the 10 NAPH C(sp²) atoms (OOPDs) of ±0.05 and ±0.09 Å, and the twist angle is 23.2°. For PDI-1,7-(Bn_F)₂, the two NAPHs are planar with average OOPDs of ±0.08 and ±0.08 Å, and the twist angle is 31.1°. These can be compared with the twist angles of 6.5° and 37° in the structures of (Ph)₂PDI-1,7-F₂ and (Ph)₂PDI-1,6,7,12-Cl₄, respectively.¹³⁵ Discussion of the solid state packing for PDI-1-Bn_F and PDI-1,7-(Bn_F)₂ is given in the following chapter (section 4.6.1).

3.5.2. NMR spectroscopy.

Obtaining crystallographic data for PDI-1-Bn_F and PDI-1,7-(Bn_F)₂ aided NMR-based structural elucidations for PDI-1,6-(Bn_F)₂, where single crystals were not of sufficient quality for X-ray diffraction. Of note, in the ¹⁹F NMR spectrum of PDI-1-Bn_F there are three aromatic signals from the Bn_F group and three (six) signals from the two Ph_F groups attached at the imide position which are no longer isochronous (see Figure 3.47 for assignment of aromatic fluorines and Figure 3.48 for full spectrum showing benzylic F(CF₂) at ca. δ -77 ppm). The signal(s) from the *para*-Ph_F (2F) fluorine can be used as an internal standard to determine how many substitutions took place via integration value, even if Bn_F groups are symmetric as is the case for both bis adducts. From the crystallographic data above, it is known that PDI-1-Bn_F (and PDI-1,7-(Bn_F)₂ for that matter) has (have) the Bn_F on the *bay* position(s) instead of the *ortho* position(s). Moreover, there is only a slight variation in the chemical shift of the F(CF₂) going from one to two Bn_F groups. It can be inferred that, as was the case for PERY-(Bn_F)_n and trifluoromethylated PDIs, Bn_F substitutions onto the different unique positions of PDI (*bay* or *ortho*) should result in the benzylic signals being in distinct regions from each other. In the case of PDI-1-Bn_F and PDI-1,7-(Bn_F)₂, the observed ¹⁹F fingerprint region for the benzylic (CF₂) *bay* position is around δ -77 ppm; it is slightly shifted from the *bay* fingerprint region of PERY at ca. δ -73 ppm. Therefore, it can be determined that the compound labeled PDI-1,6-(Bn_F)₂ contains two Bn_F groups from the integration value (using the Ph_F groups as an internal standard); while it can be inferred that it must have both Bn_F groups on the 1,6 *bay* positions. Indeed, the ¹⁹F-NMR spectrum of PDI-1,7-(Bn_F)₂ shows symmetry between the Ph_F groups on the imide and the Bn_F signals; in contrast the ¹⁹F-NMR spectrum of PDI-1,6-(Bn_F)₂ shows broken symmetry between the Ph_F groups on the imide, while the Bn_F groups remain symmetric. Hence, the structural assignment of PDI-1,6-(Bn_F)₂ is the only reasonable option.

Moreover, there is a singlet and pair of doublets in the ^1H NMR spectrum of PDI-1,7-(BnF) $_2$, from the three sets of 2 equivalent hydrogens in the product, which are very similar to the observed singlet and pair of doublets in the ^1H NMR spectrum of PDI-1,6-(BnF) $_2$. This splitting pattern is only possible with substitution on the 1,6 or the 2,5 positions. Since it is unlikely that one, let alone two, *ortho* positions are substituted before a substitution on the bay position would take place, it is reasonable to infer that the isolated compound labeled as PDI-1,6-(BnF) $_2$ indeed has both BnF groups on the bay positions, as indicated.

3.6. Conclusions

For the first time, solution-phase direct perfluorobenylation of planar polycyclic aromatic hydrocarbons, an electron-rich PERY and electron-poor PDI, has been studied. While not fully optimized, the direct perfluorobenylation of PERY reactions described afforded isolation of five new compounds of PERY(BnF) $_n$, where $n = 1, 2$ and 3 ; with evidence based on NMR of additional products with up to $n=4$, and indirect evidence based on MS for up to $n=5$. The product distribution was found to be readily controlled by reagent ratios and strongly influenced by reaction solution agitation method. Comparison of the solid-state packing in single crystals of PERY (BnF) $_n$, PERY-1-1 and PERY-2-1 with that of underivatized PERY, revealed a stepwise change from a typical herringbone packing motif of PERY, to a quasi-herringbone packing motif of mono-substituted PERY, to the rows of perylene columns with continuous large π - π overlap, where each row is separated by closely packed perfluorophenyl groups. The latter has been considered by theorists as the desired packing for ambipolar materials. In such structures, high hole mobility could be through the perylene columns, while strong Ph_F-Ph_F and C(sp²)-H \cdots F interactions might enable high electron mobility.

Furthermore, the solution phase direct perfluorobenylation of PDI afforded isolation of three new *bay*-substituted compounds of PDI-(Bn_F)_n, where $n = 1, 2$; but in contrast with PERY, had comparatively low conversion of PDI and low isolated yield of products. Interestingly, there appears to be side-reactions generating other non-Bn_F-substituted products—determined by the increase in aromatic fluorine signals in the ¹⁹F NMR spectrum but relative lack of benzylic F signals from the Bn_F groups, presumably causing the lower yield of the desired PDI-(Bn_F)_n products. While this phenomenon was observed for the perfluorobenylation of PDI at 120 °C and exacerbated when heated at 145 °C, there was no such indication for side reactions of PERY at 120 °C and only a minor increase in aromatic fluorine signals compared to benzylic signals at 145 °C. This suggests a difference in the reactivity between electron rich PERY and electron deficient PDI for direct perfluorobenylation under the experimental conditions used; which was not observed for the analogous direct perfluoroalkylation of PAHs (PERY and PDI specifically). While the molecular compositions of these side products have yet to be determined, understanding their generation should nevertheless be investigated further to avoid or minimize their formation and thereby increase the yield of PDI-(Bn_F)_n products.

3.7. EXPERIMENTAL SECTION

3.7.1. Materials and Methods.

Reagents and Solvents. The following reagents and solvents were used as received unless otherwise indicated: heptafluorobenzyl iodide (C₆F₅CF₂I, abbr. Bn_FI; SynQuest Laboratories, 90%), chloroform-*d* (abbr. CDCl₃; Cambridge Isotope Laboratories, 99.8%), hexafluorobenzene (abbr. C₆F₆; Sigma-Aldrich, >99.5% NMR grade), copper powder (Strem Chemical, 99%), perylene (abbr. PERY; Sigma-Aldrich, 99+%), 2,3,4,5,6-pentafluoroaniline (Oakwood Products, 99+%), perylene-3,4,9,10-tetracarboxylic dianhydride (abbr. PTCDA; Sigma-Aldrich, 97%), zinc

acetate dihydrate (Aldrich Chemical, 98+%), 2-propanol (abbr. IPA, EMD Millipore, ACS grade), diethyl ether anhydrous (EMD Millipore, ACS grade), dimethyl sulfoxide (abbr. DMSO; Fisher Chemical, ACS grade), acetonitrile (abbr. MeCN; Sigma-Aldrich, HPLC grade), toluene (Sigma-Aldrich, ACS grade), dichloromethane (abbr. DCM; Sigma-Aldrich, ACS grade), ethyl acetate (Sigma-Aldrich, ACS grade), hexane (Sigma-Aldrich, ACS grade), 1-methyl-2-pyrrolidone (Sigma-Aldrich, ACS grade), silica gel (Sigma Aldrich, high purity grade, 60 Å pore size, 70–230 mesh), sodium chloride (Fisher Chemical, ACS grade), and magnesium sulfate (Aldrich Chemical, anhydrous, technical grade). Distilled-deionized water (abbr. dd-H₂O) with a minimum resistance of 18 MΩ-cm was prepared using a Barnstead NANOpure ultrapure water system. DMSO was dried over activated 3 Å molecular sieves for 24 h and cannula transferred into a flame-dried Schlenk tube under a N₂ (g) purge for storage. A saturated sodium chloride solution (abbr. NaCl brine) was prepared using dd-H₂O at room temperature.

HPLC Analysis. High Performance Liquid Chromatography (HPLC) was conducted using a Shimadzu liquid chromatography instrument (CBM-20A control module, SPD-20A UV-Vis detector, LC-6AD pump, manual injector valve). The HPLC columns utilized were COSMOSIL Buckyprep 10 mm I.D. x 250 mm semi-prep and 20 mm I.D. x 250 mm prep columns (Nacalai Tesque, Inc.) at a flow rate of 5 mL min⁻¹ and 16 mL min⁻¹, respectively.

NMR Analysis. All ¹H and ¹⁹F NMR spectra were of CDCl₃ solutions recorded at room temperature with a Varian (Agilent) 400MR NMR spectrometer equipped with Automated Tuning. ¹H and ¹⁹F NMR spectra were acquired at 400 MHz and 376.1 MHz, respectively, using a 1 second relaxation time, and a 45 ° pulse angle. ¹H chemical shifts are reported relative to δ(CHCl₃) = 7.26). ¹⁹F chemical shifts are reported relative to δ(C₆F₆) = -164.9).

Mass Spectrometry. A Thermo-Finnigan LTQ LC/MS-MS linear ion-trap mass spectrometer with an electrospray ionization (ESI) source was utilized to record positive ion ESI (PI-ESI) mass spectra. Acetonitrile was used as the carrier solvent and injected at a flow rate of 50 $\mu\text{L min}^{-1}$.

3.7.2. *Synthesis of PERY-(BnF)_n*

General reaction procedure. A Schlenk tube equipped with a #9 O-ring sidearm was charged with PERY (10 mg, 40 μmol) and Cu powder (15 mg, 240 μmol , 6 equiv) and subsequently dried overnight in a 120 °C oven. The reaction tube was taken from the oven and attached to a Schlenk line to cool under dynamic vacuum. BnFI (13.4 μL , 80 μmol , 2 equiv) and dried DMSO (5.0 mL) were added via syringe with the tube open under a flow of N₂. The reaction tube was degassed by using the freeze-pump-thaw (FPT) technique three times (x3). The reaction flask was closed under vacuum and allowed to warm to room temperature before placing in a heated oil bath (145 \pm 5 °C) for 24 hours. Note: the reaction should be refluxing shortly after placing the flask in the oil bath due to the reduced pressure. Upon completion, the reaction was cooled to room temperature and the contents poured into a separatory funnel containing dd-H₂O (20 mL). The mixture was extracted with diethyl ether (3x20 mL); the organic layers were combined and washed with dd-H₂O (3x20 mL), NaCl brine (20 mL), and dried over MgSO₄. The solvent was removed by rotary evaporation and the products were separated by HPLC. After 24 hours, the flask was cooled to room temperature and opened under a positive pressure of N₂ to add more BnFI (13.4 μL , 80 μmol , 2 equiv.) to the reaction, for a total of four equiv. of BnFI added. This was FPTx3 as before and placed back into the heated oil bath (145 \pm 5 °C) for an additional 24 hours. Note that the reaction does not reflux as vigorously the second time it is placed in the oil bath compared to the first.

Reaction 1a (Schlenk tube without stir bar): The reaction was allowed to heat for 24 hours at a temperature 120 \pm 5 °C (oil-bath temperature) before it was worked up

reaction flask was under vacuum and allowed to warm to room temperature before placing in a heated oil bath ($145\pm 5\text{ }^{\circ}\text{C}$) for 24 hours.

Reaction 1b (Schlenk tube without stir bar): The reaction was allowed to heat for 24 hours at a temperature $145\pm 5\text{ }^{\circ}\text{C}$ (oil-bath temperature) before the reaction flask was cooled to room temperature and opened under a positive pressure of N_2 to add more BnFI ($13.4\text{ }\mu\text{L}$, $80\text{ }\mu\text{mol}$, 2 equiv.) to the reaction, for a total of four equiv. of BnFI added. This was FPTx3 as before and placed back into the heated oil bath ($145\pm 5\text{ }^{\circ}\text{C}$) for an additional 24 hours. Note that the reaction does not reflux as vigorously the second time it is placed in the oil bath compared to the first. Upon completion (48 h total), the reaction was cooled to room temperature worked up as normal.

Reaction 1c (pear-shaped flask with stir bar): The same general procedure as described above for reaction 1b, but with five times the amount of material used (i.e., 50 mg PERY, same concentration, and the same number of equiv. of reagents). However, to improve the mixing and efficient use of BnFI , a magnetic stir bar was used in the pear-shaped Schlenk flask, instead of a vertical reaction tube without a stirrer as in reaction 1a and 1b. This allowed for a better conversion of perylene as well as the formation of products with a greater number of BnF groups.

3.7.2.1. NMR chemical shifts, coupling constants, and yields of isolated PERY-(BnF) $_n$.

PERY-1-1. Isolated yield of 3.0 mg (reaction **1a**) (16 % yield); ^1H NMR (400 MHz, CHLOROFORM-*d*) δ ppm 8.19 - 8.29 (m, 4 H), 7.93 (d, $J=8.2\text{ Hz}$, 1 H), 7.74 (d, $J=8.2\text{ Hz}$, 2 H), 7.77 (d, $J=8.2\text{ Hz}$, 1 H), 7.49 - 7.58 (m, 3 H). ^{19}F NMR (376 MHz, CHLOROFORM-*d*) δ ppm -86.28 (t, $J=23.2\text{ Hz}$, 2 F), -141.51– -141.22 (m, 2 F), -152.92 (t, $J=21.8\text{ Hz}$, 1 F), -163.40– -163.18 (m, 2 F)

PERY-1-2. ^1H NMR (400 MHz, CHLOROFORM-*d*) δ ppm 8.25 (d, $J=7.4\text{ Hz}$, 2 H), 8.02 (d, $J=8.6\text{ Hz}$, 1 H), 7.97 (d, $J=7.0\text{ Hz}$, 1 H), 7.86 (d, $J=9.0\text{ Hz}$, 1 H), 7.82 (d, $J=8.2\text{ Hz}$, 1 H), 7.76 (d,

$J=8.2$ Hz, 1 H), 7.70 (d, $J=7.8$ Hz, 1 H), 7.66 (t, $J=7.4$ Hz, 1 H), 7.58 (t, $J=7.8$ Hz, 1 H), 7.40 (t, $J=7.8$ Hz, 1 H). ^{19}F NMR (376 MHz, CHLOROFORM-*d*) δ ppm -72.85 (t, $J=23.2$ Hz, 2 F), -141.18 (q, $J=21.8$ Hz, 2 F), -153.95 (t, $J=20.4$ Hz, 1 F), -164.64 (tsxt, $J=16.4, 16.4, 5.5, 5.5, 5.5, 5.5$ Hz, 2 F)

PERY-2-1. Isolated yield of 2.9 mg (reaction **1a**) and 11.6 mg (reaction **1b**) (10.8 and 8.5 % yield, respectively); ^1H NMR (400MHz, CHLOROFORM-*d*) δ = 8.29 (d, $J = 7.8$ Hz, 4 H), 7.99 (d, $J = 8.6$ Hz, 2 H), 7.84 (d, $J = 7.8$ Hz, 2 H), 7.58 (t, $J = 8.0$ Hz, 2 H). ^{19}F NMR (376 MHz, CHLOROFORM-*d*) δ ppm -86.31 (t, $J=23.2$ Hz, 4 F), -141.42 (td, $J=23.2, 19.1$ Hz, 4 F), -152.63 (t, $J=21.8$ Hz, 2 F), -163.27– -163.05 (m, 4 F).

PERY-3-1. Percent yield of 5.5 % (by H-NMR, reaction **1c**, see Figure 3.45) A; ^1H NMR (400 MHz, CHLOROFORM-*d*) δ ppm 8.45 (s, 1 H), 8.30 - 8.35 (m, 2 H), 8.11 (d, $J=7.8$ Hz, 1 H), 8.07 (d, $J=9.0$ Hz, 1 H), 8.00 (d, $J=8.2$ Hz, 1 H), 7.71 - 7.79 (m, 2 H), 7.66 (t, $J=8.0$ Hz, 1 H). ^{19}F NMR (376 MHz, CHLOROFORM-*d*) δ ppm -72.61 (t, $J=21.8$ Hz, 2 F), -85.64 (t, $J=23.2$ Hz, 2 F), -86.71 (t, $J=23.2$ Hz, 2 F), -141.39 (s, 4 F), -142.26– -142.00 (m, 2 F), -151.87 (s, 2 F), -152.68 (dd, $J=20.4, 17.7$ Hz, 1 F), -162.92– -162.64 (m, 4 F), -163.77 (t, $J=19.1$ Hz, 2 F).

PERY-3-2. Percent yield of 7.2 % (by H-NMR, reaction **1c**, see Figure 3.45); ^1H NMR (400 MHz, CHLOROFORM-*d*) δ ppm 8.30 - 8.36 (m, 2 H), 8.28 (d, $J=7.8$ Hz, 1 H), 8.10 (d, $J=8.2$ Hz, 1 H), 8.05 (d, $J=7.4$ Hz, 2 H), 7.91 (d, $J=8.2$ Hz, 1 H), 7.75 (t, $J=8.0$ Hz, 1 H), 7.52 (t, $J=8.0$ Hz, 1 H). ^{19}F NMR (376 MHz, CHLOROFORM-*d*) δ ppm -73.86 (t, $J=23.2$ Hz, 1 F), -85.03 (t, $J=23.2$ Hz, 2 F), -86.59 (t, $J=23.2$ Hz, 2 F), -140.95 (q, $J=21.8$ Hz, 2 F), -141.66– -141.36 (m, 4 F), -151.92 (t, $J=20.4$ Hz, 1 F), -152.19 (t, $J=21.8$ Hz, 1 F), -153.16 (t, $J=20.4$ Hz, 1 F), -162.86– -162.66 (m, 2 F), -163.03 (t, $J=19.8$ Hz, 2 F), -164.12– -163.94 (m, 2 F).

3.7.3. Synthesis of *N,N'*-bis(pentafluorophenyl)perylene diimide (PDI)

N,N'-bis(pentafluorophenyl)perylene diimide (PDI) was prepared according to the referenced literature with modifications.¹²⁸⁻¹²⁹ The procedure given here gave a modestly improved isolated yield of 60% in contrast with previously reported yield of 52%.²⁶ A 25 mL three-neck, round bottom flask, equipped with water condenser, stir bar, and septa, was attached to a Schlenk line and purged with N₂ (g) using an exit needle for 5 min. Under a N₂ (g) purge, Zn(OAc)₂·2H₂O (107 mg, 0.583 mmol) and PTCDA (300 mg, .756 mmol) were dry loaded into the reactor, followed by the addition of sparged NMP (15 mL) via cannula transfer. The reactor was kept under a N₂ (g) atmosphere with a gas bubbler outlet attached to a Schlenk line. The reaction was heated in an oil bath at 100 °C for 1 h with stirring, submerged to just above the reactor's solvent level. Under a N₂ (g) purge, pentafluoroaniline (Ph_F-NH₂) (692 mg, 3.78 mmol, 5 equiv.) was dry loaded into the reactor, and the reaction temperature was increased to 180 °C and heated for 36 h. Upon completion, the reaction was allowed to cool to room temperature and the contents were poured into a separatory funnel containing half-saturated NaCl_(aq) solution (100 mL). The mixture was extracted with toluene (3x200 mL). The organic layers were added together, washed with half-saturated NaCl_(aq) solution (3x100 mL), and dried over MgSO₄. The diimide product was purified by adsorbing the crude product mixture onto silica gel and running a silica plug twice using DCM. Isolated yield 329 mg (60 % yield); ¹H NMR (CDCl₃, 400 MHz): δ = 8.83 (d, *J* = 8Hz, 4H), 8.79 (d, *J* = 8Hz, 4H); ¹⁹F NMR (CDCl₃): -146.38 (d, *J* = 17.7, 2F), -154.76 – -154.93 (t, 1F), -164.51 – -165.72 (m, 2F).

3.7.4. Synthesis of PDI(-(BnF))_n.

Reaction 2a. A Schlenk tube equipped with a #9 O-ring sidearm was charged with PDI (10 mg, 14 μmol) and Cu powder (7.0 mg, 110 μmol, 8 equiv.) and subsequently dried overnight in a 120 °C oven. The reaction tube was taken from the oven and attached to a Schlenk line to cool

under dynamic vacuum. Bn_FI (4.7 μ L, 28 μ mol, 2 equiv.) and dried DMSO (5.0 mL) were added via syringe with the tube open under a flow of N₂. The solution was degassed by using the freeze-pump-thaw (FPT) technique three times (x3). The reaction flask was closed under vacuum and allowed to warm to room temperature before placing in a heated oil bath (120 \pm 5 $^{\circ}$ C). Note: the reaction should be refluxing shortly after placing the flask in the oil bath due to the reduced pressure. After heating for 24 hours, the reaction was allowed to cool to room temperature, and the contents were poured into a separatory funnel containing dd-H₂O (30 mL). The mixture was extracted with ethyl acetate (3x10 mL). The organic layers were added together, washed with dd-H₂O (3x10) and NaCl brine (10 mL), and dried over MgSO₄. Purification was performed in two stages. First, flash chromatography was employed using a solution of 1:2:7 EtOAc/DCM/Hexane as the eluent. Compounds with more than one perfluorobenzyl group substitution eluted together as a smear and required further separation by HPLC.

Reaction 2b. Same general procedure as rxn. **2a**, with the alteration that the temperature was 145 \pm 5 $^{\circ}$ C (instead of 120 \pm 5 $^{\circ}$ C) and that after 24 hours the flask was cooled to room temperature and opened under a positive pressure of N₂ to add more Bn_FI (4.7 μ L, 28 μ mol, 2 equiv.) to the reaction, for a total of four equiv. of Bn_FI added. This was FPTx3 as before and placed back into the heated oil bath (145 \pm 5 $^{\circ}$ C) for an additional 24 hours. Note that the reaction does not reflux as vigorously the second time it is placed in the oil bath compared to the first. Same workup and purification as reaction **2a** above.

3.8. Tables and Figures

Table 3.1. Reaction conditions for direct perfluorobenylation.

Rxn. #	Substrate	# of Bn _F I additions (2 equiv. per addition) ^(a)	Time (h)	Solvent	Temp. (°C)	Source of agitation
1a	PERY	1	24	DMSO	120	reflux
1b	PERY	2	48	DMSO	145	reflux
1c	PERY	2	48	DMSO	145	stir bar
2a	PDI	1	24	DMSO	120	reflux
2b	PDI	2	48	DMSO	145	reflux

Chromatograms for reactions 1a–c are given in Figure 3.5 and Figure 3.8
NMR spectra for reaction 2a and 2b are given Figure 3.12 Figure 3.13
^a First addition of Bn_FI was added to the reaction before heating; subsequent additions were added after 24 hours.

Table 3.2. Crystal data and final refinement parameters for the PERY-1-1 and PERY-2-1 X-ray diffraction structures.

Compound	PERY-1-1	PERY-2-1
formula	C ₂₇ H ₁₁ F ₇	C ₃₄ H ₁₀ F ₁₄
formula wt., g mol⁻¹	468.36	684.42
habit, color	plate, yellow	needle, orange
crystal system	monoclinic	monoclinic
crystal size, mm	0.101 × 0.067 × 0.005	0.276 × 0.038 × 0.031
space group, Z	P2 ₁ /c, 4	C2/c, 8
a, Å	15.548(2)	36.833(4)
b, Å	10.6962(17)	7.3678(7)
c, Å	11.3090(18)	18.8651(19)
α, deg	90	90
β, deg	93.482(3)	100.917(2)
γ, deg	90	90
V, Å³	1877.3(5)	5026.9(9)
T (K)	150	100
ρ_{calc}, g cm⁻³	1.657	1.809
Goof [all data]	1.054	0.965
R(F) (I>2σ(I))^a	0.0842	0.0568
wR(F²) [all data]^a	0.1822	0.1383

^a $R(F) = \frac{\sum ||F_o| - |F_c||}{\sum |F_o|}$; $wR(F^2) = (\frac{\sum [w(F_o^2 - F_c^2)^2]}{\sum [w(F_o^2)^2]})^{1/2}$.

Table 3. Crystal data and final refinement parameters for PDI-1-Bn_F and PDI-1,2-(Bn_F)₂ X-ray diffraction^a

<i>Compound abbreviation</i>	1-Bn_F	1,7-(Bn_F)₂
<i>empirical formula</i>	C ₄₃ H ₇ F ₁₇ N ₂ O ₄	C ₅₀ H ₆ F ₂₄ N ₂ O ₄
<i>formula weight, g mol⁻¹</i>	938.51	1154.57
<i>crystal habit</i>	rhombohedron	needle
<i>crystal color</i>	dark red	red-orange
<i>crystal size, μm</i>	175 × 124 × 82	372 × 109 × 40
<i>crystal system</i>	triclinic	triclinic
<i>space group, Z</i>	<i>P</i> $\bar{1}$, 4	<i>P</i> $\bar{1}$, 4
<i>a, Å</i>	8.1330(10)	11.6214(16)
<i>b, Å</i>	15.0581(18)	14.537(2)
<i>c, Å</i>	15.1685(18)	25.938(3)
<i>α, degree</i>	68.573(2)	75.612(2)
<i>β, degree</i>	88.677(2)	83.723(2)
<i>γ, degree</i>	88.307(2)	88.023(3)
<i>V, Å³</i>	1728.4(4)	4219.1(10)
<i>T, K</i>	100(2)	100(2)
<i>ρ_{calc}, g cm⁻³</i>	1.803	1.818
<i>R(F) [I > 2σ(I)]^c</i>	0.0646	0.0764
<i>wR(F²) [all data]^c</i>	0.1992	0.2286
<i>GoF [all data]</i>	1.050	1.018

^a All X-ray crystallographic data were collected using synchrotron radiation ($\lambda = 0.41425$ Å) at the Advanced Photon Source.

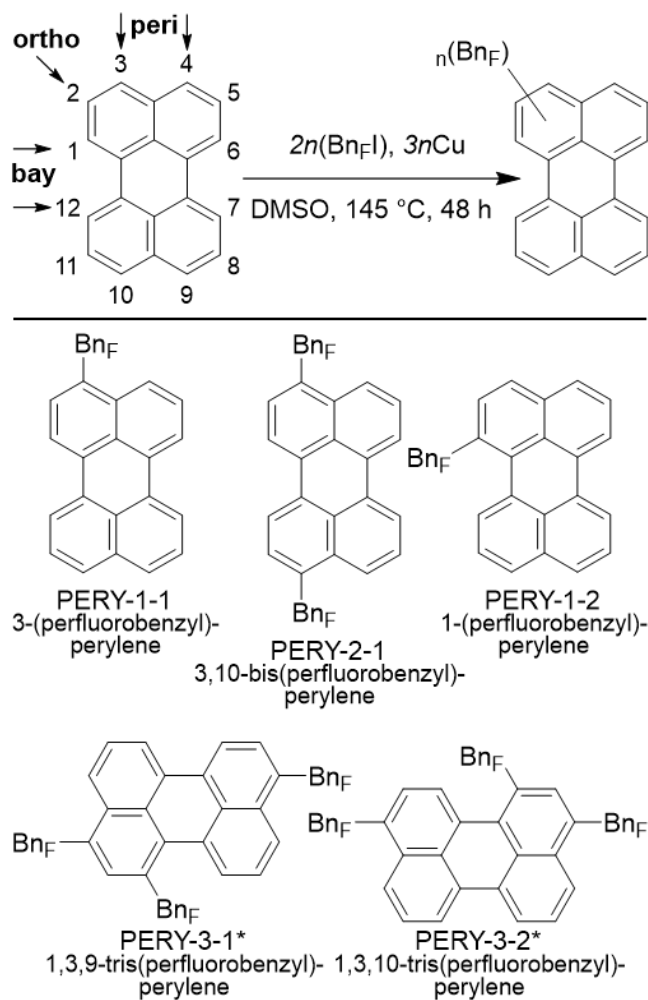


Figure 3.1. Top: General reaction scheme for direct perfluorobenylation of perylene and nomenclature for unique positions. Bottom: Drawings of molecular structures of isolated $\text{PERY}(\text{Bn}_F)_n$ compounds; for brevity, $\text{PERY}-n-x$ notations are introduced, where n is the number of Bn_F groups and x is the isomer number. Note that the compound $\text{PERY}-3-1$ could have the structure of $\text{PERY}-3-1^*$ or $\text{PERY}-3-2^*$ shown here, and the compound $\text{PERY}-3-2$ would then have the other structure.

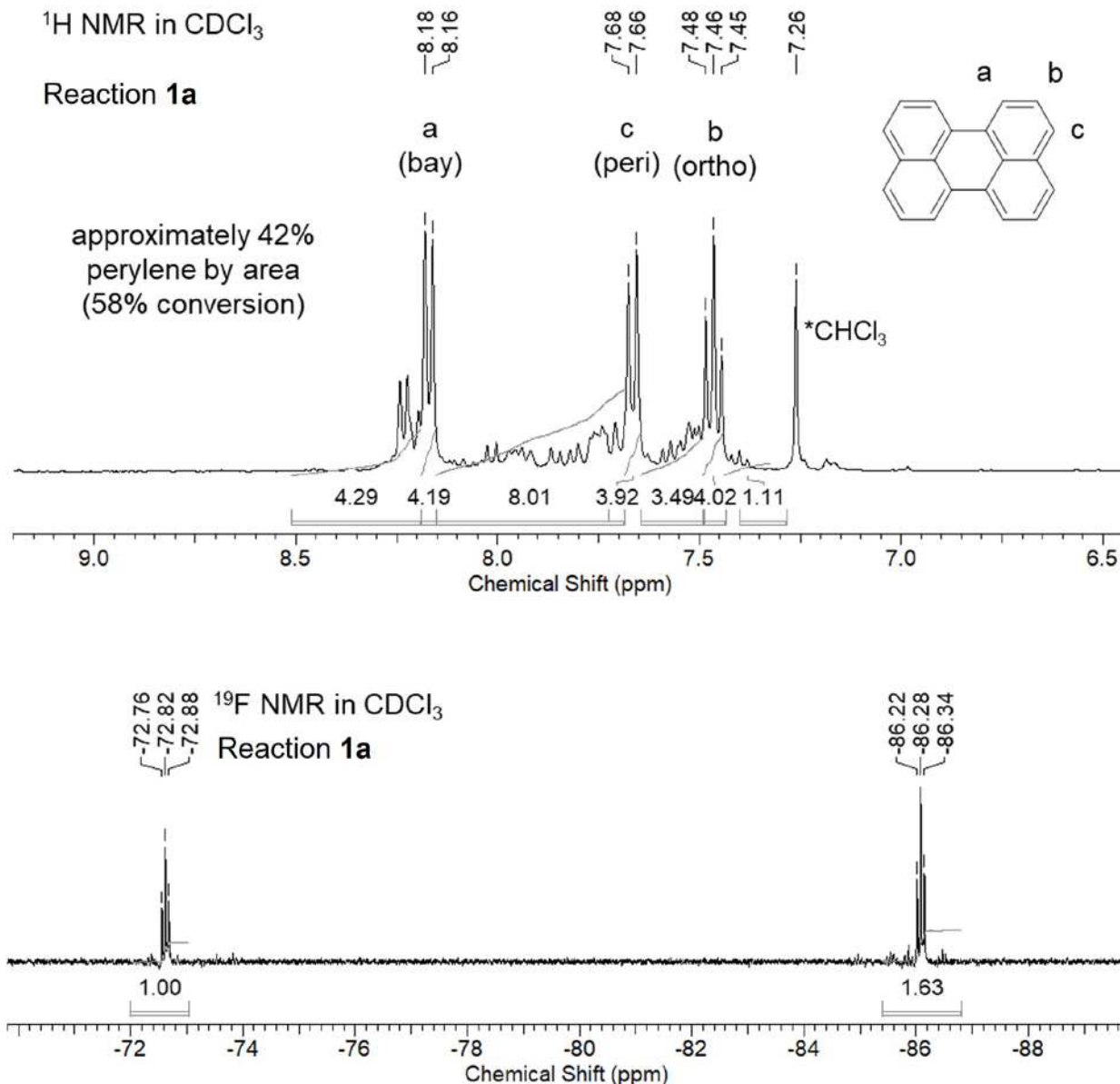


Figure 3.2. NMR spectra of crude reaction **1a**. Top: ¹H-NMR spectrum of aromatic region, showing over 40% of PERY starting material remaining unreacted after 24 hours at 120 °C. Top: ¹⁹F-NMR spectrum showing a mixture of products consisting predominately of two isomers, mono-substituted on the *peri* (PERY-1-1) and *bay* (PERY-1-2) positions, with an overall ratio of 1:1.6 *bay:peri* for all substitutions by ¹⁹F-NMR.

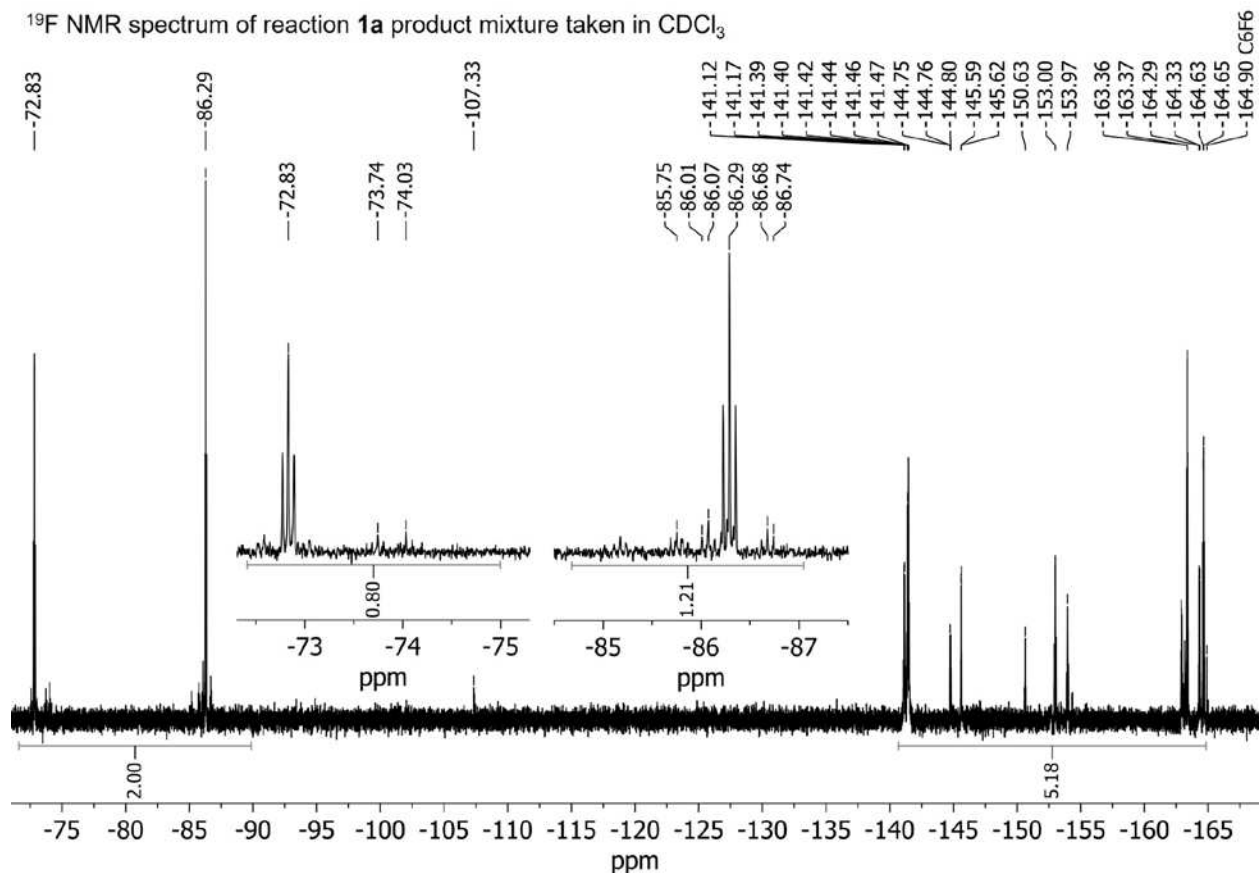


Figure 3.3. ¹⁹F-NMR spectrum of crude reaction mixture **1a**—after heating PERY in the presence of 2 equiv. of BnF for 24 h at 120 °C. Showing a mixture of products consisting predominately of two isomers, mono-substituted on the *peri* (PERY-1-1) and *bay* (PERY-1-2) positions.

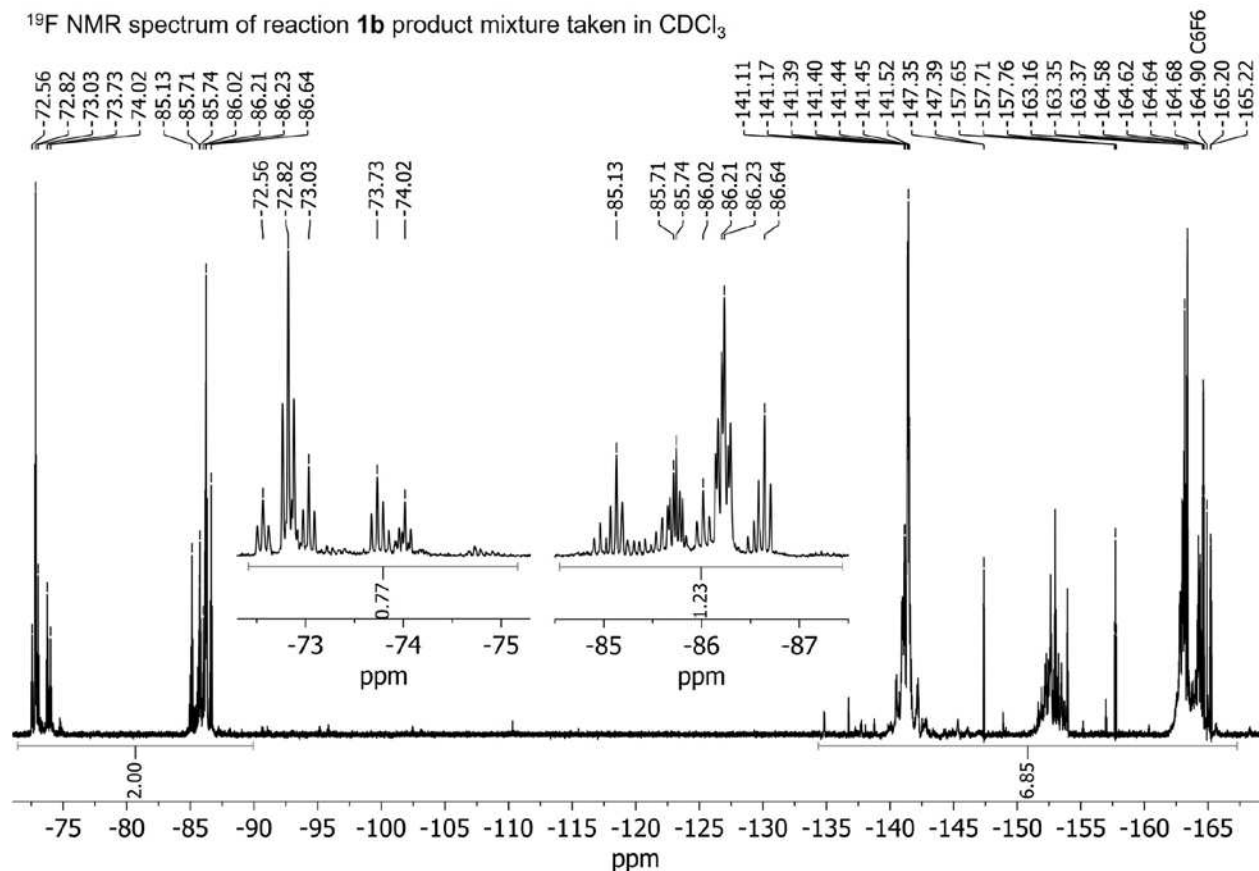


Figure 3.4. ¹⁹F-NMR spectrum of crude reaction mixture **1b**—after heating PERY in the presence of 4 equiv. of Bn_FI for 48 h at 145 °C (half of Bn_FI was added after 24 hours) Showing several triplets in the benzylic F(CF₂) regions for *peri* (ca. -72 to -75 ppm) and *bay* (ca. -84.5 to -87.5 ppm) positions.

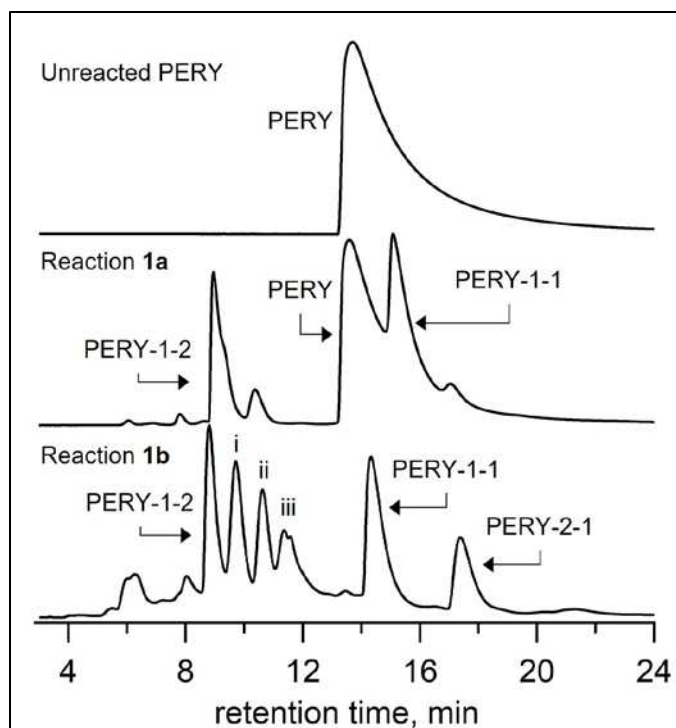


Figure 3.5. HPLC chromatograms of pure PERY and crude **1a** and **1b** reaction mixtures, separated with a semipreparative COSMOSIL Buckyprep column (250 x 10 mm i.d), MeCN eluent, 5 mL min⁻¹ flow rate, 370 nm UV detection. Top: injection of pure PERY sample. Middle: crude reaction mixture of **1a**, showing a majority of the reaction mixture remains unreacted PERY. Bottom: crude reaction mixture **1b**; PERY-1-1, PERY-1-2 and PERY-2-1 can each be isolated without the need for secondary purification. Fractions i and ii are mixtures believed to each contain two PERY-2 isomers, where each isomer has one BnF group on the *bay* and one on the *peri* position see Figure 3.8 for more discussion on isolation and characterization of products. Note that the retention time for unreacted PERY (products with higher retention times than PERY) shifted slightly depending on the relative concentration of PERY in the sample: for pure PERY and reaction **1a**, the retention times is essentially unchanged, while for **1b** PERY has a lower retention time and is found in fraction ii in the bottom chromatogram.

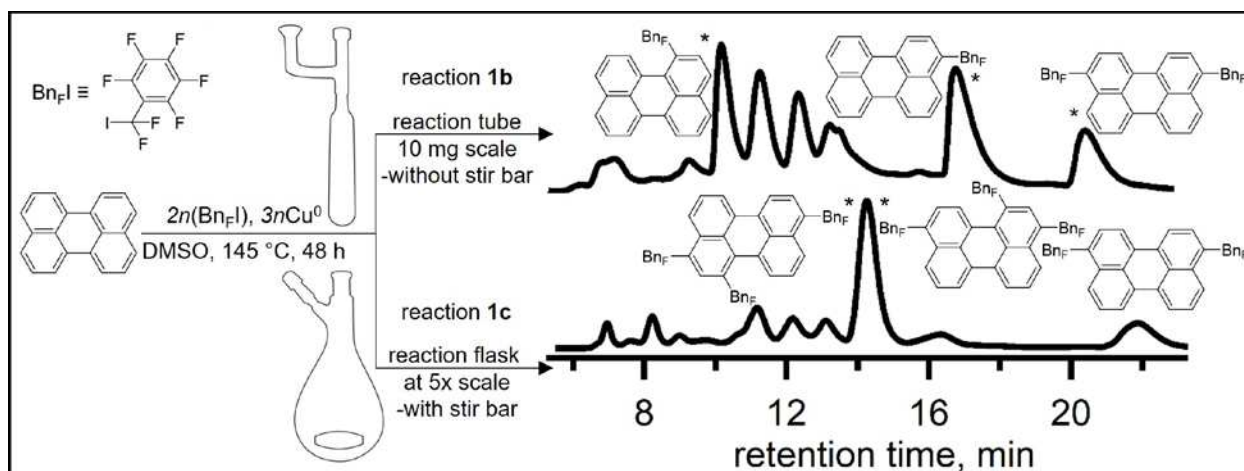


Figure 3.6. General reaction scheme for direct perfluorobenylation of perylene showing differences in reaction conditions between **1b** and **1c** with their resulting chromatograms. Note the isolable isomers are shown next to their respective peak marked with asterisk in each chromatogram; see Figure 3.8 for more discussion on isolation and characterization of products.

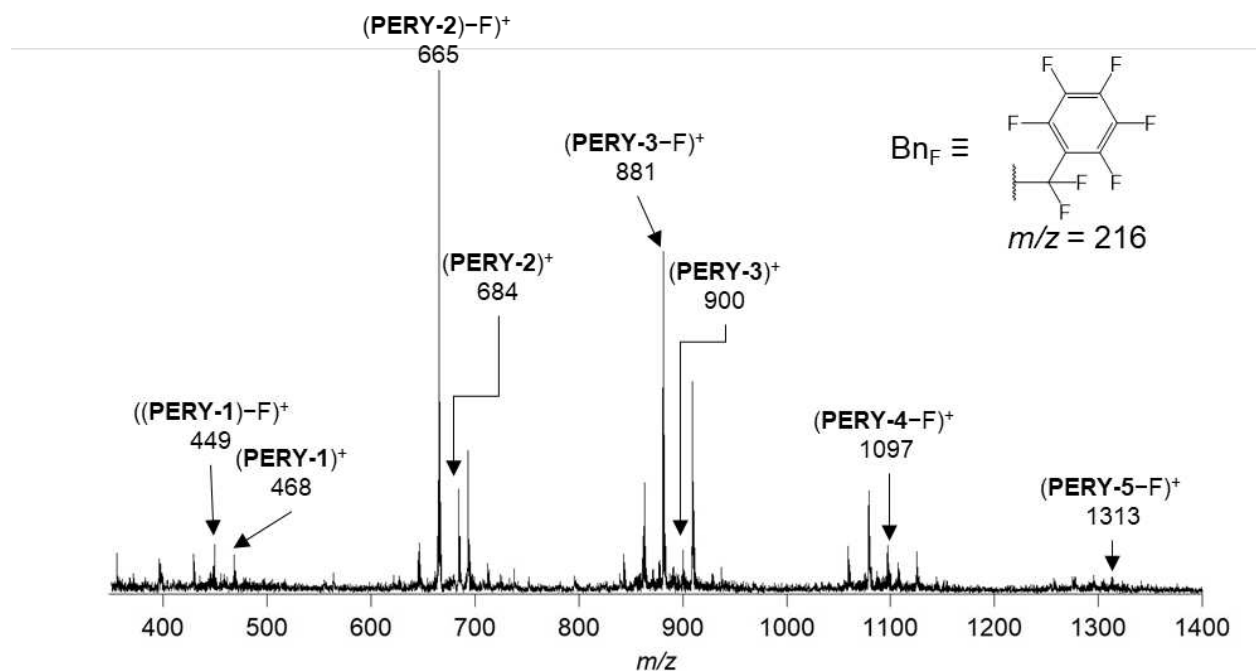


Figure 3.7. Positive-ion ESI mass spectrum of crude reaction mixture from reaction **1c**. Showing parent ion (m/z 468 for one PERY-1) and/or loss of fluoride (m/z 449) for one to five substitutions of Bn_F groups. The parent peak could not be directly observed for PERY-5, but a small peak consistent with the loss of fluoride ion (m/z 1313) is shown. Note that unsubstituted PERY is $252 \text{ g}\cdot\text{mol}^{-1}$, and each Bn_F group adds $216 \text{ g}\cdot\text{mol}^{-1}$.

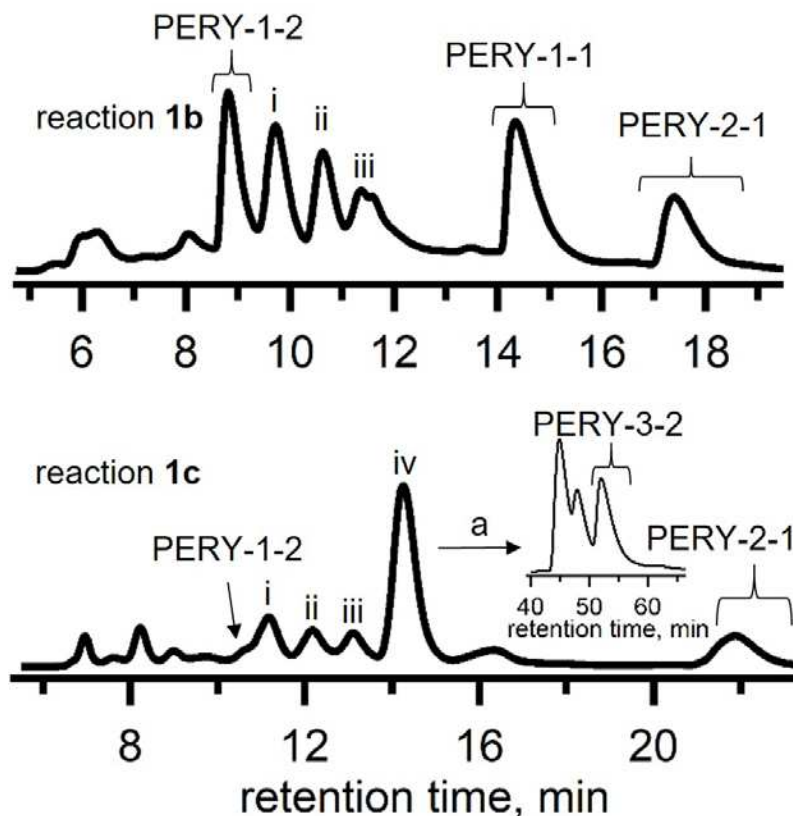


Figure 3.8. HPLC chromatograms of crude product mixtures **1b** and **1c**. Top: Reaction **1b** separated with a semipreparative COSMOSIL Buckyprep column (250 x 10 mm i.d), MeCN eluent, 5 mL min⁻¹ flow rate, 370 nm UV detection; PERY-1-1, PERY-1-2 and PERY-2-1 can each be isolated without the need for secondary purification. Fractions i and ii are mixtures believed to each contain two PERY-2 isomers, where each isomer has one Bn_F group on the *bay* and one on the *peri* position (see Figure 3.9, Figure 3.42, and Figure 3.43 for analysis and discussion). Bottom: Reaction **1c** separated with a preparative COSMOSIL Buckyprep column (250 x 20 mm i.d), acetonitrile eluent, 16 mL min⁻¹ flow rate, 370 nm UV detection. a) fraction iv was subsequently extracted with a small amount of methanol, leaving behind pure PERY-3-1 as insoluble material and using the extract for HPLC to isolate PERY-3-2. Inset shows second separation step for PERY-3-2 after solvent extraction (250 x 10 mm i.d. COSMOSIL Buckyprep column, methanol eluent, 5 mL min⁻¹ flow rate). The first fraction of this separation contains two PERY-3 isomers which could not be separated from each other, and the second peak consists of PERY-3-1 with significant contamination from the first peak. Note that difference in retention time between the two chromatograms is due to using a newer (and larger) column with different inlet tube lengths. Changing the dead time and efficacy of the column at separating. However, the fractions labeled i-iii are lined up to guide the eye and show the same general separation profile. With fraction vi not being present in reaction 1a and consisting of PERY-3 isomers (Figure 3.45).

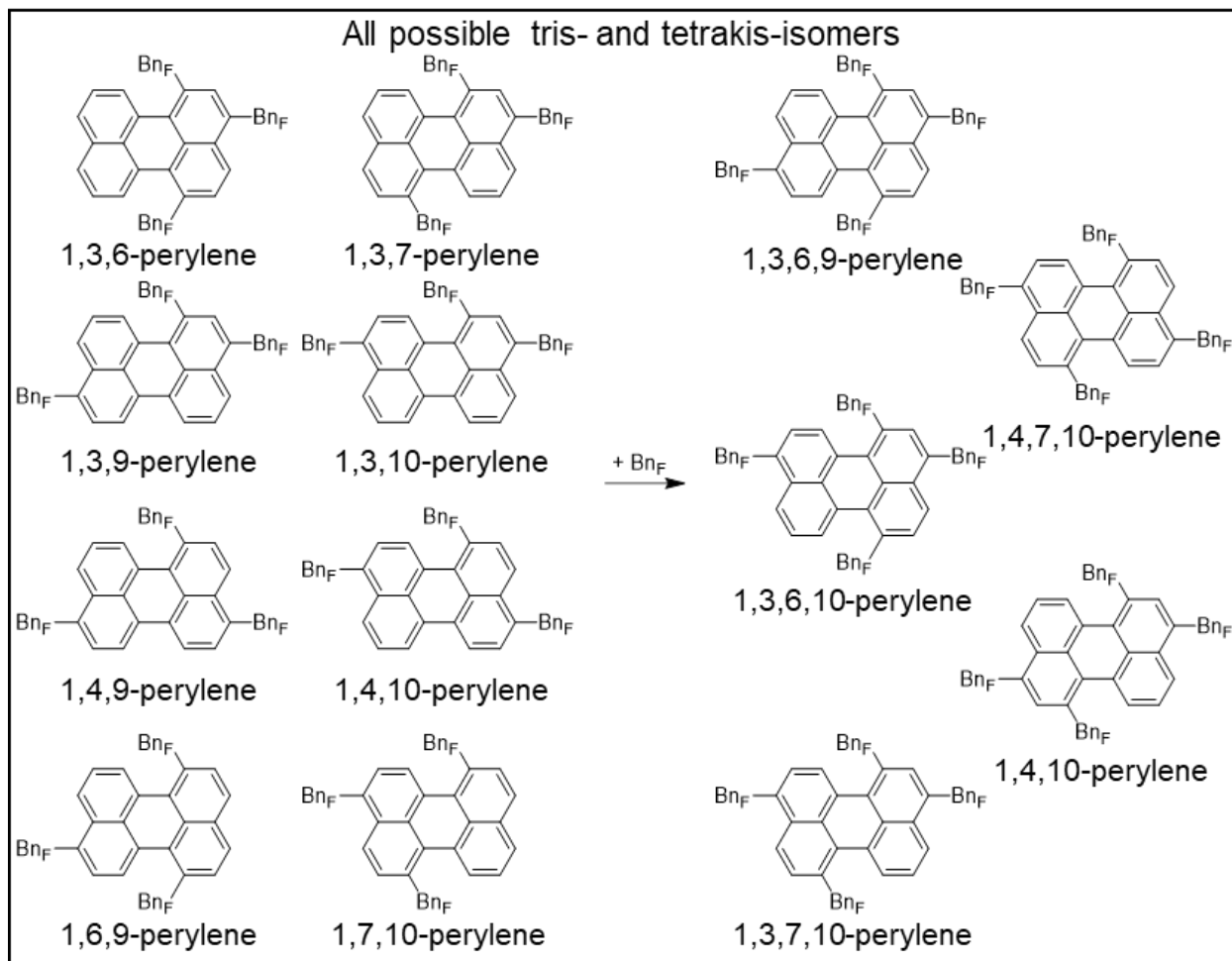


Figure 3.10. Structure and numbering of all possible isomers containing 3–4 BnF groups assuming that a) ortho positions do not react (e.g. 2-perylene), b) *peri* positions adjacent to each other cannot both be substituted (e.g. 3,4-perylene) and c) *bay* positions directly across from each other cannot both be substituted (e.g. 1,12-perylene). See also detailed explanation in Figure 3.9.

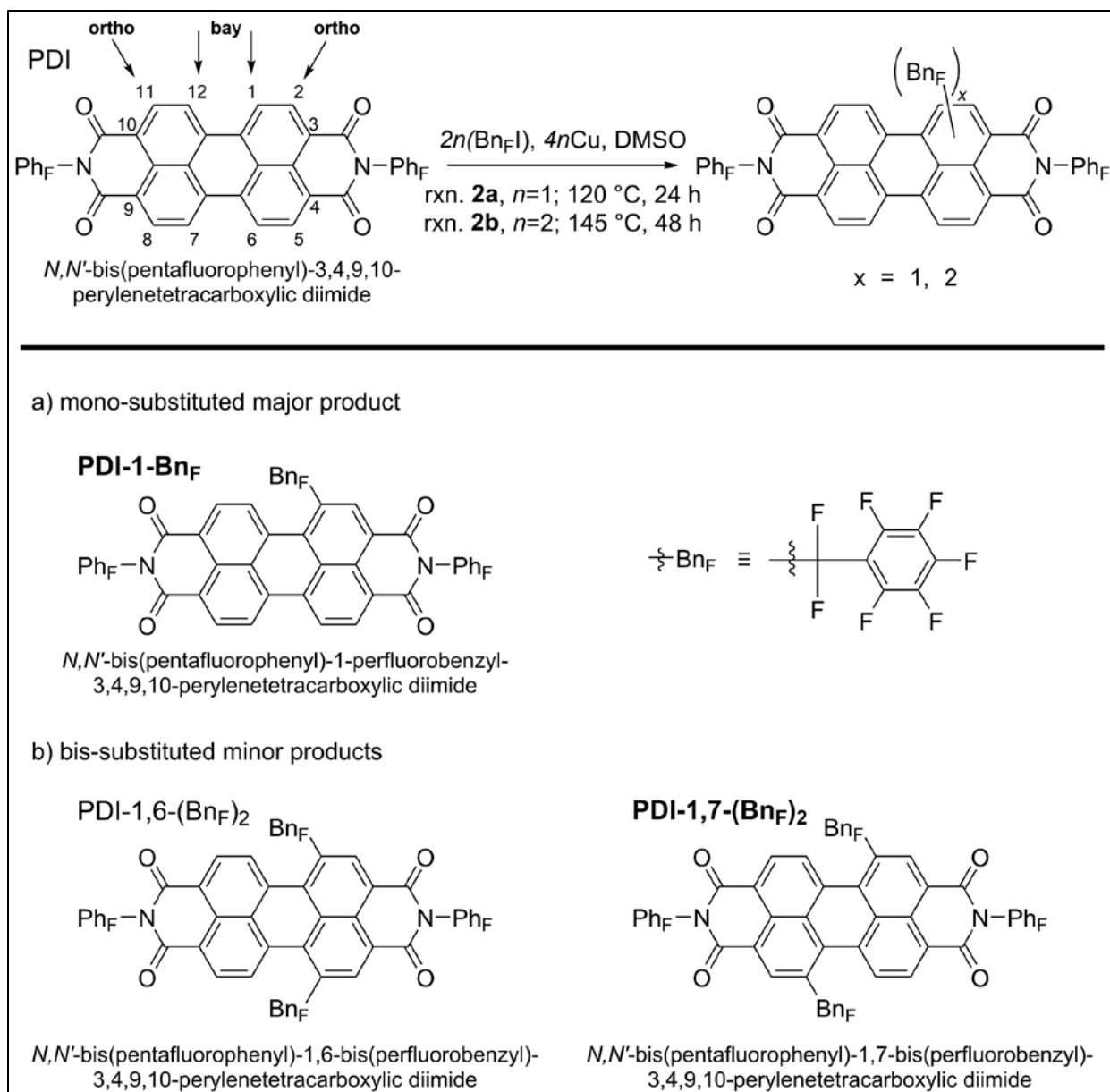


Figure 3.11. Top: General reaction scheme for direct perfluorobenylation of PDI and nomenclature for unique positions. Bottom: Drawings of molecular structures of isolated PDI- $(\text{BnF})_n$ compounds; for brevity, PDI- x - $(\text{BnF})_n$ notations are introduced, where x is (are) the position(s) of substituted BnF groups and n is the number of BnF groups substituted. Names shown in **bold** are for products that single crystal X-ray structure were obtained.

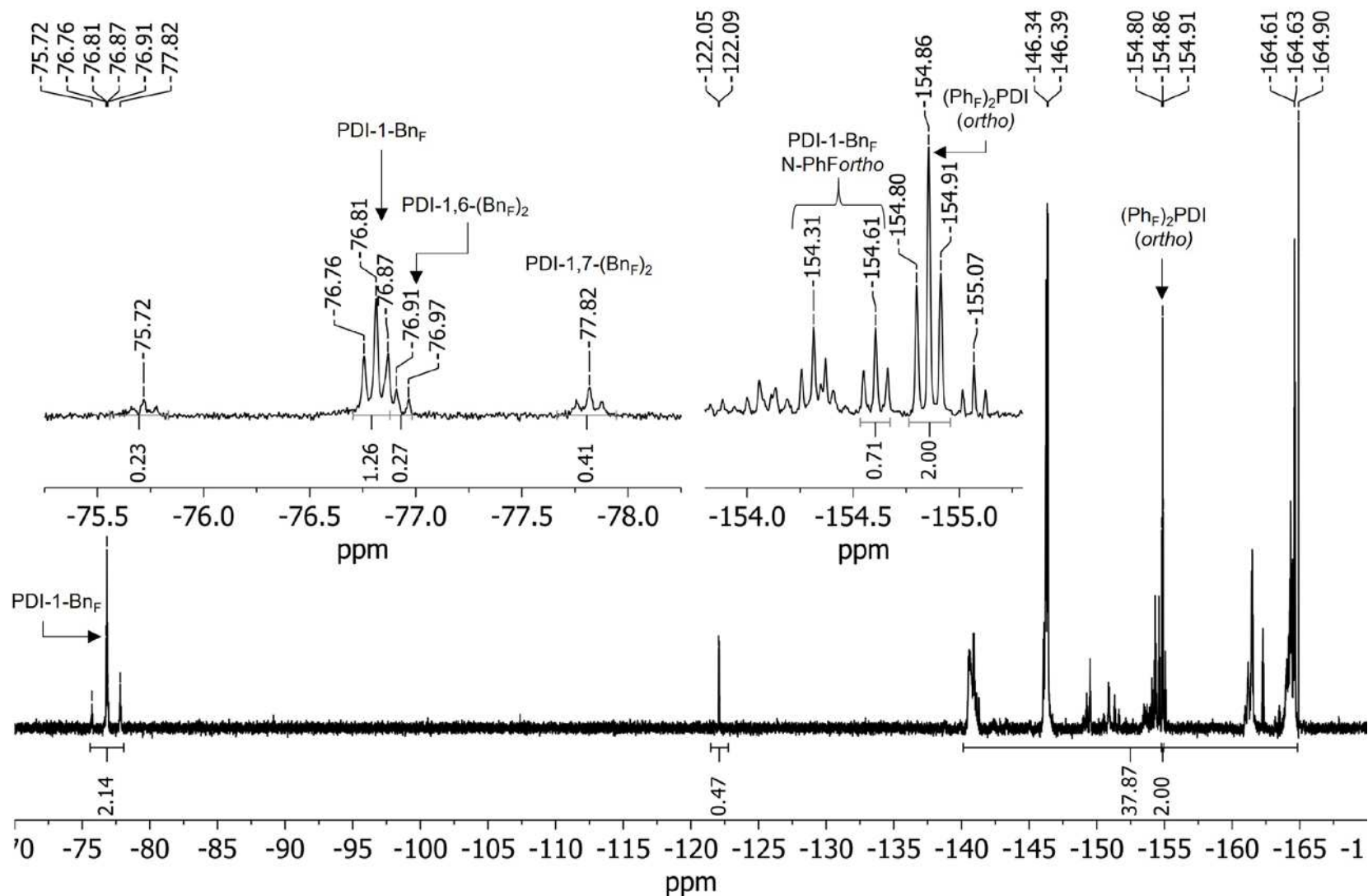


Figure 3.12. ^{19}F -NMR spectrum of crude reaction mixture **2a**—after heating PDI in the presence of 2 equiv. of BnFI for 24 h at 120 °C. Showing a mixture of products consisting predominately of the mono-substituted derivative PDI-1-BnF and two minor bis-substituted isomers PDI-1,6-(BnF)₂ and PDI-1,7-(BnF)₂.

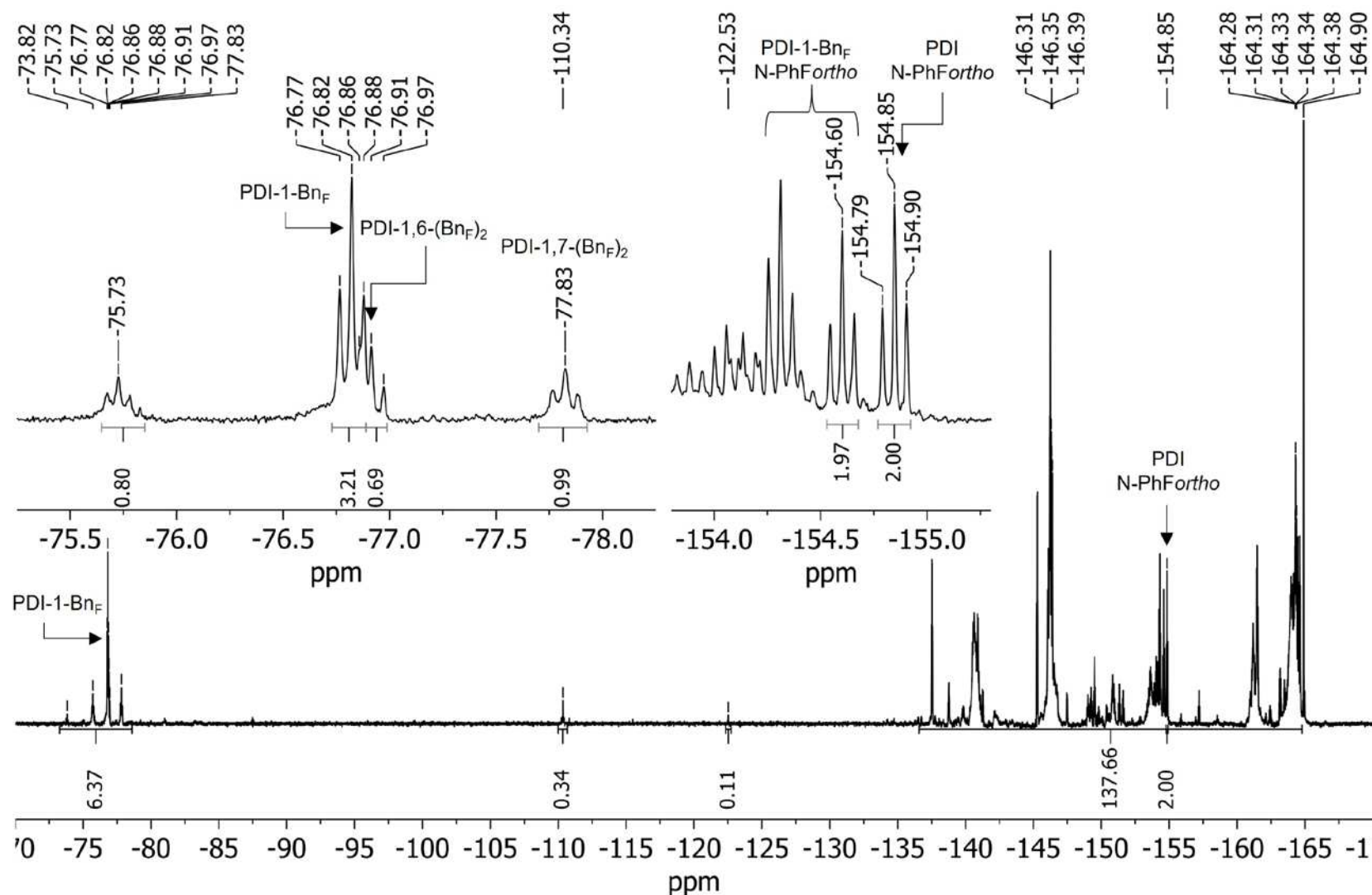


Figure 3.13. ^{19}F -NMR spectrum of crude reaction mixture **2b**—after heating PDI in the presence of 4 equiv. of $\text{Bn}_\text{F}\text{I}$ for 48 h at 145 °C (half of $\text{Bn}_\text{F}\text{I}$ was added after 24 hours) Showing a mixture of products consisting predominately of the mono-substituted derivative PDI-1- Bn_F and two minor bis-substituted isomers PDI-1,6-(Bn_F) $_2$ and PDI-1,7-(Bn_F) $_2$

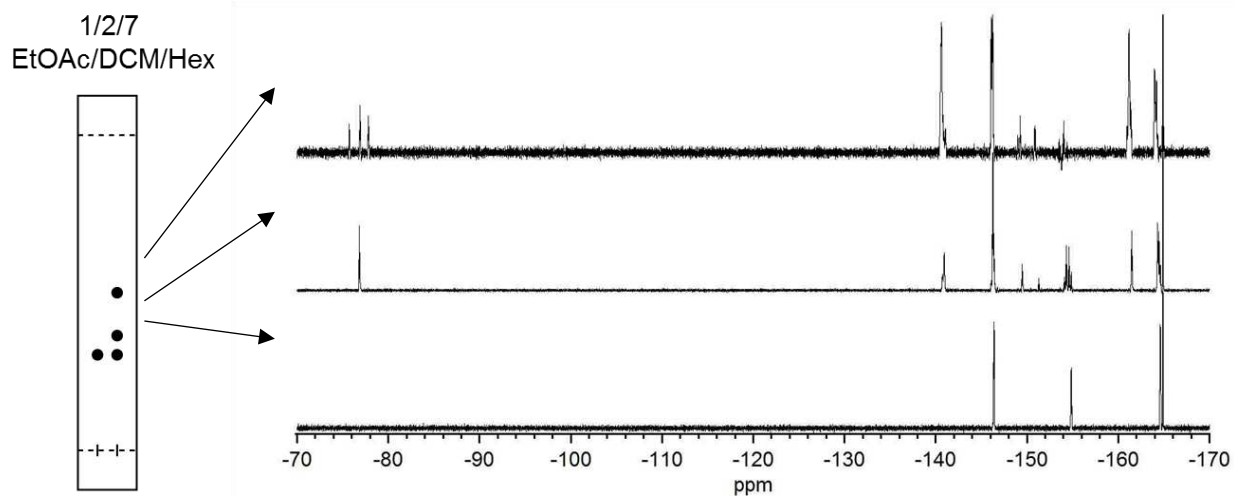


Figure 3.14. Example of primary separation by flash chromatography. Left: TLC representation of flash chromatography separation of crude product mixture of PDI perfluorobenzylation using 1:2:7 EtOAc–DCM–Hexane; left column shows position of unreacted starting material (SM), right column shows separation of the crude reaction mixture (R). Right: ^{19}F NMR spectra of corresponding fractions as they elute out of silica column, taken in CDCl_3 with C_6F_6 as an internal standard. Isolated three fractions are (from top to bottom/first to last to elute) a mixture of substituted products, a pure fraction of PDI-1- Bn_F , and the unreacted PDI starting material.

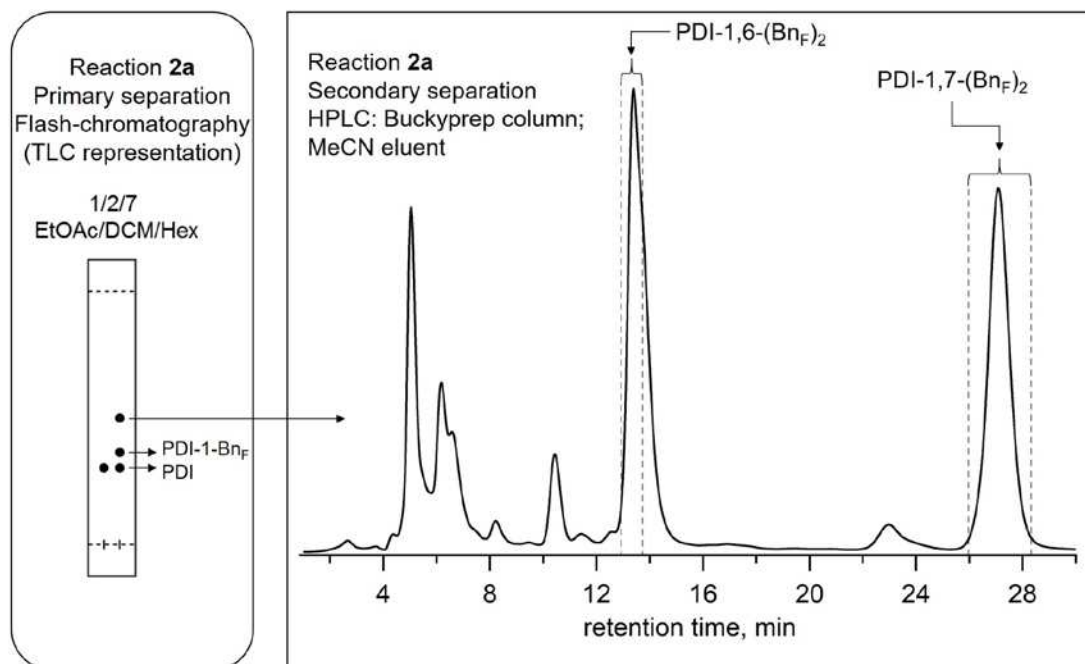


Figure 3.15. HPLC chromatogram of secondary separation post flash chromatography Left: TLC representation of flash chromatography separation of PDI perfluorobenzylation reaction. Right: HPLC chromatogram of first fraction from flash chromatography, containing bis-substituted products separated with a semipreparative COSMOSIL Buckyprep column (250 x 10 mm i.d), MeCN eluent, 5 mL min^{-1} flow rate, 530 nm UV detection

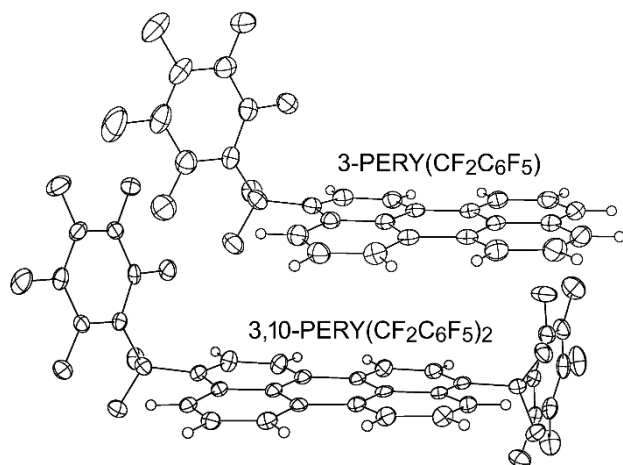


Figure 3.16. The molecular X-ray structures of 3-PERY(CF₂C₆F₅) (PERY-1-1) and 3,10-PERY(CF₂C₆F₅)₂ (PERY-2-1) (50% thermal ellipsoids except for H atoms).

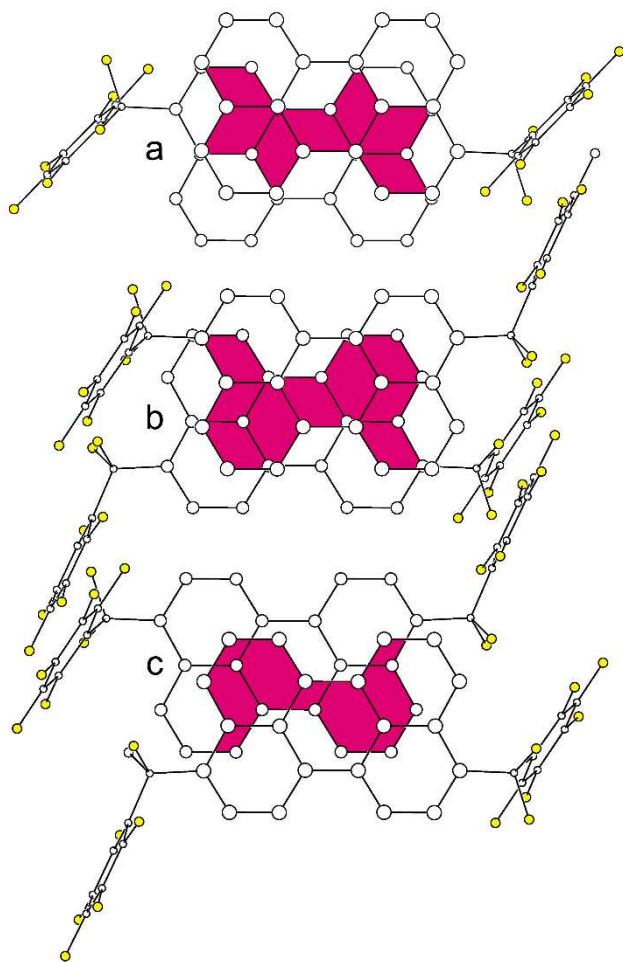


Figure 3.17. Parallel perspective drawings of the π - π overlap of perylene C(sp²) aromatic cores in the structures of PERY-1-1 (a) and PERY-2-1 (b and c; H atoms removed for clarity; F atoms shaded yellow).

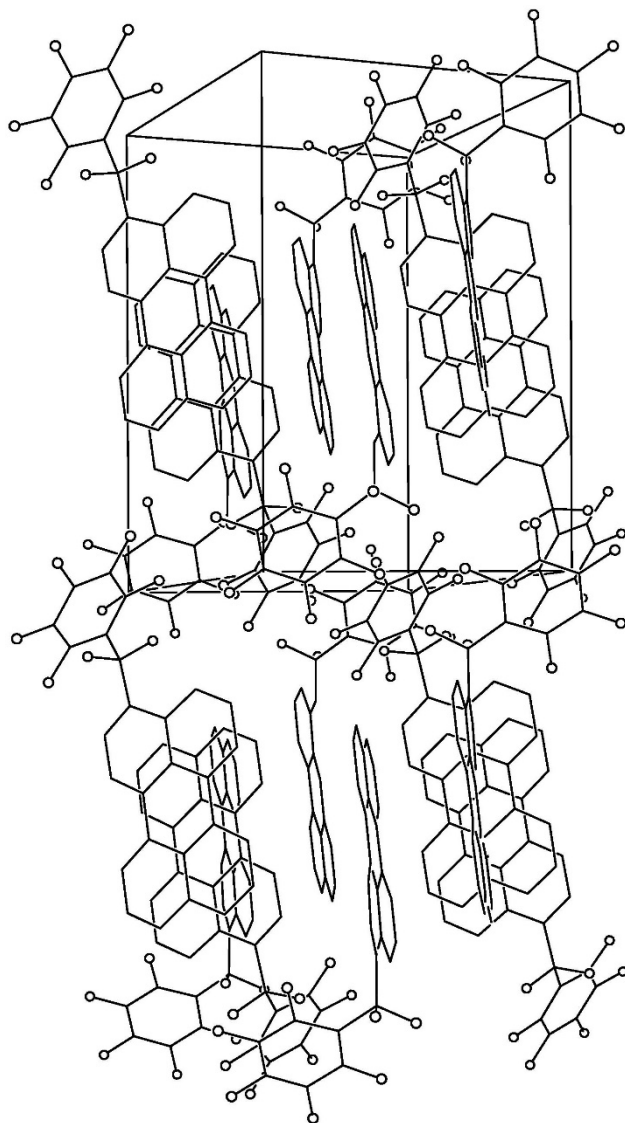


Figure 3.18. The structure of PERY-1-1 (H atoms removed for clarity; F atoms shown as circles). One unit cell is shown. The crystallographic a axis is aligned with the long axis of the page.

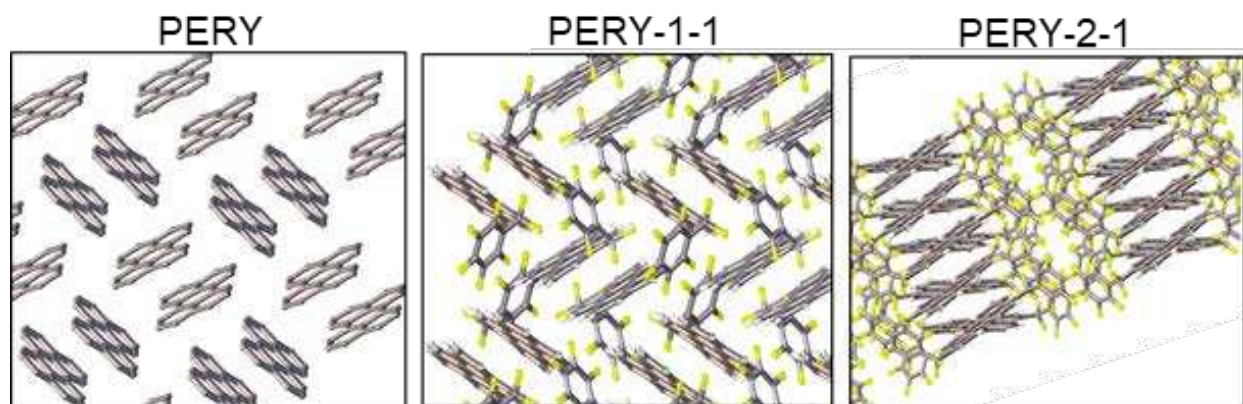


Figure 3.19. Side perspective of crystal structure packing of PERY, PERY-1-1, and PERY-2-1

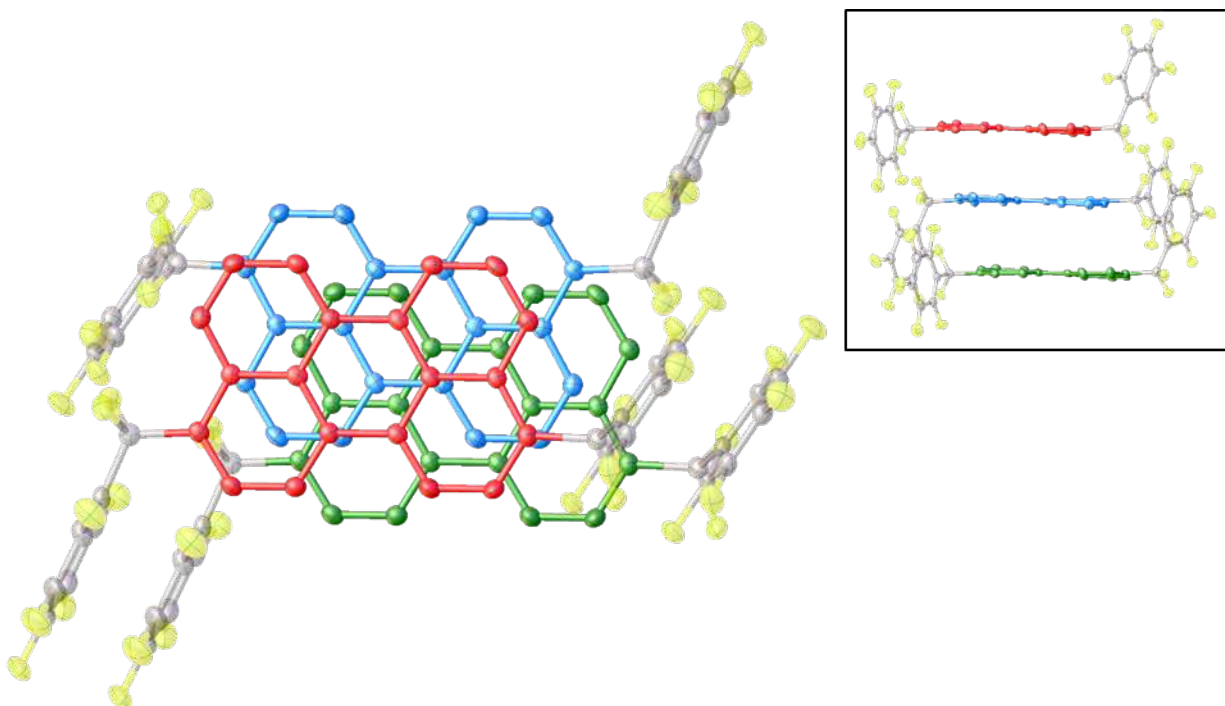


Figure 3.20. Top view of PERY-2-1 through single column of perylene cores showing degree of overlap. View shown is normal to the plane made by the innermost 6-membered carbon ring for the perylene colored in red. inset is a side view showing stacking order of colored-perylene cores.

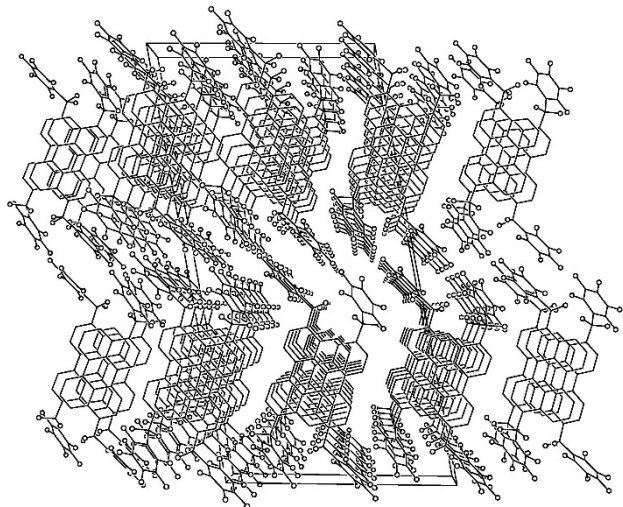


Figure 3.21. The structure of PERY-2-1. H atoms removed for clarity; F atoms shown as circles. One unit cell is shown. The crystallographic b axis is perpendicular to the plane of the page. Layers of molecules lying in bc planes are stacked in the crystallographic a direction.

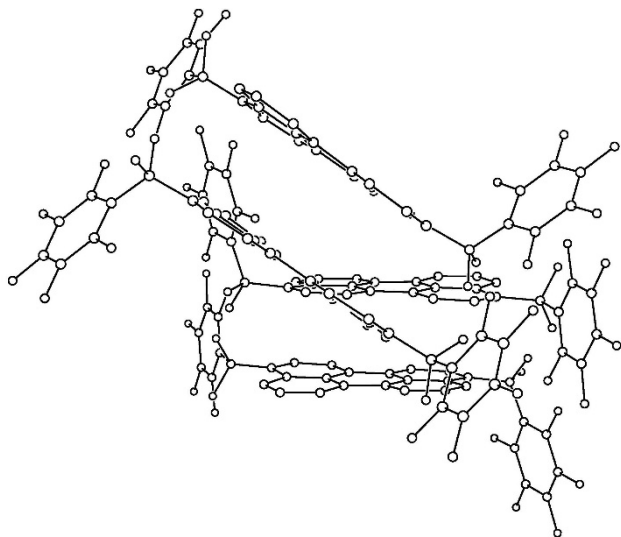


Figure 3.22. The structure of PERY-2-1 (H atoms removed for clarity). Two molecules in neighboring infinite stacks are shown. The perylene $C(sp^2)$ cores are tilted 35.6° from the cores in neighboring stacks.

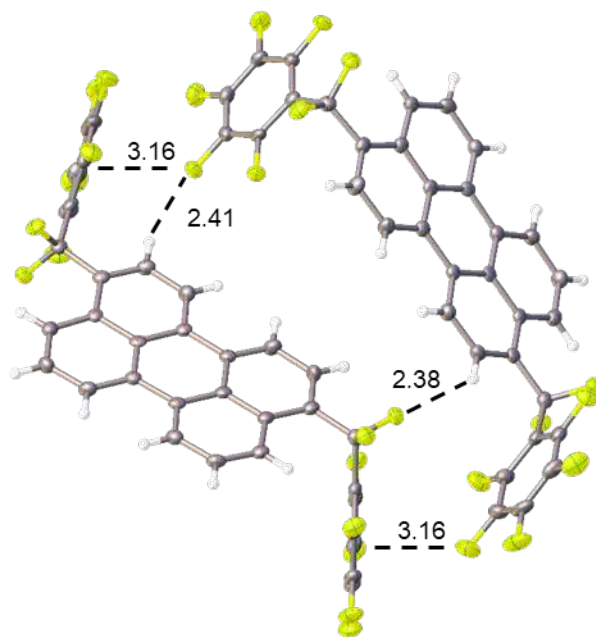


Figure 3.23. Intermolecular interactions between PERY-2-1 molecules of adjacent columns within the same row. Showing each is acting as a hydrogen bond donor and acceptor, between the close Ar-H...F-Ar (2.41 Å) and CF_2 ...H-Ar (2.38 Å) distances. As well as two close π ...F-Ar distances of 3.16 Å between each.

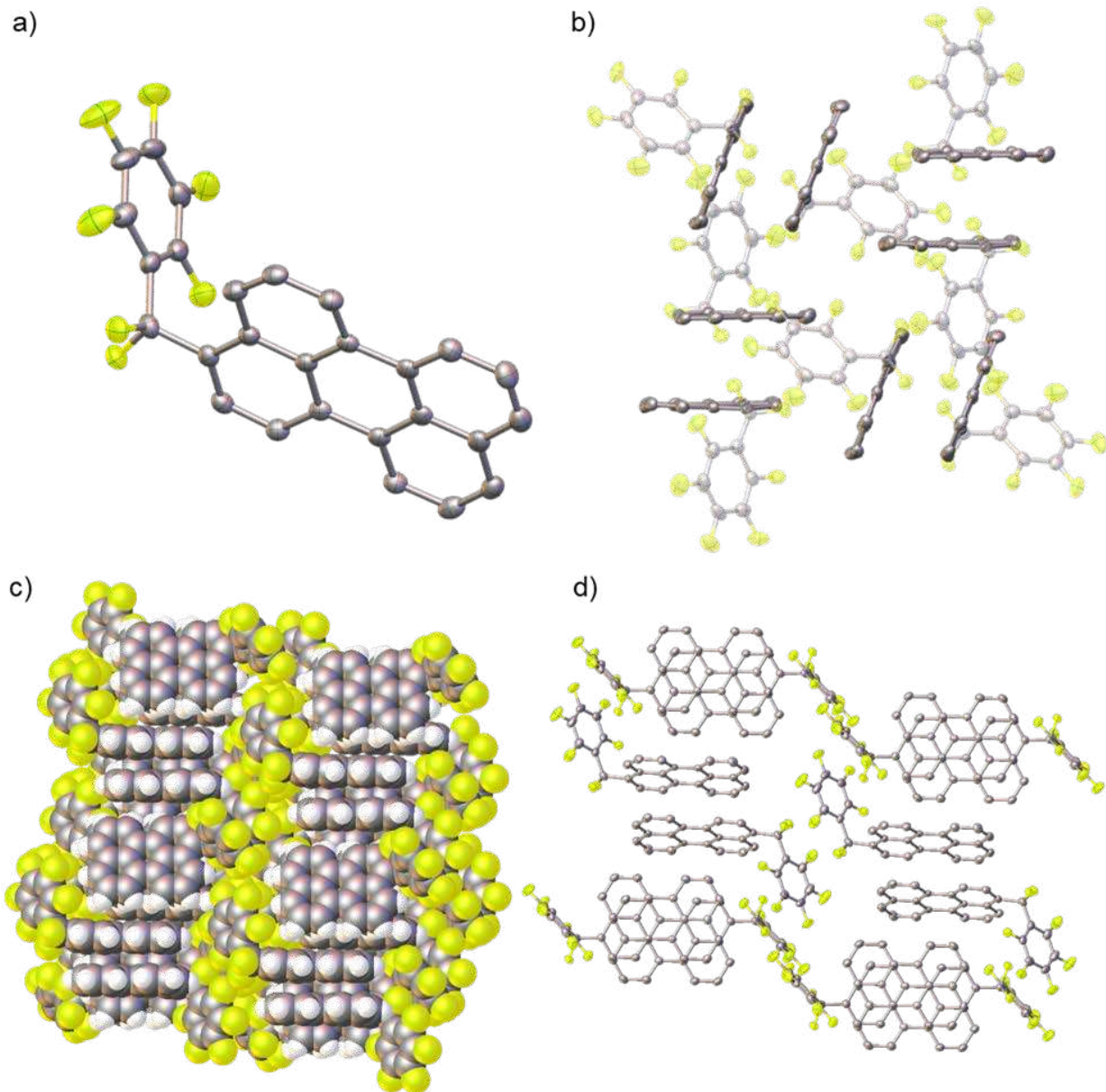


Figure 3.24. Single crystal X-ray structure and packing of PERY-1-1 (hydrogens omitted for clarity when needed). a) 50% thermal ellipsoid of single PERY-1-1 molecule b) view normal to plane of perfluorophenyls showing herringbone-stacked pairs of perylene cores (perfluorobenzyls are transparent for clarity). c) front view showing solid state packing in a space-filling model for PERY-1-1, showing columns of herringbone-stacked perylene cores separated by planes of closely packed perfluorobenzyls from adjacent molecules. d) same view as (c) but with thermal ellipsoids to show interactions between adjacent molecules.

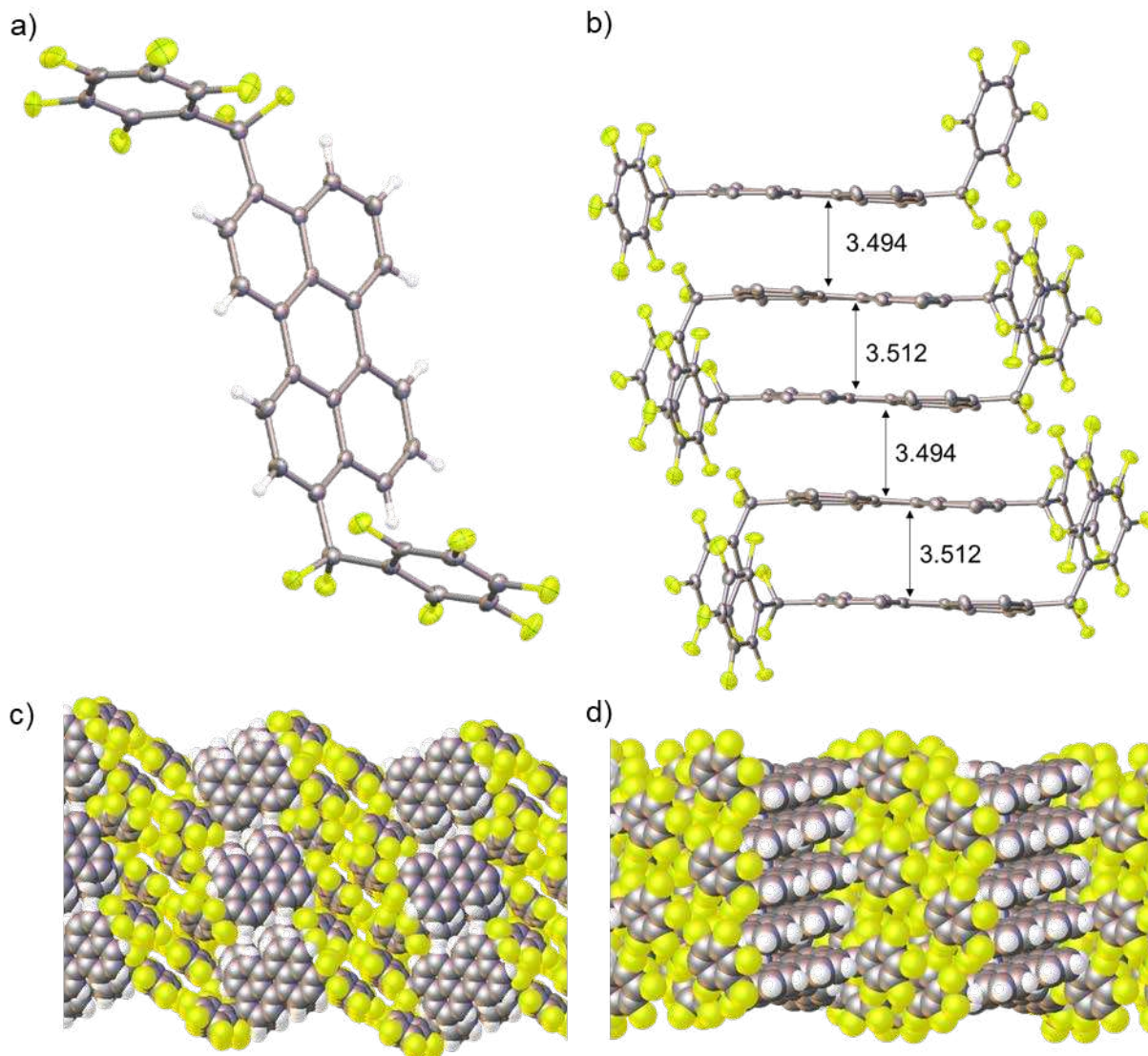


Figure 3.25. Single crystal X-ray structure and packing of PERY-2-1 (hydrogens omitted for clarity where needed). a) 50% thermal ellipsoid of single PERY-2-1 molecule. b) side view of perylene-columns showing distance between ‘hugging pairs’ where the perfluorobenzyls interact and with each other causing a larger distance between the planes of perylene (3.512 Å) compared to the non-hugging pairs (3.494 Å). c and d) space-filling model showing columns made up of stacked perylene cores from the top and side view respectively.

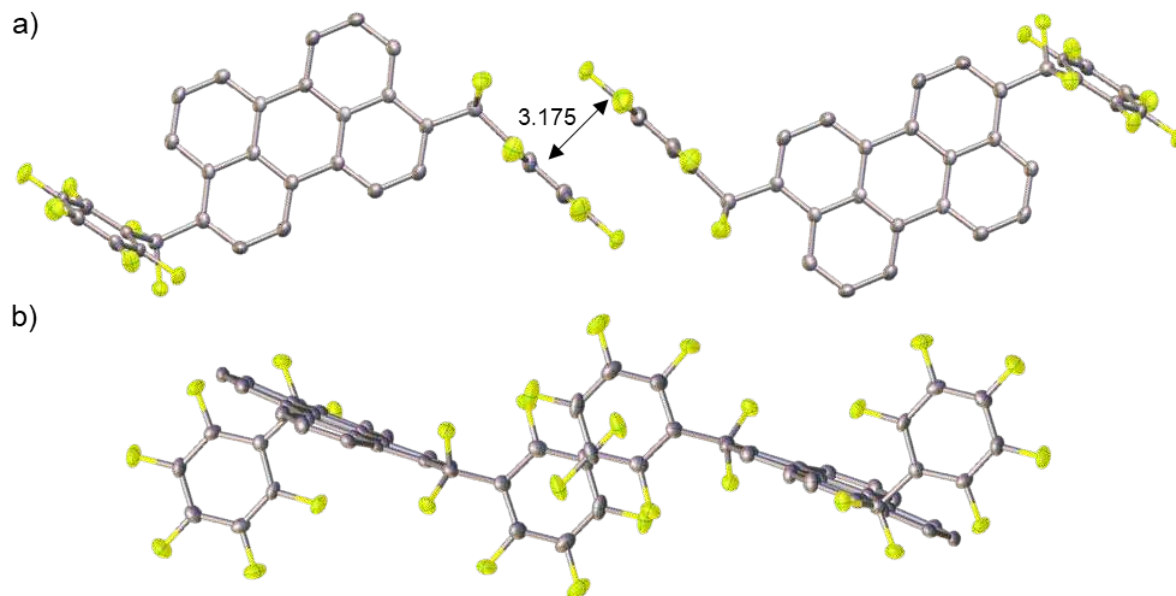


Figure 3.26. Simplified view of PERY-2-1 solid state packing between adjacent rows of perylene columns shown in Figure 3.25. a) side-view showing distance between perfluorophenyl rings of adjacent perylene rows separated by closely packed perfluorophenyls. Note that the perfluorophenyl rings are perfectly parallel with each other. b) top view showing degree of overlap between perfluorophenyl rings.

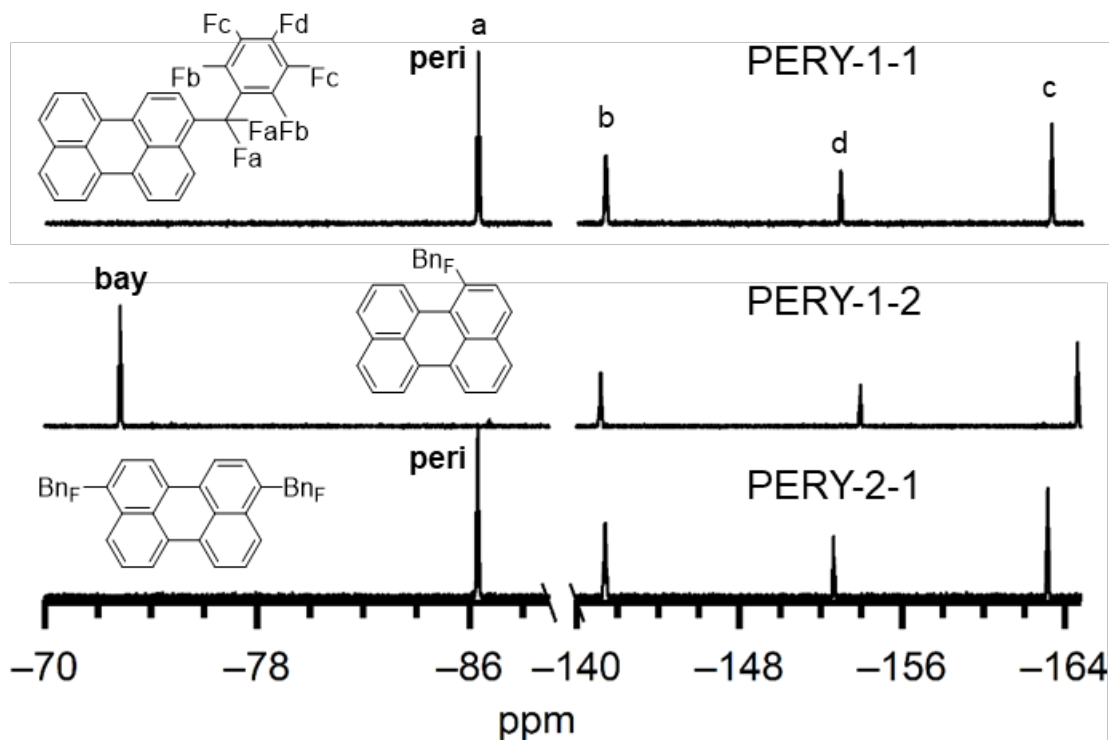


Figure 3.27. ^{19}F -NMR spectra of mono- and bis-substituted products. Showing difference in bay and peri positions for the $-\text{CF}_2-$ region (ca. -70– to -90 ppm) and relatively unchanged Ph_F region (ca. -140– to -165 ppm).

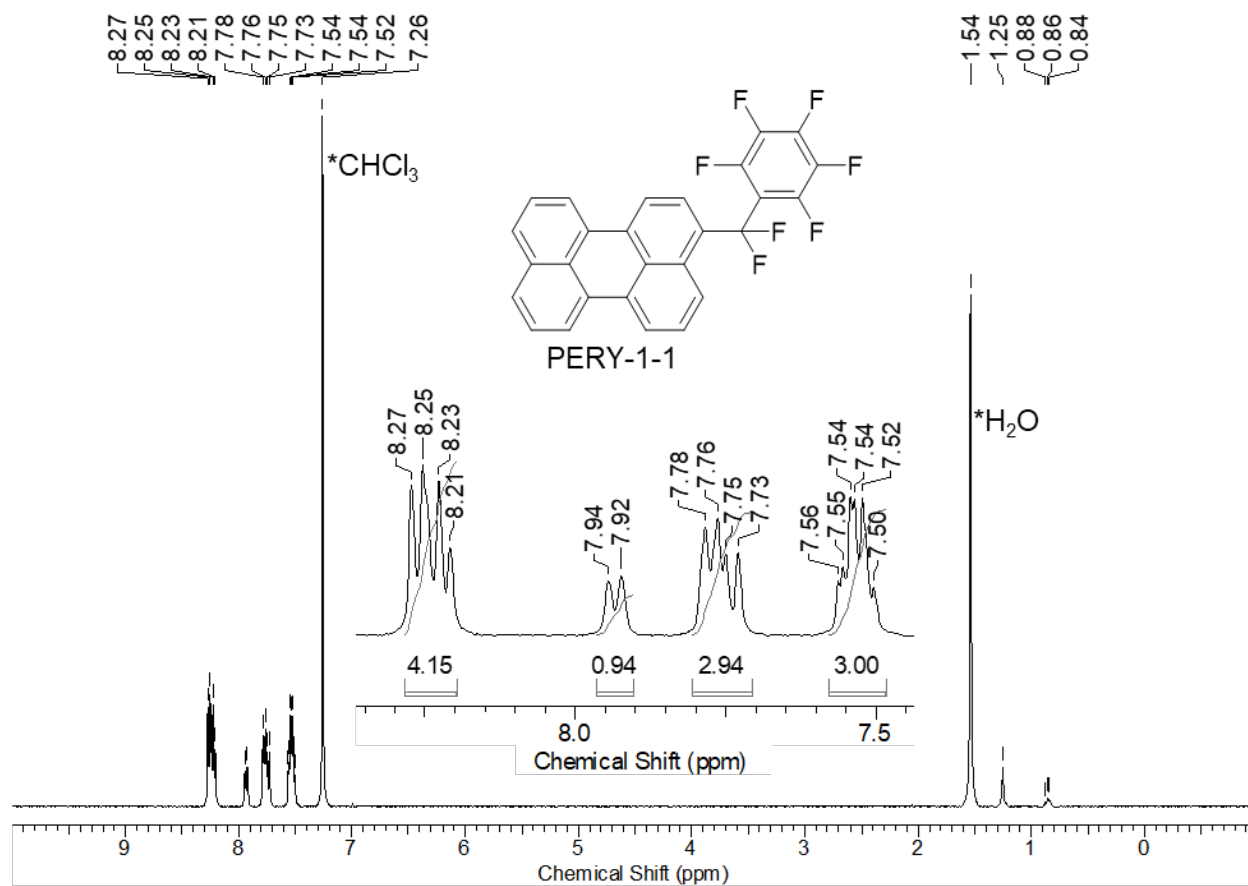


Figure 3.28. $^1\text{H-NMR}$ spectrum of PERY-1-1 in CDCl_3 .

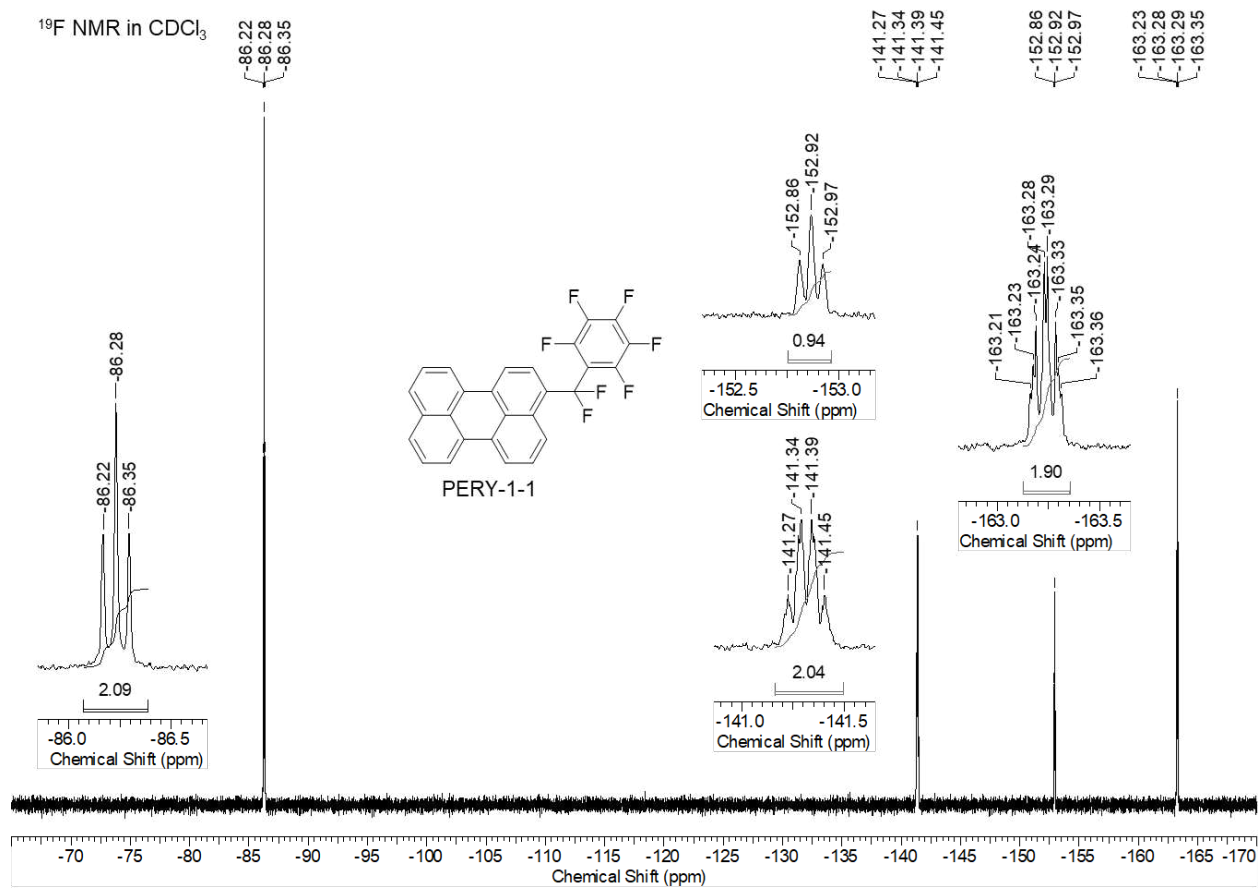


Figure 3.29. ^{19}F -NMR spectrum of PERY-1-1 in CDCl_3 .

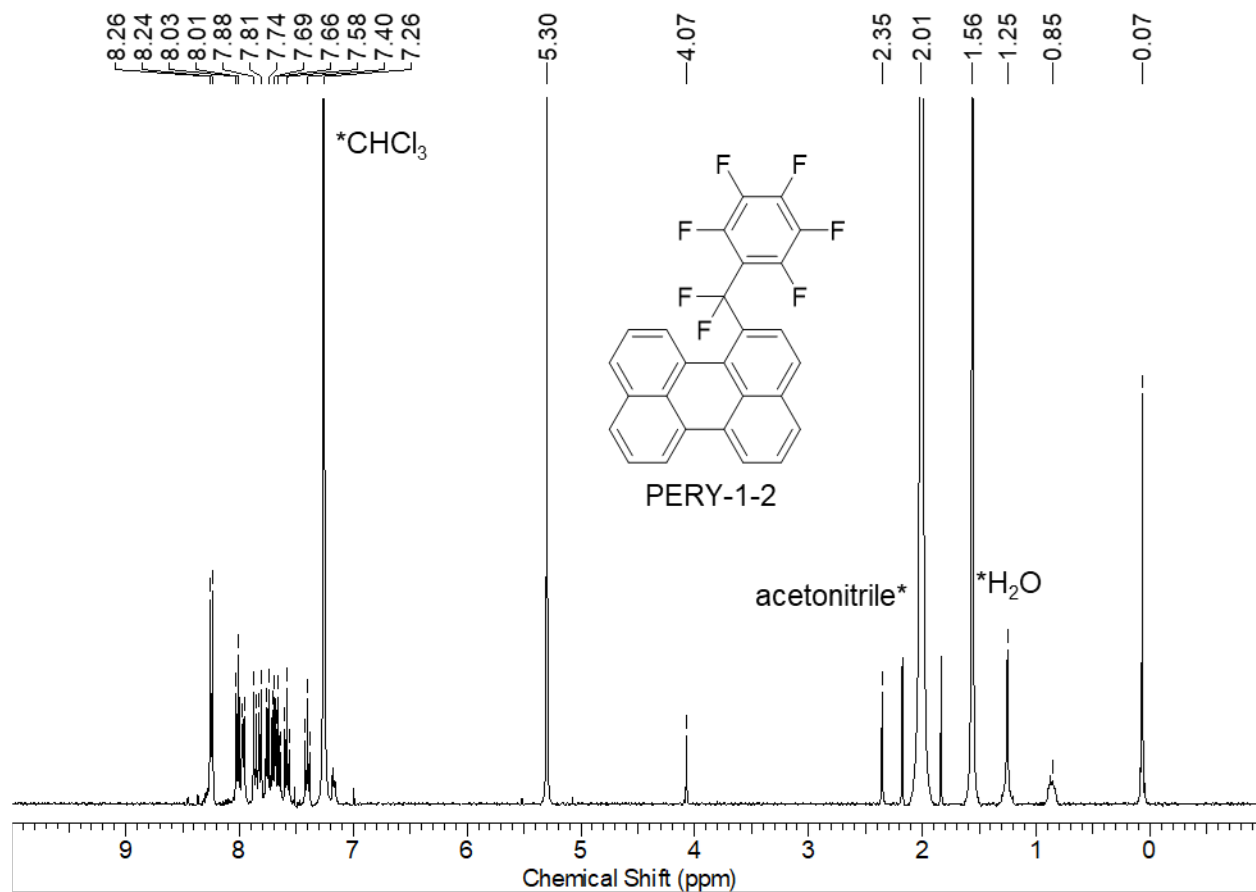


Figure 3.30. $^1\text{H-NMR}$ spectrum of PERY-1-2 in CDCl_3 .

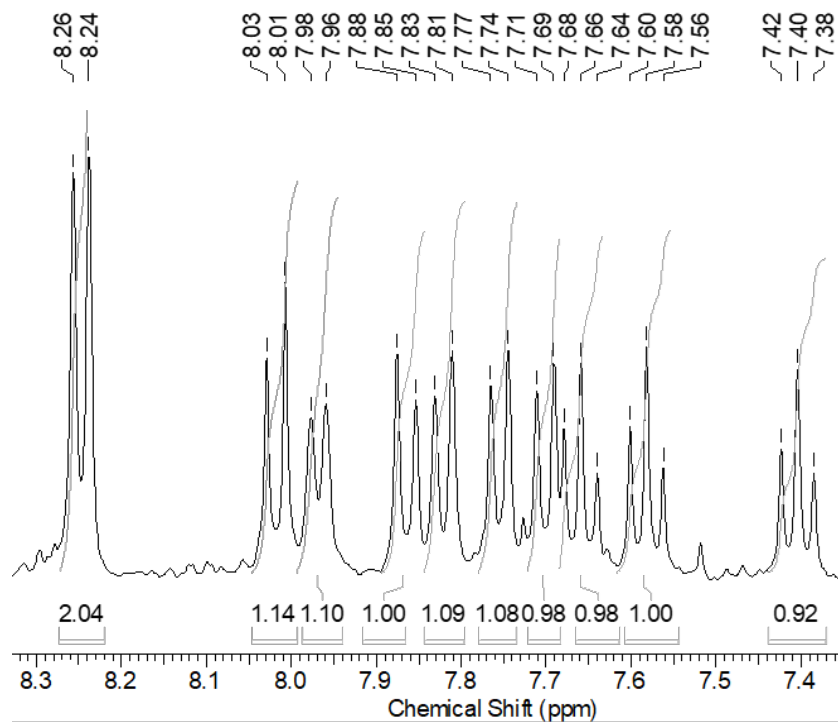


Figure 3.31. $^1\text{H-NMR}$ spectrum of PERY-1-2 aromatic region in CDCl_3 .

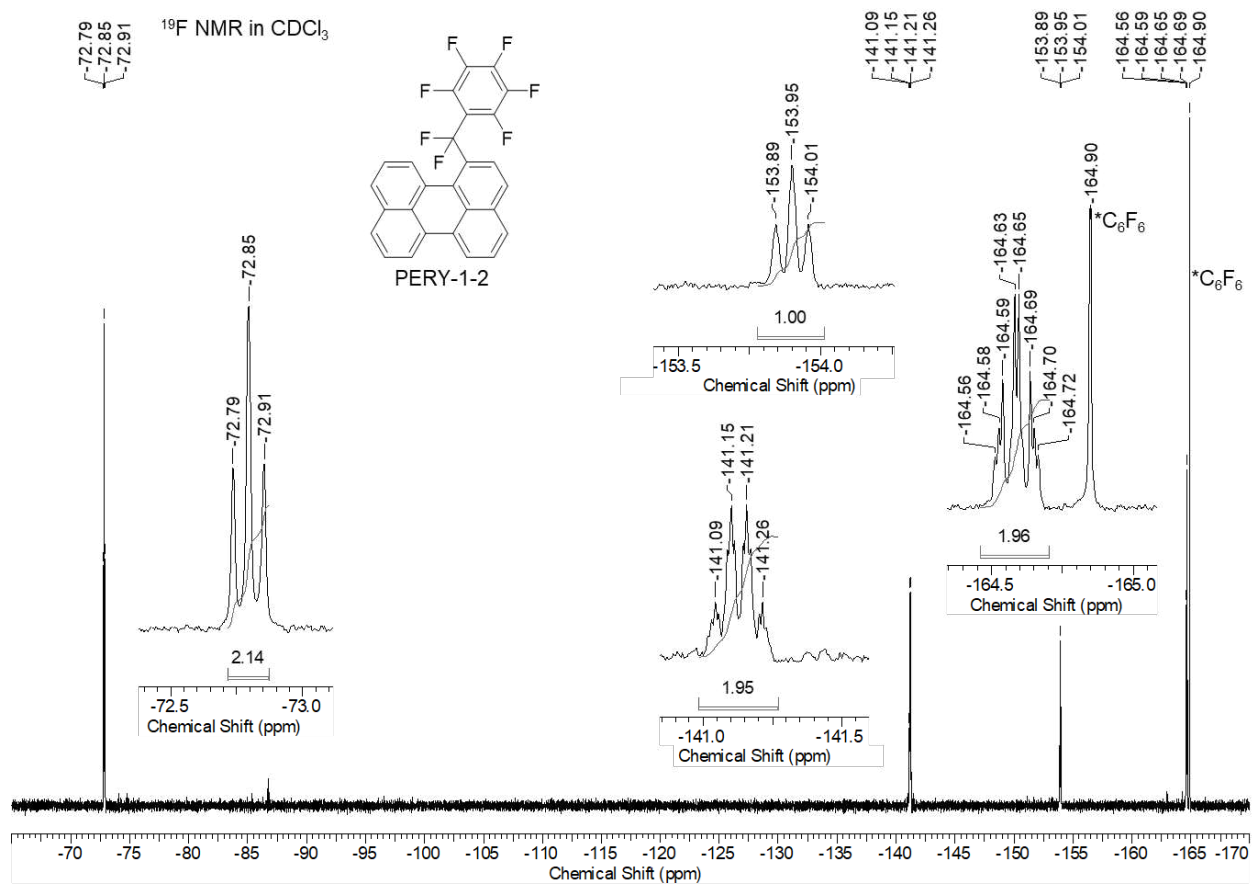


Figure 3.32. ^{19}F -NMR spectrum of PERY-1-2 in CDCl_3 .

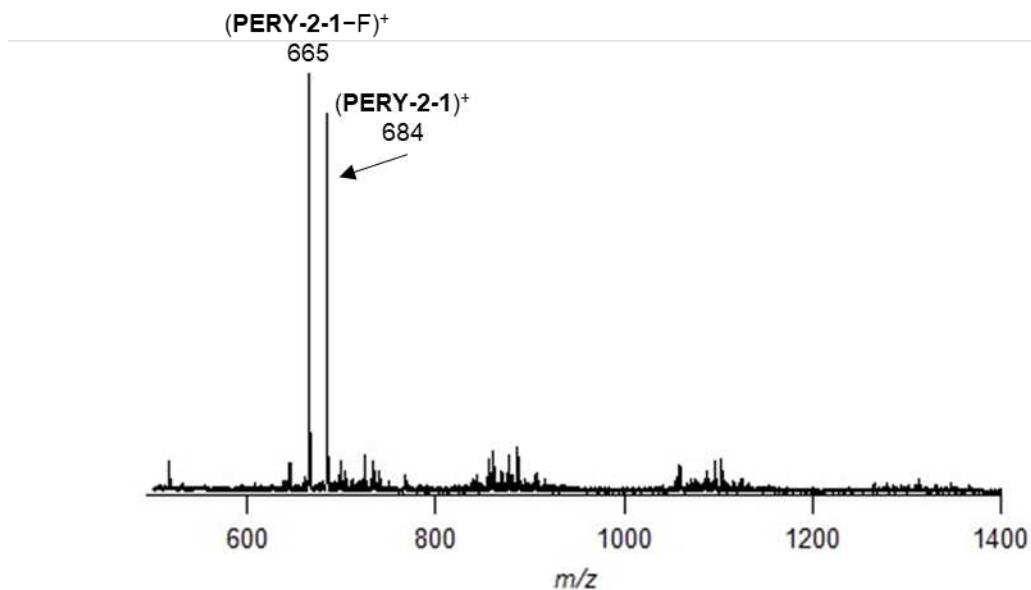


Figure 3.33. Positive-ion ESI mass spectrum of PERY-2-1.

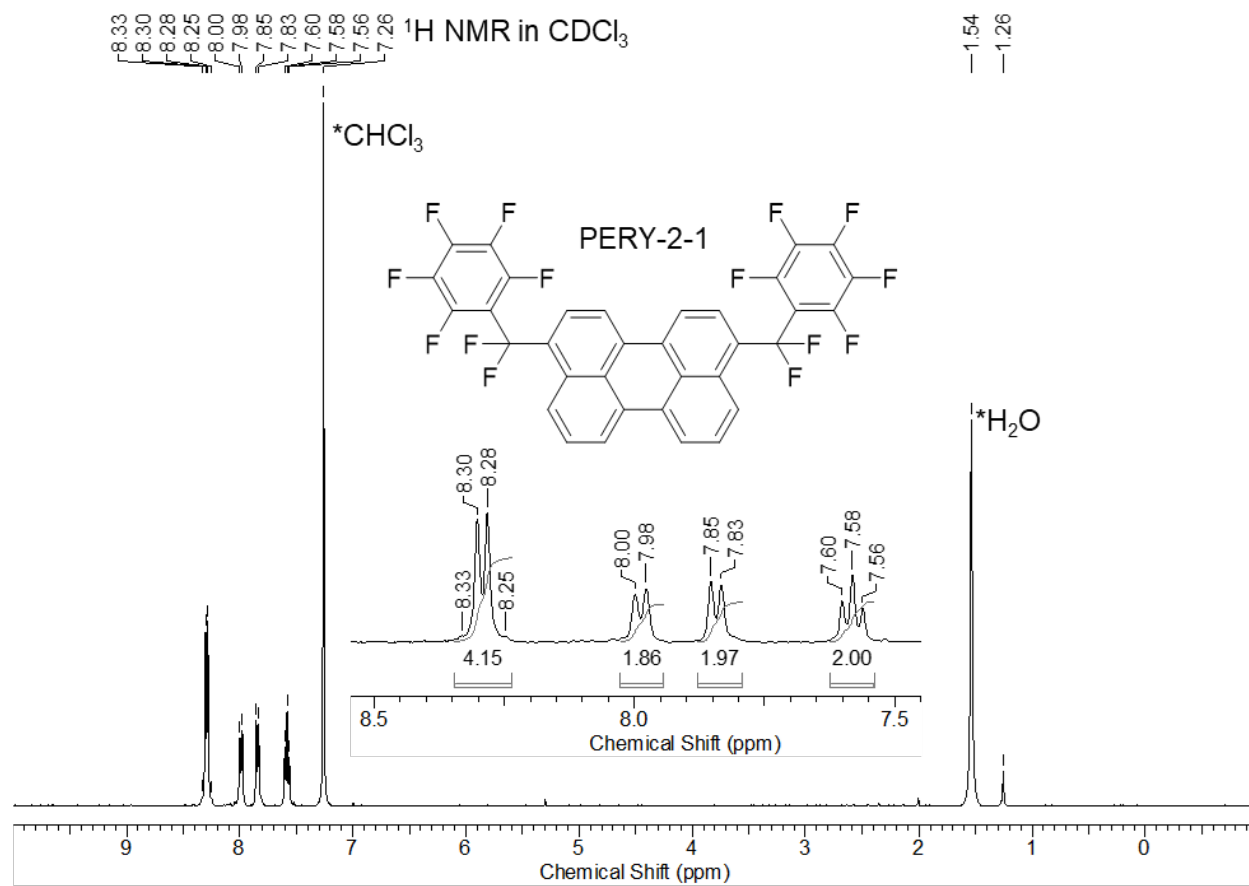


Figure 3.34. ¹H-NMR spectrum of PERY-2-1 in CDCl₃.

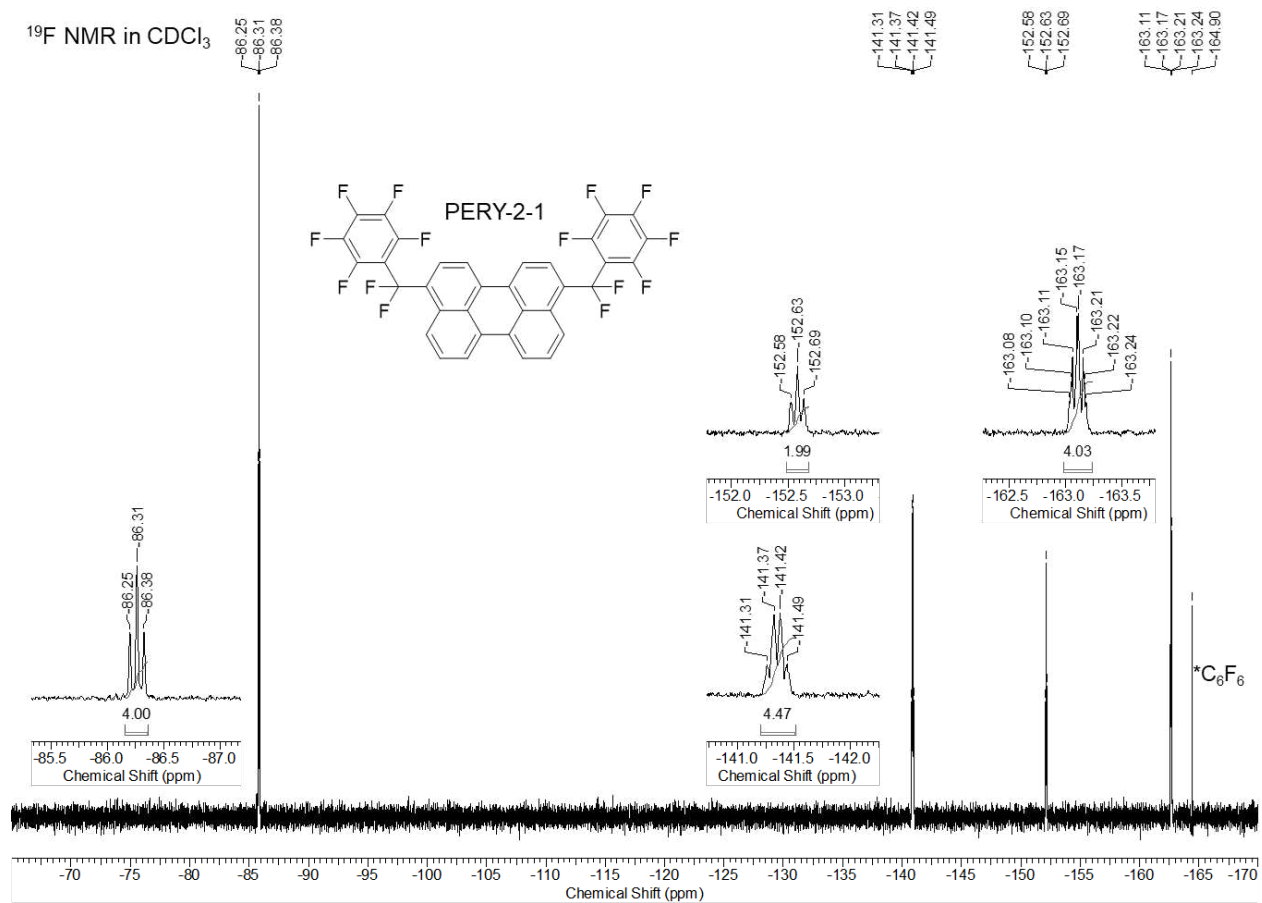


Figure 3.35. ¹⁹F-NMR spectrum of PERY-2-1 in CDCl₃.

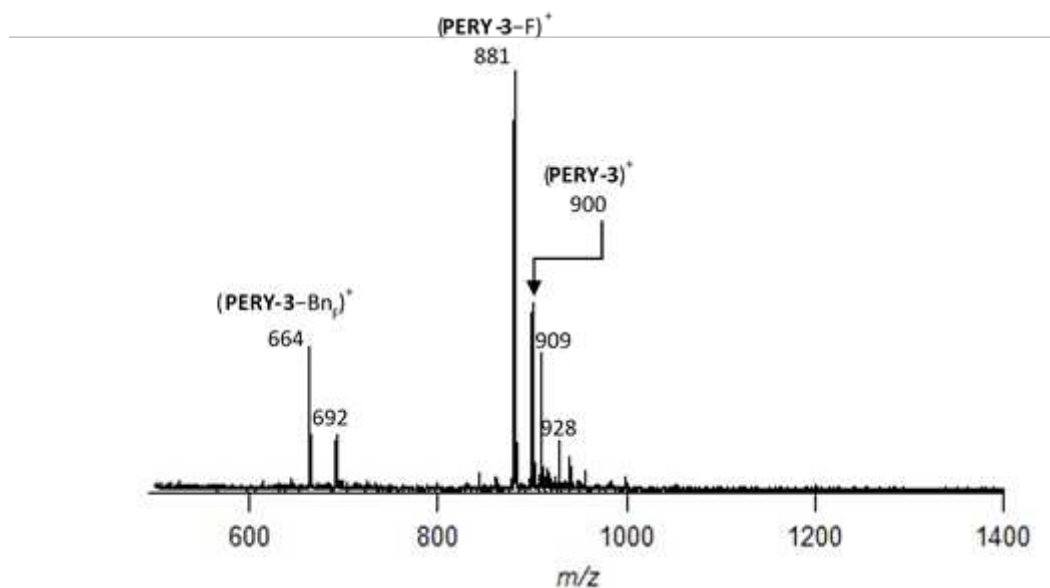


Figure 3.36. Positive-ion ESI mass spectrum of PERY-3-1.

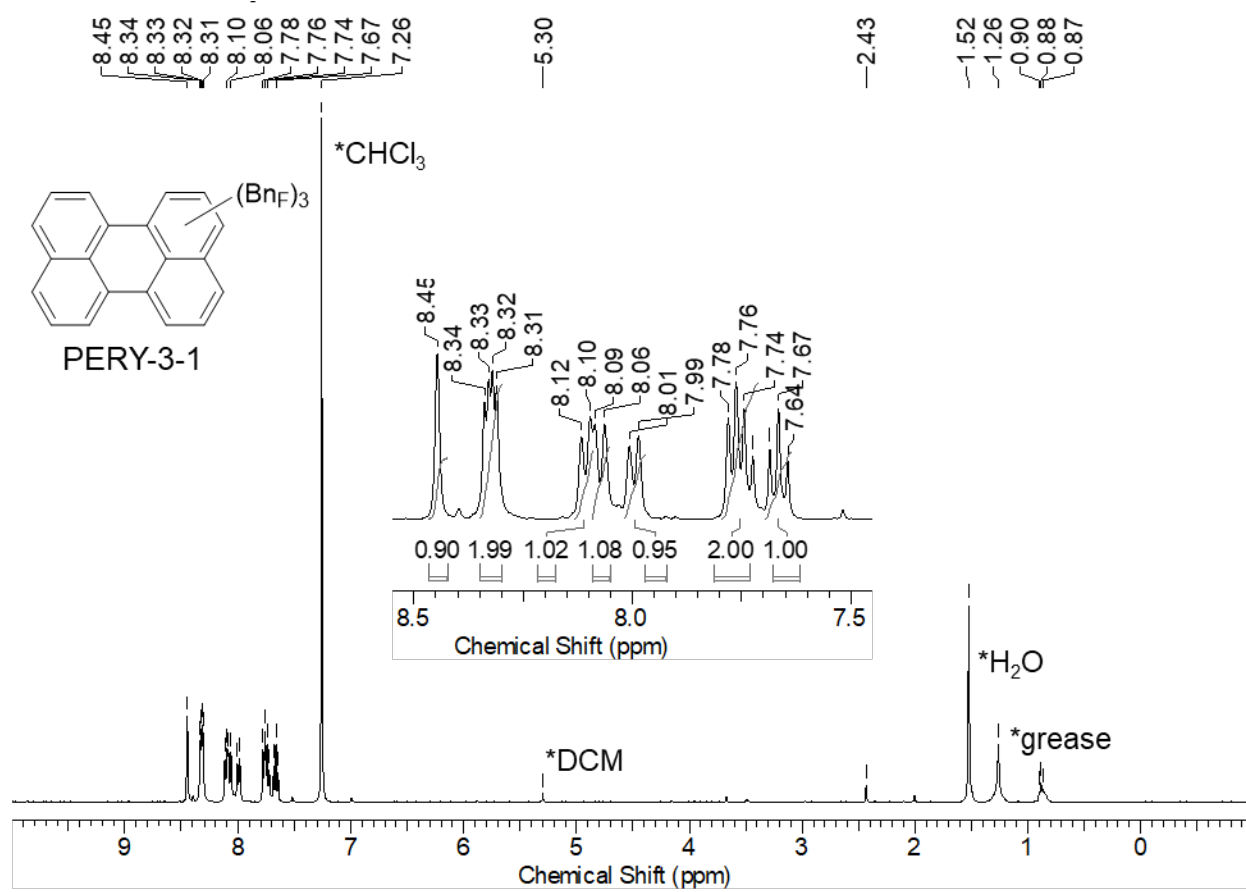


Figure 3.37. $^1\text{H-NMR}$ spectrum of PERY-3-1 in CDCl_3 .

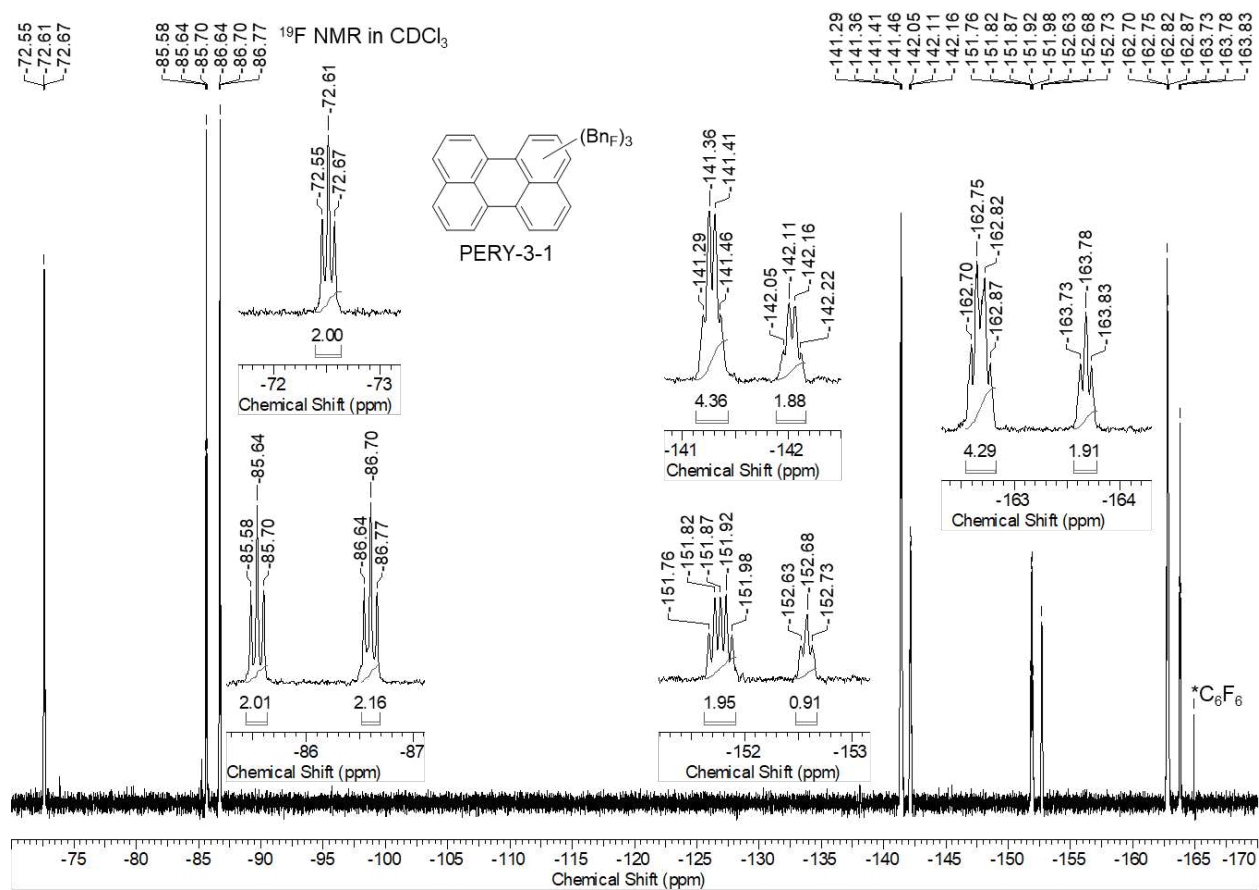


Figure 3.38. ¹⁹F-NMR spectrum of PERY-3-1 in CDCl₃.

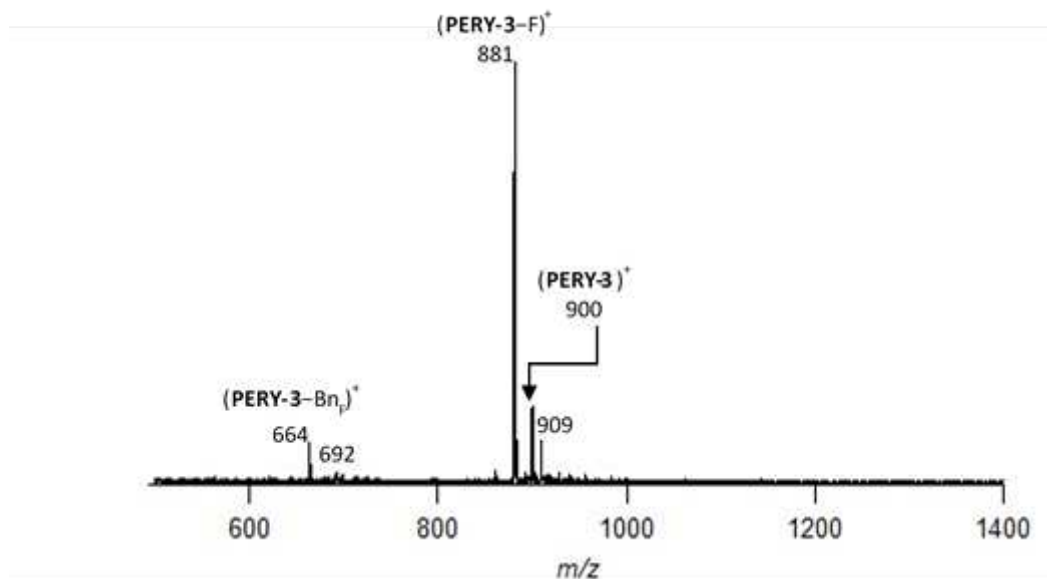


Figure 3.39. Positive-ion ESI mass spectrum of PERY-3-2 fraction.

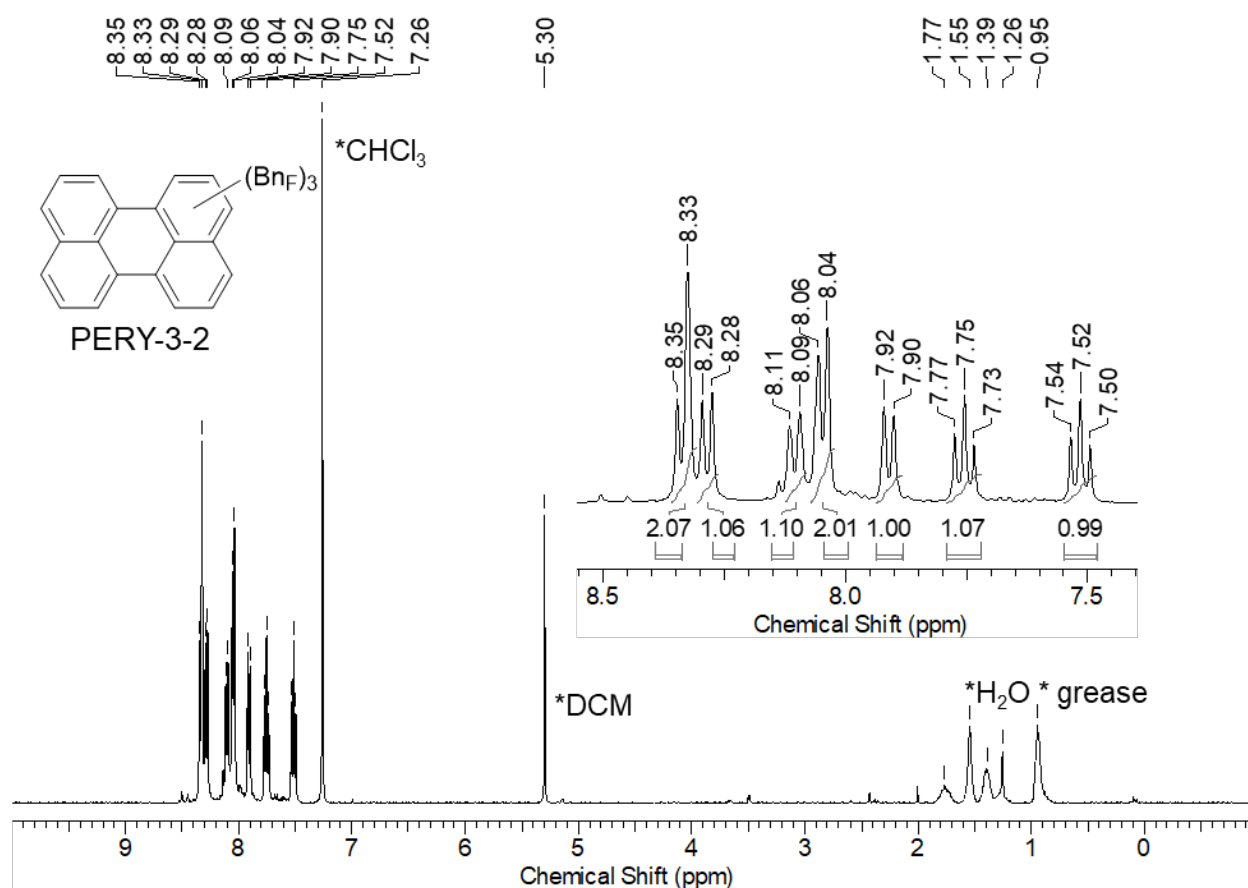


Figure 3.40. $^1\text{H-NMR}$ spectrum of PERY-3-2 in CDCl_3 .

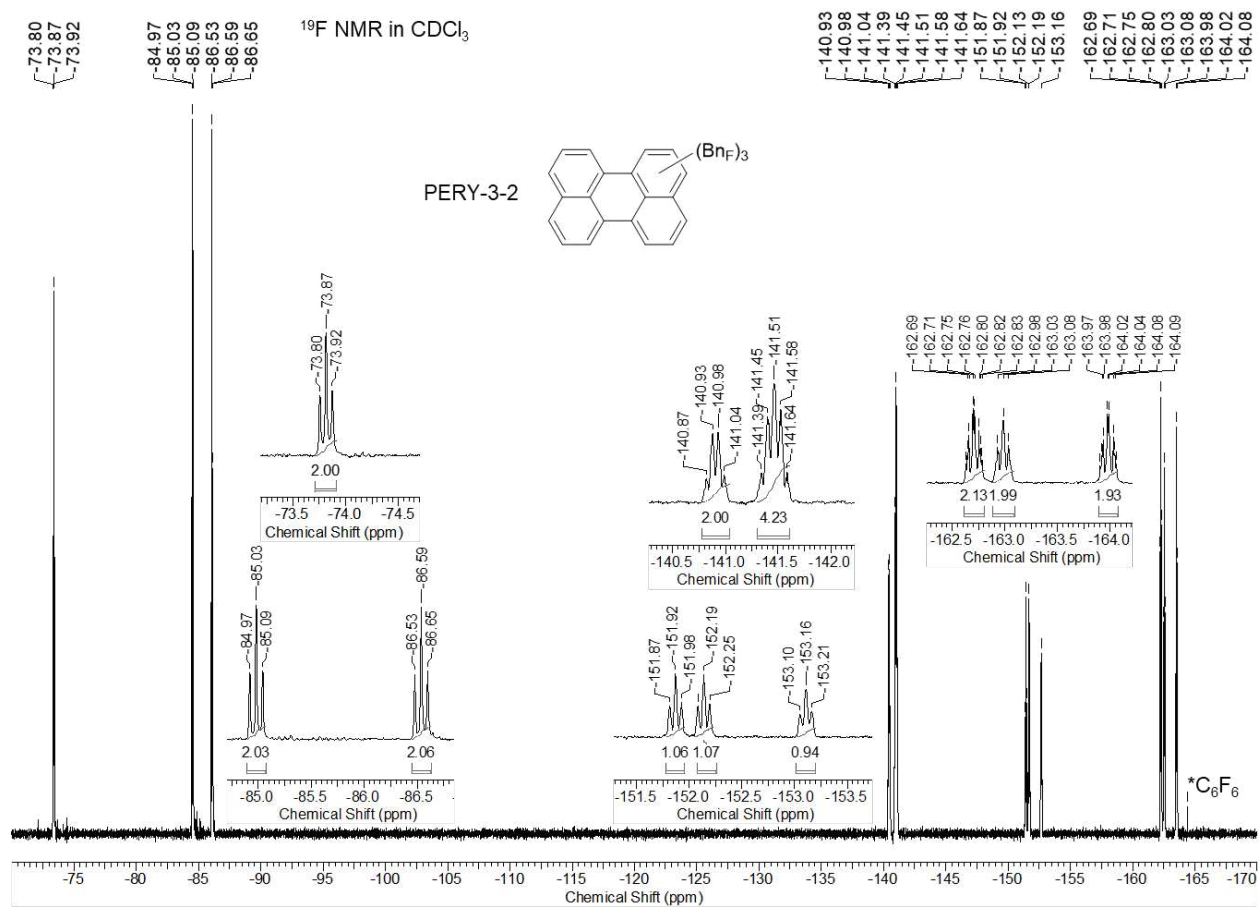


Figure 3.41. ¹⁹F-NMR spectrum of PERY-3-2 in CDCl₃.

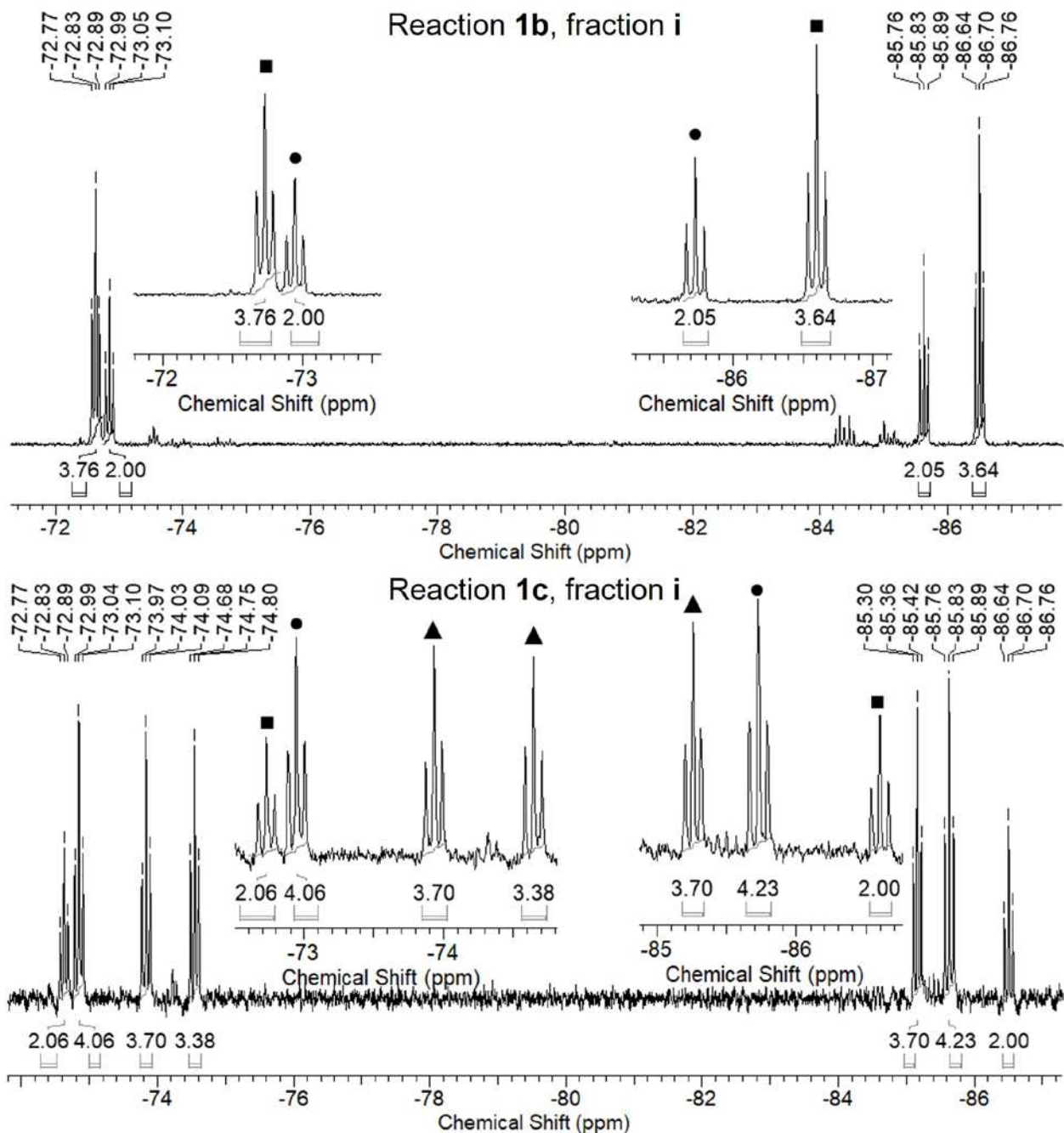


Figure 3.42. ^{19}F -NMR spectra of benzylic region for fraction i (from Figure 3.8). top) reaction **1b** showing two sets of triplets (labeled ■ and ●) for two bis-substituted PERY compounds, each with one group on the *bay* and *peri* positions. bottom) reaction **1c** showing same two sets of triplets (■ and ●) as **1a**, as well as three new triplets of similar intensity (labeled as ▲) consistent with a tris-substituted (PERY-3) containing two BnF groups on the *bay* position and one on the *peri* position, which one would expect this isomer to have a lower retention time (i) than if there were two groups on the *peri* position and one on the *bay* (i.e. PERY-3 isomers in fraction iv of Fig. 2).

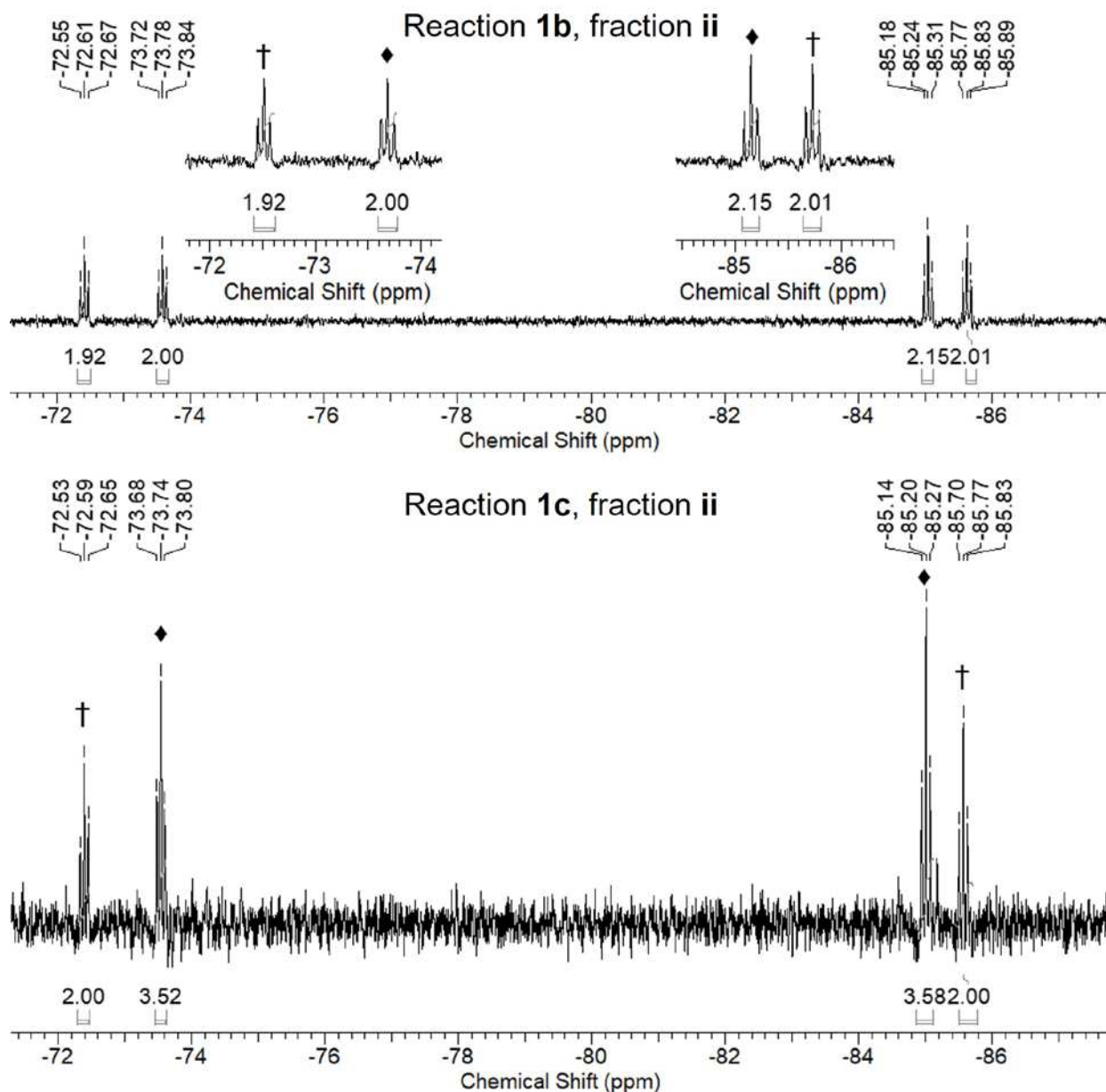


Figure 3.43. ^{19}F -NMR spectra of benzylic region for fraction ii (from Figure 3.8). top) reaction **1b** showing two sets of triplets (labeled † and ♦) for two bis-substituted PERY compounds, each with one group on the *bay* and *peri* positions. bottom) reaction **1c** showing same two sets of triplets († and ♦) but in different ratios to each other (2:3.5 vs 1.9:2.0, respectively). It indicates that these are two PERY-2 isomers instead of one PERY-4 isomer, which could not be differentiated from reaction **1b** alone without further characterization.

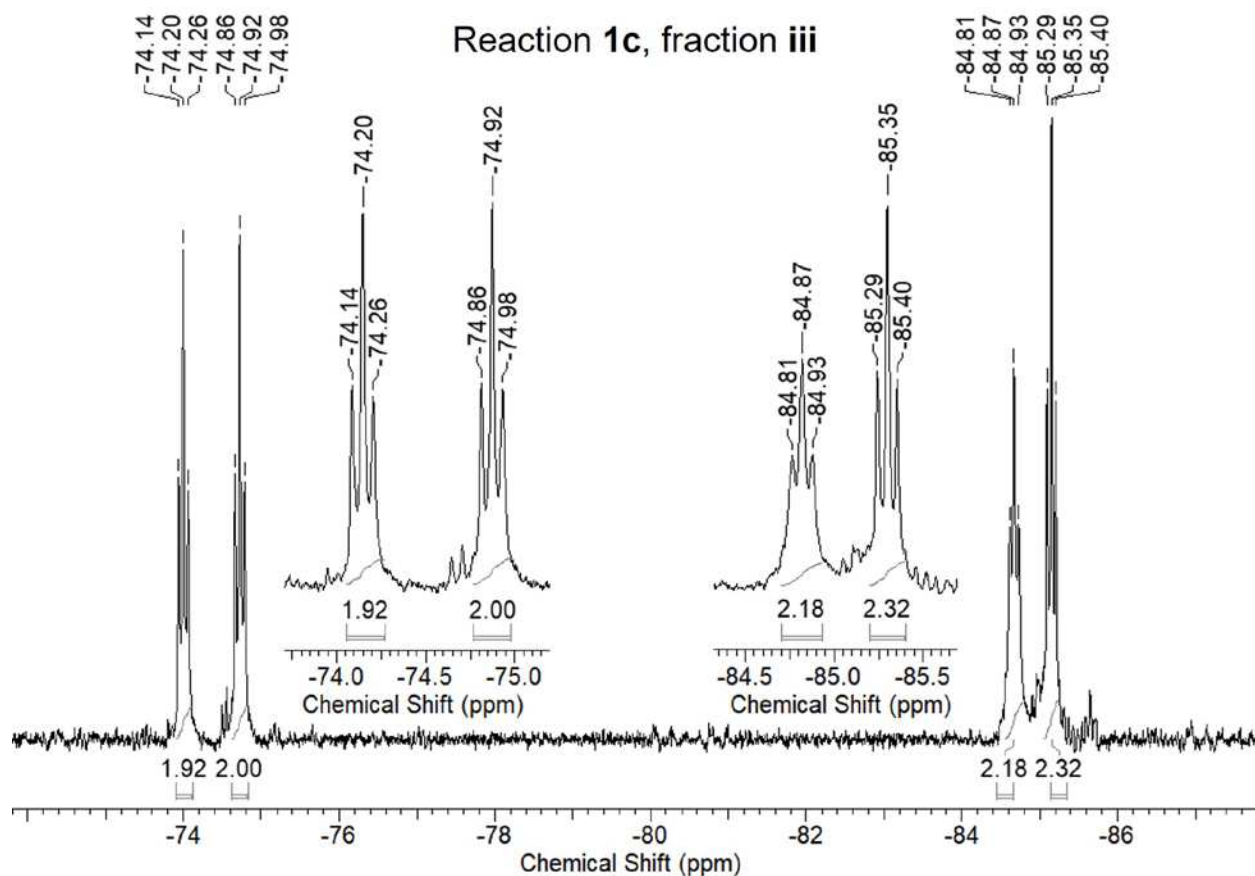


Figure 3.44. ^{19}F -NMR spectra of benzylic region for reaction **1c**, fraction iii (from Figure 3.8) showing four triplets which the author believes to be from a non-symmetric tetrakis substituted PERY compound, with two groups on the *bay* and two on the *peri* positions. Note, these signals are not observed in reaction 1a, suggesting it is a higher substitution than a bis-isomer, thus leading to the conclusion it must be a non-symmetric PERY-4-1.

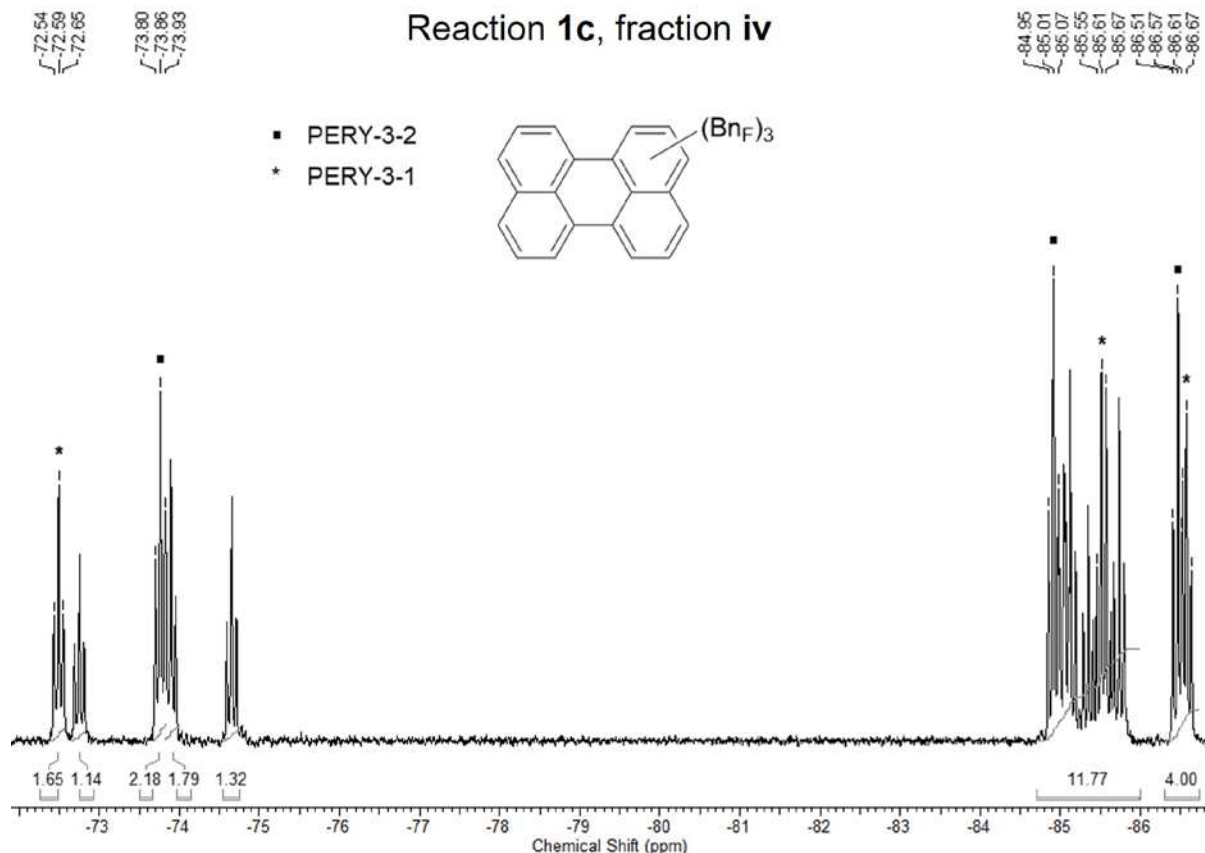


Figure 3.45. ^{19}F -NMR spectrum of largest fraction (vi) from reaction **1c** (Figure 3.8 and S4) before secondary separation or solvent extraction, showing benzylic CF_2 region to determine yield of PERY-3-1 and PERY-3-2. **F1** (45.2 mg isolated) is a mixture of four isomers containing three BnF groups and a small amount of one symmetric isomer containing four groups. By using ^{19}F -NMR, it is possible to determine the relative amount of PERY-3-1 and PERY-3-2 without the need for rigorous purification. This is done by comparing the integration for the overlapping triplets (centered at -86.70 and -86.59 ppm), which originate from one of the two *bay* positions on PERY-3-1 and PERY-3-2, with the total integration value of all *bay*- CF_2 's. When integrating these together to 4 (shown), the total value for all *bay* positions is 15.77, which includes 8 fluorines from the two *bay* positions on each of PERY-3-1 and PERY-3-2. This gives 50.7% of fraction vi being PERY-3-1 and PERY-3-2 combined. Using this and comparing the integration of the *bay*- CF_2 triplets centered at -72.61 and -73.87 ppm, which are separated enough to compare in contrast to the *bay* positions, we get that PERY-3-1 is 21.9% of fraction vi (5.5% total yield by NMR) and PERY-3-2 is 28.8% (7.2% total yield by NMR).

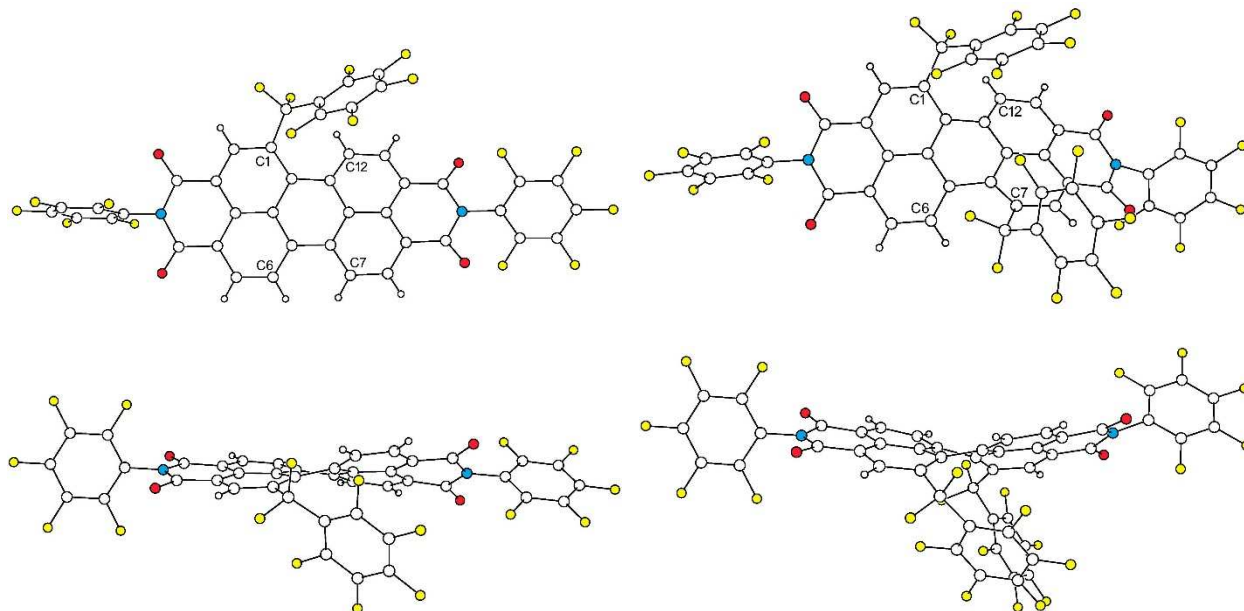


Figure 3.46. Drawings of the X-ray structures of PDI-1-BnF (left) and PDI-1,7-(BnF)₂ (right).

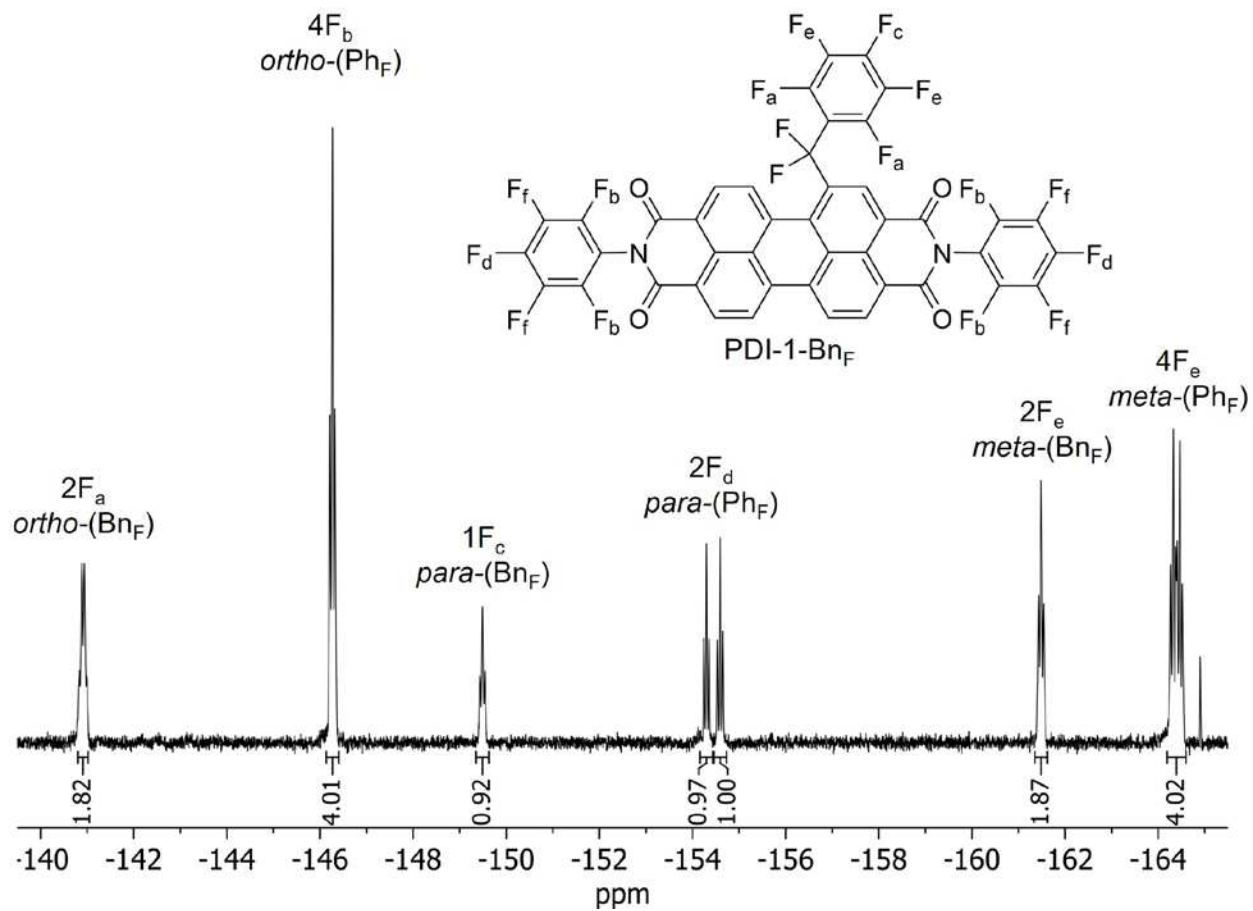


Figure 3.47. ^{19}F NMR aromatic region of purified PDI-1-(Bn_F) $_1$ (zoom in of Figure 3.48). Each peak is labeled for either being from the Ph_F groups on the imides or from the substituted Bn_F .

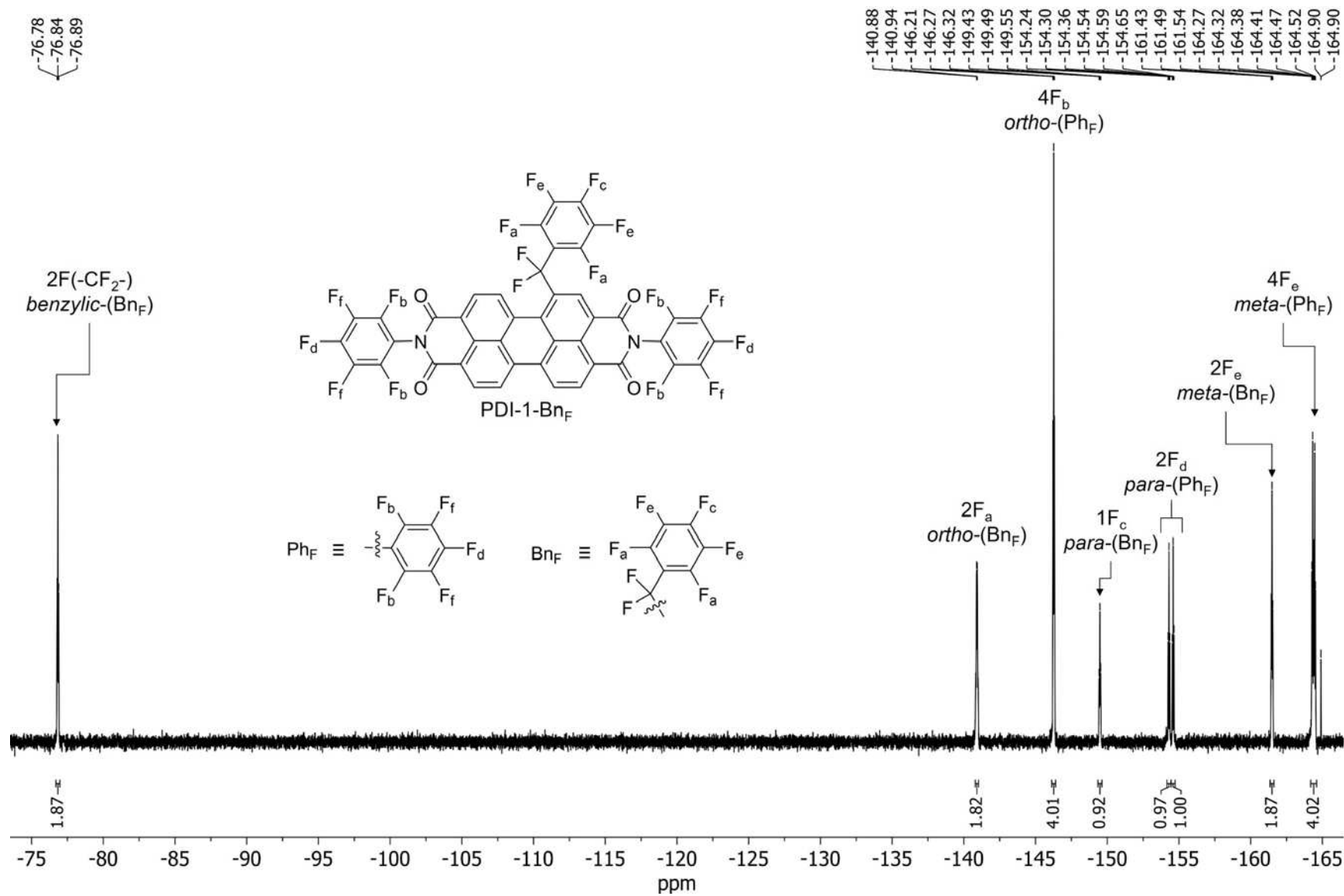


Figure 3.48: ^{19}F -NMR spectrum of PDI-1-BnF in $CDCl_3$.

^{19}F NMR (376 MHz, CDCl_3) δ -76.83 (t, $J = 21.7$ Hz, 2F), -140.91 (d, $J = 21.0$ Hz, 2F), -146.18 – -146.36 (m, 4F), -149.49 (t, $J = 21.7$ Hz, 1F), -154.30 (t, $J = 21.5$ Hz, 1F), -154.59 (t, $J = 21.3$ Hz, 1F), -161.40 – -161.60 (m, 2F), -164.32 (dd, $J = 21.2, 16.4$ Hz, 2F), -164.46 (dd, $J = 21.1, 16.4$ Hz, 2F).

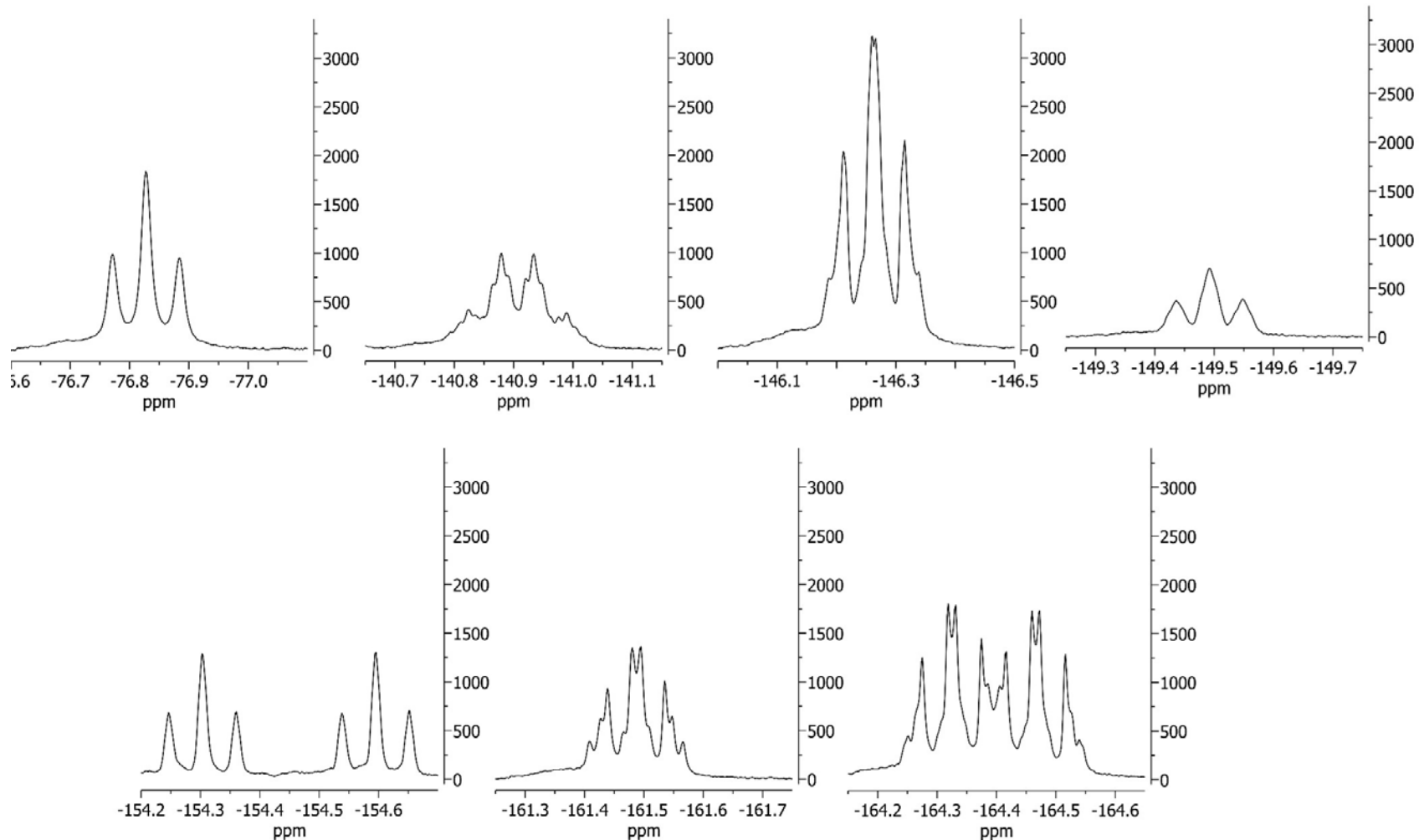


Figure 3.49: Closeup view of signals in ^{19}F -NMR spectrum of PDI-1-BnF from Figure 3.5 showing relative intensities and normalized to the same ppm scale.

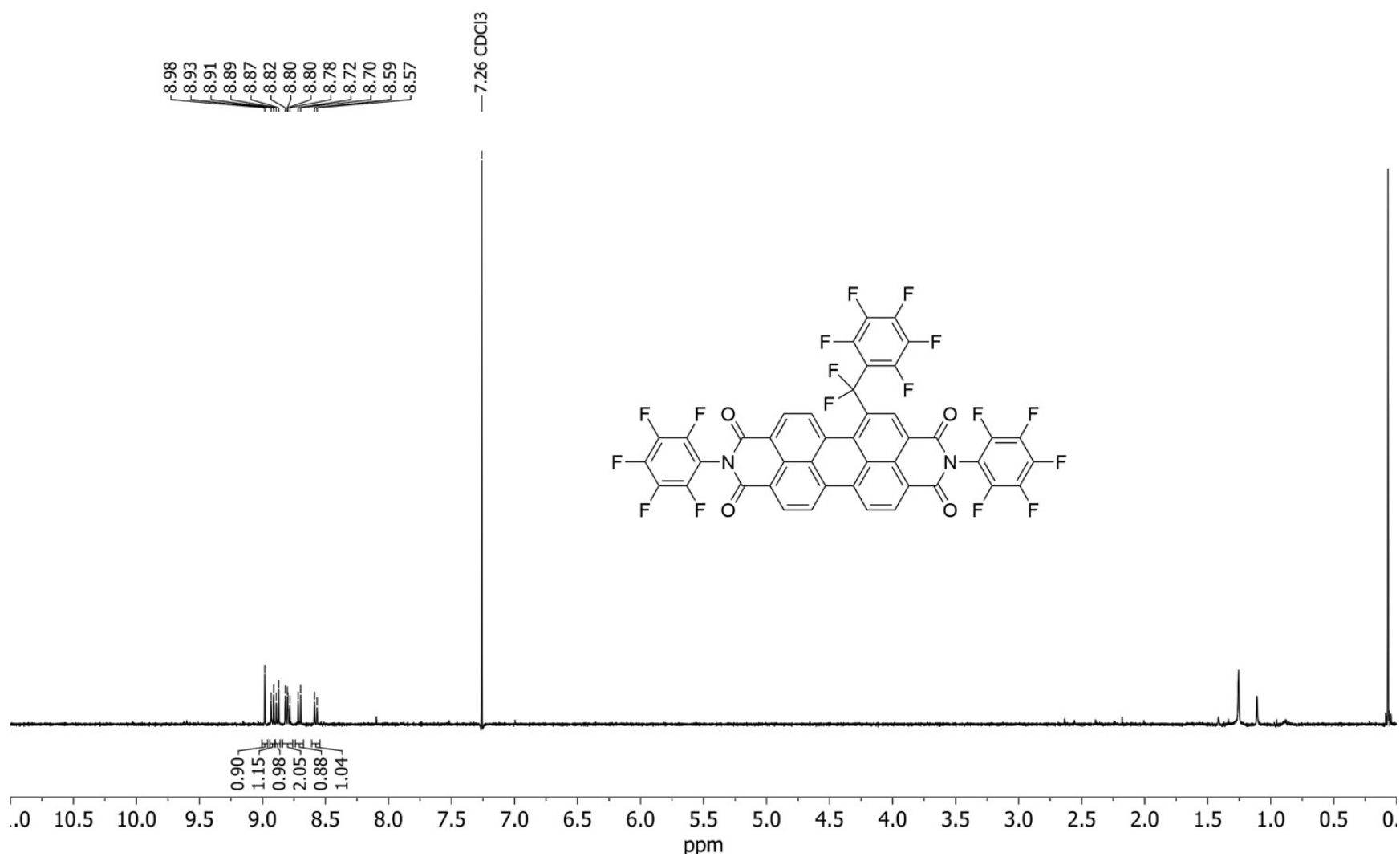


Figure 3.50: $^1\text{H-NMR}$ spectrum of PDI-1-BnF in CDCl_3 .

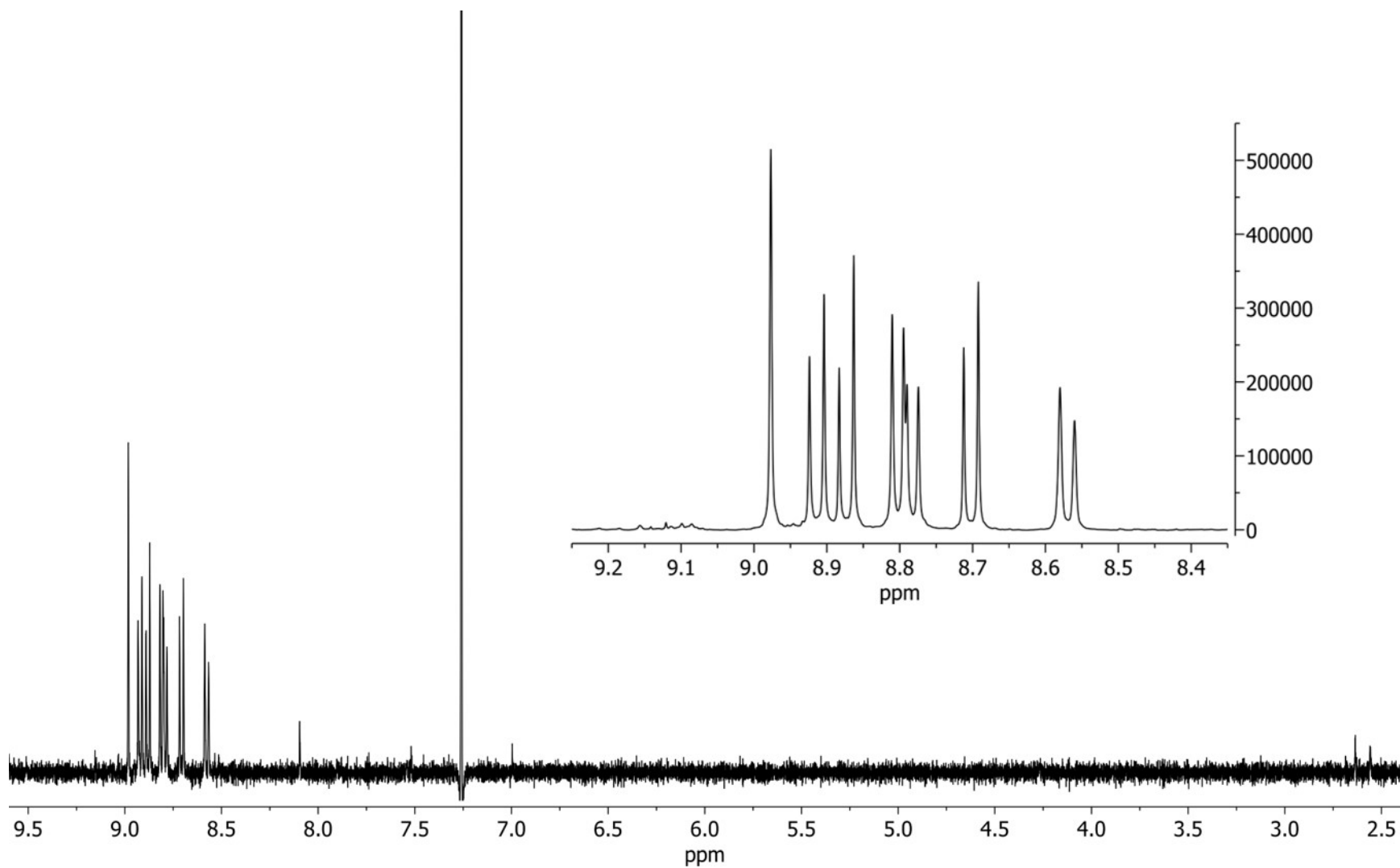


Figure 3.51: $^1\text{H-NMR}$ spectrum of PDI-1- BnF in CDCl_3 showing from 2.5 to 9.5 ppm. Inset shows aromatic region from 8.4 to 9.2 ppm.

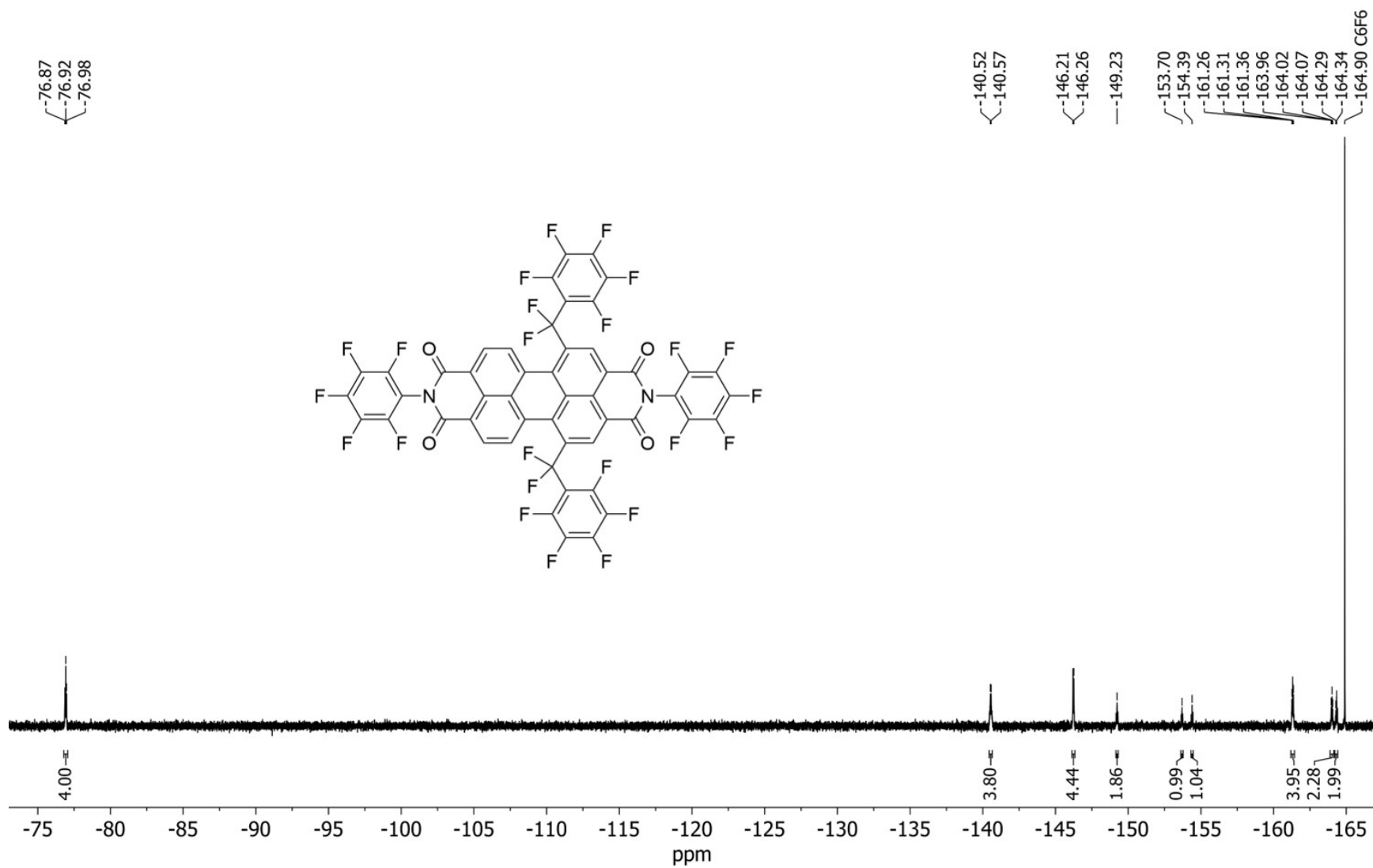


Figure 3.52: ¹⁹F-NMR spectrum of PDI-1,6-(BnF)₂ in CDCl₃.

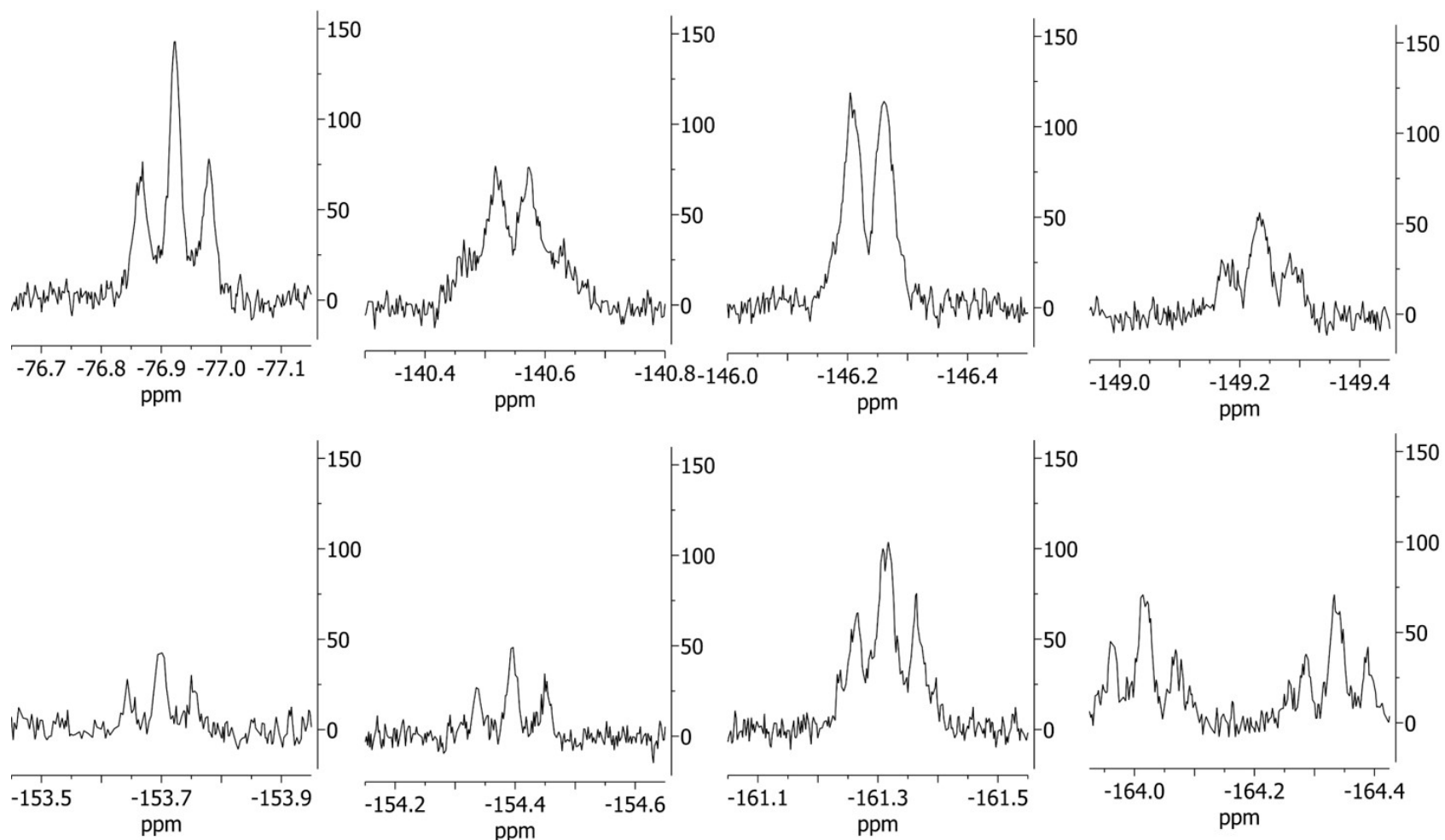


Figure 3.53: Closeup view of signals in ^{19}F -NMR spectrum of PDI-1,6-(BnF)₂ from Figure 3.10. Showing relative intensities and normalized to the same ppm scale.

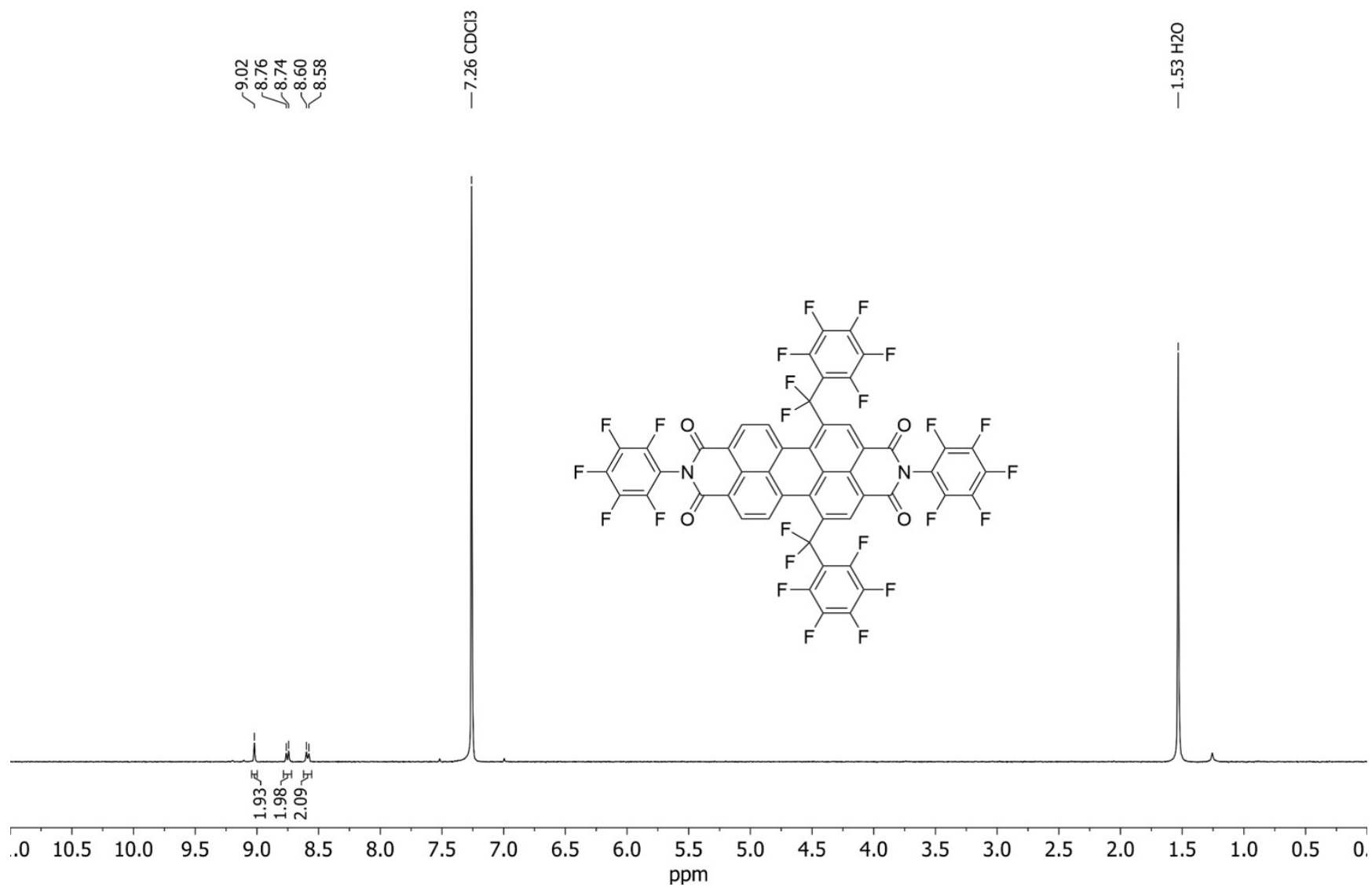


Figure 3.54: $^1\text{H-NMR}$ spectrum of PDI-1,6-(BnF) $_2$ in CDCl_3 .

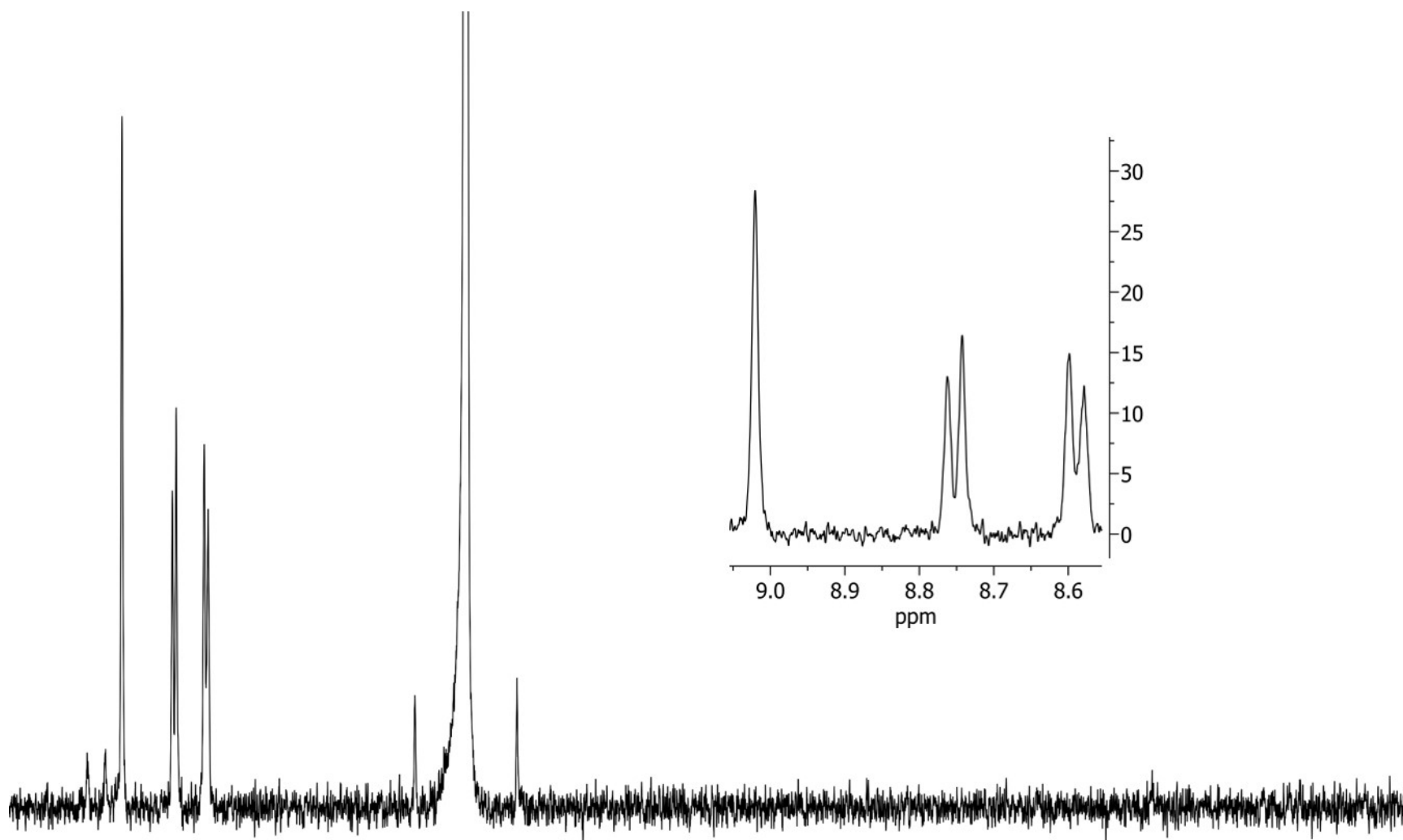


Figure 3.55: ¹H-NMR spectrum of PDI-1,6-(BnF)₂ in CDCl₃ showing from 2.5 to 9.5 ppm. Inset shows aromatic region from 8.5 to 9.1 ppm.

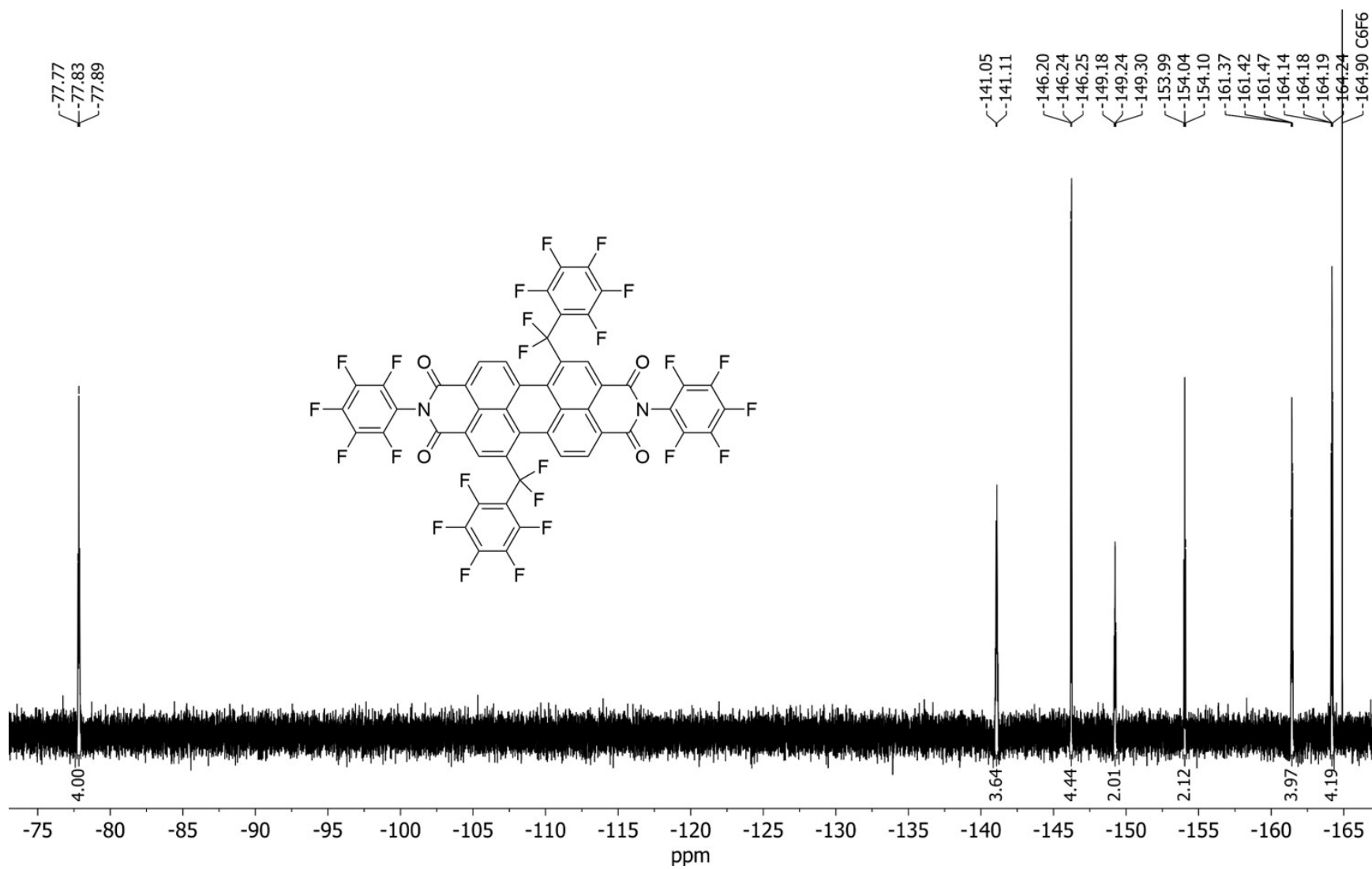


Figure 3.56: ^{19}F -NMR spectrum of PDI-1,7-(BnF) $_2$ in CDCl_3 .

^{19}F NMR (376 MHz, CDCl_3) δ -77.83 (t, $J = 22.3$ Hz, 4F), -141.08 (d, $J = 21.9$ Hz, 4F), -146.13 -- -146.31 (m, 4F), -149.24 (t, $J = 21.7$ Hz, 2F), -154.04 (t, $J = 21.5$ Hz, 2F), -161.31 -- -161.54 (m, 4F), -164.19 (dd, $J = 20.9, 16.6$ Hz, 4F).

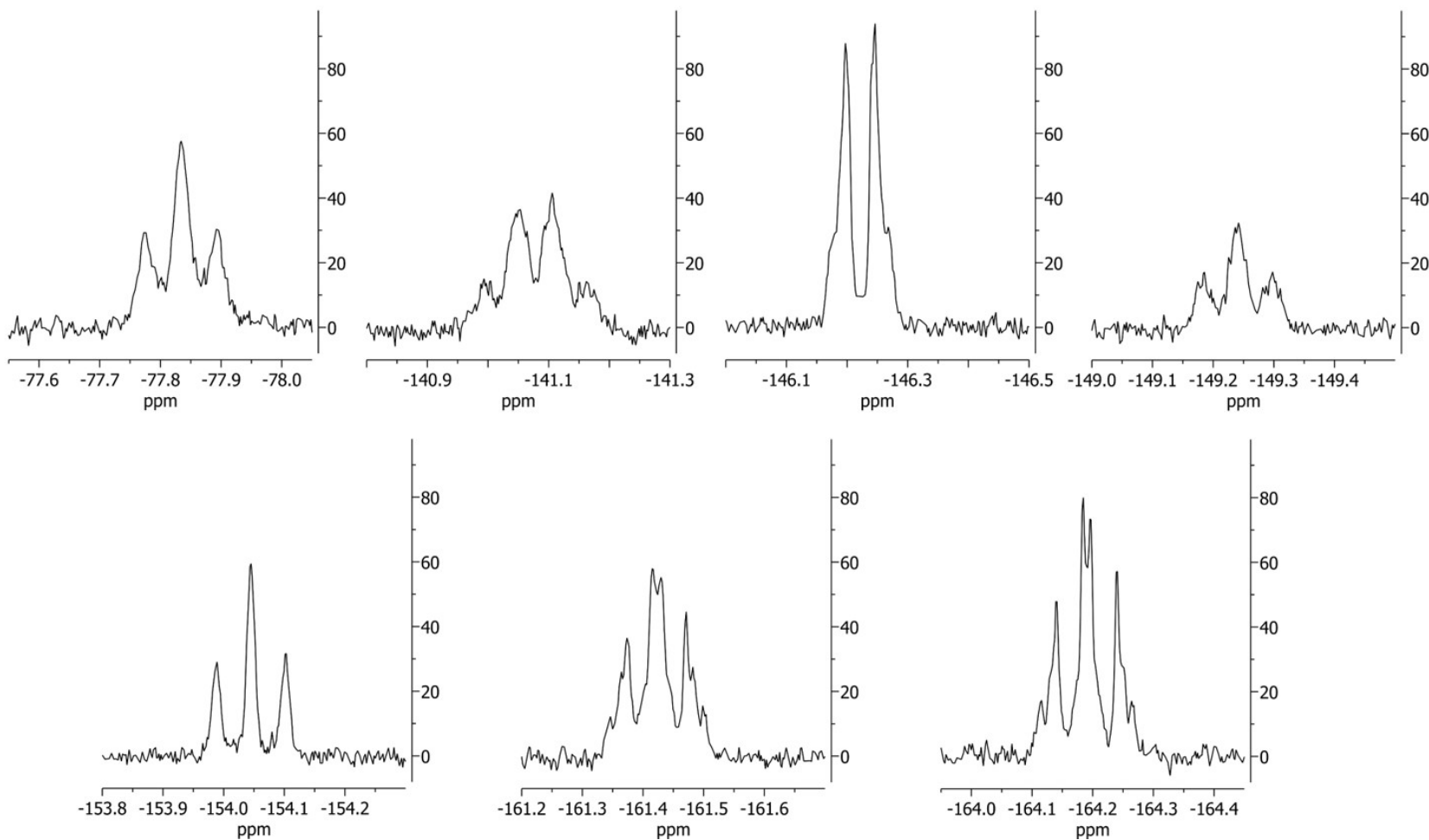


Figure 3.57: Closeup view of signals in ^{19}F -NMR spectrum of PDI-1,7-(BnF) $_2$ from Figure 3.15. Showing relative intensities and normalized to the same ppm scale.

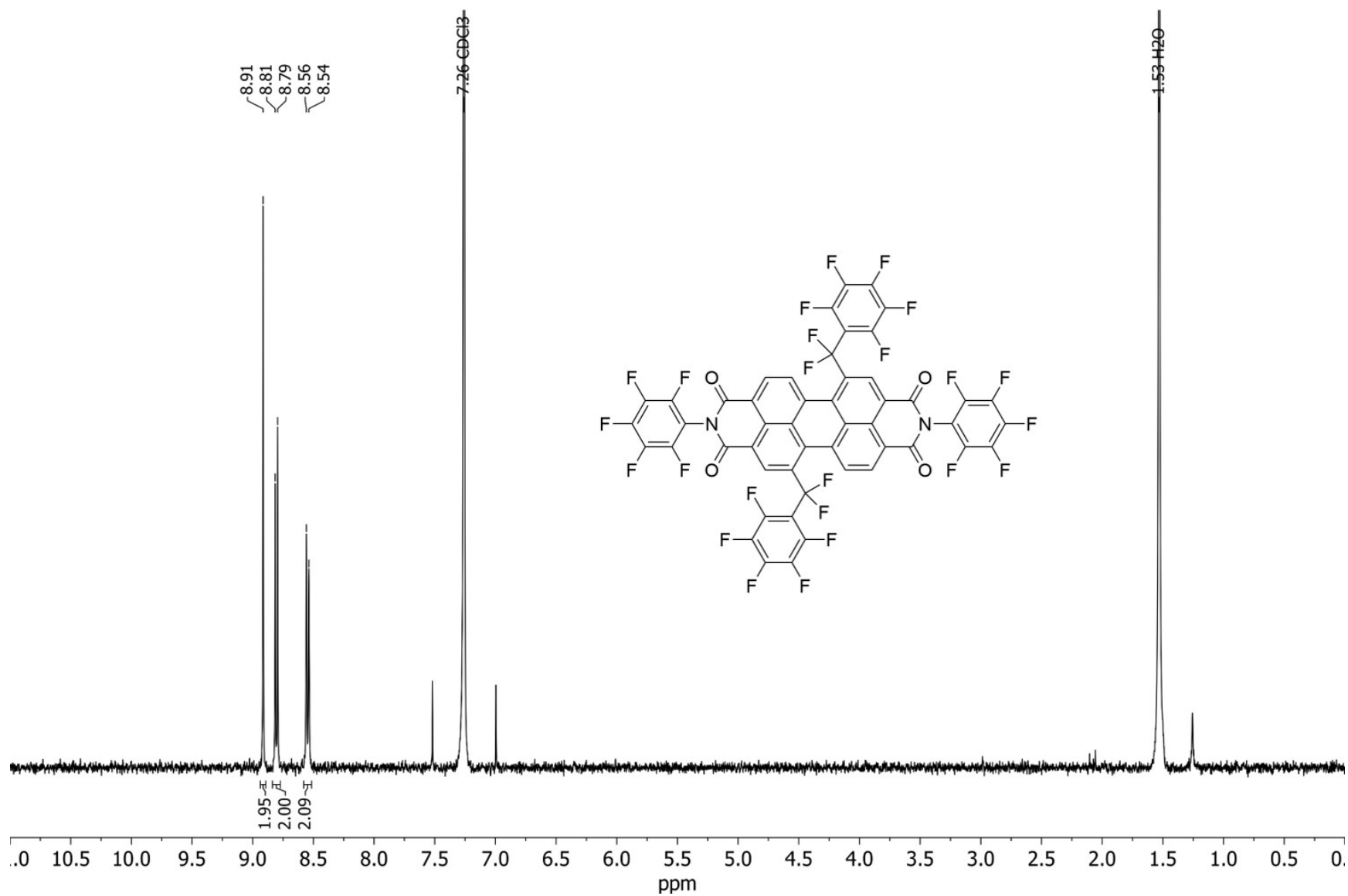


Figure 3.58: $^1\text{H-NMR}$ spectrum of PDI-1,7-(BnF) $_2$ in CDCl_3 .

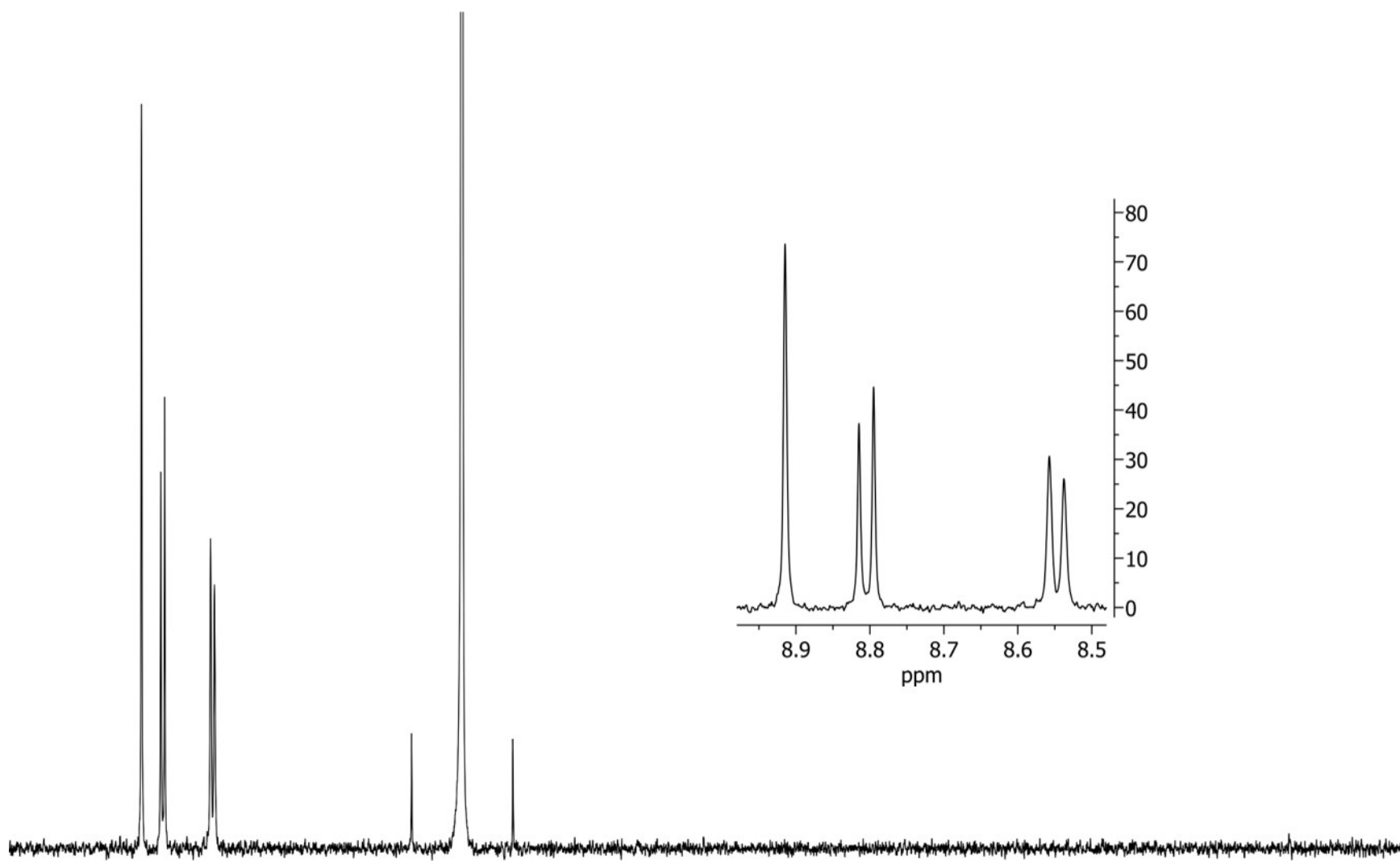


Figure 3.59: ¹H-NMR spectrum of PDI-1,7-(BnF)₂ in CDCl₃ showing from 2.5 to 9.5 ppm. Inset shows aromatic region from 8.5 to 9.1 ppm.

CHAPTER 3 REFERENCES

104. Zhang, Q.; Kelly, M. A.; Bauer, N.; You, W., The Curious Case of Fluorination of Conjugated Polymers for Solar Cells. *Acc. Chem. Res.* **2017**, *50* (9), 2401-2409.
105. Liu, C.; Qiu, N.; Sun, Y.; Ke, X.; Zhang, H.; Li, C.; Wan, X.; Chen, Y., All-Small-Molecule Organic Solar Cells Based on a Fluorinated Small Molecule Donor With High Open-Circuit Voltage of 1.07 V. *Frontiers in Chemistry* **2020**, *8* (329).
106. Ge, J.; Xie, L.; Peng, R.; Fanady, B.; Huang, J.; Song, W.; Yan, T.; Zhang, W.; Ge, Z., 13.34 % Efficiency Non-Fullerene All-Small-Molecule Organic Solar Cells Enabled by Modulating the Crystallinity of Donors via a Fluorination Strategy. *Angew. Chem. Int. Ed.* **2020**, *59* (7), 2808-2815.
107. Xie, R.; Ying, L.; Liao, H.; Chen, Z.; Huang, F.; Cao, Y., Efficient Non-fullerene Organic Solar Cells Enabled by Sequential Fluorination of Small-Molecule Electron Acceptors. *Frontiers in Chemistry* **2018**, *6* (303).
108. Guo, X.; Bu, L.; Zhao, Y.; Xie, Z.; Geng, Y.; Wang, L., Controlled phase separation for efficient energy conversion in dye/polymer blend bulk heterojunction photovoltaic cells. *Thin Solid Films* **2009**, *517* (16), 4654-4657.
109. Sun, H.; Kramer, J. H., 7 - Perfluoroalkylated PAH n-Type Semiconductors: Theory and Experiment. In *New Fluorinated Carbons: Fundamentals and Applications*, Boltalina, O. V.; Nakajima, T., Eds. Elsevier: Boston, 2017; pp 155-176.
110. Li, C.; Liu, Z.; Schöneboom, J.; Eickemeyer, F.; Pschirer, N. G.; Erk, P.; Herrmann, A.; Müllen, K., Perylenes as sensitizers in hybrid solar cells: how molecular size influences performance. *J. Mater. Chem.* **2009**, *19* (30), 5405-5415.
111. Kushwaha, K.; Yu, L.; Stranius, K.; Singh, S. K.; Hultmark, S.; Iqbal, M. N.; Eriksson, L.; Johnston, E.; Erhart, P.; Müller, C., A Record Chromophore Density in High-Entropy Liquids of Two Low-Melting Perylenes: A New Strategy for Liquid Chromophores. *Adv. Sci.* **2019**, *6* (4), 1801650.
112. Shoaee, S.; Deledalle, F.; Shakya Tuladhar, P.; Shivanna, R.; Rajaram, S.; Narayan, K. S.; Durrant, J. R., A Comparison of Charge Separation Dynamics in Organic Blend Films Employing Fullerene and Perylene Diimide Electron Acceptors. *J. Phys. Chem. Lett.* **2015**, *6* (1), 201-205.
113. Chen, H. Z.; Ling, M. M.; Mo, X.; Shi, M. M.; Wang, M.; Bao, Z., Air Stable n-Channel Organic Semiconductors for Thin Film Transistors Based on Fluorinated Derivatives of Perylene Diimides. *Chem. Mater.* **2007**, *19* (4), 816-824.
114. Sun, H.; Tottempudi, U. K.; Mottishaw, J. D.; Basa, P. N.; Putta, A.; Sykes, A. G., Strengthening π - π Interactions While Suppressing Csp²-H \cdots π (T-Shaped) Interactions via Perfluoroalkylation: A Crystallographic and Computational Study That Supports the Beneficial Formation of 1-D π - π Stacked Aromatic Materials. *Crystal Growth & Design* **2012**, *12* (11), 5655-5662.
115. Sun, H.; Putta, A.; Billion, M., Arene Trifluoromethylation: An Effective Strategy to Obtain Air-Stable n-Type Organic Semiconductors with Tunable Optoelectronic and Electron Transfer Properties. *J. Phys. Chem. A* **2012**, *116* (30), 8015-8022.
116. Liu, L.; Yang, G.; Duan, Y.; Geng, Y.; Wu, Y.; Su, Z., The relationship between intermolecular interactions and charge transport properties of trifluoromethylated polycyclic aromatic hydrocarbons. *Org. Electronics* **2014**, *15* (9), 1896-1905.
117. Botoshansky, M.; Herbstein, F. H.; Kapon, M., Towards a Complete Description of a Polymorphic Crystal: The Example of Perylene. *Helv. Chim. Acta* **2003**, *86* (4), 1113-1128.
118. Kuvychko, I. V.; Castro, K. P.; Deng, S. H. M.; Wang, X.-B.; Strauss, S. H.; Boltalina, O. V., Taming Hot CF₃ Radicals: Incrementally Tuned Families of Polyarene Electron Acceptors for Air-Stable Molecular Optoelectronics. *Angew. Chem. Int. Ed.* **2013**, *52* (18), 4871-4874.
119. Nowak-Król, A.; Würthner, F., Progress in the synthesis of perylene bisimide dyes. *Organic Chemistry Frontiers* **2019**, *6* (8), 1272-1318.

120. Sharma, V.; Koenig, J. D. B.; Welch, G. C., Perylene diimide based non-fullerene acceptors: top performers and an emerging class featuring N-annulation. *Journal of Materials Chemistry A* **2021**, *9* (11), 6775-6789.
121. Clikeman, T. T.; Bukovsky, E. V.; Wang, X.-B.; Chen, Y.-S.; Rumbles, G.; Strauss, S. H.; Boltalina, O. V., Core Perylene Diimide Designs via Direct Bay- and ortho-(Poly)trifluoromethylation: Synthesis, Isolation, X-ray Structures, Optical and Electronic Properties. *Eur. J. Org. Chem.* **2015**, *2015* (30), 6641-6654.
122. Li, Y.; Li, C.; Yue, W.; Jiang, W.; Kopecek, R.; Qu, J.; Wang, Z., Direct Functionalization of Polycyclic Aromatics via Radical Perfluoroalkylation. *Org. Lett.* **2010**, *12* (10), 2374-2377.
123. San, L. K.; Clikeman, T. T.; Dubceac, C.; Popov, A. A.; Chen, Y.-S.; Petrukhina, M. A.; Strauss, S. H.; Boltalina, O. V., Corannulene Molecular Rotor with Flexible Perfluorobenzyl Blades: Synthesis, Structure and Properties. *Chem. Eur. J.* **2015**, *21* (26), 9488-9492.
124. Wang, L.; Dai, J.; Song, Y., The impact of diperfluorophenyl and thienyl substituents on the electronic structures and charge transport properties of the fused thiophene semiconductors. *Int J. Quant. Chem.* **2019**, *119* (5), e25824.
125. Pawle, R. H.; Haas, T. E.; Muller, P.; Thomas Iii, S. W., Twisting and piezochromism of phenylene-ethynylenes with aromatic interactions between side chains and main chains. *Chem. Sci.* **2014**, *5* (11), 4184-4188.
126. Li, Y.; Li, C.; Yue, W.; Jiang, W.; Kopecek, R.; Qu, J.; Wang, Z., Direct Functionalization of Polycyclic Aromatics via Radical Perfluoroalkylation. *Org. Lett.* **2010**, *12* (10), 2374-2377.
127. Clikeman, T. T.; Bukovsky, E. V.; Wang, X.-B.; Chen, Y.-S.; Rumbles, G.; Strauss, S. H.; Boltalina, O. V., Core Perylene Diimide Designs via Direct Bay- and ortho-(Poly)trifluoromethylation: Synthesis, Isolation, X-ray Structures, Optical and Electronic Properties. *Eur. J. Org. Chem.* **2015**, *2015* (30), 6641-6654.
128. Katz, H. E.; Lovinger, A. J.; Johnson, J.; Kloc, C.; Siegrist, T.; Li, W.; Lin, Y. Y.; Dodabalapur, A., A soluble and air-stable organic semiconductor with high electron mobility. *Natur* **2000**, *404* (6777), 478-481.
129. Chen, H. Z.; Ling, M. M.; Mo, X.; Shi, M. M.; Wang, M.; Bao, Z., Air Stable n-Channel Organic Semiconductors for Thin Film Transistors Based on Fluorinated Derivatives of Perylene Diimides. *Chem. Mater.* **2007**, *19* (4), 816-824.
130. Okamoto, T.; Nakahara, K.; Saeki, A.; Seki, S.; Oh, J. H.; Akkerman, H. B.; Bao, Z.; Matsuo, Y., Aryl-Perfluoroaryl Substituted Tetracene: Induction of Face-to-Face π - π Stacking and Enhancement of Charge Carrier Properties. *Chem. Mater.* **2011**, *23* (7), 1646-1649.
131. Takeya, J.; Yamagishi, M.; Tominari, Y.; Hirahara, R.; Nakazawa, Y.; Nishikawa, T.; Kawase, T.; Shimoda, T.; Ogawa, S., Very high-mobility organic single-crystal transistors with in-crystal conduction channels. *Appl. Phys. Lett.* **2007**, *90* (10), 102120.
132. da Silva Filho, D. A.; Kim, E.-G.; Brédas, J.-L., Transport Properties in the Rubrene Crystal: Electronic Coupling and Vibrational Reorganization Energy. *Adv. Mater.* **2005**, *17* (8), 1072-1076.
133. Goldmann, C.; Haas, S.; Krellner, C.; Pernstich, K. P.; Gundlach, D. J.; Batlogg, B., Hole mobility in organic single crystals measured by a "flip-crystal" field-effect technique. *J. Appl. Phys.* **2004**, *96* (4), 2080-2086.
134. Bergantin, S.; Moret, M., Rubrene Polymorphs and Derivatives: The Effect of Chemical Modification on the Crystal Structure. *Crystal Growth & Design* **2012**, *12* (12), 6035-6041.
135. Schmidt, R.; Oh, J. H.; Sun, Y.-S.; Deppisch, M.; Krause, A.-M.; Radacki, K.; Braunschweig, H.; Könemann, M.; Erk, P.; Bao, Z.; Würthner, F., High-Performance Air-Stable n-Channel Organic Thin Film Transistors Based on Halogenated Perylene Bisimide Semiconductors. *J. Am. Chem. Soc.* **2009**, *131* (17), 6215-6228.

CHAPTER 4. New Approaches to Fluoroannulation of PAHs

4.1. Introduction

A considerable effort in the molecular design and synthesis of the PAH-based organic semiconductors has been dedicated to the development of the methods that allow expansion of their conjugated π -systems, for improved charge transport. Among such methods, aryl-aryl couplings have been achieved with UV irradiation under *oxidative* conditions (O_2 or I_2 ; Mallory reactions), but these mostly lead to unsubstituted PAHs, such as picene, benzo(c)phenanthrene, and hexabenzocoronene, and partially fluorinated triphenylenes,¹³⁶⁻¹³⁹ and by Kubota and coworkers on dibenzoanthracene and benzoperylene with perfluorocyclopentene groups.¹⁴⁰ Treatment of precursors having strategically-placed F atoms with activated TiO_2 or Al_2O_3 at 200 °C produced large, but unsubstituted, PAHs and even graphene nanoribbons by loss of HF ¹⁴¹⁻¹⁴⁷ (cyclodehydrofluorination; e.g., trifluoropentaphenylene tribenzopyrene¹⁴⁵). Diels-Alder reactions were employed to prepare extended PAH structures,¹⁴⁸ with one example being a monofluorinated tetraphene.¹⁴⁹ Mono- and difluorophenacenes were prepared via multi-step syntheses involving the Pd(II)-catalyzed Friedel–Crafts-type cyclization of 1,1,2-trifluoro- and 1,1-difluoro-1-alkenes and the In(III)-catalyzed tandem cyclization of bis(1,1-difluoroallene)s.¹⁵⁰ In this chapter, new methods of annulation of PAHs are described, which are *fundamentally* different from the above literature examples, as the new π -system-extending reactions discovered by the author are based on reductive defluorination/aromatization and reductive dehydrofluorination/cyclization reactions of $PDI(BnF)_n$ derivatives to form PDI derivatives with extended π systems.

To better understand the reasons of the presence of products that contribute to the greater relative intensity of aromatic fluorines found in the ^{19}F -NMR spectra of the crude products of PDI

perfluorobenylation reactions (see Chapter 3), it is useful to hypothesize *a priori* the likely side reactions involved so they can be either readily ruled out or confirmed to be the cause. To begin, it can be reasonably assumed that the direct (C–H) perfluorobenylation using perfluorobenzyl iodide with copper promoter proceeds through a similar reaction pathway as the perfluoroalkylation of PAHs with perfluoroalkyl iodides. That is, copper is acting as a reducing agent for R_F-I and/or consumes iodine byproduct generated during the thermally-induced homolytic cleavage of the R_F-I bond, this process is followed by $PAH(R_F)$ product formation. Figure 4.1 depicts two potential pathways for Bn_F-I where copper, as a reducing agent, reacts with Bn_F-I to form $(Bn_F-I)^-$, which will subsequently decompose by ejecting I^- (forming CuI_2 or CuI with oxidized copper) and Bn_F^\bullet radicals capable of substitution. If, instead, Bn_F^\bullet radicals are formed by thermally induced homolytic bond cleavage of the Bn_F-I bond, then copper will react with the iodine byproduct formed in the equilibrium reaction to irreversibly form CuI and favor further Bn_F-I bond cleavage. Either method is possible (i.e., not yet disproven), and each lead to generation of radicals involved in the direct (C–H) perfluoroalkyl (perfluoroaryl)-radical aromatic substitution of PAHs (see general mechanism in Figure 4.1). Due to electrophilic character of perfluoroalkyl radicals, perfluoroalkylation reactions with electron-rich aromatics typically proceed under mild conditions and with high yields.¹⁵¹ This mechanism is different from copper-coupling reactions of PAHs, such as the Ullman coupling, where there is no radical intermediate but it requires an activated carbon to proceed (e.g. a brominated carbon).¹⁵²

With that said, given the postulated mechanisms in Figure 4.1, there are four potential “sources” of aromatic fluorines that must be investigated: they could originate from 1) perfluorobenzyl iodide (Bn_F-I), which, if the perfluorobenzyl group were to react and one or both of the benzylic fluorines were to be removed in the process, would skew the ^{19}F NMR spectrum

towards higher content of the aromatic fluorines; 2) the pentafluorophenyl groups on (Ph_F)₂PDI, which, if the PDI were to react with any reagent (which is not Bn_FI) to form a new PDI derivative, the pentafluorophenyl signals would shift and there would be “new” aromatic fluorine signals, regardless of the derivatization involved; 3) the benzylic fluorines could be removed *in the process* of forming PDI-1-Bn_F, and this would result in derivatives without benzylic fluorines, but with the “new” set of fluorophenyl signals; or 4) the benzylic fluorines could be removed only *after* PDI-1-Bn_F has formed in a one-pot cascade reaction, also resulting in a PDI-1-Bn_F derivative without any benzylic fluorines present.

4.2. Investigation into PDI-perfluorobenylation side-reactions in DMSO

To consider these hypotheses in turn, the author designed and performed several control experiments aimed at testing the stability of each analyte involved in the reaction in question, i.e., the perfluorobenylation of PDI. Table 4.1 shows the conditions of reactions **2w–z** chosen for these tests, which are analogous to the conditions used in rxn. **2b** from Chapter 3 (see Table 3.1), in which the product had an uncharacteristically low amount of benzylic fluorines and excessive amount of aromatic fluorine signals in NMR. In each case, the analytes were dissolved in degassed anhydrous DMSO and heated at 145 °C in the presence of copper metal promoter; times varied depending on the rate of decomposition (or lack thereof) observed for each analyte.

The first analyte to be studied was perfluorobenzyl iodide, which is generally known to be both photo- and thermally unstable, and it degrades unless stored in the dark in a refrigerator. Therefore, it was presumed that when heated to 145 °C in the presence of copper promoter, Bn_FI will generate Bn_F• radicals and it will subsequently convert into final product(s) within a shorter period of time than the time used in reactions **2a** or **2b** in Chapter 3 (24 and 48 h, respectively). Indeed, when heating together Bn_FI and copper in DMSO (exp. **2w** in Table 4.1), an essentially complete

degradation of BnFI was observed after 60 minutes of heating. Figure 4.2 shows the concentration of BnFI over time; determined from aliquots taken every 15 minutes for ^{19}F -NMR analysis (the spectra recorded from 0 to 60 minutes are shown in Figure 4.3). After 60 minutes the fluorine signals due to BnFI nearly vanished, indicating presence of only trace amounts of BnFI, and in its place, several new high-intensity multiplets appeared in the aromatic region of the ^{19}F NMR spectrum. These signals may belong to a single compound, but it was not possible to unambiguously identify its structure at this time. Notably, while there is only a minor shift in the aromatic fluorine signals of this product compared to aromatic signals from the BnFI starting material (top of Figure 4.3), in contrast, there is a drastic change in the chemical shifts of benzylic fluorine signals: after 60 minutes, the benzylic fluorine signals from BnFI are essentially absent, and in their place there are new signals close to -120 ppm, which is outside of the region typically associated with aromatic fluorine signals. It is likely that under reaction conditions **2w**, BnF^\bullet radicals could presumably either self-react to form $[\text{BnF}]_2$ or react with the solvent, DMSO. The third possibility is that copper might react with BnFI, however, the observed ^{19}F -NMR spectrum is unlikely to be that of a BnF-Cu complexes, as these have been documented to be thermally unstable even at dry-ice slush bath temperatures.¹⁵³ Such behavior is different from $\text{R}_\text{F-Cu}$ complexes, which have been isolated at -78 °C and in some cases, even at room temperature, notably when the copper is also stabilized with neocuproine or similar ligands and derivatives thereof.¹⁵² However, by comparing the signals of the BnFI decomposition product (bottom of Figure 4.3) to the ^{19}F NMR spectrum of the crude product mixture from reaction **2a**, it is evident that the compound generated in reaction **2w** was not generated in reaction **2a** or **2b** (at least not in observable quantities). Therefore, heating BnFI in conditions **2w** does not generate the unknown

byproducts responsible for a disproportionate amount of aromatic and benzylic fluorine signals in the ^{19}F -NMR, and thus it can be ruled out as the (sole) source.

The second control experiment involved analyte PDI. It is notable that the side reactions under question were not observed during the perfluorobenylation of PERY performed under similar conditions (see Chapter 3), therefore it is reasonable to assume that the nature of the substrate can be important to consider, for example, chemical reactivity intrinsic to PDI, but absent in PERY substrate. However, when only PDI was heated for 8 hours in the presence of copper (exp. **2x** in Table 4.1), there was no observable reaction by either NMR or MS. Notably, Figure 4.4 shows the mass spectrum of the PDI sample after reaction **2x**, in which only the molecular ion peak of PDI at $722\ m/z$ is observed. Therefore, it can be concluded that the underivatized PDI is perfectly stable under conditions **2x**.

The third possible source could be from a side reaction between PDI and BnF_I , where the benzylic fluorines on the BnF group are displaced in the process of substitution. A detailed analysis of the mass spectrum of the crude PDI-perfluorobenylation product mixture of reaction **2a** provides evidence that the byproducts in question are likely derivatives of BnF substituted PDIs (Figure 4.5). The mass spectrum contains a series of peaks due to molecular ions of $\text{PDI}(\text{BnF})_{1-4}$, while there are also series of peaks with m/z values that are consistently either 39 or 42 lower than the molecular ion peaks of $\text{PDI}(\text{BnF})_{1-4}$. For example, for PDI-1-(BnF)_1 , m/z 938, there are two accompanying ions with m/z 899 and 896. Furthermore, even though the molecular ion peak of $\text{PDI}(\text{BnF})_5$ is not present in the mass spectrum, the peak with m/z lower by 39 with respect to m/z value of $\text{PDI}(\text{BnF})_5$ is present. Repeating regular intervals of $216\ a.u.$ correspond to the added molar mass of a BnF ($217\ a.u.$) replacing hydrogen on PDI. This implies either that these side products are from a “decomposed” BnF group, or that there is a side reaction other than a

substitution reaction which is adding functional groups with 174 and 177 m/z to the PDI (722 *a.u.*) starting material.

One must take into consideration that the observed ions in the mass spectrum may originate from mass-spectrometry-specific effects, i.e., fragmentation accompanying ionization.

For example, fragmentation was observed for the molecular ions of purified PERY-(BnF)_{*n*} compounds during mass spectrometry, albeit in the positive ion mode and only fragmentation via a single fluoride ion (19 m/z) loss was noted. Therefore, the possibility of the unknown signals in the mass spectrum shown in Figure 4.5 being from fragmentation via fluorine loss must also be ruled out. The collision-induced dissociation experiments (also known as MS-MS analysis) were carried out for each molecular ion of PDI-(BnF)_{*n*} to determine their fragmentation patterns, however, the resulting fragmentation spectra did not form product ions via loss of 39 or 42 m/z . Moreover, these fragmentation patterns (recorded at higher collision energy than when recording mass spectra for the product analysis) are not present in the mass spectrum for purified PDI-1-(BnF)₁ (see Figure 4.6), which shows the PDI-1-(BnF)₁^{-•} radical anion as the base peak without any observable fragment ion formation. Therefore, the two series of signals starting as at 896 and 899 m/z represent molecular ions of the distinct homolog compounds and are not ions generated in the mass spectrometer through fragmentation.

Before proceeding to the discussion of the possible chemical nature of these side products, it is useful to be mindful of the possible combinations of groups of atoms that could be lost (and subsequently gained) to result in a decrease of 39 or 42 m/z compared to molecular ions PDI(BnF)₁₋₄. One such possibility that would lower the m/z by 39 is if two fluorides and a hydrogen were to leave a PDI(BnF)₁₋₄ compound, and in the case of PDI(BnF)₁ this would yield a derivative with m/z 899. A possibility to lower molecular mass by 42 *a.u.* would be if three fluorides and a

hydrogen were removed with an oxide being added, and in the case of PDI(BnF)₁ this would yield a derivative with m/z 896, with the general formula PDI(C₆F₄CO). However, without additional characterization this is merely a speculation and only gives information on the difference in molecular constitution and not the regio- or stereochemistry.

The fourth possible source of excess aromatic fluorines that was investigated is a cascade reaction where PDI(BnF)_{*n*} products lose their benzylic fluorines only after they are generated. To test this hypothesis, the stability of a purified sample of PDI-1-BnF analyte was examined. Interestingly, when PDI-1-BnF was heated using conditions **2y** (Table 4.1) for 8 hours, there was a complete decomposition of the analyte, according to ¹H-NMR (Figure 4.7): no signals from PDI-1-BnF were present while a group of new closely positioned signals appeared at around 9 ppm. Moreover, it is noteworthy that the ¹⁹F-NMR spectrum of the sample after heating no longer contained a signal within the benzylic region of the spectrum; other signals were not sufficiently resolved to make structural assignments. The disappearance of benzylic fluorines implies either that the two benzylic fluorines have been removed or are no longer in a chemical environment similar to that of analyte PDI-1-BnF. Interestingly, when the product of reaction **2y** was analyzed by MS—spectrum shown in Figure 4.8—the most intense signal was 896 m/z , which would represent a decrease of 42 m/z from PDI-1-BnF (938 m/z); while the molecular ion for PDI-1-BnF itself was barely above the noise of the baseline in the mass spectrum. The second most intense signal in Figure 4.8 is another unexplained signal at 924 m/z which is 14 m/z lower than the molecular ion.

Finally, it was investigated if the presence of copper is relevant for the observed transformation of PDI-1-BnF, or if it is simply the thermal decomposition of PDI-1-BnF in DMSO (rxn. **2z**, Table 4.1). Figure 4.9 shows the mass spectrum of decomposed PDI-1-BnF after heating for 8 hours in

DMSO at 145 °C (without copper added), under conditions **2z**. Indeed, MS analysis of reaction **2z** shows that copper is not necessary for this transformation to occur, as the dominant peak at m/z 896 was the same as was observed in the analogous experiment with copper present (**2y**). While the signals present in the mass spectrum for reaction **2z** are not identical to the mass spectrum of the product of reaction **2y**, (e.g., there was a noticeable signal at 924 m/z in the case of **2y**, but this signal was not observed in **2z**) the largest peak is the same in either case: 896 m/z . So, one may conclude that the Bn_F group on PDI-1- Bn_F is not stable to heating, at least, when it is dissolved in DMSO and heated at 145° C for 8 hours.

The decomposition products of PDI-1- Bn_F from reaction **2z** were analyzed by HPLC using 1:1 toluene–heptane on a Buckyprep column. This was found to give partial separation between PDI-1- Bn_F and the major compounds formed during decomposition (see Figure 4.10). When the largest fraction (other than PDI-1- Bn_F) was isolated, the mass spectrum confirmed that, indeed, the only signal present is of 896 m/z : thus, confirming both its molecular (and not fragmentation) nature, and this compound is the major product generated by thermal decomposition of PDI-1- Bn_F . Interestingly, when comparing the UV-vis absorption spectra for PDI and PDI-1- Bn_F , shown in Figure 4.11, it is apparent that other than a minor blue shift in the wavelength of maximum absorption, there is little change in the absorption profile when only a single Bn_F group is substituted. However, the UV-vis absorption spectrum of the decomposition product (with m/z 896) shows that a new broad featureless absorption band grows in 250-350 nm range, while maintaining the typical PDI-absorption profile with three bands at 450-550 nm. This suggests that this “decomposition” product has a different, or additional, π -conjugated system; and it may be worthwhile studying in its own right, if it could be isolated in sufficient quantities and characterized. Hypotheses for possible structural assignments of this unknown decomposition

product are discussed in the last section of this chapter. With that said, the main goal of experiments **2w–z** described above was to identify the likely causes(s) of the formation of these PDI side products that do not contain benzylic fluorines; and subsequently to design reactions that avoid said decomposition from occurring; as a consequence, this will lead to generation of sufficient quantities of PDI-(BnF)_n products to allow for study in OPV devices. Therefore, alterations to the perfluorobenylation reaction conditions were investigated in order to avoid PDI-1-BnF decomposing into the compound with a base peak of 896 *m/z* and described in the following sections.

4.3. Effects of reaction variables on product distribution and PDI conversion

4.3.1. Reaction optimization in DMSO: effects of reduced copper and sequential addition of BnFI

One can speculate that, since PDI-1-BnF decomposes when heating in DMSO at 145 °C, the same conditions used to synthesize PDI-1-BnF from PDI and BnFI, a shorter perfluorobenylation reaction time could hinder PDI-BnF degradation, as long as the initial reaction to generate PDI-BnF is significantly faster than the rate of the subsequent reaction consuming and/or decomposing PDI-BnF. A shorter reaction time might then allow for isolation of PDI-(BnF)_n products in greater isolated yield than obtained using rxn. **2a** and **2b**, (see Chapter 3), and favoring mono-substituted product over poly-substituted products. Moreover, after experiment **2w** showed that essentially all BnF–I bonds will be cleaved within an hour under the reaction conditions used, it does not seem beneficial to allow the reaction to proceed significantly longer than this (e.g., 24 hours in this and similar work on perfluorobenylation and perfluoroalkylations of PAHs).

Table 4.2 shows the variations in reaction conditions tested in this study while keeping the solvent (DMSO) and temperature (145 °C) constant. To be able to compare changes in reaction

variables utilizing a shorter reaction time, a control experiment was performed to get a reference data for comparison—reaction **2m** in Table 4.2 —by heating PDI in DMSO at 145 °C for 2 hours with 4 equiv. of BnFI and 8 equiv. of copper (stored on the benchtop). This reaction resulted in PDI-BnF being the major product formed, although the majority of the crude reaction mixture remained unreacted PDI (see top of Figure 4.12 for chromatogram).

To analyze the product distribution and conversion of PDI starting material more efficiently for the reactions shown in in Table 4.2, a more rapid method of analysis was used, instead of the analysis of the NMR spectra of crude products. These product mixtures have multiple overlapping signals in the NMR spectra and it is not straightforward to determine either the starting material conversion or molecular constituents in the product other than PDI-(BnF)_n derivatives. Ideally, one would perform complete product separation, identification of the isolated compounds and determine their yields, but this process is very laborious and not practical for such tests: it includes two stages of separation (silica flash chromatography, then HPLC with Buckyprep column). Therefore, HPLC analysis has been chosen for rapid analysis of product distribution, after it was found that baseline separation of PDI and PDI-1-BnF could be achieved using a mixture of 20/80 IPA–toluene on a Cosmosil Buckyprep-semipreparative column (see chromatogram shown in Figure 4.12): allowing for direct comparison between both the conversion of PDI and the relative yield of PDI-1-BnF compared to all other products generated in each reaction (including bis-PDI-BnF isomers). Other products were coeluting together at t_R around 3 to 5.8 min and attempts to find an eluent to separate them were not successful.

The top of Figure 4.12 shows the chromatogram of the crude product mixture from a reference-reaction **2m**, with low conversion of PDI (peak at 22 min) and (in which the most abundant product present is PDI-1-BnF (6 min).

To improve the conversion compared to **2m**, the effect of sequential addition of the 4 equiv. of BnFI over time instead of simply adding all amount of the reagent at the beginning of the reaction was investigated. Since the relative amount of copper used is kept constant with respect to BnFI , the amount of time required for the formation of perfluorobenzyl radicals from BnFI and Cu should be relatively constant regardless of the concentration of BnFI . Therefore, each addition of BnFI requires the same “reaction time” (2 hours) before another portion is added. Therefore, to test sequential addition of BnFI , reaction **2n** (Table 4.2) started with 1 equiv. of BnFI and then 1 equiv. of BnFI was added every 2 hours for the same total equiv. of BnFI as reaction **2m** (4 molar equiv. of BnFI), for a total reaction time of 8 hours. The bottom of Figure 4.12 shows the chromatogram of reaction **2n**'s crude product mixture, which has significantly greater conversion of PDI compared to **2m**, which was run without sequential addition of BnFI . This result appears to suggest that without sequential addition of the BnFI reagent, its prolong heating was causing either dimerization of BnF radicals or side reactions of BnFI with the solvent, these processes were indeed hindering the preferred reaction of perfluorobenylation of PDI from taking place. At the same time, it was demonstrated that maintaining a low concentration of BnFI with respect to PDI during the synthesis provides an efficient way to favor PDI substitution. However, it should be noted that while PDI-1- BnF is the major product in rxn **2n**, the relative amounts of minor PDI derivative products eluting at short retention times from 3 to 5.8 min and labeled as fraction **a** in Figure 4.12, also increased (see more discussion on these products below)

Another hypothesis for improving conversion was put forward: to investigate the quality of copper metal used. Up to this point, each PDI-perfluorobenylation reaction had utilized copper metal powder, which was stored on the benchtop. In this state, the copper metal surface is presumably coated in a layer of copper oxides and carbonates. While it has been observed that

copper ions play important role in many organic synthesis and catalytic cycles (especially, CuI), the working hypothesis for the radical-based direct perfluoroalkylation requires non-oxidized copper metal. Therefore, using copper metal coated in oxide is, at best, lowering the actual equivalents of copper available for the reaction—and it is very problematic for adding stoichiometric amounts—and, at worst, could be a source for oxide which could react in unknown ways. It should be noted that the high-yielding perfluoroalkylation of PDIs and PAHs by Li et. al.¹⁵⁴ was performed with unspecified commercially bought copper powder and used as is, without any treatment.

To remove surface oxides and carbonates from the copper metal, the same benchtop copper used for prior reactions was treated (reduced) by heating at elevated temperatures under a reducing atmosphere (2% H₂). When this was done, water vapor came off the copper surface and could be collected by dry-ice trap to monitor the progress. Once water ceased to be collected, it was assumed that no more surface oxides remained on the copper. The newly reduced copper (Cu_{H2}) was then kept in an air- and moisture-free glovebox to avoid oxidation.

When this treated copper was used (rxn. **2o** in Table 4.2), a significant improvement in the conversion and product distribution compared to reaction **2m** with untreated copper (Cu). was observed: the middle of Figure 4.12 depicts the chromatograms for reactions **2o** and **2m**. —using this reduced copper (Cu_{H2})— Interestingly, using (Cu_{H2}) results in a similar product distribution as when BnF₄I was added sequentially (rxn. **2n**), although the conversion of PDI was still higher for reaction **2n** (based on HPLC peak area). Notably, the compositions of the HPLC fraction-**a** in both reactions **2n** and **2m** were similar: they contained a mixture of PDI(BnF)_n and by-products with enhanced content of aromatic functional groups. This was confirmed when fraction **a** was analyzed by ¹⁹F NMR (spectrum shown in Figure 4.13): a disproportionate amount of fluorine

signals in the aromatic region (generally defined as ca. -135 – -170 here) per benzylic $F(CF_2)$ fluorine signal was found.

From these results one can infer that using treated copper *and* adding BnF in smaller sequential additions should give the highest conversion of PDI. However, this is hypothesized to concomitantly increase the relative amount of fraction-**a** containing undesirable by-products, instead of simply increasing the yield of PDI-1- BnF . Therefore, in order to improve the selectivity for PDI- BnF derivatives, further alterations to the reaction conditions must be found, which would suppress the side-product formation.

One approach is to alter the solvent used in the reaction: this can (ideally) result in increased rate of reaction for the desired product and a decrease in the rate for side reactions. On the other hand, alterations to the solvent can hinder the desired reaction and, even worse still, result in more side products. While DMSO is frequently used for perfluoroalkylation reactions, and commonly used for nucleophilic aromatic substitution reactions in general (radical and non-radical based), that does not make it the sole option for such reactions. There are many solvents available to use for the perfluorobenylation, which are considered stable for radical based reactions, have sufficiently high boiling points, and dissolve PAHs in high concentrations at elevated temperatures.

4.3.2. Testing alternative solvents: reaction results and PDI-1- BnF stability

Examples of available solvents other than DMSO include similarly water-miscible polar aprotic solvents such as NMP, DMF, DMAc... etc.; as well as hydrophobic and comparatively non-polar electron-deficient aromatic solvents. For example, chlorinated aromatics such as chlorobenzene (PhCl) and *ortho*-dichlorobenzene (*o*-DCB), which have dielectric constants of 5.62 and 9.93, respectively (Table 4.3), or the more polar—but still hydrophobic—cyanated

aromatic solvents such as benzonitrile (PhCN) which has a dielectric constant of 25.9 (in the middle-range of those mentioned above). In contrast, NMP and DMSO are water-miscible with high dielectric constants of 32.2 and 46.7, respectively. In total, five solvents were investigated in this work (including DMSO, a complete list in Table 4.3) for their effects on the product distribution and/or stability of PDI-1-Bn_F while heating in the presence of reduced copper metal.

When NMP was used as a solvent in place of DMSO (rxn. **2h**) with all other conditions analogous to reaction **2n**—namely, 145 C with 4 equiv. of Bn_FI and 8 equiv. of Cu(H₂), heated for 2 hours—most of the crude product mixture remained unreacted PDI starting material. Figure 4.14 shows the ¹H-NMR spectrum of the aromatic region where the largest signals (ca. 75% by area) are from the PDI's two doublets centered at approximately 8.8 ppm. Moreover, the ¹⁹F-NMR in Figure 4.15 shows that there is still unreacted Bn_FI, in addition to PDI; suggesting that Bn_FI is less reactive—at least slower to generate thermally activated Bn_F radicals—in NMP compared to DMSO. Interestingly, as it follows from the analysis of the mass spectrum of the crude product of rxn **2h** shown in Figure 4.16, there is evidence for PDI-(Bn_F)_n products as well as formation of the side products observed in DMSO reactions, and even some molecular ions, which were not observed previously (such as 882 m/z). Therefore, to achieve the goal of hindering side reactions and favoring PDI-(Bn_F)_n products, NMP does not appear to be any better than DMSO.

Since polar aprotic solvents DMSO and NMP readily allow for side reactions to occur, the least polar solvent available, chlorobenzene (PhCl), was tested to determine if these side-reactions are not dependent of solvent. Before testing PhCl as a solvent in a perfluorobenzylation reaction, the stability of PDI-1-Bn_F in PhCl was investigated by heating it at 145 °C for 8 hours (the maximum length of the reactions tested in Table 4.2) in the presence of Cu(H₂) powder. After heating, there was no observable decomposition of PDI-1-Bn_F by ¹H NMR; in comparison, there

was complete decomposition under the same conditions with DMSO (rxn. **2y** in Table 4.1). Consequently, replacing DMSO with PhCl in a perfluorobenylation reaction was investigated to test if this would avoid decomposition while also forming the desired PDI(Bn_F)_n products. Curiously, the perfluorobenylation reaction of PDI in PhCl (**2i**) using analogous conditions as **2n** resulted in only trace amounts of any PDI-1-Bn_F forming—with no detectable conversion of PDI in either the ¹H- or ¹⁹F-NMR spectra, even when extending the total time to 8 hours. Indeed, it is only when analyzing the crude product mixture by HPLC or MS after 8 hours of heating that there is any indication of a reaction occurring. The chromatogram of a concentrated aliquot of the crude product mixture is shown in Figure 4.17 with only a trace amount of PDI-1-Bn_F product detectable while the unreacted PDI is oversaturating the detector and represents over 99% of total chromatogram area. Interestingly, when the product mixture was analyzed by MS there is evidence for substitution products *and* addition products being present (see mass spectrum in Figure 4.18); while there is no indication of the decomposition products previously observed (896 and 899 *m/z*). Moreover, even though the products are only produced in trace amounts, their molecular ion peaks are more intense in the mass spectrum than the PDI starting material: suggesting that MS can be used to verify the trace presence products in these reactions but not for estimating the relative amounts. One can speculate that the low polarity of PhCl is not favorable for radical formation (and subsequent aromatic substitution), such that the conditions used are not sufficient to generate substituted products. If this is indeed the case, then increasing the dielectric constant of the solvent would improve the conversion.

Compared to PhCl, *o*-dichlorobenzene (*o*-DCB) is more polar and with a relatively higher dielectric constant but is still significantly less polar than NMP or DMSO. As was observed for PhCl, when PDI-1-Bn_F was heated in *o*-DCB at 145 °C, there was no observable decomposition

by ^1H NMR after 8 hours. However, the perfluorobenylation reaction of PDI in *o*-DCB (**2j**) using analogous conditions as **2n** resulted in negligible conversion of PDI. HPLC analysis of the crude product mixture shows small amounts of PDI-1-Bn_F as the major product generated (see chromatogram in Figure 4.19), but this is only visible when the aliquot is so concentrated that the PDI starting material saturates the UV-vis detector. Interestingly, the chromatogram shows that PDI-1-Bn_F is the largest peak of the products generated, but there is a peak at ca. $t=7.5$ min that has not been observed in other product mixtures up to this point. In fact, when the crude product mixture was analyzed by MS, the spectrum showed the presence of PDI-Bn_F products as well as addition products PDI(Bn_F)_nH_n (Figure 4.20) similar to when PhCl was used as a solvent, but these are only observable for bis-adducts and higher additions. This implies that there is “broken” aromaticity within the perylene core of the PDI for some bis and higher adducts generated. If the general mechanism for substitution proceeds through a pathway similar to Figure 4.1, where after a perfluorobenzyl radical adds to the aromatic core—forming an sp³ hybridized carbon intermediate—a second perfluorobenzyl radical abstracts the sp³ hybridized carbon’s hydrogen to rearomatize the perylene core, then there appears to be a competing pathway where instead a perfluorobenzyl radical *adds* and results in two sp³ hybridized carbons in the product. These Bn_F additions are presumably on the more reactive *bay*-positions, but this cannot be determined from MS data alone and would require additional information.

Finally, benzonitrile (PhCN) was tested as a solvent replacement in the perfluorobenylation of PDI; with a dielectric constant of 25.9, PhCN is roughly halfway between the polarity of the chlorinated aromatic solvents tested and DMSO. When condition **2c** was used with PhCN instead of DMSO, an aliquot was taken after 2 hours for analysis before the reaction was worked up (rxn **2i**). Interestingly, the ^{19}F -NMR spectrum of the 2-hour aliquot given in the top of Figure 4.21

shows triplets indicative of formation of *bay*-substituted compounds as well as triplets ca. -14 ppm from the *bay* position, which one can speculate are from Bn_F substitutions in another (different) chemical environment such as *ortho*-substitution, although the compounds responsible for these triplets were not isolable. Moreover, most of the crude product mixture remained unreacted Bn_FI . To test if the yield of $\text{PDI}-(\text{Bn}_F)_n$ products could be increased by continuing the reaction to allow for complete conversion of Bn_FI the 2-hour crude reaction mixture was heated at 145 °C for an additional 22 hours (for 24 hours total) before a second aliquot was taken out for analysis.

The middle of Figure 4.21 shows the ^{19}F -NMR spectrum after 24 hours, where the relative amount of Bn_FI has decreased while the intensity and number of triplets in the benzylic region (and intensity thereof) has increased compared to a 2-hour rxn **2i**. Interestingly, when the 24-hour reaction product was analyzed by MS (see Figure 4.22) there was no evidence of the molecular ion at m/z 896, the most common decomposition product of $\text{PDI}-1-\text{Bn}_F$ observed in DMSO. Moreover, the intensity of signals for $\text{PDI}-(\text{Bn}_F)_n$ (where $n=1$ or 2) are greater than the intensity of signals with lower m/z values that could represent their decomposition products; suggesting that $\text{PDI}-(\text{Bn}_F)_n$ compounds were being generated and not degrading during the reaction (at least rapidly). That being the case, there is still a surprisingly large amount of unreacted Bn_FI for the length of reaction time.

It is important to note that when solvents such as DMSO, and the others tested above, are heated at 145 °C in a reduced pressure reaction tube used here they reflux and/or bump and enable mixing the solution. However, PhCN was not observed bumping or refluxing at any point while heating in a sealed tube at 145 °C; thereby reducing the rate of intermolecular interactions between reagents and slowing the process of forming Bn_F radicals and subsequent $\text{PDI}-(\text{Bn}_F)_n$ products. Conveniently, by increasing the temperature of the oil bath used for heating the reaction tube from

145 to 160 °C, it was possible to achieve a similar refluxing and bumping, and hence, mixing, as observed with DMSO and other solvents.

When the 24-hour reaction mixture was placed back into the hot bath (now at 160 °C instead of 145 °C) and heated for an additional 48 hours, there was a moderate increase in conversion of Bn_FI (see Figure 4.21 bottom spectrum). Moreover, unlike reactions with other solvents, which showed any substantial conversions (e.g., DMSO and NMP), the benzylic F(CF₂) signals have not disappeared over time—even at an elevated temperature of 160 °C. Indeed, from Figure 4.21 it can be seen that the intensity of signals for benzylic F(CF₂) in the *bay* region of PDI only increased with time—and maintained a similar product distribution—whereas when heating in DMSO these same signals disappear due to decomposition, suggesting that PDI-(Bn_F)_n products are relatively stable under reaction conditions with PhCN as the solvent.

After heating for 72 hours total (24 h at 145 °C, then 48 h at 160 °C), the reaction in PhCN was worked up and analyzed by HPLC. Figure 4.23 shows the chromatogram of the crude product mixture, where there is indeed a fair amount of PDI-1-Bn_F, also confirmed by the ¹⁹F-NMR spectrum.

Of the solvents tested in Table 4.3, the (relatively) non-polar aromatic solvents PhCl and *o*-DCB did not cause PDI-1-Bn_F decomposition or any side reaction forming products with the loss of groups of atoms that account for molecular mass decrease by 39 or 42 m/z. However, using these solvents in the perfluorobenylation reactions of PDI resulted in negligible conversion of starting material; and more interestingly, they resulted in the formation of (not only) the expected Bn_F substitution products, but also *addition* products, which had not been observed previously. In contrast, the most polar solvents (of the tested here) NMP and DMSO allowed for decomposition

post-substitution, perhaps by either bond homolysis or annulation after a Bn_F group is substituted. The latter has previously been observed after addition of Bn_F groups to C₆₀ fullerene.⁴

Interestingly, in between these two extremes of solvent polarity, when PhCN was used, not only is there desirable PDI-(Bn_F) product formation and moderate conversion of PDI starting material but there is also an additional product was detected with the molecular ion peak in the MS that equals 1078 *m/z* (76 *m/z* lower than PDI-(Bn_F)₂, the difference formally accounts for the loss of four fluorine atoms), which was observed with both *o*-DCB and NMP, but not DMSO. When performing MS/MS experiments with ions with *m/z* > 1078 that were present in the product mixture, the ion at 1078 *m/z* does not get produced from a fragmentation of any of them. Initially, this compound could not be isolated or identified by HPLC using any conditions, which had already been tested: MS analysis of all fractions that eluted before the PDI starting material via HPLC using 20:80 IPA–toluene on a Cosmosil Buckyprep column never showed the same signal at 1078 *m/z* observed in the crude MS spectrum.

With the goal of generating PDI-(Bn_F)_{*n*} in greater yields (greater relative product abundance), and ultimately aiming at a selective synthesis of fully saturated PDI-(Bn_F)_{*n*}, PhCN appeared most suitable of the solvents readily available and tested in this work, thereby warranting further detailed investigation described in the following section.

4.4. Cascade synthesis of bis(perfluorophenyl)benzo[*g,h,i*]perylene diimide: isolation, characterization, and effects of reducing agent

*4.4.1. Discovery and isolation of bis(perfluorophenyl)benzo[*g,h,i*]perylene diimide derivatives*

Initial perfluorobenzoylation reactions using PhCN as a solvent instead of DMSO showed promising results with respect to product yields and conversion, and suppression of undesirable side reactions that were prevalent in DMSO. Therefore, further optimizations were attempted

targeting PDI-Bn_F products (see Table 4.4 for conditions). Preliminary reactions in PhCN showed that 145 °C was not sufficiently high temperature to achieve good mixing of the reagents in the reaction vessel used (see Experimental for detail) and the reaction rates were too slow, therefore, a higher temperature was applied, 160 °C, at which good mixing of reaction mixture was achieved and complete consumption of Bn_FI occurred within 2 hours. Moreover, sequential addition of 2 equivalents of Bn_FI every 2 hours was implemented in reactions **3a–3d** to improve the conversion of PDI with the same relative amount of Bn_FI (see Figure 4.24 for general reaction scheme).

For example, when PDI was dissolved in PhCN with Bn_FI (2 equiv. initially; 2 more equiv. after 2 hours) and heated at 160 °C for 4 hours total (reaction **3a**) it resulted in greater conversion of PDI and selectivity for PDI-1-Bn_F than in reaction **2n** under the comparable conditions used with DMSO (i.e., 4 equiv. Bn_FI, 2 h, 145 °C). Indeed, the chromatogram for reaction **3a** in Figure 4.25 shows PDI-1-Bn_F as the most abundant compound in the crude product mixture.

The effects of adding an excess of copper (5 times the moles of Bn_FI (rxn **3b**) compared to 2 times as in rxn **3a**) were also investigated. It can be seen from the HPLC chromatograms in Figure 4.25 that adding an excess of copper changes the product distribution compared to having a stoichiometric amount. This is not necessarily surprising, as the heterogeneous reaction with copper metal requires collisions with the relatively sparse amount of copper powder. An excess of copper powder should therefore allow for more frequent collisions between the surface of the copper and any soluble reagents and lead to higher conversion of the starting material. However, comparison of the chromatograms of the products of reactions **3a** and **3b** recorded at 530 nm wavelength detection, which was originally chosen as the wavelength of max absorbance for PDI(Ph_F)₂, provided incomplete and somewhat inconsistent information on the product relative abundances, as if the conversion in reaction **3b** was lower than in reaction **3a**. However, examining HPLC

traces at other wavelengths (with the UV detector on the HPLC system allowing for that) revealed drastic differences in their appearances at lower wavelengths, e.g., 470 nm. This was supposedly due to the presence of the products that do not have absorption at 530 nm but absorb strongly at lower wavelengths. It can be clearly seen in Figure 4.25 where chromatograms recorded at 530 nm (dashed line) are overlaid with chromatograms recorded at 470 nm (solid line).

It is important to note that each of the isolated PDI-(BnF)_{1,2} compounds and even the side products (with m/z (896 + 216*n*), where $n = 0-4$, identified in DMSO reactions, see above) all maintained the general absorption profile characteristic of a perylene motif of three prominent peaks, each increasing in intensity with increasing wavelength; either with the same or close (+/- 3 nm) wavelength of max absorbance of PDI(PhF)₂ at 530 nm (see Figure 4.11 for example). In contrast, these new products in reactions **3a** and **3b** are not observable when analyzing the chromatograms recorded at 530 nm because their wavelength of max absorbance is 50 nm blue shifted to 470 nm and they practically do not absorb at 530 nm (see absorption spectra section below).

Note that the relative absorbance for PDI starting material at 470 nm is ca. one third of the absorbance at 530 nm. While the fractions of PDI and PDI-1-BnF appear to “decrease” in intensity at 470 compared to 530 nm by about as much as would be expected based on the lower relative absorbance at 470 nm, the intensity of the peak of fraction-**a** increases substantially. Also, it appears that relative amounts of the new product(s) in fraction **a** are higher in reaction **3b** than in reaction **3a**, the only difference in the conditions being amounts of copper. From this it can be inferred that copper metal is (or can be) involved in the formation of these new PDI-derivatives, either from the PDI starting material directly or from PDI-BnF as an intermediate.

The role of copper was therefore investigated further. Reaction **3e** was carried out under the conditions identical to **3a–c**, but no copper was added. This resulted in no observable conversion of PDI (or BnFI) for reaction **3e** when the reaction mixture was analyzed by ^{19}F -NMR (see spectrum at the bottom of Figure 4.26); in contrast to when copper was used under the same conditions (rxn. **3c**, top of Figure 4.26). Therefore, it can be inferred that copper is indeed necessary for the reaction to proceed. This naturally brings about the question of whether copper metal is unique in its role in this reaction, or a different reducing agent could replace copper.

A notably inexpensive and easy to use reducing agent is sodium thiosulfate ($\text{Na}_2\text{S}_2\text{O}_3$), which is not as strong reducing agent as Cu^0 but it is known to readily consume I_2 byproduct; for example, it has been routinely used in the work up procedures to remove I_2 from perfluoroalkylated PAH crude products. Reaction **3d** was performed using the same number of molar equivalents of $\text{Na}_2\text{S}_2\text{O}_3$ as was used in reaction **3c** with copper powder. According to the MS and NMR analysis of the product of reaction **3d** (see Figure 4.26 and Figure 4.27), there is evidence for direct perfluorobenylation in reaction **3d** as well as the generation of the new product with m/z 1078. Thus, copper is not unique in its role as a reducing agent to form perfluorobenzyl radicals and yield PDI products and it can be replaced by other, even weaker reducing agents. Interestingly, not all BnFI was consumed in reaction **3d**, in contrast to reaction **3c**.

Finally, an effort was undertaken to identify new abundant products formed in reactions **3b**, **3c** and **3d** when excess of reducing agents was used. As mentioned above, three facts were established from the preliminary analysis of NMR, MS and HPLC data of crude products. (1) The new products have substantially different absorption spectra, and likely modified π -system compared to perylene core. (2) They have short retention times when using Buckyprep column, and hence do not interact with pyrene-based stationary phase as strongly as PDI and PDI-BnF

derivatives, under applied conditions. (3) One of the most prominent new products has molecular mass of 1078 a.u., which is consistent with the loss of *four* fluorine atoms from PDI-(Bn_F)₂. Figure 4.28 shows the HPLC traces of the crude product from reaction **3d** recorded at 470 nm and using two eluents: 1:9 and 2:8 IPA/toluene mixtures, respectively. The latter trace (shown on the inset of Figure 4.28) shows a better resolution of fraction **a**, which allowed for isolation and characterization of the most abundant compound in the mixture eluting at 3.8 min. Its complete characterization (see NMR and X-ray sections below), including MS, NMR and X-ray single crystal data definitively established that a new product in question was a unique bis(perfluorophenyl)*benzo*[*g,h,i*]perylene diimide (Ph_F)₂PDI-1,12-benzo(PhF)₂ (BPDI-7-Bn_F) that was generated *via* a cascade reaction involving chemical-reductant initiated direct perfluorobenylation—reductive benzylic defluorination/bay-bay annulation—and π -extension (APEX reaction).¹⁵⁵ Figure 4.24 shows the general reaction scheme for the one-pot cascade synthesis of BPDI and several other new isolated (Ph_F)₂PDI-1,12-benzo(PhF)₂ derivatives (as well as perfluorobenzylated PDI products) shown in the lower part of Figure 4.24. Interestingly, while BPDI-7-Bn_F compound has a small retention time of 3.8 min, its parent compound, BPDI eluted only after 60 min with the same eluent mixture, indicating a strong affinity of benzoperylene core (that is not sterically hindered by bulky Bn_F group across the bay) to pyrene-based stationary phase of the column, possibly via donor-acceptor interactions between electron poor BPDI and electron-rich pyrene. Besides BPDI and BPDI-Bn_F compounds, (Figure 4.66–Figure 4.68 and Figure 4.75–Figure 4.77, respectively) a bis-BPDI compound was isolated, and its structure was elucidated by NMR spectroscopy. (See Figure 4.70–Figure 4.72).

4.5. Na₂S₂O₃ promoted cascade perfluorobenylation and annulation of PDIs to give a chiral *bay-bay* annulated seven membered ring derivative

4.5.1. Synthesis and isolation

When PDI was heated in PhCN at 160 °C in the presence of Na₂S₂O₃ reductant and 4 equiv. of Bn_FI for a total of 4 hours (2 equiv. Bn_FI initially, 2 more equiv. after 2 hours) there was a significant amount of unreacted Bn_FI (reaction **3d**). One can infer from this that two hours is not sufficient time between additions for the Bn_FI reagent to be consumed from the prior addition before more is added. When the reaction time was increased from 2 to 3 hours between additions, there was no observable unreacted Bn_FI in the ¹⁹F-NMR. However, unreacted PDI still made up a non-negligible amount of the crude product mixture, even while higher substitution products were being generated. Therefore, it became apparent that further optimization targeting a high yield of a mono substituted PDI-Bn_F product might not be feasible with Na₂S₂O₃ under the conditions described. On the other hand, saturation of the PDI could be achievable given that sufficient equivalents of Bn_FI are added to the reaction. Surprisingly, when this was done in reaction **4a** by simply doubling the total reaction time and equivalents of Bn_FI with respect to PDI, higher substituted PDI-(Bn_F)_{n>1} products did not become dominant. Rather, analysis of the products revealed another type of the product that was not previously generated. This new PDI product, (Ph_F)₂PDI-1,12-*cyclo*-CH₂C₆F₄ (PDI-C7H2) (depicted in Figure 4.29 and Figure 4.30), was isolable using 10% (or 20%) IPA–toluene as the eluent with a Cosmosil Buckyprep column and gave a maximum achieved isolated yield of 24% with 98+% purity (see detailed separation conditions below).

In addition to isolating PDI-C7H2, two bis-isomers of the same PDI derivative were isolated and characterized: (Ph_F)₂PDI-1,12:7,6-(*cyclo*-CH₂C₆F₄)₂ and (Ph_F)₂PDI-1,12:6,7-(*cyclo*-CH₂C₆F₄)₂. These could be isolated by secondary HPLC separation of the earlier eluting fractions shown in Figure 4.32. Compound (Ph_F)₂PDI-1,12:7,6-(*cyclo*-CH₂C₆F₄)₂ is chiral. The enantiomers

of $(\text{Ph}_F)_2\text{PDI-1,12:7,6-(cyclo-CH}_2\text{C}_6\text{F}_4)_2$ are related by inversion of both 7-membered-rings and are therefore rare examples of a fundamental, newly-recognized type of conformational isomerism, named akamptisomerization by Crossley et al.¹⁵⁶ Our DFT calculations show that the barrier to akamptisomerization of $(\text{Ph}_F)_2\text{PDI-1,12:7,6-(cyclo-CH}_2\text{C}_6\text{F}_4)_2$ is 120–150 kJ mol⁻¹, high enough that the two akamptisomers could be separated by chiral HPLC¹⁵⁷⁻¹⁵⁸ in the future.

Conceptually, the reductive dehydrofluorination/cyclization process proceeds with loss of HF, but the byproducts may be separate F⁻ and H⁺ species (e.g., insoluble NaF and soluble HSO₃⁻). There is precedent for HF loss and cyclization of Bn_F ligands in organometallic Co and Rh complexes.¹⁵⁹⁻¹⁶⁰ There is also precedent for hydrolysis of CF₂Ar_F groups to form C(=O)Ar_F groups in Hughes' Co and Rh complexes.¹⁵⁹⁻¹⁶⁰ If active reducing agent was present during the aqueous workup, the reduction of the C=O moieties to CH₂ groups could have occurred (i.e., CF₂ → C=O → CH₂ instead of CF₂ → CH₂). The mechanism of such remarkable transformations needs to be studied in detail in the future, which will help design new functional materials with extended π-systems.

4.5.2. Isolation of PDI-C7H2 (and BPDI) derivatives

4.5.2.1. Primary HPLC separation: isolation of PDI-C7H2 and BPDI (and PDI).

Figure 4.31 shows a chromatogram of the crude product of reaction 4b used for isolation of new annulated PDIs. The crude product mixture (post work-up) was dissolved in a solution of 1:9 IPA–toluene such that there was no visible precipitate, this was then filtered through a microfiber filter paper. At this stage, if there was any colored material trapped on the filter paper, it was BPDI and it was redissolved and isolated in pure form by rinsing with excess toluene. (Note that BPDI was the least soluble compound observed from reactions 4a,c,d; bisBPDI was only isolated in reactions using copper and was not observed when using Na₂S₂O₃ coupled with sequential

additions of BnFI). The filtered solution was then separated by HPLC using a Cosmosil Buckyprep semipreparative (or preparative) column with 1:9 IPA–toluene eluent at a flow rate of 5 mL·min⁻¹ (or 16 mL·min⁻¹ for preparative column) (see Figure 4.31 for chromatogram). During this primary separation, PDI-C7H2, PDI starting material and BPDI could each be isolated as single fractions collected at retention times (t_R) from 9.6–11.2 min, 26–36 min, and 61–75 min, respectively, without need for further purification. All compounds, which elute out before PDI-C7H2 ($t_R < 9.6$ min), were collected together and referred to as “F1” (fraction 1).

4.5.2.2. Secondary and tertiary HPLC separation: isolation of PDI-*cis*(C7H2)2 (F1F2), PDI-*trans*(C7H2)2 (F1F3) and PDI-C7FH (F1F4) (Figure 4.32).

Explanation of methodology. In order to isolate the compounds in fraction F1 in reasonably high purity, multiple stages of separation are required. However, simply increasing the relative content of IPA in the IPA–toluene eluent has limits due to the decrease in solubility with increasing amount of IPA. Moreover, as the amount of IPA is increased the retention times of the products in F1 are also increased, but each peak broadens considerably (see chromatogram for F1) and causes a significant peak overlap. Using alternative weak solvents available as eluents for the Buckyprep column, such as methanol and acetonitrile, or mixtures thereof and with toluene, were also unsuccessful in achieving baseline separation of any single compound: where some compounds increased in retention times and others decreasing, but in such a way that there was always considerable overlap between peaks. Of the the multiple mixtures investigated (not shown), a 1:1 mixture of IPA–toluene resulted in distinguishable peaks for almost all of the major compounds in F1; even though there is a great deal of overlap still for essentially all compounds. Therefore, if the fractions are collected using this method, they will either each have to be individually re-separated a third or fourth time to get highly pure material, or only the middle-most part of the

peak would be able to get collected at a large loss of yield. However, while there is overlap between each peak and the peaks immediate before and after it, there is minimal overlap between any single peak and the peaks that are 2 away from it; that is, peak 1 and 2 overlap, but peak 1 and 3 do not. Therefore, rather than trying to collect each peak individually and separating them again, requiring 6+ subsequent individual HPLC separations (or more) to achieve highly pure samples, this process can instead be expedited using a separation scheme where during the (secondary) separation of F1, every odd-numbered fraction is collected together, and every even-numbered fraction is added together. Then, using the same eluent as the secondary separation, even-numbered fractions can all be separated during a single (tertiary) HPLC separation and fractions, which are single products, are isolated as highly pure samples (see ^{19}F -NMRs of characterized products); during this process, the “impurities” with respect to the even-numbered separations are the compounds to be isolated in the odd-numbered fractions, and can be directly added to the mixture of odd-numbered fractions. Then, the same process is applied to the odd-numbered fractions using the same eluent as the secondary separation, odd-fractions can all be separated during a single (tertiary) HPLC separation and fractions which are single products are isolated as highly pure samples (see ^{19}F -NMRs of characterized products).

Secondary HPLC separation (Figure 4.32). F1 was dissolved in a solution of 1:1 IPA–toluene taken in sufficient volume such that there is no visible precipitate and filtered through a microfiber filter paper. The filtered F1 was then separated by HPLC using a Cosmosil Buckyprep preparative column with 1:1 IPA–toluene eluent at a flow rate of $16 \text{ mL} \cdot \text{min}^{-1}$. Every odd-numbered fraction other than F1F7, (i.e., F1F1, F1F3, and F1F5) was collected together as F1-odd; every even-numbered fraction (i.e., F1F2, F1F4, and F1F6) was collected together as F1-even; F1F7 was

collected individually at this stage, but there was not sufficient material collected of F1F7 to show sufficient signal-to-noise ratio when analyzed by ^{19}F -NMR.

Tertiary HPLC separation (Figure 4.32). F1-odd and F1-even were each (separately) dissolved in solutions of 1:1 IPA–toluene, then separated by HPLC using a Cosmosil Buckyrep preparative column with 1:1 IPA–toluene eluent. This resulted in pure fractions of PDI-*cis*(C7H2)2 (F1F2), PDI-*trans*(C7H2)2 (F1F3) and PDI-C7FH (F1F4); the majority of fraction F1F5 was constituted of PDI-1-Bn_F, with one or two minor unknown products also being present; F1F6 was a mixture of two products, which could be isolated with additional HPLC. Fraction F1F1 was a mixture and did not have a discernable major product when analyzed by ^{19}F -NMR. Examples of the ^{19}F -NMR spectra for the major fractions collected after tertiary separation are stacked in Figure 4.33 and Figure 4.34.

4.5.2.3. Quaternary HPLC separation: isolation of PDI-1-Bn_F, BPDI-C7H2, PDI-C7H2-5-Bn_F.

Fractions F1F5 and F1F6 could each be further purified by HPLC with the Buckyrep column using a different eluent, 3:1 MeCN–toluene (see chromatogram in Figure 4.35). After being dissolved in 3:1 MeCN–toluene, F1F5 was separated further to give pure PDI-1-Bn_F, while the other major product in the fraction could not be determined.

F1F6 has only two compounds present which appear to be comparable in abundance based on the ^{19}F -NMR of the fraction before separation. Notably, the two products in F1F6 have different absorbance maxima, 470 nm and 530 nm. When F1F6 is separated using 3:1 MeCN–toluene, the two compounds (see Figure 4.36), F1F6F1 and F1F6F2, were determined to be BPDI-C7H2 (where both *bay* regions of the PDI are annulated, but one *bay* has a π -extended (bis-perfluoro)benzo, and the other *bay* region has a *cyclo*-C7H2 group) and PDI-C7H2-5-Bn_F, respectively.

4.6. Structural Characterization of PDI derivatives from this work.

4.6.1. X-ray Crystallography

Preliminary Comments. For clarity, the PDI and derivatives thereof prepared in this work, namely *N,N'*-bis(perfluorophenyl)perylene diimide, will be referred to as (Ph_F)₂PDI for the rest of this section. The literature structure of *N,N'*-bis(*n*-perfluorobutyl)perylene diimide ((*n*-Bu_F)₂PDI) is shown in Figure 4.37.¹³⁵ It shows the locant numbering that will be used in this chapter. It also shows that a PDI compound with perfluoroalkyl groups (or other sterically-innocent groups) on the N atoms and no other substituents has a planar PDI core with considerable intermolecular π - π overlap.

The literature structure of 1,7-difluoro-*N,N'*-bis(perfluorophenyl)perylene diimide ((Ph_F)₂PDI-1,7-F₂) is shown in Figure 4.38.¹⁶¹ It shows that a compound with a (Ph)₂PDI core and two sterically-innocent substituents also has a planar core. However, the presence of the *N*-perfluorophenyl groups prevents any significant (i.e., < 4 Å) intermolecular π - π overlap of the PDI cores of neighboring molecules in the lattice (not shown).

Seven compounds prepared with (Ph)₂PDI as the starting material have been structurally characterized in this work. They are listed in Table 4.8 and shown in Figure 4.39. They will be discussed in detail below. Two of them are present in co-crystals with either pyrene (PYRN) or perylene (PERY), and these structures are preliminary in that crystallographic information files (CIFs) have not been deposited in the Cambridge Structural Database. Nevertheless, they are of sufficient quality to unambiguously confirm the structure of the PDI derivatives identified by NMR spectroscopy. The co-crystallizations were necessary because single crystals of these two pure PDI compounds suitable for X-ray diffraction could not be obtained. Co-crystallization with an

unsubstituted PAH has proven to be a good method to obtain X-ray quality crystals of compounds that otherwise were difficult to crystallize.¹⁶¹

The seven (Ph)₂PDI derivatives shown in Figure 4.39 are based on the addition of one or two perfluorobenzyl groups (CF₂C₆F₅, abbreviated Bn_F) to C1, C6, C7, C8, or C12 of the (Ph_F)₂PDI core, in five cases followed by additional transformations of one or both of the Bn_F groups involving, inter alia, the loss of F atoms and the formation of new C(sp²)-C(sp²) bonds.

Data Collection and Structure Refinement. Synchrotron X-ray diffraction data were collected at the Advanced Photon Source at Argonne National Laboratory on beamline 15ID-D, using a diamond 111 monochromator, an X-ray wavelength of 0.41425 Å, and a Bruker D8 goniometer. Multiscan absorption corrections were applied using SADABS v 2016/2. Unit cell parameters were determined by the least squares fit of the angular coordinates of all reflections. Integrations of all frames were performed using APEX III software, and the structures were solved using SHELXTL/OLEX 2 software. The structure of (Ph_F)₂PDI-1-Bn_F was refined as a perfect two-component twin. Listed in Table 4.9 are crystal Data and Final Refinement Parameters for the five structures for which CIFs were acceptable for publication (i.e., with no CheckCIF A alerts) by the Cambridge Structural Database (CSD). These five CIFs have been deposited with the CSD pending publication of this work. Thermal ellipsoid plots for these five structures are shown in Figure 4.40.

The Structures of (Ph_F)₂PDI-1-Bn_F and (Ph_F)₂PDI-1,7-(Bn_F)₂. Crystals of these two compounds were grown by slow evaporation of saturated DCM-MeCN and MeOH solutions (respectively). These two structures are the simplest of the seven to describe. They resulted for reactions in which Bn_F groups were substituted for the H atom on C1 in (Ph_F)₂PDI-1-Bn_F and for the H atoms on C1 and C7 in (Ph_F)₂PDI-1,7-(Bn_F)₂, as shown in Figure 4.39 and Figure 4.40. The

presence of the Bn_F substituents resulted in significant distortion of the PDI cores from planarity in both compounds, as shown in Figure 4.41.

The packing of molecules in the unit cells in these two structures are shown in Figure 4.42. In both structures there is no significant intermolecular π - π overlap of aromatic portions of the molecules (i.e., the PDI cores and C₆F₅ groups).

The Donor/Acceptor Co-crystal Structure of PYRN/(Ph_F)₂PDI-1,12-cyclo-CH₂C₆F₄. The PDI compound that co-crystallized with PYRN from a DCM–EtOH solution has a seven-membered ring presumably formed in situ from (Ph_F)₂PDI-1-Bn_F. It is not known whether (i) the elimination of HF and concomitant formation of the new C(sp²)–C(sp²) bond between C12 and an *ortho* C atom of the Bn_F group or (ii) the transformation of the CF₂ group into a CH₂ group occurs first.

Several drawings of this structure are shown in Figure 4.43 and Figure 4.44. Figure 4.43 shows a portion of the unit cell. The PYRN and PDI molecules are stacked alternately along the crystallographic *a* axis. The perpendicular distance between the least-squares planes of the two PYRN molecules shown in the figure is 6.9 Å (the *a* axis length is 7.711(4) Å). The nonplanar PDI aromatic core and the nonplanar conformation of the seven-membered ring that includes PDI atoms C1 and C12 are readily apparent. Figure 4.44 shows the significant π - π overlap between neighboring PYRN and (Ph_F)₂PDI-1,12-cyclo-CH₂C₆F₄ molecules. More than half of the PYRN π system overlaps with the PDI aromatic core in one nearest neighbor in the stack, and the other half of the PYRN π system overlaps equally with its other PDI nearest neighbor (not shown). The perpendicular out-of-plane displacements (OOPDs) of the PDI C(sp²) atoms from the least-squares plane of the PYRN π system range from 3.35 to 3.63 Å (the average displacement of these eight

PDI C(sp²) atoms is 3.43 Å). The shortest of these distances equals the interplanar π - π separation in graphite.¹⁶²

The (Ph_F)₂PDI-1,12-*cyclo*-CH₂C₆F₄ molecule is asymmetric. Both enantiomers are present in the $P\bar{1}$ unit cell. The enantiomers are shown side-by-side in Figure 4.45. The seven-membered ring adopts a boat configuration, as shown in Figure 4.46. The enantiomers are related by inverting the seven-membered ring. Ring-inversion isomers such as these are referred to as akamptisomers, enantiomers that do not require breaking and reforming covalent single bonds for racemization to occur.¹⁶³ The CH₂ hydrogen atoms in (Ph_F)₂PDI-1,12-*cyclo*-CH₂C₆F₄ are inequivalent and give rise to an *AB* quartet in the ¹H NMR spectrum (see Figure 4.78). If the ring inversion had been rapid on the NMR timescale, a singlet for the CH₂ group would have been observed instead.

A literature compound with a seven-membered ring containing a CH₂ group, an N-Et group, and five C(sp²) atoms is also shown in Figure 4.46.¹⁶⁴ This asymmetric compound also adopts a boat configuration. Variable temperature ¹H NMR spectroscopy revealed that equilibration of the enantiomers by ring inversion had a barrier (i.e., a transition state energy) of 90.4 kJ mol⁻¹. The compound with C=O and N-H instead of C=S and N-Et had a ring inversion barrier of 45.6 kJ mol⁻¹.¹⁶⁴ Other seven-membered-ring compounds with multiple C(sp²) atoms in the ring have been found to have ring-inversion barriers of 48–67 kJ mol⁻¹.¹⁶⁵

The ring inversion of (Ph_F)₂PDI-1,12-*cyclo*-CH₂C₆F₄ was studied by DFT collaborator Dr. Alexey A. Popov of the IFW Dresden, Germany. The ground-state structure was optimized starting with the X-ray structure coordinates of the co-crystal with PYRN. The transition-state structure and its energy relative to the ground state was then determined. The results are shown in Figure 4.47. The DFT-predicted transition-state energy is 105 kJ mol⁻¹, significantly higher than the experimentally-determined 90.4 kJ mol⁻¹ barrier to inversion discussed above for a compound

with a less rigid structure than $(\text{Ph}_F)_2\text{PDI-1,12-cyclo-CH}_2\text{C}_6\text{F}_4$. The predicted high barrier to racemization suggests that it might be possible to separate the enantiomers of $(\text{Ph}_F)_2\text{PDI-1,12-cyclo-CH}_2\text{C}_6\text{F}_4$, potentially using HPLC chromatography columns with chiral stationary phases,¹⁶⁶⁻¹⁶⁷ including those that have been shown to resolve structural isomers of PAHs.¹⁶⁸⁻¹⁶⁹

The Donor/Acceptor Co-crystal Structure of PERY/ $(\text{Ph}_F)_2\text{PDI-8-Bn}_F\text{-1,12-cyclo-CH}_2\text{C}_6\text{F}_4$. The PDI compound that co-crystallized with PERY from a MeCN–MeOH solution also has a seven-membered ring presumably formed in situ from $(\text{Ph}_F)_2\text{PDI-1,8-Bn}_F$ (also identified by NMR spectroscopy. Interestingly, although the Bn_F group on C1 underwent annulation and concomitant $\text{CF}_2 \rightarrow \text{CH}_2$ transformation, the Bn_F group on C8 did not undergo either reaction.

A portion of the unit cell in this structure is shown in Figure 4.48. The PERY and PDI molecules are stacked alternately along the crystallographic a axis. The perpendicular distance between the least-squares planes of the PERY molecules is 7.10 Å (the a axis length is 7.930(4) Å). As in the other donor/acceptor co-crystal structure discussed above, the nonplanar PDI aromatic core and the nonplanar conformation of the seven-membered ring that includes PDI atoms C1 and C12 are readily apparent. The seven membered ring adopts a boat conformation (not shown).

Figure 4.49 displays parallel projection drawings of the PERY donors on either side of the $(\text{Ph}_F)_2\text{PDI-8-Bn}_F\text{-1,12-cyclo-CH}_2\text{C}_6\text{F}_4$ acceptor. The least-squares planes of the PERY $\text{C}(\text{sp}^2)$ atoms are both in the plane of the page (i.e., their least-squares planes are rigorously parallel). The regions of overlap of the aromatic π systems of the pairs of molecules are different. The perpendicular OOPDs of the PDI C atoms underneath the plane of the PERY π system in the top drawing range from 3.42 to 3.56 Å and average 3.47 Å. In the bottom drawing the OOPDs range from 3.42 to 3.69 Å and average 3.58 Å.

The Structures of (Ph_F)₂PDI-1,12:6,7-(*cyclo*-CH₂C₆F₄)₂ ("*cis*") and (Ph_F)₂PDI-1,12:7,6-(*cyclo*-CH₂C₆F₄)₂ ("*trans*"). Crystals of these compounds were grown by evaporation of saturated solutions of DCM–MeCN and DCM–MeOH, respectively. They are presumably formed in situ from (Ph_F)₂PDI-1,6-(Bn_F)₂ (identified by NMR spectroscopy) and (Ph_F)₂PDI-1,7-(Bn_F)₂ (X-ray structure discussed above), respectively. The 1,12:6,7 compound is referred to as "*cis*" because the CH₂ moieties are attached to C atoms the same side of the PDI (i.e., the left naphthalene (NAPH) fragment of the PDI in Figure 4.39 and Figure 4.40), while the 1,12:7,6 "*trans*" compound has its CH₂ moieties on opposite sides of the PDI (i.e., one on the left and one of the right NAPH fragments of the PDI). The seven-membered rings are, as in (Ph_F)₂PDI-1,12-*cyclo*-CH₂C₆F₄ and (Ph_F)₂PDI-8-Bn_F-1,12-*cyclo*-CH₂C₆F₄, nonplanar and adopt boat conformations, as shown in Figure 4.50.

The PDI cores in these two compounds are distinctly nonplanar as shown in Figure 4.51 and Figure 4.52. The NAPH fragments are twisted relative to one another by 26.4° in the *cis* compound and by 27.7° in the *trans* compound). Both compounds are dissymmetric, each with a single idealized (not crystallographic) C₂ axis. Therefore, the CH₂ groups are symmetry related, but the H atoms on each CH₂ group have different ¹H NMR chemical shifts. The fact that there is an *AB* quartet for the CH₂ groups in each compound, and not a time-averaged singlet, demonstrates that the seven-membered rings are not rapidly undergoing ring inversions.

Figure 4.52 also shows that the CH₂ groups in the seven-membered rings in the *cis* isomer lie on opposite sides of the mean plane of the PDI aromatic core (i.e., not including the C₆F₅ groups at either end of the molecule). In contrast, the CH₂ groups in the *trans* isomer lie on the same side of the mean PDI plane. Thus, the X-ray structures exhibit what can be called CH₂-up-CH₂-down (or simply *up,down*) orientations in the *cis* isomer and CH₂-up-CH₂-up (*up,up*) orientations in the

trans isomer. To see if the *up,down* structure of the *cis* isomer and the *up,up* structure of the *trans* isomer are the result of crystal packing forces (i.e., intermolecular interactions) or the result of intrinsic, intramolecular steric interactions, the relative energies of DFT-optimized *up,up* and *up,down* structures for the *cis* compound and for the *trans* compound were determined.

The results for the *cis* isomer are shown in Figure 4.53. The hypothetical *cis_up,up* structure is less stable by 26.7 kJ mol⁻¹ than the observed *cis_up,down* structure. Even if seven-membered ring inversion could occur slowly, the equilibrium concentration of the *cis_up,down* structure would be 200,000 times greater than the *cis_up,up* structure. The lower stability of the *cis_up,up* structure is because it forces the PDI core to be much flatter than in the observed *cis_up,down* structure (note that the four red O atoms for the *cis_up,up* in Figure 4.53 are nearly co-planar). The twist angle of the NAPH fragments in the high-energy DFT *cis_up,up* structure is only 3.8°, whereas the twist angle in the observed DFT *cis_up,down* structure is 27.7° (cf. 26.4° in the X-ray structure). In point of fact, to say that the NAPH/NAPH twist angle of the *cis-up,up* isomer is 3.8° is misleading. Each NAPH fragment is individually bent into a shallow bowl, one bent up and one bent down, as shown in Figure 4.54. So the two NAPH fragments are not really "twisted" relative to one another, but the result is that the PDI core is relatively flat in the high-energy structure.

The DFT results for the *trans* isomer tell the same story. The NAPH fragments in the DFT *trans-up,up* isomer are twisted by 27.9° (cf. 28.0° in the X-ray structure). In contrast, the PDI core in the high-energy DFT *trans-up,down* structure is relatively flat, and the NAPH fragments are bent in opposite directions in a similar way as in the *cis-up,up* isomer shown in Figure 4.54.

The structure of benzo[ghi](Ph_F)₂PDI-1,12-(Ph_F)₂. Crystals of this compound were grown by evaporation of a [[solvent]] solution. It results from a different type of annulation of the putative compound (Ph_F)₂PDI-1,12-(Bn_F)₂. In this case the two presumed Bn_F groups would have been on

the same side of the PDI core (i.e., across the bay from one another), so the same type of seven-membered ring formation seen in the previous two compounds would not have been possible. Presumably, the two sterically-crowded CF₂ groups lost all four F atoms and, by forming a new C(sp²)–C(sp²) bond, resulted in the formation of a new aromatic ring, producing the benzo[*ghi*]-PDI derivative (Ph_F)₂PDI-1,12-benzo(Ph_F)₂ shown in Figure 4.55 (a thermal ellipsoid plot of the molecule was shown in Figure 4.40).

The benzo-PDI core is relatively flat. The average OOPDs of the 26 C(sp²) core atoms is ±0.07 Å (the range of OOPDs is from 0.18 to –0.16 Å; the OOPDs for the two benzo C(sp²) atoms connected with the highlighted green line are 0.01 and 0.04 Å). The two NAPH fragments in (Ph_F)₂PDI-1,12-benzo(Ph_F)₂ are twisted by only 5.9°. The two Ph_F groups on the N atoms are rotated by 69° and 72° relative to the least-squares plane of the benzo-PDI aromatic core, and the two Ph_F groups on the benzo substituent are rotated by 67° and 74° from the benzo-PDI core.

Even though there are four Ph_F groups on the molecule, here is no π–π overlap in the X-ray structure. Figure 4.56 shows (i) the packing of four molecules in the unit cell and (ii) the central portion of the unit cell contents with the same orientation).

4.7. Mechanistic insight and DFT calculation for bis(perfluorophenyl)benzo[*g,h,i*]perylene diimide formation

When hypothesizing about the possible pathways to formation of BPDI and its derivatives, it is clear that it results from a reductive annulation/π-extension of the putative compound (Ph_F)₂PDI-1,12-(Bn_F)₂ (see Figure 4.57). In the case of BPDI, the two Bn_F groups would have been on the same side of the PDI core (i.e., across the bay from one another), Presumably, the two sterically-crowded CF₂ groups lost all four F atoms and, by forming a new C(sp²)–C(sp²) bond, resulted in the formation of a new aromatic ring, producing the benzo[*ghi*]-PDI derivative (Ph_F)₂PDI-1,12-

benzo(Ph_F)₂ shown in Figure 4.57. Similarly, formation of BPDI-Bn_F and bis-BPDI would proceed in similar manner, for these compounds both bay regions of PDI molecules are involved, as shown in the lower part of Figure 4.57.

In an effort to understand the formation of (Ph_F)₂PDI-1,12-benzo(Ph_F)₂, the DFT-optimized structure of the putative precursor, (Ph_F)₂PDI-1,12-(Bn_F)₂, was determined to see how crowded the CF₂ moieties would be. It is shown in Figure 4.58. The hypothetical intermediate is significantly distorted as a result of the crowding between the perfluorobenzyl groups. The F...F distance shown in Figure 4.58 is 2.59 Å, which is shorter than twice the van der Waals radius of an F atom, 2.70–2.94 Å.¹⁷⁰ As a result, the NAPH fragments of the PDI core are twisted with respect to one another, and, more importantly, each one is significantly warped from planarity.

4.8. Electrochemical properties and absorption spectra of fluoromodified PAHs

4.8.1. Redox properties of PERY(Bn_F)_n in solution, comparison to PERY(CF₃)_n

Cyclic voltammetry was used to determine the redox properties of each isolated compound by measuring the $E_{1/2}^{0/-}$ reduction potential. Prior work with various classes of PAH(R_F)_n compounds provided ample evidence that they exhibit reversible redox behavior in solution, and thus cyclic voltammetry is a viable technique for evaluation of their electronic properties. In this study, for the purpose of direct comparison, the same solvent and electrolyte system were chosen as used for PERY(CF₃)_n derivatives. PERY-1-1 showed an irreversible first- and quasi-reversible second-electron reduction

(Figure 4.60). Derivatives with two and three Bn_F groups per PERY showed increasingly irreversible behavior, in striking contrast to electrochemically reversible PERY(CF₃)_n compounds regardless of the number of substitutions.¹¹⁸ Therefore, the half peak potential ($E_{p/2}^{0/-}$) was

measured instead so as to compare the electronic properties within the family of PERY(BnF)_n compounds.

Figure 4.59 shows the graphs of $E_{p/2}^{0/-}$ as a function of $n(\text{BnF})$ (left) and $E_{1/2}^{0/-}$ as a function of $n(\text{CF}_3)$ (right). Very similar linear trends were found for both families of PERY derivatives, with the slopes of ca. 0.23 V/BnF and 0.20 V/CF₃ from their best fit lines.¹¹⁸

Interestingly, this unusual electrochemical behavior sheds some light on the fact that attempts to use negative ion mode of electrospray mass spectrometry for characterization of PERY(BnF)_n compounds proved unsuccessful. No molecular ions or typical fragment ions were observed in the negative mode, suggesting radical anion instability under ESI conditions. The molecular ion for each PERY(BnF)_n could only be observed when using positive-ion mode, and notably a considerable fragmentation due to loss of fluoride was observed, with the signal intensity higher than that of the molecular ion peak. Such behavior precluded measurements of the gas-phase electron affinity (EA) via low-temperature photoelectron spectroscopy technique, since it utilizes generation of the molecular negative-ion beams in the electrospray ion source.

The nature of such electrochemical instability is unclear at this point and further investigations are currently under way in our laboratories. We hypothesize that it is specific to the perfluorobenzyl groups attached to PAH core, which undergo (yet to be determined) chemical transformations under reducing conditions. In line with these observations, CORA(BnF)_n exhibited similar irreversible electrochemical behavior, in contrast to the trifluoromethylated analogs, which were electrochemically reversible in the solution phase and stable enough to measure their EAs in the gas phase.¹⁷¹

4.8.2. Redox properties of PDI(PhF)₂ and its derivatives in the gas and solution phase.

One of the motivations for this work on the synthesis of PDI(Bn_F)_n compounds was to determine electron withdrawing effect of Bn_F groups on PDIs. A very limited data is available on electrochemical properties of PAH(Bn_F)_n; in fact, the corannulene derivative with five Bn_F groups, CORA(Bn_F)₅ was shown to have irreversible redox behavior in solution, as were most of the PERY(Bn_F)_n compounds synthesized and studied by the author (see above). Interestingly, DFT calculations performed for the series of CORA(Bn_F)_n, *n* = 1–5, revealed that the gas-phase *E*A_s of CORA((Bn_F)_n are 0.06–0.10 eV higher than *E*A_s of CORA((CF₃)_n, when compounds with the same *n* are compared. The DFT-calculated *E*_{1/2}^{0/-} values had the opposite trend, i.e., CORA((CF₃)_n were shown to be stronger acceptors in solution than corresponding CORA((Bn_F)_n compounds, this was due to differences in their respective solvation energies in the neutral state.

Indirect evidence of the irreversible redox behavior of CORA(Bn_F)_n and PERY(Bn_F)_n could be already deduced from their behavior under electrospray mass spectrometry conditions: molecular anions were not stable in both cases and fragmented with the loss of fluorine. In contrast, in the ESI mass spectra of the purified PDI(Bn_F)_n compounds, molecular ions were the only ionic species, and no fragment ions were observed.

Table 4.7 lists experimentally determined *E*_{1/2}^{0/-} from cyclic voltammetry, and gas-phase *E*A_s measured using low-temperature photoelectron spectroscopy (LT-PES) of negative ions, which were generated in the ESI ion source with TDAE as a reducing agent. Figure 4.61 shows cyclic voltammograms for PDI(Bn_F)_n, where *n* = 0,1,2. All compounds exhibit two reversible reductions, and the *E*_{1/2}^{0/-} values of PDI(Bn_F)_n and PDI(Bn_F)_n are 130 and 250 mV, respectively, cathodically shifted relative to parent PDI, confirming that Bn_F group has a strong electron withdrawing effect, and it increases as more Bn_F groups are added to PDI. Attempt to measure *E*A of PDI(Bn_F)_n was not successful: molecular anions generated using TDAE in acetonitrile solution were not stable

and quickly fragmented. At the same time, EA of the parent $PDI(Ph_F)_2$ was measured to be 3.01 eV, which is significantly higher than the estimated $EA = 2.88$ eV for $PDI(Bu)_2$, thereby confirming that Ph_F substituents in the imide positions contribute to the acceptor properties of PDIs.

Electronic properties of BPDI in DCM solution were studied by cyclic voltammetry (see Figure 4.62) and it exhibited reversible redox behavior, however, its $E_{1/2}^{0/-}$ was 40 mV more negative than the $E_{1/2}^{0/-}$ of the parent $PDI(Ph_F)_2$. i.e., it is a slightly weaker acceptor in solution, despite the presence of two electron deficient Ph_F groups on the BPDI core. In contrast, in the gas phase, BPDI has a 100 meV higher EA than $PDI(Ph_F)_2$. Presumably, differences in solvation energies of these two compounds could be responsible for such deviation in $E_{1/2}^{0/-}$ trend.

In the case of other annulated PDI derivatives, $PDI-C7H2$, $PDI-cis(C7H2)_2$ and $PDI-trans(C7H2)_2$, (see Figure 4.63 and Table 4.7), they all show two reversible waves in the cyclic voltammograms, and cathodic shifts relative to the parent $PDI(Ph_F)_2$, by 20, 50 and 60 mV, respectively. Similarly, in the gas phase, their EAs are higher than that of $PDI(Ph_F)_2$, and even BPDI.

These new data on the electronic properties in the gas phase and in solution for the new PDIs prepared in this work characterize them as very strong electron acceptors, with reversible electrochemical behavior and thus they can be considered as viable candidates for the studies in the optoelectronic devices as n -type organic semiconductors in OFETs, or low-LUMO acceptor materials in the donor-acceptor photoactive layers in the OPVs.

4.8.3. Absorption spectra of PDI and its derivatives

The absorption spectra of underivatized PDI, measured during HPLC using 1:9 IPA–toluene, is shown in the top left of Figure 4.64 and exhibits three intense peaks of increasing absorbance with increasing wavelength ($\lambda_{max} = 530$ nm). When Bn_F groups are substituted onto PDI, the first

Bn_F results in a 5 nm blue shift to the absorption profile, $\lambda_{\text{max}} = 525$ nm for PDI-1-Bn_F (top right of Figure 4.64). When two Bn_F groups are substituted, see middle two spectra in Figure 4.64, there is a more significant blue shift: $\lambda_{\text{max}} = 507$ nm for PDI-1,6-(Bn_F)₂, $\lambda_{\text{max}} = 508$ nm for PDI-1,7-(Bn_F)₂. Furthermore, having two Bn_F groups somewhat increases the relative absorbance at lower values (ca. 300 nm) compared to the three absorbance peaks of the parent PDI structure.

In contrast to the more subtle changes in the absorption profile during Bn_F substitutions just mentioned, the conversion of PDI into BPDI is an extension to the π -system of the perylene-core. This results in BPDI being blue shifted by ca. 60 nm, $\lambda_{\text{max}} = 473$ nm; and a new intense, and broad, absorption band being present from ca. 270 to 350 nm (spectrum in bottom left of Figure 4.64). Interestingly, this new absorption band at lower wavelengths grows in relative intensity with Bn_F substitution: such is the case for BPDI-7-Bn_F (bottom right of Figure 4.64), $\lambda_{\text{max}} = 470$ nm, which exhibits the strongest absorption below 350 nm of any derivatives prepared in this work.

Figure 4.65 shows the UV-Vis absorption spectra of isolated PDI-C7H₂ derivatives. When analyzing the spectrum of PDI-C7H₂, $\lambda_{\text{max}} = 524$ nm, the spectrum is only blue shifted slightly; comparable to a Bn_F substitutions on PDI, rather than the significant shift observed for BPDI. However, there is a new broad signal from ca. 270 to 350 nm observed for all PDI-C7H₂ derivatives, though less intense than BPDI. This lower-wavelength absorption is intensified going from a PDI-C7H₂ to either PDI-*cis*(C7H₂)₂, $\lambda_{\text{max}} = 512$ nm, or PDI-*trans*(C7H₂)₂, $\lambda_{\text{max}} = 520$ nm. Interestingly, comparing the spectra in middle of Figure 4.65 show that is negligible change in the absorption profile when there is a Bn_F groups added onto the *ortho*-positions, $\lambda_{\text{max}} = 524$ nm for PDI-C7-Bn_F.

4.9. Conclusions

This chapter describes the serendipitous discovery of new type of fluoroannulations of PAHs that led to the preparation and characterization of the new families of PDI-based molecules with extended pi-systems. In the course of optimization of perfluorobenylation of PDI, the author paid attention to an unexpected change in the ^{19}F NMR spectra of the products of certain reactions, and appearance of new molecular species in their mass spectra. Eliminating proposed hypotheses one by one by performing a range of control experiments, it was determined that reductive defluorination/aromatization was responsible for the formation of new benzoPDIs and PDIs bearing a seven-membered ring(s) across the bays. Studies of the electronic properties of these compounds demonstrate reversible redox behavior in solution and significantly improved acceptor properties, which in combination with the favorable solid-state packing motifs, make them potentially valuable candidates as non-fullerene acceptors.

This discovery opens a wide avenue for molecular designs of unprecedented large PAH molecules with both planar, 2-dimensional aromatic cores, and 3-dimensional warped structures, which are in great demand for the modern organic optoelectronic applications extending beyond organic photovoltaics. The fact that the new reactions can be applied to the electron-deficient PAH substrates, extends the scope of the substrates even further. Future studies on the mechanistic aspects of these reactions are needed to improve the selectivity and yields.

4.10. Experimental section

4.10.1. Materials and Methods.

Reagents and Solvents. The following reagents and solvents were used as received unless otherwise indicated: heptafluorobenzyl iodide ($\text{C}_6\text{F}_5\text{CF}_2\text{I}$, abbr. $\text{Bn}_\text{F}\text{I}$; SynQuest Laboratories, 90%), chloroform-*d* (abbr. CDCl_3 ; Cambridge Isotope Laboratories, 99.8%), hexafluorobenzene (abbr. C_6F_6 ; Sigma-Aldrich, >99.5% NMR grade), copper powder (Strem Chemical, 99%), sodium

thiosulfate ($\text{Na}_2\text{S}_2\text{O}_3$; Fisher Chemical, anhydrous, >98%), dimethyl sulfoxide (abbr. DMSO; Fisher Chemical, ACS grade), 1-methyl-2-pyrrolidone (abbr. NMP; Sigma-Aldrich, ACS grade), chlorobenzene (abbr. PhCl; Sigma-Aldrich, HPLC grade), *ortho*-dichlorobenzene (abbr. *o*-DCB; Sigma-Aldrich, HPLC grade), benzonitrile (abbr. PhCN; Sigma-Aldrich, ACS grade), acetonitrile (abbr. MeCN; Sigma-Aldrich, HPLC grade), toluene (Sigma-Aldrich, ACS grade), dichloromethane (abbr. DCM; Sigma-Aldrich, ACS grade), methanol (abbr. MeOH; Sigma-Aldrich, ACS grade), ferrocene (abbr. $\text{Fe}(\text{Cp})_2$, Acros Organics, 98%), tetrabutylammonium perchlorate ($\text{N}(n\text{-Bu})_4\text{ClO}_4$, TBAClO₄, Eastman Kodak, 98%) diethyl ether anhydrous (EMD Millipore, ACS grade), dimethyl ethoxide (abbr. DME; EMD, ACS grade), sodium chloride (Fisher Chemical, ACS grade), and magnesium sulfate (Aldrich Chemical, anhydrous, technical grade). Distilled-deionized water (abbr. dd-H₂O) with a minimum resistance of 18 M Ω -cm was prepared using a Barnstead NANOpure ultrapure water system. Solvents used for reactions and cyclic voltammetry—namely, DMSO, NMP, PhCl, *o*-DCB, PhCN, DCM, and DME—were dried over activated 3 Å molecular sieves for 24 h and cannula transferred into a flame-dried Schlenk tube under a N₂ (g) purge for storage.

HPLC Analysis. High Performance Liquid Chromatography (HPLC) was conducted using a Shimadzu liquid chromatography instrument (CBM-20A control module, SPD-20A UV-Vis detector, LC-6AD pump, manual injector valve). The HPLC columns utilized were COSMOSIL Buckyprep 10 mm I.D. x 250 mm semi-prep and 20 mm I.D. x 250 mm prep columns (Nacalai Tesque, Inc.) at a flow rate of 5 mL min⁻¹ and 16 mL min⁻¹, respectively.

NMR Analysis. All ¹H and ¹⁹F NMR spectra were of CDCl₃ solutions recorded at room temperature with a Varian (Agilent) 400MR NMR spectrometer equipped with Automated Tuning. ¹H and ¹⁹F NMR spectra were acquired at 400 MHz and 376.1 MHz, respectively, using a 1 second

relaxation time, and a 45 ° pulse angle. ^1H chemical shifts are reported relative to $\delta(\text{CHCl}_3) = 7.26$ ppm. ^{19}F chemical shifts are reported relative to $\delta(\text{C}_6\text{F}_6) = -164.9$ ppm.

Mass Spectrometry. A Thermo-Finnigan LTQ LC/MS-MS linear ion-trap mass spectrometer with an electrospray ionization (ESI) source was utilized to record negative ion ESI (NI-ESI) mass spectra. Acetonitrile was used as the carrier solvent and injected at a flow rate of $50 \mu\text{L min}^{-1}$.

Cyclic voltammetry. Cyclic voltammetry (CV) measurements were carried out in an inert (N_2) atmosphere glove box using a PAR 263 potentiostat/galvanostat and a three-electrode electrochemical cell equipped with a platinum counter and working electrode (0.125 mm diameter) and a silver quasi reference electrode. CV measurements of PERY derivatives were performed in 0.1 M $\text{N}(n\text{-Bu})_4\text{ClO}_4$ in DME; measurements of PDI derivatives were performed in 0.1 M $\text{N}(n\text{-Bu})_4\text{PF}_6$ in DCM.

4.10.2. General procedure for PDI perfluorobenzoylation and stability experiments

A Schlenk tube equipped with a #9 O-ring sidearm was charged with PDI (10 mg, $14 \mu\text{mol}$) and Cu powder (if used, 7.0 mg, $110 \mu\text{mol}$, 8 equiv.) and subsequently dried overnight in a $120 \text{ }^\circ\text{C}$ oven. The reaction tube was taken from the oven and attached to a Schlenk line to cool under dynamic vacuum. Dried solvent (1.0 mL) and BnFI (if applicable) is added via syringe with the reaction tube open and with a positive flow of N_2 . The solution was degassed by the freeze-pump-thaw (FPT) technique three times (x3). The reaction flask was closed under vacuum and allowed to warm to room temperature before placing in a heated oil bath ($145 \pm 5 \text{ }^\circ\text{C}$). Note: the reaction should be refluxing shortly after placing the flask in the oil bath due to the reduced pressure. After heating for the desired amount of time, the reaction was allowed to cool to room temperature.

For NMP and DMSO solvents: the contents were poured into a separatory funnel containing dd- H_2O (30 mL). The mixture was extracted with ethyl acetate ($3 \times 10 \text{ mL}$). The organic layers

were added together, washed with dd-H₂O (3x10) and NaCl brine (10 mL), and dried over MgSO₄. Samples were then analyzed by either NMR, MS and/or HPLC. For water immiscible solvents tested, the crude reaction mixtures were filtered and the solvents removed by attaching to a vacuum line and leaving under reduced pressure overnight. Crude mixtures were then analyzed by either NMR, MS and/or HPLC.

4.10.3. General reaction procedure for BPDI derivatives (3a,b)

A Schlenk tube equipped with a Rodaviss joint and PTFE side-arm and was charged with PDI (10 mg, 14 μ mol) and reduced-Cu powder (Cu_{H2}, 35.0 mg, 550 μ mol, 40 equiv.) and subsequently dried overnight in a 120 °C oven. The Schlenk tube was taken from the oven, attached to a Schlenk line and capped with a Rodaviss stopper, and allowed to cool under dynamic vacuum. BnFI (4.7 μ L, 28 μ mol, 2 equiv.) and dried PhCN (1.0 mL) were added via syringe with the tube open under a flow of N₂. The solution was degassed by using the freeze-pump-thaw (FPT) technique three times (x3). The reaction flask was closed under vacuum and allowed to warm to room temperature before placing in a heated oil bath (160 \pm 1 °C). Note: the reaction should be refluxing shortly after placing the flask in the oil bath due to the reduced pressure in the system. After heating for 2 hours, the flask was cooled to room temperature and opened under a positive pressure of N₂ to add more BnFI (4.7 μ L, 28 μ mol, 2 equiv.) to the reaction, for a total of four equiv. of BnFI added. This was FPTx3 as before and placed back into the heated oil bath (160 \pm 1 °C) for an additional 2 hours. Note that the reaction does not reflux as vigorously the second time it is placed in the oil bath compared to the first. Once the reaction is done (4 hours total), the flask is cooled and toluene (10x reaction volume) is added: the solution is then decanted and filtered using glass microfiber filter paper to remove any reducing agent or their byproducts salts (e.g. Cu and CuI), which are essentially insoluble in toluene at room temperature. PhCN (and toluene) was

removed by successive azeotroping with isopropanol under reduced pressure with a rotovap until the crude material was solvent free. Isolation of products is achieved using HPLC with a Cosmosil Buckyprep semi-preparative or preparative column.

4.10.4. General reaction procedure for PDI-C₇H₂ derivatives (4a,b,d)

A Schlenk tube equipped with a Rodaviss joint and PTFE side-arm and was charged with PDI (96.0 mg, 0.133 mmol) and anhydrous Na₂S₂O₃ (841 mg, 5.32 mmol, 40 equiv.) and subsequently dried overnight in a 120 °C oven. The Schlenk tube was taken from the oven, attached to a Schlenk line and capped with a Rodaviss stopper, and allowed to cool under dynamic vacuum. BnFI (44.6 μL, 0.266 mmol, 2 equiv.) and dried PhCN (10.0 mL) were added via syringe with the tube open under a flow of N₂. The solution was degassed by using the freeze-pump-thaw (FPT) technique three times (x3). The reaction flask was closed under vacuum and allowed to warm to room temperature before placing in a heated oil bath (160 ± 1 °C). Note: the reaction should be refluxing shortly after placing the flask in the oil bath due to the reduced pressure in the system. After heating for 3 hours, the flask was cooled to room temperature and opened under a positive pressure of N₂ to add more BnFI (44.6 μL, 0.266 mmol, 2 equiv.) to the reaction: this was FPTx3 as before and placed back into the heated oil bath (160 ± 1 °C) for an additional 3 hours. This process is repeated 2 more times to give a total of four additions of BnFI for a total of 178.4 mL added (2.128 mmol, 8 equiv.) and a total reaction time of 12 hours (3 hours per addition). Note that the reaction does not reflux as vigorously after the first time it is placed in the oil bath.

Work-up. At the end of a reaction (12 hours total), the crude reaction mixture is allowed to cool and is decanted into a beaker containing toluene (x10 the volume of the reaction solution). The reaction flask is then rinsed at least x3 times with toluene (the flask is rinsed until there is no more colored material being extracted) and the toluene extracts were decanted into the crude

reaction mixture; leaving behind unreacted sodium sulfate and other salt-biproducts. The crude product mixture was then filtered using a glass microfiber filter paper to remove any remaining insoluble organic salts dispersed in the solution. PhCN (and toluene) is removed by successive azeotroping with isopropanol under reduced pressure with a rotovap until the crude material was solvent free. Isolation of products is achieved using HPLC with a Cosmosil Buckyprep semi-preparative or preparative column, discussed below.

4.11. Tables and Figures

Table 4.1. Stability experiments for PDI perfluorobenylation reaction's substrates and products.

Exp. #	Substrate	Cu present (Y/N)	Time (h)	Solvent	Temp. (°C)
2w	Bn _F I	Y	1	DMSO	145
2x	PDI	Y	8	DMSO	145
2y	PDI-Bn _F	Y	8	DMSO	145
2z	PDI-Bn _F	N	8	DMSO	145

Table 4.2. Reaction conditions tested for perfluorobenylation of PDI(Ph_F) in DMSO

Rxn.	Bn _F I per addition (equiv.)	# of Bn _F I additions ^(a)	Time (h)	Solvent	Temp. (°C)	copper used
2a	2	1	24	DMSO	120	benchtop
2m	4	1	2	DMSO	145	benchtop
2n	4	1	2	DMSO	145	H ₂ -treated
2o	1	4 ^a	8	DMSO	145	benchtop

Table 4.3 Reaction conditions tested for perfluorobenylation of PDI(Ph_F).

Exp.	Solvent	Dielectric constant (ε)	Observable PDI-Bn _F decomposition? (Y/N)	Significant PDI conversion (Y/N)	Time (h)
2c^(a)	DMSO	46.7	Y	Y	2
2h	NMP	32.2	Y	Y	2
2i	PhCN	25.9	Y	Y	
3j	<i>o</i> -DCB	9.93	N	N	8
2k	PhCl	5.62	N	N	8

Table 4.4. Reaction conditions tested for perfluorobenylation of PDI(Ph_F) in PhCN resulting in BPDI(Ph_F).

Exp.	Bn _F I eq. (total)	Additions of Bn _F I(a)	Time (h)	Reducing agent used	Reducing agent eq.	Solvent	Temp. (°C)
3a	4	2	4	Cu	8	PhCN	160
3b	4	2	4	Cu	40	PhCN	160
3c	4	2	4	Cu	40	PhCN	160
3d	4	2	4	Na ₂ S ₂ O ₃	40	PhCN	160
3e	4	2	4	none	-	PhCN	160

Table 4.5. Reaction conditions to generate PDI-C₇H₂ derivatives.

Exp.	Starting mass of PDI (mg)	Bn _F I eq. ^(a) (total)	# of Bn _F I additions (2 eq. per addition) ^(b)	Source of agitation	Time (h)	Na ₂ S ₂ O ₃ eq.	Solvent	Temp. (°C)
4a	100	8	4	reflux	12	40	PhCN	160
4b	1000	8	4	stir bar	12	40	PhCN	160
4c	100	8	1	reflux	12	40	PhCN	160
4d	100	8	4	reflux	12	40	PhCN	160

^a Total number of equivalents added is split equally amongst the number of additions.

^b First addition of Bn_FI was added to the reaction before heating; subsequent additions were added after 3 hours.

Table 4.6. Half-peak reduction potentials of PERY derivatives

PERY-(BnF) _n	$E_{p/2}^{0/-}$ (V) (± 0.010 V) ^a	$\Delta E_{p/2}^{0/-}$ (mV)
PERY	-2.14 ^b	-
PERY-1-1	-1.86	+280
PERY-2-1	-1.73	+130
PERY-3-1	-1.46	+270
PERY-3-2	-1.46	+270

^a $E_{p/2}^{0/-}$ potential calculated from cyclic voltammetry (CV) measurements; anaerobic; 0.1 M N(*n*Bu)₄ClO₄ in DME; platinum working and counter electrodes; silver wire quasi-reference electrode; 500 mV·s⁻¹; values are referenced vs. $E_{1/2}^{+/0}$ of ferrocene (Fe(Cp)₂).[

^b Value used for unsubstituted perylene is the $E_{p/2}^{0/-}$ potential (not this work).¹¹⁸.

Table 4.7. Electrochemical properties of PDI derivatives

Substrate	$E_{1/2}^{0/-}$ (V) ^a (± 0.010 V)	$\Delta E_{1/2}^{0/-}$ (mV)	$E_{1/2}^{-/-2}$ (V)	$\Delta E_{1/2}^{-/-2}$ (mV)	EA (eV) (± 0.010 eV)
PDI	-0.87	-	-1.07	-	3.01
PDI-1-BnF	-0.74	+130	-0.97	+100	unstable
PDI-1,7-(BnF) ₂	-0.62	+250	-0.92	+150	unstable
BPDI	-0.91	-40	-1.16	-90	3.110
PDI-C7H2	-0.857	+20	-1.08	-10	3.135
PDI- <i>cis</i> (C7H2) ₂	-0.824	+50	-1.11	-40	3.255
PDI- <i>trans</i> (C7H2) ₂	-0.813	+60	-1.10	-30	3.260

^a $E_{p/2}^{0/-}$ potential calculated from cyclic voltammetry (CV) measurements; anaerobic; 0.1 M N(*n*Bu)₄PF₆ in DCM; platinum working and counter electrodes; silver wire quasi-reference electrode; 100 mV·s⁻¹; referenced vs. $E_{1/2}^{+/0}$ of ferrocene (Fe(Cp)₂).

Table 4.8. The seven compounds characterized by single-crystal X-ray diffraction described in this chapter^a

Compound ^b	Abbreviations in Table 2 and Figure 3
(Ph _F) ₂ PDI-1-Bn _F	1-Bn _F
(Ph _F) ₂ PDI-1,7-(Bn _F) ₂	1,7-(Bn _F) ₂
(Ph _F) ₂ PDI-1,12:7,6-(<i>cyclo</i> -CH ₂ C ₆ F ₄) ₂	<i>trans</i> -(<i>c</i> -CH ₂ C ₆ F ₄) ₂
(Ph _F) ₂ PDI-1,12:6,7-(<i>cyclo</i> -CH ₂ C ₆ F ₄) ₂	<i>cis</i> -(<i>c</i> -CH ₂ C ₆ F ₄) ₂
benzo[<i>ghi</i>](Ph _F) ₂ PDI-1,12-(Ph _F) ₂	benzo(Ph _F) ₂
PYRN/(Ph _F) ₂ PDI-1,12- <i>cyclo</i> -CH ₂ C ₆ F ₄ ^b	<i>c</i> -CH ₂ C ₆ F ₄
PERY/(Ph _F) ₂ PDI-8-Bn _F -1,12- <i>cyclo</i> -CH ₂ C ₆ F ₄ ^b	(Bn _F)(<i>c</i> -CH ₂ C ₆ F ₄)

^a Ph_F = perfluorophenyl; Bn_F = perfluorobenzyl; PYRN = pyrene; PERY = perylene; PDI = 3,4,9,10-perylenetetracarboxylic diimide, abbreviated perylene diimide throughout this chapter; (Ph_F)₂PDI = *N,N'*-bis(perfluorophenyl)PDI.

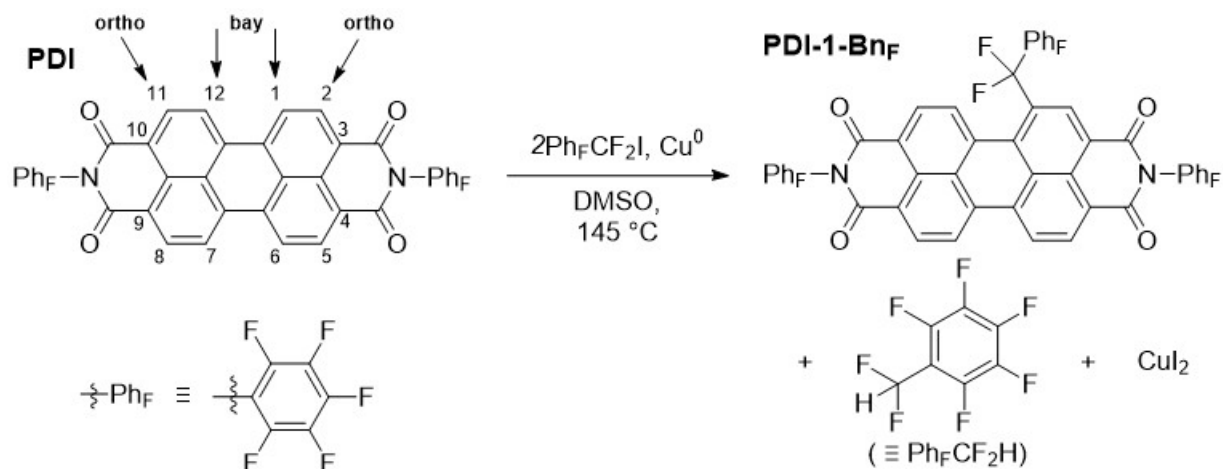
^b Co-crystal with 1/1 stoichiometry

Table 4.9. Crystal data and final refinement parameters for five X-ray diffraction structures deposited with the Cambridge structural database^a

Compound abbreviation ^b	1-BnF	1,7-(BnF) ₂	<i>trans</i> -(<i>c</i> -CH ₂ C ₆ F ₄) ₂	<i>cis</i> -(<i>c</i> -CH ₂ C ₆ F ₄) ₂	benzo(PhF) ₂
empirical formula	C ₄₃ H ₇ F ₁₇ N ₂ O ₄	C ₅₀ H ₆ F ₂₄ N ₂ O ₄	C ₅₀ H ₈ F ₁₈ N ₂ O ₄	C ₅₀ H ₈ F ₁₈ N ₂ O ₄	C ₅₀ H ₆ F ₂₀ N ₂ O ₄
formula weight, g mol ⁻¹	938.51	1154.57	1042.58	1042.58	1078.57
crystal habit	rhombohedron	needle	plate	plate	rhombohedron
crystal color	dark red	red-orange	yellow-orange	yellow-orange	red-orange
crystal size, μm	175 × 124 × 82	372 × 109 × 40	103 × 52 × 26	91 × 45 × 24	60 × 48 × 38
crystal system	triclinic	triclinic	monoclinic	triclinic	monoclinic
space group, <i>Z</i>	<i>P</i> , 4	<i>P</i> , 4	<i>P</i> 2 ₁ / <i>n</i> , 4	<i>P</i> , 4	<i>C</i> 2/ <i>c</i> , 8
<i>a</i> , Å	8.1330(10)	11.6214(16)	20.166(7)	11.0028(14)	31.195(9)
<i>b</i> , Å	15.0581(18)	14.537(2)	10.878(4)	14.2130(18)	12.594(3)
<i>c</i> , Å	15.1685(18)	25.938(3)	21.652(10)	26.687(3)	23.882(6)
<i>α</i> , degree	68.573(2)	75.612(2)	90	85.700(2)	90
<i>β</i> , degree	88.677(2)	83.723(2)	117.369(5)	81.799(2)	104.147(10)
<i>γ</i> , degree	88.307(2)	88.023(3)	90	75.930(2)	90
<i>V</i> , Å ³	1728.4(4)	4219.1(10)	4218(3)	4003.2(9)	-6
<i>T</i> , K	100(2)	100(2)	100(2)	100(2)	100(2)
<i>ρ</i> _{calc} , g cm ⁻³	1.803	1.818	1.642	1.73	1.59
<i>R</i> (<i>F</i>) [<i>I</i> > 2σ(<i>I</i>)]	0.0646	0.0764	0.0795	0.0624	0.0478
<i>wR</i> (<i>F</i> ²) [all data]	0.1992	0.2286	0.2519	0.1849	0.1342
GoF [all data]	1.05	1.018	1.017	1.015	1.05

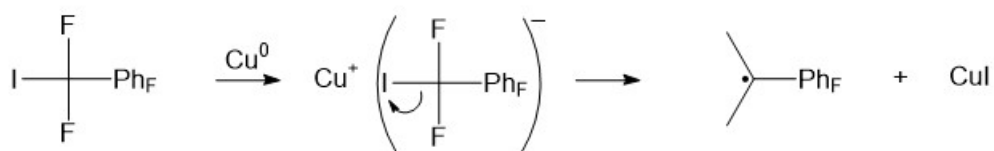
a) All X-ray crystallographic data were collected using synchrotron radiation ($\lambda = 0.41425$ Å) at the Advanced Photon Source.

b) See Table 4.8 for a list of compounds along with the abbreviations used in this table.

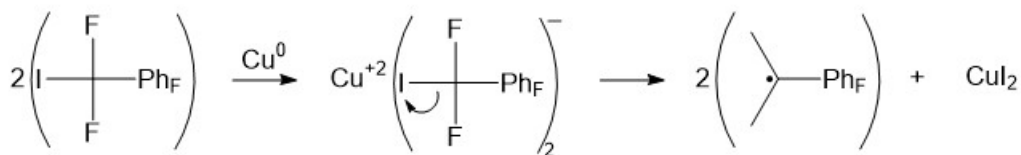


Pathways to generate perfluorobenzyl radicals.

one-electron transfer pathway forming CuI (process repeats twice in balanced equation)



two-electron transfer pathway forming CuI_2



Substitution of of perfluorobenzyl by benzylic-radical addition and hydrogen atom abstraction

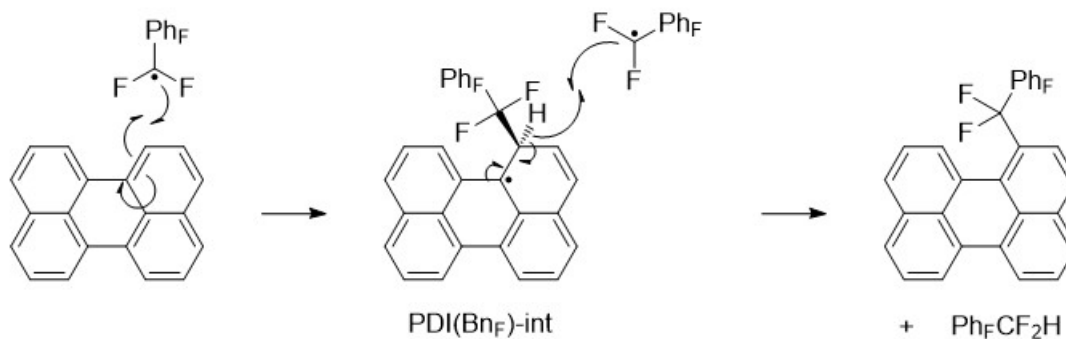


Figure 4.1. Top: Balanced chemical equation for direct perfluorobenylation of PDI. Bottom: Proposed mechanism for the perfluorobenylation of PDI (and PERY); imide groups are removed for clarity.

percent BnFI remaining (%)	time (min)
100.0%	0
49.0%	15
11.9%	30
3.22%	45
0.23%	60

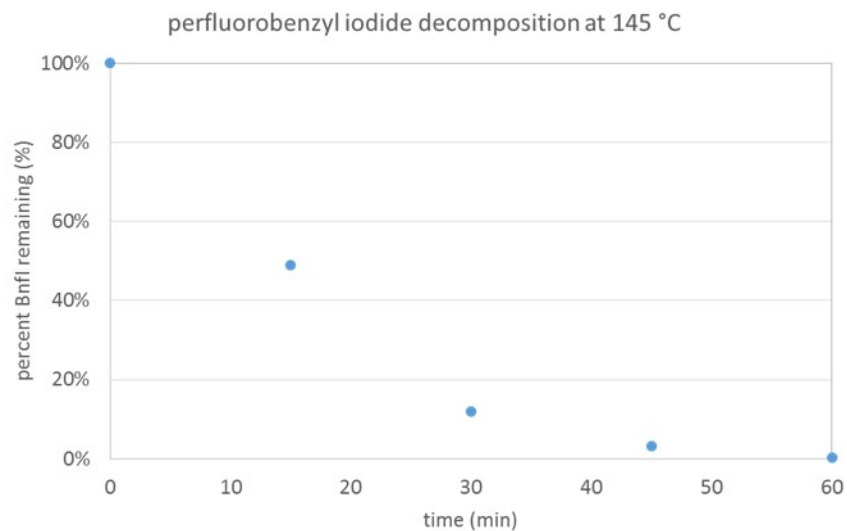


Figure 4.2. Concentration of perfluorobenzyl iodide (BnFI) over time when heated in DMSO and in the presence of copper.

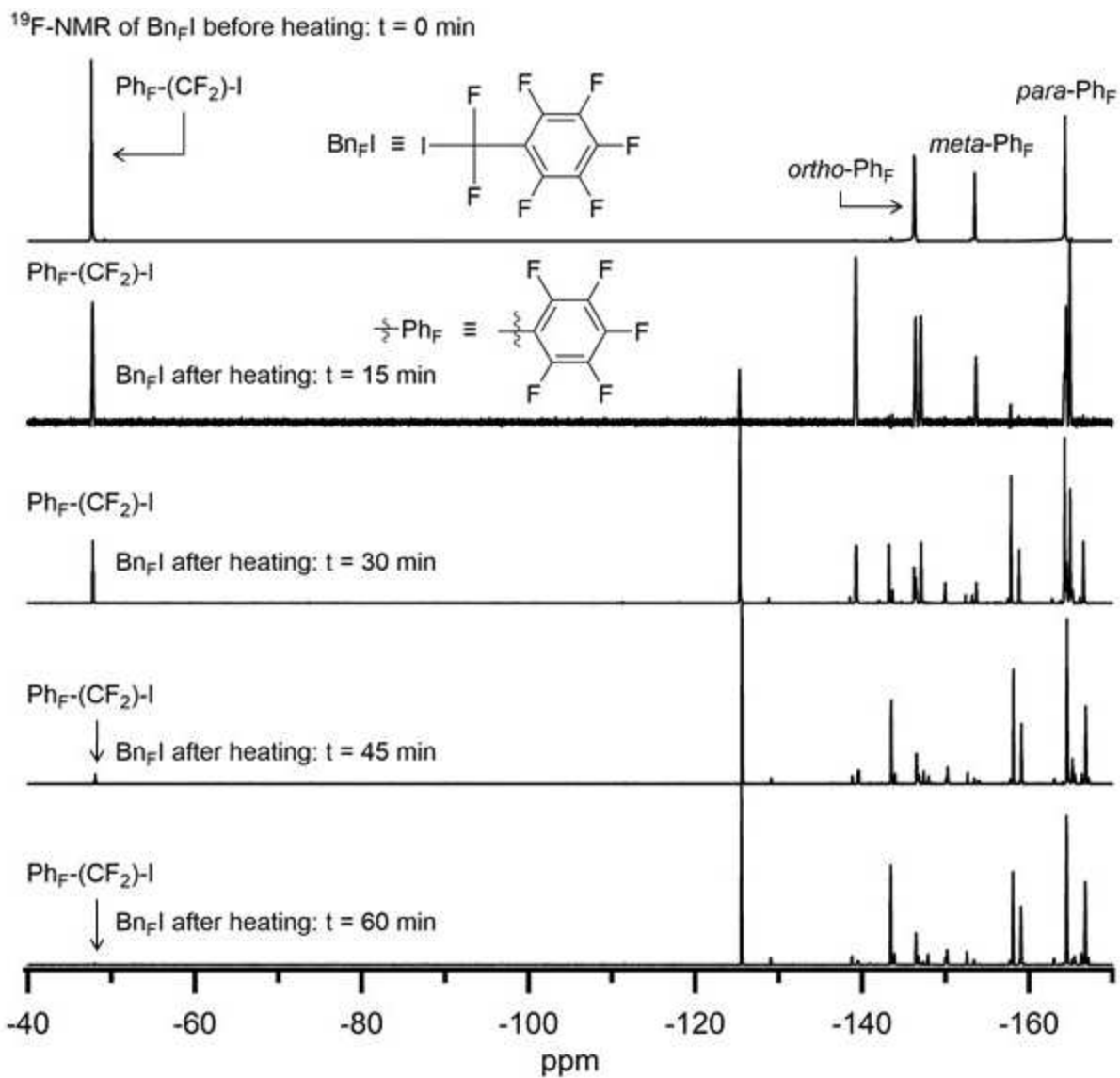


Figure 4.3. ^{19}F -NMR spectrum of perfluorobenzyl iodide ($\text{Bn}_\text{F}\text{I}$) over time when heated in DMSO and in the presence of copper. Taken in CDCl_3 .

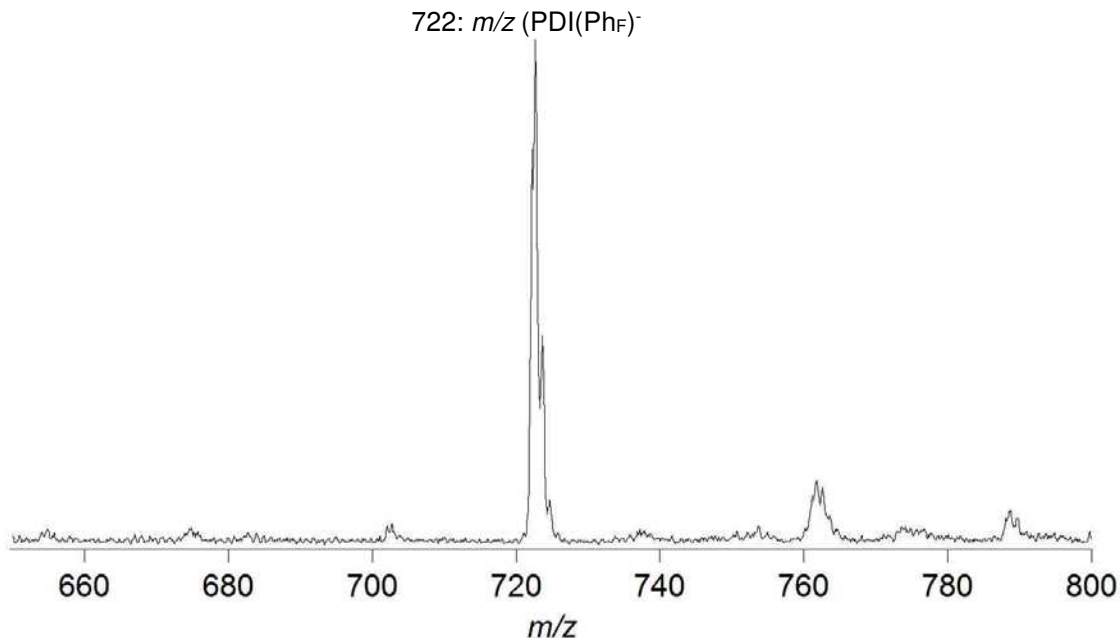


Figure 4.4. Negative-ion ESI mass spectrum of PDI after heating for 8 hours at 145 C in DMSO with copper (rxn 2d conditions without BnF added). Showing no observable decomposition of PDI.

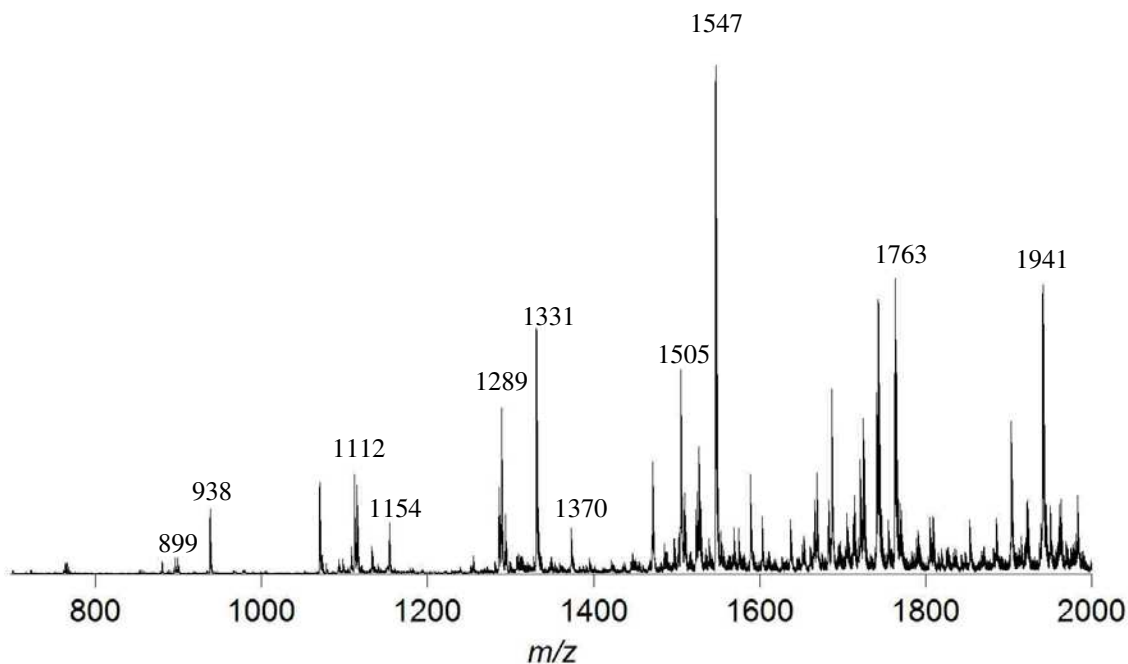


Figure 4.5. Mass spectrum of crude product mixture of reaction **2a**. Note, $m/z = 938, 1154, 1370, 1586$ and 1802 for 1, 2, 3, 4 and 5 substitutions of BnF groups onto PDI(PhF). For each molecular ion peak of a BnF substituted compound, there are peaks associated with either a difference of 39 or 42 m/z less than the molecular ion peak. Taken in negative mode with acetonitrile used as the carrier solvent.

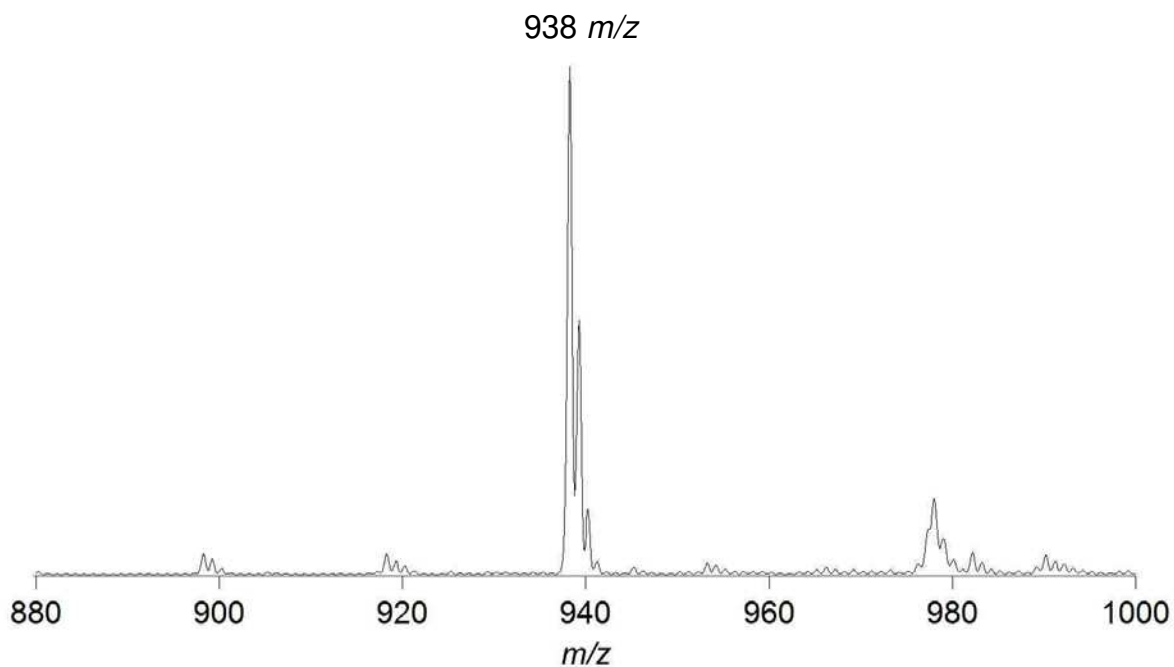


Figure 4.6. Negative-ion ESI mass spectrum of PDI-1-BnF.

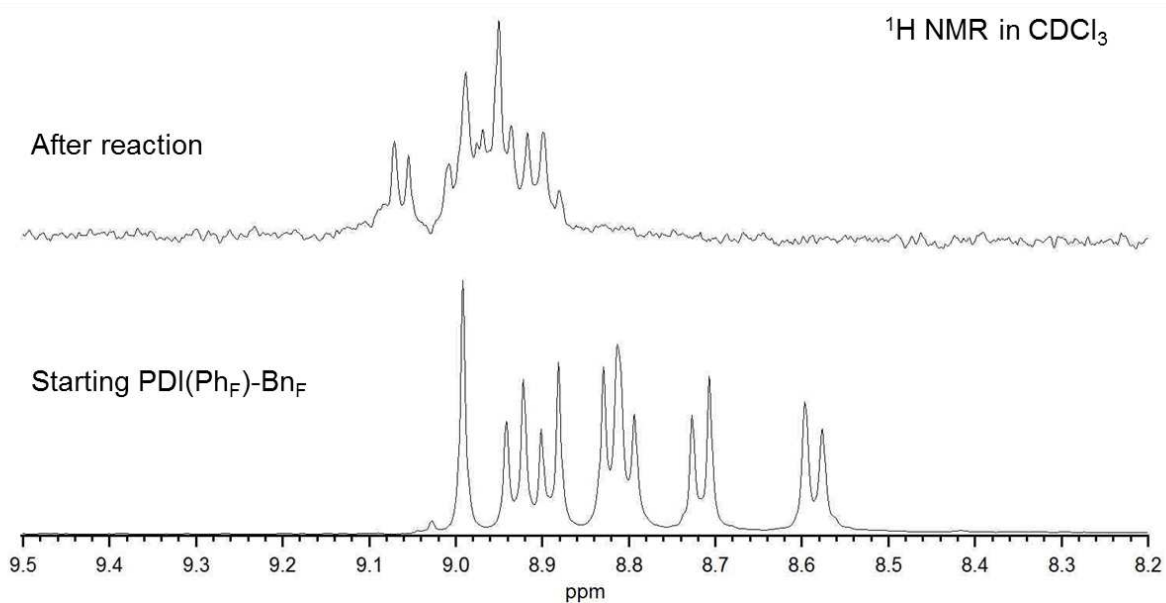


Figure 4.7. Change in ^1H NMR spectra of PDI-1-BnF after decomposition Top: PDI-1-BnF decomposition after heating for 8 hours at 145 °C in DMSO with copper (rxn. **2d** conditions without BnFI added). Bottom: unreacted PDI-1-BnF.

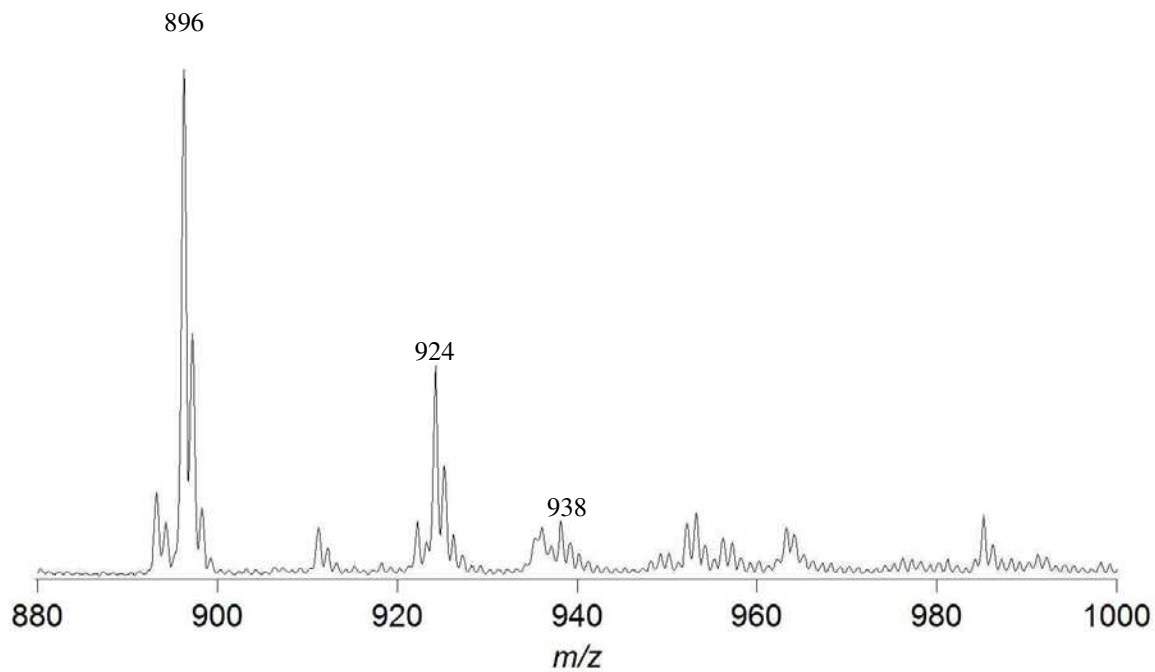


Figure 4.8. Negative-ion ESI mass spectrum of PDI-1-BnF after decomposition with copper by heating 8 hours at 145 °C in DMSO (rxn 2d conditions without BnFI added). Taken from the same sample as the NMR in the bottom part of Figure 4.7.

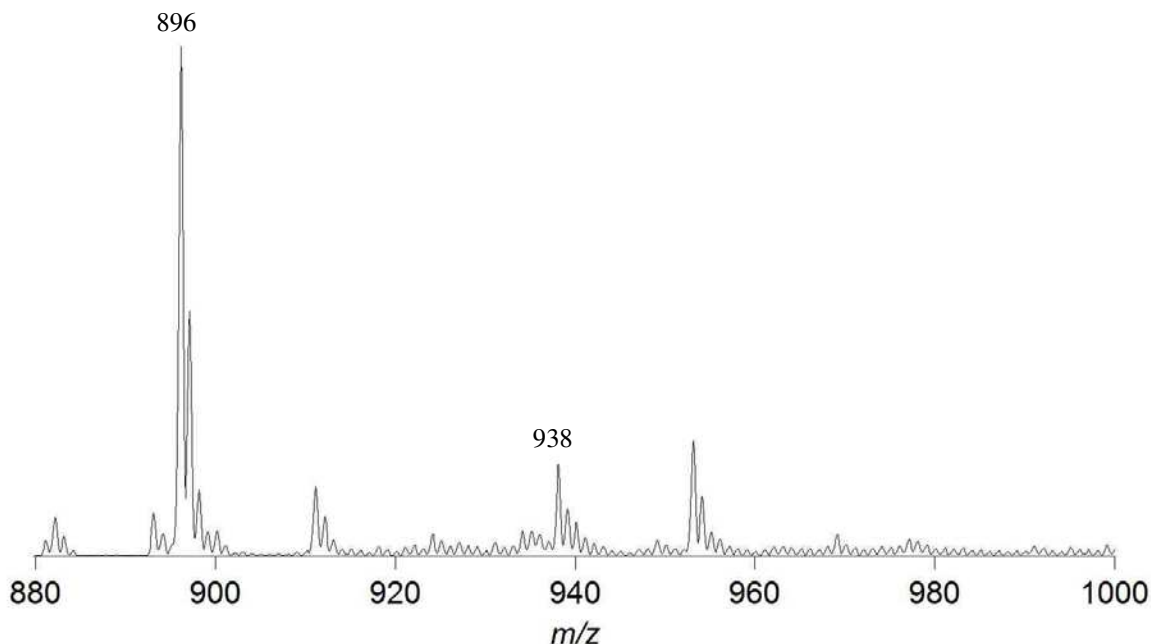


Figure 4.9. Negative-ion ESI mass spectrum of PDI-1-BnF after thermal decomposition (without copper) by heating for 8 hours at 145 °C in DMSO (rxn 2d conditions without copper or BnFI added).

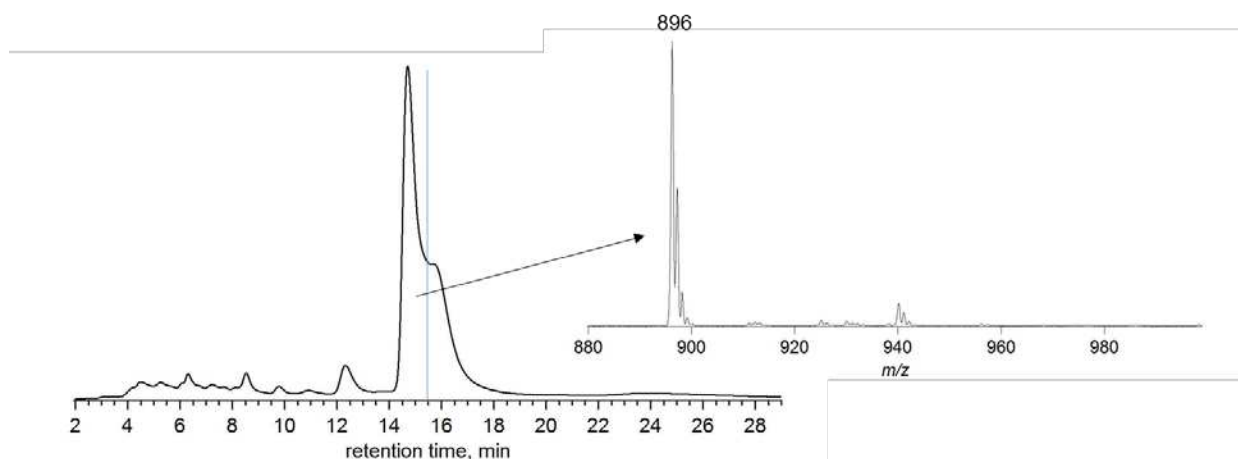


Figure 4.10. HPLC chromatogram of crude perfluorobenzylation reactions of PDI-1-BnF after thermal decomposition by heating for 8 hours at 145 C in DMSO. (rxn 2d conditions without copper or BnFI added). Showing several minor compounds and a major decomposition product forming. Separation was achieved using a 250 x 10 mm i.d. COSMOSIL Buckyprep column, 1:2 toluene–MeCN eluent, 5 mL min⁻¹ flow rate, set to 530 nm UV detection. Largest peak was determined to be PDI-1-BnF by MS (not shown). Inset shows mass spectrum of major decomposition product of PDI-1-BnF after separation, showing only $m/z = 896$ is present and the major decomposition product.

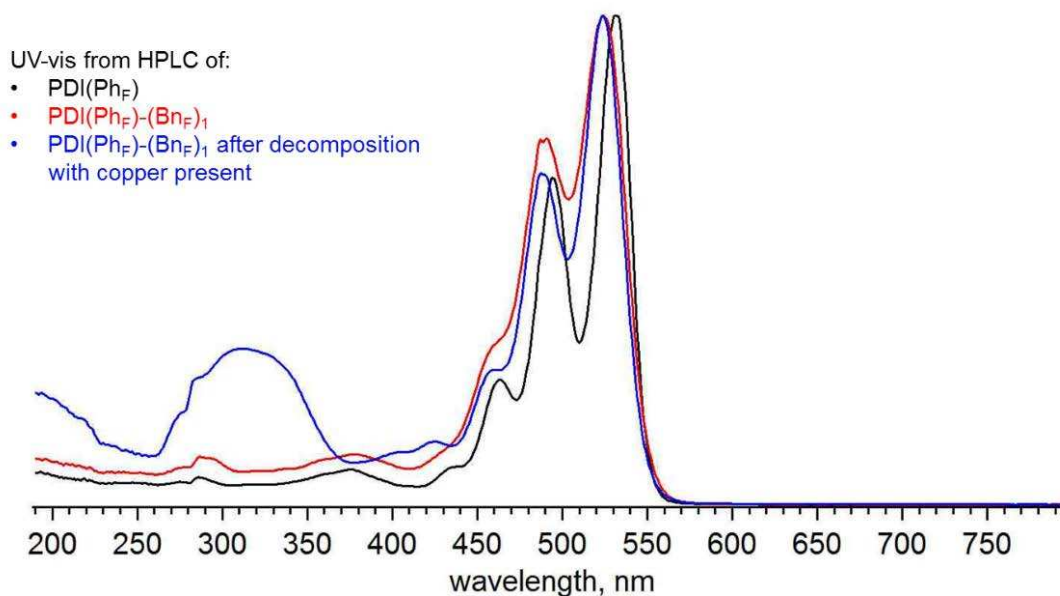


Figure 4.11. Comparison between UV-vis absorption profiles of unreacted PDI, PDI-1-Bn_F and the major decomposition product of PDI-1-Bn_F isolated from HPLC separation (shown in Figure 4.10, $m/z = 896$); depicted in black, red, and blue respectively. Illustrating a new absorption band that has grown in from ca. 260 to 370 nm, while maintaining the same three-forked perylene absorption profile of the starting material.

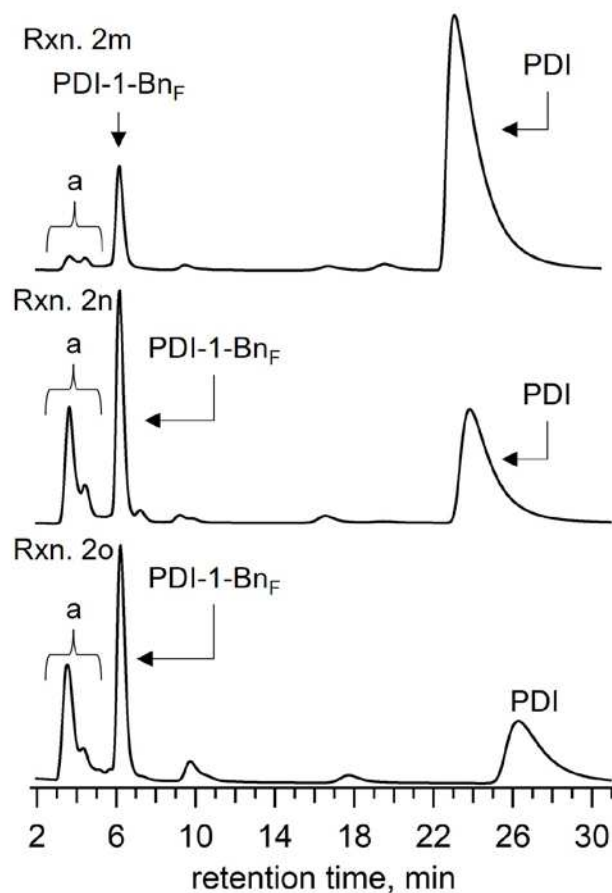


Figure 4.12. HPLC chromatograms of crude product mixtures of 145 °C reactions from Table 4.2. Rxn. B: One addition of BnFI with untreated copper. Rxn. C: One addition of BnFI with treated copper. Rxn D: sequential additions of BnFI with untreated copper. HPLC separation was achieved using a 250 x 10 mm i.d. COSMOSIL Buckyprep column, 2:8 IPA–toluene eluent, 5 mL min^{-1} flow rate, set to 530 nm UV detection.

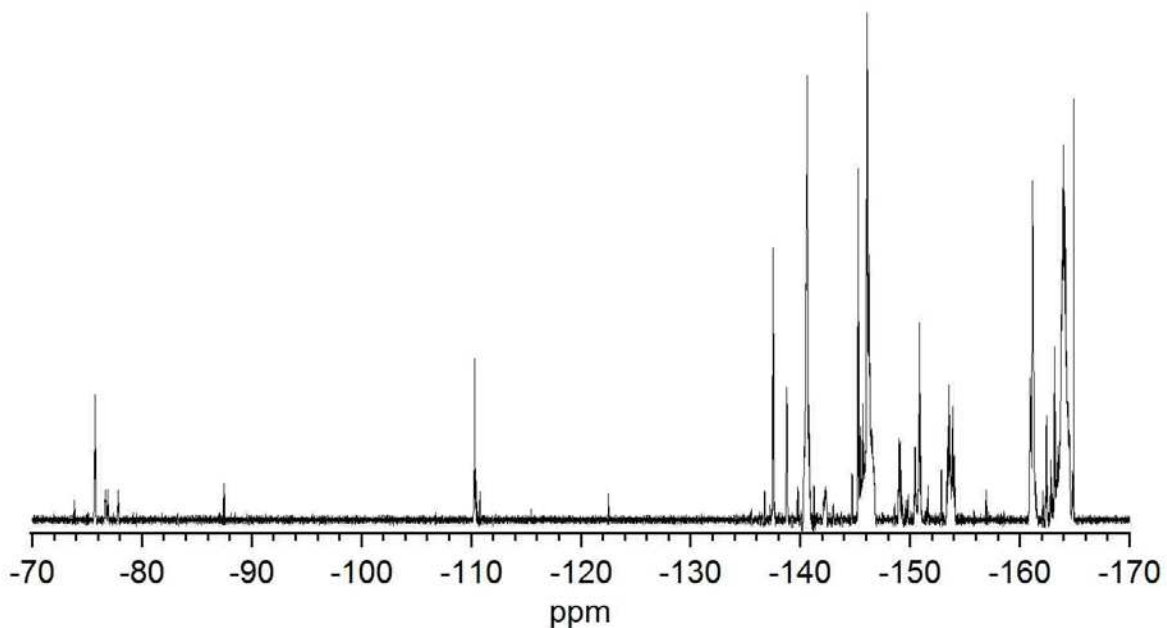


Figure 4.13: ^{19}F NMR spectrum of fraction-a in Figure 4.12 (ca. 3–4 min) from reaction **2d**. Showing an excess of aromatic fluorines per number of benzylic fluorines in spectrum. When integrating whole benzylic region (ca. -70 – -90) to 2 gives a value of 72 for whole aromatic region (ca. -135 – -170), which is significantly higher than what could be expected for substituted PDI.

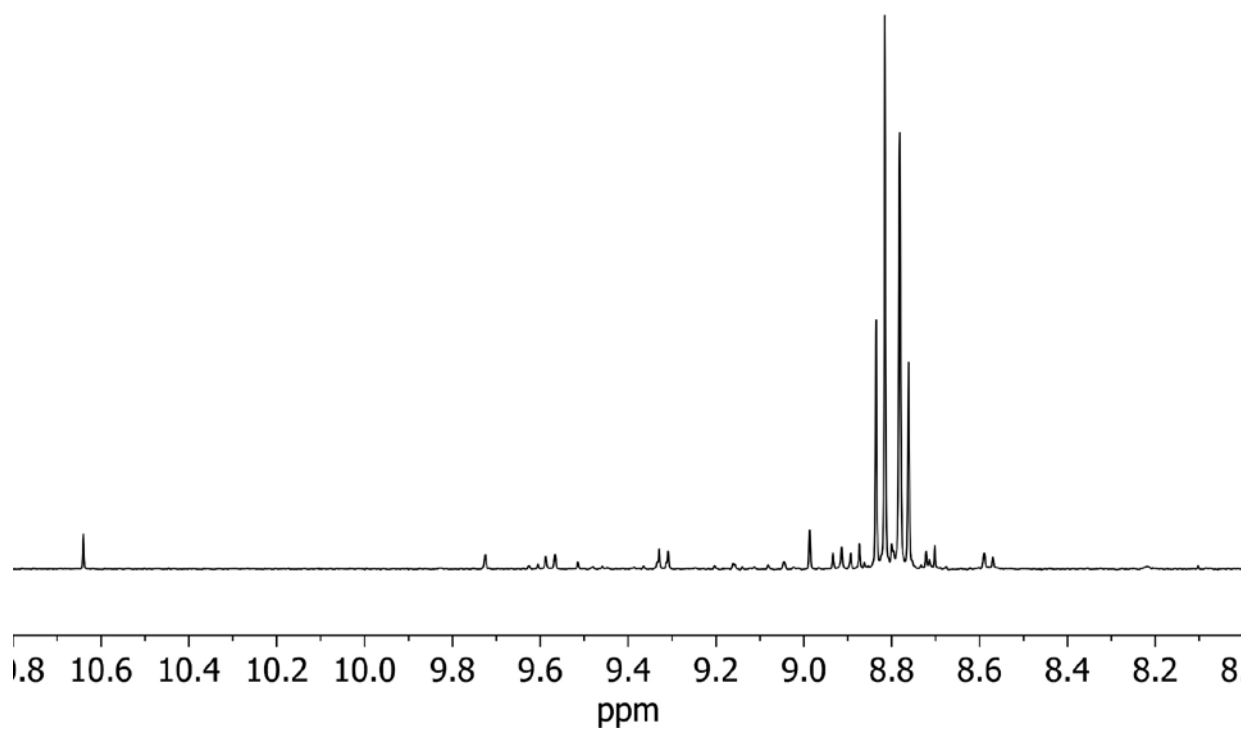


Figure 4.14. ^1H -NMR of crude perfluorobenzylation reactions of PDI in NMP after heating for 2 hours at $145\text{ }^\circ\text{C}$ with copper (rxn. **2c** with NMP instead of DMSO).

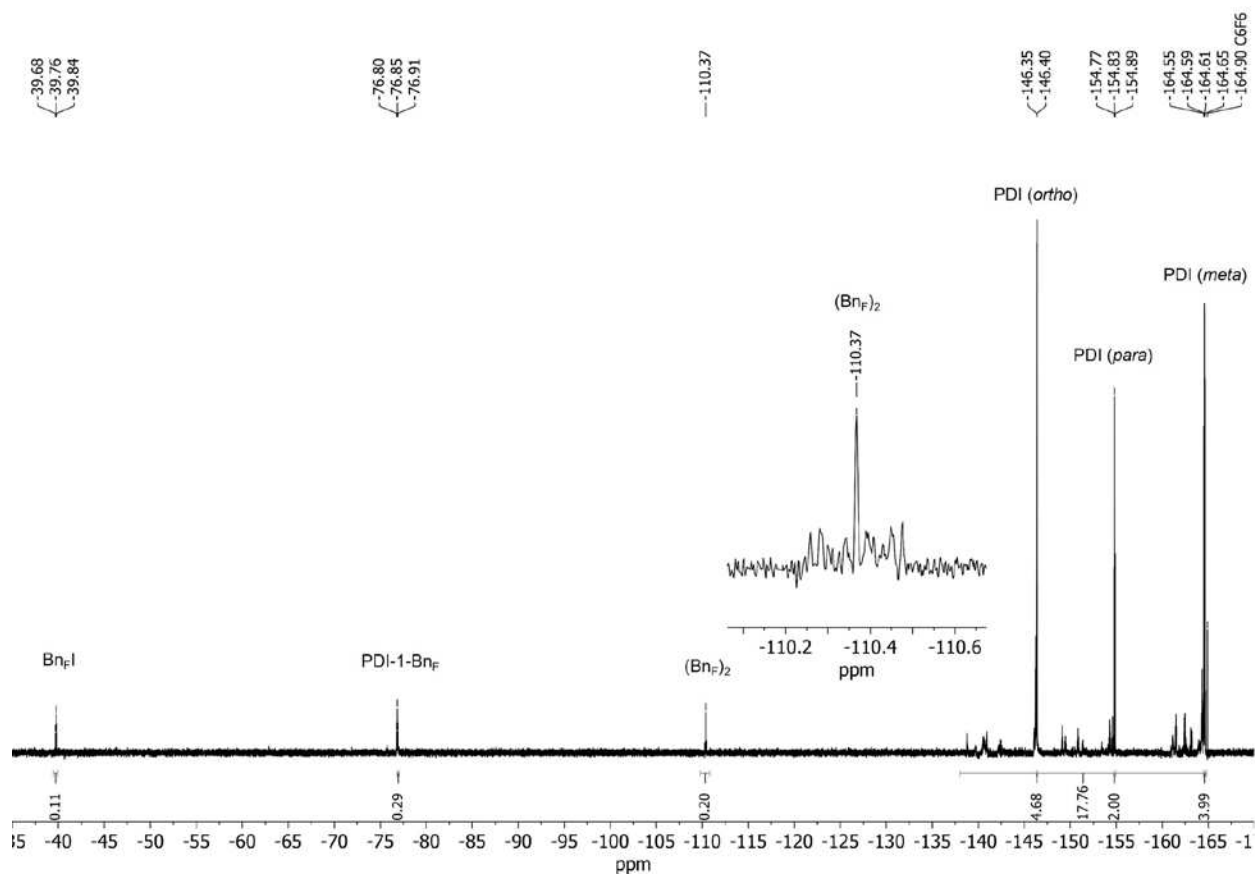


Figure 4.15. ^{19}F -NMR of crude perfluorobenzylation reactions of PDI in NMP after heating for 2 hours at 145 °C with copper (rxn. **2c** with NMP instead of DMSO).

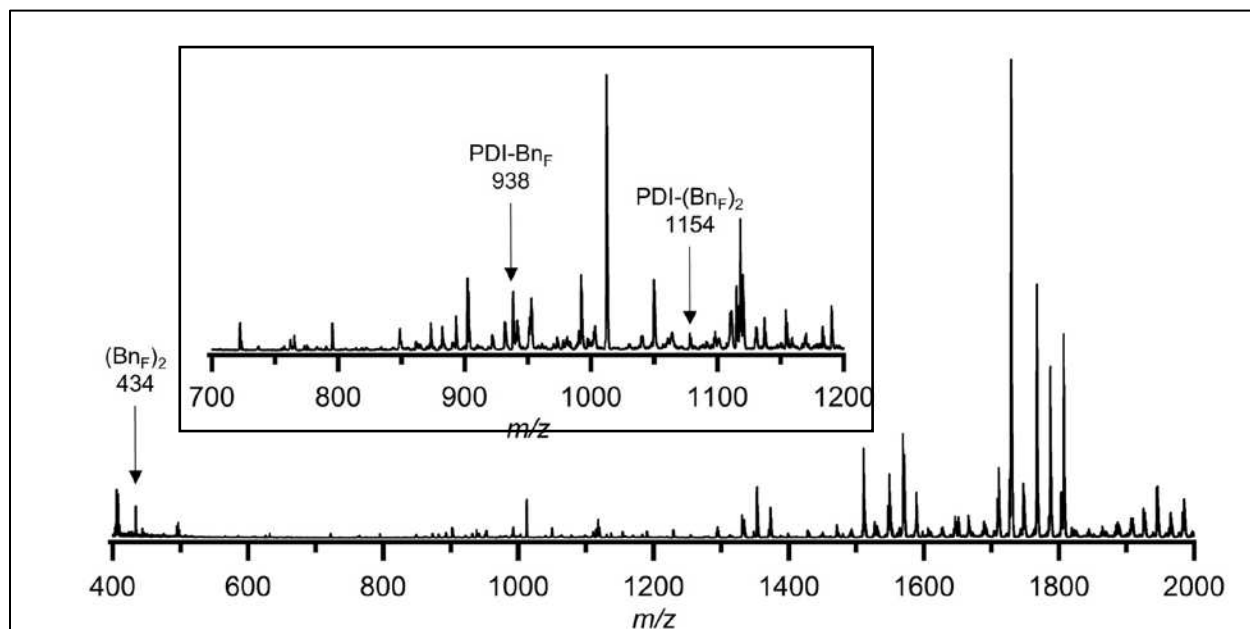


Figure 4.16. Mass spectrum of crude perfluorobenzylation reactions of PDI in NMP after heating for 2 hours at 145 °C with copper (rxn. **2c** with NMP instead of DMSO).

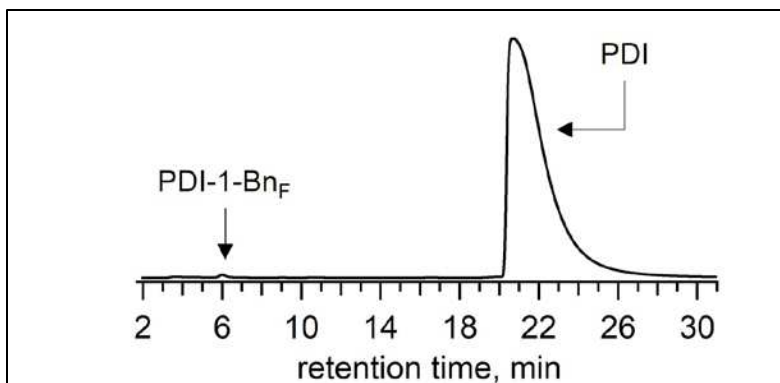


Figure 4.17: HPLC chromatogram of crude perfluorobenylation reactions of PDI in PhCl. Separation was achieved using a 250 x 10 mm i.d. COSMOSIL Buckyprep column, 1:9 IPA-toluene eluent, 5 mL min⁻¹ flow rate, set to 530 nm UV detection. Showing very little conversion of starting material into PDI-(Bn_F)_n products.

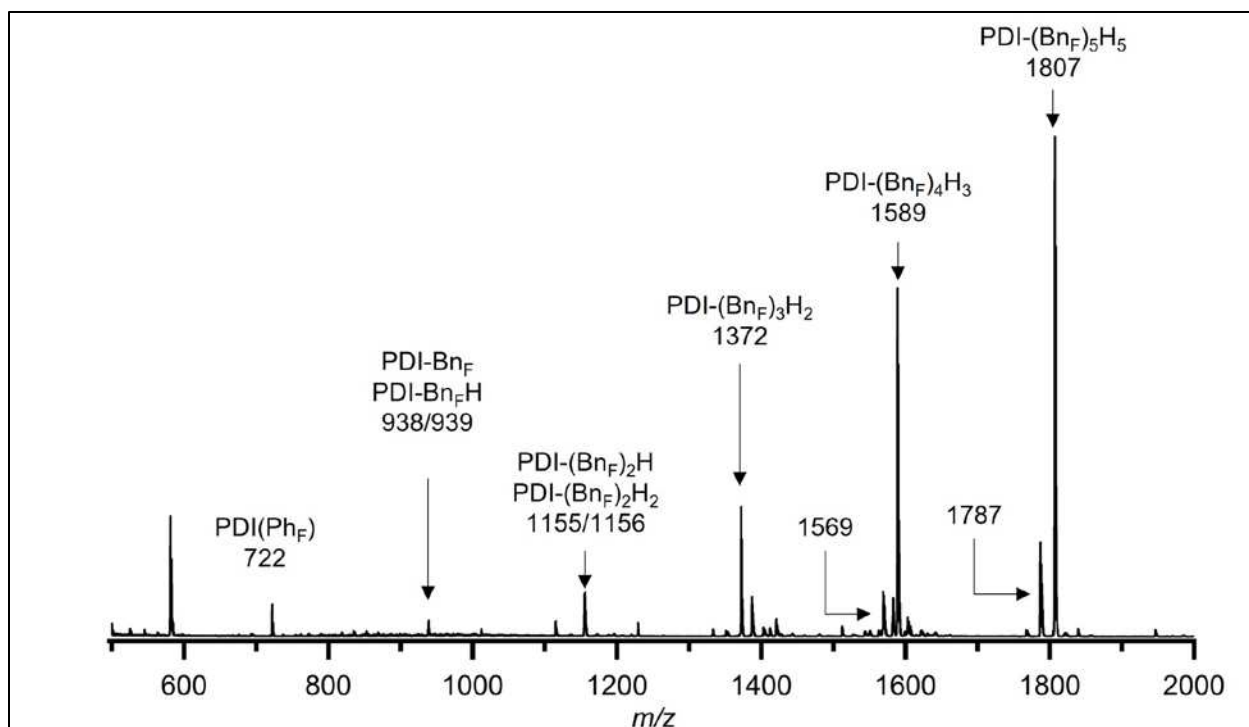


Figure 4.18: Negative-ion ESI mass spectrum of crude reaction mixture of perfluorobenylation reaction of PDI in PhCl. Showing both substitution products and addition products containing Bn_F groups.

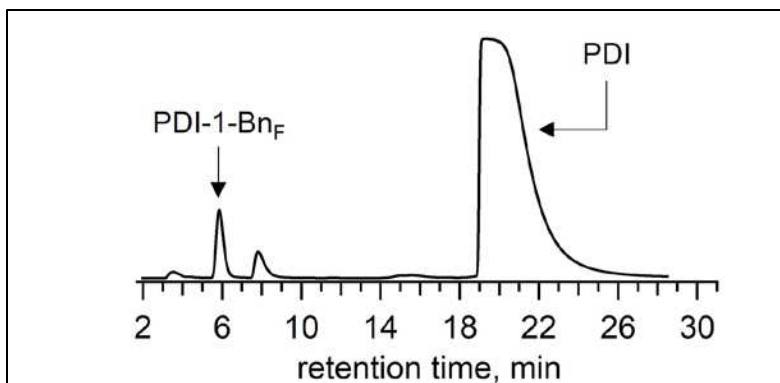


Figure 4.19. HPLC chromatogram of crude perfluorobenylation reactions of PDI in ODCB. Separation was achieved using a 250 x 10 mm i.d. COSMOSIL Buckyprep column, 1:9 IPA–toluene eluent, 5 mL min⁻¹ flow rate, set to 530 nm UV detection. Showing very little conversion of starting material into PDI-(Bn_F)_n products.

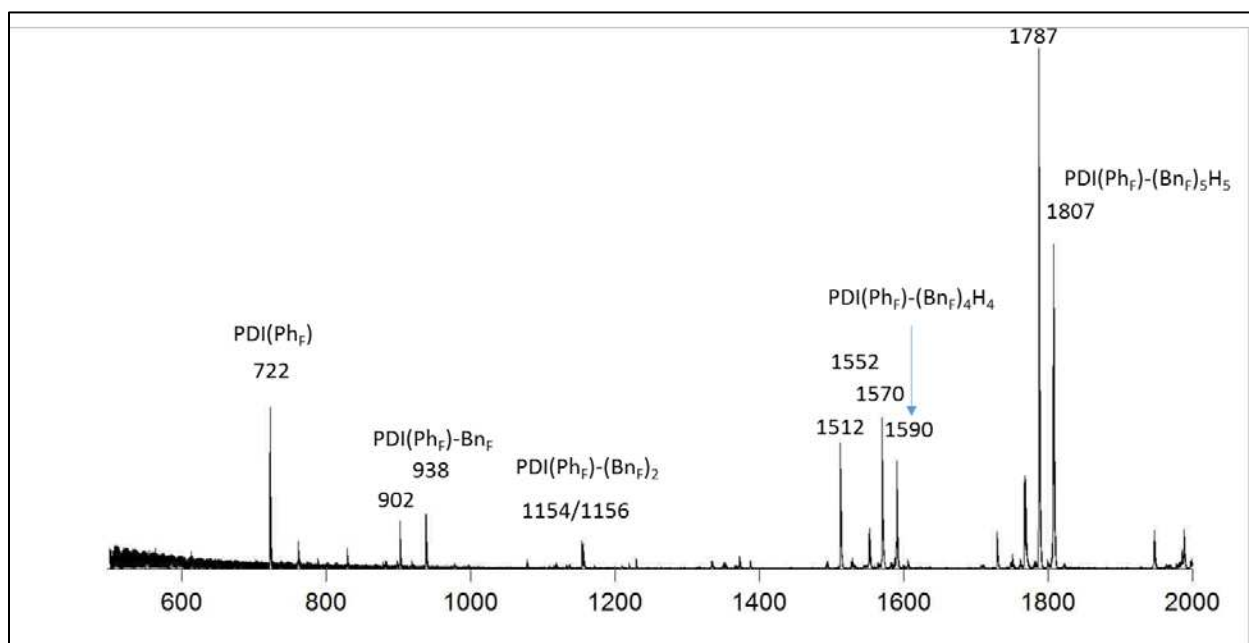


Figure 4.20. Negative-ion ESI mass spectrum of crude reaction mixture of perfluorobenylation reaction of PDI in ODCB. Showing both substitution products and addition products containing Bn_F groups.

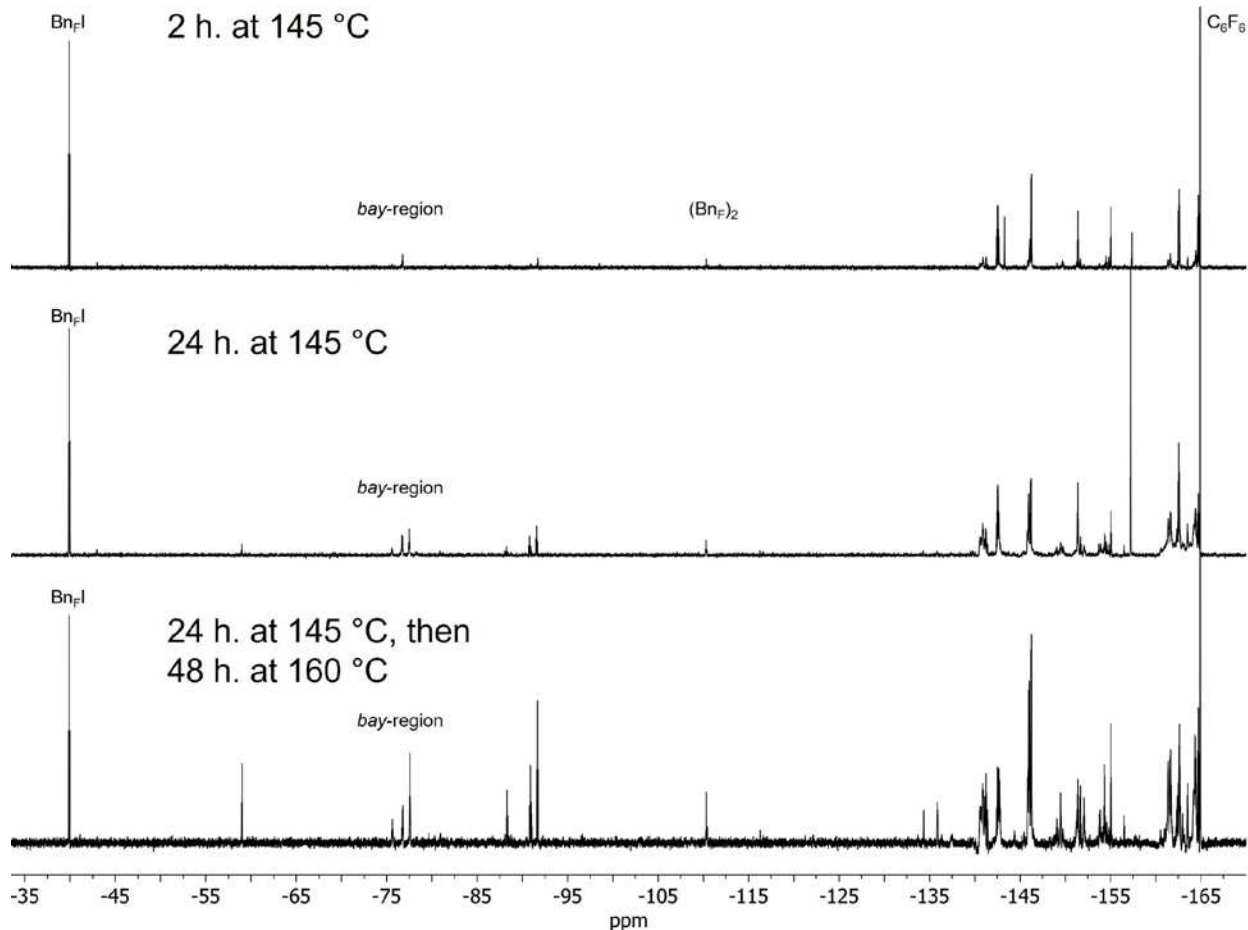


Figure 4.21. ^{19}F -NMR spectra of aliquots taken over time of perfluorobenzoylation reaction of PDI in PhCN with 4 equiv. of BnF-I and 8 equiv. of copper. Top: spectrum of aliquot taken after heating for 2 hours at 145 °C with copper (rxn. **2c** with PhCN instead of DMSO). Middle: after heating for 24 hours. Bottom: after heating for 72 hours total (24 h at 145 °C then 48 h at 160 °C). Each spectrum is normalized to have the same intensity for the benzylic $\text{F}(\text{CF}_2)$ signal from unreacted BnF-I .

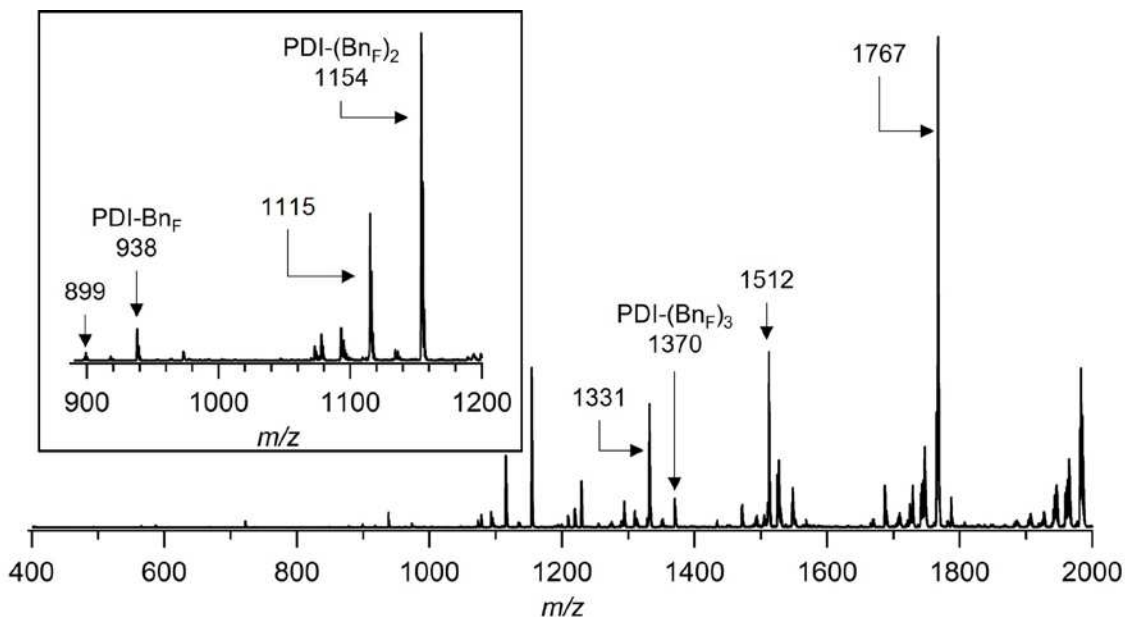


Figure 4.22. Negative-ion ESI mass spectrum of crude perfluorobenylation reaction of PDI in PhCN with 4 equiv. of BnF_I and 8 equiv. of copper after heating for 24 h at 145 °C. Inset shows expansion of region from 900 to 1200 m/z .

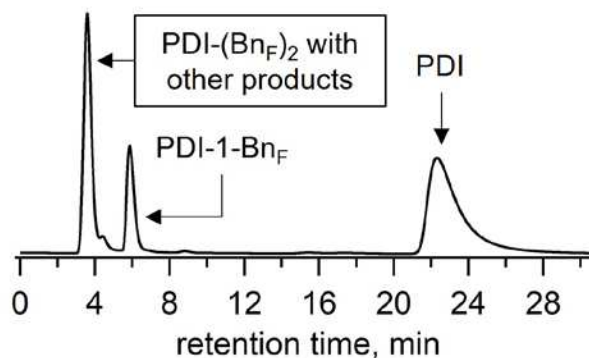


Figure 4.23. HPLC chromatogram of crude perfluorobenylation reaction of PDI in PhCN with 4 equiv. of BnF_I and 8 equiv. of copper after heating for 72 hours (24 h at 145 °C then 48 h at 160 °C). Separation was achieved using a 250 x 10 mm i.d. COSMOSIL Buckyprep column, 1:9 IPA-toluene eluent, 5 mL min^{-1} flow rate, set to 530 nm UV detection.

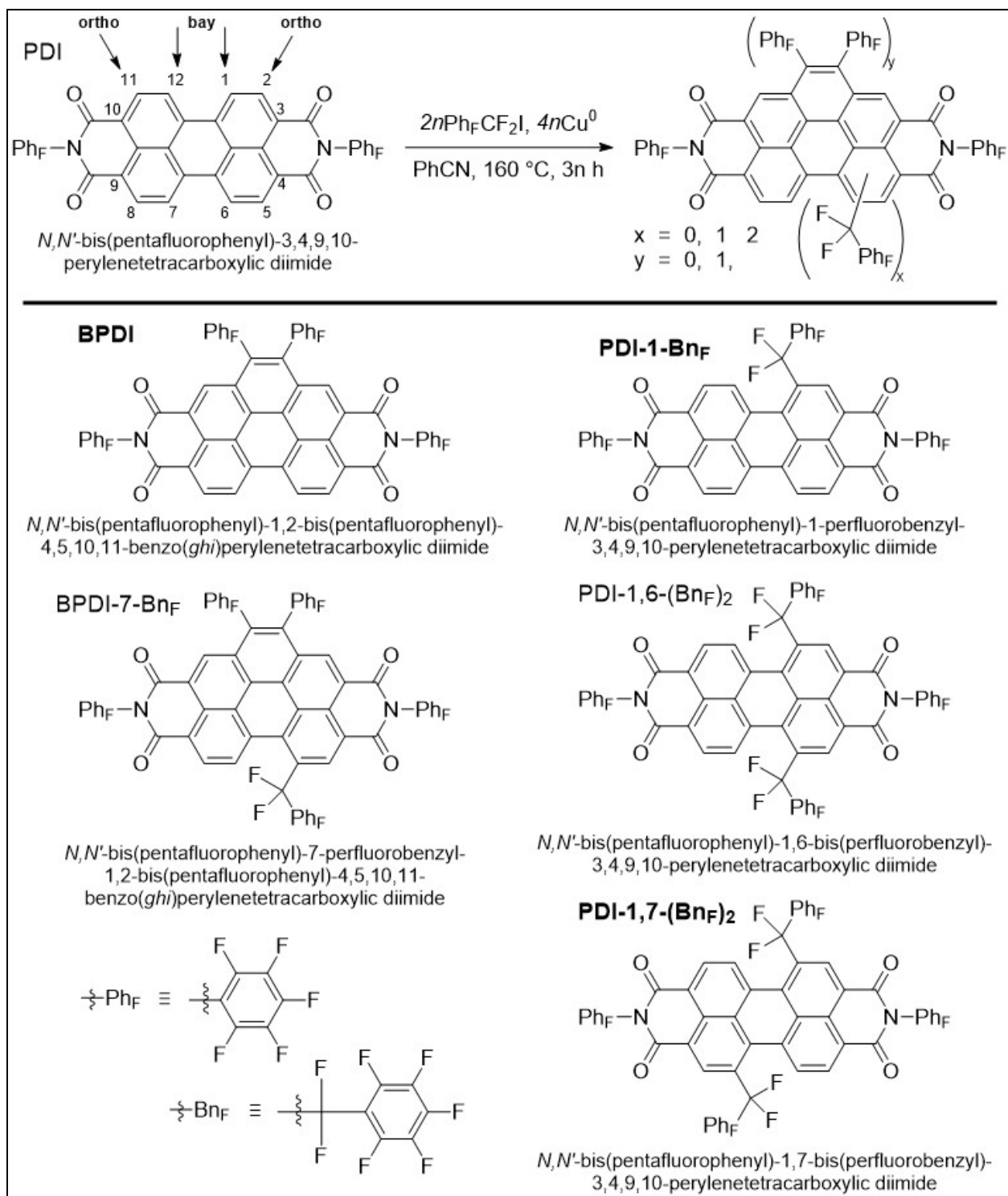


Figure 4.24: Top: General reaction scheme for direct perfluorobenylation and annulation of PDI with nomenclature for unique positions. Bottom: Drawings of molecular structures of isolated perylene diimides, PDI(BnF)_n, and benzoperylene diimides, BPDI(BnF)_n; for brevity, PDI-*x*-(BnF)_n and BPDI-*x*-(BnF)_n notations are introduced, where *x* is (are) the position(s) of substituted BnF groups and *n* is the total number of BnF groups substituted. Names shown in **bold** are for products that single crystal X-ray structure were obtained.

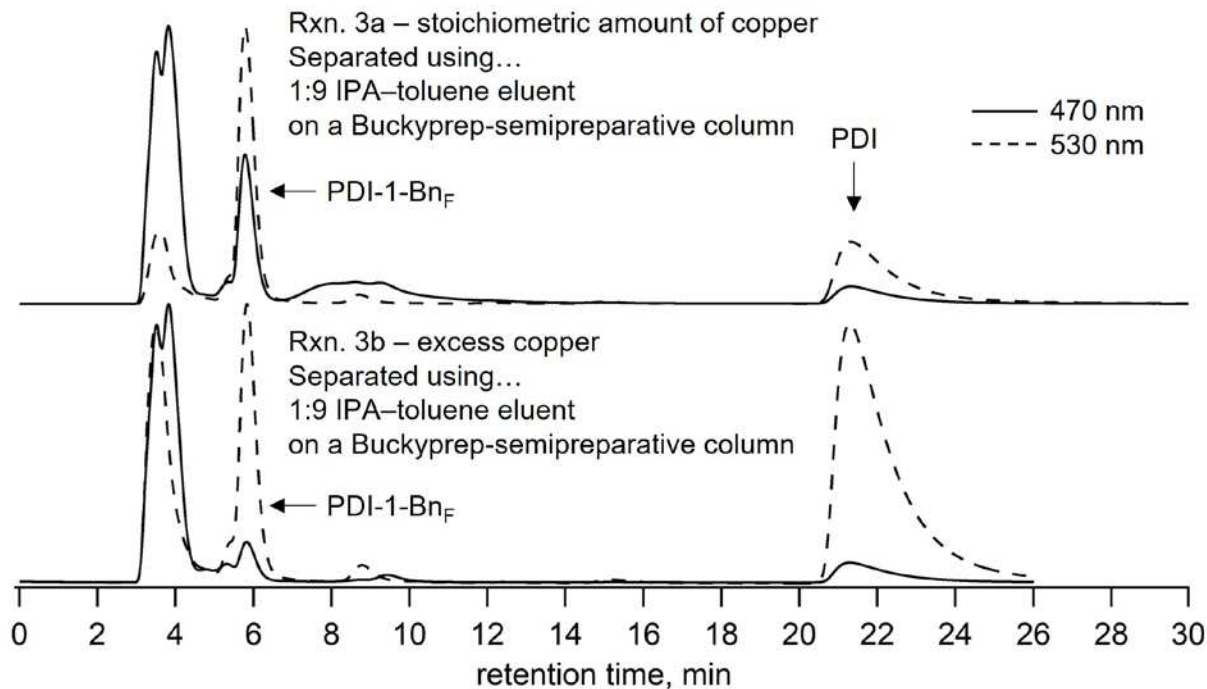


Figure 4.25. HPLC chromatograms of crude perfluorobenzylation reactions of PDI in PhCN, normalized to the highest peak. Top: chromatogram for crude reaction **3a**, using 8 equiv. copper with 4 equiv. Bottom: chromatogram for crude reaction **3b**, using 40 equiv. copper with 4 equiv. Bn_FI. Solid lines (—) show chromatogram at 470 nm detection (λ_{max} for BPDI and BPDI-Bn_F products); dashed trace (---) show chromatogram at 530 nm detection (λ_{max} for PDI and PDI-Bn_F products). HPLC separation was achieved using a 250 x 10 mm i.d. COSMOSIL Buckyprep semipreparative column, 1:9 IPA–toluene eluent, 5 mL min⁻¹ flow rate.

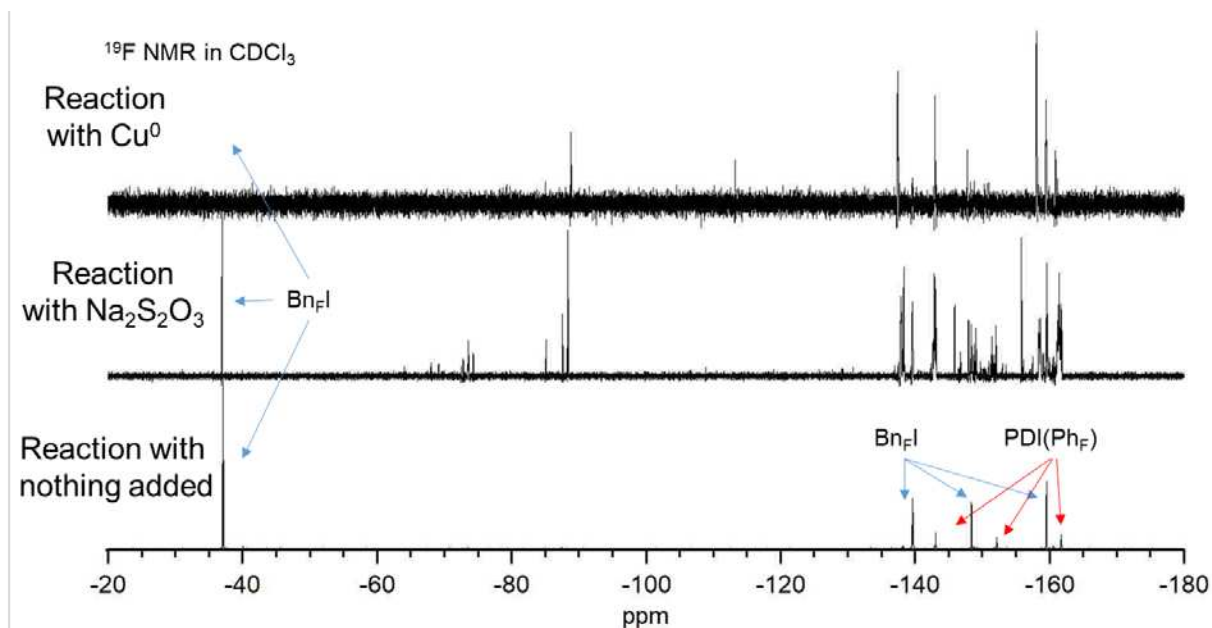


Figure 4.26 Stacked ¹⁹F-NMR spectra of crude reactions 3c (top), 3d (middle), and 3e taken in CDCl₃; comparing reaction conditions using PhCN solvent at 160 °C with Cu metal, Na₂S₂O₃ salt, or neither. Note that there is no reaction without a reductant being present.

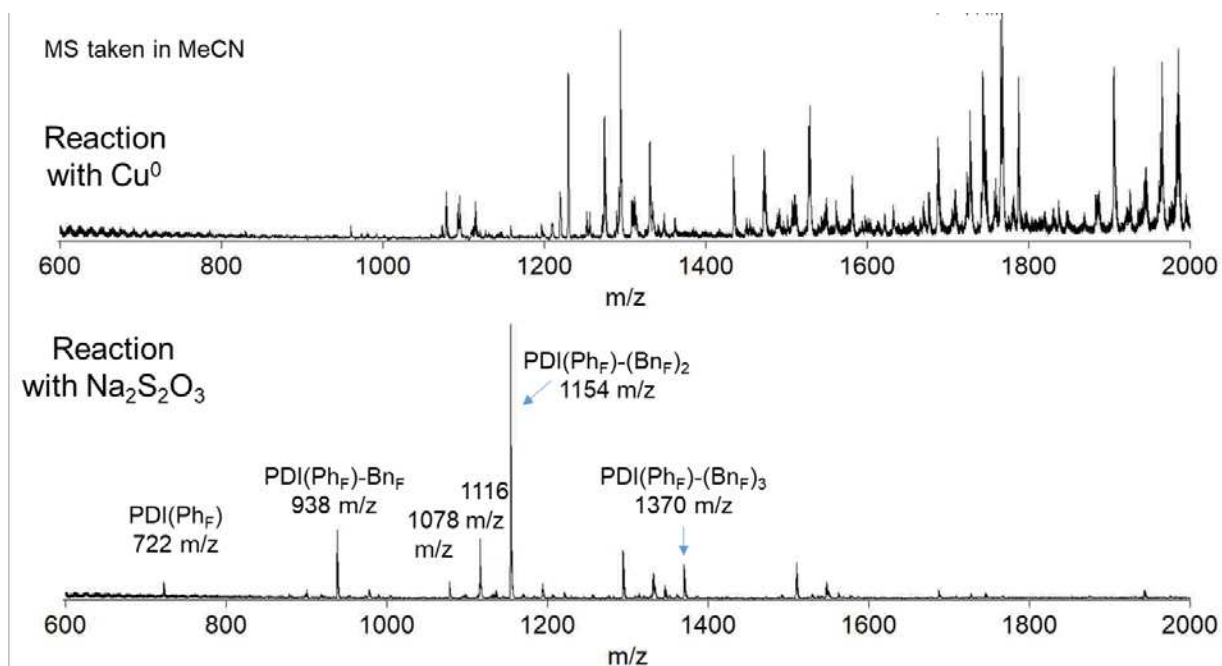


Figure 4.27. Stacked negative-ion ESI mass spectra of crude reactions 3c (top) and 3d (bottom) using MeCN as the carrier solvent. Comparing the effects of using Cu metal versus Na₂S₂O₃ as the reducing agent for perfluorobenylation and/or BPDI formation.

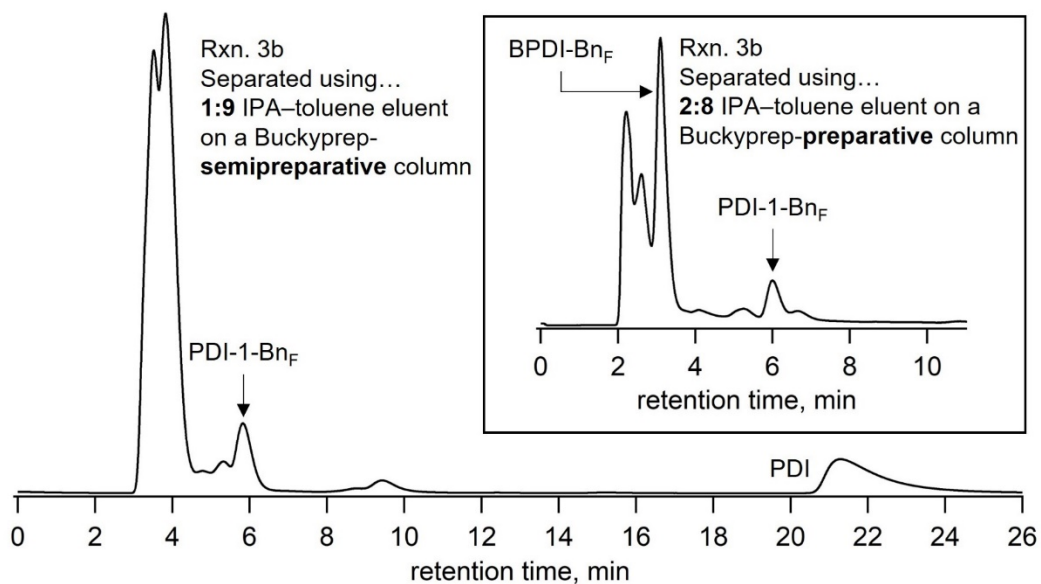


Figure 4.28. HPLC separations of reaction **3b**, showing chromatogram for 470 nm wavelength detection (λ_{max} for BPDI and BPDI-Bn_F products) using a 1:9 IPA-toluene eluent. Inset shows separation using a weaker eluent (2:8 IPA-toluene) which allows for isolation of the major BPDI derivative: BPDI-Bn_F. HPLC separation was achieved using a 250 x 10 mm i.d. COSMOSIL Buckyprep semipreparative column, 5 mL min⁻¹ flow rate.

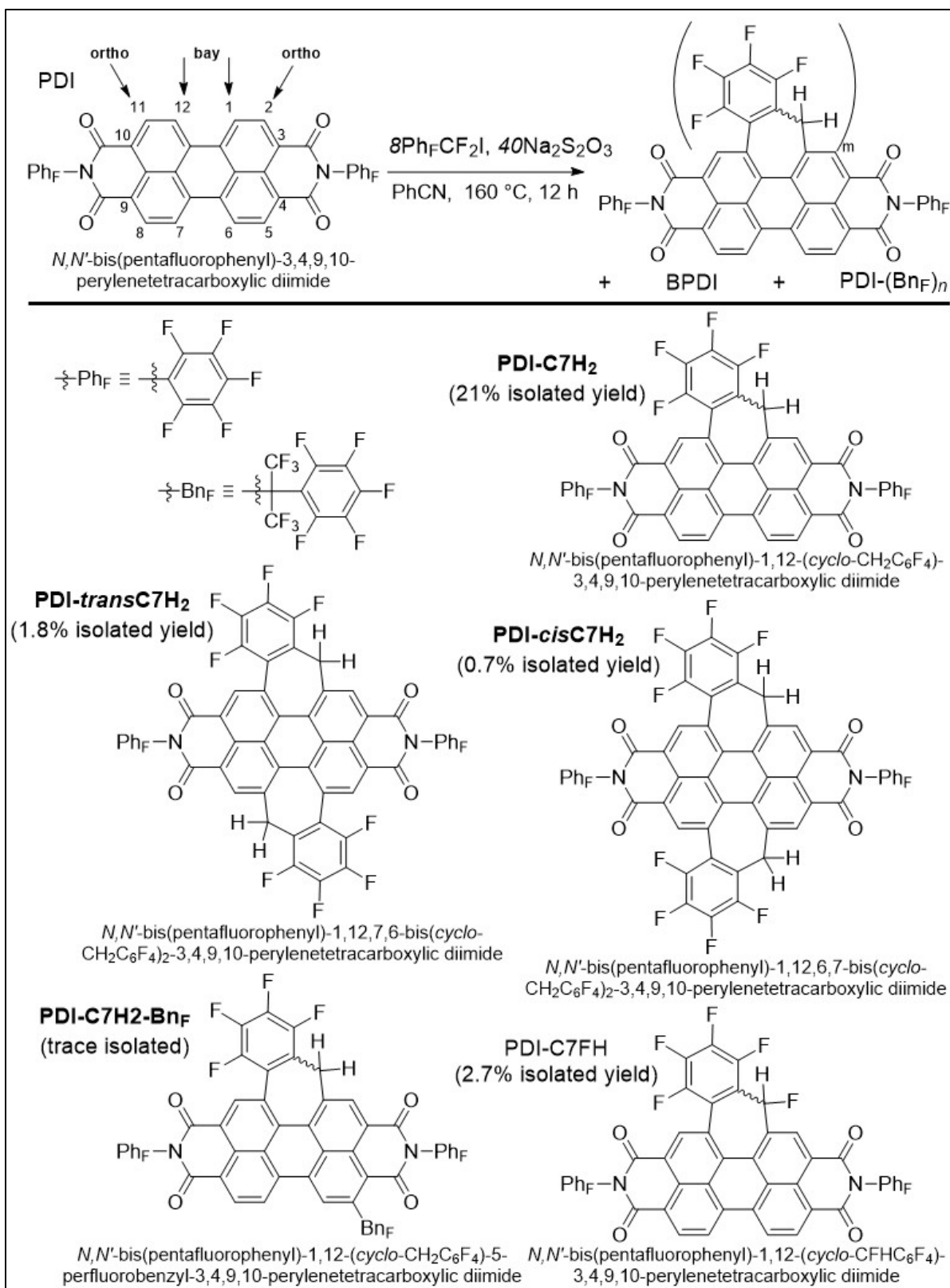


Figure 4.29 General reaction scheme for direct perfluorobenylation and annulation of PDI with nomenclature for unique positions. Bottom: Drawings of molecular structures of isolated PDI-C7H₂ derivatives.

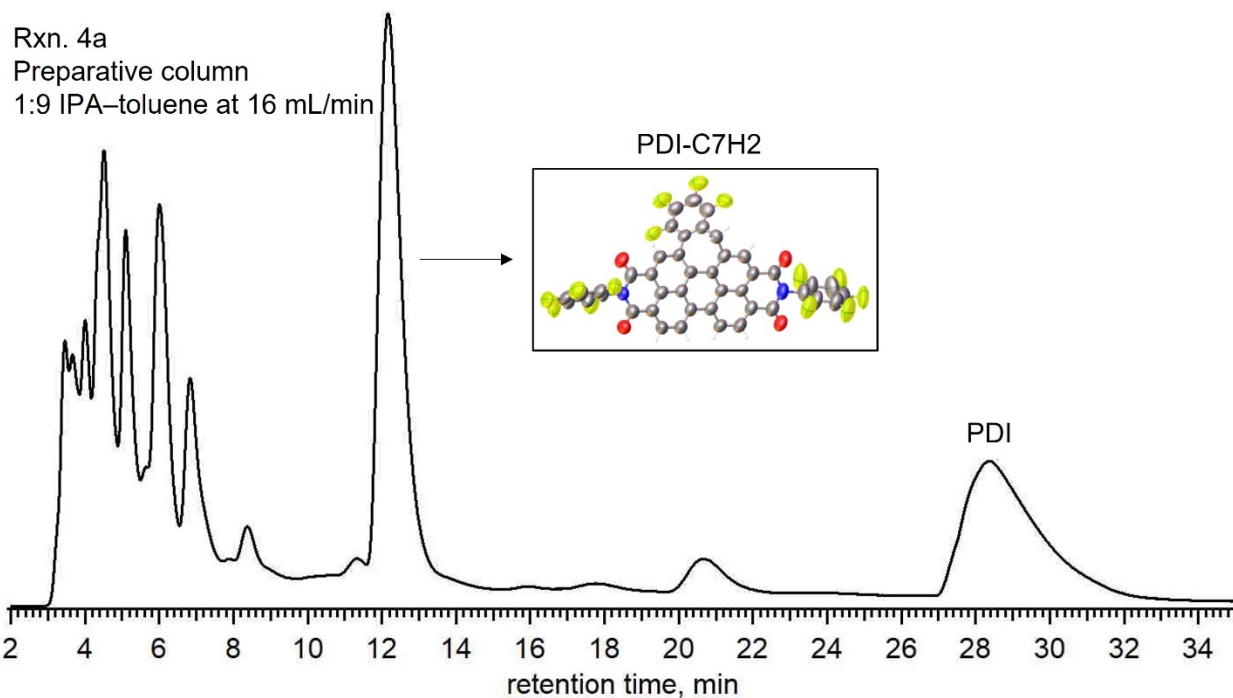


Figure 4.30. HPLC chromatograms of crude product mixture of reaction **4a** (in Table 4.5), resulting in the highest yield of PDI-C7H2 in a single reaction (isolated yields shown in Figure 4.29). HPLC separation was achieved using a 250 x 10 mm i.d. COSMOSIL Buckyprep preparative column, 1:9 IPA-toluene eluent, 16 mL min⁻¹ flow rate, set to 530 nm UV detection.

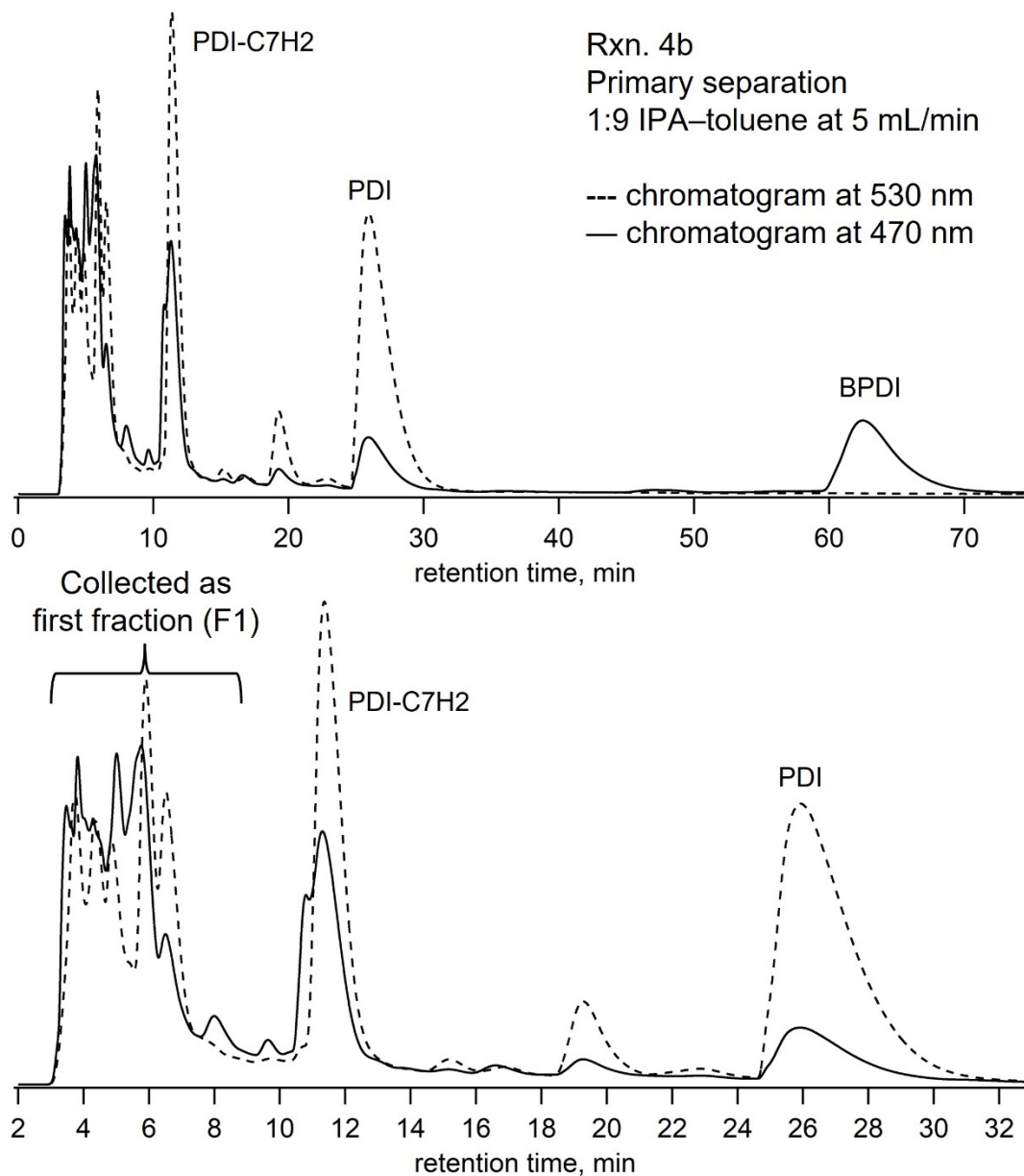


Figure 4.31. Example of primary separation of reaction 4b. Solid lines (—) show chromatogram at 470 nm detection (λ_{\max} for BPDI and BPDI-Bn_F products); dashed trace (---) show chromatogram at 530 nm detection (λ_{\max} for PDI and PDI-Bn_F products). Top) shows full chromatogram from 0 to 75 min of reaction 4b, where BPDI is observable at longer retention times. Bottom) closeup of top figure, showing chromatogram from 0 to 33 min of reaction 4b. Major products in fraction F1 can be separated with additional HPLC, shown in Figure 4.32. HPLC separation was achieved using a 250 x 10 mm i.d. COSMOSIL Buckyprep preparative column, 1:9 IPA–toluene eluent, 16 mL min⁻¹ flow rate, set to 530 nm UV detection.

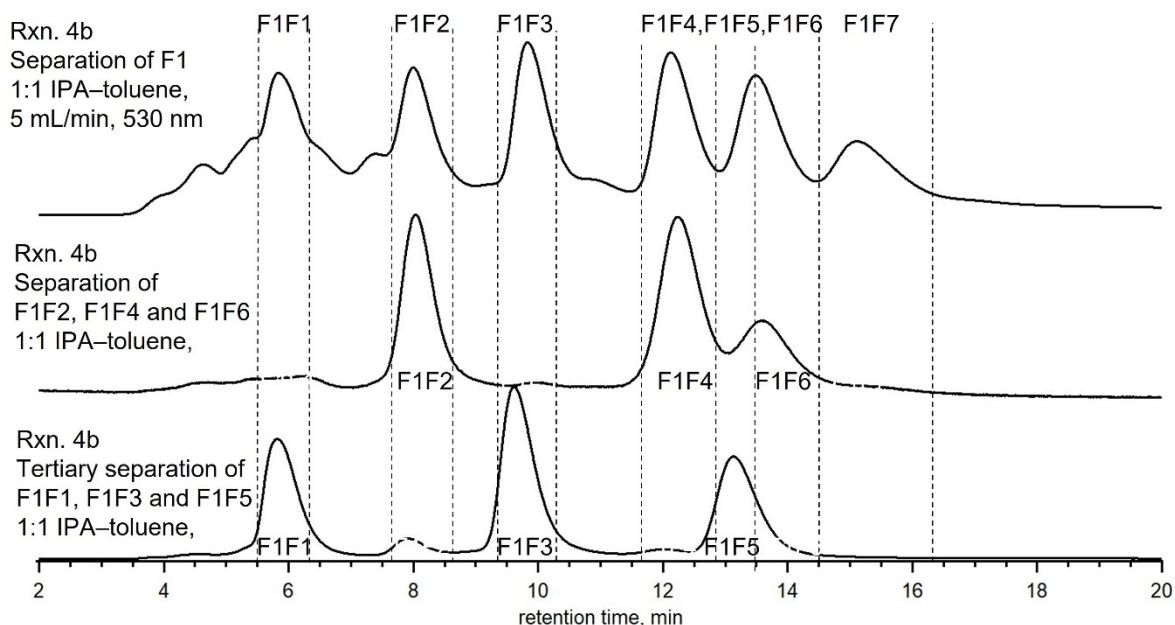


Figure 4.32 Example of secondary and tertiary separation of reaction 4b. All chromatogram traces shown at 530 nm. Dashed lines show where each fraction was collected in each chromatogram Top) representative example of secondary separation of F1 from reaction 4b (F1 shown in Figure 4.31). Each odd numbered fraction (other than F1F7) was added together, and each even numbered fraction was added together. Middle) representative example of tertiary separation of F1-even, giving pure F1F2 and F1F4, with F1F6 needing additional separation Bottom) representative example of tertiary separation of F1-odd, giving pure F1F3, with F1F1 and F1F5 needing additional separation. HPLC separation was achieved using a 250 x 10 mm i.d. COSMOSIL Buckyprep preparative column, 1:9 IPA-toluene eluent, 16 mL min⁻¹ flow rate, set to 530 nm UV detection.

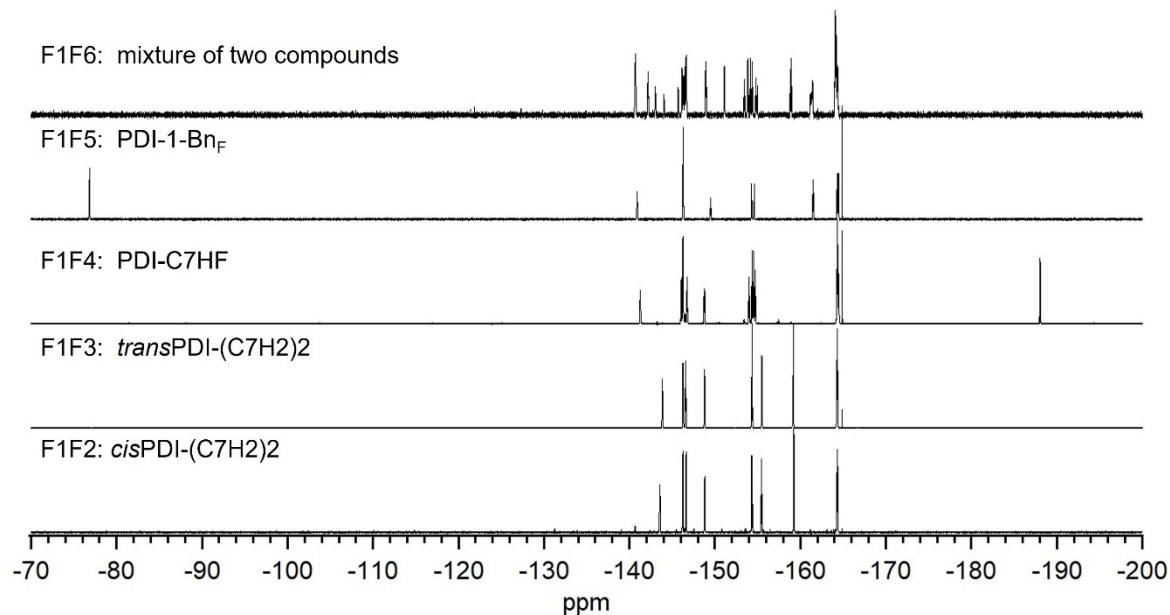


Figure 4.33. Stacked ¹⁹F-NMR spectra of major fractions shown in Figure 4.32.

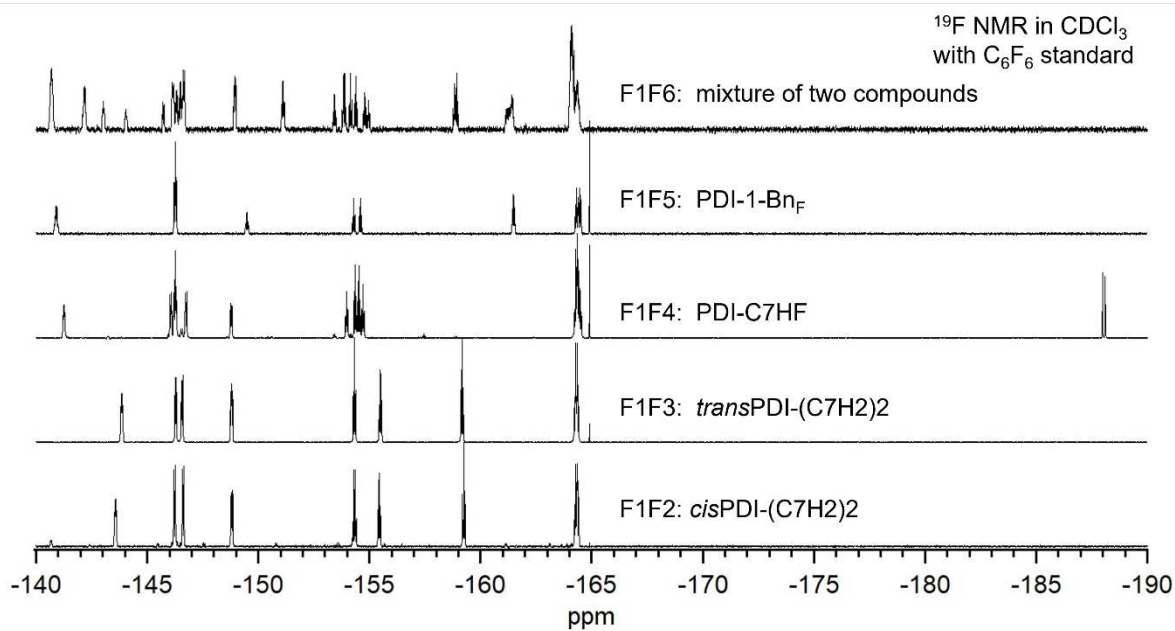


Figure 4.34. Closeup view of aromatic region of Figure 4.33.

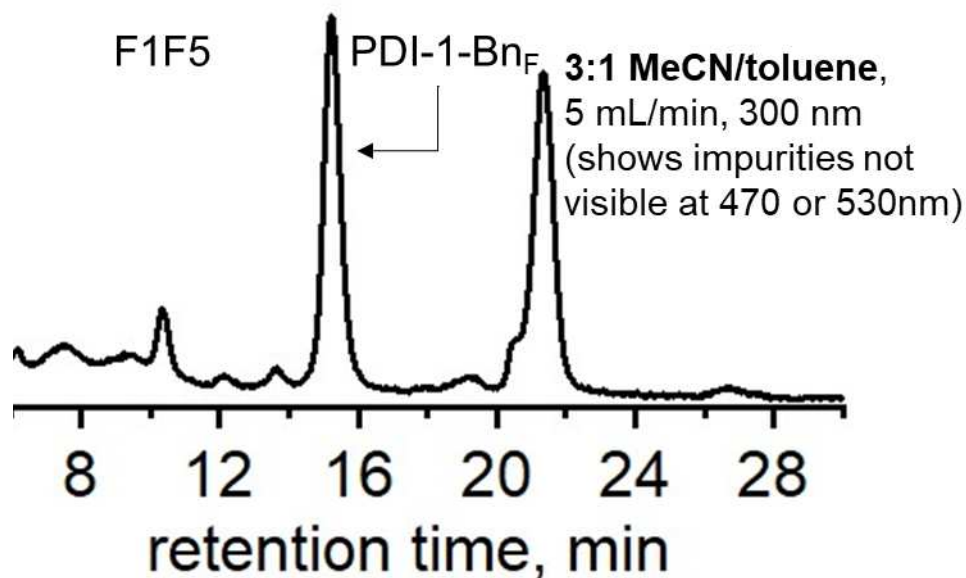


Figure 4.35. Example of quaternary separation of reaction 4b, F1F5, to give pure PDI-1-Bn_F. HPLC separation was achieved using a 250 x 10 mm i.d. COSMOSIL Buckyrep preparative column, 3:1 MeCN–toluene eluent, 5 mL min⁻¹ flow rate, set to 300 nm UV detection.

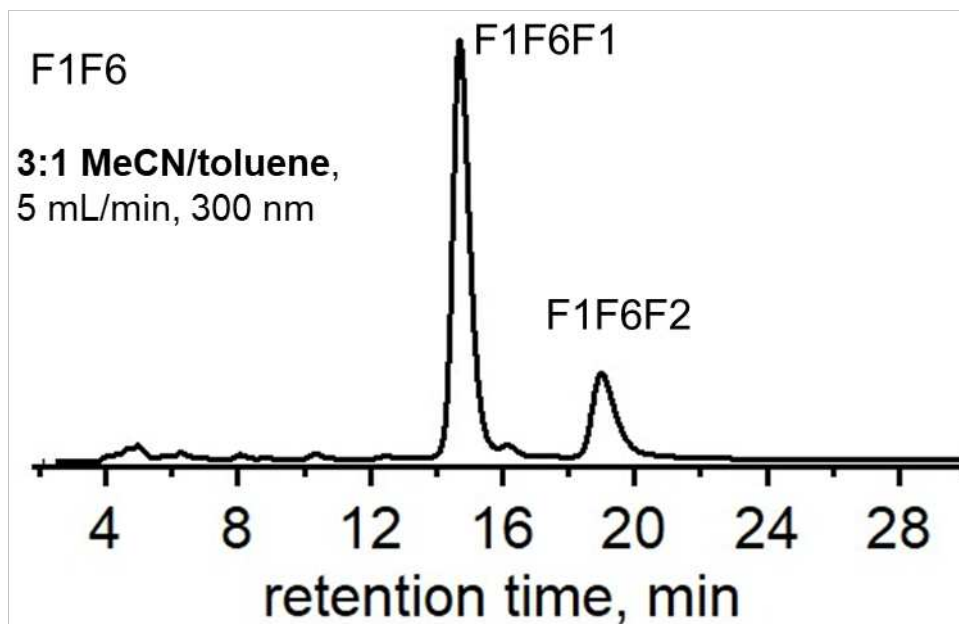


Figure 4.36. Example of quaternary separation of reaction 4b, F1F6. HPLC separation was achieved using a 250 x 10 mm i.d. COSMOSIL Buckyrep preparative column, 3:1 MeCN–toluene eluent, 5 mL min⁻¹ flow rate, set to 300 nm UV detection.

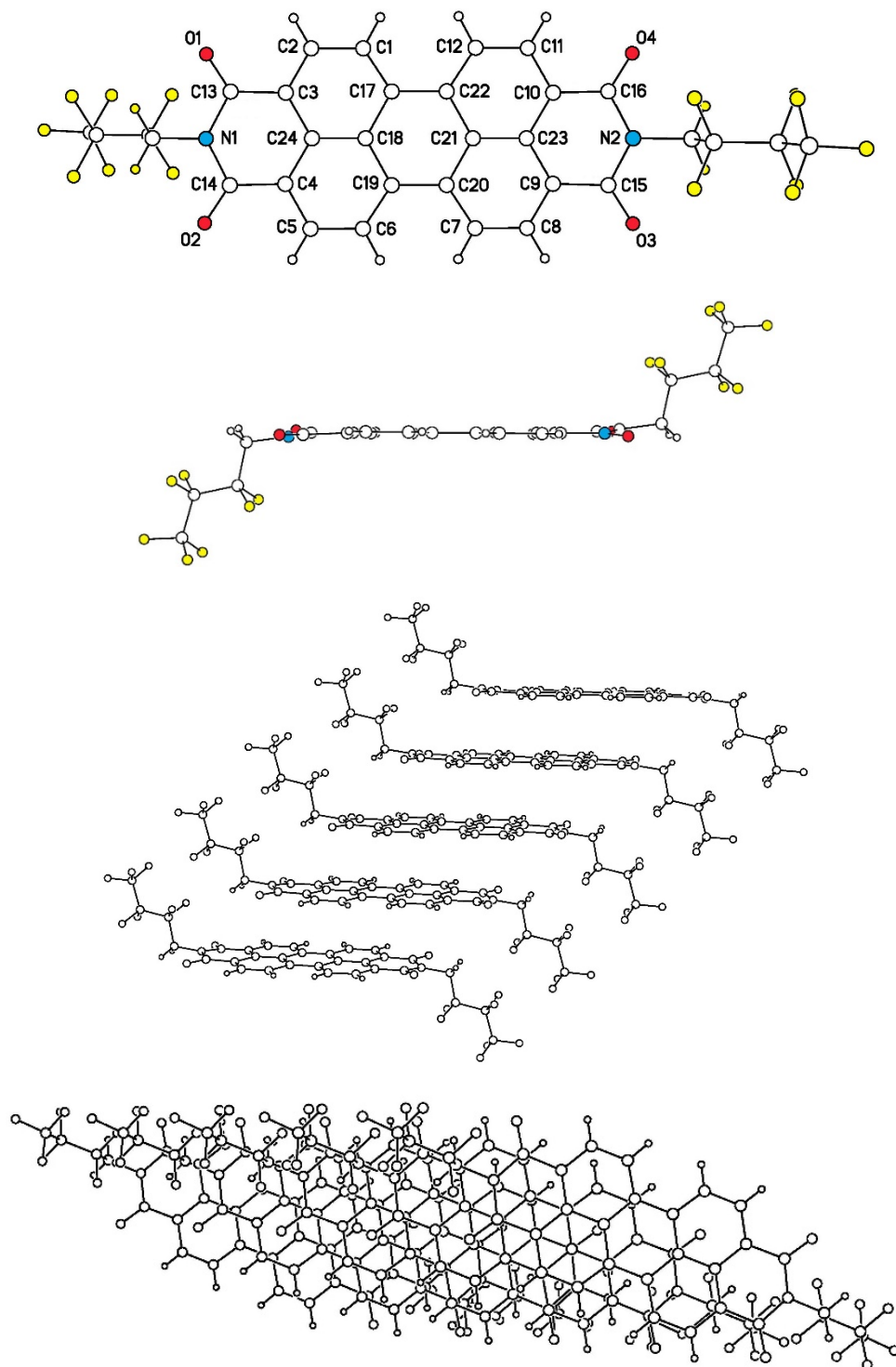


Figure 4.37. The literature structure of $(C_3F_7CH_2)_2PDI$.¹³⁵ The locant scheme used in this chapter is shown in the top drawing.

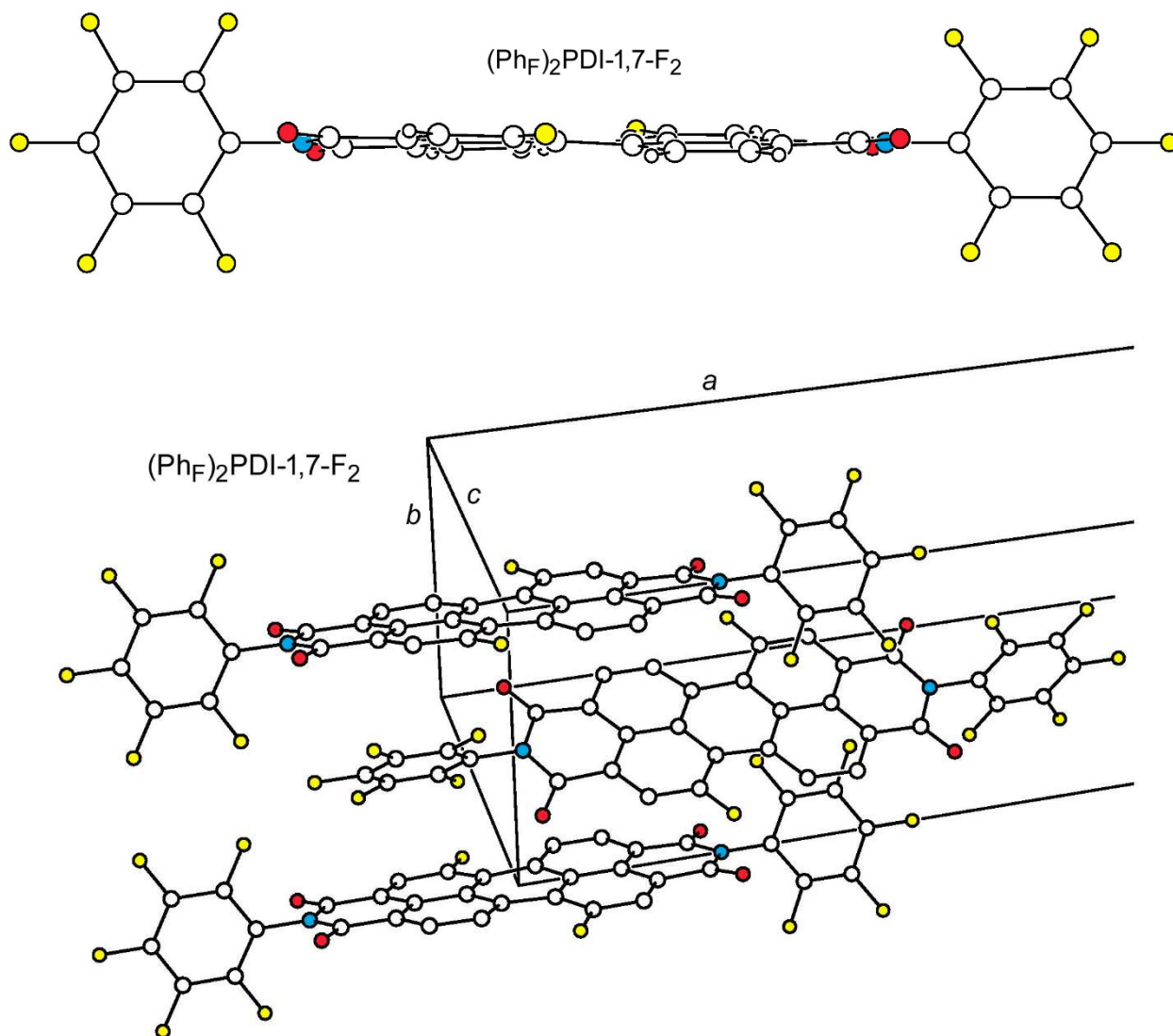


Figure 4.38. The literature structure of (Ph_F)₂PDI-1,7- F_2 .¹⁶¹ The PDI core is relatively planar but the Ph_F groups prevent any significant intermolecular π - π overlap of the PDI cores or the Ph_F groups in neighboring molecules in the lattice. Every other molecule along the crystallographic *b* axis is rotated 24.4° from its nearest neighbor molecules. The Ph_F groups are rotated 83.3° relative to the PDI core.

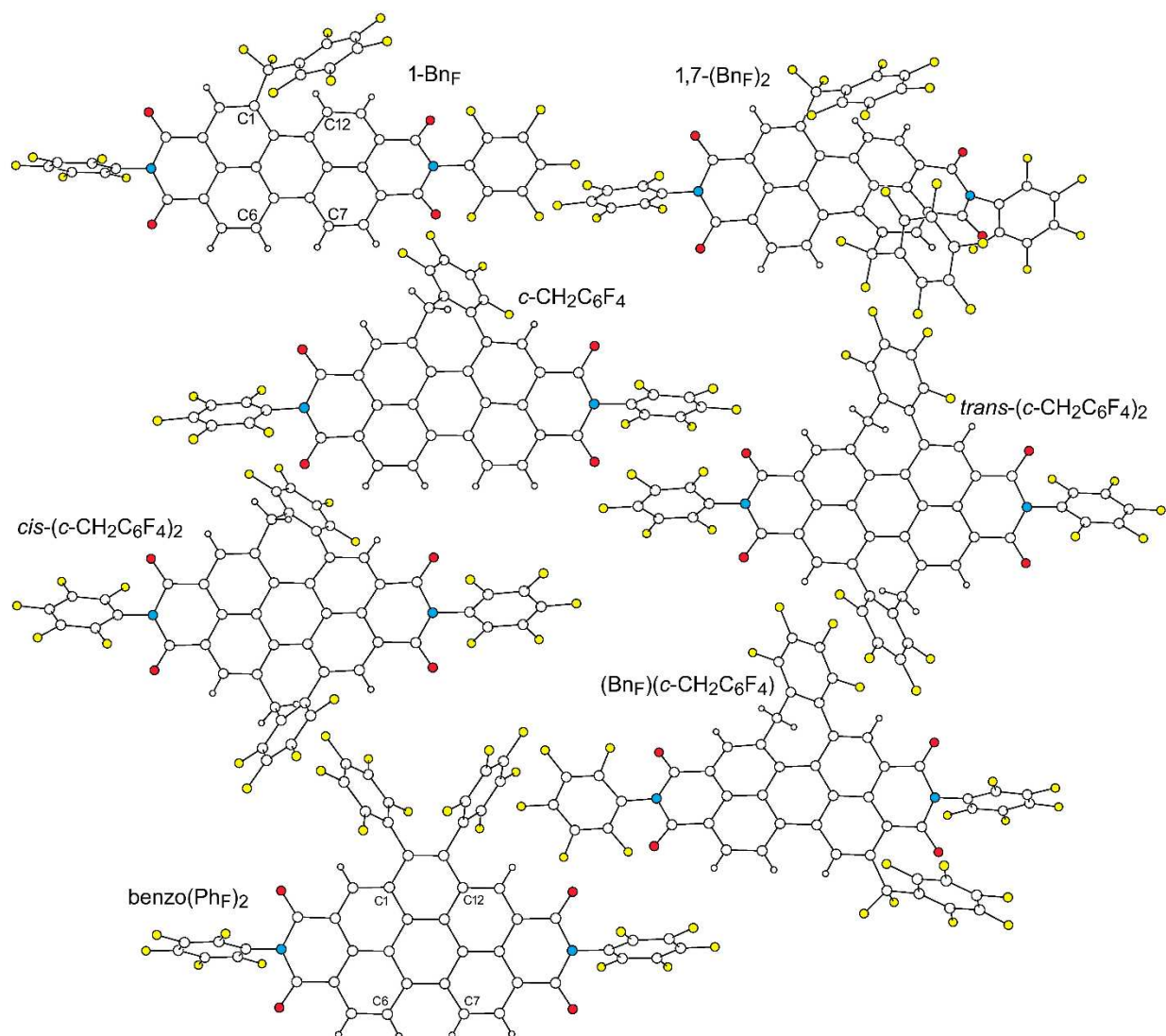


Figure 4.39. Ball-and-stick plots for the seven structures listed in Table 4.8 (the abbreviations used in this figure are defined in Table 4.8).

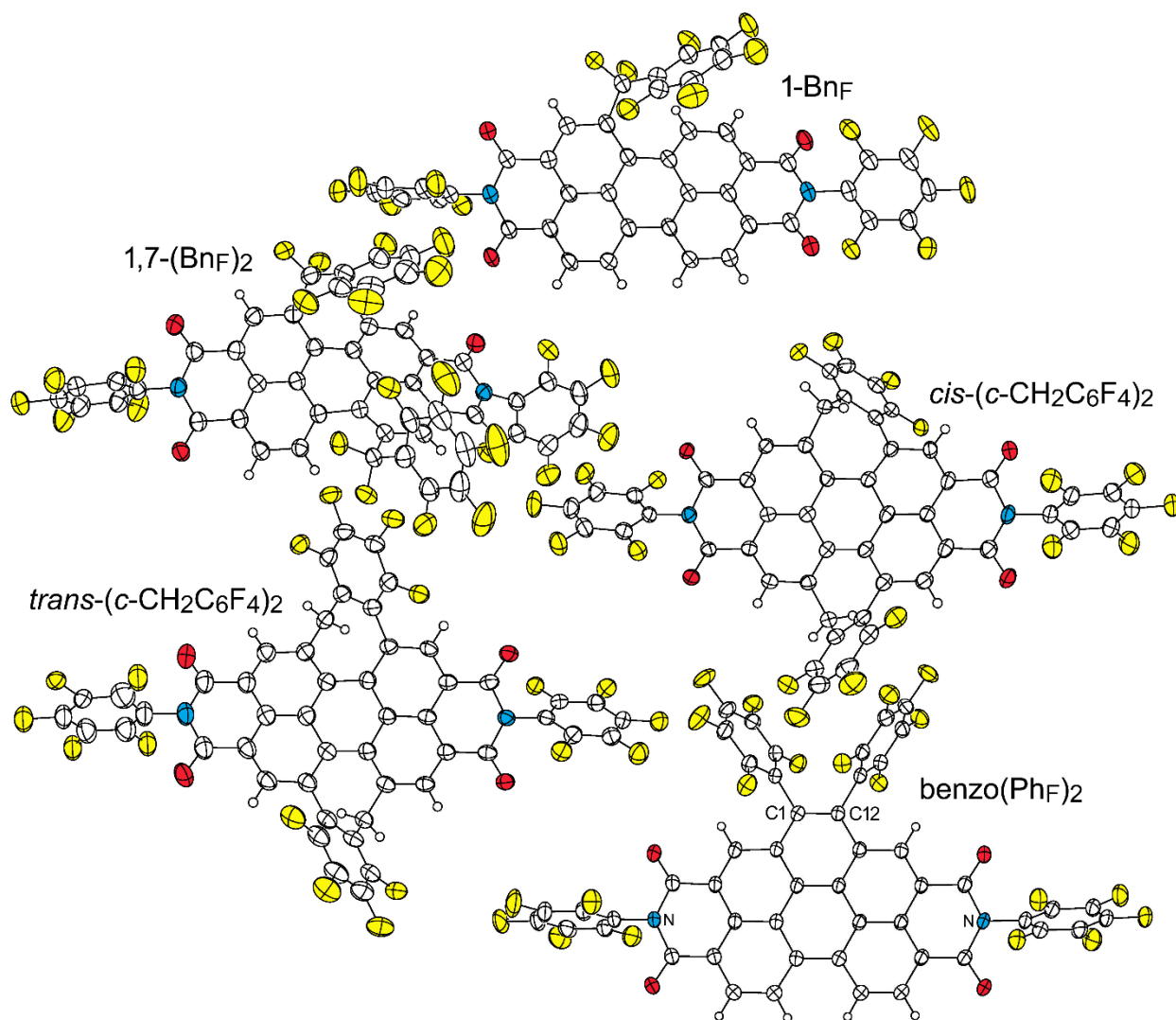


Figure 4.40. Thermal ellipsoid plots for the first five structures listed in Table 4.8, which are also the five structures listed in Table 4.9. Hydrogen atoms are drawn as spheres of arbitrary size. All nonhydrogen atoms are drawn as 50% probability ellipsoids except for the drawing of *trans*-(*c*-CH₂C₆F₄)₂, in which the atoms are drawn as 40% probability ellipsoids.

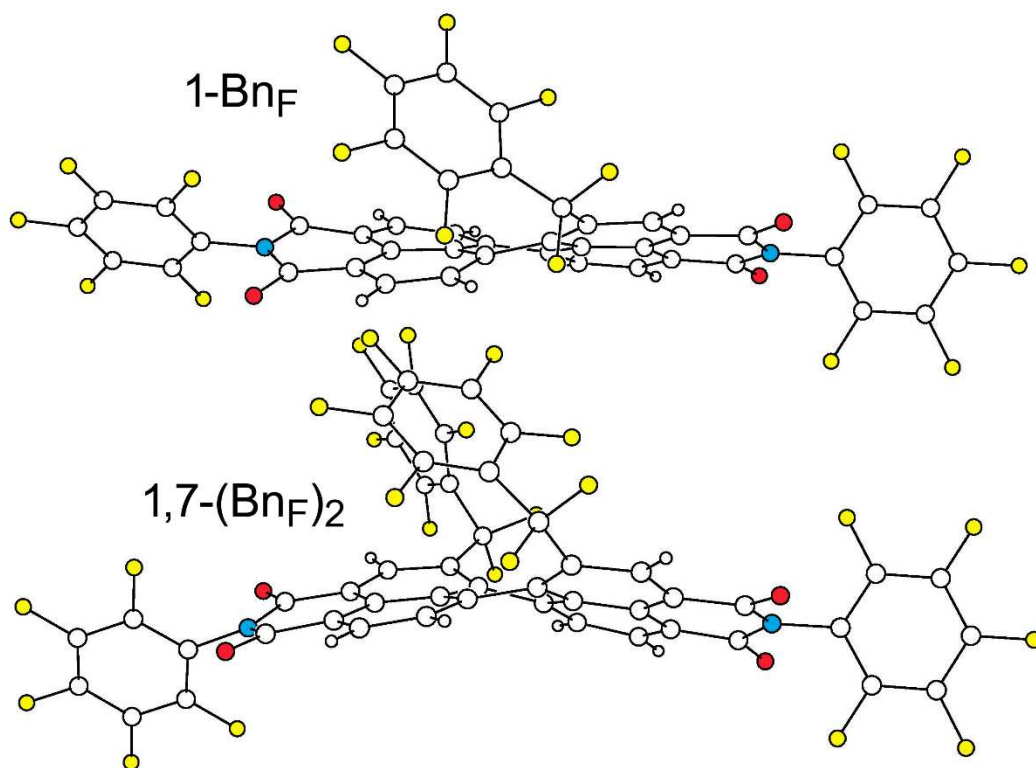


Figure 4.41. Views of the structures of $(\text{Ph}_F)_2\text{PDI-1-Bn}_F$ and $(\text{Ph}_F)_2\text{PDI-1,7-(Bn}_F)_2$ showing the distortions of the PDI aromatic cores from planarity (H atoms omitted for clarity; only N (blue), O (red), and F atoms (not colored) are shown as spheres).

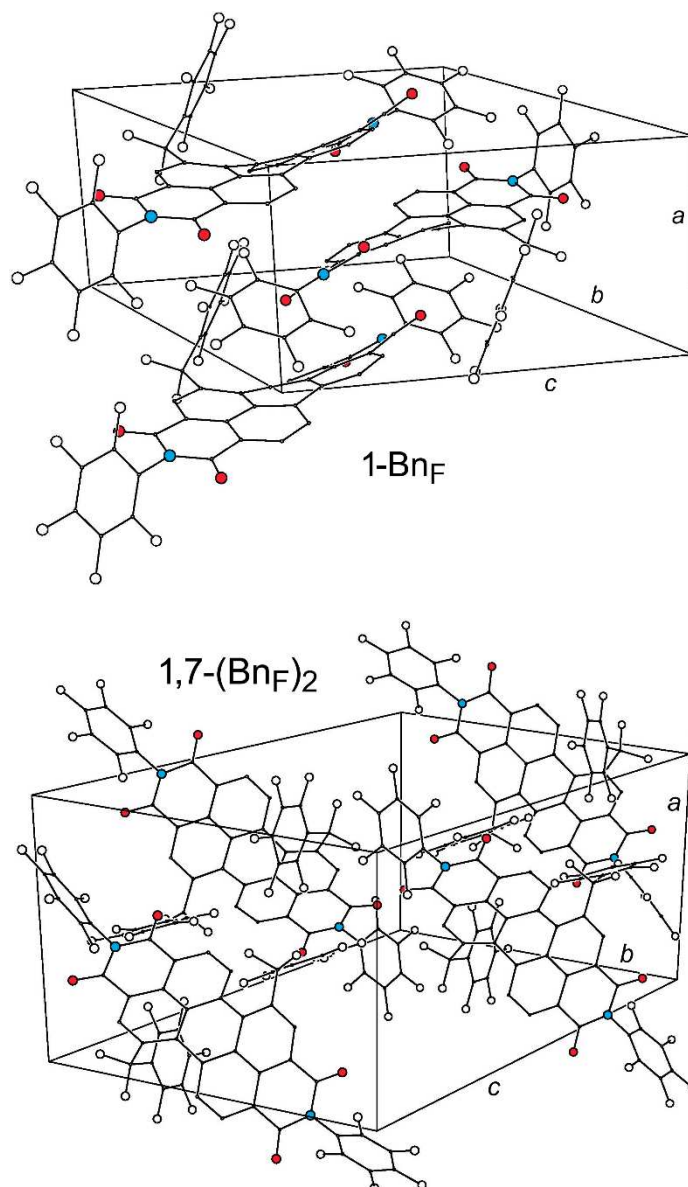


Figure 4.42. Views of the structures of $(\text{Ph}_F)_2\text{PDI-1-Bn}_F$ and $(\text{Ph}_F)_2\text{PDI-1,7-(Bn}_F)_2$ showing the packing of molecules in the unit cells (H atoms omitted for clarity; only N (blue), O (red), and F atoms (not colored) are shown as spheres). There is no significant intermolecular π - π overlap of aromatic portions of the molecules (i.e., the PDI cores and C_6F_5 moieties).

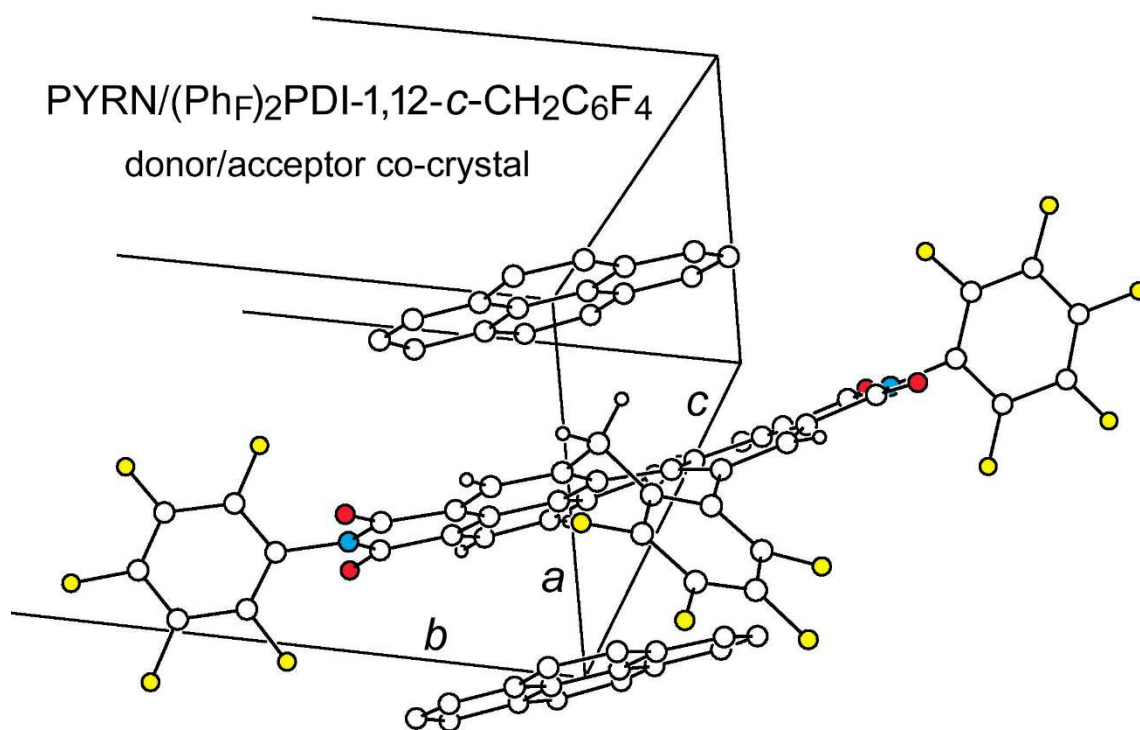


Figure 4.43. A portion of the unit cell in the donor/acceptor co-crystal structure of PYRN/(Ph_F)₂PDI-1,12-*cyclo*-CH₂C₆F₄ (H atoms omitted from the PYRN molecules; N, O, and F atoms are colored blue, red, and yellow, respectively). The PYRN and PDI molecules are stacked alternately along the crystallographic *a* axis. The perpendicular distance between the least-squares planes of the PYRN molecules is 6.90 Å (the *a* axis length is 7.711(4) Å). The nonplanar PDI aromatic core and the nonplanar conformation of the seven-membered ring that includes PDI atoms C1 and C12 are readily apparent.

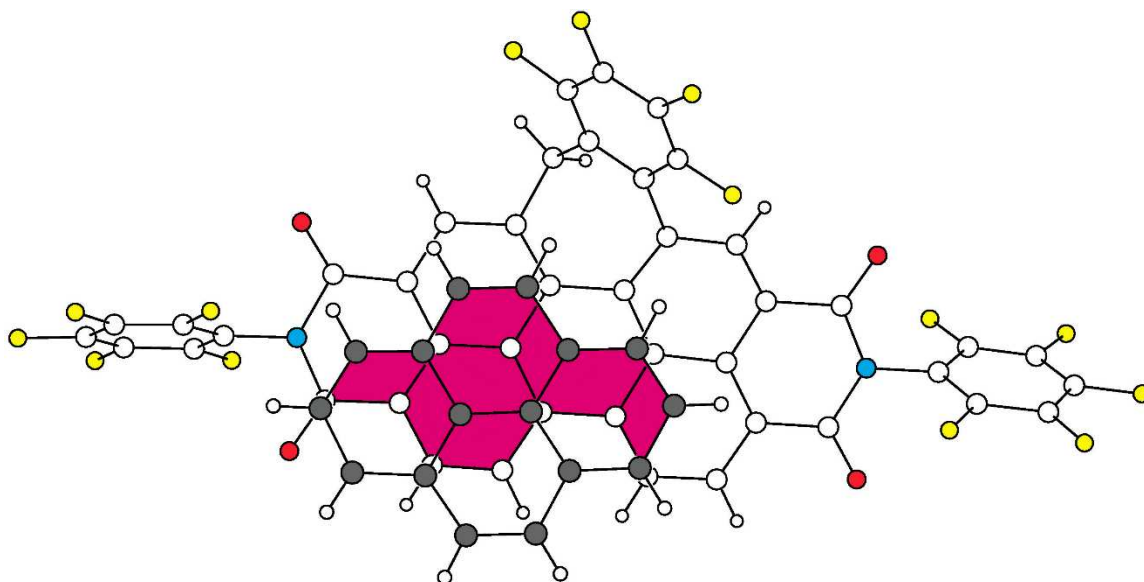


Figure 4.44. Parallel projection drawing of the PYRN donor (grey C atoms) and one of its neighboring $(\text{Ph}_F)_2\text{PDI-1,12-cyclo-CH}_2\text{C}_6\text{F}_4$ acceptors in the donor/acceptor co-crystal structure of $\text{PYRN}/(\text{Ph}_F)_2\text{PDI-1,12-cyclo-CH}_2\text{C}_6\text{F}_4$ (N, O, and F atoms are colored blue, red, and yellow, respectively). The least-squares plane of the PYRN C atoms is in the plane of the page. The region of overlap of the aromatic π systems of the two molecules is colored magenta. The perpendicular out-of-plane displacements of the PDI C atoms underneath the plane of the PYRN π system range from 3.35 to 3.63 Å (the average displacement of these eight PDI C atoms is 3.43 Å).

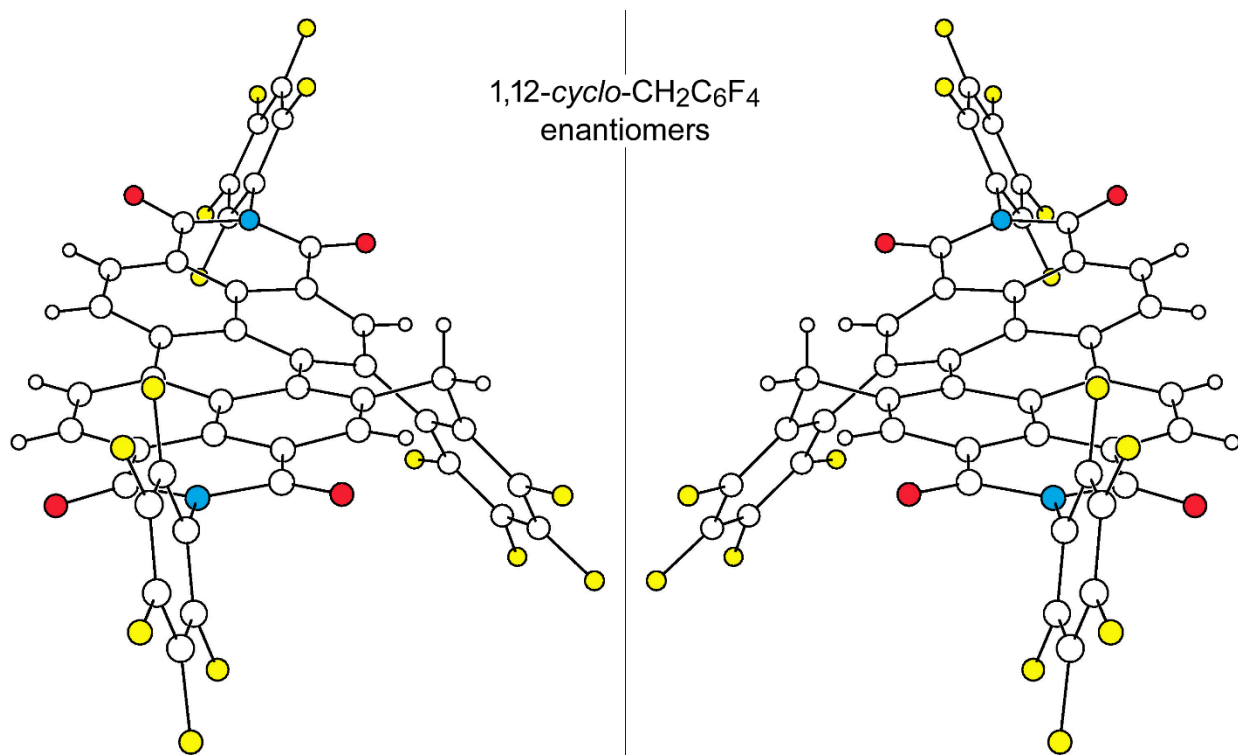


Figure 4.45. The PDI enantiomers in the donor/acceptor co-crystal X-ray structure of PYRN/(Ph_F)₂PDI-1,12-*cyclo*-CH₂C₆F₄ (PYRN omitted for clarity; N, O, and F atoms are colored blue, red, and yellow, respectively). The enantiomers are related by inversion of the seven-membered ring.

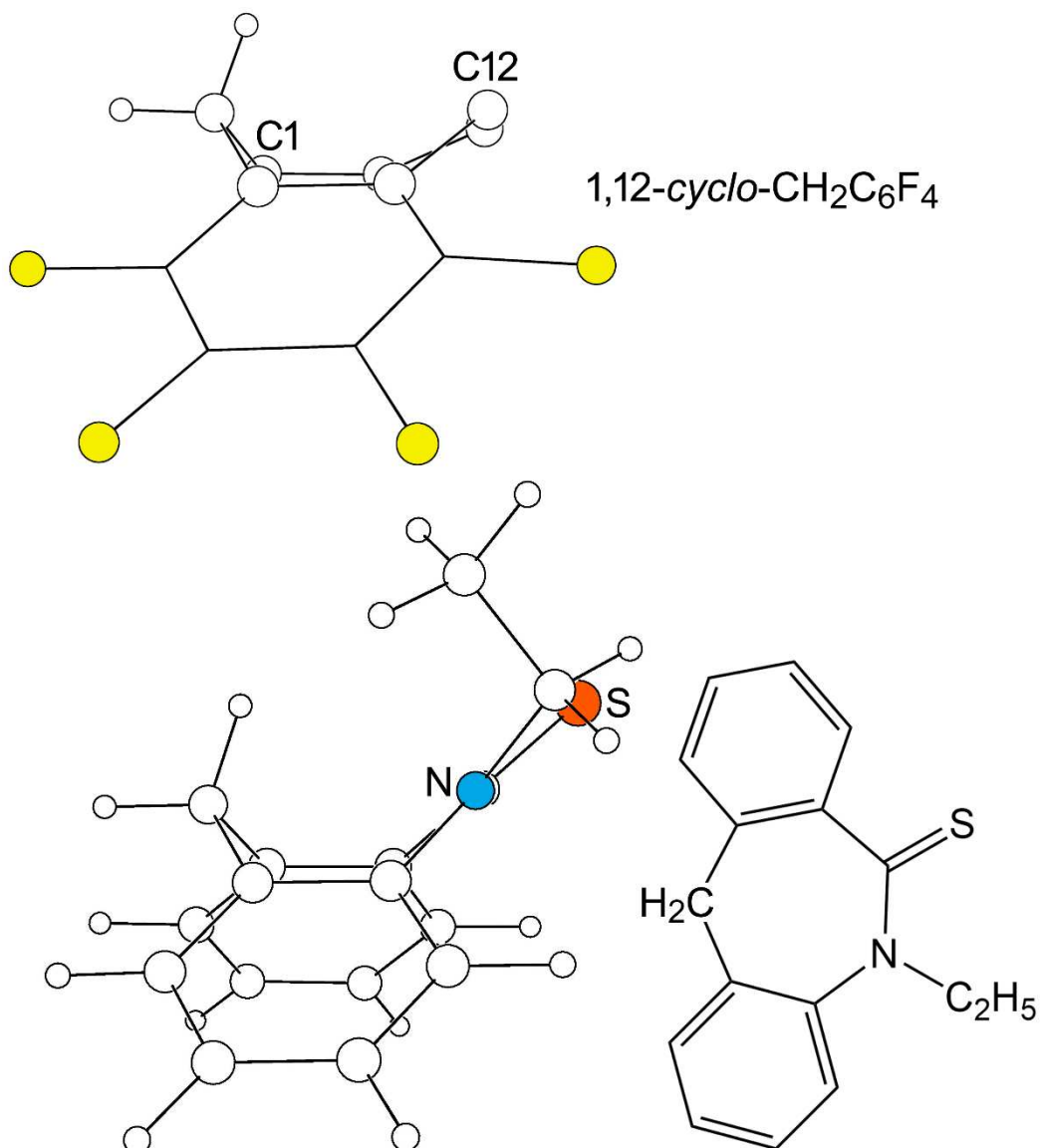


Figure 4.46. The X-ray structure of 5-ethyl-5,6-dihydro-11*H*-dibenzo[*b,e*]azepine-6-thione, oriented to highlight the boat configuration of the seven-membered ring.¹⁶⁴ The N and S atoms are colored blue and orange, respectively. This compound was shown to have a barrier to ring inversion (i.e., racemization) of 90.4 kJ mol⁻¹.

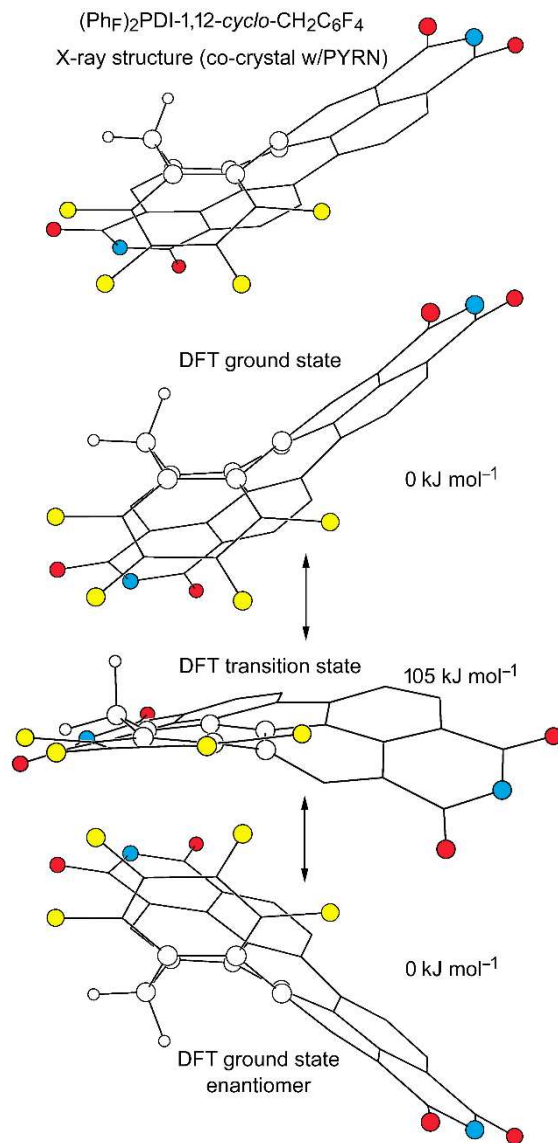


Figure 4.47. Four drawings of the structure of $(\text{Ph}_F)_2\text{PDI-1,12-cyclo-CH}_2\text{C}_6\text{F}_4$ oriented to highlight the boat configuration of the seven-membered rings (C_6F_5 groups and H atoms other than the CH_2 group omitted for clarity). The top drawing is from the donor/acceptor co-crystal X-ray structure of $\text{PYRN}/(\text{Ph}_F)_2\text{PDI-1,12-cyclo-CH}_2\text{C}_6\text{F}_4$. The next drawing down is the DFT-optimized structure of the PDI compound starting with the X-ray coordinates, demonstrating that the PYRN molecule in the co-crystal structure did not significantly affect the structure of the PDI compound. The last two drawings are the DFT ring-inversion transition state and the other enantiomer. The DFT-predicted transition-state energy is 105 kJ mol^{-1} higher than the ground-state energy.

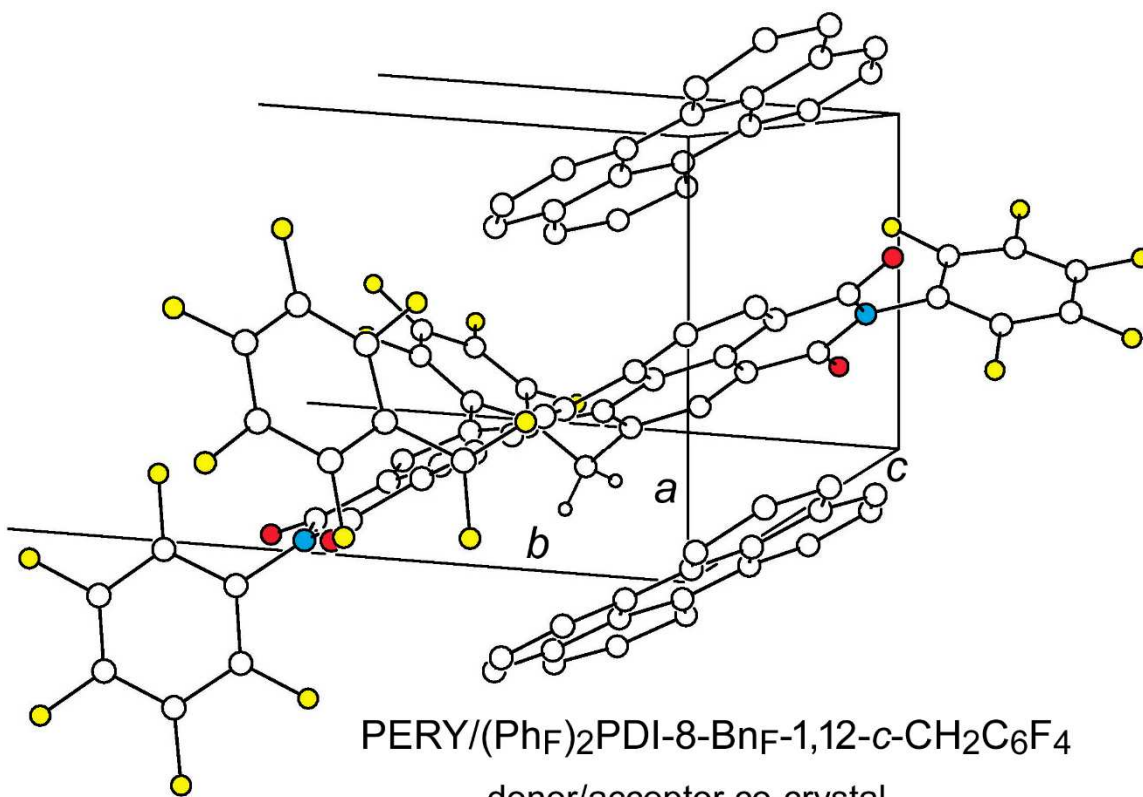


Figure 4.48. A portion of the unit cell in the donor/acceptor co-crystal structure of PERY/(Ph_F)₂PDI-8-Bn_F-1,12-*cyclo*-CH₂C₆F₄ (H atoms omitted except for the CH₂ group in the seven-membered ring; N, O, and F atoms are colored blue, red, and yellow, respectively). The PERY and PDI molecules are stacked alternately along the crystallographic *a* axis. The perpendicular distance between the least-squares planes of the PERY molecules is 7.10 Å (the *a* axis length is 7.930(4) Å). The nonplanar PDI aromatic core and the nonplanar conformation of the seven-membered ring that includes PDI atoms C1 and C12 are readily apparent.

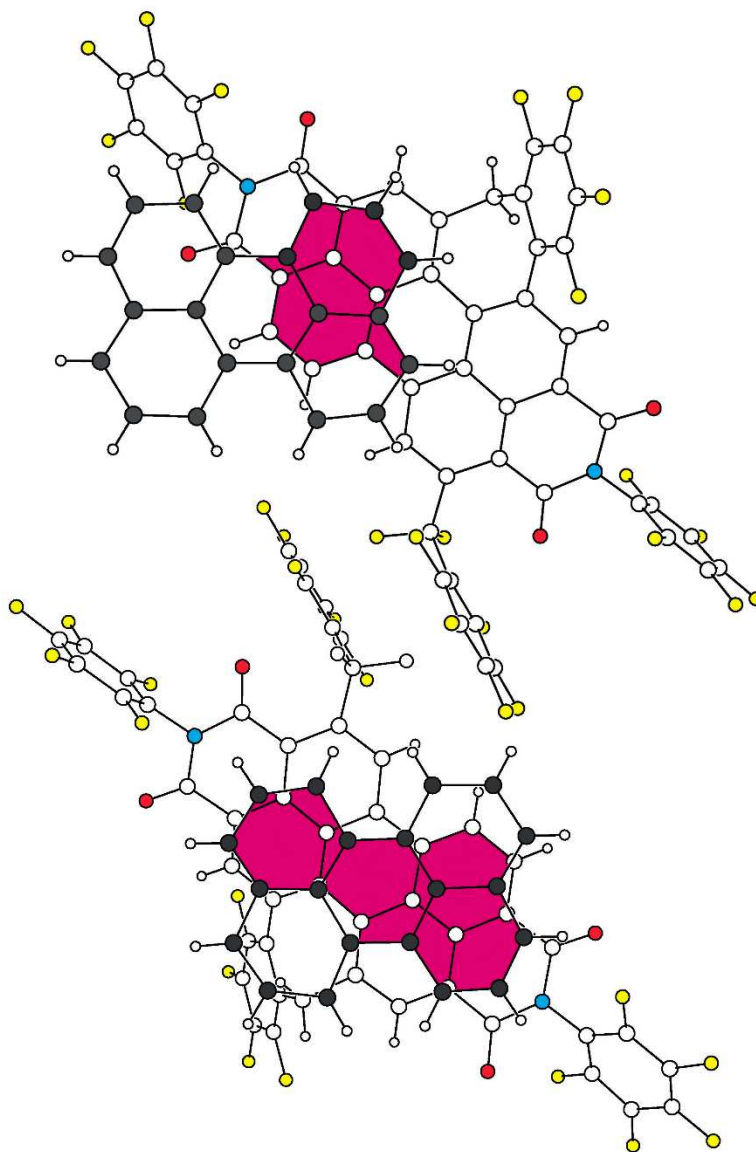


Figure 4.49. Parallel projection drawings of the PERY donors (grey C atoms) on either side of the $(\text{Ph}_F)_2\text{PDI-8-Bn}_F\text{-1,12-cyclo-CH}_2\text{C}_6\text{F}_4$ acceptor in the co-crystal structure of $\text{PERY}/(\text{Ph}_F)_2\text{PDI-8-Bn}_F\text{-1,12-cyclo-CH}_2\text{C}_6\text{F}_4$ (N, O, and F atoms are colored blue, red, and yellow, respectively). The least-squares planes of the PERY C atoms are both in the plane of the page (i.e., their least-squares planes are rigorously parallel). The regions of overlap of the aromatic π systems of the pairs of molecules are colored magenta. The perpendicular out-of-plane displacements of the PDI C atoms underneath the plane of the PERY π system (OOPDs) in the upper drawing range from 3.42 to 3.56 Å and average 3.47 Å. In the lower drawing the OOPDs range from 3.42 to 3.69 Å and average 3.58 Å.

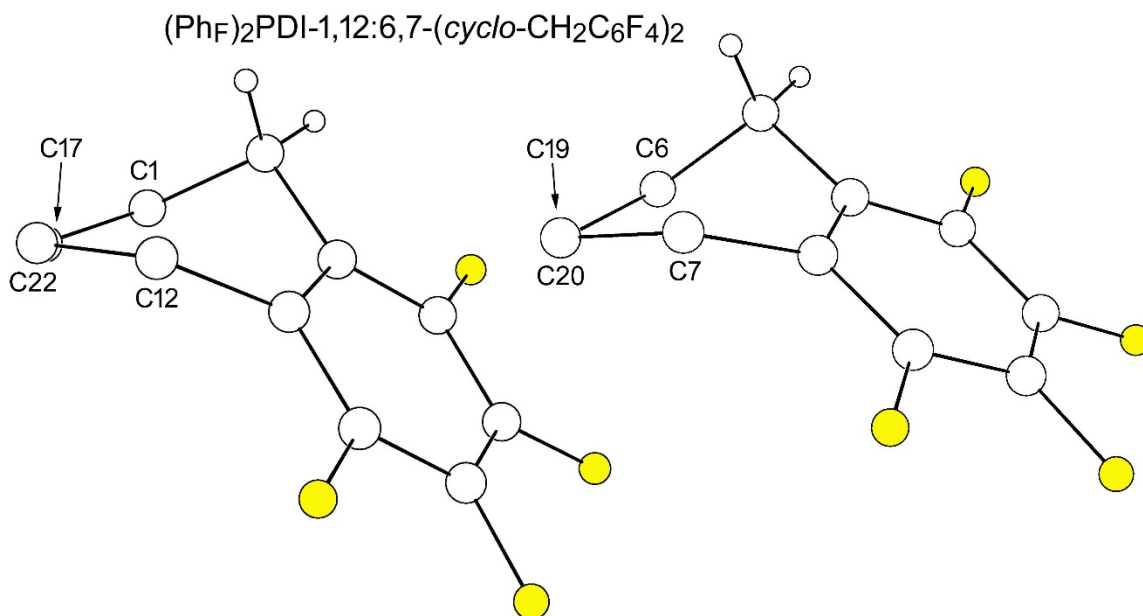


Figure 4.50. The nonplanar conformations of the seven-membered rings in the *cis* isomer (Ph_F)₂PDI-1,12:6,7-(*cyclo*-CH₂C₆F₄)₂. The atom numbering is based on the locants shown in Figure 4.37. The conformations of the seven-membered rings in the *trans* isomer (Ph_F)₂PDI-1,12:6,7-(*cyclo*-CH₂C₆F₄)₂ (not shown) are similar.

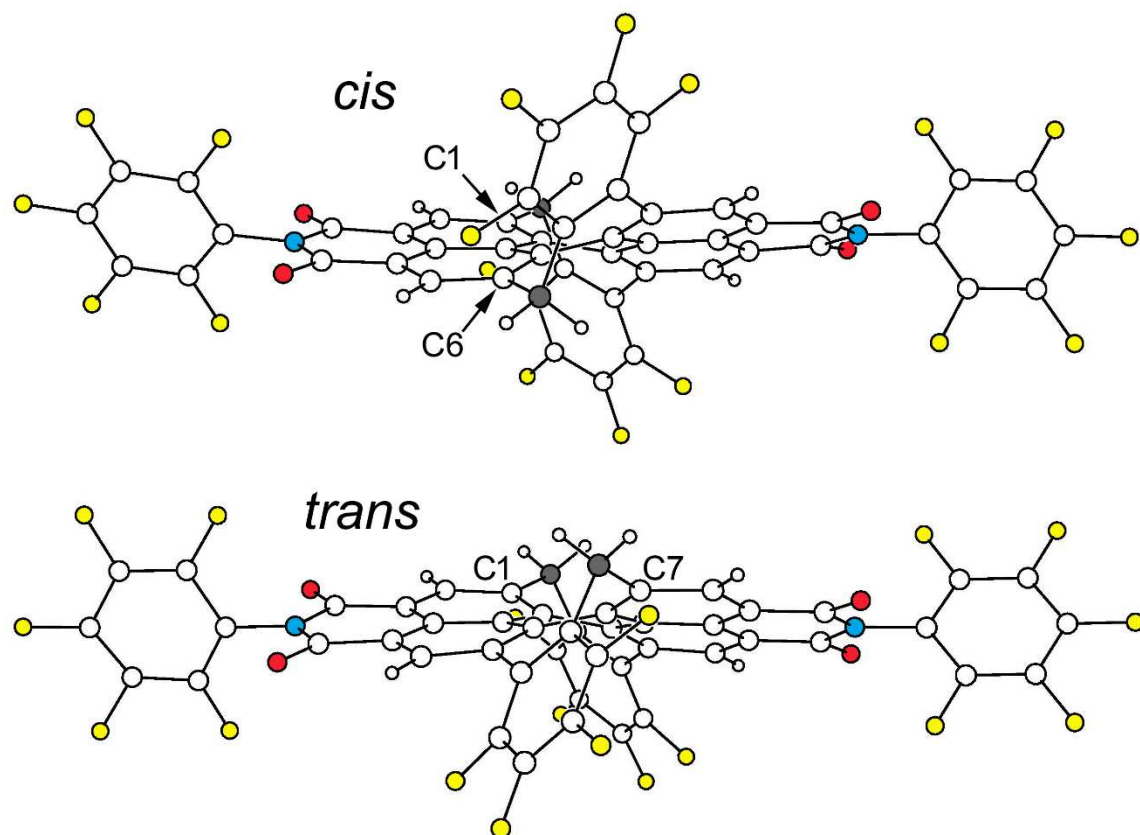


Figure 4.51. Drawings of $(\text{Ph}_F)_2\text{PDI-1,12:6,7-(cyclo-CH}_2\text{C}_6\text{F}_4)_2$ (*cis*; top) and $(\text{Ph}_F)_2\text{PDI-1,12:7,6-(cyclo-CH}_2\text{C}_6\text{F}_4)_2$ (*trans*; bottom). The N, O, and F atoms are colored blue, red, and yellow, respectively, and the CH_2 carbon atoms are highlighted as gray spheres. The distortion of the PDI core in both compounds is readily apparent. In addition, note that the CH_2 groups attached to C1 and C6 are on opposite sides of the distorted PDI plane in the *cis* compound, and the CH_2 groups attached to C1 and C7 are on the same side of the PDI plane in the *trans* compound. The orientations of the CH_2 groups are more readily seen in Figure 4.52.

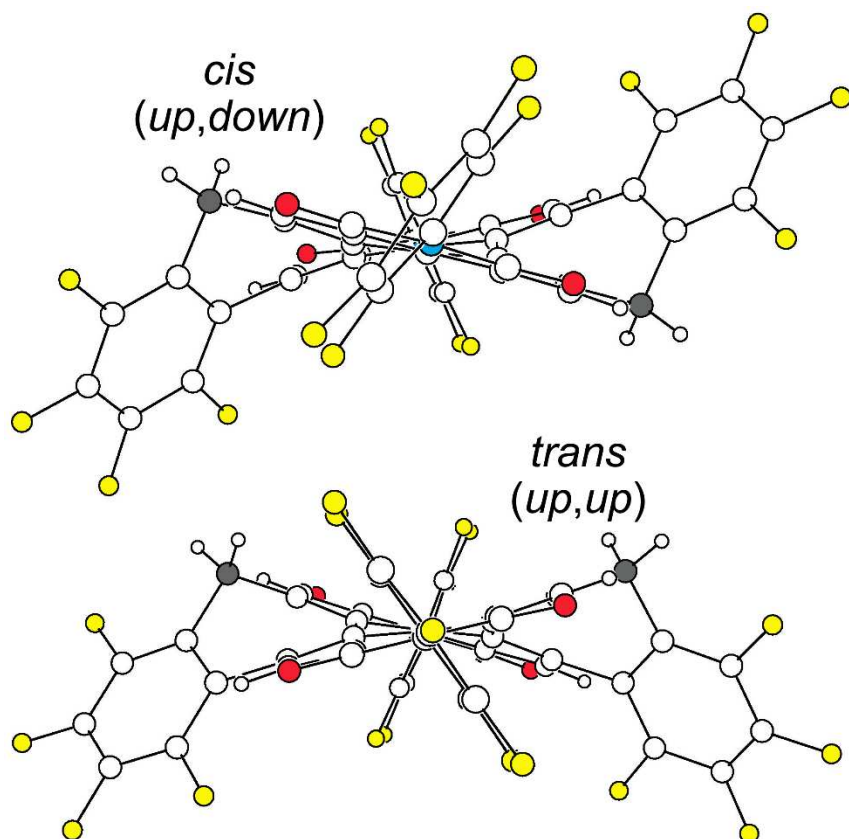


Figure 4.52. Drawings of $(\text{Ph}_F)_2\text{PDI-1,12:6,7-(cyclo-CH}_2\text{C}_6\text{F}_4)_2$ (*cis*; top) and $(\text{Ph}_F)_2\text{PDI-1,12:7,6-(cyclo-CH}_2\text{C}_6\text{F}_4)_2$ (*trans*; bottom) rotated 90° from their positions in Figure 4.44. The N, O, and F atoms are colored blue, red, and yellow, respectively, and the CH_2 carbon atoms are highlighted as gray spheres. With respect to the mean PDI plane in each compound, the CH_2 -up- CH_2 -down (*up,down*) orientations in the *cis* isomer and the CH_2 -up- CH_2 -up (*up,up*) orientations in the *trans* isomer are readily apparent.

(Ph_F)₂PDI-1,12:6,7-(cyclo-CH₂C₆F₄)₂ akamptisomers

DFT-optimized structures

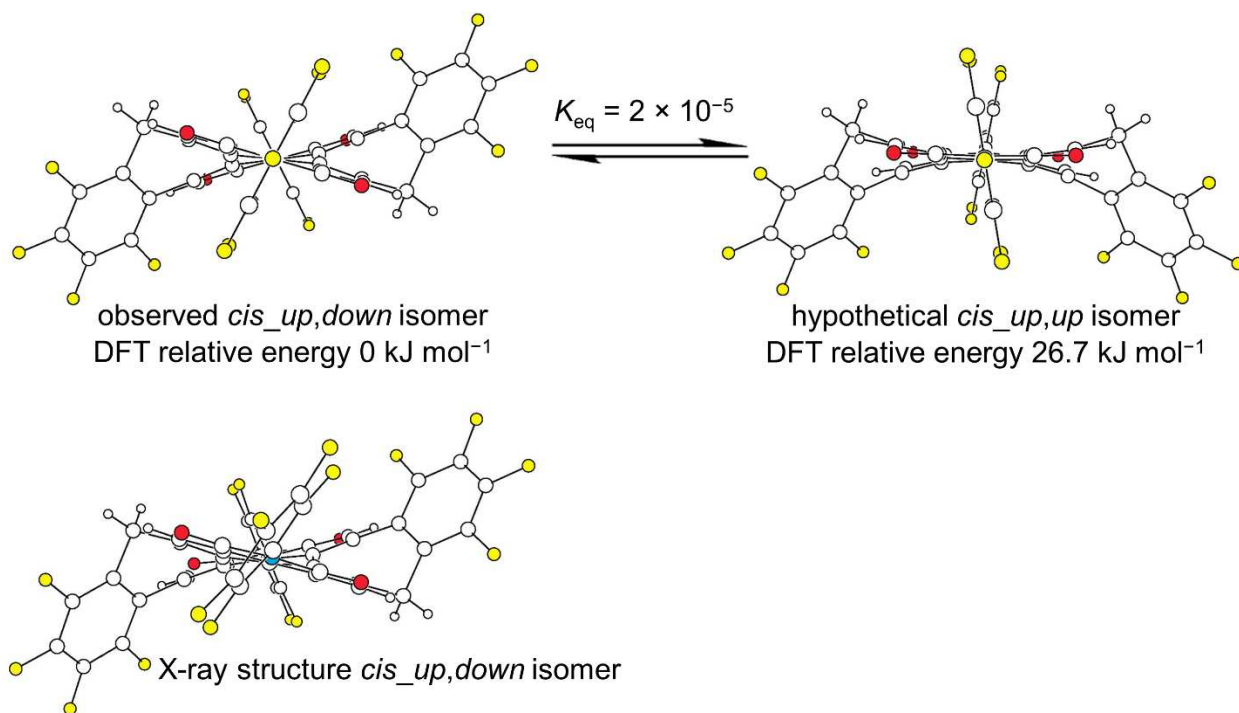


Figure 4.53. (Top) The DFT-optimized structures of the *up,down* and *up,up* seven-membered ring conformers of the *cis* isomer (Ph_F)₂PDI-1,12:6,7-(cyclo-CH₂C₆F₄)₂ (O and F atoms are red and yellow, respectively; N atoms are hidden from view). (Bottom) The X-ray structure of the *cis* isomer (Ph_F)₂PDI-1,12:6,7-(cyclo-CH₂C₆F₄)₂ (see also Figure 4.52), showing that the DFT-optimized lower-energy *up,down* conformer structure is virtually identical to the observed X-ray structure (N, O, and F atoms are blue, red, and yellow, respectively). The DFT-predicted relative energies show that the observed *up,down* conformer structure is favored over the hypothetical *up,up* structure by 26.7 kJ mol⁻¹.

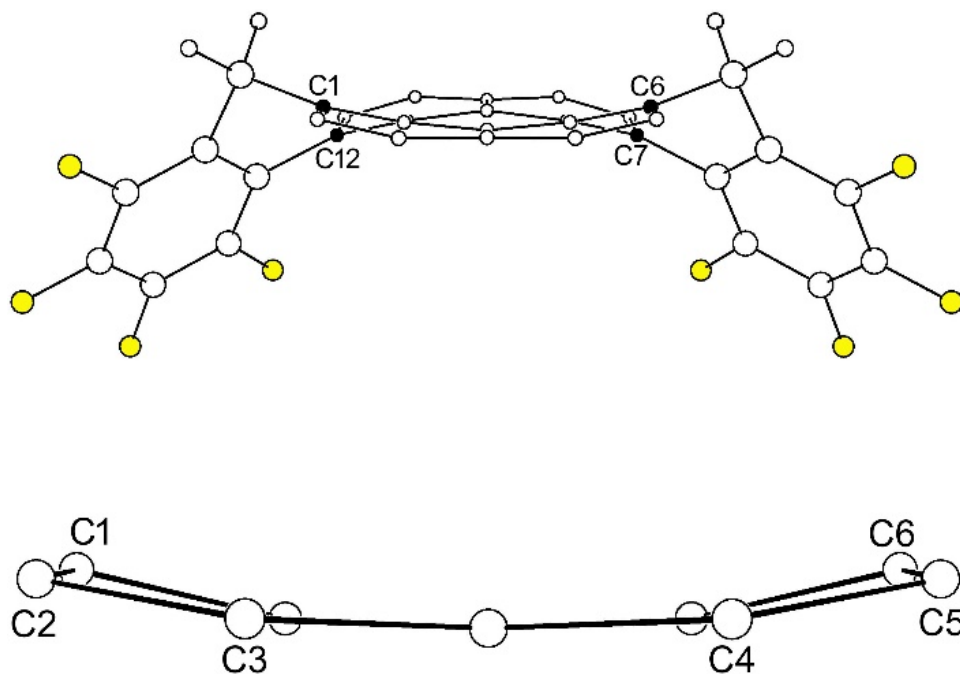


Figure 4.54. Fragments of the DFT *cis-up,up* isomer of $(\text{PhF})_2\text{PDI-1,12:6,7-(cyclo-CH}_2\text{C}_6\text{F}_4)_2$. The upper drawing shows only the two naphthalene (NAPH) fragments and the two seven-membered-ring *cyclo-CH*₂C₆F₄ substituents. The NAPH C atoms are small spheres so that their bent, shallow bowl conformations can be readily seen. The lower drawing shows only the front NAPH fragment that contains C1 and C6.

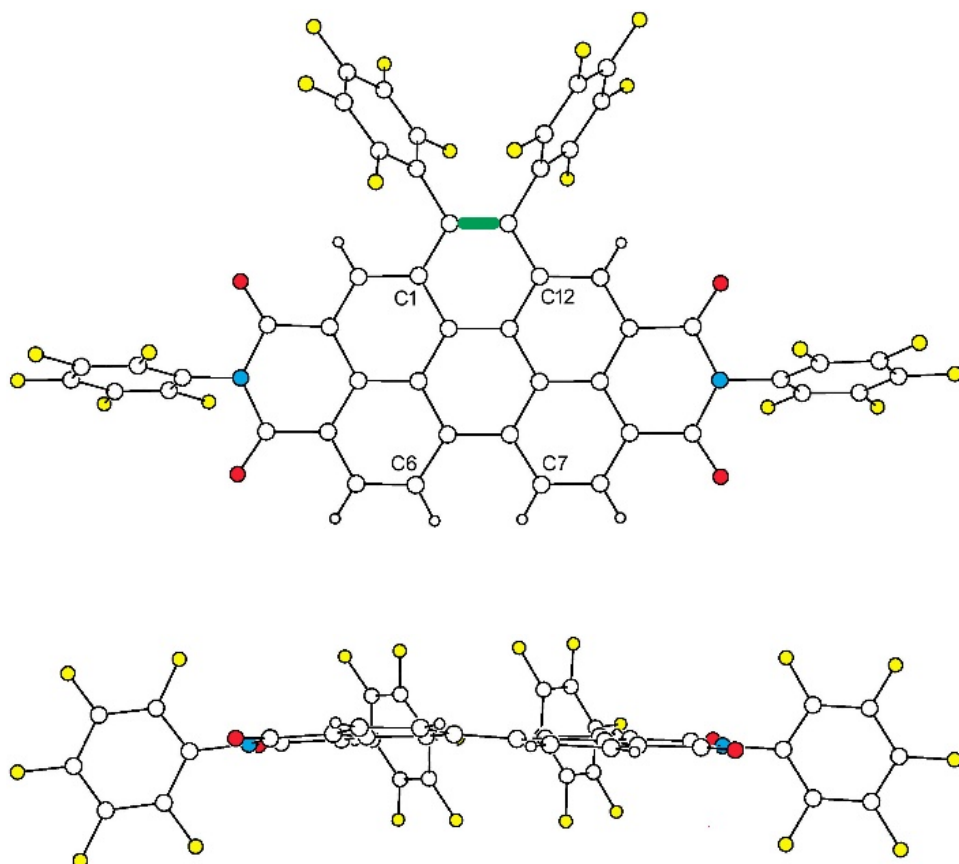


Figure 4.55. The X-ray structure of $(\text{PhF})_2\text{PDI-1,12-benzo}(\text{PhF})_2$. The new $\text{C}(\text{sp}^2)\text{-C}(\text{sp}^2)$ bond is highlighted in green in the upper drawing. The N, O, and F atoms are, blue, red, and yellow, respectively.

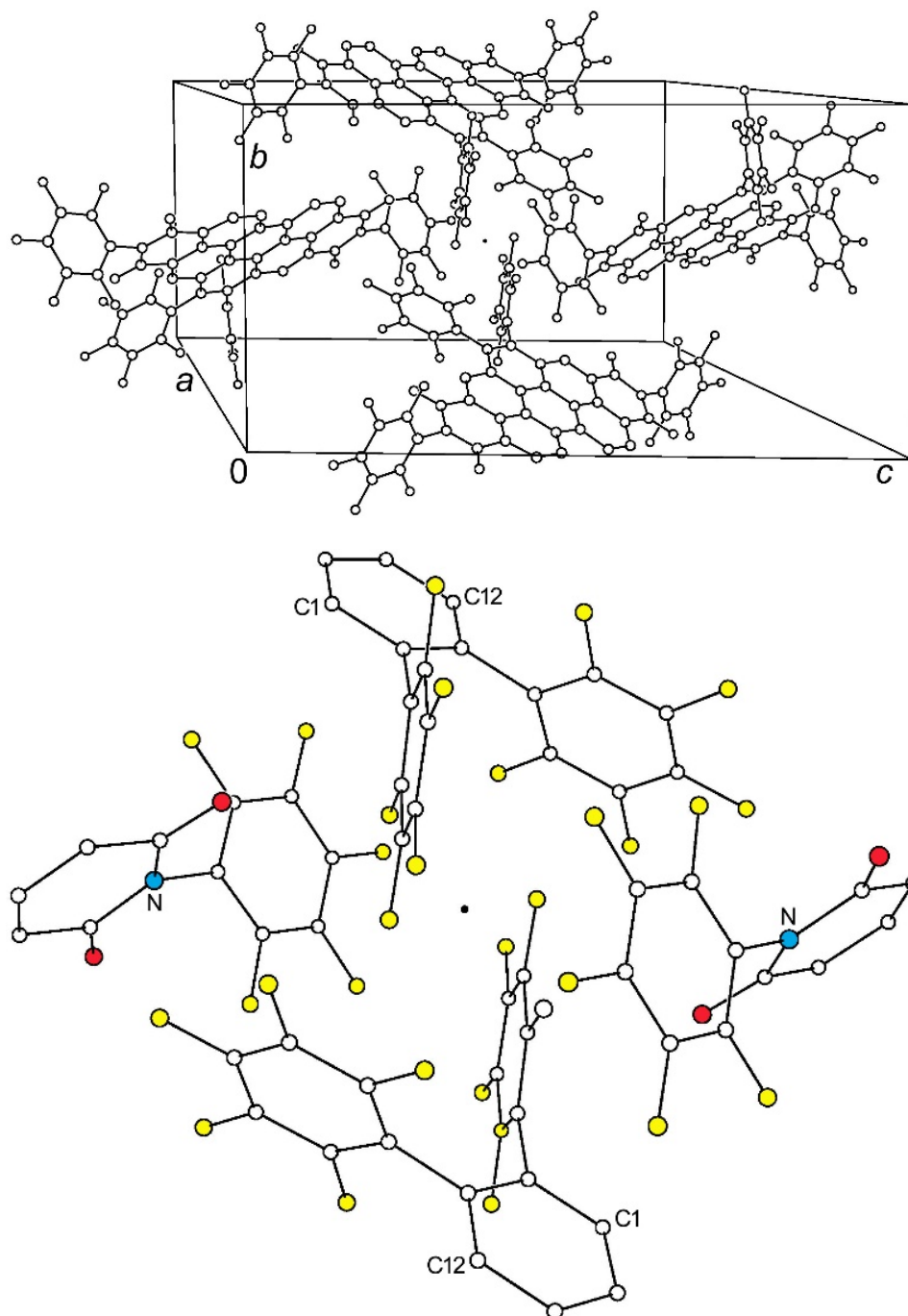


Figure 4.56. The packing of molecules in the X-ray structure of $(\text{PhF})_2\text{PDI-1,12-benzo}(\text{PhF})_2$. The bottom drawing is an expansion of the central part of the unit cell drawing, showing the lack of π - π overlap with the six PhF groups on the four closest molecules (N, O, and F atoms are blue, red, and yellow, respectively). In both drawings the central black dot is the centroid of the four molecules.

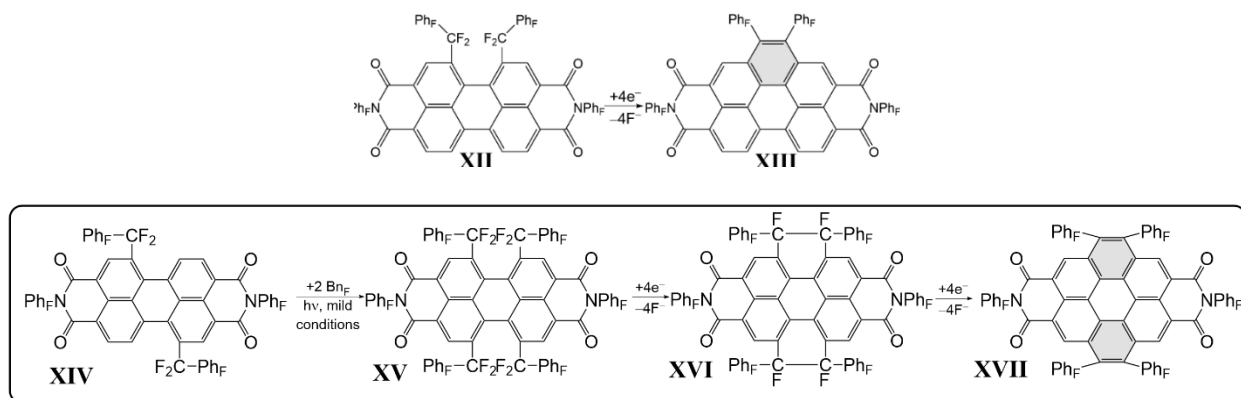


Figure 4.57 Possible pathways to formation of BPDI (and *bis*BPDI) and its derivatives.

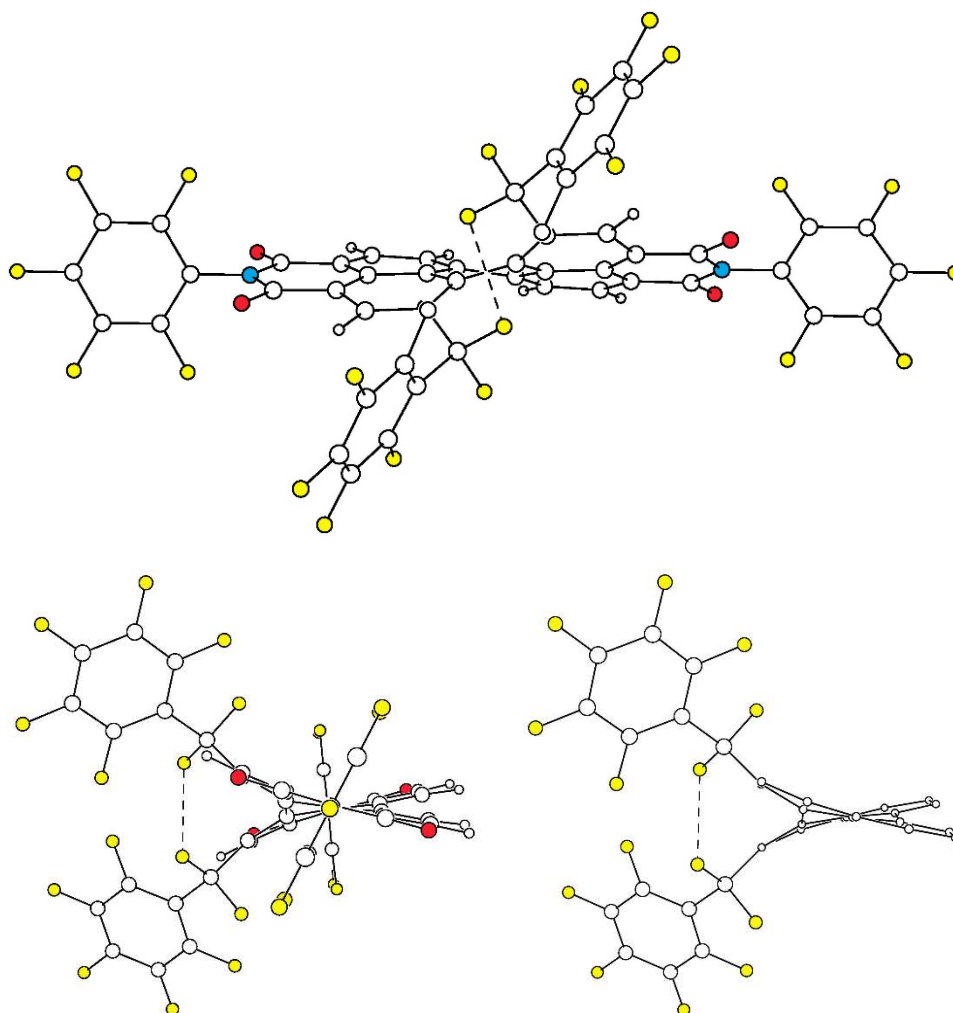


Figure 4.58. The DFT-optimized structure of the putative intermediate $(\text{Ph}_F)_2\text{PDI-1,12-(BnF)}_2$ (N, O, and F atoms are blue, red, and yellow, respectively). The distance between the closest F atoms of the perfluorobenzyl CF_2 groups (dashed lines) is 2.59 Å. The lower-right drawing only includes the two NAPH fragments and the $\text{CF}_2\text{C}_6\text{F}_5$ substituents.

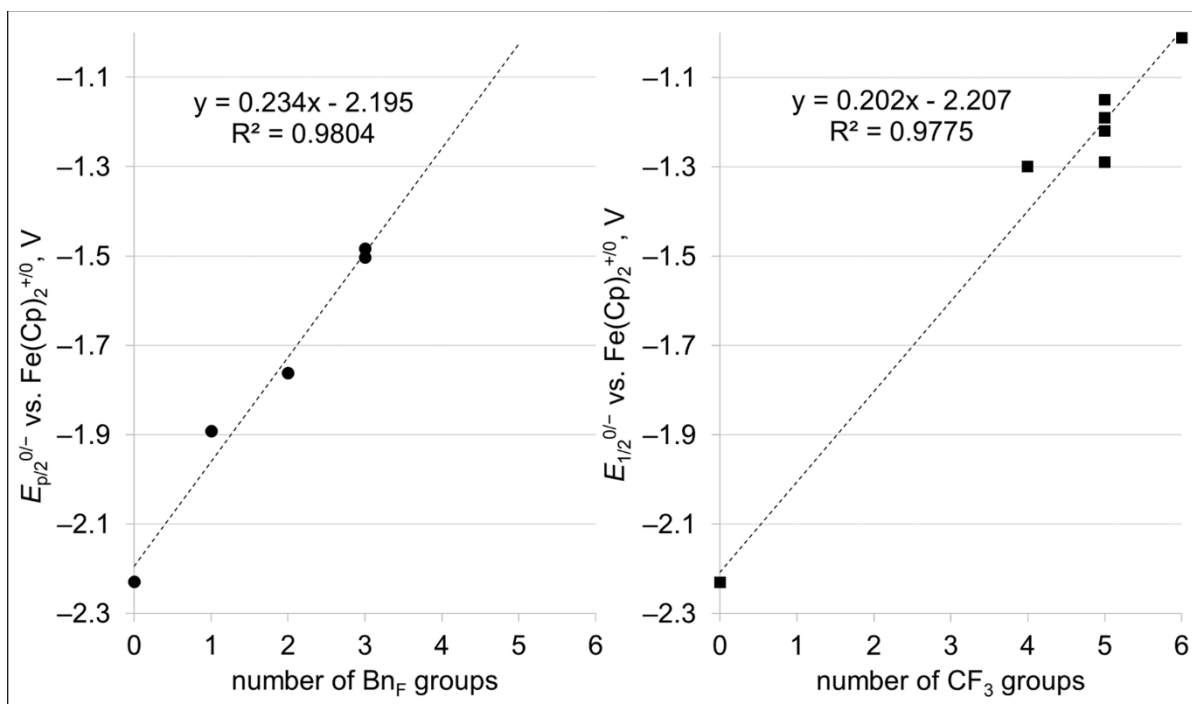


Figure 4.59. Left) change in $E_{p/2}^{0/-}$ as a function of number of Bn_F groups substituted onto perylene. Value used for unsubstituted perylene is also the $E_{p/2}^{0/-}$ potential.¹¹⁸ Right) change in $E_{1/2}^{0/-}$ as a function of CF_3 groups (not this work).¹¹⁸ All values are referenced vs. $E_{1/2}^{+/0}$ of ferrocene ($\text{Fe}(\text{Cp})_2$).

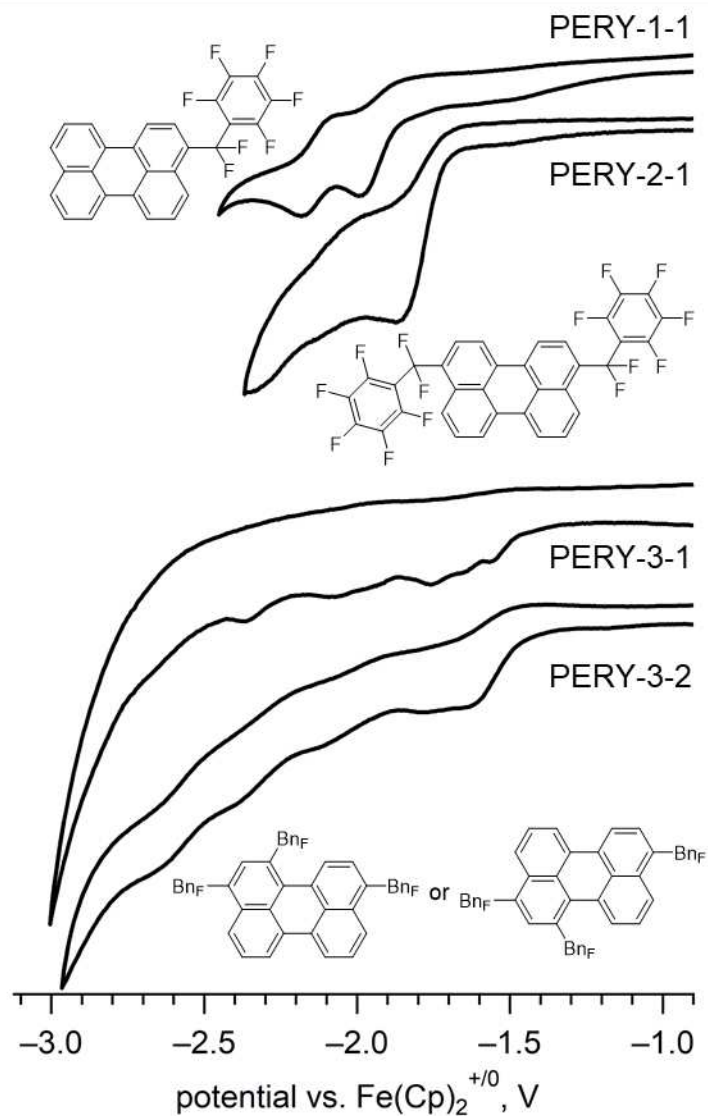


Figure 4.60. Cyclic voltammogram of PERY-1-1, PERY-2-1, PERY-3-1 and PERY-3-2 taken in 0.1 M $\text{N}(\text{nBu})_4\text{ClO}_4$ in dimethoxyethane, using a platinum working and counter electrodes, silver wire quasi-reference electrode, at a scan rate of 500 mV s^{-1} . Ferrocene ($\text{Fe}(\text{Cp})_2$) was used as an internal reference.

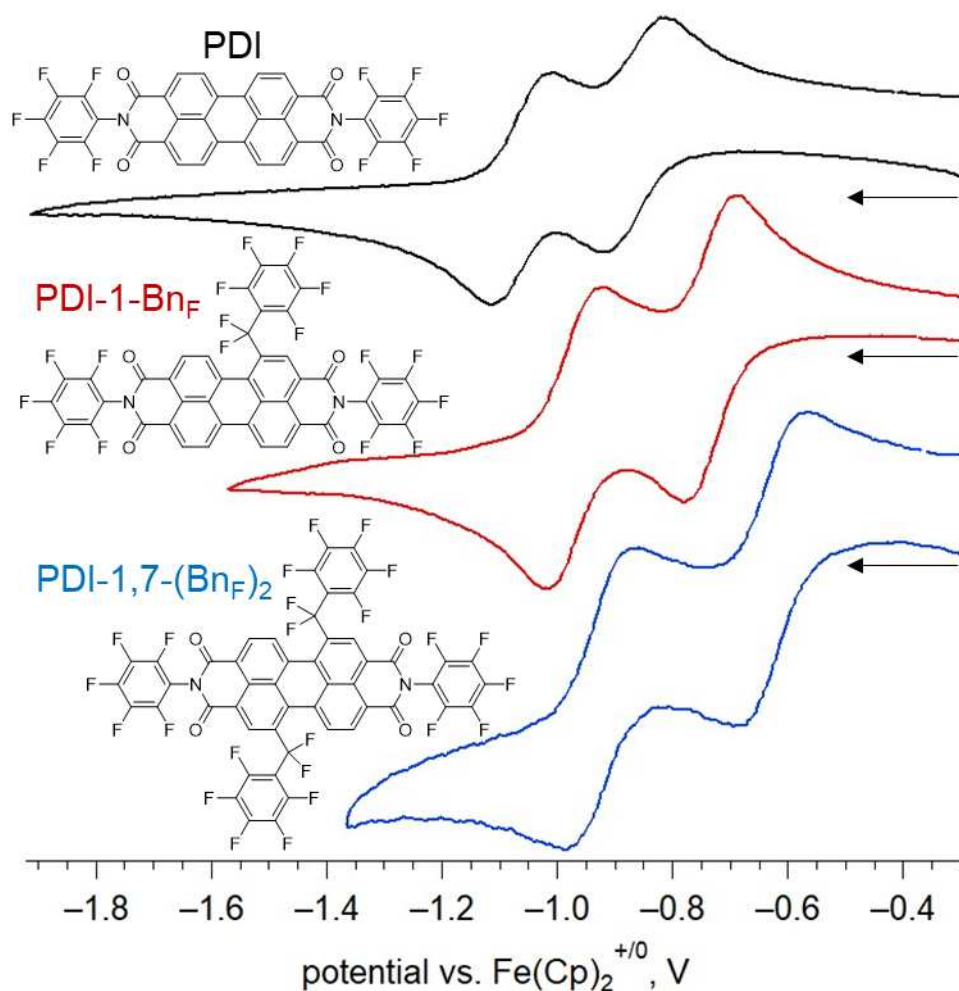


Figure 4.61. Cyclic voltammograms of PDI, PDI-1-Bn_F, and PDI-1,7-(Bn_F)₂, taken in 0.1 M TBAPF₆ in DCM using a platinum working and counter electrodes and silver wire quasi-reference electrode at a scan rate of 100 mV s⁻¹. Ferrocene (Fe(Cp)₂) was used as an internal reference.

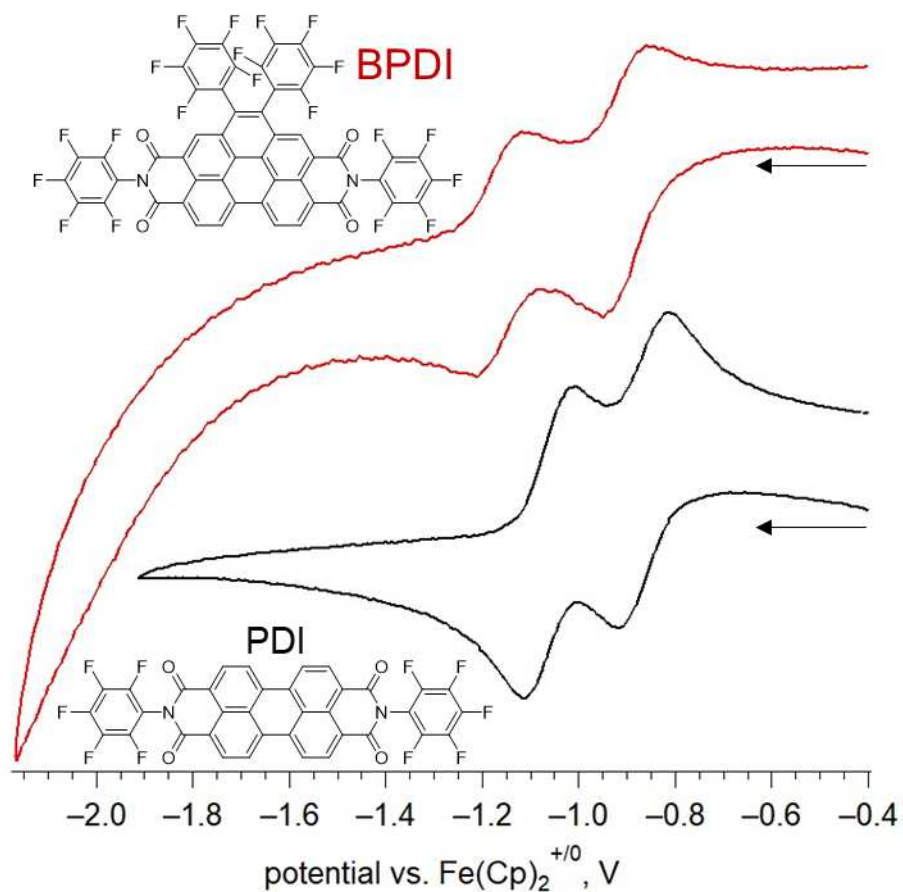


Figure 4.62. Cyclic voltammograms of PDI and BPDI taken in 0.1 M TBAPF₆ in DCM using a platinum working and counter electrodes and silver wire quasi-reference electrode at a scan rate of 100 mV s⁻¹. Ferrocene ($\text{Fe}(\text{Cp})_2$) was used as an internal reference.

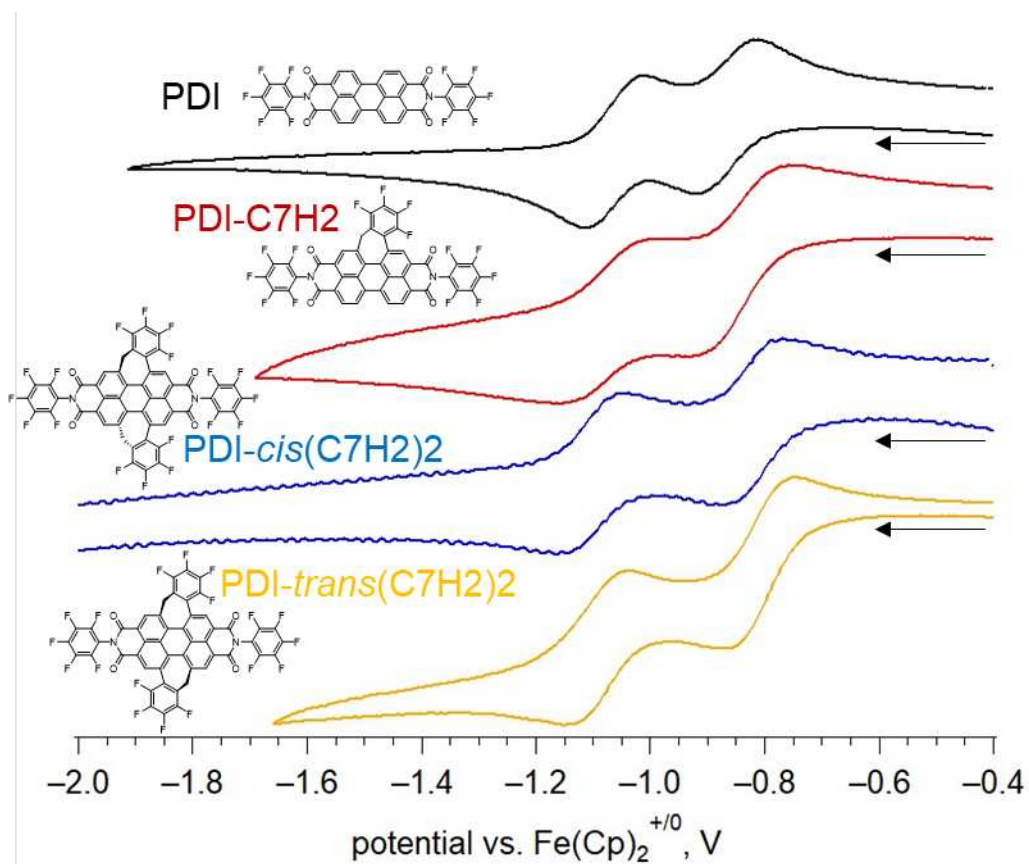


Figure 4.63. Cyclic voltammograms of PDI, PDI-C7H2, PDI-*cis*(C7H2)2 and PDI-*trans*(C7H2)2 taken in 0.1 M TBAPF₆ in DCM using a platinum working and counter electrodes and silver wire quasi-reference electrode at a scan rate of 100 mV s⁻¹. Ferrocene (Fe(Cp)₂) was used as an internal reference.

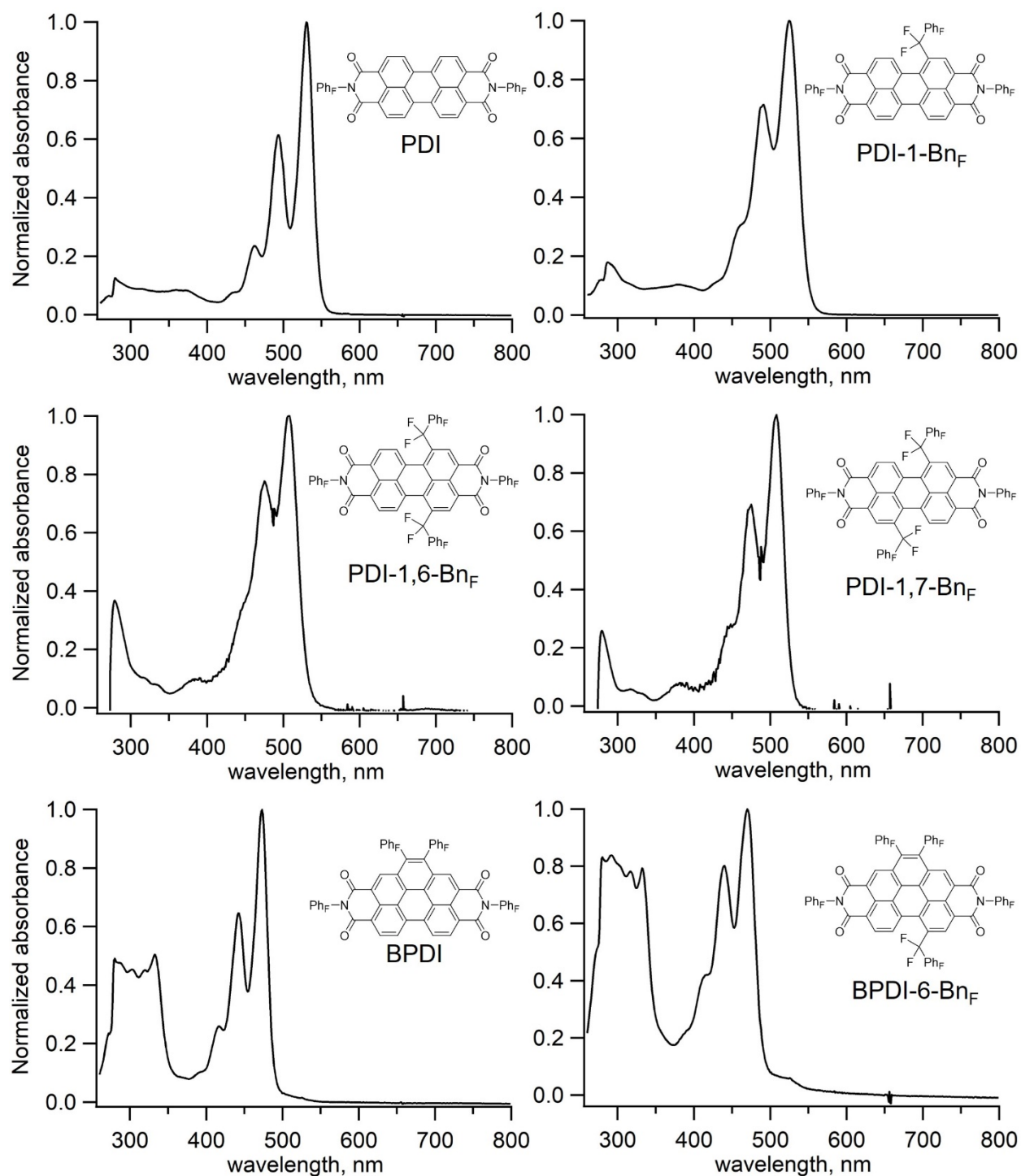


Figure 4.64. UV-vis absorbance spectra of PDI, BPDI, and their respective perfluorobenzylated derivatives. All spectra are normalized to their highest absorption peak.

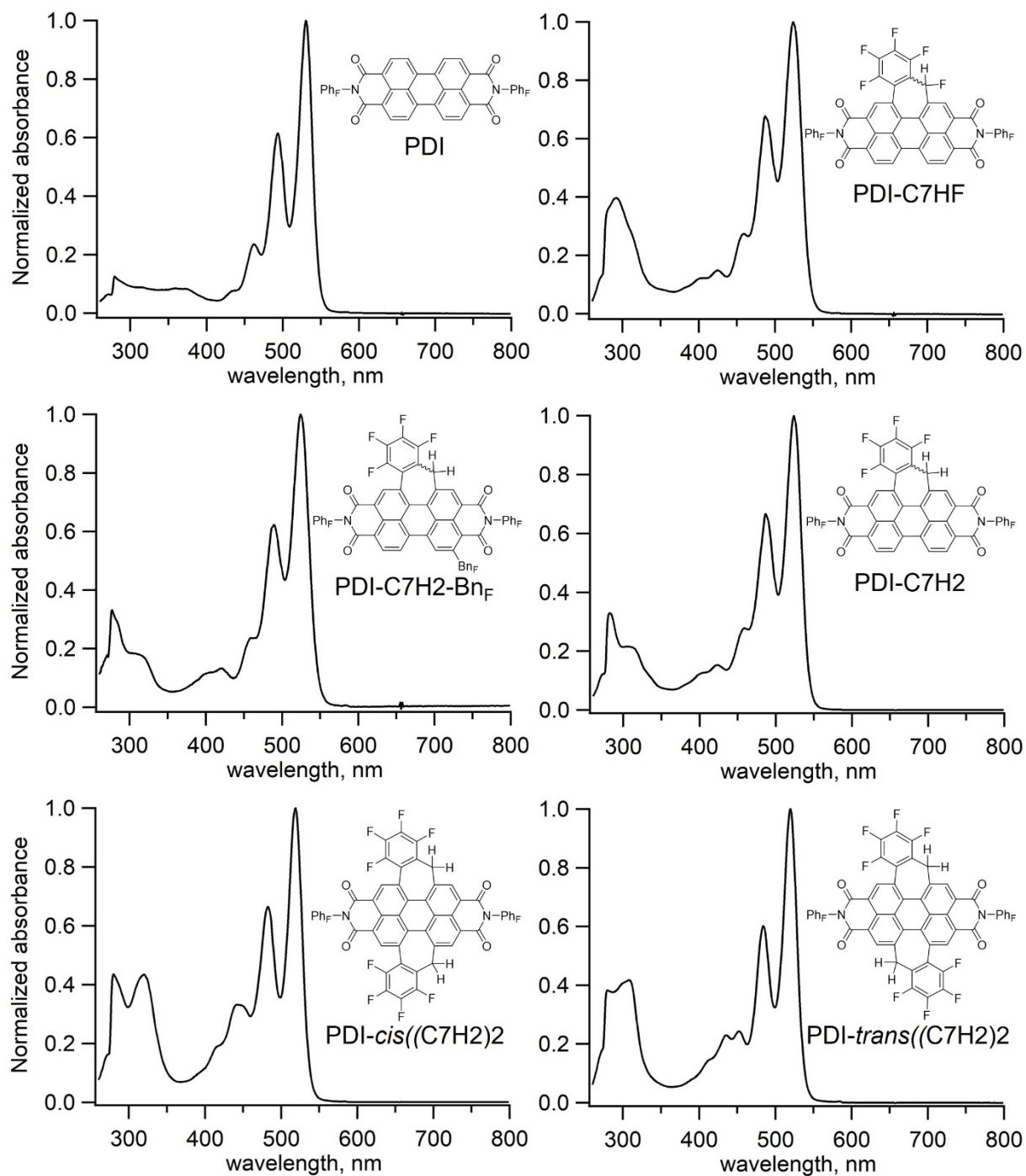


Figure 4.65. UV-vis absorbance spectra of PDI and PDI-C7H2 derivatives. All spectra are normalized to their highest absorption peak.

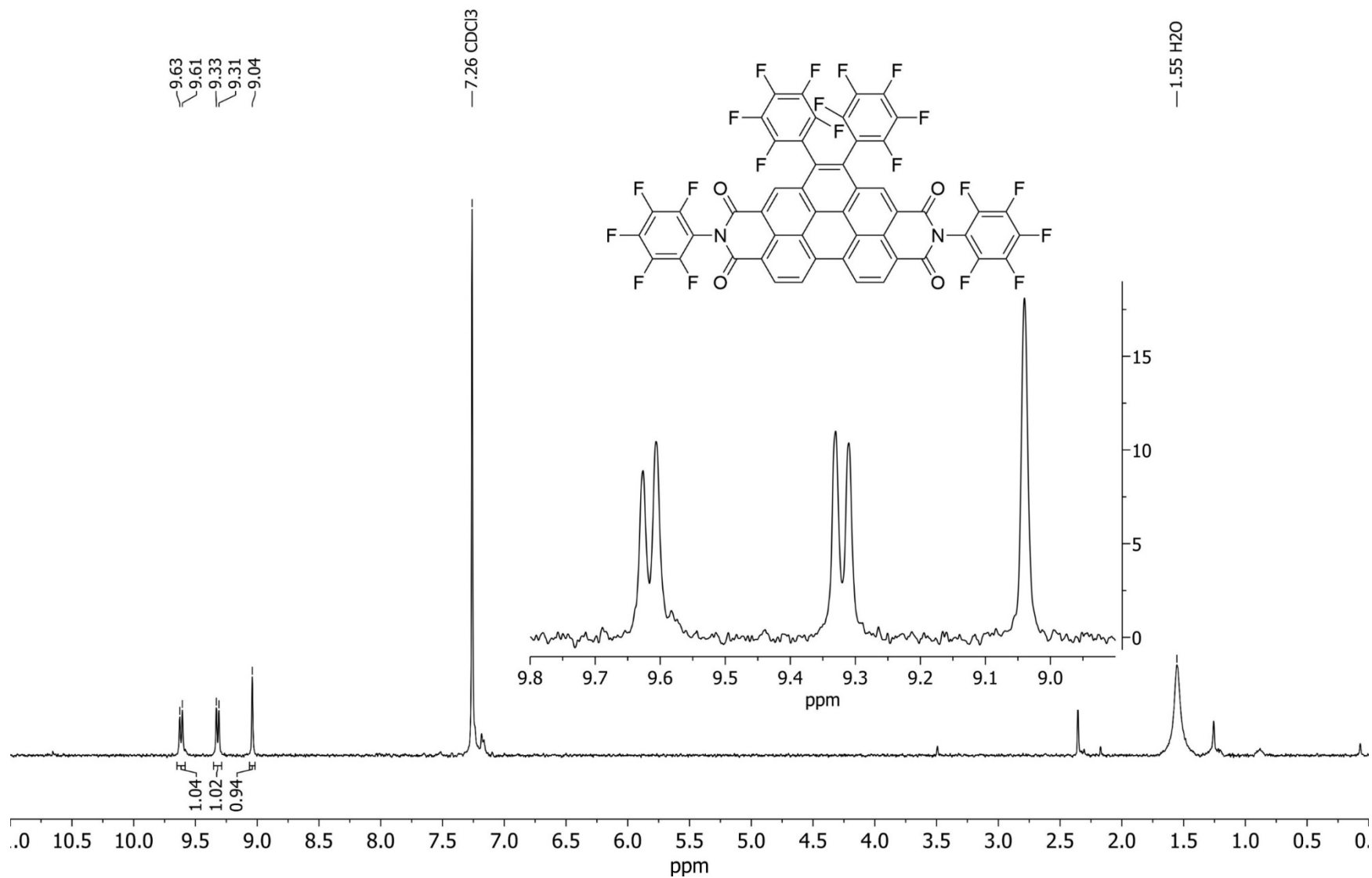


Figure 4.66. $^1\text{H-NMR}$ spectrum of BPDI in CDCl_3 . Inset shows expanded aromatic region from 8.9 to 9.8 ppm.

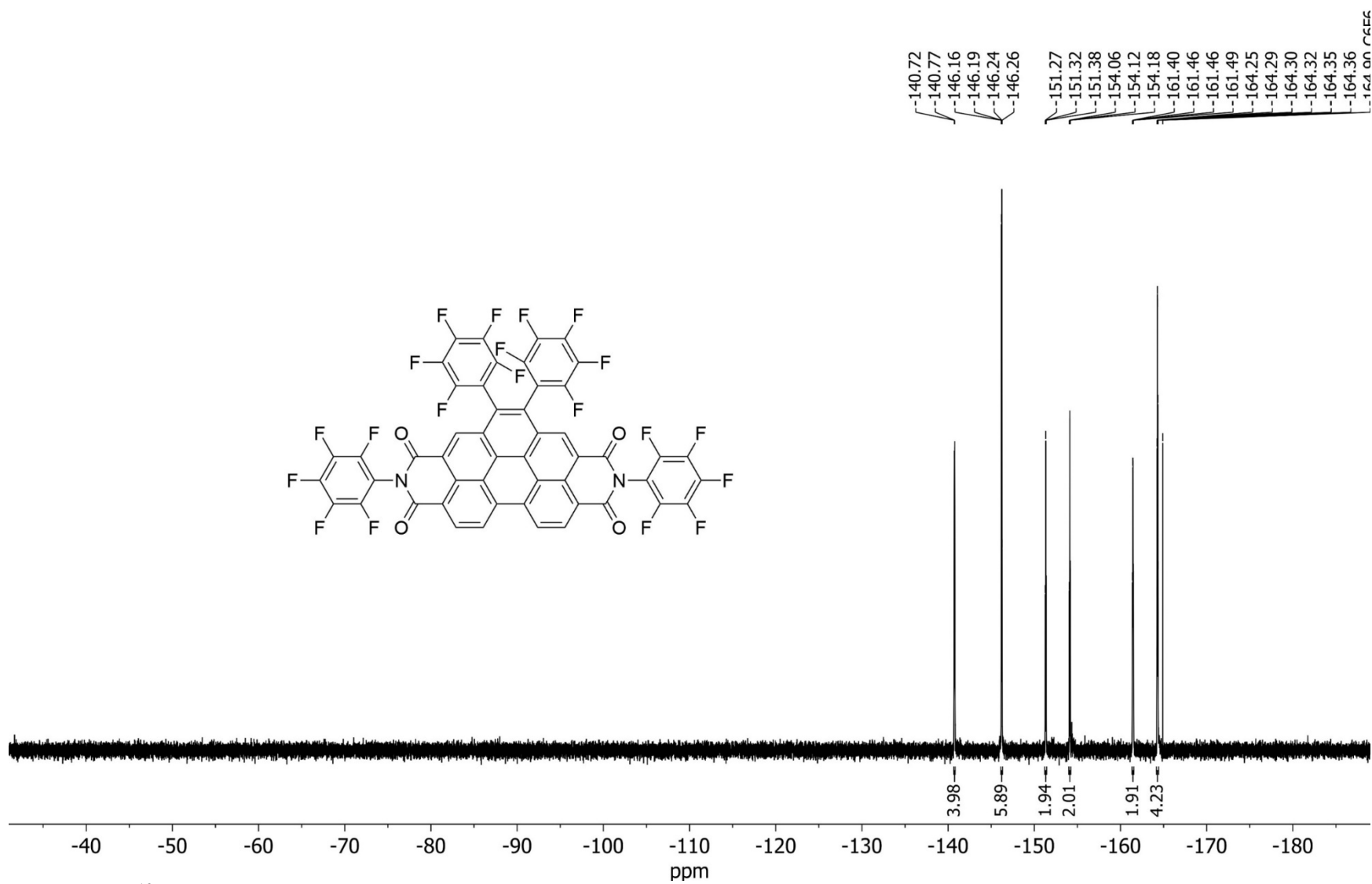


Figure 4.67. ¹⁹F-NMR spectrum of BPDI in CDCl₃.

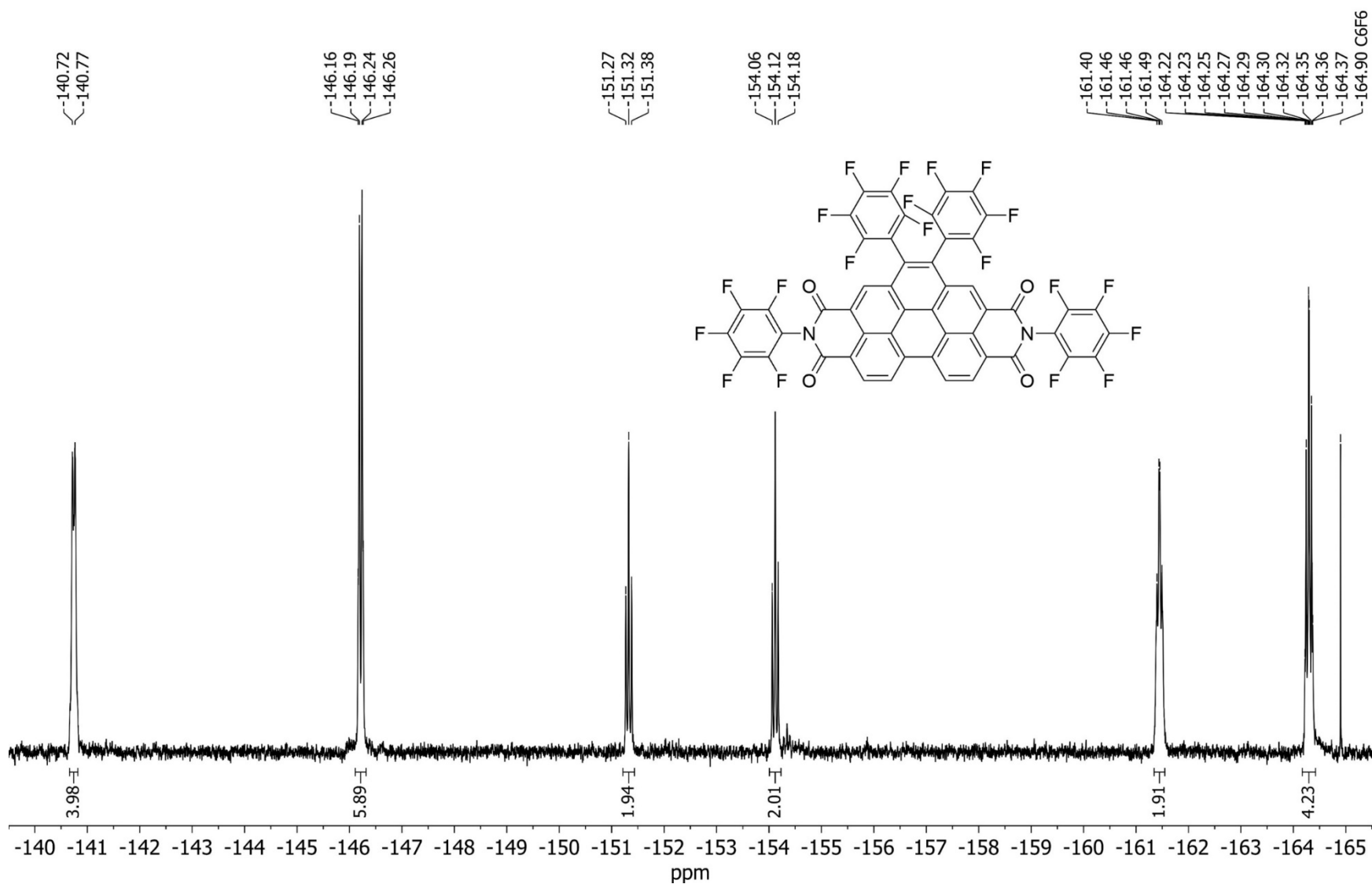


Figure 4.68. Expanded aromatic region of BPDl's ^{19}F -NMR spectrum shown in Figure 4.67.

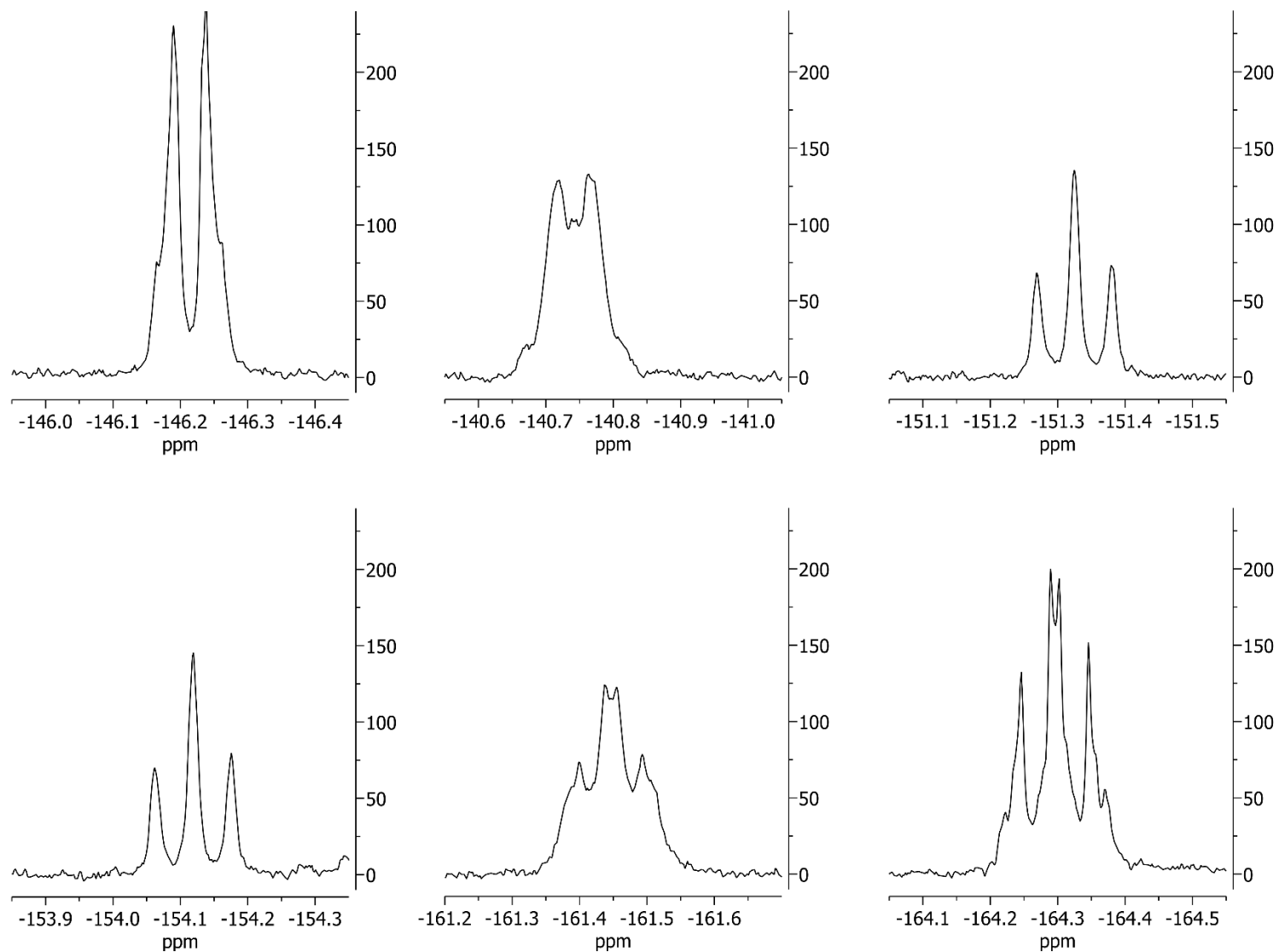


Figure 4.69. Closeup view of BPDI's ^{19}F -NMR signals shown in in Figure 4.67. All signals are proportional in intensity (y-axis) to each other with respect to their original spectrum, while all x-axes are at the same scale (normalized such that each x-axis is the same width and 0.5 ppm across).

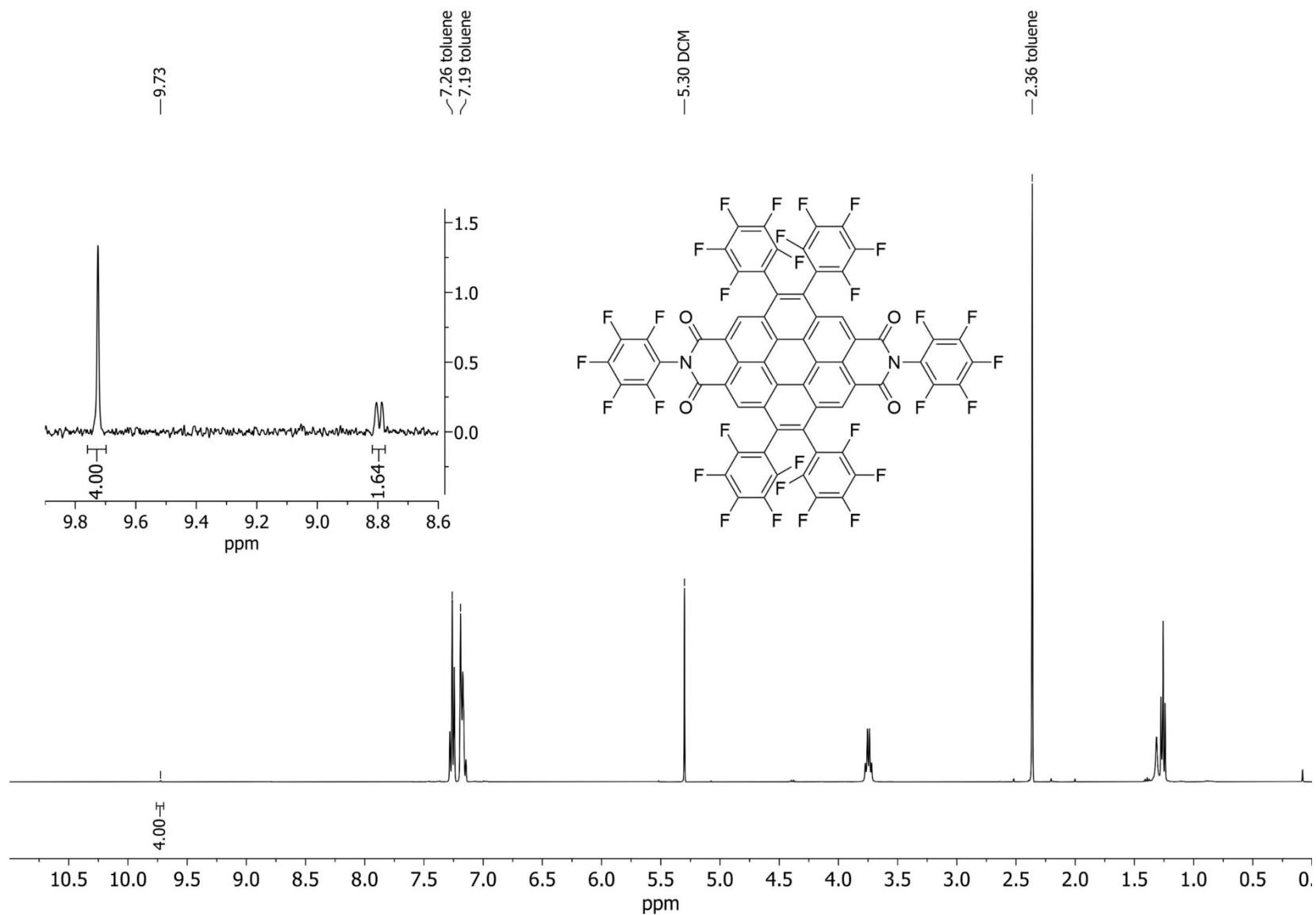


Figure 4.70. $^1\text{H-NMR}$ spectrum of *bis*BPDI in CDCl_3 . Inset shows expanded aromatic region from 8.60 to 9.85 ppm.

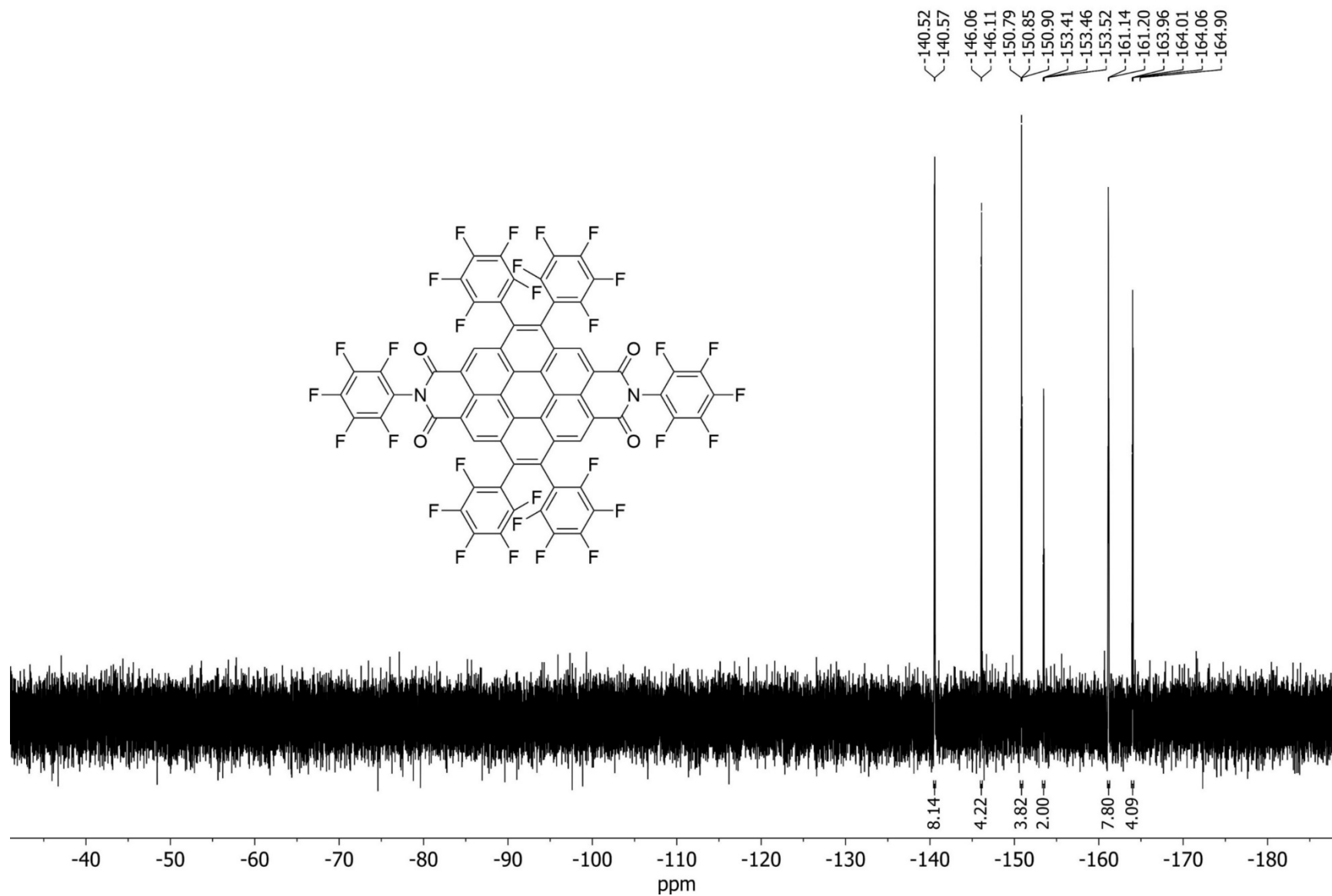


Figure 4.71. ^{19}F -NMR spectrum of *bis*BPDI in CDCl_3 .

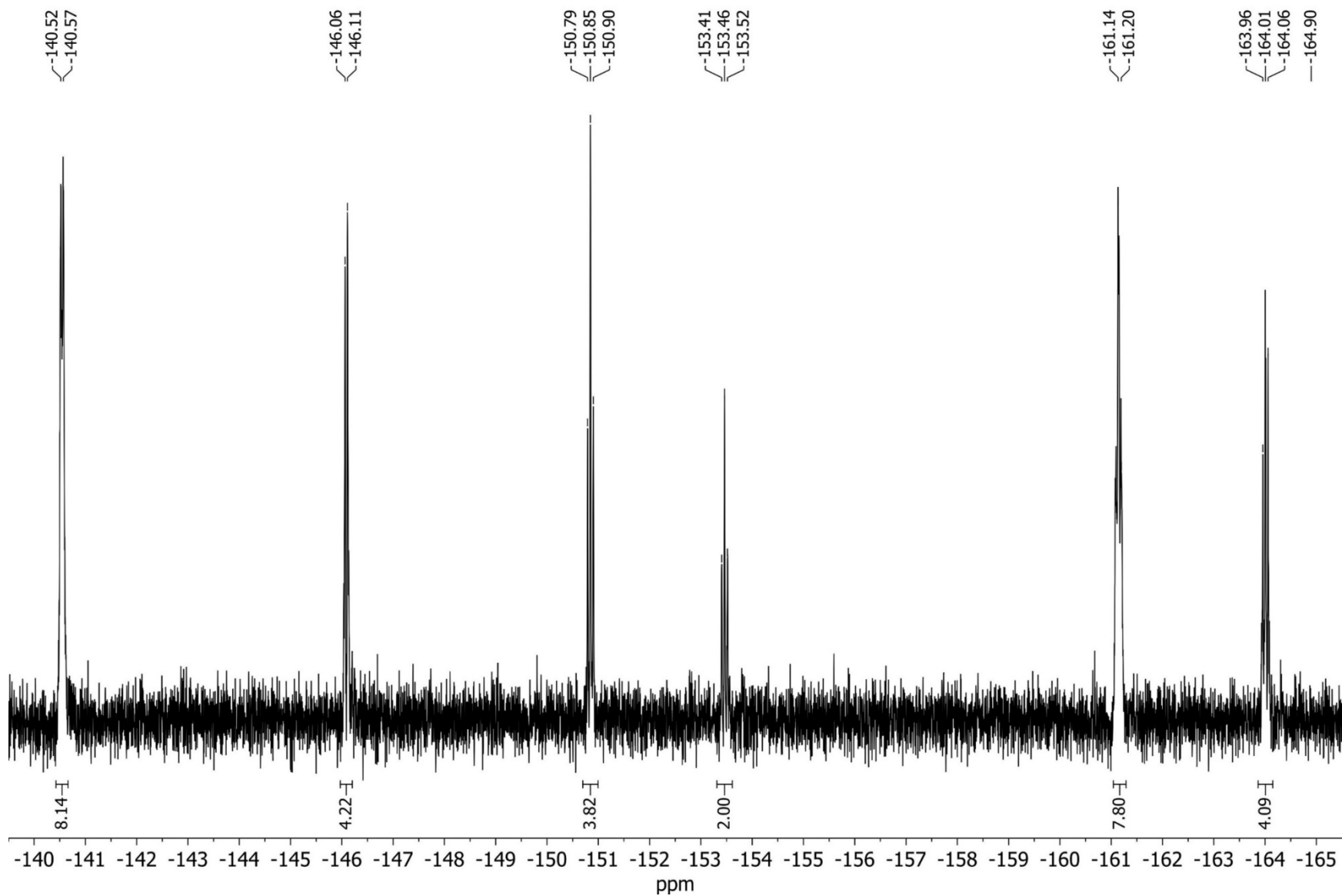


Figure 4.72. Expanded aromatic region of *bis*BPDI's ^{19}F -NMR spectrum shown in Figure 4.71.

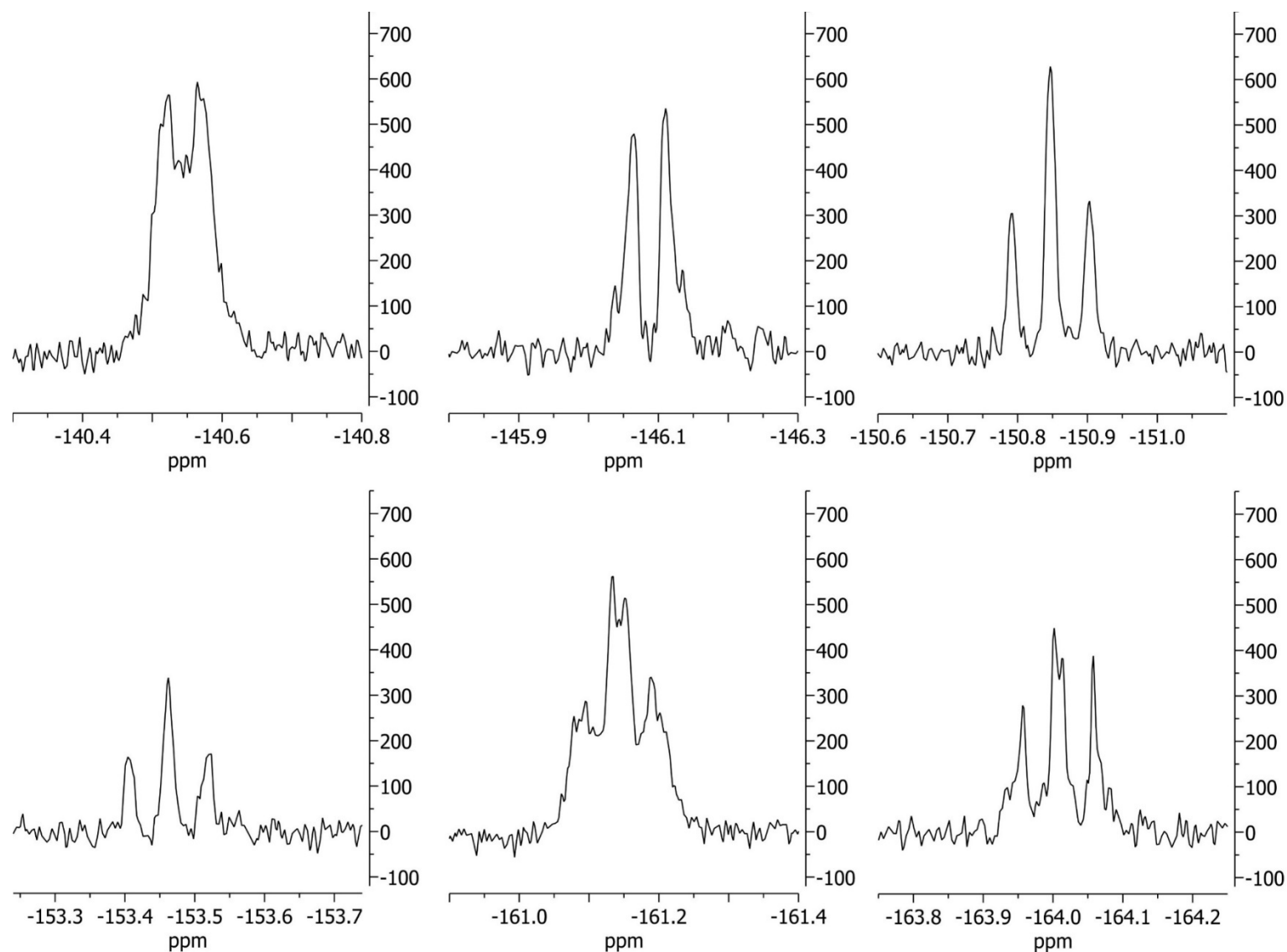


Figure 4.73. Closeup view of *bisBPDI*'s ^{19}F -NMR signals shown in Figure 4.71. All signals are proportional in intensity (y-axis) to each other with respect to their original spectrum, while all x-axes are at the same scale (normalized such that each x-axis is the same width and 0.5 ppm across).

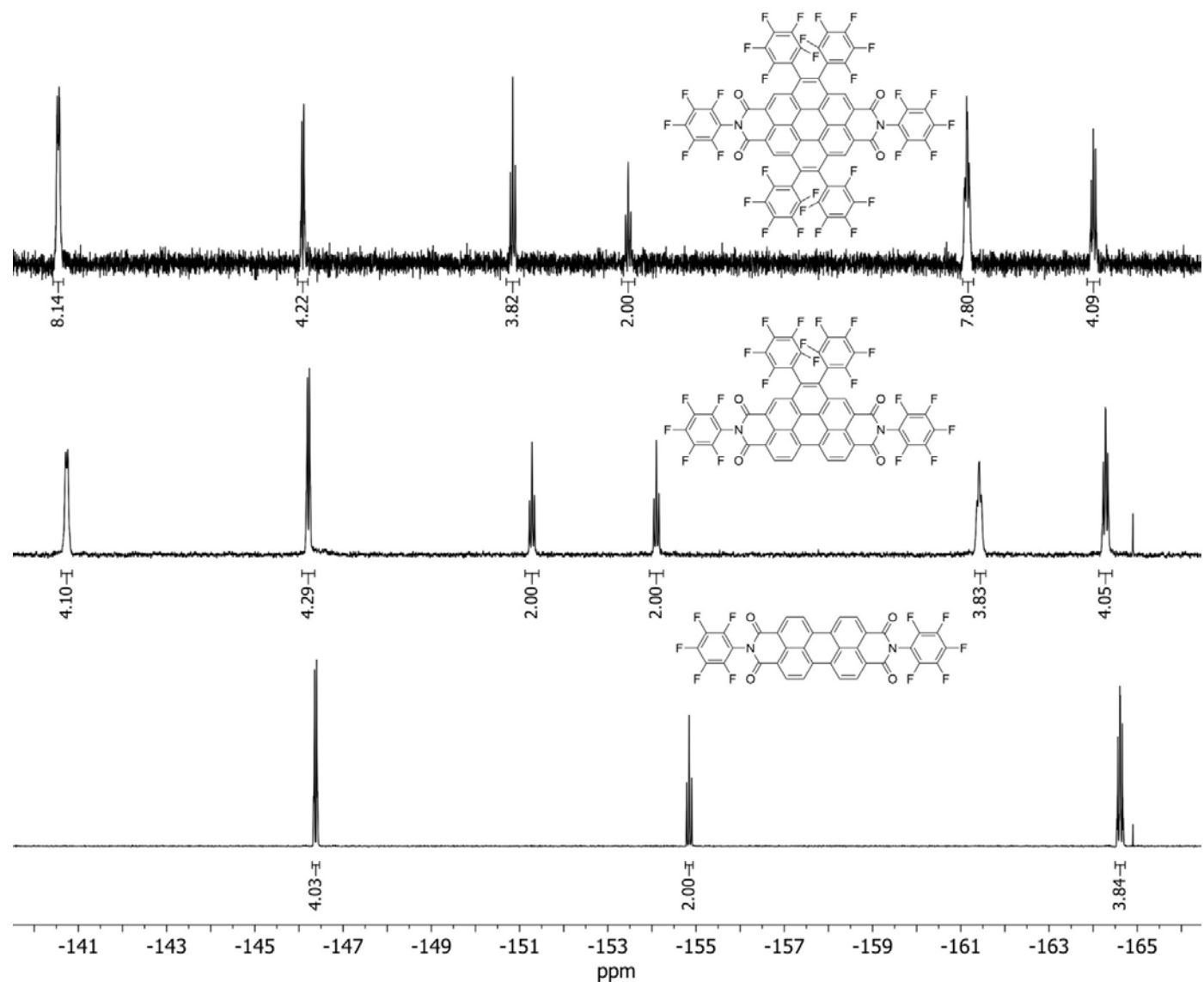


Figure 4.74. Comparison between ^{19}F -NMR spectra of PDI, BPDI, and bisBPDI (bottom, middle and top respectively). The relative integration values are normalized with respect to the two *para*-fluorines of the imide's perfluorophenyl group, set to 2.00 in each spectrum.

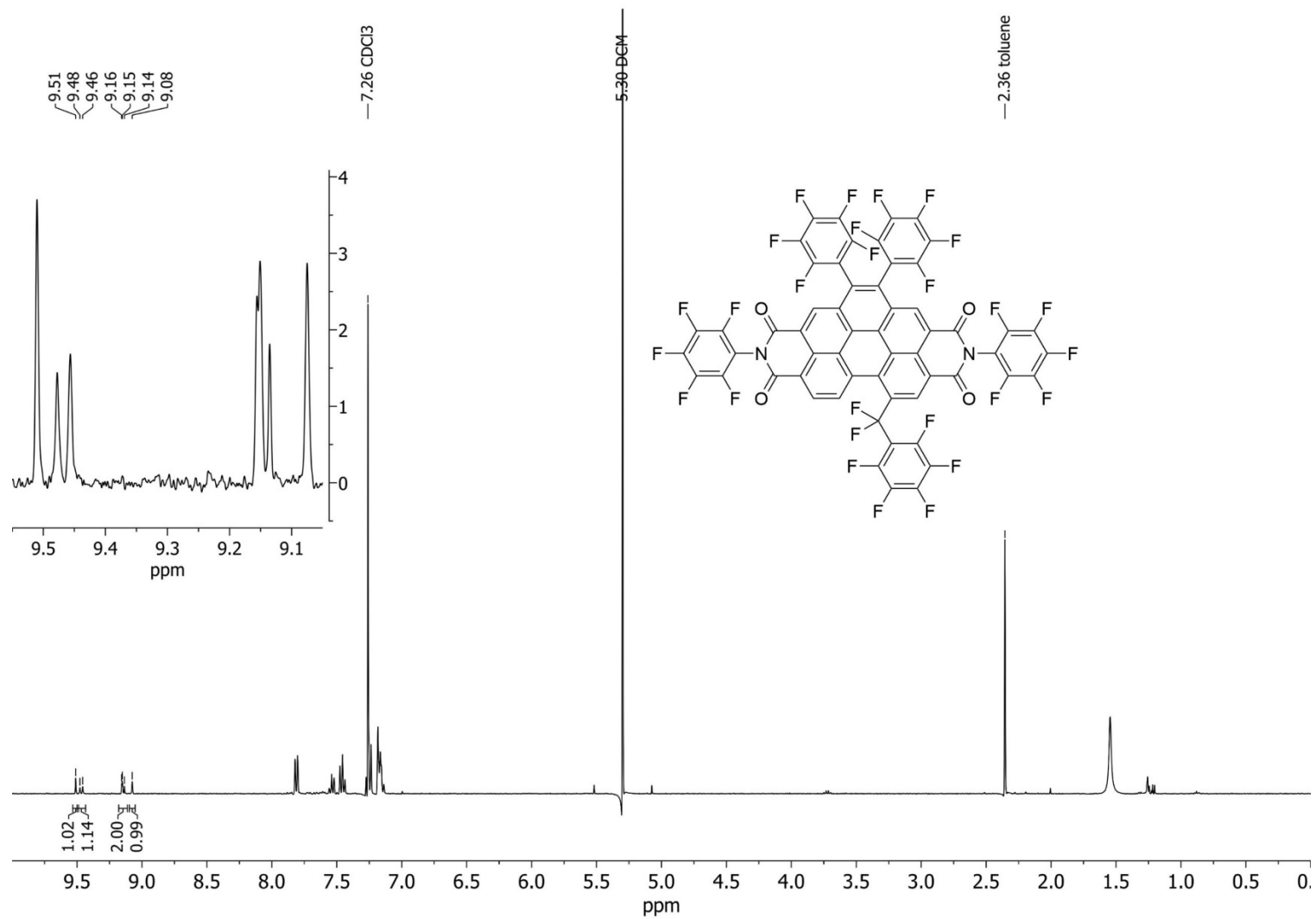


Figure 4.75. $^1\text{H-NMR}$ spectrum of BPDI-6-Bn_F in CDCl_3 . Inset shows expanded aromatic region from 9.05 to 9.55 ppm.

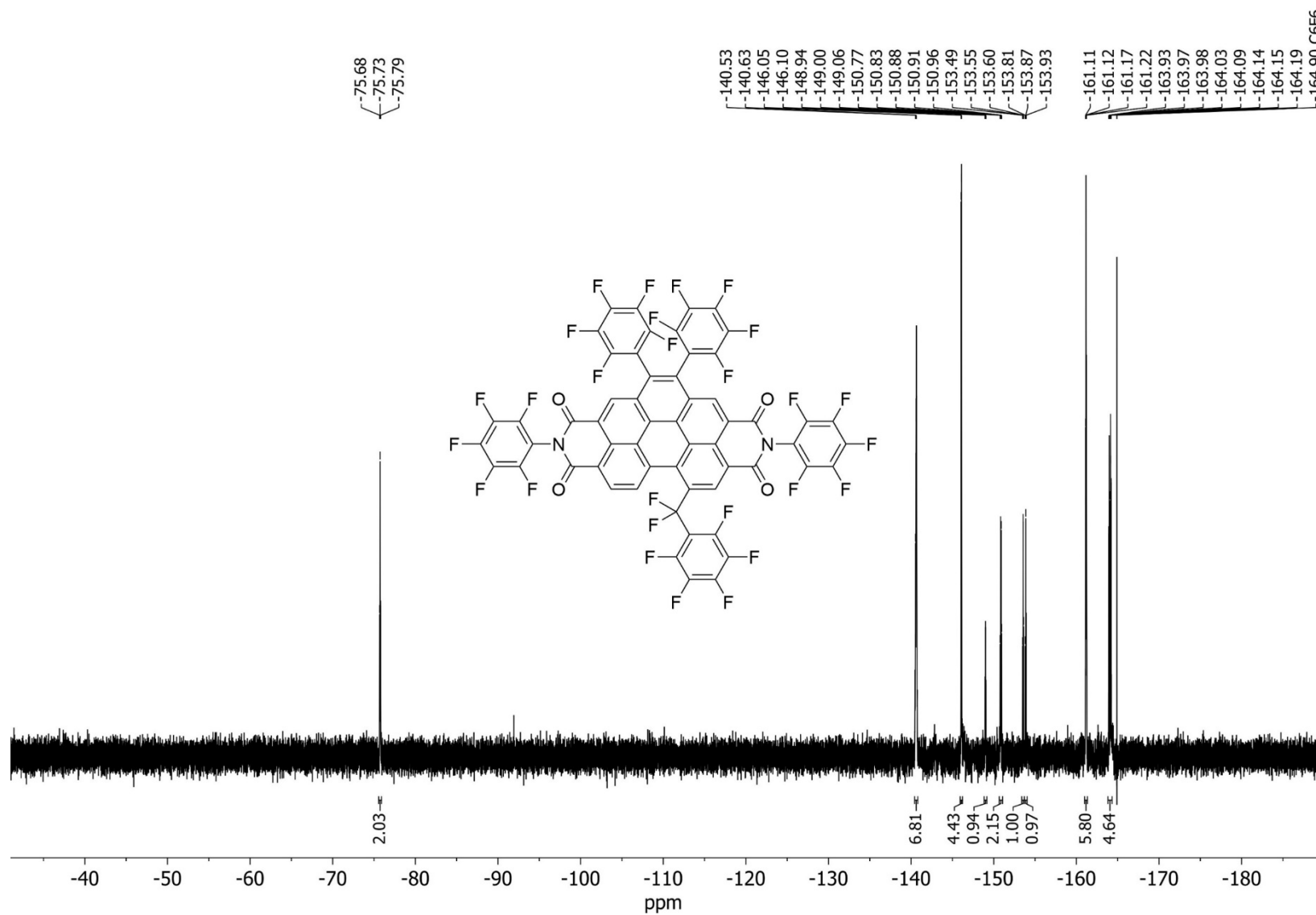


Figure 4.76. ¹⁹F-NMR spectrum of BPDI-6-BnF in CDCl₃.

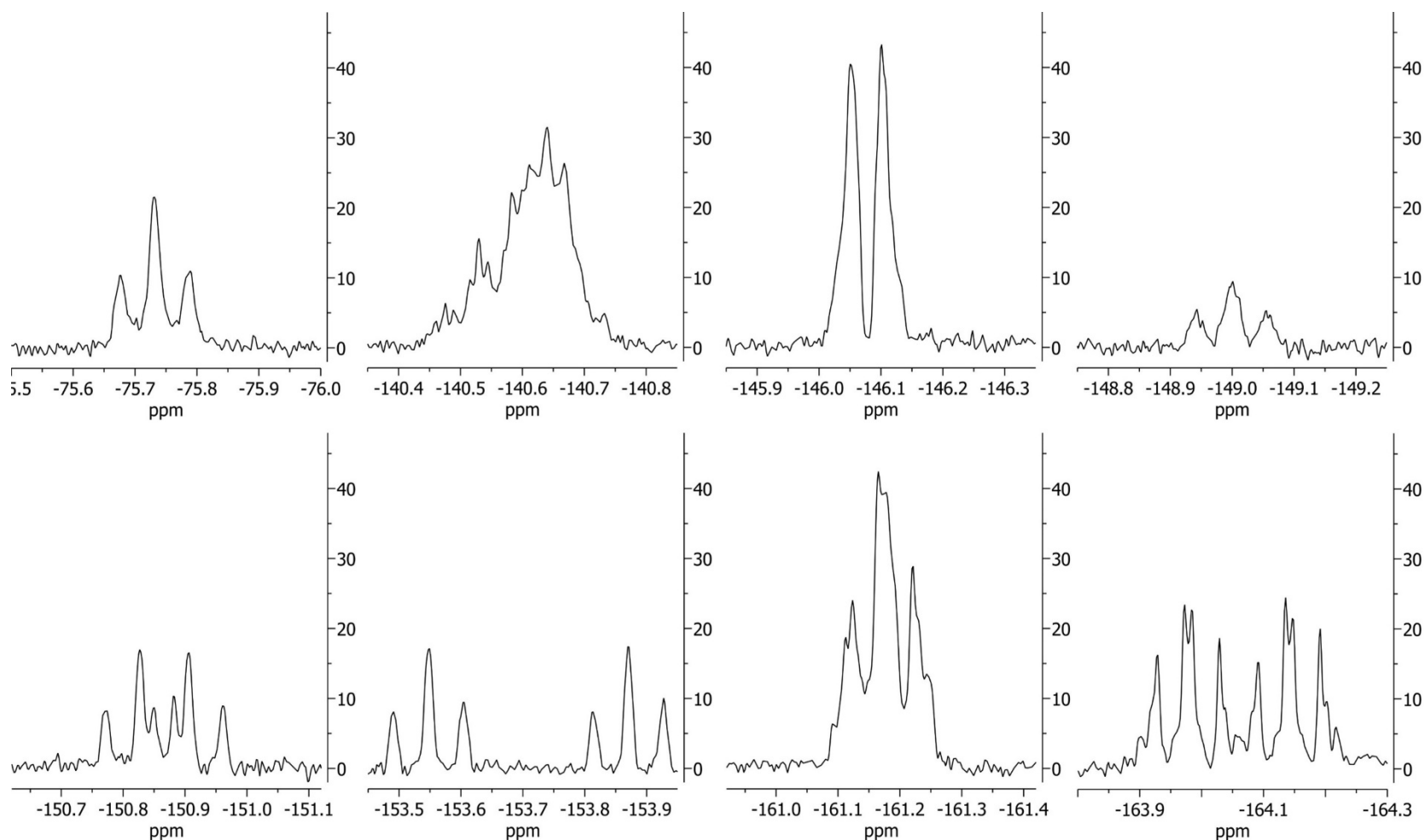


Figure 4.77. Closeup view of BPDI-6-BnF's ^{19}F -NMR signals shown in Figure 4.76. All signals are proportional in intensity (y-axis) to each other with respect to their original spectrum, while all x-axes are at the same scale (normalized such that each x-axis is both the same width and 0.5 ppm across).

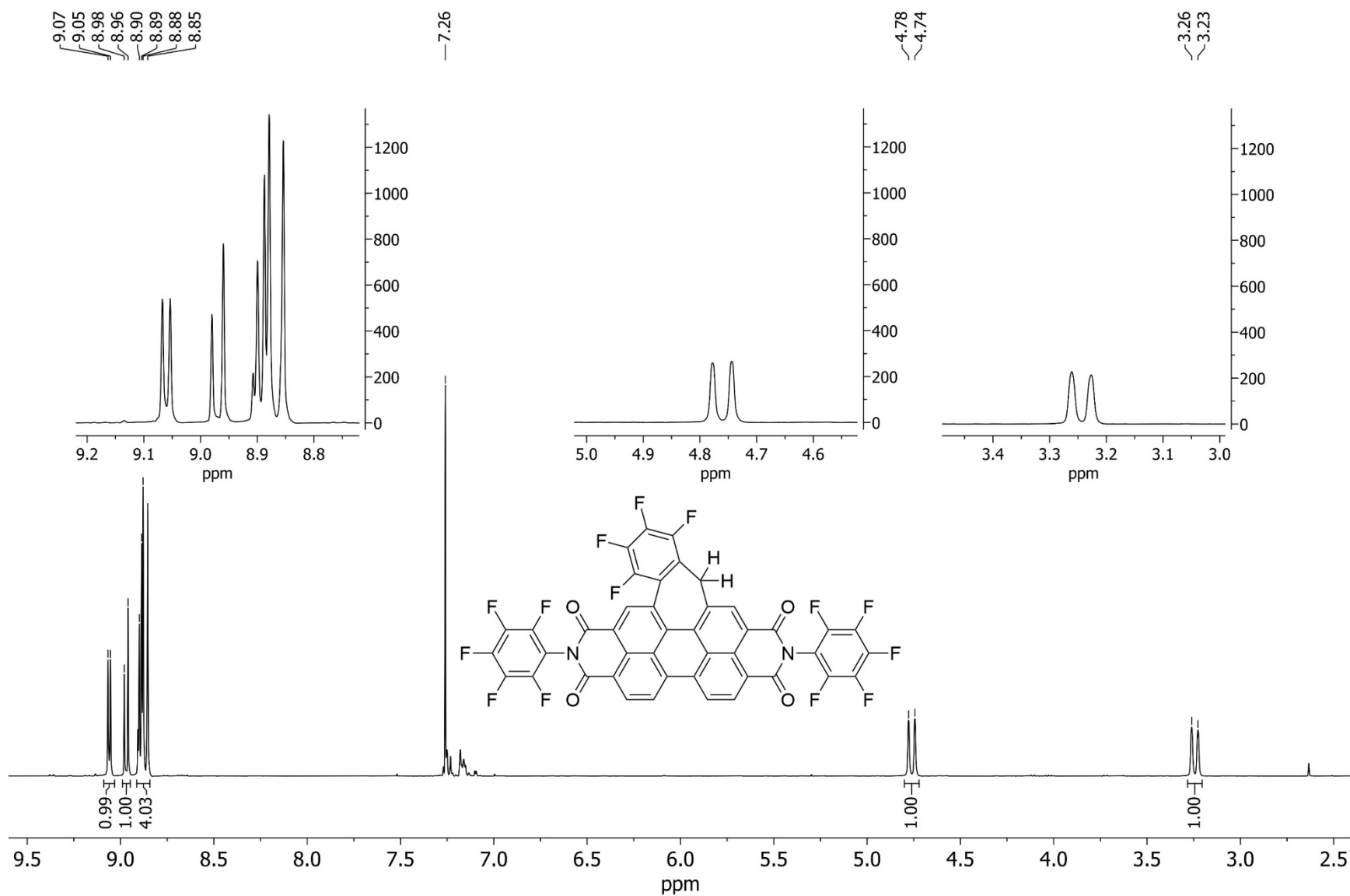


Figure 4.78. $^1\text{H-NMR}$ spectrum of PDI-C7H2 in CDCl_3 from 2.4 to 9.6 ppm. Left inset shows expanded region for aromatic proton signals (8.70 to 9.25 ppm); middle and right insets show expanded regions for each signal from the two benzylic hydrogens.

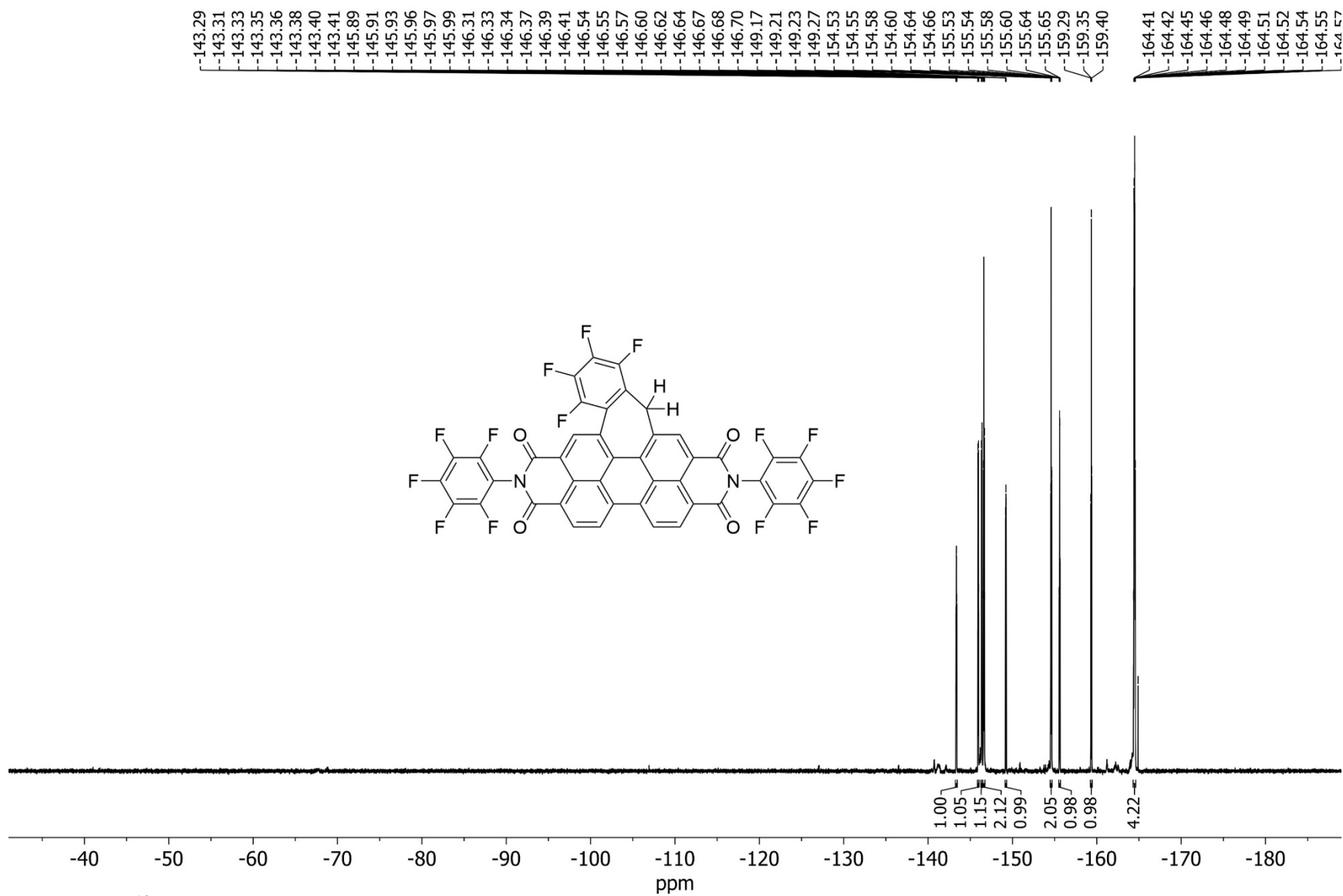


Figure 4.79. ¹⁹F-NMR spectrum of PDI-C7H2 in CDCl₃.

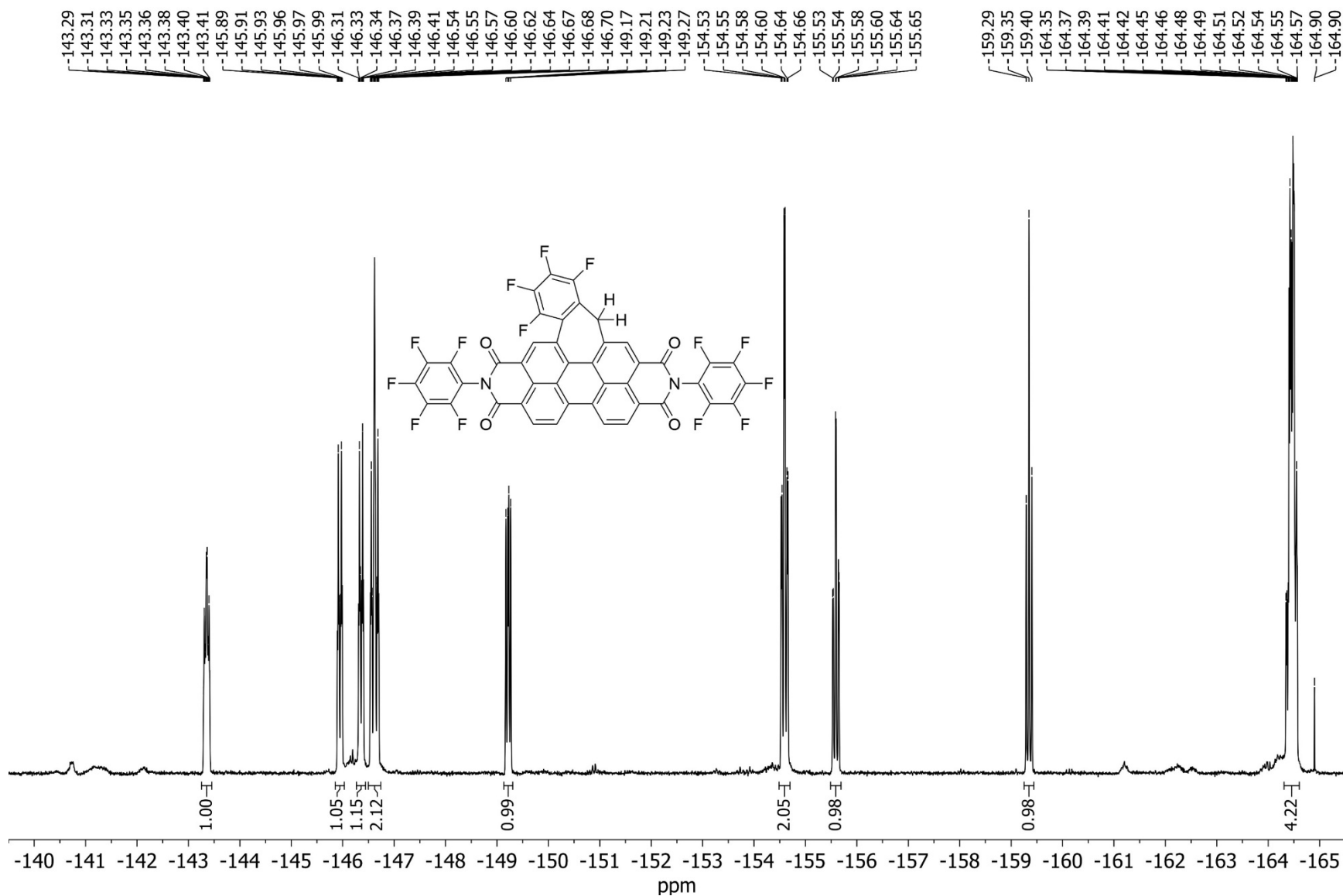


Figure 4.80. Expanded aromatic region of PDI-C7H2's ^{19}F -NMR spectrum—full spectrum shown in Figure 4.79.

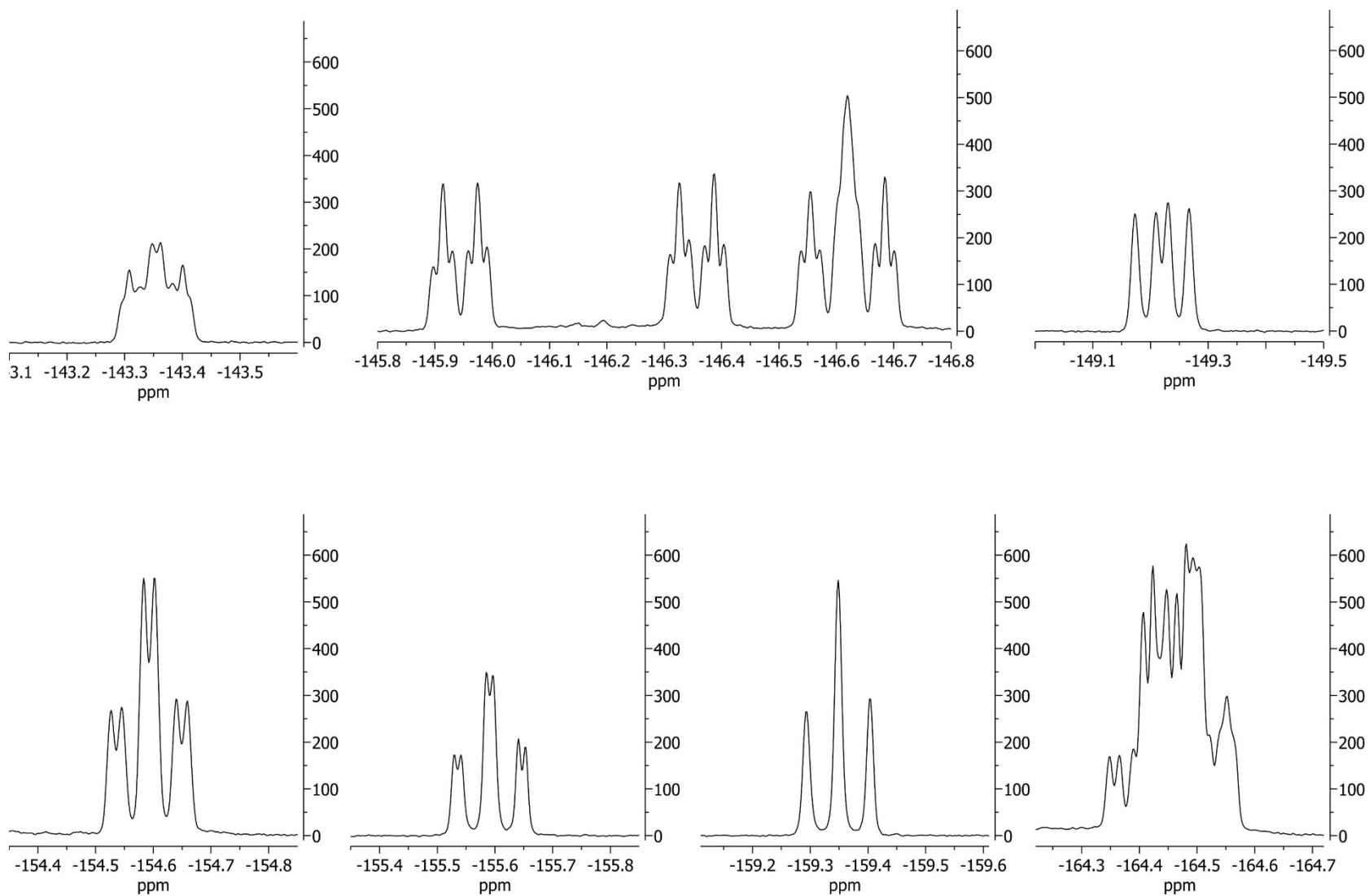


Figure 4.81. Closeup view of PDI-C7H2's ^{19}F -NMR signals shown in Figure 4.79. All signals are proportional in intensity (y-axis) to each other with respect to their original spectrum, while all x-axes are at the same scale (normalized such that each x-axis is both the same width and 0.5 ppm across).

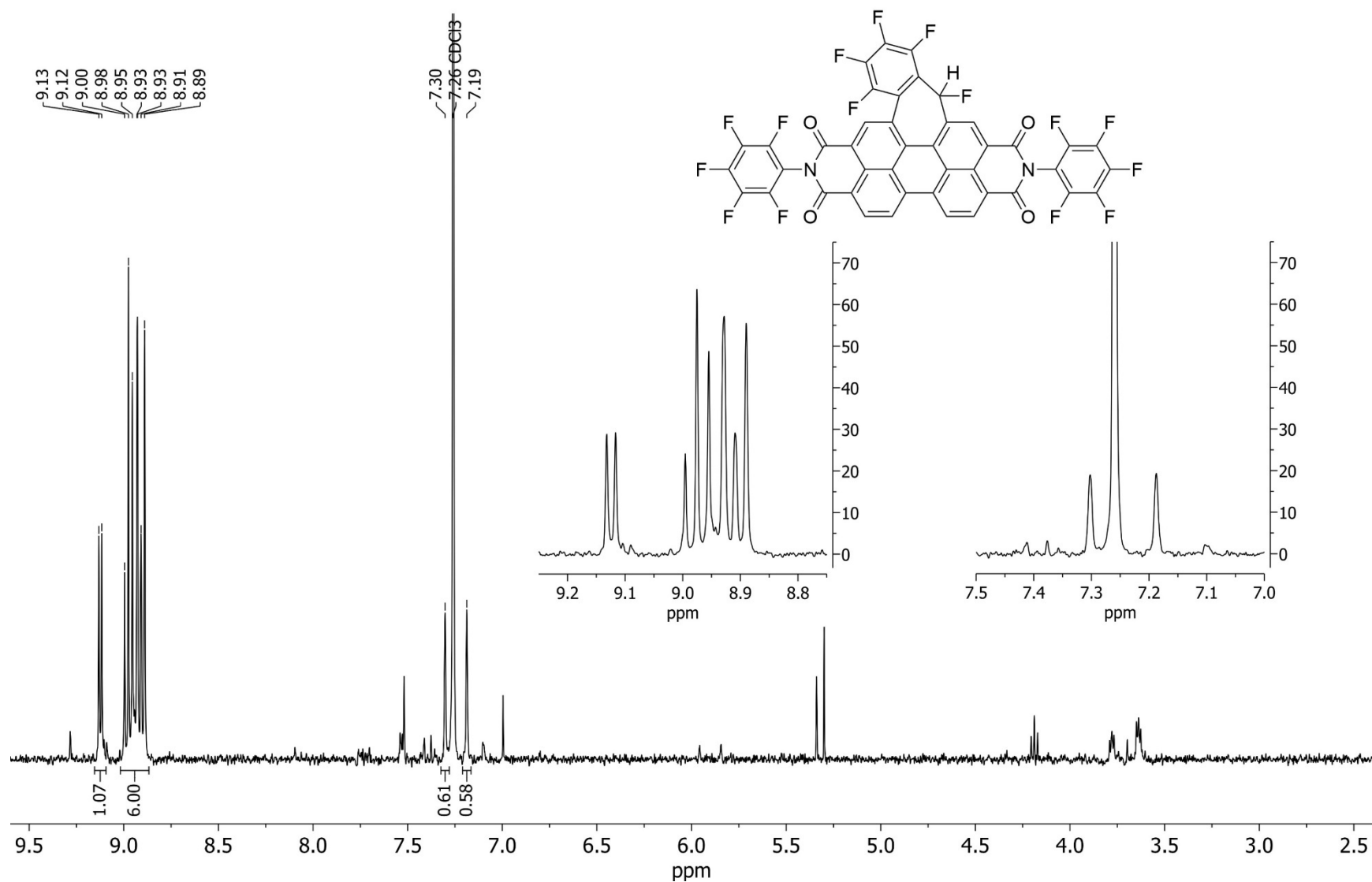


Figure 4.82. ¹H-NMR spectrum of PDI-C7HF in CDCl₃ from 2.4 to 9.6 ppm. Left inset shows expanded region for aromatic proton signals (8.70 to 9.25 ppm); right inset shows expanded regions for the doublet of the benzylic hydrogen coupled to the benzylic fluorine (off centered from the CDCl₃ residual solvent peak at 7.26 ppm).

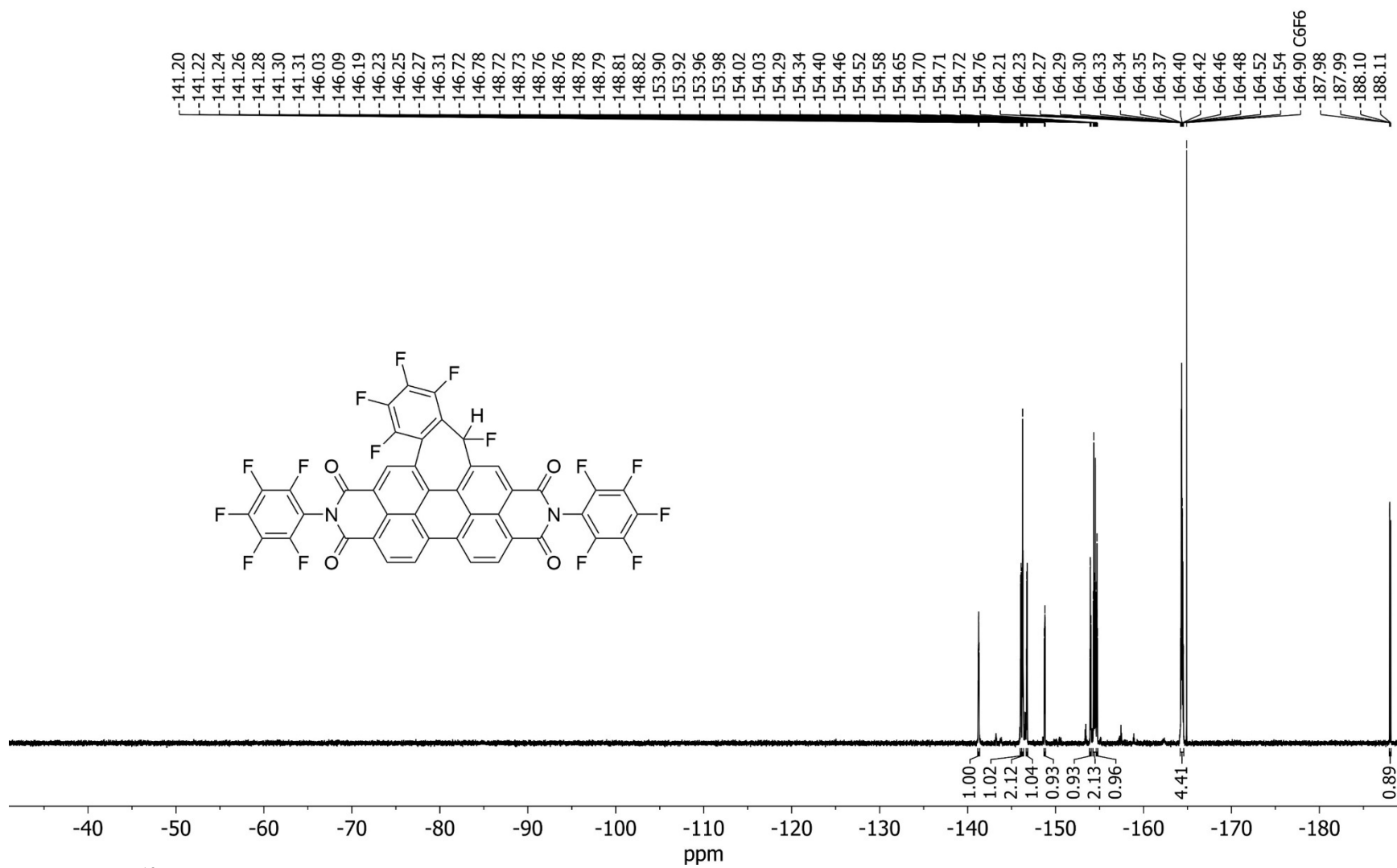


Figure 4.83. ¹⁹F-NMR spectrum of PDI-C7HF in CDCl₃.

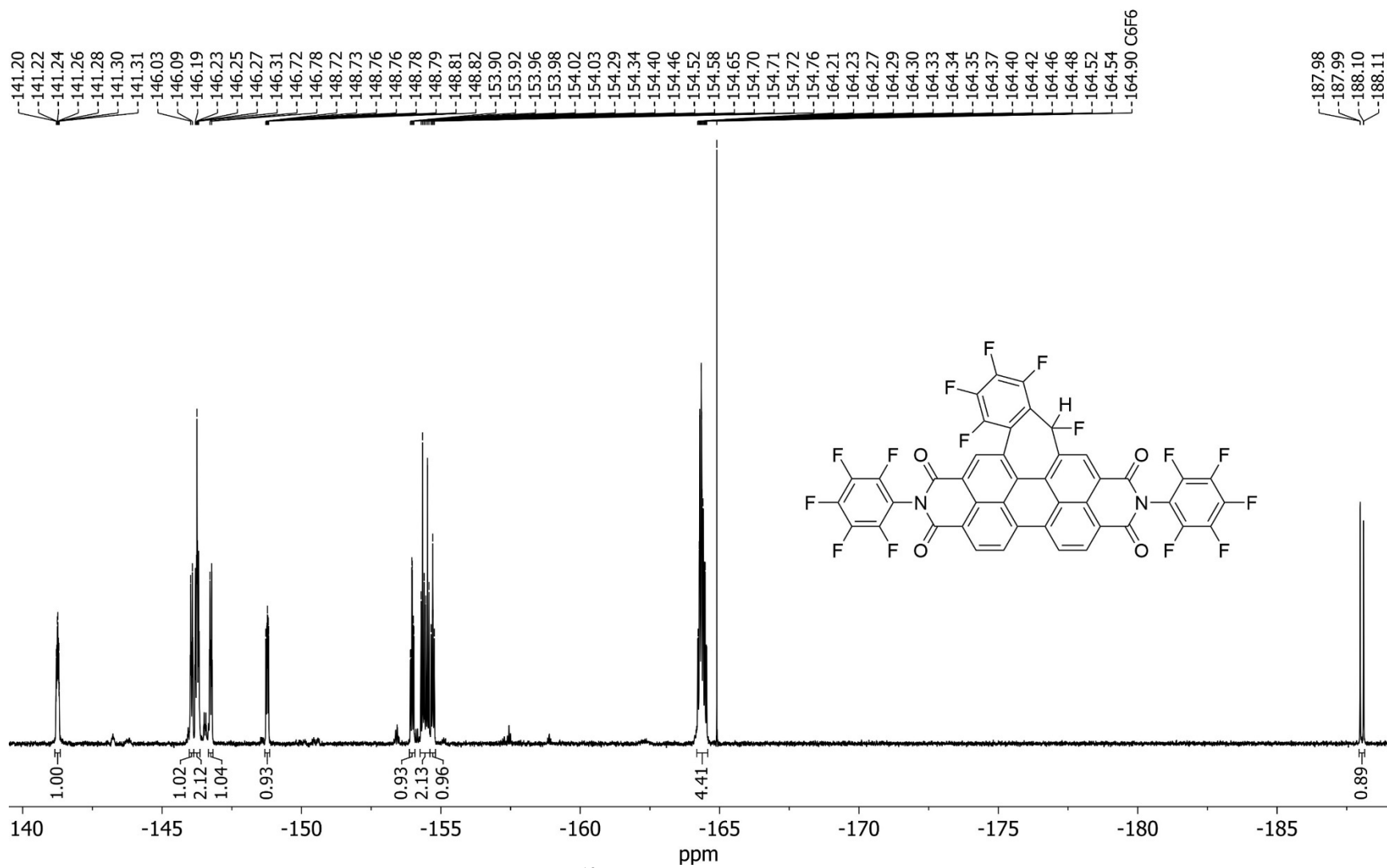


Figure 4.84. Expanded aromatic region of PDI-C7HF's ^{19}F -NMR spectrum—full spectrum shown in Figure 4.83.

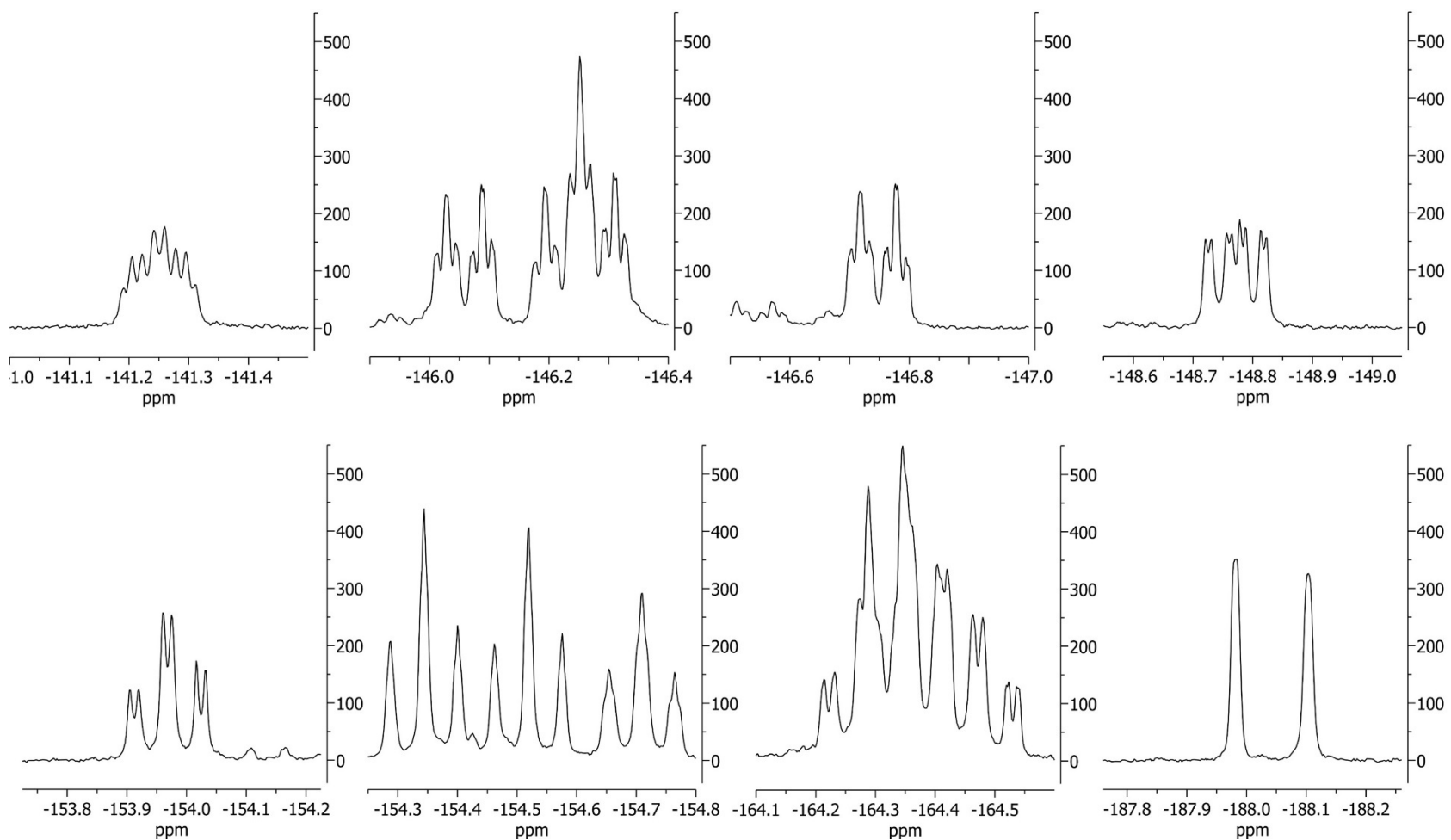


Figure 4.85. Closeup view of PDI-C7HF's ^{19}F -NMR signals shown in Figure 4.83. All signals are proportional in intensity (y-axis) to each other with respect to their original spectrum, while all x-axes are at the same scale (normalized such that each x-axis is both the same width and 0.5 ppm across).

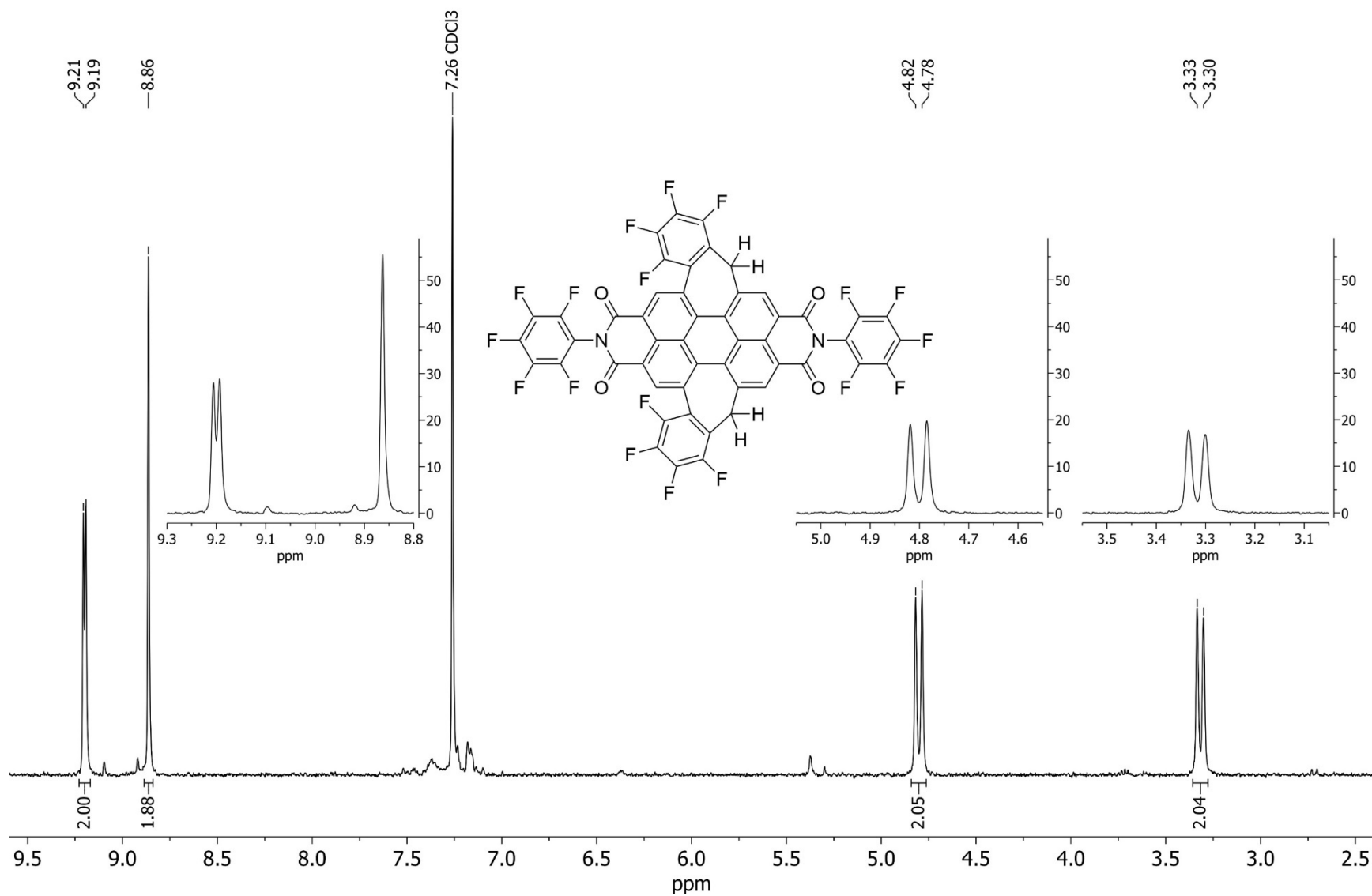


Figure 4.86. $^1\text{H-NMR}$ spectrum of PDI-*cis*(C_7H_2) $_2$ in CDCl_3 from 2.4 to 9.6 ppm. Left inset shows expanded region for aromatic proton signals (8.80 to 9.30 ppm); middle and right insets show expanded regions for the two signals from the four benzylic hydrogens.

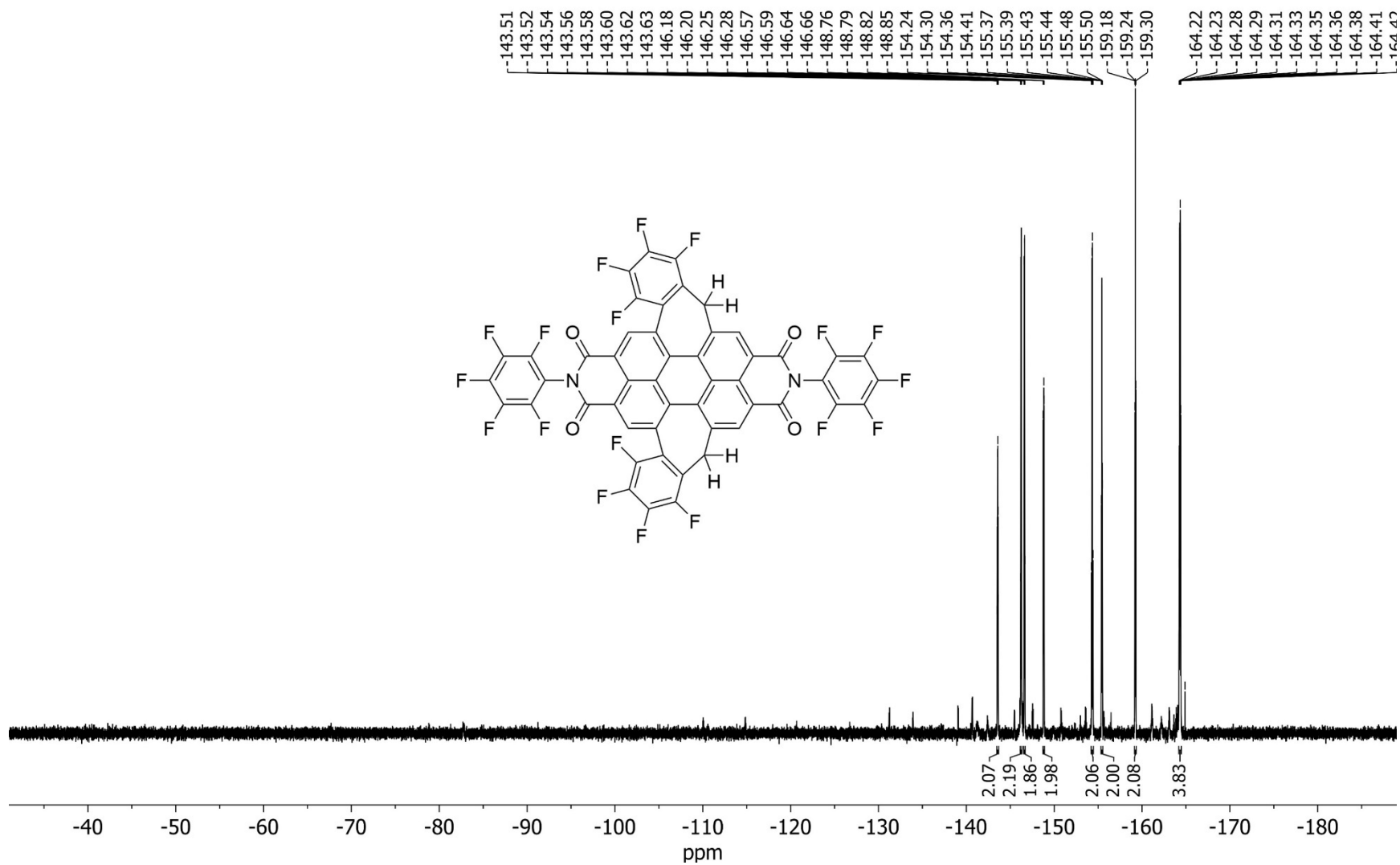


Figure 4.87. ^{19}F -NMR spectrum of PDI-*cis*(C₇H₂)₂ in CDCl₃.

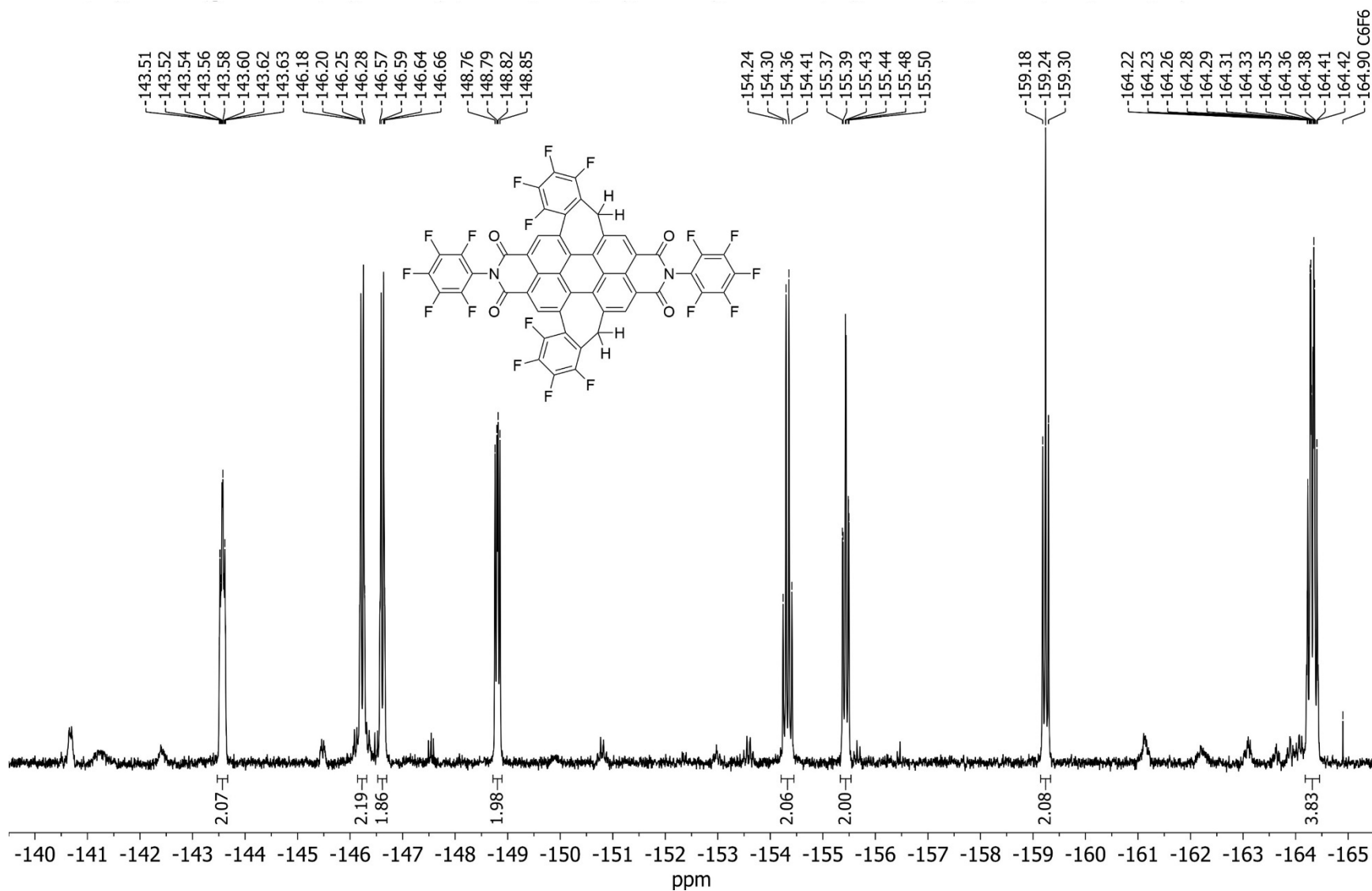


Figure 4.88 Expanded aromatic region of PDI-*cis*(C₇H₂)₂'s ¹⁹F-NMR spectrum—full spectrum shown in Figure 4.87.

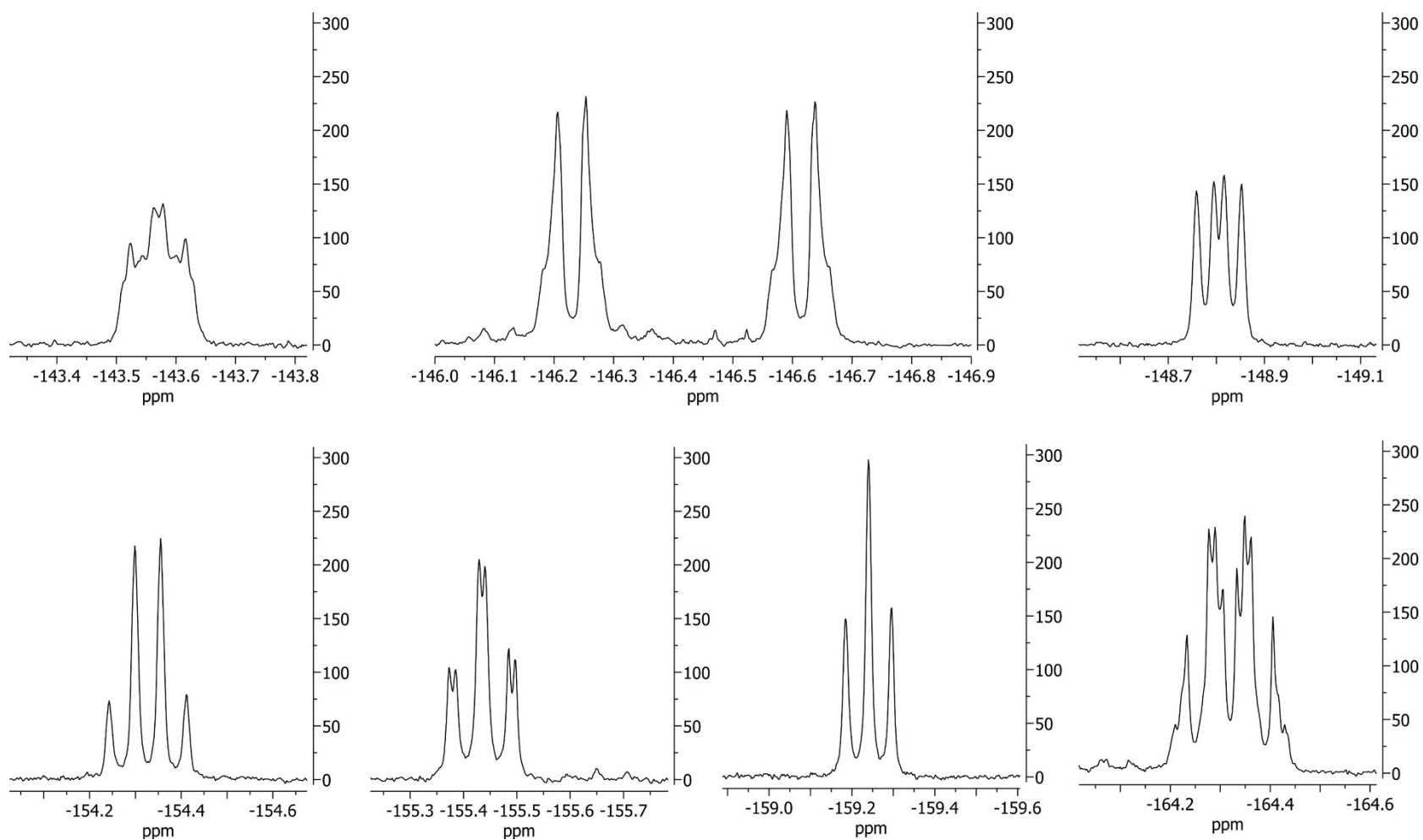


Figure 4.89. Closeup view of PDI-*cis*(C₇H₂)₂'s ¹⁹F-NMR signals shown in Figure 4.87. All signals are proportional in intensity (y-axis) to each other with respect to their original spectrum, while all x-axes are at the same scale (normalized such that each x-axis is both the same width and 0.5 ppm across).

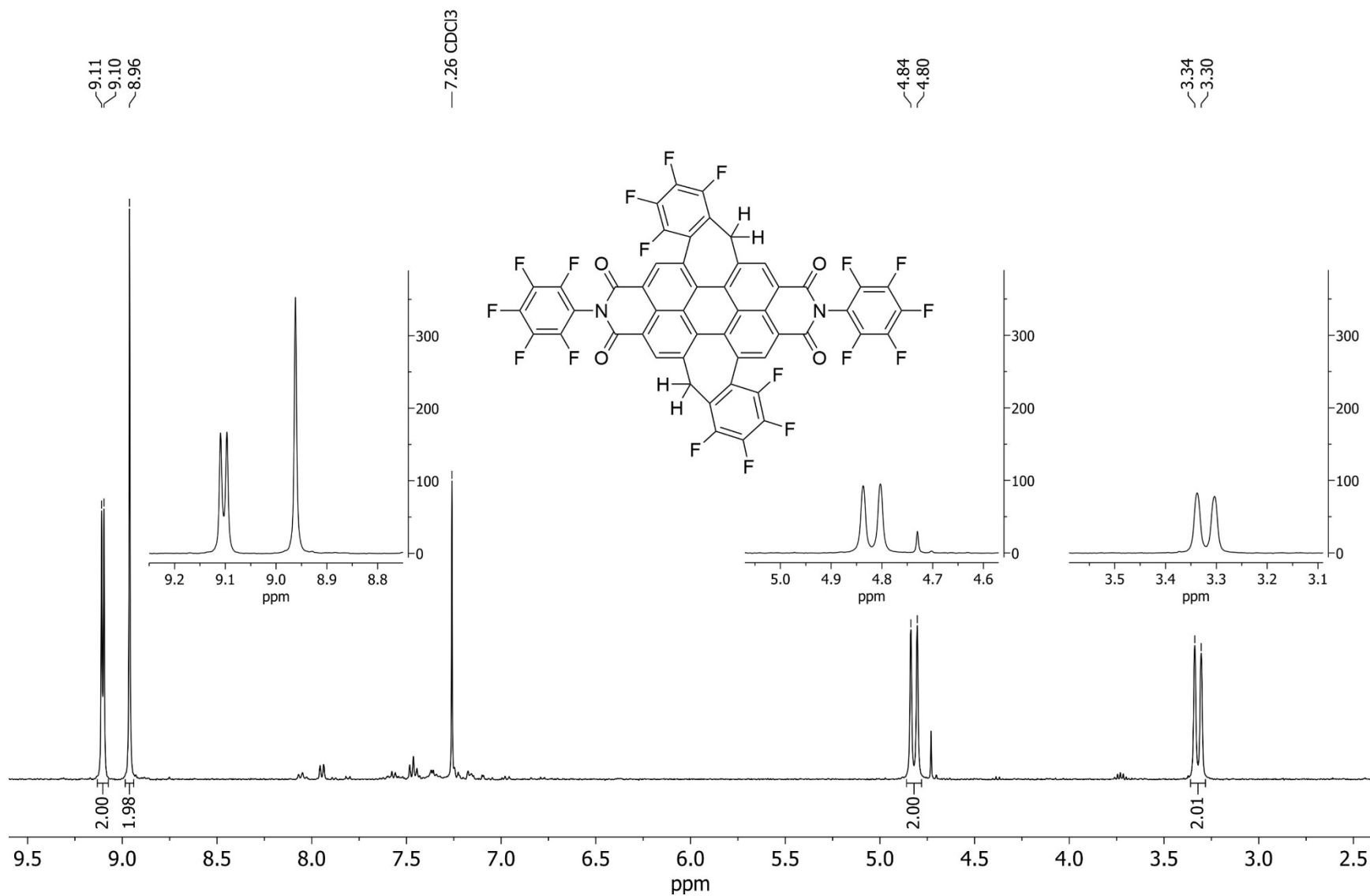


Figure 4.90. ¹H-NMR spectrum of PDI-*trans*(C₇H₂)₂ in CDCl₃ from 2.4 to 9.6 ppm. Left inset shows expanded region for aromatic proton signals (8.75 to 9.25 ppm); middle and right insets show expanded regions for the two signals from the four benzylic hydrogens.

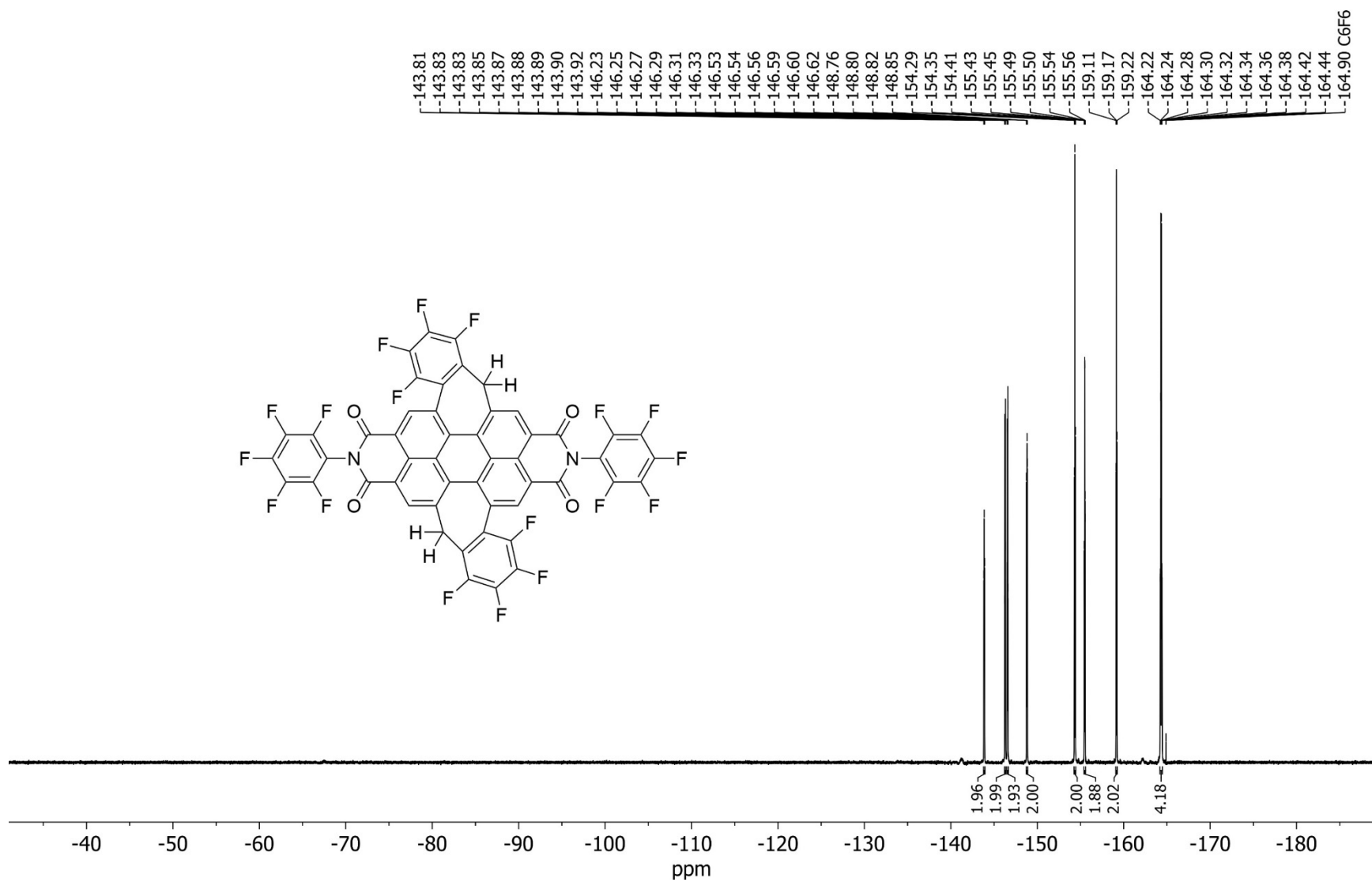


Figure 4.91. ^{19}F -NMR spectrum of PDI-trans(C7H2)2 in CDCl_3 .

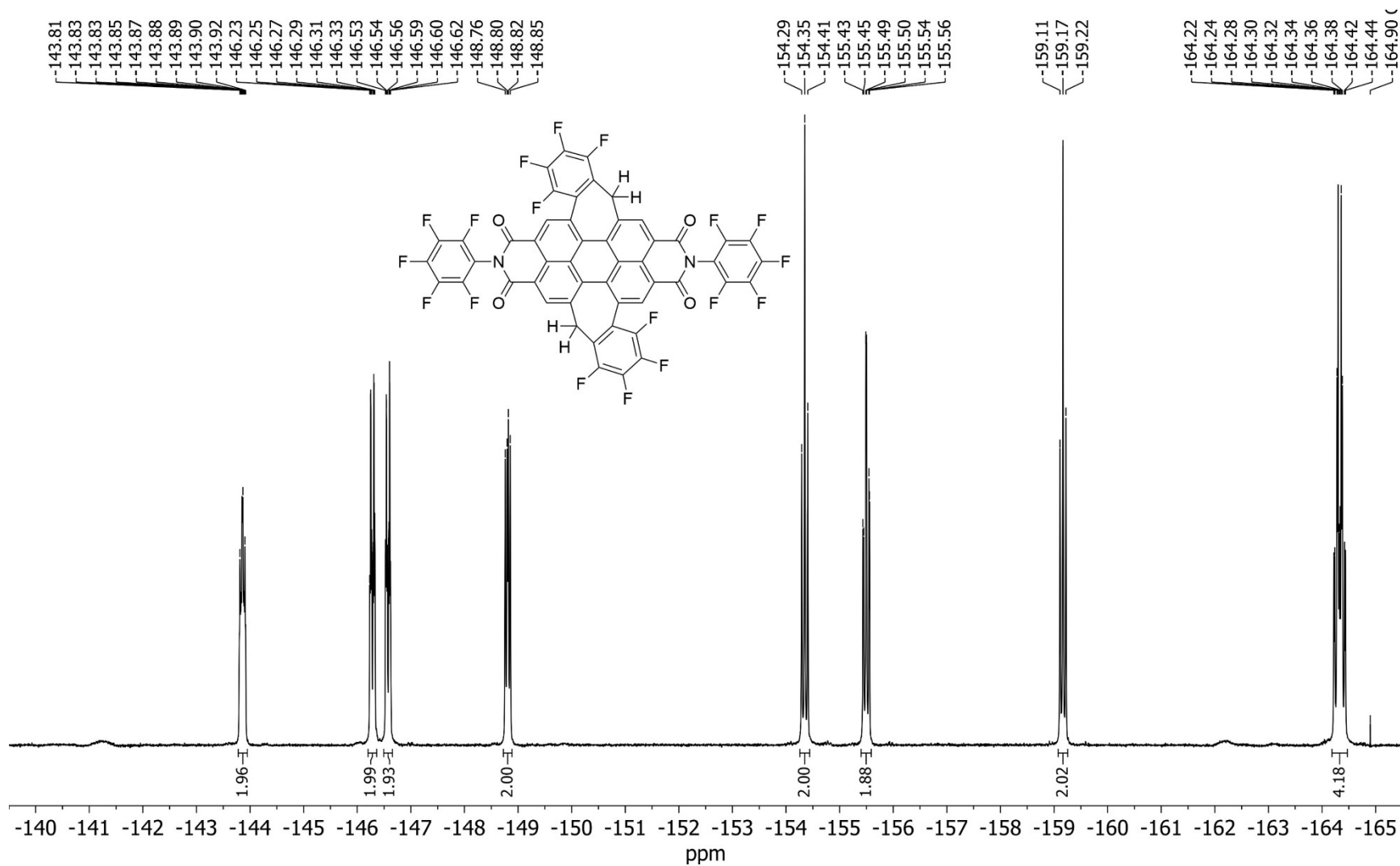


Figure 4.92. Expanded aromatic region of PDI-*trans*(C₇H₂)₂'s ¹⁹F-NMR spectrum—full spectrum shown in Figure 4.91.

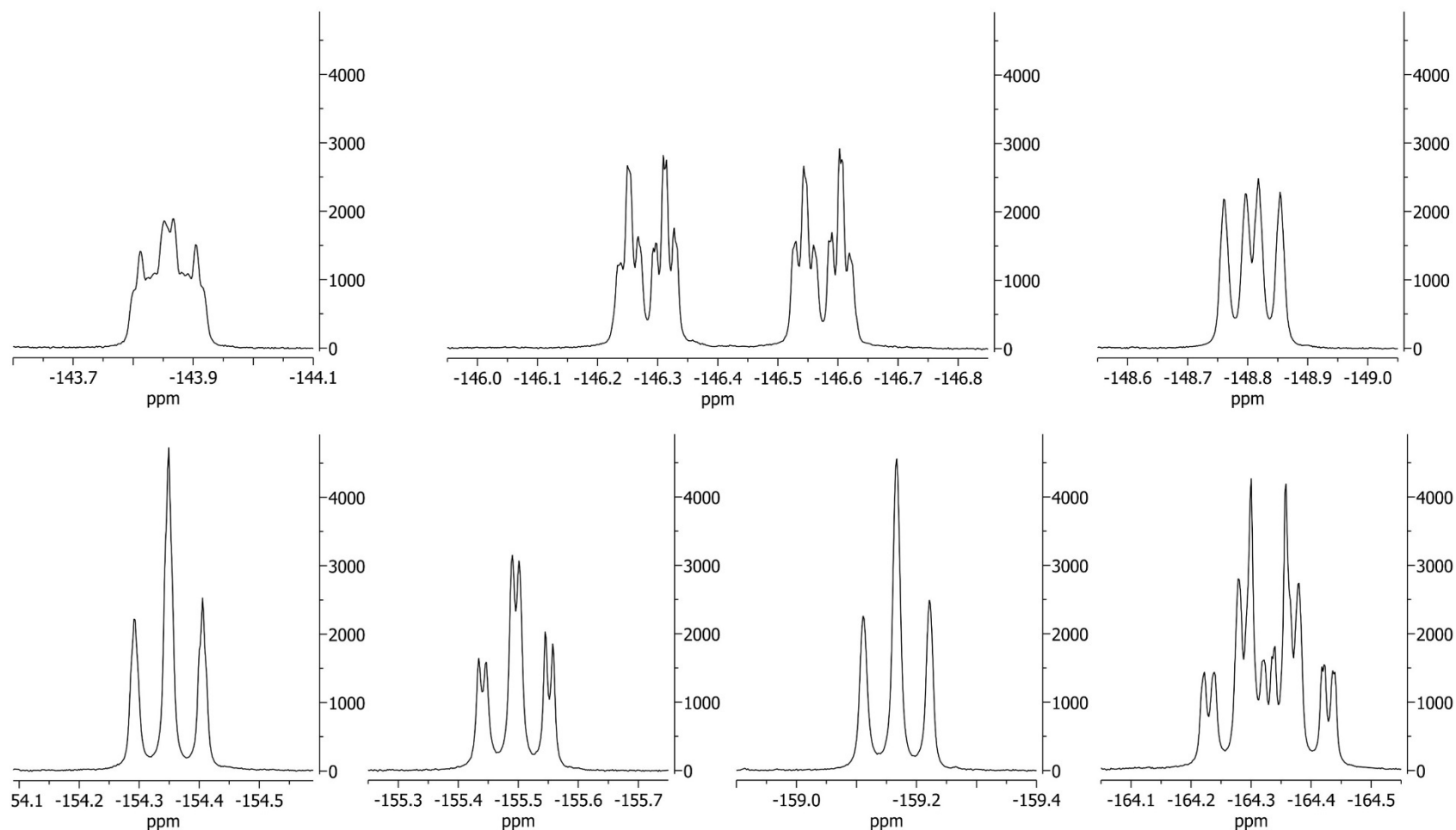


Figure 4.93. Closeup view of PDI-*trans*(C₇H₂)₂'s ¹⁹F-NMR signals shown in Figure 4.91. All signals are proportional in intensity (y-axis) to each other with respect to their original spectrum, while all x-axes are at the same scale (normalized such that each x-axis is both the same width and 0.5 ppm across).

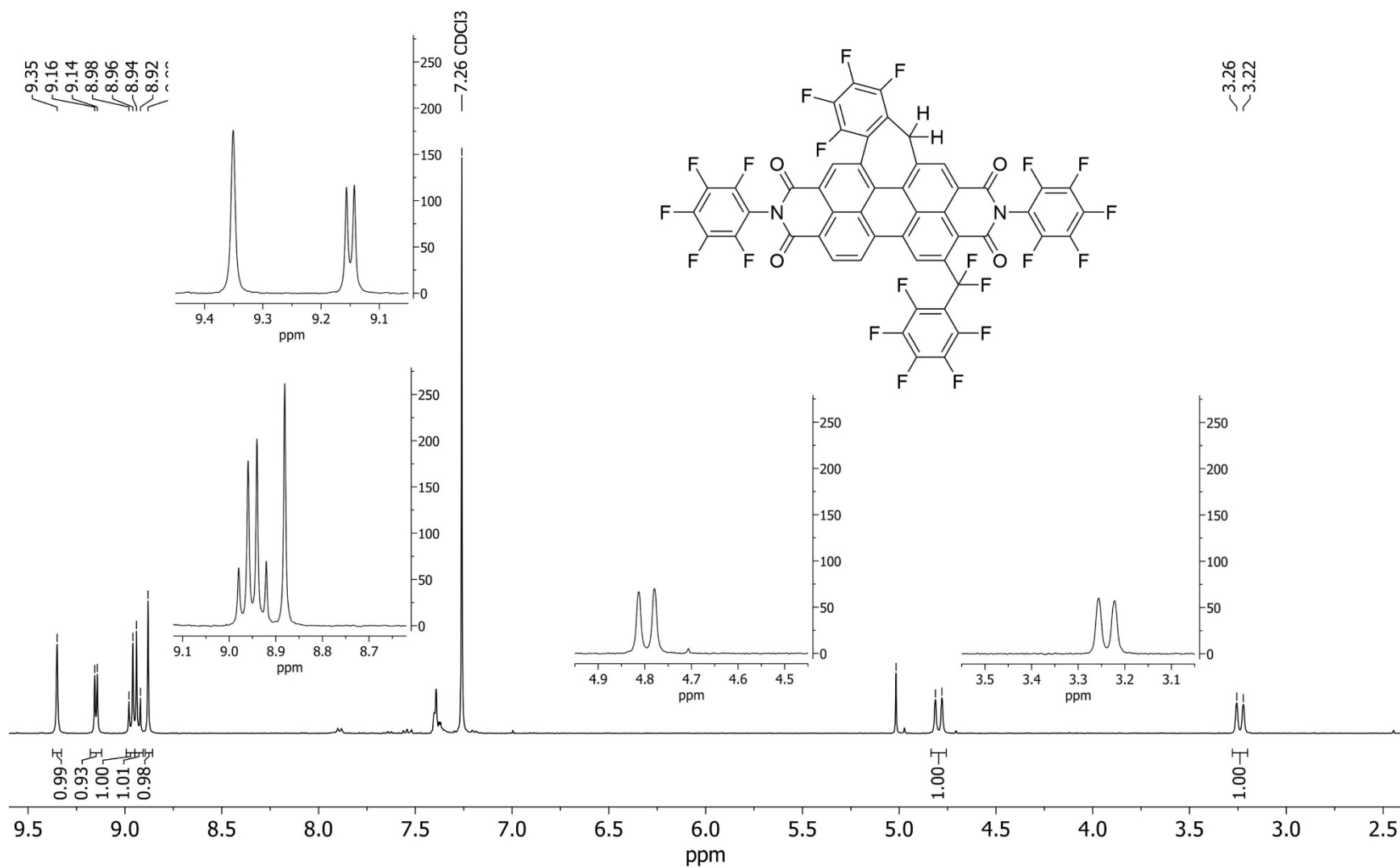


Figure 4.94. ¹H-NMR spectrum of PDI-C₇H₂-BnF in CDCl₃ from 2.4 to 9.6 ppm. Left two (stacked) inset shows expanded region for aromatic proton signals (9.05 to 9.45 ppm and 8.60 to 9.10 ppm); middle and right insets show expanded regions for the two signals from the two unique benzylic hydrogens.

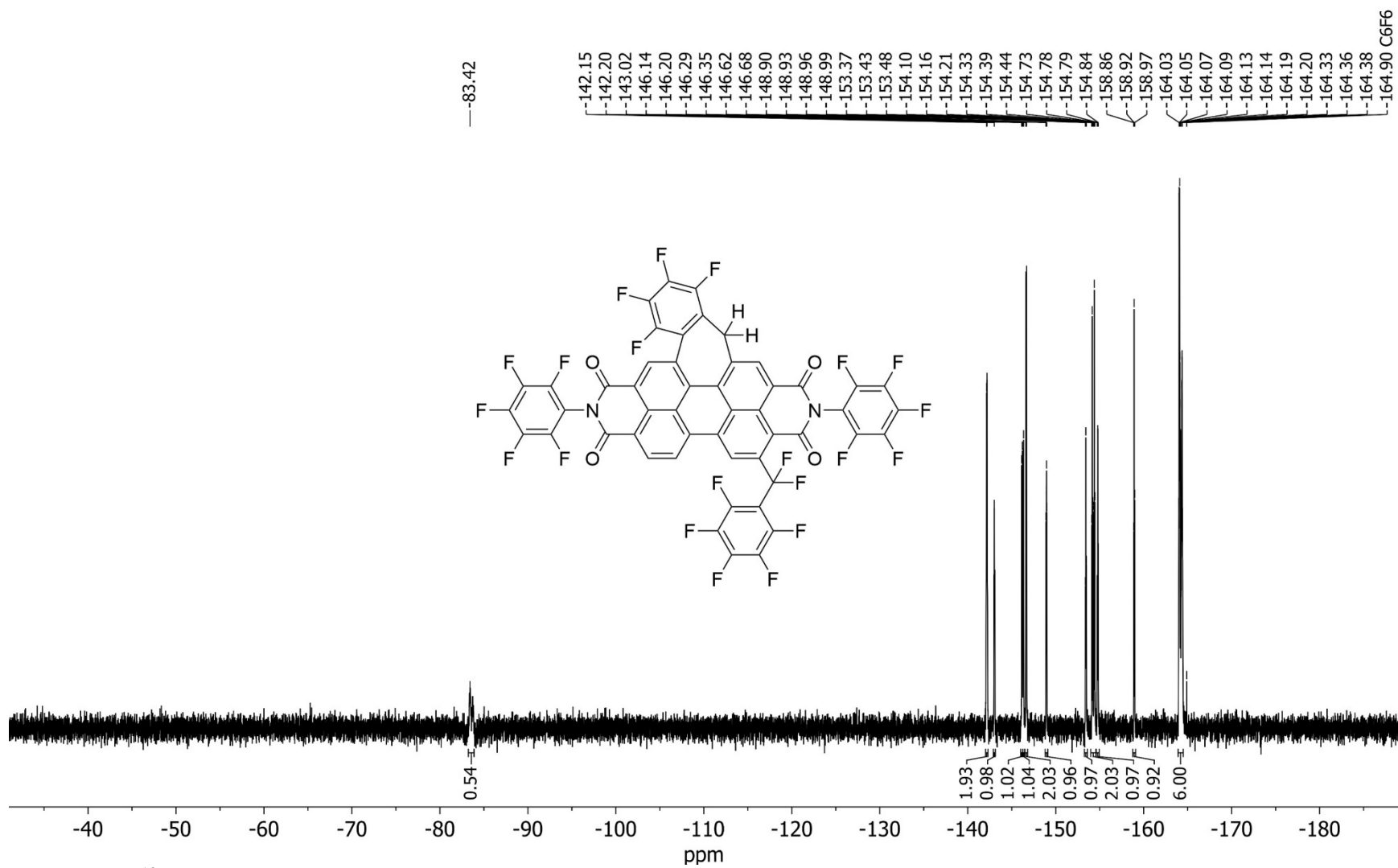


Figure 4.95. ^{19}F -NMR spectrum of PDI-C $_7$ H $_2$ -BnF in CDCl_3 .

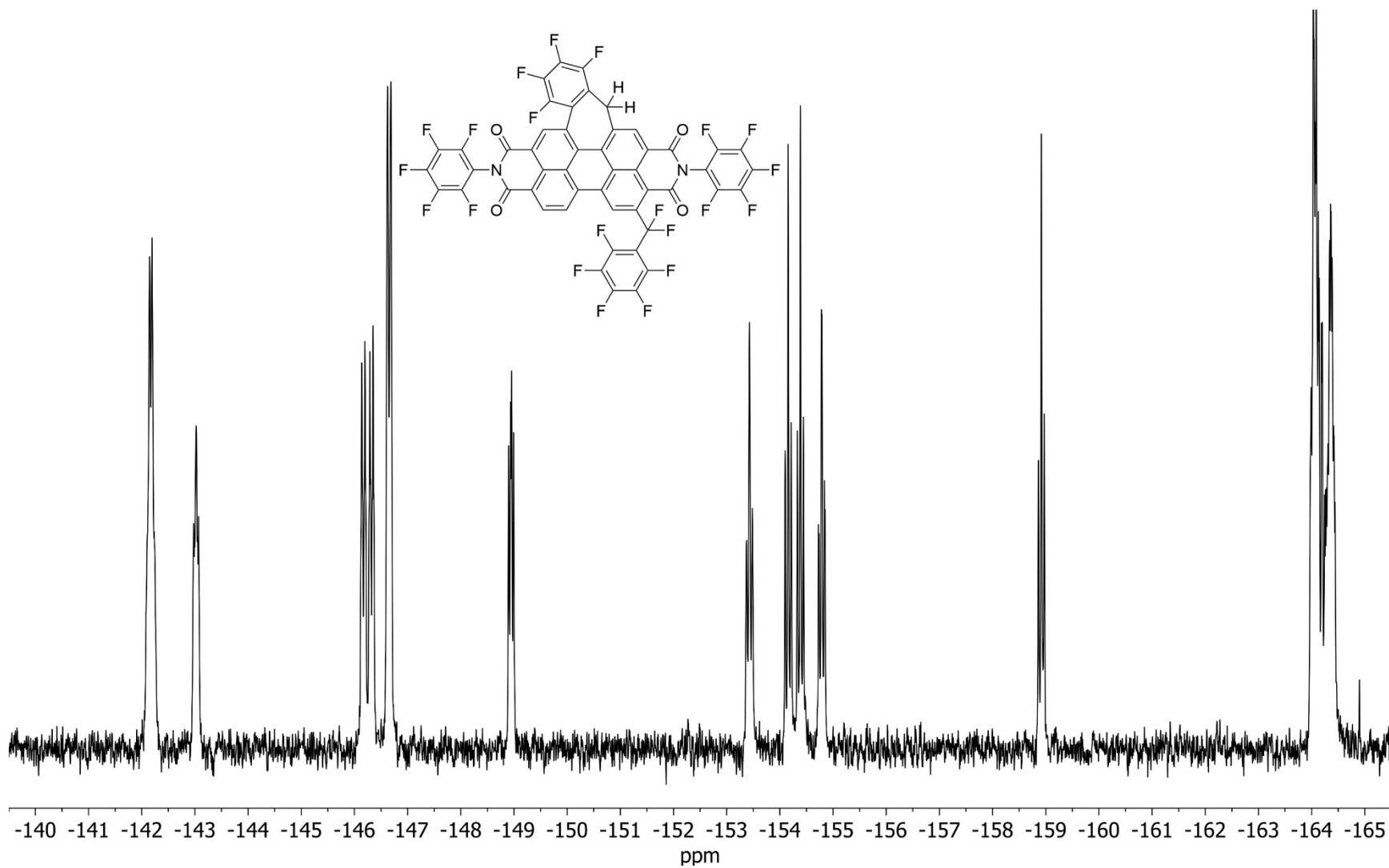


Figure 4.96. Expanded aromatic region of PDI-C7H2-BnF's ^{19}F -NMR spectrum—full spectrum shown in Figure 4.95.

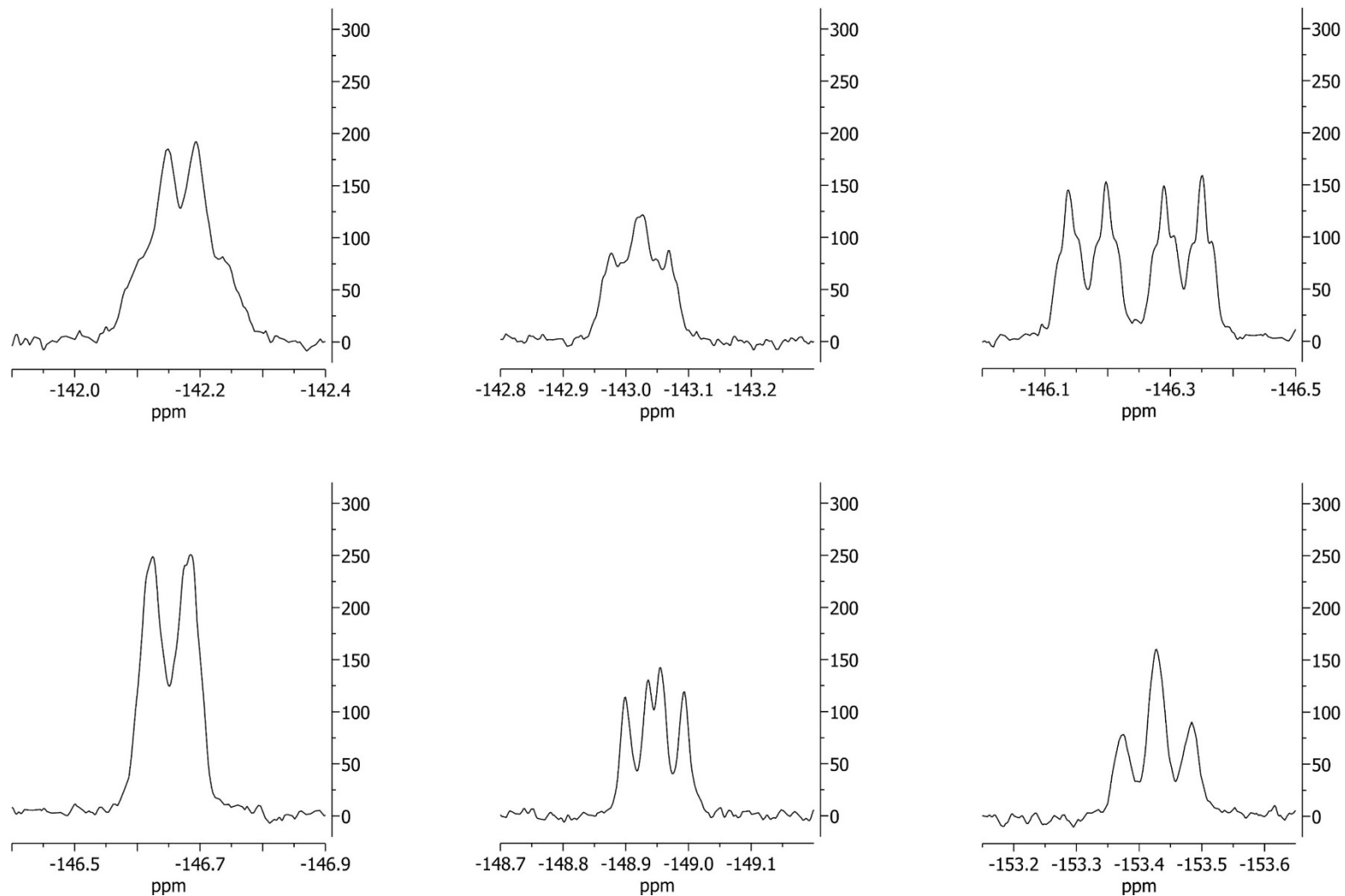


Figure 4.97. First of two closeup views of PDI-C7H₂-BnF's ¹⁹F-NMR signals shown in Figure 4.95. All signals are proportional in intensity (y-axis) to each other with respect to their original spectrum, while all x-axes are at the same scale (normalized such that each x-axis is both the same width and 0.5 ppm across).

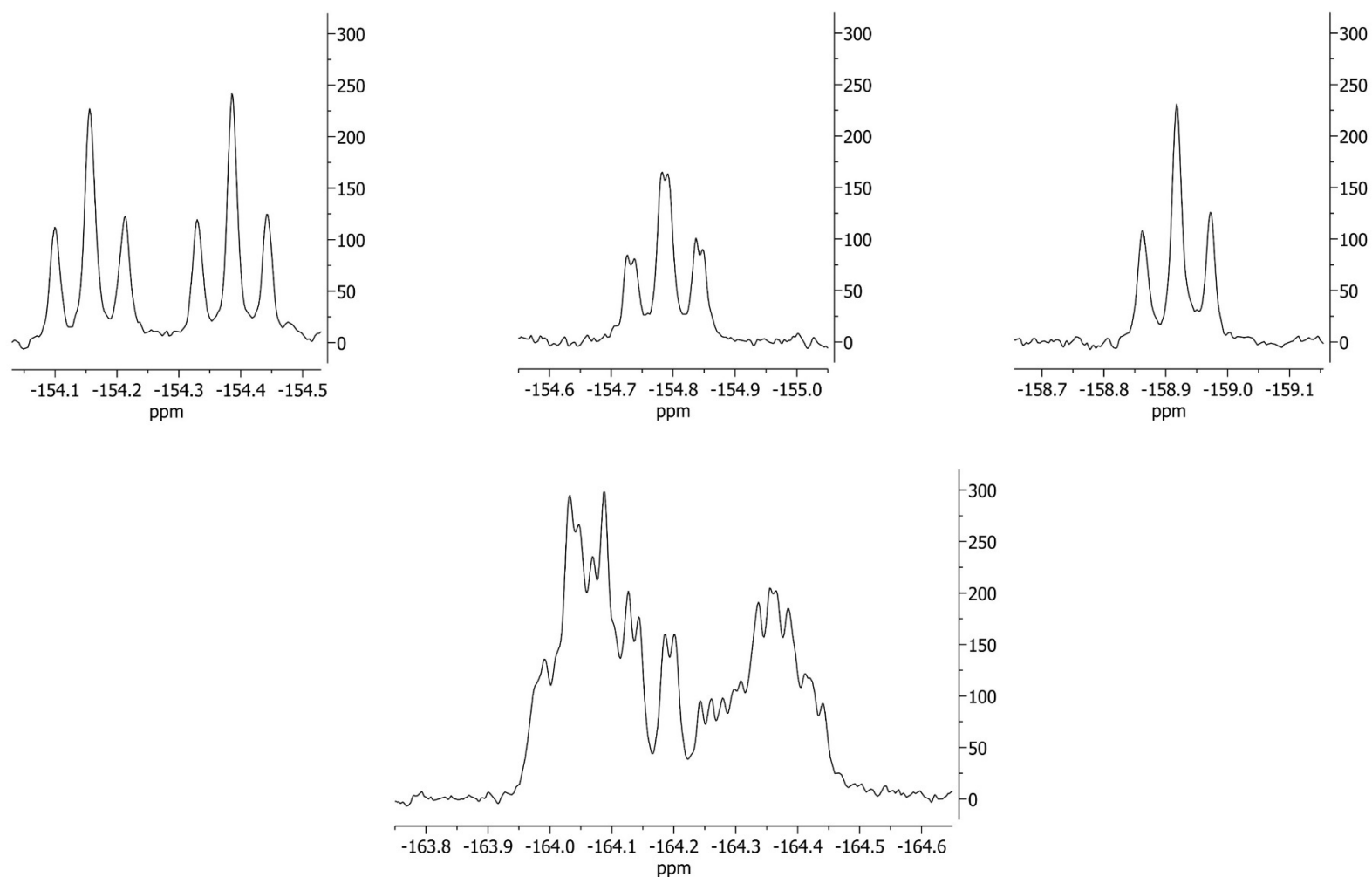


Figure 4.98. Second of two closeup views of PDI-C₇H₂-Bn_F's ^{19}F -NMR signals shown in Figure 4.95. All signals are proportional in intensity (y-axis) to each other with respect to their original spectrum, while all x-axes are at the same scale (normalized such that each x-axis is both the same width and 0.5 ppm across).

CHAPTER 4 REFERENCES

4. San, L. K.; Bukovsky, E. V.; Larson, B. W.; Whitaker, J. B.; Deng, S. H. M.; Kopidakis, N.; Rumbles, G.; Popov, A. A.; Chen, Y.-S.; Wang, X.-B.; Boltalina, O. V.; Strauss, S. H., A faux hawk fullerene with PCBM-like properties. *Chemical Science* **2015**, *6* (3), 1801-1815.
118. Kuvychko, I. V.; Castro, K. P.; Deng, S. H. M.; Wang, X.-B.; Strauss, S. H.; Boltalina, O. V., Taming Hot CF₃ Radicals: Incrementally Tuned Families of Polyarene Electron Acceptors for Air-Stable Molecular Optoelectronics. *Angew. Chem. Int. Ed.* **2013**, *52* (18), 4871-4874.
130. Postigo, A., Aromatic radical perfluoroalkylation reactions. *Can. J. Chem.* **2012**, *90* (6), 493-497.
131. Lantano, B.; Torviso, M. R.; Bonesi, S. M.; Barata-Vallejo, S.; Postigo, A., Advances in metal-assisted non-electrophilic fluoroalkylation reactions of organic compounds. *Coord. Chem. Rev.* **2015**, *285*, 76-108.
132. Burton, D. J.; Yang, Z.-Y.; Platonov, V., The preparation, stability and reactivity of perfluorobenzyl-cadmium and-copper reagents. *J. Fluorine Chem.* **1994**, *66* (1), 23-24.
133. Li, Y.; Li, C.; Yue, W.; Jiang, W.; Kopecek, R.; Qu, J.; Wang, Z., Direct functionalization of polycyclic aromatics via radical perfluoroalkylation. *Org. Lett.* **2010**, *12* (10), 2374-2377.
134. Ito, H.; Ozaki, K.; Itami, K., Annulative π -Extension (APEX): Rapid Access to Fused Arenes, Heteroarenes, and Nanographenes. *Angew. Chem. Int. Ed.* **2017**, *56* (37), 11144-11164.
135. Canfield, P. J.; Blake, I. M.; Cai, Z.-L.; Luck, I. J.; Krausz, E.; Kobayashi, R.; Reimers, J. R.; Crossley, M. J., A new fundamental type of conformational isomerism. *Nature Chem.* **2018**, *10* (6), 615-624.
135. Schmidt, R.; Oh, J. H.; Sun, Y.-S.; Deppisch, M.; Krause, A.-M.; Radacki, K.; Braunschweig, H.; Könemann, M.; Erk, P.; Bao, Z.; Würthner, F., High-Performance Air-Stable n-Channel Organic Thin Film Transistors Based on Halogenated Perylene Bisimide Semiconductors. *J. Am. Chem. Soc.* **2009**, *131* (17), 6215-6228.
136. Mallory, F. B.; Wood, C. S.; Gordon, J. T.; Lindquist, L. C.; Savitz, M. L., Photochemistry of Stilbenes. I. *J. Am. Chem. Soc.* **1962**, *84* (22), 4361-4362.
137. Mallory, F. B.; Mallory, C. W., Photocyclization of stilbenes and related molecules. *Org. React.* **2004**, *30*, 1-456.
138. Xiao, S.; Myers, M.; Miao, Q.; Sanaur, S.; Pang, K.; Steigerwald, M. L.; Nuckolls, C., Molecular wires from contorted aromatic compounds. *Angew. Chem. Int. Ed.* **2005**, *44* (45), 7390-7394.
139. Li, Z.; Twieg, R. J., Photocyclodehydrofluorination. *Chem. Eur. J.* **2015**, *21* (44), 15534-15539.
140. Gotsu, O.; Shiota, T.; Fukumoto, H.; Kawasaki-Takasuka, T.; Yamazaki, T.; Yajima, T.; Agou, T.; Kubota, T., Fluorine-Containing Dibenzoanthracene and Benzoperylene-Type Polycyclic Aromatic Hydrocarbons: Synthesis, Structure, and Basic Chemical Properties. *Molecules* **2018**, *23* (12), 3337.
141. Sharapa, D.; Steiner, A. K.; Amsharov, K., The Mechanism of Cyclodehydrofluorination on gamma-Alumina. *Phys. Status Solidi B* **2018**, *255* (12), article 1800189.
142. Suzuki, N.; Fujita, T.; Amsharov, K. Y.; Ichikawa, J., Aluminium-mediated aromatic C-F bond activation: regio-switchable construction of benzene-fused triphenylene frameworks. *Chem. Commun.* **2016**, *52* (88), 12948-12951.
143. Feofanov, M.; Akhmetov, V.; Sharapa, D. I.; Amsharov, K., Modular Approach to the Synthesis of Two-Dimensional Angular Fused Acenes. *Org. Lett.* **2020**, *22* (5), 1698-1702.
144. Akhmetov, V.; Fortsch, A.; Feofanov, M.; Troyanov, S.; Amsharov, K., Folding of fluorinated oligoarylenes into non-alternant PAHs with various topological shapes. *Org. Chem. Frontiers* **2020**, *7* (10), 1271-1275.
145. Steiner, A. K.; Amsharov, K. Y., The Rolling-Up of Oligophenylenes to Nanographenes by a HF-Zipping Approach. *Angew. Chem. Int. Ed.* **2017**, *56* (46), 14732-14736.

146. Zhao, B. L.; Feofanov, M.; Lungerich, D.; Park, H.; Rejek, T.; Wittmann, J.; Sarcletti, M.; Amsharov, K.; Halik, M., Non-substituted fused bis-tetracene based thin-film transistor with self-assembled monolayer hybrid dielectrics. *Front. Mater. Sci.* **2020**, 1-9.
147. Kabdulov, M.; Jansen, M.; Amsharov, K. Y., Bottom-Up C₆₀ Fullerene Construction from a Fluorinated C₆₀H₂₁F₉ Precursor by Laser-Induced Tandem Cyclization *Chem. Eur. J.* **2013**, *19*, 17262.
148. Dyan, O. T.; Borodkin, G. I.; Zaikin, P. A., The Diels–Alder Reaction for the Synthesis of Polycyclic Aromatic Compounds. *Eur. J. Org. Chem.* **2019**, *2019* (44), 7271-7306.
149. Dyan, O. T.; Zaikin, P. A.; Fadeev, D. S.; Gatilov, Y. V.; Borodkin, G. I., 1, 1-Difluoronaphthalen-2 (1H)-ones as building blocks for fluorinated tetraphenes. *J. Fluorine Chem.* **2018**, *210*, 88-93.
150. Fuchibe, K.; Shigeno, K.; Zhao, N.; Aihara, H.; Akisaka, R.; Morikawa, T.; Fujita, T.; Yamakawa, K.; Shimada, T.; Ichikawa, J., Pinpoint-fluorinated polycyclic aromatic hydrocarbons (F-PAHs): Syntheses of difluorinated subfamily and their properties. *J. Fluorine Chem.* **2017**, *203*, 173-184.
151. Postigo, A., Aromatic radical perfluoroalkylation reactions. *Can. J. Chem.* **2012**, *90* (6), 493-497.
152. Lantano, B.; Torviso, M. R.; Bonesi, S. M.; Barata-Vallejo, S.; Postigo, A., Advances in metal-assisted non-electrophilic fluoroalkylation reactions of organic compounds. *Coord. Chem. Rev.* **2015**, *285*, 76-108.
153. Burton, D. J.; Yang, Z.-Y.; Platonov, V., The preparation, stability and reactivity of perfluorobenzyl-cadmium and-copper reagents. *J. Fluorine Chem.* **1994**, *66* (1), 23-24.
154. Li, Y.; Li, C.; Yue, W.; Jiang, W.; Kopecek, R.; Qu, J.; Wang, Z., Direct functionalization of polycyclic aromatics via radical perfluoroalkylation. *Org. Lett.* **2010**, *12* (10), 2374-2377.
155. Ito, H.; Ozaki, K.; Itami, K., Annulative π -Extension (APEX): Rapid Access to Fused Arenes, Heteroarenes, and Nanographenes. *Angew. Chem. Int. Ed.* **2017**, *56* (37), 11144-11164.
156. Canfield, P. J.; Blake, I. M.; Cai, Z.-L.; Luck, I. J.; Krausz, E.; Kobayashi, R.; Reimers, J. R.; Crossley, M. J., A new fundamental type of conformational isomerism. *Nature Chem.* **2018**, *10* (6), 615-624.
157. Hu, Y.; Paternò, G. M.; Wang, X.-Y.; Wang, X.-C.; Guizzardi, M.; Chen, Q.; Schollmeyer, D.; Cao, X.-Y.; Cerullo, G.; Scotognella, F., π -extended pyrene-fused double [7] carbohelicene as a chiral polycyclic aromatic hydrocarbon. *J. Am. Chem. Soc.* **2019**, *141* (32), 12797-12803.
158. Medel, M. A.; Tapia, R.; Blanco, V.; Miguel, D.; Morcillo, S. P.; Campaña, A. G., Octagon-Embedded Carbohelicene as a Chiral Motif for Circularly Polarized Luminescence Emission of Saddle-Helix Nanographenes. *Angew. Chem. Int. Ed.* **2021**, *60* (11), 6094-6100.
159. Hughes, R. P.; Lindner, D. C.; Rheingold, A. L.; Yap, G. P. A., Perfluorobenzyl complexes of cobalt and rhodium. Unusual coupling between pentafluorophenyl and pentamethylcyclopentadienyl rings. *Organometallics* **1996**, *15*, 5678-5686.
160. Hughes, R. P.; Lindner, D. C.; Liable-Sands, L. M.; Rheingold, A. L., Conversion of Perfluorobenzyl Complexes of Rhodium to Fluorinated Oxarhodacycles. *Organometallics* **2001**, *20*, 363-366.
161. Castro, K. P.; Bukovsky, E. V.; Kuvychko, I. V.; DeWeerd, N. J.; Chen, Y.-S.; Deng, S. H. M.; Wang, X.-B.; Popov, A. A.; Strauss, S. H.; Boltalina, O. V., PAH/PAH(CF₃)_n Donor/Acceptor Charge-Transfer Complexes in Solution and in Solid-State Co-Crystals. *Chemistry – A European Journal* **2019**, *25* (59), 13547-13565.
162. Chung, D. D. L., Review Graphite. *JMatS* **2002**, *37* (8), 1475-1489.
163. Canfield, P. J.; Blake, I. M.; Cai, Z.-L.; Luck, I. J.; Krausz, E.; Kobayashi, R.; Reimers, J. R.; Crossley, M. J., A new fundamental type of conformational isomerism. *Nature Chemistry* **2018**, *10* (6), 615-624.
164. Iurre, J.; Marquillas, F.; Alvarez-Larena, A.; Piniella, J. F., Synthesis, conformational analysis, and molecular structure of 5-ethyl-5,6-dihydro-11H-dibenzo[b,e]azepine-6-thione. *Can. J. Chem.* **1994**, *72* (2), 334-338.

165. Altamura, M.; Dapporto, P.; Guidi, A.; Harmat, N. J. S.; Jierry, L.; Libralesso, E.; Paoli, P.; Rossi, P., Investigation on the flexibility of chiral tricyclic derivatives. *New J. Chem.* **2008**, *32* (9), 1617-1627.
166. Bui, C. V.; Rosenau, T.; Hettegger, H., Polysaccharide- and β -Cyclodextrin-Based Chiral Selectors for Enantiomer Resolution: Recent Developments and Applications. *Molecules* **2021**, *26* (14), 4322.
167. Medel, M. A.; Tapia, R.; Blanco, V.; Miguel, D.; Morcillo, S. P.; Campaña, A. G., Octagon-Embedded Carbohelicene as a Chiral Motif for Circularly Polarized Luminescence Emission of Saddle-Helix Nanographenes. *Angew. Chem. Int. Ed.* **2021**, *60* (11), 6094-6100.
168. Ryu, J. J., An Important Application of Pirkle Type π -Acidic Chiral Stationary Phases: Resolution of Polynuclear Aromatic Hydrocarbon Mixtures by Normal-Phase Conventional and Capillary HPLC. *Bull. Korean Chem. Soc.* **2009**, *30* (no. 4), 945-947.
169. Judson L. Haynes III; Isiah M. Warner, POLYMERIC SURFACTANTS AS PSEUDOSTATIONARY PHASES FOR SEPARATIONS IN ELECTROKINETIC CHROMATOGRAPHY (EKC): A REVIEW. *Rev. Anal. Chem* **1999**, *18* (6), 317-382.
170. Bondi, A., van der Waals Volumes and Radii. *The Journal of Physical Chemistry* **1964**, *68* (3), 441-451.
171. Kuvychko, I. V.; Spisak, S. N.; Chen, Y.-S.; Popov, A. A.; Petrukhina, M. A.; Strauss, S. H.; Boltalina, O. V., A Buckybowl with a Lot of Potential: C₅-C₂₀H₅(CF₃)₅. *Angew. Chem. Int. Ed.* **2012**, *51* (20), 4939-4942.

LIST OF ACRONYMS AND ABBREVIATIONS

Acronym/abbreviation	Full name
BDT	benzodithiophene
BHJ	bulk heterojunction
Bn _F	perfluorobenzyl
BT	benzothiadiazole
CF ₃ I	trifluoromethyl iodide
CO ₂ (s)	dry ice
CPDT	cyclopentadithiophene
CSU	Colorado state university
DFT	density functional theory
DMSO	dimethyl sulfoxide
DOS	density of states
EA	electron affinity
FBT	fluorinated benzothiadiazole
FF	fill factor
FHF	faux-hawk fullerene
GTGS	gradient-temperature gas–solid
GTGS-I (II–VI)	gradient-temperature gas–solid configuration I (II–VI)
HOMO	Highest occupied molecular orbital
HPLC	high performance liquid-chromatography
IPA	isopropyl alcohol
<i>J</i> _{sc}	short circuit current
LGR	liquid-gas reservoir
LUMO	lowest unoccupied molecular orbital
MeCN	acetonitrile
MS	mass spectroscopy
N _{2(l)}	liquid nitrogen
NMP	<i>n</i> -methyl-2-pyrrolidone
NMR	nuclear magnetic resonance
NREL	National Renewable Energy Lab
OFET	organic field effect transistor
<i>o</i> -DCB	<i>ortho</i> -dichlorobenzene
OPV	organic photovoltaics
<i>o</i> -DCB	<i>ortho</i> -dichlorobenzene
<i>P</i> (CF ₃ I)	CF ₃ I pressure
PAF	perfluoroalkyl fullerene
PAH	polycyclic aromatic hydrocarbon
PC ₆₀ BM	phenyl-C ₆₁ -butyric acid methyl ester
PCE	power conversion efficiency
PDI	perylene diimide
PERY	perylene

PhCl	chlorobenzene
PhCN	benzonitrile
Ph _F	perfluorophenyl
PHJ	planar heterojunction
PL	photoluminescence
PTCDA	perylene tetracarboxylic dianhydride
R _F	perfluoroalkyl
RT	room temperature
Rxn	reaction
STM	scanning tunneling microscopy
STS	Scanning tunneling spectroscopy
<i>T</i> ₆₀	time required to photobleach film to 60% of its initial absorbance
<i>T</i> ₈₀	time required to photobleach film to 80% % of its initial absorbance
<i>T</i> _{hp}	hot-plate temperature
TMC ₆₀ F	trifluoromethylated C ₆₀ -fullerenes
TMC ₇₀ F	trifluoromethylated C ₇₀ -fullerenes
TMF	trifluoromethylated fullerenes
TPD	thienopyrrolodione
TRMC	time-resolved microwave conductivity
TRPL	time-resolved photoluminescence
V _{oc}	open circuit voltage